

**EXPERIMENTAL INVESTIGATION AND MODELING OF KEY DESIGN  
PARAMETERS IN FLOW BOILING AND CONDENSATION**

by

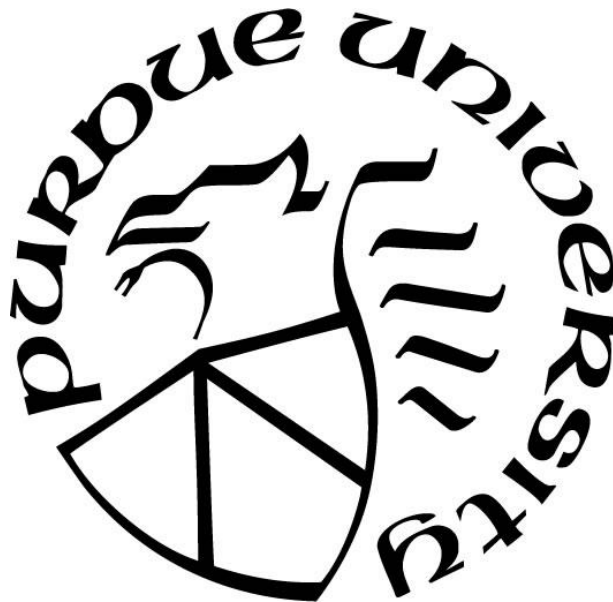
**Lucas E. O'Neill**

**A Dissertation**

*Submitted to the Faculty of Purdue University*

*In Partial Fulfillment of the Requirements for the degree of*

**Doctor of Philosophy**



School of Mechanical Engineering

West Lafayette, Indiana

August 2019

**THE PURDUE UNIVERSITY GRADUATE SCHOOL  
STATEMENT OF COMMITTEE APPROVAL**

Dr. Issam Mudawar, Chair

Department of Mechanical Engineering

Dr. Steven Collicott

Department of Aeronautics and Astronautics

Dr. Amy Marconnet

Department of Mechanical Engineering

Dr. Carlo Scalò

Department of Mechanical Engineering

**Approved by:**

Dr. Jay Gore

Head of the Graduate Program

## ACKNOWLEDGMENTS

I would like to start by thanking my advisor Dr. Issam Mudawar, whose tutelage, motivation, and support made this work possible. His expertise in the field of two-phase flow heat transfer is matched only by his skill at conveying it to his students. His role as a mentor for me, both professionally and personally, has set an amazing standard for the remainder of my career. I consider myself incredibly fortunate to have had the opportunity to work with him over the past five years.

Additionally, I would like to thank my frequent research collaborators Dr. Mohammad (Mojib) Hasan, Dr. R. (Bala) Balasubramaniam, and Dr. Henry Nahra, all of the Microgravity Sciences branch at NASA GRC. They were always available to answer questions, discuss results, and provide feedback on my work. They greatly assisted my development as a researcher over the course of my Ph.D. with their consistent feedback, direction, and encouragement.

I would also like to acknowledge my friends and colleagues in the Purdue Boiling and Two Phase Flow Laboratory who have been an enormous help both in my research and daily life. I want to thank Chirag, Devah, Vish, Jeongmin, Seung-Hyun, and Dr. Liang, without whom writing this thesis would have been very difficult.

I would also like to thank Dr. Steven Collicott, Dr. Amy Marconnet, and Dr. Carlo Scalo for serving on my advisory committee. At different points over the course of my degree each contributed to my technical and professional development, and I am fortunate to have had them as mentors.

I am grateful for financial support provided by NASA Space Technology Research Fellowship NNX15AP29H, as well as the technical support of countless people at NASA Glenn Research Center.

Finally, I want to thank my family and friends, whose support for me has been unwavering.

## TABLE OF CONTENTS

LIST OF TABLES .....	10
LIST OF FIGURES .....	11
NOMENCLATURE .....	20
ABSTRACT.....	25
1. INTRODUCTION .....	29
1.1 Flow Boiling Dynamic Behavior .....	29
1.1.1 <i>Importance of Flow Boiling Dynamic Behavior in Space-based Applications</i> .....	29
1.1.2 <i>Flow Boiling Instabilities and Transient Phenomena</i> .....	30
1.1.3 <i>Density Wave Oscillations</i> .....	31
1.2 Flow Condensation .....	34
1.2.1 <i>Flow Condensation as an Enabling Technology for Phase Change Thermal Management</i> .....	34
1.2.2 <i>Flow Condensation Dynamic Behavior</i> .....	35
1.2.3 <i>Predictive Tools for Condensation Flow Regime</i> .....	37
1.2.4 <i>Impact of Body Force Effects on Flow Condensation Heat Transfer</i> .....	39
1.3 Objectives of Study.....	41
1.3.1 <i>Flow Boiling</i> .....	41
1.3.2 <i>Flow Condensation</i> .....	42
2. EXPERIMENTAL METHODS .....	44
2.1 Flow Boiling .....	44
2.1.1 <i>Flow Boiling Module</i> .....	44
2.1.2 <i>Flow Boiling Test Loops</i> .....	48
2.1.3 <i>Operating Conditions and Measurement Uncertainty</i> .....	53
2.2 Flow Condensation .....	55
2.2.1 <i>Condensation Module for Heat Transfer Measurements</i> .....	55
2.2.2 <i>Condensation Module for Flow Visualization</i> .....	59
2.2.3 <i>Condensation Experimental Facility</i> .....	61
2.2.4 <i>Operating Conditions, Operating Procedure, and Measurement Uncertainty</i> .....	65
3. FLOW BOILING.....	67

3.1	Impact of Density Wave Oscillations on Flow Boiling System Dynamic Behavior and Stability .....	67
3.1.1	<i>Analysis of System Dynamics</i> .....	67
3.1.1.1	Approach for Determining Influence of Fluid Components .....	67
3.1.1.2	Region I: Filter between Pump and Pre-heater.....	75
3.1.1.3	Region II: Pre-heater Outlet and FBM Inlet.....	79
3.1.1.4	Region III: Flow Boiling Module (FBM).....	83
3.1.1.5	Region IV: Condenser .....	91
3.1.1.6	Region V: Accumulator.....	95
3.1.1.7	Overall Outcomes .....	98
3.1.2	<i>Analysis of Flow Boiling Transient Behavior</i> .....	98
3.1.2.1	Recap of Trends from Prior Investigation .....	98
3.1.2.2	Transient Evolution of Key Parameters with Increases in Heat Flux.....	101
3.1.3	<i>Stability Map Evaluation</i> .....	114
3.1.3.1	Utilization of Stability Maps in Two-phase Flow Analysis .....	114
3.1.3.2	New Qualitative Stability Maps for Density Wave Oscillations .....	122
3.2	Frequency and Amplitude of Density Wave Oscillations in Vertical Upflow Boiling ..	125
3.2.1	<i>Analysis of Density Wave Oscillation (DWO) Phenomenon</i> .....	125
3.2.1.1	Density Wave Oscillations (DWOs) in Micro-channels versus Mini/macro-channels	125
3.2.2	<i>Analysis of Transient Pressure Signals</i> .....	126
3.2.2.1	Flow Visualization Images .....	130
3.2.2.2	Explanation of Density Wave Oscillation Phenomenon .....	143
3.2.3	<i>Frequency and Amplitude of Density Wave Oscillations</i> .....	148
3.2.3.1	Detection Method for Frequency and Amplitude of Oscillation .....	148
3.2.3.2	Frequency and Amplitude of Oscillation in Response to Changes in Mass Velocity, Inlet Quality, and Heat Flux .....	152
3.2.3.3	<i>Frequency and Amplitude of Oscillation in Response to Changes in Relevant Dimensionless Groups</i> .....	159
3.2.3.4	Coupling of Frequency and Amplitude of Oscillation .....	167
3.2.4	<i>Utilizing Frequency and Amplitude Information</i> .....	169

3.2.4.1	Reconstruction of Experimental Pressure Fluctuations .....	169
3.2.4.2	Key Trends/Outcomes useful for Future Model Development .....	175
3.3	Mechanistic Model to Predict Frequency and Amplitude of Density Wave Oscillations in Vertical Upflow Boiling .....	177
3.3.1	<i>Density Wave Oscillation (DWO) Model Development</i> .....	177
3.3.1.1	Model Setup and Advancement.....	177
3.3.1.2	Full Solution Procedure .....	188
3.3.1.3	Investigation of Model Sub-component Trends .....	196
3.3.2	<i>DWO Model Evaluation</i> .....	209
3.3.2.1	Parametric Trends of Model Predictions .....	209
3.3.2.2	Model Evaluation using Experimental Database.....	214
3.3.2.3	Parametric Extensions using Model Predictions .....	224
3.3.2.4	Discussion of Model Limitations and Focus for Future Work.....	230
4.	FLOW CONDENSATION.....	232
4.1	Flow Condensation Pressure Oscillations at Different Orientations .....	232
4.1.1	<i>Transient Pressure Results and Existence of Key Oscillatory Modes</i> .....	232
4.1.1.1	Observation of Oscillatory Modes within CM-HT.....	232
4.1.1.2	Existence of Peak Oscillatory Mode within CM-HT .....	240
4.1.2	<i>Characterization of Dominant Oscillatory Mode</i> .....	251
4.1.2.1	Peak Frequency of Oscillation.....	254
4.1.2.2	Peak Amplitude of Oscillation .....	259
4.1.2.3	Impact of Oscillatory Modes .....	264
4.1.3	<i>Relationship to Observed Interfacial Behavior</i> .....	269
4.2	Identification of Condensation Flow Regime at Different Orientations using Temperature and Pressure Measurements.....	280
4.2.1	<i>Condensate Liquid Distribution</i> .....	280
4.2.1.1	Summary of Qualitative Trends for Condensate Liquid Behavior.....	280
4.2.1.2	Utility of a new Method for Flow Regime Identification.....	283
4.2.2	<i>Flow Regime Identification</i> .....	284
4.2.2.1	Co-current and Counter-current Flows.....	284
4.2.2.2	Stratified and Axisymmetric Horizontal Flows.....	292

4.2.2.3	Summary of New Method for Identifying Condensation Flow Regime .....	297
4.2.3	<i>Comparison of Results with Flow Regime Maps</i> .....	300
4.2.3.1	Vertical Upflow Condensation Regime Map .....	300
4.2.3.2	Horizontal Flow Condensation Regime Maps.....	305
4.3	Flow Condensation Heat Transfer in a Smooth Tube at Different Orientations: Experimental Results and Predictive Models .....	314
4.3.1	<i>Data Selection and Heat Transfer Reduction</i> .....	314
4.3.1.1	Condensation Heat Transfer Coefficient Calculation.....	314
4.3.1.2	Condensation Heat Transfer Coefficient Uncertainty Analysis .....	322
4.3.2	<i>Heat Transfer Results</i> .....	327
4.3.2.1	Local Results .....	327
4.3.2.2	Channel-average Results .....	335
4.3.2.3	Influence of Body Force .....	342
4.3.3	<i>Evaluation of Predictive Models</i> .....	348
4.3.3.1	Separated Flow Model (SFM) Predictions for Vertical Downflow .....	348
4.3.3.2	Common Correlations for Horizontal Flow.....	357
4.3.3.3	Challenges with Predicting Vertical Upflow .....	371
5.	CONCLUSIONS .....	373
5.1	Flow Boiling .....	373
5.1.1	<i>DWO Existence and Impact on System Stability</i> .....	373
5.1.2	<i>Frequency and Amplitude of DWOs in Vertical Upflow Boiling</i> .....	374
5.1.3	<i>Mechanistic Model to Predict Frequency and Amplitude of DWOs in Vertical Upflow Boiling</i> .....	375
5.2	Flow Condensation .....	376
5.2.1	<i>Condensation Pressure Oscillations at Different Orientations</i> .....	376
5.2.2	<i>Identification of Condensation Flow Regime Using Temperature and Pressure Measurements</i> .....	377
5.2.3	<i>Flow Condensation Heat Transfer</i> .....	379
	REFERENCES .....	381
	APPENDIX A: REVIEW OF TWO-PHASE FLOW INSTABILITIES IN MACRO- AND MICRO-CHANNEL SYSTEMS .....	419

A.1	Introduction.....	419
A.1.1	<i>Phase Change Heat Transfer and Multiphase Flow</i> .....	419
A.1.2	<i>Study of Two-Phase Flow Instabilities</i> .....	419
A.1.3	<i>Classification of Macro- and Micro-Scale Systems</i> .....	420
A.1.4	<i>Objectives of the Present Review</i> .....	426
A.2	Static Instabilities.....	430
A.2.1	<i>Critical Heat Flux (CHF)</i> .....	430
A.2.2	<i>Ledinegg (Excursive) Instability</i> .....	431
A.2.2.1	Characteristic Pressure Curves .....	431
A.2.2.2	Existence and Characteristics of Ledinegg Instability.....	435
A.2.2.3	Studies Investigating Ledinegg Instability .....	437
A.2.2.4	Differences in Micro-Channel Systems.....	450
A.2.2.5	Concluding Remarks on Ledinegg Instability .....	451
A.2.3	<i>Boiling Curve Hysteresis and Vapor Burst</i> .....	454
A.2.4	<i>Flow Regime Transition Instability</i> .....	457
A.3	Dynamic Instabilities .....	458
A.3.1	<i>Density Wave Oscillations</i> .....	458
A.3.1.1	Existence and Characteristics of Density Wave Oscillations in Macro-Channels.....	459
A.3.1.2	Existence and Characteristics of Density Wave Oscillations in Macro-Channels.....	464
A.3.1.3	Atypical Density Wave Oscillations in Macro-Channels.....	475
A.3.1.4	Existence and Characteristics of Density Wave Oscillations in Micro-Channels .....	479
A.3.1.5	Studies Investigating Density Wave Oscillations in Micro-Channels .....	483
A.3.1.6	Density Wave Oscillations in Flow Condensation.....	484
A.3.1.7	Summary of Findings Relating to Density Wave Oscillations.....	486
A.3.2	<i>Parallel Channel Instability</i> .....	486
A.3.2.1	Existence and Characteristics of Parallel Channel Instability .....	486
A.3.2.2	Studies on Parallel Channel Instability in Macro-Channel Systems .....	491
A.3.2.3	Studies on Parallel Channel Instability in Micro-Channel Systems.....	494
A.3.2.4	Geometry Modifications to Suppress/Eliminate PCI in Parallel Micro-Channel Heat Sinks .....	497
A.3.2.5	Summary of Key Information Related to Parallel Channel Instability .....	501

A.3.3	<i>Pressure Drop Oscillations</i> .....	501
A.3.3.1	Existence and Characteristics of Pressure Drop Oscillations .....	502
A.3.3.2	Comments on Ledinegg Instability versus Pressure Drop Oscillations .....	505
A.3.3.3	Studies Investigating Pressure Drop Oscillations .....	509
A.3.3.4	Atypical Interactions between Boiling Systems and Compressible Volume(s) ...	513
A.3.3.5	Summary of Important Findings Related to PDOs .....	513
A.3.4	<i>Acoustic Oscillations</i> .....	514
A.3.5	<i>Other Reported Two-Phase Dynamic Instabilities</i> .....	515
A.4	Current State of Instability Literature .....	517
A.5	Conclusions .....	522
VITA	.....	524
PUBLICATIONS	.....	528

## LIST OF TABLES

Table 2.1: Test Matrix for Year 1. ....	54
Table 2.2: Test Matrix for Year 2. ....	54
Table 2.3: Operating conditions used for DWO analysis. ....	54
Table 2.4: Target operating conditions for condensation portion of current study. ....	66
Table 3.1: Key operating conditions for system dynamic analysis cases. Indicated cases correspond to parts (b) – (e) in Figs. 3.1 – 3.7. ....	75
Table 3.2: Predicted and experimental frequencies for DWOs shown in Figs. 3.4(c) and 3.4(e). ....	90
Table 3.3: Description of works on which stability maps are based. ....	115
Table 3.4: Cross correlation coefficients for waveform pairs in Fig. 3.27. ....	172
Table 3.5: Cross correlation coefficients for inlet and outlet pressure fluctuations under various operating conditions. ....	173
Table 3.6: Key findings from the present section. ....	176
Table 3.7: Relevant assumptions, relations, and references for Region 2 control volume. ....	182
Table 3.8: Relevant assumptions, relations, and references for Region 3 control volumes. ....	183
Table 3.9: Model relationships associated with each respective step in the model solution procedure outlined in Fig. 3.29. ....	191
Table 4.1: Summary of trends governing oscillatory behavior in each orientation. ....	269
Table 4.2: Summary of flow regime identification approach in each orientation. ....	298
Table 4.3: Summary of flow regime identification approach in vertical upflow. ....	305
Table 4.4: Summary of flow regime identification approach in horizontal flow. ....	313
Table 4.5: Annular flow model relations [141]. ....	349
Table 4.6: Condensation heat transfer coefficient correlations evaluated. ....	358
Table A.1: Mini/macro- to micro-channel transition criteria. ....	422
Table A.2: Key topics in two-phase flow instabilities and dynamic behavior. ....	428
Table A.3: Works dealing with OFI correlations. ....	447
Table A.4: Uncommon findings related to Ledinegg Instability. ....	453
Table A.5: Parametric trends for traditional (macro-channel) Density Wave Oscillations. ....	473
Table A.6: Overview of strengths and weaknesses of current instability literature. ....	519

## LIST OF FIGURES

- Figure 2.1: (a) Exploded view of the flow boiling module (FBM). (b) Schematics of FBM fluid path and heated wall temperature measurement locations. (c) Photos of FBM with key components labeled. .... 45
- Figure 2.2: (a) Schematic and (b) photos of year 1 (2015) experimental flow boiling facility, and (c) schematic and (d) photo of year 2 (2016) experimental flow boiling facility. .... 49
- Figure 2.3: Condensation Module for Heat Transfer Measurements (CM-HT) (a) schematics and (b) 3-D drawing, and Condensation Module for Flow Visualization (CM-FV) (c) schematics and (d) 3-D drawing..... 57
- Figure 2.4: (a) Schematic of flow loop used in condensation portion of current study, and (b) photos of facility with key components identified. .... 63
- Figure 3.1: (a) Five regions for analysis of dynamic pressure behavior, along with transient records of operating conditions for vertical upflow with (b)  $G \sim 200 \text{ kg/m}^2\text{s}$  and subcooled inlet, (c)  $G \sim 200 \text{ kg/m}^2\text{s}$  and saturated inlet, (d)  $G \sim 800 \text{ kg/m}^2\text{s}$  and subcooled inlet, and (e)  $G \sim 800 \text{ kg/m}^2\text{s}$  and saturated inlet. .... 70
- Figure 3.2: (a) Sample plot of transient pressure drop across the filter (region I), along with amplitude versus frequency plots of the same for vertical upflow, vertical downflow, and horizontal flow with (b)  $G \sim 200 \text{ kg/m}^2\text{s}$  and subcooled inlet, (c)  $G \sim 200 \text{ kg/m}^2\text{s}$  and saturated inlet, (d)  $G \sim 800 \text{ kg/m}^2\text{s}$  and subcooled inlet, and (e)  $G \sim 800 \text{ kg/m}^2\text{s}$  and saturated inlet. .... 76
- Figure 3.3: (a) Sample plot of transient pre-heater outlet pressure (region II), along with amplitude versus frequency plots of the same for vertical upflow, vertical downflow, and horizontal flow with (b)  $G \sim 200 \text{ kg/m}^2\text{s}$  and subcooled inlet, (c)  $G \sim 200 \text{ kg/m}^2\text{s}$  and  $x_{e,in} \sim 0.10$ , , (d)  $G \sim 800 \text{ kg/m}^2\text{s}$  and subcooled inlet, and (e)  $G \sim 800 \text{ kg/m}^2\text{s}$  and  $x_{e,in} \sim 0.05$ . .... 80
- Figure 3.4: (a) Sample plots of transient pressure drop across heated length of FBM (region III), along with amplitude versus frequency plots of the same for vertical upflow, vertical downflow, and horizontal flow with (b)  $G \sim 200 \text{ kg/m}^2\text{s}$  and subcooled inlet, (c)  $G \sim 200 \text{ kg/m}^2\text{s}$  and saturated inlet, (d)  $G \sim 800 \text{ kg/m}^2\text{s}$  and subcooled inlet, and (e)  $G \sim 800 \text{ kg/m}^2\text{s}$  and saturated inlet. Negative values of average pressure drop reported for highly subcooled inlet conditions in vertical downflow and horizontal flow orientations are attributed to difficulties in measuring small pressure drops coupled with limitations in measurement accuracy. .... 84
- Figure 3.5: (a) Flow visualization images depicting the cycle of low density (bright) and high density (dark) fronts passing through the heated length of FBM in vertical upflow with finite inlet quality, with (b) six consecutive High Density Fronts (HDFs) identified from images and the time between them used to calculate single-event frequencies, which are shown to fall within the range of peak oscillatory behavior in (c). .... 88
- Figure 3.6: (a) Sample plot of transient pressure drop through the condenser (region IV), along with amplitude versus frequency plots of the same for vertical upflow, vertical downflow, and horizontal flow with (b)  $G \sim 200 \text{ kg/m}^2\text{s}$  and subcooled inlet, (c)  $G \sim 200 \text{ kg/m}^2\text{s}$  and saturated inlet, (d)  $G \sim 800 \text{ kg/m}^2\text{s}$  and subcooled inlet, and (e)  $G \sim 800 \text{ kg/m}^2\text{s}$  and saturated inlet. .... 92

Figure 3.7: Sample plot of accumulator transient pressure (region V), along with amplitude versus frequency plots of the same for vertical upflow, vertical downflow, and horizontal flow with (b)  $G \sim 200 \text{ kg/m}^2\text{s}$  and subcooled inlet, (c)  $G \sim 200 \text{ kg/m}^2\text{s}$  and saturated inlet, (d)  $G \sim 800 \text{ kg/m}^2\text{s}$  and subcooled inlet, and (e)  $G \sim 800 \text{ kg/m}^2\text{s}$  and saturated inlet. .... 95

Figure 3.8: Qualitative trends for magnitude of flow boiling dynamic behavior in FBM versus (a) mass velocity, (b) heat flux, and (c) inlet quality. .... 100

Figure 3.9: Transient results for vertical upflow with (a) highly subcooled and (b) saturated inlet conditions. Fast Fourier transforms of key steady-state parameters corresponding to heat flux levels ‘C’ and ‘D’ for each are compared in (c) and (d). .... 103

Figure 3.10: Transient results for vertical downflow with (a) highly subcooled and (b) saturated inlet conditions. Fast Fourier transforms of key steady-state parameters corresponding to heat flux levels ‘C’ and ‘D’ for each are compared in (c) and (d). .... 107

Figure 3.11: Transient results for horizontal flow with (a) highly subcooled and (b) saturated inlet conditions. Fast Fourier transforms of key steady-state parameters corresponding to heat flux levels ‘C’ and ‘D’ for each are compared in (c) and (d). .... 111

Figure 3.12: Data from the present experiments superimposed on stability maps of (a) Bogojevic *et al.* [158] and (b) Brutin and Tadrist [38]. .... 118

Figure 3.13: Flow boiling stability maps adapted from (a) Ishii and Zuber [37], (b) Lee and Pan [157], and (c) Chang and Pan [58]. .... 120

Figure 3.14: Stability maps indicating conditions under which Density Wave Oscillations are present for (a) vertical upflow, (b) vertical downflow, and (c) horizontal flow orientations. .... 123

Figure 3.15: Plots of FBM heated length inlet and outlet pressures versus time over 20 s, zoomed in on the first 3 s, and associated fast Fourier transforms over the 20-s period for (a)  $G = 234.2 \text{ kg/m}^2\text{s}$ , (b)  $G = 834.1 \text{ kg/m}^2\text{s}$ , and (c)  $G = 1978.9 \text{ kg/m}^2\text{s}$ , .... 128

Figure 3.16: Consecutive flow visualization image sequences for vertical upflow boiling with  $G = 407.8 \text{ kg/m}^2\text{s}$ ,  $x_{e,in} = 0.03$ ,  $P_{in} = 116.0 \text{ kPa}$ , and  $q'' = 7.2 \text{ W/cm}^2$ , spanning (a) 0.005 – 0.100s, (b) 0.105-0.200 s, (c) 0.205-0.300 s, (d) 0.30-0.400 s, and (e) 0.405-0.500 s. Time difference between consecutive images is  $\Delta t = 0.005 \text{ s}$ . .... 131

Figure 3.17: Consecutive flow visualization image sequences for vertical upflow boiling with  $G = 821.6 \text{ kg/m}^2\text{s}$ ,  $x_{e,in} = 0.06$ ,  $P_{in} = 123.8 \text{ kPa}$ , and  $q'' = 7.2 \text{ W/cm}^2$ , spanning (a) 0.005 – 0.100s, (b) 0.105-0.200 s, (c) 0.205-0.300 s, (d) 0.30-0.400 s, and (e) 0.405-0.500 s. Time difference between consecutive images is  $\Delta t = 0.005 \text{ s}$ . .... 134

Figure 3.18: Consecutive flow visualization image sequences for vertical upflow boiling with  $G = 1636.5 \text{ kg/m}^2\text{s}$ ,  $x_{e,in} = 0.01$ ,  $P_{in} = 154.6 \text{ kPa}$ , and  $q'' = 7.2 \text{ W/cm}^2$ , spanning (a) 0.005 – 0.100s, (b) 0.105-0.200 s, (c) 0.205-0.300 s, (d) 0.30-0.400 s, and (e) 0.405-0.500 s. Time difference between consecutive images is  $\Delta t = 0.005 \text{ s}$ . .... 137

Figure 3.19: (a) Select flow visualization image sequences for  $G = 1221.9 \text{ kg/m}^2\text{s}$ ,  $x_{e,in} = 0.02$ ,  $P_{in} = 129.1 \text{ kPa}$ , and  $q'' = 7.3 \text{ W/cm}^2$  depicting the cycle of low density (bright) fronts and high density (dark) fronts passing through the heated length of the FBM. (b) Tabulated values of single-event frequencies of high density fronts (HDFs) identified from the images and time between HDFs. (c)

Transient pressure signals and corresponding fast Fourier transforms confirming the frequencies in (b).....	141
Figure 3.20: Schematics outlining cyclical process behind DWOs, with (a) nominal conditions, (b) liquid accumulation in inlet region, (c) liquid slug/HDF advance, (d) HDF passage through heated lengths, and (e) return to nominal conditions. ....	145
Figure 3.21: Plots showing detection methodology for DWO frequency and amplitude: (a) transient inlet and outlet pressure signals for entire fast Fourier transform (FFT) window, (b) associated FFTs with peak frequencies identified, (c) low-pass filtered pressure signals to isolate DWO behavior, and (d) DWO amplitude detection using filtered signals. ....	150
Figure 3.22: Plots of DWO frequency versus mass velocity for three heat flux levels and (a) $x_{e,in} = 0.00 - 0.04$ , (b) $x_{e,in} = 0.07 - 0.13$ , (c) $x_{e,in} = 0.19 - 0.25$ , and (d) $x_{e,in} = 0.30 - 0.40$ . ....	154
Figure 3.23: Plots of DWO amplitude versus mass velocity for three heat flux levels and (a) $x_{e,in} = 0.00 - 0.04$ , (b) $x_{e,in} = 0.07 - 0.13$ , (c) $x_{e,in} = 0.19 - 0.25$ , and (d) $x_{e,in} = 0.30 - 0.40$ . ....	157
Figure 3.24: Plots of DWO frequency versus (a) liquid Reynolds number, $Re_f$ , (b) liquid Weber number, $We_f$ , (c) liquid Froude number, $Fr_f$ , (d) boiling number, $Bo$ , and (e) phase change number, $N_{pch}$ . ....	161
Figure 3.25: Plots of DWO amplitude versus (a) liquid Reynolds number, $Re_f$ , (b) liquid Weber number, $We_f$ , (c) liquid Froude number, $Fr_f$ , (d) boiling number, $Bo$ , and (e) phase change number, $N_{pch}$ . ....	164
Figure 3.26: Plot of DWO amplitude versus frequency for all data from years 1 and 2 of the study. ....	168
Figure 3.27: Plot of FBM heated length inlet pressure fluctuations along with (a) curve reconstructed from DWO amplitude and frequency, (b) 2 <sup>nd</sup> order Fourier series expansion, (c) 3 <sup>rd</sup> order Fourier series expansion, (d) 4 <sup>th</sup> order Fourier series expansion, and (e) 8 <sup>th</sup> order Fourier series expansion. ....	170
Figure 3.28: (a) General model setup, key characteristics of which are presence of annular flow throughout, segmentation into Upstream Region 1, High Density Front Region 2, and Downstream Region 3, and separate adiabatic and diabatic lengths. (b) Control-volume encompassing HDF Region. (c) Description of force terms in separated flow model used in Downstream Region 3. ....	180
Figure 3.29: (a) Depiction of primary solution equations for each region of the DWO model, and (b) evolution of model control volumes with time. ....	186
Figure 3.30: Flow chart for model solution. ....	190
Figure 3.31: Plots of Region 3 model subcomponent predictions versus time: (a) SFM force terms for liquid phase and (b) vapor phase, (c) phase momentum terms, (d) phase velocities, (e) mass velocities, (f) average quality, (g), phase cross-sectional areas, and (h) flow lengths, all for the case with mass velocity $G = 835.9 \text{ kg/m}^2 \text{ s}$ , inlet pressure $P_{in} = 122 \text{ kPa}$ , inlet quality $x_{e,in} = 0.04$ , and FBM heat flux $q'' = 2.5 \text{ W/cm}^2$ . ....	198

- Figure 3.32: Plots of Region 2 (HDF) model subcomponents predictions versus time: (a) relative velocities entering and exiting HDF, (b) mass accumulation within HDF, (c) HDF momentum balance components, (d) HDF momentum, (e) HDF velocity, and (f) HDF length and position, all for the case of mass velocity  $G = 835.9 \text{ kg/m}^2\text{s}$ , inlet pressure  $P_{in} = 122 \text{ kPa}$ , inlet quality  $x_{e,in} = 0.04$ , and FBM heat flux  $q'' = 2.5 \text{ W/cm}^2$ : ..... 203
- Figure 3.33: Measurements of HDF length for three different sets of operating conditions..... 208
- Figure 3.34: Comparison of parametric trends for model predictions and experimental results: (a) DWO frequency versus mass velocity, (b) DWO amplitude versus mass velocity, (c) frequency versus inlet quality, (d) amplitude versus inlet quality, (e) frequency versus heat flux, and (f) amplitude versus heat flux. .... 211
- Figure 3.35: Plots of DWO frequency predicted by the model versus experimentally determined values for (a) low mass flux, (b) high mass flux, (c) low inlet quality, (d) high inlet quality, (e) low heat flux, (f) high heat flux, and (g) overall range of parameters. .... 215
- Figure 3.36: Plots of DWO amplitude predicted by the model versus experimentally determined values for (a) low mass flux, (b) high mass flux, (c) low inlet quality, (d) high inlet quality, (e) low heat flux, (f) high heat flux, and (g) overall range of parameters. .... 220
- Figure 3.37: Plot presenting model predictions for parametric changes to operating environment and test section geometry: (a) DWO frequency versus local acceleration (gravity), (b) DWO amplitude versus local acceleration, (c) frequency versus heated length, (d) amplitude versus heated length, (e) frequency versus adiabatic length, (f) amplitude versus adiabatic length, (g) frequency versus mass velocity for different working fluids, and (h) amplitude versus mass velocity for different working fluids. .... 226
- Figure 4.1: Transient CM-HT inlet and outlet pressure curves over 20-s and 3-s periods, along with associated fast Fourier transforms taken over the 20-s period for (a) vertical upflow, (b) vertical downflow, and (c) horizontal flow orientations with superheated vapor inlet. .... 233
- Figure 4.2: Transient CM-HT inlet and outlet pressure curves over 20-s and 3-s periods along with associated fast Fourier transforms taken over the 20-s period for (a) vertical upflow, (b) vertical downflow, and (c) horizontal flow orientations with saturated mixture inlet..... 235
- Figure 4.3: Sample transient plots and associated fast Fourier transforms for (a) FC-72 pump inlet and outlet pressures, (b) bulk heater power input, (c) CM-HT water inlet and outlet pressures, and (d) CM-HT FC-72 inlet and outlet pressures. .... 238
- Figure 4.4: Process of determining  $Q$  Factor for peak frequency of oscillation by taking fast Fourier transform of 20-s duration inlet pressure signal, applying 10-Hz low pass filter to FFT curve, determining if a true peak exists, identifying the frequency associated with the peak, and determining the associated  $Q$  Factor for cases with (a) high  $Q$ , (b) moderate  $Q$ , and (c) no peak. .... 242
- Figure 4.5: Plots of  $Q$  Factor versus FC-72 mass velocity, inlet quality, exit quality, and inlet pressure, for all cases in (a) vertical upflow, (b) vertical downflow, and (c) horizontal flow orientations..... 246

- Figure 4.6: Plots of  $Q$  Factor versus FC-72 inlet vapor Reynolds, Weber, and Froude numbers, and exit liquid Reynolds, Weber, and Froude numbers, for all cases in (a) vertical upflow, (b) vertical downflow, and (c) horizontal flow orientations..... 249
- Figure 4.7: Plots showing detection methodology for peak frequency and amplitude of oscillation: (a) transient FC-72 inlet and outlet pressure signals for entire fast Fourier transform window, (b) associated FFTs with peak frequencies identified, as well as filter frequency (used in later steps) identified, (c) low-pass filtered pressure signals, and (d) amplitude detection using filtered signals..... 252
- Figure 4.8: Plots of peak frequency of oscillation versus FC-72 mass velocity, inlet quality, exit quality, and inlet pressure, for all cases in (a) vertical upflow, (b) vertical downflow, and (c) horizontal flow orientations..... 255
- Figure 4.9: Plots of peak frequency of oscillation versus FC-72 inlet vapor Reynolds, Weber, and Froude numbers, and exit liquid Reynolds, Weber, and Froude numbers, for all cases in (a) vertical upflow, (b) vertical downflow, and (c) horizontal flow orientations..... 257
- Figure 4.10: Plots of peak amplitude of oscillation versus FC-72 mass velocity, inlet quality, exit quality, and inlet pressure, for all cases in (a) vertical upflow, (b) vertical downflow, and (c) horizontal flow orientations..... 260
- Figure 4.11: Plots of peak amplitude of oscillation versus FC-72 inlet vapor Reynolds, Weber, and Froude numbers, and exit liquid Reynolds, Weber, and Froude numbers, for all cases in (a) vertical upflow, (b) vertical downflow, and (c) horizontal flow orientations..... 262
- Figure 4.12: Plots of (a) peak frequency of oscillation versus  $Q$  factor, (b) amplitude of peak oscillation versus  $Q$  factor, and (c) peak frequency versus peak amplitude for vertical upflow, vertical downflow, and horizontal flow orientations..... 266
- Figure 4.13: Sequential images of horizontal flow with  $G_{FC} = 82.9 \text{ kg/m}^2\text{s}$ ,  $G_{H_2O} = 696.8 \text{ kg/m}^2\text{s}$ ,  $P_{FC,in} = 123.1 \text{ kPa}$ ,  $P_{WRBH} = 1361.9$ , and  $x_{e,in} = 1.15$ , centered (a) near the inlet ( $z = 28 \text{ mm}$ ), (b) at the middle of the channel ( $z = 294 \text{ mm}$ ), and (c) near the exit ( $z = 560 \text{ mm}$ ), with individual images in each sequence separated by  $0.0075 \text{ s}$ ..... 272
- Figure 4.14: Sequential images of vertical downflow at the middle region (centered at  $z = 294 \text{ mm}$ ) with (a)  $G_{FC} = 34.6 \text{ kg/m}^2\text{s}$ ,  $G_{H_2O} = 926.1 \text{ kg/m}^2\text{s}$ ,  $P_{FC,in} = 130.1 \text{ kPa}$ ,  $P_{WRBH} = 570.3 \text{ W}$ , and  $x_{e,in} = 1.10$ , (b)  $G_{FC} = 33.5 \text{ kg/m}^2\text{s}$ ,  $G_{H_2O} = 931.8 \text{ kg/m}^2\text{s}$ ,  $P_{FC,in} = 130.5 \text{ kPa}$ ,  $P_{WRBH} = 416.7 \text{ W}$ , and  $x_{e,in} = 0.68$ , and (c)  $G_{FC} = 34.2 \text{ kg/m}^2\text{s}$ ,  $G_{H_2O} = 934.7 \text{ kg/m}^2\text{s}$ ,  $P_{FC,in} = 130.0 \text{ kPa}$ ,  $P_{WRBH} = 323.4 \text{ W}$ , and  $x_{e,in} = 0.38$ , with individual images in each sequence separated by  $0.0075 \text{ s}$ ..... 276
- Figure 4.15: Sequential images of (a) falling film in inlet region (centered at  $z = 190 \text{ mm}$ ) with  $G_{FC} = 13.32 \text{ kg/m}^2\text{s}$  and  $G_{H_2O} = 6.09 \text{ kg/m}^2\text{s}$ , (b) flooding in inlet region with  $G_{FC} = 53.29 \text{ kg/m}^2\text{s}$  and  $G_{H_2O} = 73.36 \text{ kg/m}^2\text{s}$ , and (c) climbing film in outer region (centered at  $z = 952 \text{ mm}$ ) with  $G_{FC} = 106.45 \text{ kg/m}^2\text{s}$  and  $G_{H_2O} = 97.79 \text{ kg/m}^2\text{s}$ , with individual images in each sequence separated by  $0.0125 \text{ s}$ . Adapted from [93]..... 278
- Figure 4.16: Schematics of liquid film circumferential distribution and axial flow characteristics for (a) vertical upflow, (b) vertical downflow, and (c) horizontal flow orientations..... 282

- Figure 4.17: Plots of stainless steel wall temperature and CM-HT inlet and outlet pressures for (a) vertical upflow with  $G \sim 300 \text{ kg/m}^2 \text{ s}$ , (b) vertical upflow with  $G \sim 60 \text{ kg/m}^2 \text{ s}$ , (c) vertical downflow with  $G \sim 300 \text{ kg/m}^2 \text{ s}$ , and (d) vertical downflow with  $G \sim 50 \text{ kg/m}^2 \text{ s}$ . ..... 286
- Figure 4.18: Plots of scaled temperature fluctuations versus mass velocity for (a) superheated vapor and (b) two-phase mixture inlet conditions, and scaled pressure fluctuations at channel inlet and outlet for (c) superheated vapor and (d) two-phase mixture inlet conditions. .... 290
- Figure 4.19: Plots of stainless steel ( $T_{ss}$ ) and water ( $T_{H2O}$ ) temperature measurements at all axial locations as well as standard deviation between respective measurements in all three orientations for (a)  $G_{FC} \sim 300 \text{ kg/m}^2 \text{ s}$  and  $x_{e,in} \sim 1.00$ , (b)  $G_{FC} \sim 300 \text{ kg/m}^2 \text{ s}$  and  $x_{e,in} \sim 0.80$ , (c)  $G_{FC} \sim 100 \text{ kg/m}^2 \text{ s}$  and  $x_{e,in} \sim 1.10$ , and (d)  $G_{FC} \sim 100 \text{ kg/m}^2 \text{ s}$  and  $x_{e,in} \sim 0.80$ . ..... 294
- Figure 4.20: Standard deviation between circumferential stainless-steel wall temperature measurements versus mass velocity for all three orientations. Values show signs of convergence by  $G \sim 200 \text{ kg/m}^2 \text{ s}$ , indicating this is the mass velocity at which horizontal flow transitions from *stratified* to *annular* flow in the current test section. .... 297
- Figure 4.21: (a) Vertical upflow condensation regime map of Park and Mudawar [93] providing predictions of flow regime for all local measurements in the current dataset, along with (b) predicted flow regime versus mass velocity and (c) channel length-average predicted flow regime versus mass velocity. .... 303
- Figure 4.22: Flow regime map of (a) Park *et al.* [94] used to evaluate current dataset, with (b) identified flow regimes across the range of mass velocities tested. Similar plots for flow regime maps of Kim *et al.* [96] (c), (d), Breber *et al.* [113] (e), (f), and Song *et al.* [122] (g), (h). ..... 310
- Figure 4.23: (a) Schematics for heat transfer coefficient data reduction methodology used here, along with (b) schematic illustrating the importance of capturing radial temperature variations present along the condensation length. .... 317
- Figure 4.24: Values of (a) local pressure and (b) local temperature used to calculate local heat transfer coefficient values shown in (c). Includes comparison between use of local superheated vapor temperature and interface (saturation) temperature to calculate heat transfer coefficient values. .... 320
- Figure 4.25: Uncertainty of (a) local heat transfer coefficient calculations averaged over all cases with superheated vapor inlet conditions (inset in Fig. 6 (b)) versus measurement position, and (b) uncertainty of channel length average heat transfer coefficient values versus FC-72 mass velocity. .... 325
- Figure 4.26: Evaluation of heat transfer coefficient versus axial location for all three orientations with (a) multiple flowrates and  $x_{e,in} \sim 1.05$ , (b) multiple inlet qualities and  $G_{FC} \sim 300 \text{ kg/m}^2 \text{ s}$ , and (c) multiple inlet qualities and  $G_{FC} \sim 100 \text{ kg/m}^2 \text{ s}$ . .... 329
- Figure 4.27: Evaluation of heat transfer coefficient versus local quality for multiple mass velocities with (from left to right)  $x_{e,in} > 1.00$ ,  $x_{e,in} \sim 0.80$ , and  $x_{e,in} \sim 0.60$ , in (a) vertical upflow, (b) vertical downflow, and (c) horizontal flow orientations. .... 333

- Figure 4.28: Plots of channel-average condensation heat transfer coefficient and total condensation energy transfer versus cooling water mass velocity for (a) vertical upflow, (b) vertical downflow, and (c) horizontal flow orientations. .... 336
- Figure 4.29: Evaluation of condensation length average heat transfer coefficient versus FC-72 mass velocity for (a) vertical upflow, (b) vertical downflow, and (c) horizontal flow orientations. .... 338
- Figure 4.30: Evaluation of condensation length average heat transfer coefficient versus FC-72 inlet quality for (a) vertical upflow, (b) vertical downflow, and (c) horizontal flow orientations. .... 340
- Figure 4.31: (a) Average condensation heat transfer coefficient versus mass velocity for three water flowrates in all three orientations, and (b) ratio of Vertical Upflow and Horizontal Flow (respectively) to Vertical Downflow average heat transfer coefficient, showing the effect of increases in mass velocity on converging values. .... 344
- Figure 4.32: Evaluation of gravity independence criteria developed by O'Neill et al. [137] using the current data. Subfigures correspond to the influence of body force acting (a) parallel or opposite to flow direction and (b) perpendicular to flow direction. .... 347
- Figure 4.33: Separated flow model local heat transfer predictions for vertical downflow with (a), (b), (c) superheated vapor inlet and descending mass velocity, (d), (e), (f) two-phase inlet and descending mass velocity, and (g) overall performance of SFM channel-average heat transfer predictions. .... 353
- Figure 4.34: Ratio of experimental to predicted heat channel average heat transfer coefficient versus liquid-only Reynolds number and  $X_{tt}$ , with heat transfer coefficient values predicted by correlations of (a) Akers and Rosson [180], (b) Cavallini and Zecchin [181], (c) Shah [182], (d) Haraguchi et al. [183], (e) Dobson and Chato [89], (f) Moser et al. [184], and (g) the updated Shah correlation [168]. Correlations shown here are recommended for use with macro-channels. .. 363
- Figure 4.35: Ratio of experimental to predicted heat channel average heat transfer coefficient versus liquid-only Reynolds number and  $X_{tt}$ , with heat transfer coefficient values predicted by correlations of (a) Wang et al. [119], (b) Koyama et al. [186], (c) Huang et al. [187], (d) Bohdal et al. [188], (e) Park et al. [189], and (f) Kim and Mudawar [56]. Correlations shown here are recommended for use with mini/micro-channels. .... 368
- Figure A.1: Plots of channel hydraulic diameter and reduced pressure representing operating conditions for many common studies on (a) flow boiling and (b) flow condensation with FC-72, water, and R134a as working fluids. Mini/macro-to-micro channel transition criteria of Ong and Thome [217], Kew and Cornwell [218], Brauner and Ullmann [219] are superimposed with boiling studies, while that of Li and Wang [220] is superimposed for condensation studies. Provided in (c) are flow visualization images highlighting differences between macro- to micro-channel transition for FC-72 and water (adapted from Mukherjee and Mudawar [14]). .... 424
- Figure A.2: Pressure versus mass velocity characteristic curves for (a) flow boiling (internal characteristic,  $q'' > 0$ ), (b) flow condensation (internal characteristic,  $q'' < 0$ ), (c) different pump types (external characteristic), and (d) sample cases for describing existence/non-existence of Ledinegg instability with (1) positive displacement pump, (2) centrifugal pump, and (3) fixed pressure drop boundary condition. .... 433

- Figure A.3: Sample test cases indicating (a) nominal progression of heat flux increments leading to CHF, and (b) Ledinegg instability (Flow Excursion) leading to CHF. Adapted from Mishima *et al.* [269]. ..... 438
- Figure A.4: Avoidance of Ledinegg instability may be achieved through elimination of the negative slope of the boiling curve as shown in (a) (adapted from Genglei *et al.* [273]) which may result in appreciable improvements in CHF values (b) as seen by Mishima *et al.* [269]. Also shown are methods for avoiding operating conditions where Ledinegg instability is likely to occur (negative-slope region), including (c) correlation for Onset of Flow Instability (OFI), adapted here from Lee *et al.* [43], and (d) stability maps, adapted here from Achard *et al.* [287]. ..... 444
- Figure A.5: Examples highlighting key features of boiling curve hysteresis. (a) Differences in ascending and descending boiling curves for flow boiling of FC-72 (adapted from Heindel *et al.* [312]). (b) ‘Vapor Burst’ phenomenon associated with flow boiling of FC-72 [244,328-329]. The sharp pressure increase in (b) due to rapid vaporization of a significant mass of liquid is observable in most boiling configurations with well de-gassed, low contact angle working fluids. .... 455
- Figure A.6.: Illustration of simplified Density Wave Oscillation (DWO) process. Information corresponds to a half-cycle of the instability, and includes (a) schematics and (b) plots of representative parameters. .... 462
- Figure A.7: Experimental examples of Density Wave Oscillations (DWOs), including (a) isolated DWOs, adapted from Dogan *et al.* [339], (b) DWOs induced by PDOs, adapted from Yuncu [62] with (c) superposition of PDO and DWO conditions on system pressure curves, also from Yuncu [62], and (d) DWO following Ledinegg instability, adapted from Mishima *et al.* [269]. ..... 465
- Figure A.8: Examples of results from analytic models used to determine under what conditions Density Wave Oscillations will occur in a given system: (a) stability map of Ishii and Zuber [37] and (b) transient model results of Colombo *et al.* [340]. ..... 469
- Figure A.9: (a) Experimental evidence for and (b) explanation of an atypical DWO mechanism investigated in a series of studies by O’Neill *et al.* [53-56]. ..... 477
- Figure A.10: (a) Schematic illustrating the key condition for Density Wave Oscillation in a micro-channel (presence of fully confined vapor growth) based on the work of He *et al.* [377]. (b) Illustration of orifice use at inlet to micro-channel, and (c) experimental results depicting impact of inlet orifice on damping/elimination of DWOs in the micro-channel, adapted from Fan and Hassan [381]. ..... 481
- Figure A.11: Schematics depicting (a) nominal operation of two parallel boiling channels, (b) parallel boiling channels experiencing Flow Maldistribution (Ledinegg instability), and (c) parallel channels exhibiting out-of-phase Density Wave Oscillations (DWOs), referred to as Parallel Channel Instability (PCI). ..... 488
- Figure A.12: Plots of (a) inlet velocity versus time showing Parallel Channel Instability 180° out-of-phase between two channels, adapted from Aritomi *et al.* [386-390], (b) fluctuations in non-dimensional inlet velocity versus non-dimensional time showing PCI in a five-channel system, adapted from analytic work of Lee and Pan [157], and (c) experimental results highlighting the difference between Pressure Drop Oscillations (left) and PCI (right) in parallel micro-channel heat sinks, adapted from Qu and Mudawar [57]. ..... 493

Figure A.13: Image of (a) parallel micro-channels with inlet restrictions adapted from Szczukiewicz *et al.* [416], (b) schematic of expanding parallel micro-channels adapted from Lu and Pan [421], and (c) comparison of results for straight micro-channels with expanding micro-channels (top) and those with inlet orificing (bottom), adapted from Lee *et al.* [414]..... 499

Figure A.14: Series of schematics presenting the process of Pressure Drop Oscillations, from (a) nominal operation, (b) attempting flow excursion, (c) max flowrate condition, (d) reduction in flowrate, (e) minimum flowrate condition, and (f) continuation of the cycle ..... 503

Figure A.15: (a) Stability map (for fixed mass flowrate, pressure, and heat flux) showing conditions for which Ledinegg instability, Flow Excursion with Compressible Volume (FECV), and Pressure Drop Oscillations will occur (adapted from Rahman and Singh [433]). (b) Operating conditions exhibiting PDOs, and (c) operating conditions showing FECV, adapted from Mishima *et al.* [269]. ..... 507

Figure A.16: Examples of analytic model results for Pressure Drop Oscillations adapted from (a) Ozawa *et al.* [46] and (b) Zhang *et al.* [451]. Also, (c) example of atypical interaction between compressible volume and system dynamic behavior resulting in a new instability mode termed *Charge Transition Instability* (CTI), adapted from Lee *et al.* [452]. ..... 511

## NOMENCLATURE

$A$	amplitude; area
$Bo$	boiling number; Bond number
$C$	Wallis parameter
$c_p$	specific heat at constant pressure
$Co$	confinement number
$D$	diameter
$D_h$	hydraulic diameter
$E$	measurement error
$E\ddot{o}$	Eötvös number
$Eu$	Euler number
$F$	force
$f$	frequency; friction factor
$f_r$	resonant frequency
$Fr$	Froude number
$Fr_f$	liquid Froude number
$G$	mass velocity
$g$	Earth's gravitational constant
$h$	enthalpy
$H$	height of flow channel's cross-section; digital filter transfer function
$h_{cond}$	condensation heat transfer coefficient
$h_{fg}$	latent heat of vaporization
$I$	inertia
$j$	superficial velocity
$k$	conductivity
$K$	constant used in calculating eddy momentum diffusivity; restriction coefficient
$K_{orf}$	inlet orifice loss coefficient
$L$	length
$L_{cond}$	condensation length
$l$	length
$L_d$	development length of flow channel
$L_e$	exit length of flow channel
$L_h$	heated length of flow channel
$M$	momentum

$m$	mass
$\dot{m}$	mass flow rate
$MAE$	mean absolute error
$N$	number of data points; number of samples
$N_{pch}$	phase change number
$N_{sub}$	subcooling number
$P$	pressure
$p$	perimeter
$P'$	mean-subtracted pressure fluctuations
$P_{in}$	pressure at inlet to diabatic portion of channel
$P_{out}$	pressure at outlet to diabatic portion of channel
$P_R$	reduced pressure
$Pe$	Peclet number
$Pr$	Prandtl number
$P_{wr}$	power supplied (by pre-heater)
$\Delta P$	pressure drop across heated portion of channel
$Q$	total heat input; $Q$ Factor, measure of oscillatory mode intensity
$\dot{q}''$	heat flux on diabatic perimeter of channel
$Q_{cond}$	total condensation energy transfer in test section
$\Delta q_{cond}$	local incremental condensation energy transfer
$R$	temperature ratio (OFI correlation); force ratio (DWOs in micro-channels)
$r$	radius
$Re$	Reynolds number
$Re_f$	superficial liquid Reynolds number, $Re_f = G(1-x)D_h/\mu_f$
$S_2$	flow transition parameter
$St$	Stanton number
$Su$	Suratman number
$T$	temperature
$T'$	amplitude of temperature fluctuations
$t$	time
$T_{in}$	temperature at channel inlet
$T_{sat}$	saturation temperature
$T_{sat,in}$	saturation temperature of fluid at inlet to heated portion of channel
$T_{tr}$	transport time
$U$	mean velocity; uncertainty
$u$	velocity

$U_{char}$	characteristic velocity
$v$	specific volume
$W$	width of flow channel's cross-section
$We$	Webber number
$x$	quality
$x_e$	thermodynamic equilibrium quality
$x_f$	flow quality
$X_{tt}$	Lockhart-Martinelli parameter
$y$	wall-normal coordinate
$z$	variable indicating digital domain; stream-wise position

### ***Greek Symbol***

$\alpha$	void fraction; channel inclination
$\delta$	condensate film thickness; indicates a perturbation
$\Gamma$	mass transfer rate; liquid film mass flowrate
$\Lambda$	friction number
$\zeta$	percentage of predictions within 50% of experimental value
$\theta$	percentage of predictions within 30% of experimental value; test section orientation
$\varphi$	two-phase multiplier
$\mu$	dynamic viscosity
$\mu_P$	mean of pressure set, statistical parameter
$\eta$	correlation constant
$\rho$	density
$\rho_{cc}$	cross correlation coefficient, statistical parameter
$\sigma$	surface tension; standard deviation
$\sigma_P$	standard deviation of pressure set, statistical parameter
$\tau$	shear stress

### ***Subscripts***

$0-n$	indicates a time span ( $t=0$ to $t=n$ ) over which an average or max is found
$12$	evaluated between regions 1 and 2
$23$	evaluated between regions 2 and 3
$A$	accelerational; amplitude
$a$	adiabatic
$ave$	average
$BH$	bulk heater
$c$	cross-section; core; channel
$cap$	capillary

<i>d</i>	diabatic (heated)
<i>DWO</i>	property of Density Wave Oscillation (such as amplitude or frequency)
<i>exp</i>	experimental (measured)
<i>F</i>	friction; condensate liquid film
<i>f</i>	saturated liquid
<i>FBM</i>	flow boiling module
<i>FC</i>	FC-72 fluid
<i>fdb</i>	fully-developed boiling
<i>film</i>	referring to condensate liquid film
<i>fo</i>	liquid only
<i>FWHM</i>	full width half maximum
<i>G</i>	gravitational
<i>g</i>	saturated vapor
<i>go</i>	vapor only
<i>h</i>	hydraulic (diameter)
<i>H</i>	heated (length, diameter)
<i>H2O</i>	water, cooling fluid
<i>HDF</i>	property of HDF
<i>i</i>	inner (refers to diameter)
<i>in</i>	inlet to diabatic portion of channel
<i>interface</i>	evaluated at the interface (such as shear stress or perimeter)
<i>k</i>	Fourier series index; phase indicator
<i>m</i>	heated wall identifier ( <i>a</i> for heater $H_a$ or <i>b</i> for heater $H_b$ )
<i>max</i>	max value over range evaluated
<i>mean</i>	mean value over range evaluated
<i>n</i>	axial measurement station ( $n = 0 - 11$ )
<i>o</i>	outer (refers to diameter)
<i>out</i>	outlet to diabatic portion of channel
<i>P</i>	pressure
<i>PC</i>	phase change
<i>PH</i>	pre-heater
<i>pred</i>	predicted
<i>rec</i>	reconstructed
<i>res</i>	reservoir
<i>sat</i>	saturation
<i>SE</i>	single event

<i>SS</i>	stainless-steel (inner condensation tube)
<i>T</i>	turbulent
<i>tot</i>	total (indicates parameter is evaluated over the total length of Region 3)
<i>Tp</i>	two-phase
<i>tran</i>	transition
<i>w</i>	wall; wetted
<i>wall</i>	evaluated for the channel wall (such as shear stress or perimeter)
<i>z</i>	stream-wise position
<i>Zivi</i>	evaluated using Zivi void fraction correlation
$2\phi$	two-phase

### ***Superscripts***

<i>0</i>	value at initial time (equal to Region 1 value for all Region 3 parameters)
<i>n</i>	indicates current time step

### ***Acronyms***

CHF	critical heat flux
CTI	charge transition instability
CM-FV	condensation module for flow visualization
CM-HT	condensation module for heat transfer measurements
DWO	density wave oscillation
FBCE	Flow Boiling and Condensation Experiment
FBM	flow boiling module
FECV	flow expansion with compressible volume
HDF	high density front
LDF	low density front
LDV	Laser Doppler Velocimetry
OFI	onset of flow instability
ONB	onset of nucleate boiling
OSV	onset of significant vapor
PCI	parallel channel instability
PDO	pressure drop oscillation

## ABSTRACT

Author: O'Neill, Lucas, E. PhD

Institution: Purdue University

Degree Received: August 2019

Title: Experimental Investigation and Modeling of Key Design Parameters in Flow Boiling and Condensation.

Major Professor: Issam Mudawar

In order to better understand and quantify the effect of instabilities in systems utilizing flow boiling heat transfer, the present study explores dynamic results for pressure drop, mass velocity, thermodynamic equilibrium quality, and heated wall temperature to ascertain and analyze the dominant modes in which they oscillate. Flow boiling experiments are conducted for a range of mass velocities with both subcooled and saturated inlet conditions in vertical upflow, vertical downflow, and horizontal flow orientations. High frequency pressure measurements are used to investigate the influence of individual flow loop components (flow boiling module, pump, pre-heater, condenser, *etc.*) on dynamic behavior of the fluid, with fast Fourier transforms of the same used to provide critical frequency domain information. Conclusions from this analysis are used to isolate instabilities present within the system due to physical interplay between thermodynamic and hydrodynamic effects. Parametric analysis is undertaken to better understand the conditions under which these instabilities form and their impact on system performance. Several prior stability maps are presented, with new stability maps provided to better address contextual trends discovered in the present study.

Further, this study utilizes experimental results for vertical upflow boiling of FC-72 in a rectangular channel with finite inlet quality to investigate Density Wave Oscillations (DWOs) and assess their potential impact on design of two-phase systems for future space missions. High-speed flow visualization image sequences are presented and used to directly relate the cyclical passage of High and Low Density Fronts (HDFs and LDFs) to dominant low-frequency oscillations present in transient pressure signals commonly attributed to DWOs. A methodology is presented to determine frequency and amplitude of DWO induced pressure oscillations, which are then plotted for a wide range of relevant operating conditions. Mass velocity (flow inertia) is seen to be the dominant parameter influencing frequency and amplitude of DWOs. Amplitude of pressure oscillations is at most 7% of the time-averaged pressure level for current operating

conditions, meaning there is little risk to space missions. Reconstruction of experimental pressure signals using a waveform defined by frequency and amplitude of DWO induced pressure fluctuations is seen to have only moderate agreement with the original signal due to the oversimplifications of treating DWO induced fluctuations as perfectly sinusoidal in nature, assuming they occur at a constant frequency value, and neglecting other transient flow features. This approach is nonetheless determined to have potential value for use as a boundary condition to introduce DWOs in two-phase flow simulations should a model be capable of accurately predicting frequency and amplitude of oscillation.

Additionally, this study presents a new mechanistic model for Density Wave Oscillations (DWOs) in vertical upflow boiling using conclusions drawn from analysis of flow visualization images and transient experimental results as a basis from which to begin modeling. Counter to many prior studies attributing DWOs to feedback effects between flow rate, pressure drop, and flow enthalpy causing oscillations in position of the bulk boiling boundary, the present instability mode stems primarily from body force acting on liquid and vapor phases in a separated flow regime leading to liquid accumulation in the near-inlet region of the test section, which eventually departs and moves along the channel, acting to re-wet liquid film along the channel walls and re-establish annular, co-current flow. This process was modeled by dividing the test section into three distinct control volumes and solving transient conservation equations for each, yielding predictions of frequencies at which this process occurs as well as amplitude of associated pressure oscillations. Values for these parameters were validated against an experimental database of 236 FC-72 points and show the model provides good predictive accuracy and capably captures the influence of parametric changes to operating conditions.

Also, this study shows analysis of pressure signals in condensing systems reveal the presence of relevant oscillatory phenomena during flow condensation as well, which may impact performance in applications concerned with precise system control. Towards this end, the present study presents results for oscillatory behavior observed in pressure measurements during flow condensation of FC-72 in a smooth circular tube in vertical upflow, vertical downflow, and horizontal flow orientations. Dynamic behavior observed within the test section is determined to be independent of other components within the flow loop, allowing it to be isolated and interpreted as resulting from physical aspects of two-phase flow with condensation. The presence of a peak oscillatory mode (one of significantly larger amplitude than any others present) is seen for 72% of

vertical upflow test cases, 61% of vertical downflow, and 54% of horizontal flow. Relative intensities of this peak oscillatory mode are evaluated through calculation of  $Q$  Factor for the corresponding frequency response peak. Frequency and amplitude of peak oscillatory modes are also evaluated. Overall, vertical upflow is seen to exhibit the most significant oscillatory behavior, although in its maximum case amplitude is only seen to be 7.9% of time-averaged module inlet pressure, indicating there is little safety risk posed by oscillations under current operating conditions. Flow visualization image sequences for each orientation are also presented and used to draw parallels between physical characteristics of condensate film behavior under different operating conditions and trends in oscillatory behavior detected in pressure signals

Further, the present work outlines a new methodology utilizing temperature and pressure measurements to identify condensation flow regimes. For vertical upflow condensation, amplitude of dynamic temperature and pressure oscillations are shown to clearly indicate transition from counter-current flow regimes (*i.e.*, *falling film*, *oscillating film*, *flooding*) to annular, co-current flow (*climbing film* flow regime). In horizontal flow condensation, standard deviation between multiple thermocouple measurements distributed around the tube circumference was calculated at all axial (stream-wise) measurement locations. High values of standard deviation are present for stratified flow (*stratified flow*, *wavy-stratified*, *plug flow*), while axisymmetric flow regimes (*i.e.*, *slug flow*, *annular flow*) yield significantly lower values. Successful development of this technique represents a valuable contribution to literature as it allows condensation flow regime to be identified without the often-costly restriction of designing a test section to allow optical access. Identified flow regimes in both vertical upflow and horizontal flow orientations are compared to regime maps commonly found in the literature in pursuit of optimum performing maps.

Finally, the present study aims to better analyze the influence of body force on flow condensation heat transfer by conducting tests at multiple orientations in Earth's gravity. Dielectric FC-72 is condensed in a smooth stainless-steel tube with 7.12 mm diameter and 574.55 mm condensing length by counterflow of cooling water across the outer surface of the tube. Test conditions span FC-72 mass velocities of 50.3 – 360.3 kg/m<sup>2</sup>s, test section inlet pressures of 127.0 – 132.1 kPa, and test section inlet thermodynamic equilibrium qualities of 0.13 – 1.15. A subset of data gathered corresponding to axisymmetric, annular condensation heat transfer is identified and a detailed methodology for data reduction to calculate heat transfer coefficient presented. Uncertainty analysis is also presented and indicates channel average heat transfer coefficients are

calculated within  $\pm 3.6\%$  to  $\pm 26.7\%$  (depending on operating conditions). Analysis of parametric trends for condensation heat transfer reveals the dominant influence of mass velocity (flow inertia), secondary influence of vapor mass fraction (thermodynamic equilibrium quality), and strong dependence on orientation (body force) at low mass velocities. At higher mass velocities results for all orientations investigated begin to converge, indicating body force independent annular condensation heat transfer is achieved. Separated Flow Model predictions of vertical downflow condensation heat transfer provide reasonable agreement with experimental results, evidence by a Mean Absolute Error (MAE) of 31.2%. Evaluation of condensation heat transfer correlations for horizontal flow reveal most correlations struggle for cases with high liquid content. Specific correlations are identified for superior accuracy in predicting the measured data.

# 1. INTRODUCTION

## 1.1 Flow Boiling Dynamic Behavior

### 1.1.1 *Importance of Flow Boiling Dynamic Behavior in Space-based Applications*

To meet increasingly stringent thermal design constraints posed by dual trends of miniaturization and increased performance across multiple industries, thermal design engineers are considering two-phase flow thermal management systems which capitalize on both sensible and latent heat to offer orders of magnitude improvements in heat transfer performance [1]. Researchers at the Purdue University Boiling and Two-Phase Flow Laboratory (PU-BTPFL) and other organizations have investigated many different configurations to best utilize phase change heat transfer for varying applications, including capillary-driven devices [2-4], pool boiling thermosyphons [5-7], falling film [8,9], channel flow boiling [10,11], micro-channel boiling [12-16], jet impingement [17-20], and spray [21-27], as well as hybrid configurations [28-31] involving two or more of these schemes.

Thermal management systems utilizing phase change heat transfer are particularly attractive options for utilization in aerospace thermal-fluid systems where their high heat transfer coefficients allow significant reductions in size and weight of hardware, both critical design parameters in aerospace applications. This has led space agencies worldwide to fund further development of the technology to allow implementation in both space vehicles and planetary bases. Current targets for adoption of phase change technologies include Thermal Control Systems (TCSs), which control temperature and humidity of the operating environment, heat receiver and heat rejection systems for power generating units, and Fission Power Systems (FPSs), which are projected to provide high power as well as low mass to power ratio [32-34].

Limiting the adoption rate of phase-change heat transfer for these technologies is the presence of complex phenomena related to buoyancy and surface tension present in multiphase flows which can affect critical aspects such as flow regime, phase distribution, and even the nucleation process itself. Many design tools for phase change thermal management rely on empirically correlated expressions for key parameters that were developed based on testing in a certain orientation in Earth's gravity. From the hyper-gravity associated with launch, to the micro-gravity of orbit and/or deep space, to the varying gravitational fields associated with operation on

various extra-terrestrial bodies, any system designed for aerospace applications will need to be robust to drastic changes in operating conditions which fall outside the intended range of existing empiric and semi-empiric design tools. Prior studies conducted with the aid of parabolic flight have shown changes in local acceleration lead to dynamic changes in flow boiling behavior, with similar operating conditions tested in micro-gravity and hyper-gravity environments yielding significant difference in flow boiling heat transfer [35,36]. It is likely more sophisticated design tools, such as mechanistic models and computational schemes, could better predict this behavior as they are based less on prior experimental results, which may or may not apply, and more on the dominant underlying physical processes.

In addition to changes in system performance due to varying local acceleration across a mission's lifecycle, continuous changes to ambient thermal environment of the system often necessitate changes in operation mode. Whether due to cyclical solar exposure in orbiting vehicles, differences in ambient temperature between operations in space (transit) and some terrestrial environment (Moon, Mars, etc.), or changes in thermal loading associated with periodic operation of high-energy instruments, it is likely any dedicated space-based two-phase flow thermal management system will need to operate across a range of flow rates, heat fluxes, and pressures. Many studies have shown how changes to these parameters can instigate the onset of flow boiling instabilities, expressing transition criteria in the form of both stability maps [37-39] and transition correlations [40-43], but further study of the characteristics of these instabilities and other transient phenomena is necessary.

### 1.1.2 *Flow Boiling Instabilities and Transient Phenomena*

The origin of the study of two-phase flow instabilities is commonly attributed to Ledinegg [44], who discovered for certain operating conditions two-phase flow systems experience a jump from an unstable location to a stable location on the system's internal-external pressure curve. This manifests as a change in both system mass velocity and operating pressures.

Throughout the latter half of the 20<sup>th</sup> century, researchers investigated less noticeable, more persistent transient phenomena found in two-phase flow systems [45-47], with special attention paid to Density Wave Oscillations (DWOs) [48,49]. It was around this time that Boure *et al.* published their seminal review of two-phase flow instabilities [50], which both summarized state-

of-the-art understanding of two-phase flow transient phenomena and instabilities at the time and paved the way for future investigations in the field.

Present day researchers continue characterizing instabilities and transient behavior observed in experimental two-phase flow systems, focusing on DWOs [51-56], Parallel Channel Instability (PCI) [57-59], Pressure Drop Oscillations (PDOs) [46,60-61], and interaction of multiple instability modes [62,63]. Recent reviews, such as those by Tadrist [64], Kakac and Bon [65], and Ruspini *et al.* [66] provide updated surveys of literature relating to phenomena first reported by Boure *et al.* [50].

Recent experimental studies concerning other facets of two-phase flows (such as heat transfer, pressure drop, *etc.*) have also begun to focus more on aspects of transient system behavior, centering on bubble dynamics in micro-channels [67], temperature, pressure, and heat transfer fluctuations unassociated with instabilities [68-72], transient flow pattern transitions [73], and even system response to manually induced periodicity [74]. Much of the transient behavior observed in these studies can likely be related to either instabilities present in two-phase flow systems or externally induced oscillations, and use of a systematic analysis approach by the two-phase flow community could greatly homogenize interpretation of results.

Of the many aspects of transient two-phase flow currently being studied, however, only DWOs are of particular interest to the present study, and, as such, a more detailed review of key works in the field will be provided. For additional information on all two-phase flow instabilities, Appendix A provides a comprehensive review.

### 1.1.3 *Density Wave Oscillations*

There are many heading styles that have been added to the Styles Ribbon. There are Purdue Headings 1-6 above. You will have to manually change the text back to normal style after you Although the first experimental observation of DWOs is commonly attributed to Serov [48], it wasn't until nearly two decades later that researchers began devoting significant time to better understanding and categorizing these oscillations. It is commonly held that their occurrence is due to feedback effects between vapor generation rate, flow rate, and system pressure drop, which cause the Onset of Significant Vapor (OSV, also sometimes referred to as the onset of bulk boiling) point within the boiling channel to oscillate, thereby altering channel pressure drop characteristics

and causing flow rate to fluctuate, and this is the point from which analytic works sought to begin modeling.

Ishii provided one of the first comprehensive experimental and analytic assessments of the phenomenon [75]. The phenomenon was modeled using classic stability analysis whereby governing equations were transformed into the  $s$ -domain (frequency domain) and expressed in terms of transfer function between different parameters. This allowed system stability at a given operating point to be assessed using graphical ‘stability test criterion’ (such as that presented by Nyquist [76]). Stability boundaries for full ranges of operating conditions were determined by employing the D-Partition Method, which divides the multi-dimensional parameter space into regions bounded by harmonic frequency surfaces and singular surfaces, with stability of each surface found by testing a single point within each using the aforementioned graphical stability test criterion.

Ishii utilized experimental results from several studies [77-79], demonstrating his method for determining overall system stability by reducing the multi-dimensional parameter space to 2-dimensional for presentation, using subcooling and phase-change numbers as  $x$ - and  $y$ -coordinates, respectively. These parameters were defined as

$$N_{sub} = \frac{h_f - h_{in}}{h_{fg}} \frac{v_g - v_f}{v_f} \quad (1.1)$$

and

$$N_{pch} = \frac{Q}{\dot{m} h_{fg}} \frac{v_g - v_f}{v_f}, \quad (1.2)$$

and are still commonly utilized in literature presenting stability maps for flow boiling.

Following shortly after Ishii, Yadigaroglu and Bergles [49] performed both analytic and experimental investigations into DWOs occurring in flow boiling of Freon-113. Their analytic work followed similar lines of analysis as that of Ishii [75], and their experimental work revealed periods of oscillation in the range of 2 – 10 s.

Fukuda and Kobori [80] also investigated DWOs using both experimental and analytic methods, employing a test section composed of two parallel channels. They distinguished two separate types of DWOs from experimental observations: Type I, occurring at near-zero steam exit quality and largely influenced by gravitational pressure drop, and Type II, occurring at high steam exit quality and largely influenced by frictional pressure drop. This classification of DWOs

into different types based on key driving behavior is particularly relevant for the analysis to be presented in the present study.

Around the same time, Belblidia and Bratianu [81] presented a review of existing literature concerning DWOs. They also noted the possibility of different driving forces leading to the manifestation of the instability, and provided detailed analysis of the different modeling approaches used (mixture models, two-fluid models, *etc.*) and their effect on predictions of stability. Further, they made the key observation that existing literature was far more concerned with prediction of boundaries for stable system observation, and characterization of unstable behavior was of little importance.

Achard *et al.* [82] built on previous analytic works concerning DWOs by utilizing Hopf-Bifurcation analysis in an attempt to characterize frequency and amplitude of oscillations. Their analysis indicated that the concept of a ‘stability-boundary’ was an oversimplification, and that for operating conditions in a region sufficiently close to calculated stability bounds the system would likely exhibit limit-cycle oscillations.

Although largely building on aforementioned analysis approaches, Lahey and Podowski [47] provided a very comprehensive, detailed analytic treatment of DWOs and other instability modes within multi-phase flow systems. Their analytic work primarily utilizes a drift flux modeling approach to the system(s) in question.

In the early 1990’s two experimental studies by Yuncu [62] and Wang *et al.* [83], respectively, served to significantly advance the understanding of mechanisms behind and manifestation of DWOs. Yuncu investigated flow boiling of Freon 11 and observed both DWOs and PDOs, with DWOs occurring at higher frequencies than PDOs within his experimental system. Period of DWOs was found to be 1 – 1.5 s, and amplitude of DWOs was found to increase with increases in both mass flux and heat flux. Wang *et al.* investigated flow boiling of water in a single channel. Instead of the classic stability-theory approach to modeling onset of instability used in many prior works, they chose to correlate their experimental data to develop expressions for ‘limiting heat flux’ and ‘limiting quality’ for onset of DWOs. They also observed DWO periods on the order of 1.5 s.

More recently, Schlichting *et al.* [63] presented detailed numeric analysis on stability boundaries and behavior of interacting DWO and PDO instability modes for a proposed NASA testbed using FC-72 as the working fluid. Building on prior stability analysis work of Lahey and

Podowski [47], they employed Hopf-bifurcation analysis and characterized limit cycle oscillations expected to be present within the system.

This classic stability analysis approach was taken even further by Pandey and Singh [84], who modeled the interaction between Ledinegg instability and DWOs as phenomena giving rise to Bogdanov-Takens bifurcation. Their work was purely analytic, and constitutes one of the most comprehensive uses of classic stability theory available in contemporary literature.

Despite significant advances in both experimental and analytic investigations into DWOs, many questions remain surrounding their formation and characteristic behavior. In particular, the idea proposed by Fukuda and Kobori [80] (among others) that DWOs can form as a result of different dominant forces based on operating conditions has relevance to the current work, as the test section and operating conditions explored here are atypical for DWO investigation. Almost all prior studies based their analysis on flow boiling through long channels with highly subcooled inlet conditions and finite quality outlet. The present heated length, however, is significantly shorter than that explored in many prior works, and only exhibits typical DWO behavior for cases with finite inlet quality [54]. Due to this, modeling work will follow a novel approach, based on experimentally observed, dominant physical mechanisms.

## **1.2 Flow Condensation**

### *1.2.1 Flow Condensation as an Enabling Technology for Phase Change Thermal Management*

A key trend across all energy applications in recent years has been that of miniaturization coupled with increased capacity. System modifications following these trends have led to increased performance and smaller size, both advantageous features from product design standpoints. From a heat transfer perspective, however, this leads to a necessity of higher flux thermal management systems to reject heat [1].

To satisfy these increasingly stringent thermal management requirements, engineers have begun turning to schemes relying on phase change heat transfer. These systems typically rely on boiling to acquire heat from the device being cooled and condensation to reject heat from the working fluid and return it to a pre-boiling (subcooled or saturated liquid) state. Condensation has been investigated in several configurations, including falling film [85-87], flow through single circular mini-channels [88-94], and flow through parallel micro-channel arrays [95-97]. A

common deficiency found across most studies on condensation, however, is lack of emphasis on transient flow behavior and analysis of potential instability modes brought on by the condensation process.

Transient flow behavior is particularly important for aerospace applications (for which phase change thermal management systems are attractive due to their ability to offer superior heat transfer performance while allowing reductions in system weight and volume) due to the likelihood of encountering many different operating environments. Whether utilized in aircraft performing a variety of high-acceleration maneuvers at a range of altitudes, or in spacecraft intended to launch, travel through space, and operate in a distant planetary environment, thermal management systems for these applications will be required to operate across a wide range of thermal conditions and body force fields. Operation across a variety of body force conditions is particularly important for thermal management systems capitalizing on phase change, as the orders of magnitude difference in phase densities can cause these systems to respond strongly to changes in body force [98].

Due to the difficulty of performing system tests under microgravity, partial-gravity, and hyper-gravity conditions associated with intended use environments, precise knowledge of how changes in operating conditions affect system performance is imperative to design of phase-change thermal management systems for these applications. In particular, the potential for changes in operating environment to cause instabilities to manifest within the system and adversely affect performance mean a detailed understanding of two-phase flow dynamics and instabilities and their effects on thermal and hydrodynamic characteristics is critical.

Another key aspect of flow condensation often underemphasized is the need to accurately determine condensation flow regime. Flow regimes are used to classify flow conditions based on distribution of liquid and vapor within the condensation length. This distribution has a significant impact on local heat transfer, meaning accurate identification and prediction of flow regime is paramount to system design and interpretation of observed behavior.

### 1.2.2 *Flow Condensation Dynamic Behavior*

The vast majority of work on two-phase flow transient behavior and instabilities concerns only boiling, however, due to the perception that condensation is a more stable process. While this may be true by comparison with boiling, pressure and mass flow rate fluctuations are also

commonly seen during flow condensation, meaning it may be that instabilities are present which have not been as thoroughly investigated as those for boiling.

One of the earliest studies including transient flow condensation results was performed by Westendorf and Brown [99] in the mid 1960's, who saw that, for condensation occurring between concurrent flow of saturated vapor and subcooled liquid, high and low frequency oscillatory modes do occur and could be related to subcooling of the liquid phase.

Around the same time, Goodykoontz and Dorsch [100] investigated flow condensation in a more traditional tube-in-tube counterflow configuration. They observed pressure oscillations with frequencies in the 1-10 Hz range, although only for moderate condensation lengths of 1.7-3.7 feet (longer and shorter test sections did not exhibit any fluctuations). Amplitude of oscillation remained below 1 psi in all cases, indicating the oscillations posed no appreciable threat to safe system operation.

Also around this period, Soliman and Berenson [101] performed a detailed investigation of flow condensation in a multi-tube condenser in multiple orientations (vertical upflow, vertical downflow, and horizontal flow) using Freon-113 as working fluid. They observed two distinct oscillatory modes for pressure, one for horizontal and vertical downflow orientations and another for vertical upflow orientation, and correlated amplitude of oscillation for each using experimental data. Also of interest is their observation that amplitude of oscillation is always less than 5% of inlet pressure for vertical downflow and horizontal orientations, and less than 10% of inlet pressure for vertical upflow. This study in particular was found to be particularly relevant to the present work and is referenced throughout.

Over the ensuing decades, several condensation studies made mention of transient condensation behavior and pressure fluctuations, including flow condensation in a U-tube condenser [102], flow through an annulus [103], multi-tube condensers [104], and micro-channels [95]. Some studies present detailed descriptions, analytic models, and/or computational models including aspects of transient system behavior, ranging from traditional linearized stability models similar to those seen for DWOs and PDOs [105,106] to models attempting to assess the impact of interfacial waves formed by classic hydrodynamic instability present for concurrent flow of two fluids (in this case two phases) [107] on system pressure fluctuations and flow regime transition [95,108-109].

Overall, the available literature dealing with transient aspects of flow condensation is useful in capturing the existence of flow field parameter (*e.g.*, pressure and mass flow rate) oscillations in a majority of test cases, and providing some insight to the physical mechanisms that may be causing them, but lacking a generalized, fundamental approach to analysis which would allow comparison of results across studies and provide means towards achieving a full understanding of the fundamental processes causing oscillations to manifest.

### 1.2.3 *Predictive Tools for Condensation Flow Regime*

Many prior studies in the field have devoted significant effort to identifying two-phase flow regimes and developing tools for their prediction. In vertical downflow orientation, where body force acts to stabilize the flow by ensuring liquid phase flows along with vapor and out of the channel, regime maps are considered largely unnecessary as flow is always axisymmetric and co-current. In vertical upflow, horizontal, and intermediate flow angles, however, the relative magnitude of body force to flow inertia is critical to determining both motion and position of liquid phase within the condensation length.

One of the earliest studies to focus on flow regime in vertical tubes by Wallis [110] provided a method for predicting flooding velocities (*i.e.*, velocities at which liquid phase will remain largely stationary while vapor phase continues to flow) for adiabatic mixtures of water and air in vertical upflow orientation. His work paved the way for development of flow regime maps for vertical upflow by future researchers [93], who expanded his analysis to provide regime transition criteria for *falling film*, *flooding*, *oscillating film*, and *climbing film* flow regimes.

Investigation into flow regimes for horizontal flows has been far more prolific than vertical flows. One of the most commonly cited works is that of Taitel and Dukler [111] who developed flow regime transition criteria (and thus a flow regime map) for horizontal, adiabatic two-phase flows. They utilized the air-water data of Mandhane *et al.* [112] to validate their map.

Although developed for adiabatic two-phase flows, Breber *et al.* [113] showed the map of Taitel and Dukler [111] provided good prediction for flow regime in condensing flows as well. They then provided a simplified method for flow regime prediction based on that of Taitel and Dukler. This basic form was again leveraged when Tandon *et al.* [114] provided a modified version of Breber *et al.*'s map [113].

A slightly different approach to modeling flow regime transitions was taken by Soliman [115,116], who modeled transitions from *annular flow* to *wavy flow* and *mist flow* to *annular flow* in separate studies. Similar to Wallis in vertical upflow [110], Soliman's approach has been adapted in recent studies to provide predictions of many additional flow regimes in horizontal flow, including *stratified flow*, *wavy-stratified flow*, *wavy-annular flow with gravity influence*, *wavy-annular flow without gravity influence*, *slug flow*, and others (depending on test geometry) [94,96,117].

In addition to these, recent years have seen a significant increase in the number of flow transition criteria (and associated flow regime maps) available for use in the literature. Notable works include those of Cavallini *et al.* [118], Wang *et al.* [119], Hajal *et al.* [120], Coleman and Garimella [121], and Song *et al.* [122]. In addition to this, almost all works presenting flow condensation heat transfer results provide some discussion on observed and/or predicted flow regime.

Historically, all investigation of condensation flow regime has been done through direct (optical) observation of liquid film distribution within the flow channel. This typically requires compromises to be made during test section design, as providing an optically transparent region for direct image capture often eliminates the option of gathering detailed heat transfer data for that portion of the module. Liebenberg *et al.* attempted some characterization of flow regime based on power spectral density of pressure fluctuations during condensation in both smooth and enhanced tubes [123,124], but ultimately relied upon images for determination of flow regime.

The present work aims to present a new method for identifying flow regime in both horizontal and vertical flows using only temperature and pressure data. Although not as comprehensive as direct visualization of flow behavior, it allows interpretation of heat transfer behavior and heat exchanger performance based on observed flow regime without the necessity of optical transparency within the condensation length. This is particularly useful in industrial applications, as temperature and pressure monitoring are commonly available but optical access rarely is. It will also be very helpful in interpreting flow condensation heat transfer data gathered on the International Space Station (ISS) as part of NASA's Flow Boiling and Condensation Experiment in the absence of direct visualization behavior.

#### 1.2.4 *Impact of Body Force Effects on Flow Condensation Heat Transfer*

Due to the orders of magnitude difference in liquid and vapor phase densities, body force plays a significant role in phase change heat transfer processes. It may act to stabilize or destabilize liquid film motion in vertical flow condensation, drive stratification in horizontal flows, or even act as the driving force in systems operating by natural circulation. Prior studies focusing on the influence of body force on flow condensation have either compared microgravity results to those obtained in 1-g [125] or investigated multiple orientations in 1-g [126].

Some of the earliest works on flow condensation in microgravity were performed by Albers and Macosko [127-129], who investigated nonwetting condensation of mercury during parabolic flights. Results were compared to those obtained from ground testing in horizontal orientation, and show differences depending on operating conditions (*i.e.*, flow quality and mass velocity) investigated.

Similar conclusions were drawn by Keshock [130] who developed an analytic model for flow condensation of R-12 (validated using 1-g data) to investigate potential development of refrigeration systems for application in microgravity. Due to difficulty obtaining microgravity data, however, it was not possible to compare analytic results to corresponding 0-g experiments.

Recently, experimental microgravity data were collected by Lee *et al.* [98,131] during parabolic flights corresponding to flow condensation of FC-72 in a smooth, 791.12 mm long, 7.12 mm inner diameter tube. An interesting facet of their work is the transition from hyper-gravity through 1-g to microgravity, highlighting the continuously changing flow characteristics dependent on body force intensity.

In 1-g, Wang and Du [132] developed an analytic model and compared results with experimental values obtained for laminar film condensation of steam in inclined tubes. Their model provided reasonable predictive accuracy and validated the key experimental trend of gravity effects decreasing as tube diameter decreases (commonly referred to as confinement effects).

Particularly relevant to the present study are the works of Lips and Meyer, who investigated flow condensation of R-134a in a smooth, 1488-mm long, 8.38-mm inner diameter tube at multiple orientations between  $-90^\circ$  (vertical downflow) and  $+90^\circ$  (vertical upflow) orientations [91,133]. They provided discussion on influence of body force on parameters including flow regime, heat transfer coefficient, pressure drop, and void fraction, all key design parameters for condensers. In particular, their work noted the strong influence of orientation on condensation pressure drop for

cases with low quality (high liquid content), which diminished as quality was increased in the channel.

A concept of gravity-independent flows is seen in the works of Narain and collaborators, who investigated flow condensation of FC-72 experimentally using a smooth, 700-mm long, 6.6-mm inner diameter tube in vertical downflow orientation. They also performed numerical simulations using a 1-D approach, and later 2-D computational (CFD) simulations [134,135]. Although not comparing results from multiple orientations, this work is important as it indicates flow behavior in a single orientation may be dominated by body-force (gravity driven) or interfacial shear effects depending on key operating conditions including mass velocity and flow quality.

O'Neill *et al.* recently investigated flow condensation of FC-72 in a smooth, 1259.8-mm long, 11.89-mm inner diameter tube in vertical upflow, vertical downflow, and horizontal flow orientations [136,137]. Their work focused on experimental investigation of differences between heat transfer coefficient and liquid film interfacial waves across the three orientations. Conclusions drawn from analysis of experimental results were used to formulate a set of mechanistic criteria, expressed in terms of relevant dimensionless groups, which could be used to determine whether operating conditions could be considered 'gravity-independent' (meaning heat transfer performance would be near-identical for any orientation) or not. Similar to the work of Narain *et al.* [134,135], flows dominated by body force effects were distinguished from those driven primarily by interfacial shear.

Recent advances in computational capabilities have allowed for full 3-D, unsteady, turbulent flow condensation simulations to be run in multiple orientations. Noori Rahim Abadi *et al.* recently investigated flow condensation of R134a inside inclined smooth tubes using ANSYS Fluent [138], which complemented earlier experimental work by Lips and Meyer [91,133]. Their conclusion that orientation effects become negligible at high mass velocities (leading to shear-dominated flows) matches well with conclusions from experimental work and helps validate the physicality of computational simulations for flow condensation.

Although the continuing emergence of computational capabilities is expected to eliminate the need for costly experimental payloads in some cases, computational methods for multiphase flows with phase change are not yet at the point where purely predictive results (with no comparison to experimental results under similar operating conditions) may be accepted with high

confidence. Because of this, continued experimentation is critical to gain further understanding of how body force affects flow condensation, particularly in the micro-gravity environment. It is here NASA's Flow Boiling and Condensation Experiment (FBCE) aims to obtain unique long-duration microgravity flow condensation data collected onboard the International Space Station (ISS).

### **1.3 Objectives of Study**

#### **1.3.1 *Flow Boiling***

This work is part of an ongoing collaboration between Purdue University Boiling and Two-Phase Flow Laboratory (PU-BTPFL) and NASA Glenn Research Center (GRC) whose ultimate goal is development of the Flow Boiling and Condensation Experiment (FBCE) for the International Space Station (ISS). A summary of scientific developments from the project thus far, including key objectives, experimental methodology, analytic approaches, and other relevant works, can be found in a recent summary article [139].

Part of the current study deals with flow boiling and augments prior work dealing with experimental investigation and prediction of key design parameters including heat transfer coefficient [140-143], pressure drop [53,144], and critical heat flux [145-151], with development of a mechanistic model for prediction of frequency and amplitude of DWO induced pressure oscillations evident in vertical upflow boiling with finite inlet quality. Objectives for the study are as follows:

- 1) Determine the contribution of fluid machinery and fluid components on dynamic flow boiling behavior, so as to isolate the influence of physical phenomena that occur independent of fluid machinery and components in use.
- 2) Having isolated transient, physical phenomena of interest, perform parametric evaluation of trends relative to changes in key parameters such as mass velocity, inlet conditions, heat flux, and orientation.
- 3) Use transient pressure signals and flow visualization images to provide a comprehensive characterization of DWOs along with a physically consistent explanation for their manifestation in vertical upflow boiling.

- 4) Analyze a large database of vertical upflow cases exhibiting DWO behavior to better draw conclusions regarding trends for frequency and amplitude of DWO induced pressure oscillations.
- 5) Present analysis regarding the viability of reconstructing transient pressure results using detected frequency and amplitude, with the aim of better informing DWO model development.
- 6) Use key findings from experimental results as a basis from which to begin mechanistic modeling of the DWO phenomenon as observed in the present dataset, with the goal of creating a model capable of providing valid predictions for frequency and amplitude of DWO induced oscillations for a wide range of operating conditions.
- 7) Evaluate model performance using experimental results to determine strengths and weaknesses of the modeling approach, identifying key goals for future analysis work.

### **1.3.2** *Flow Condensation*

Another part of the current study deals with condensation and augments prior work dealing with computational prediction of flow condensation [152-154] and correlation of pressure drop and heat transfer coefficient for condensing flows using a large database from available literature [155,156] with presentation of dynamic behavior, flow regime identification strategies, and new heat transfer results. Key goals for the present work are:

- 1) Analysis of transient pressure signals throughout the flow loop to determine potential impact on flow condensation dynamic behavior within the test section.
- 2) Determination of key characteristics of dynamic behavior, including frequency and amplitude of peak oscillatory modes, which may then be evaluated over different ranges of key operating parameters to determine parametric trends.
- 3) Relation of key signal characteristics to physical behavior observed through capture of flow visualization image sequences.
- 4) Qualitatively present the competing influences of body force and flow inertia on condensate liquid film behavior using select flow visualization image sequences.
- 5) Present new methods for determining flow regime in horizontal and vertical upflow orientations using only temperature and pressure measurements.

- 6) Provide validation of new flow regime identification methodology through comparison with flow regime predictions from popular regime maps available in the literature.
- 7) Presentation of a data reduction method for determining flow condensation heat transfer data. This method includes uncertainty analysis and will also be used to process data gathered during the ISS experiments.
- 8) Interpretation of key physical trends observable for changes in values of heat transfer coefficient, with special attention paid to the influence of body force.
- 9) Evaluation of the Separated Flow Model and commonly used condensation heat transfer coefficient correlations using the new dataset.

## 2. EXPERIMENTAL METHODS

### 2.1 Flow Boiling

#### 2.1.1 Flow Boiling Module

As a part of the FBCE designed towards eventual use on the ISS, the Flow Boiling Module (FBM) is a test section instrumented to allow capture of high-speed photography through transparent polycarbonate sidewalls while simultaneously allowing detailed flow boiling heat transfer and pressure drop measurements to be made over a heated length composed of copper top and bottom walls with resistive heaters soldered to their backs and thermocouples imbedded. Figure 2.1(a) illustrates how the FBM is constructed by clamping three pieces of transparent polycarbonate plastic (Lexan) between two aluminum support plates. Although Fig. 2.1(a) indicates two o-rings are used to seal the fluid path, only one is actually used due to difficulties in assembly with two. Figure 2.1(b) shows the middle polycarbonate piece is milled out to create a rectangular 2.5-mm wide, 5-mm tall flow channel with a development length of 327.9 mm followed by a heated length of 114.6 mm, constructed by recessing oxygen-free copper slabs flush with the channel's top and bottom walls. Each copper slab has six 4.5-mm wide, 16.4-mm long, 188- $\Omega$  resistive heaters soldered to their backs, evenly spaced with small gaps between successive heaters to allow temperature measurements to be made using type-E thermocouples. Heat flux to each wall can be controlled separately, although the present study deals only with cases where heat is supplied evenly to both heated walls.

Figure 2.1(c) shows images of the actual FBM with key points identified. The top view shows the five pressure measurement points, comprised of three along the development length, one upstream of the heated length, and one downstream of the heated length. Figure 2.1(c) also illustrates the location of inlet and outlet fluid temperature measurements, performed using type-E thermocouples inserted directly into the flow.

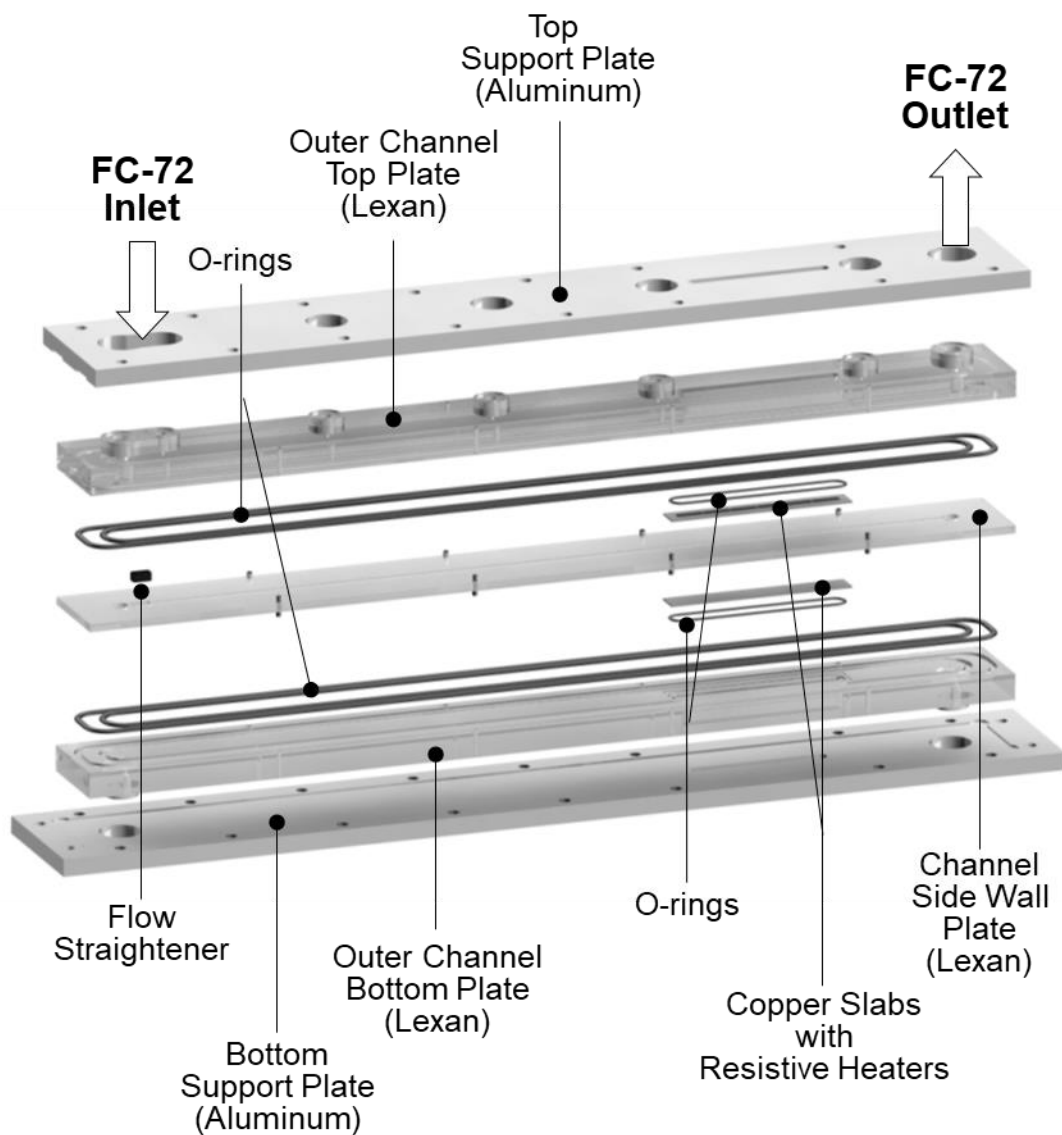
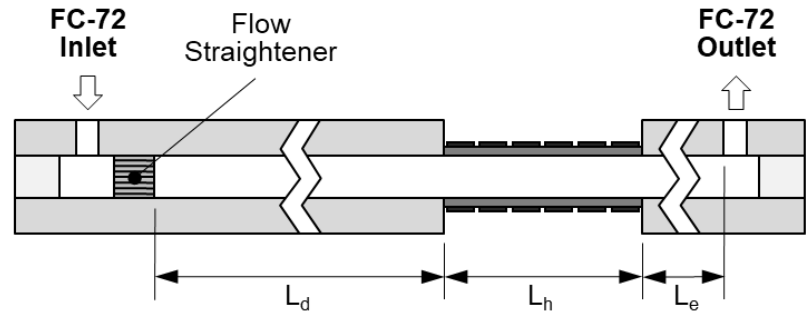
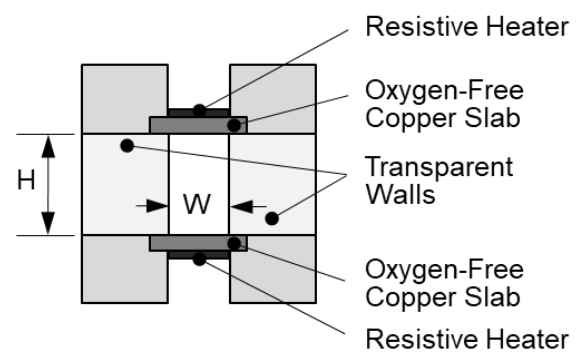


Figure 2.1: (a) Exploded view of the flow boiling module (FBM). (b) Schematics of FBM fluid path and heated wall temperature measurement locations. (c) Photos of FBM with key components labeled.



Development Length:  $L_d = 327.9$  mm  
 Heated Length:  $L_h = 114.6$  mm  
 Exit Length:  $L_e = 60.9$  mm



Channel Height:  $H = 5.0$  mm  
 Channel Width:  $W = 2.5$  mm

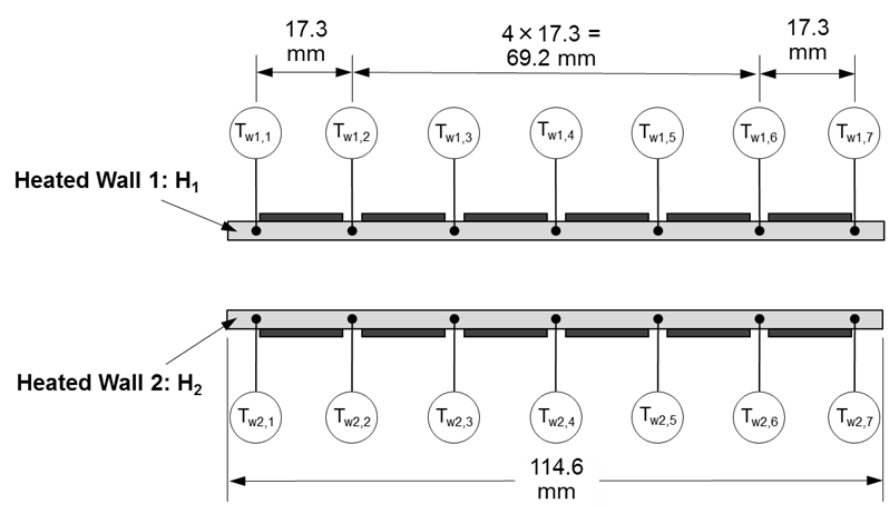


Figure 2.1 (b).

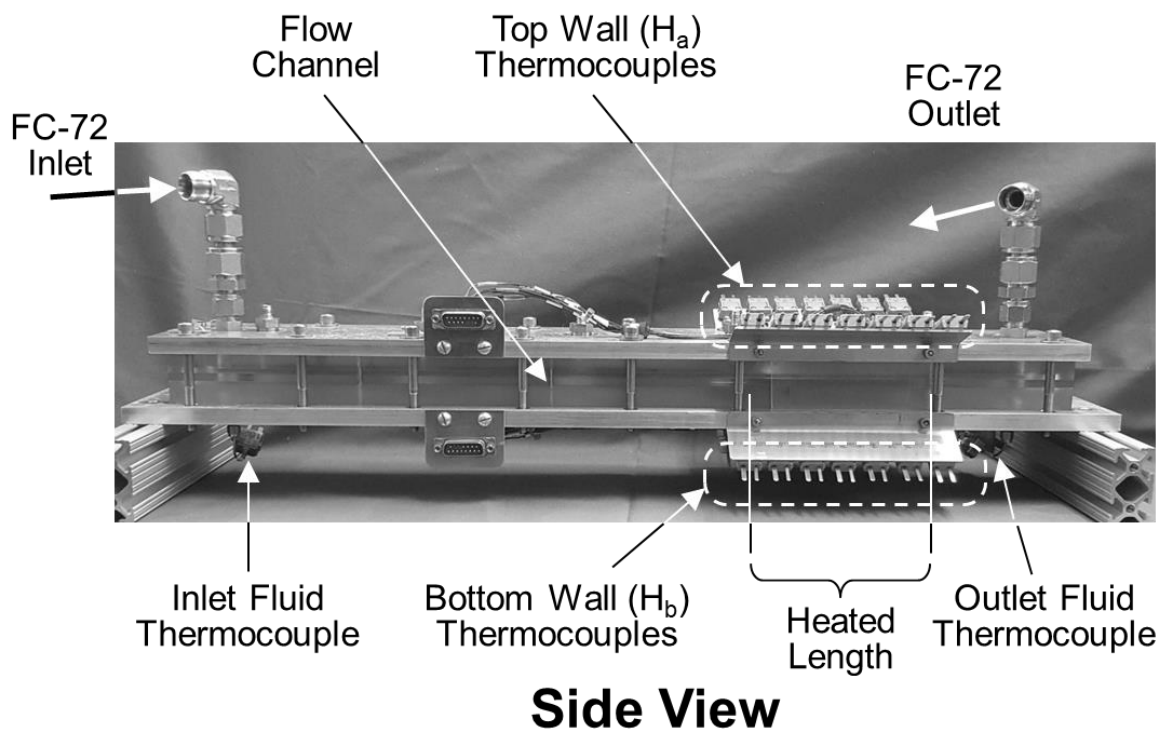
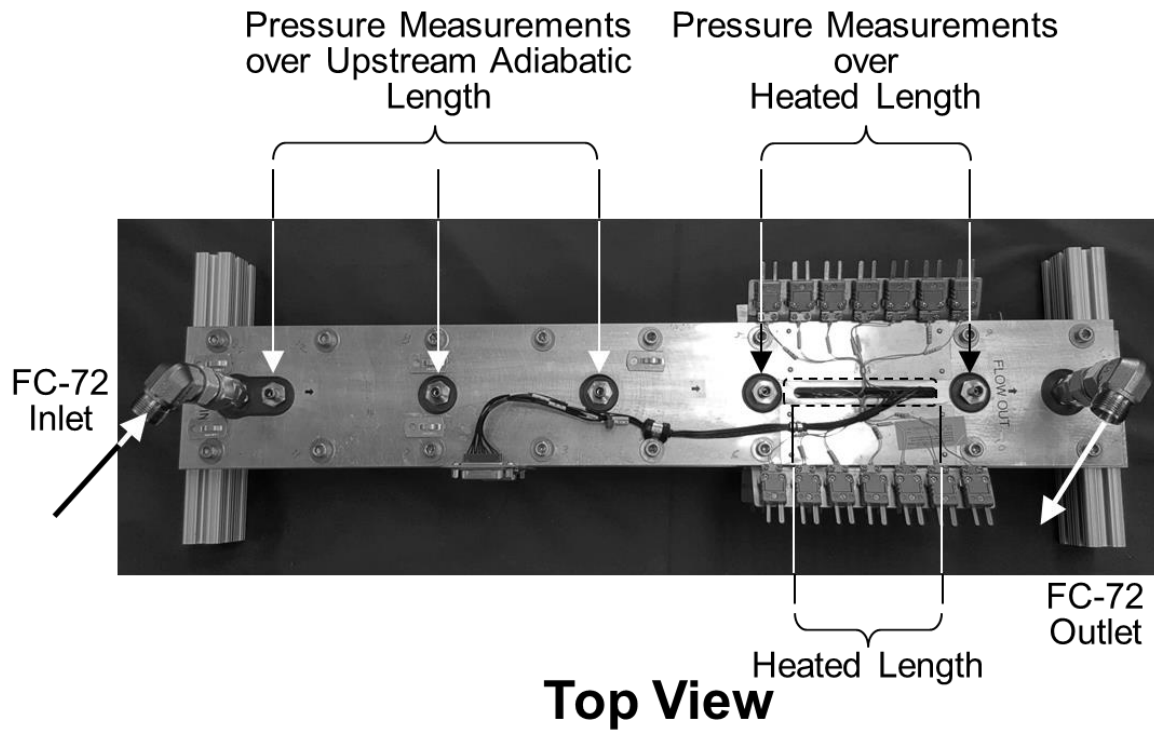


Figure 2.1 (c).

### 2.1.2 *Flow Boiling Test Loops*

The present study utilizes results from two separate sets of flow boiling experiments performed over a two-year period (2015 and 2016), both performed with FBM as test module, but using different peripheral equipment.

Figures 2.2(a) – 2.2(d) provide both schematics and photos of hardware used in each respective set of experiments. In both cases, an Ismatech MCP-z magnetically-coupled gear pump is used to circulate the working fluid, FC-72, through the system. Exiting the pump, the fluid passes through a filter to remove any particulates before entering a turbine flow meter for flow rate measurement. After the flow meter, the fluid enters the bulk heater(s) where power is supplied to set the fluid's thermodynamic conditions before entering the FBM.

In both sets of experiments wall heat flux in the flow boiling module is controlled using the FBM heater control module, which also ensures the module's safety by automatically disabling the power supply should any of the heated wall temperatures exceed 125°C (occurring only during the CHF transient). Upon exiting the test section, the fluid passes through a condenser to return to a subcooled, single-phase liquid state before entering the pump.

Key differences to note between the two systems are:

- 1) The use of two small Cast-X bulk heaters in Fig. 2.2(a) versus one larger Cast-X bulk heater in Fig. 2.2(c).
- 2) A liquid-to-liquid heat exchanger is used to condense the fluid in Fig. 2.2(a), versus a liquid-to-air heat exchanger in Fig. 2.2(c).
- 3) Use of a reservoir in Fig. 2.2(a) versus an accumulator in Fig. 2.2(c).

It is also worth noting that the system used in year 2 (2016) and depicted schematically in Fig. 2.2(c) contains a far greater number of pressure transducers throughout the loop to better assess the impact of different system components of flow dynamic behavior.

Data throughout both systems are obtained with an NI SCXI-1000 data acquisition system controlled by a LabVIEW code. Pressure transducers are sampled at 200 Hz, allowing high fidelity transient analysis of pressure signals.

Images are captured at a rate of 2000 frames per second (fps) with a pixel resolution of 2040 x 156 spanning the total 114.6-mm heated length. Illumination is provided from the opposite side of the flow channel by blue LEDs, with light passing through a light shaping diffuser (LSD) to enhance illumination uniformity.

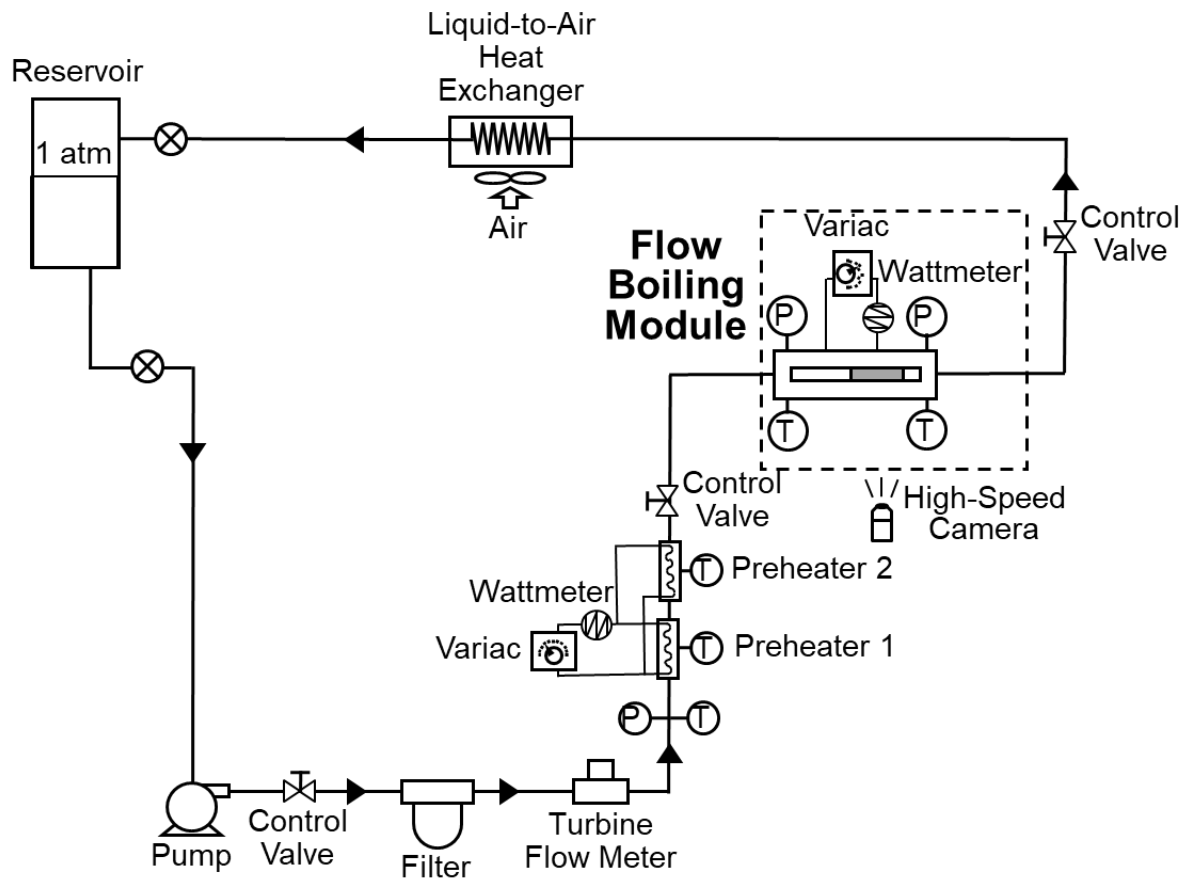


Figure 2.2: (a) Schematic and (b) photos of year 1 (2015) experimental flow boiling facility, and (c) schematic and (d) photo of year 2 (2016) experimental flow boiling facility.

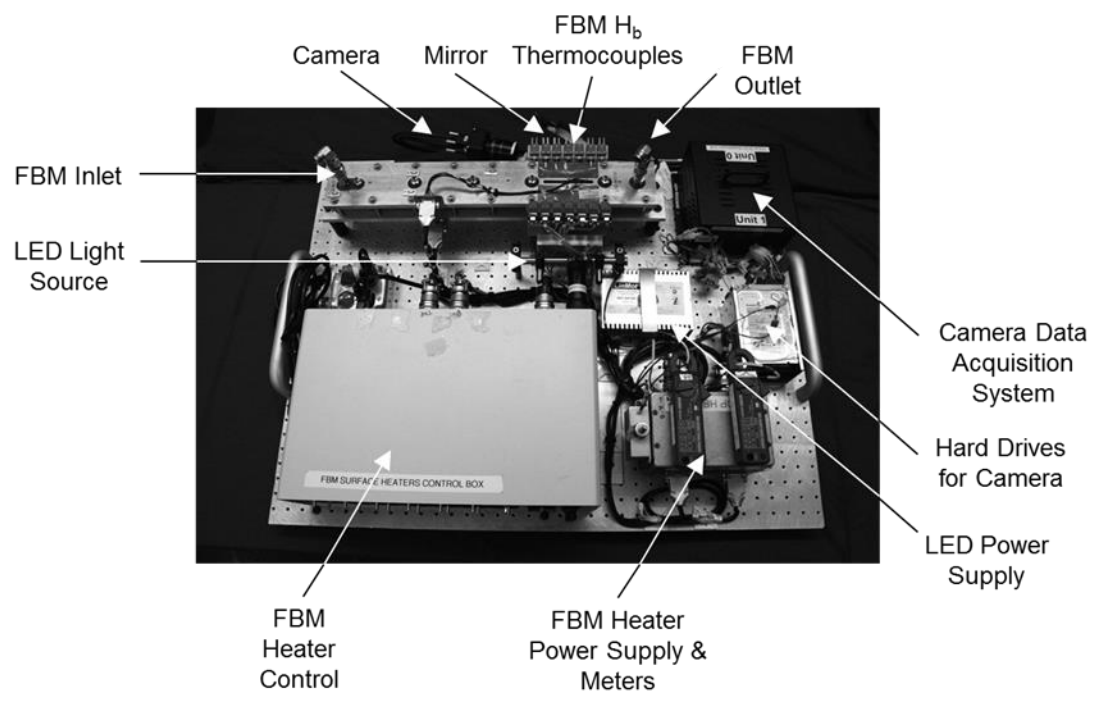
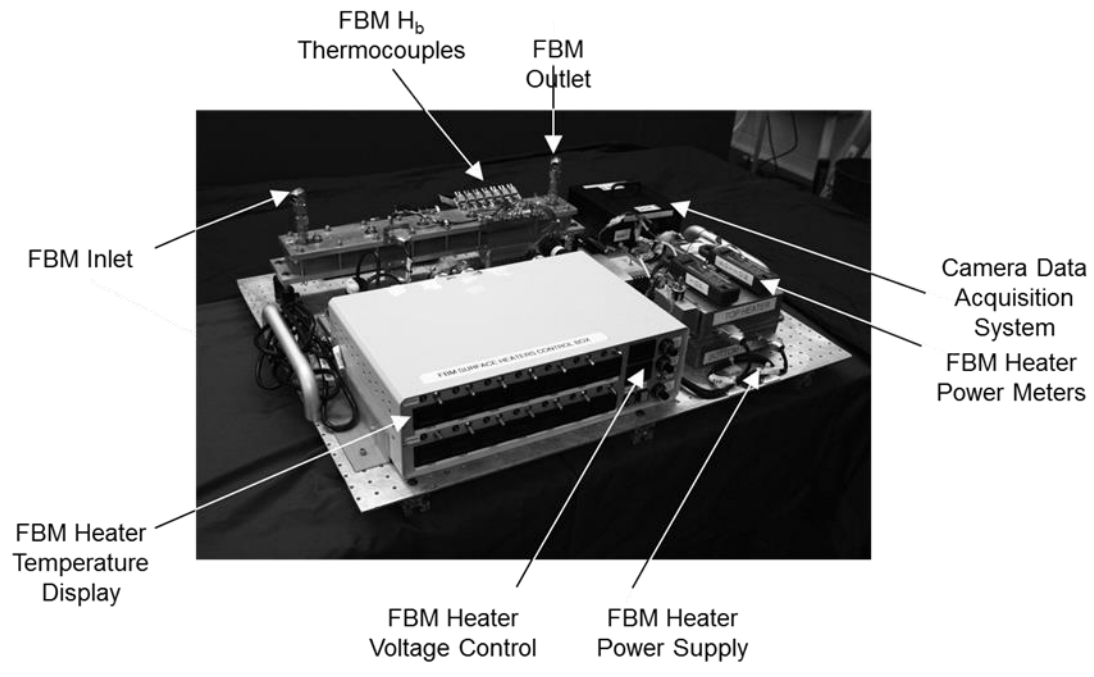


Figure 2.2 (b).

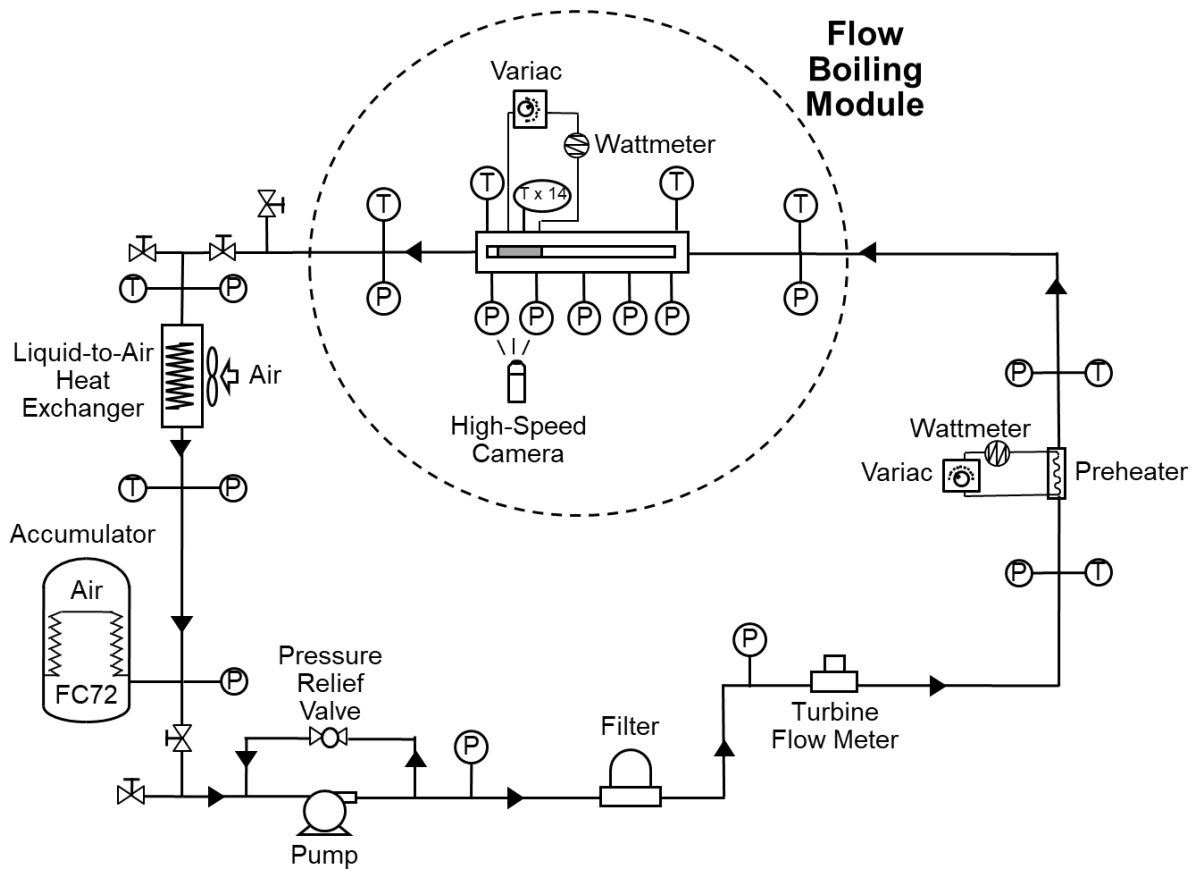


Figure 2.2 (c).

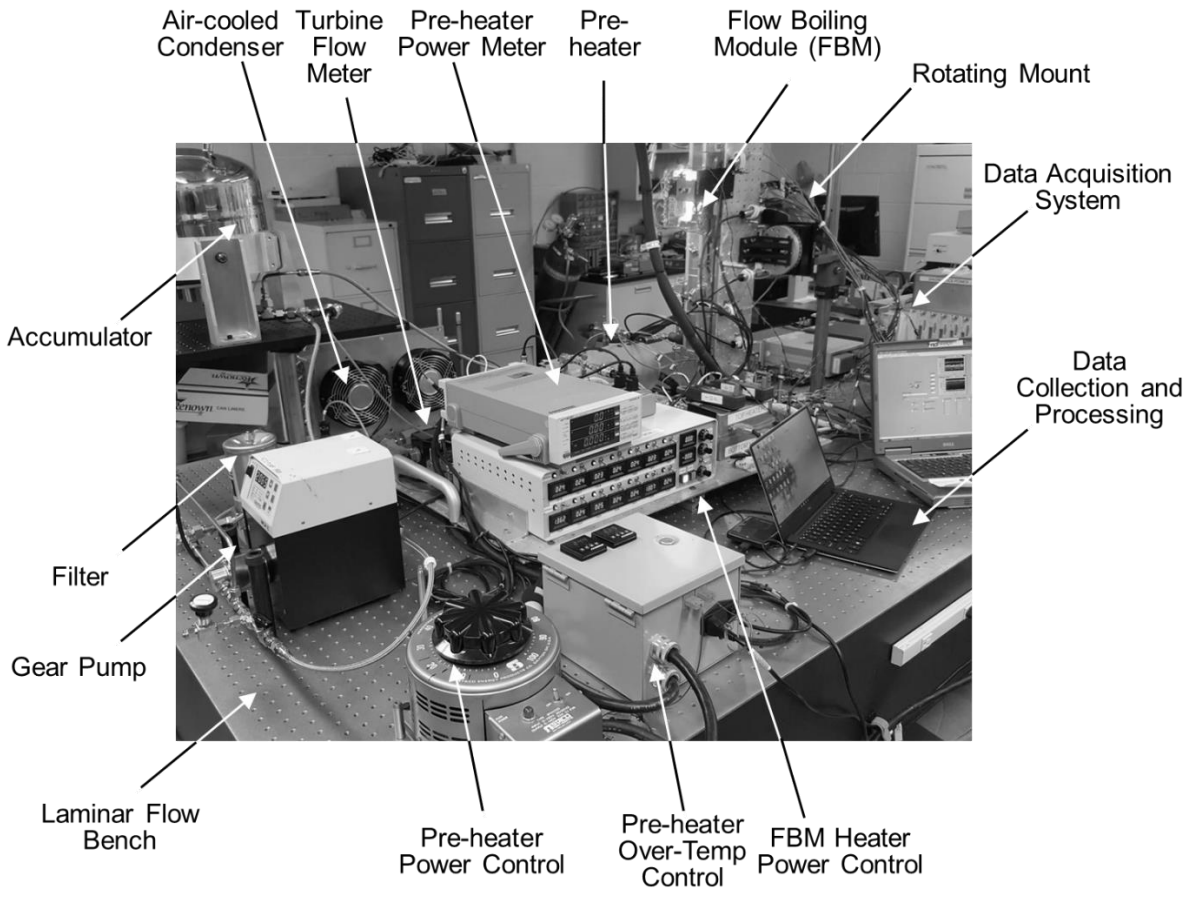


Figure 2.2 (d).

### 2.1.3 Operating Conditions and Measurement Uncertainty

Target operating conditions for each set of experiments conducted can be found in Tables 2.1 and 2.2, corresponding to testing performed during years 1 and 2, respectively. The subset of operating conditions used for DWO analysis and modeling is provided in Table 2.3, and corresponds to the full range of operating conditions (mass velocities  $G$ , inlet qualities  $x_{e,in}$ , heat fluxes  $q''$ , and inlet pressures  $P_{in}$ ) for which DWOs are observed in vertical upflow orientation. Only vertical upflow is selected for DWO investigation and modeling in later sections to limit analysis to a commonly employed flow boiling orientation for Earth-based systems.

It is important to note that negative inlet quality relates to inlet subcooling by the relationship

$$x_{e,in} = \frac{P_{wr_{PH}} - \dot{m} c_{p,f} (T_{FC,sat} - T_{PH,in})}{\dot{m} h_{fg}}, \quad (2.1)$$

where  $P_{wr_{PH}}$  is the power supplied by the pre-heater,  $\dot{m}$  is the mass flow rate,  $T_{FC,sat}$  and  $T_{PH,in}$  are saturation and inlet fluid temperatures at the preheater, respectively, and  $c_{p,f}$  and  $h_{fg}$  are, respectively, the specific heat and latent heat of vaporization of the fluid. Negative inlet quality is used instead of subcooling to better represent the combined influence of transient pressure and mass velocity changes within the system.

Tests are initiated by setting pump speed and pre-heater power to achieve the desired inlet conditions. After monitoring temperature and pressure signals in the LabVIEW code to confirm steady state has been reached, power to the heated walls in the FBM is turned on, and heat flux is increased in small increments. After each increment, wall temperatures are monitored to determine when steady state is achieved, after which data are captured for an additional 30-60 s. In the present study, steady state is achieved when wall and fluid temperatures cease to change over a period of 15 s. Heated wall power is increased until CHF is encountered.

Type-E thermocouples with an accuracy of  $\pm 0.5^\circ\text{C}$  are used to measure fluid and heated wall temperatures throughout the facility. Pressure measurements throughout the flow loop are made using pressure transducers with an accuracy of  $\pm 0.1\%$ , which corresponds to an accuracy for all pressure drop measurements of  $\pm 0.2\%$ . Pressure transducers used in the present study possess a mechanical response time of less than 1 ms, allowing the signal to be sampled at 200 Hz (once every 0.005 s). The turbine flow meter has an accuracy of  $\pm 0.1\%$ . The wall heat input is measured with an accuracy of  $\pm 0.5$  W.

Table 2.1: Test Matrix for Year 1.

Mass Velocity, $G$ [kg/m <sup>2</sup> s]	Inlet Quality, $x_{e,in}$							
	0.01	0.05	0.10	0.15	0.20	0.30	0.40	0.60
~ 200	√	√	√	√	√	√	√	√
~ 400	√	√	√	√	√	√	√	√
~ 800	√	√	√	√	√	√	√	NA
~ 1200	√	√	√	√	√	NA	NA	NA
~ 1600	√	√	√	NA	NA	NA	NA	NA
~ 2000	√	NA						

Table 2.2: Test Matrix for Year 2.

Mass Velocity, $G$ [kg/m <sup>2</sup> s]	Inlet Condition			
	$T_{sub} = -40^{\circ}\text{C}$	$x_{e,in} = 0.00$	$x_{e,in} = 0.10$	$x_{e,in} = 0.20$
~ 200	√	√	√	√
~ 400	√	√	√	√
~ 800	√	√	√	√
~ 1600	√	NA	NA	NA
~ 2400	√	NA	NA	NA

Table 2.3: Operating conditions used for DWO analysis.

Experiment Subset	$G$ [kg/m <sup>2</sup> s]	$x_{e,in}$	$q''$ [W/cm <sup>2</sup> ]	$P_{in}$ [kPa]	Datapoints
<b>Year 1 (2015)</b>	190.7 – 1978.9	0.00 – 0.69	1.0 – 22.5	109.7 – 190.3	192
<b>Year 2 (2016)</b>	199.5 – 808.8	0.00 – 0.18	0.0 – 28.3	130.7 – 229.3	44
<b>Overall</b>	190.7 – 1978.9	0.00 – 0.69	0.0 – 28.3	109.7 – 229.3	236

## 2.2 Flow Condensation

Due to the necessary presence of a second fluid acting as coolant against which condensation may take place, design of test modules for flow condensation experience a strong trade between detailed heat transfer measurement and capture of high speed flow visualization images. To overcome this limitation, the present study employs two test sections, one designed specifically for heat transfer measurements (Condensation Module for Heat Transfer measurements, CM-HT), and one for capture of flow visualization images (Condensation Module for Flow Visualization, CM-FV). These modules are described in detail below.

### 2.2.1 *Condensation Module for Heat Transfer Measurements*

As its name implies, the CM-HT was designed for the express purpose of gathering detailed flow condensation heat transfer measurements. Figure 2.3 (a) provides schematics of the module, illustrating its construction as a counterflow heat exchanger created by clamping a stainless-steel tube inside two pieces of polycarbonate with the working fluid, FC-72, condensing along the inner 7.12-mm i.d. tube and cooling water flowing through the outer annulus between the 7.94-mm o.d. tube and the 12.7-mm i.d. channel created by the polycarbonate. Both FC-72 and water flows pass through honeycomb flow straighteners before proceeding through the channel, and short lengths of insulation are present on the outside of the stainless-steel tube near the channel inlet and outlet to allow flow to develop before condensation takes place.

The total condensation length is 574.55 mm, and direct measurement of fluid temperature and pressure is made at the start and end of the length (for both FC-72 and water flows). Both water and tube wall temperatures are made at numerous locations along the channel length, with water measurements made at each axial location by direct immersion in the water flow at two diametrically opposed ( $180^\circ$  separation) locations, and tube wall temperatures at each axial location made at three equally spaced ( $120^\circ$  separation) locations by thermocouples brazed directly to the tube surface. Measurement locations are concentrated towards the FC-72 inlet to allow detailed information to be gathered in the inlet region (where the condensate film is thin and the condensation heat transfer coefficient changes quickly with axial position), with wider spacing near the FC-72 exit region (where the condensate film is thicker and condensation heat transfer coefficient commonly exhibits less dependence on axial position).

Figure 2.3 (b) shows a 3-D CAD drawing of the module, prepared for packaging along other modules as part of the FBCE payload intended for use on the ISS. Key points are identified, including water and FC-72 inlet and outlets, thermocouple insertion points, fluid connection points (for interfacing with other modules), and waterside pressure transducers. More so than the schematics presented in Fig. 2.3 (a), the module's construction as a stainless-steel tube suspended between two polycarbonate pieces clamped together by aluminum support plates is clearly apparent here.

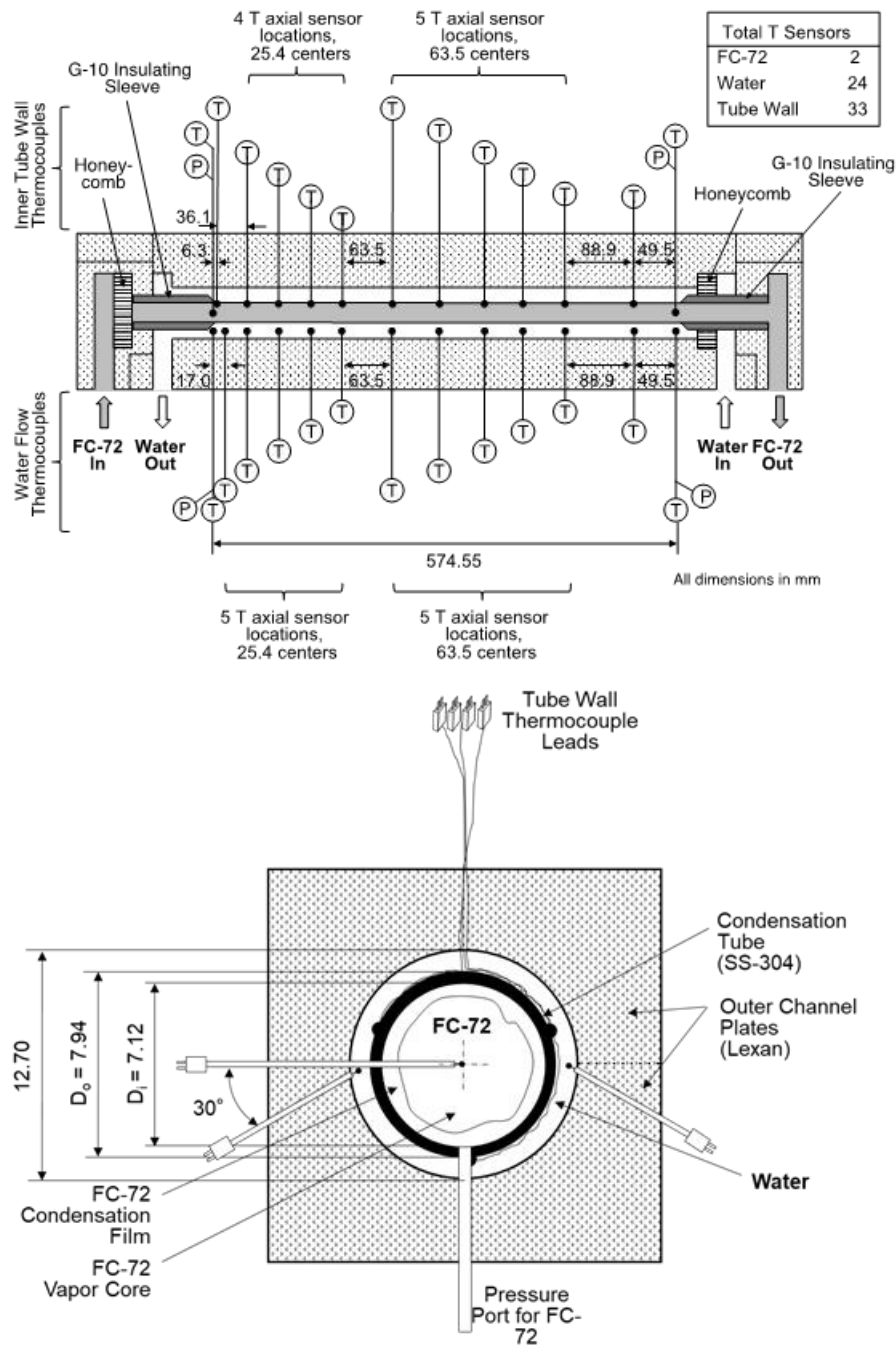


Figure 2.3: Condensation Module for Heat Transfer Measurements (CM-HT) (a) schematics and (b) 3-D drawing, and Condensation Module for Flow Visualization (CM-FV) (c) schematics and (d) 3-D drawing.

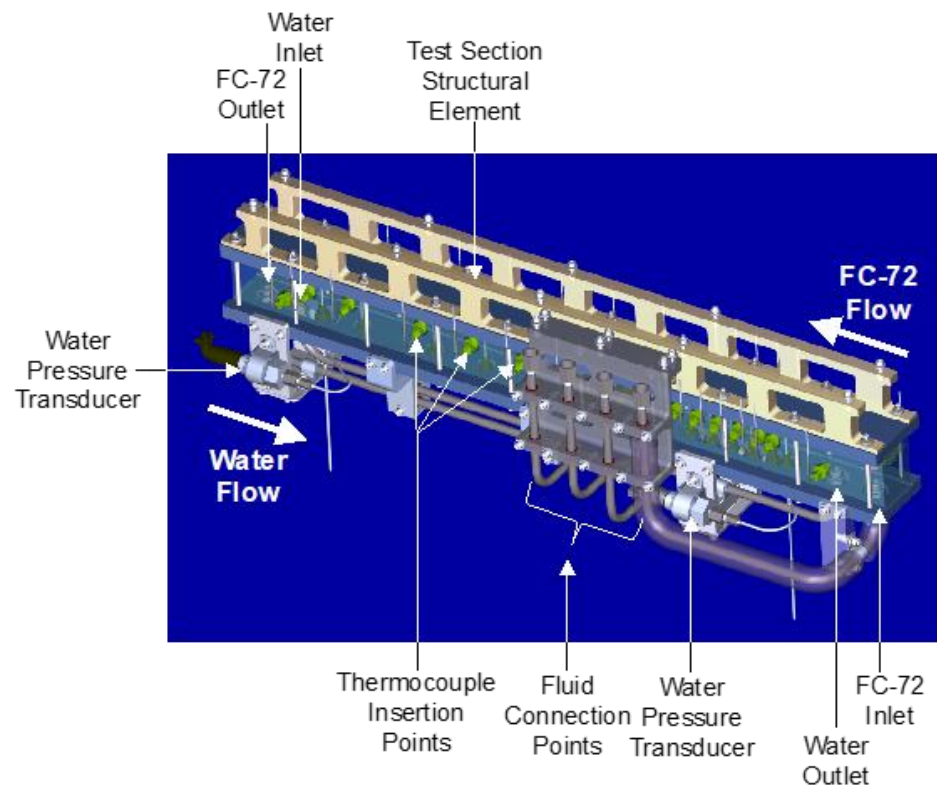


Figure 2.3 (b).

### 2.2.2 *Condensation Module for Flow Visualization*

Similar to CM-HT, CM-FV is constructed as a counterflow heat exchanger with FC-72 as the working fluid and water acting as coolant. Different from CM-HT, however, is the presence of FC-72 in the annular region, condensing along the outside of the stainless-steel tube through which water now flows as shown in Fig. 2.3 (c). This is done to allow easy optical access to the condensate film as it forms and travels along the outside of the tube.

It should be noted that both stainless-steel tube and polycarbonate channel cross-sectional dimensions have been altered from those in CM-HT, with water now flowing through a 5.23-mm i.d. tube and FC-72 condensing along the same tube's 6.04-mm outer diameter as it flows through the annular region between tube o.d. and the 12.2-mm square polycarbonate channel walls. These differences in dimension from CM-HT are implemented to match hydraulic diameters of the two condensate flow paths, with the hydraulic diameter of the annular region in CM-FV equivalent to that of the 7.12-mm i.d. tube along which FC-72 condenses in CM-HT.

As shown in Fig. 2.3 (c), optical access to the condensate film is provided in three locations along the test module, each roughly 55.9-mm in length, with the first beginning at the start of the 587.88-mm condensation length, the second centered on the center of the condensation length, and the third ending at the end of the condensation length.

In order to avoid disturbing FC-72 as it condenses, temperature and pressure measurements of the working fluid are limited to inlet and outlet locations. On the waterside, however, in addition to inlet and outlet temperature and pressure measurements made by direct immersion, wall temperatures are also recorded at five axial positions within the stainless-steel tube. These positions correspond to just upstream and downstream of the first and third imaging location as well as the center of the second imaging location. Each axial measurement location has three measurement points (created by brazing thermocouples to the heated walls) separated by 90°. Thermocouple wires are routed along the channel to the nearest exit (inlet or outlet) where they are removed from the flow through appropriate fittings.

Similar to Fig. 2.3 (b), Fig. 2.3 (d) shows a 3-D CAD drawing of CM-FV with key features identified. Of particular note in this subfigure are the three sets of LEDs used to provide backlighting for images, as well as the use of mirrors to direct the field of view of each camera towards the condensate film.

High speed images captured during CM-FV tests are performed at two speeds (depending on flow rate of condensate): 2000 frames per second (fps) with pixel resolution of 2040 x 174, and 4000 fps with pixel resolution of 2040 x 81.

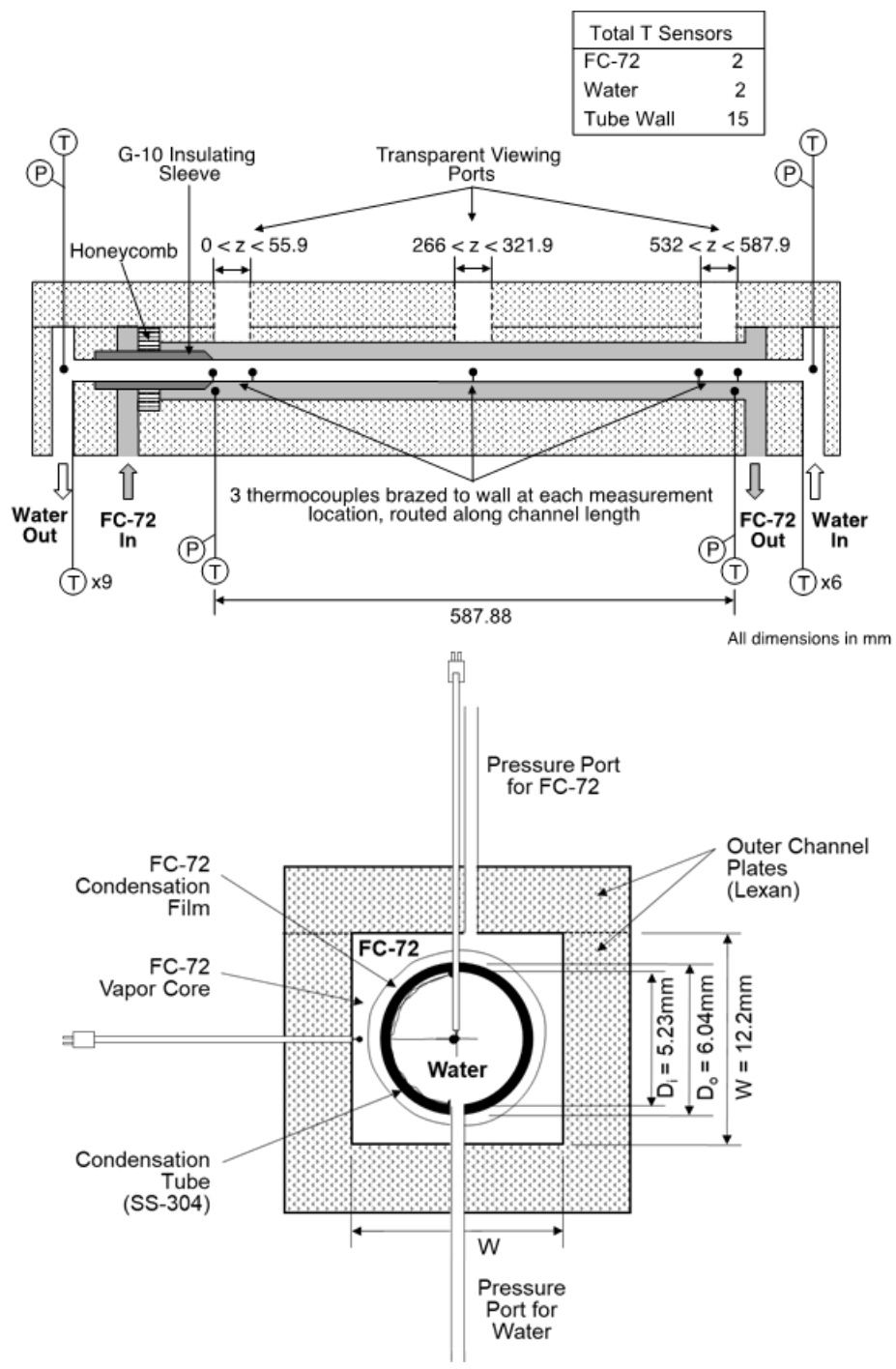


Figure 2.3 (c).

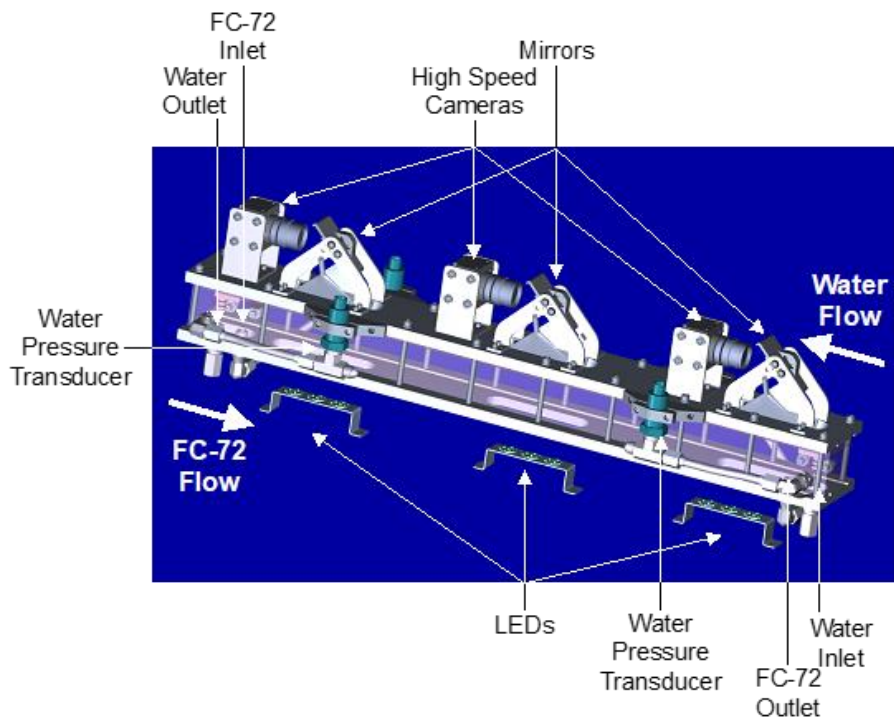


Figure 2.3 (d).

### 2.2.3 Condensation Experimental Facility

The experimental facility used for the present tests was developed as part of NASA's ongoing FBCE and intended to serve as a brass-board system useful for testing of flight hardware prototypes. Figures 2.4 (a) and 2.4 (b) provide schematics and images of the facility, respectively, with key components labeled.

Figure 2.4 (a) shows the working fluid, dielectric FC-72, is circulated within the primary loop by use of a magnetically coupled Micropump gear pump. Flow first passes through a 5-micron filter to remove any particulates entrained, then progresses through a Coriolis flow meter used to measure mass flow rate. Exiting the flow meter the fluid enters the bulk heater, used to set thermodynamic state at the inlet of the test section.

The bulk heater used in the current experiments is configured to reflect the manner in which it will be utilized in the final ISS experiments. Two modes of operation are possible, one with PID control of bulk heater metal temperature and one with constant power provided to the bulk heater. Cases with two-phase (saturated mixture) inlet conditions are run in constant power mode to allow calculation of thermodynamic quality at the bulk heater outlet without the need to integrate a power

curve in time (necessary for cases with PID temperature control). Cases with superheated inlet conditions are run in temperature control mode, with power supplied to the bulk heater varied to maintain a set-point temperature measured within the bulk heater wall.

Continuing past the bulk heater, the working fluid passes through a short insulated length and enters the test section. As mentioned when discussing each respective module in the preceding sections, flow through the test section is condensed by use of cooling water supplied in counterflow configuration. Figure 2.4 (a) illustrates cooling water is conditioned and supplied through use of a secondary loop containing a water conditioning system and multiple digital flow controllers. Water flow for both the test section and secondary condenser (used to ensure FC-72 is returned to a subcooled, single phase liquid state prior to returning to the pump) is supplied by a water conditioning unit, which includes a Merlin M33 chiller, pump, and filter. Both flow controllers are computer controlled and allow precise control of water flow rates through both the test section and the secondary condenser.

Upon exiting the test section, the fluid enters the secondary condenser. This unit is a custom built, liquid-to-liquid, helical tube-in-tube heat exchanger operated in counterflow configuration, and represents a prototype for the condenser to be used during ISS experiments. Exiting the condenser, the fluid passes an accumulator (used to accommodate volume changes within the loop due to phase change) prior to returning to the pump.

Similar to the condenser, the accumulator is a custom build prototype of the unit to be used during ISS experiments. Important to note is the presence of a small pump and solenoid valve on the air side of the accumulator, allowing active system pressure adjustment during experiments and evaluation of parametric trends relating to changes in system pressure during data analysis.

It should be noted that all primary loop hardware (including accumulator airside components) are mounted on a rotating bench-top, shown in Fig. 2.4 (b). This, coupled with the connection of water lines through flexible tubing, allows for easy transition between operating orientations during testing.

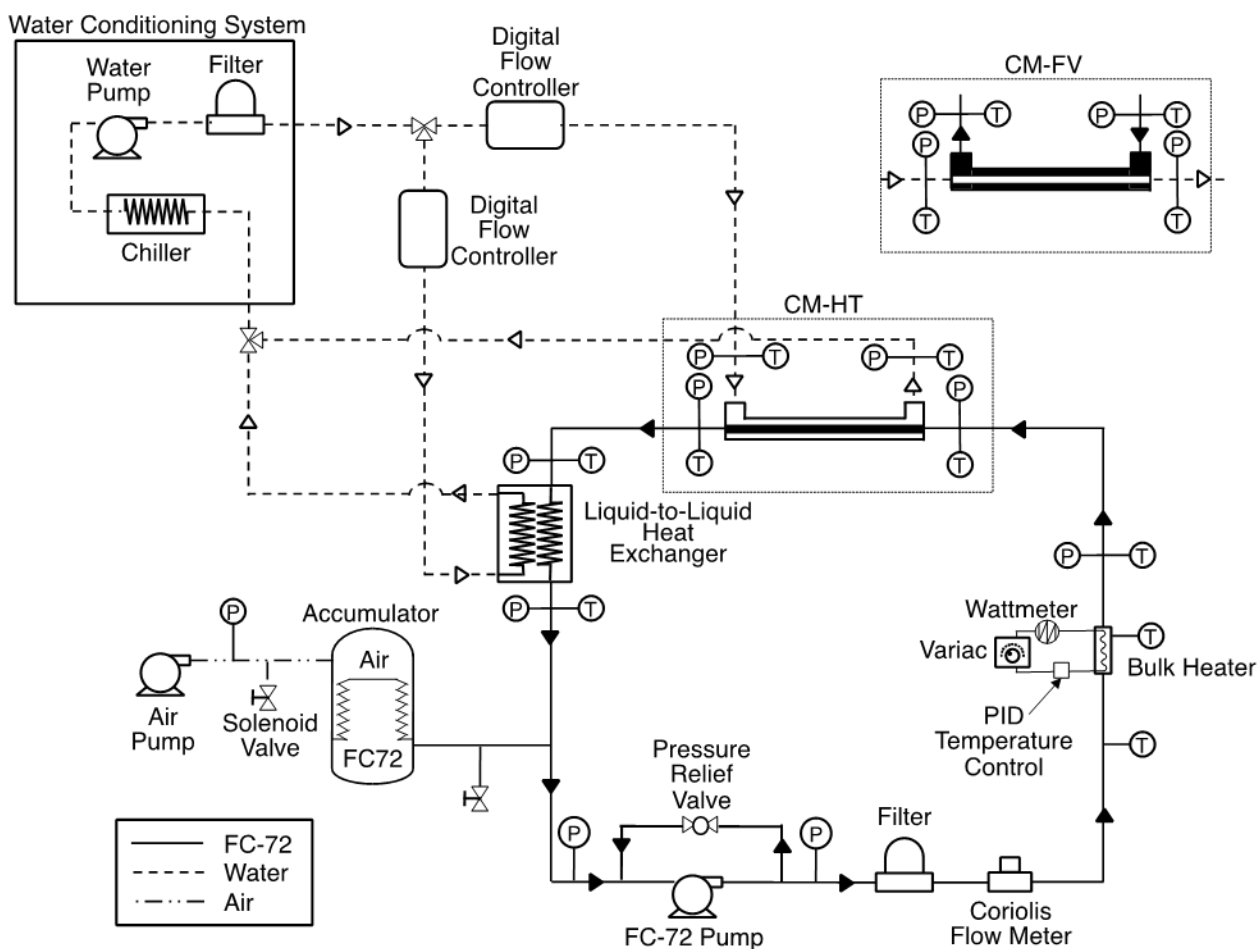


Figure 2.4: (a) Schematic of flow loop used in condensation portion of current study, and (b) photos of facility with key components identified.

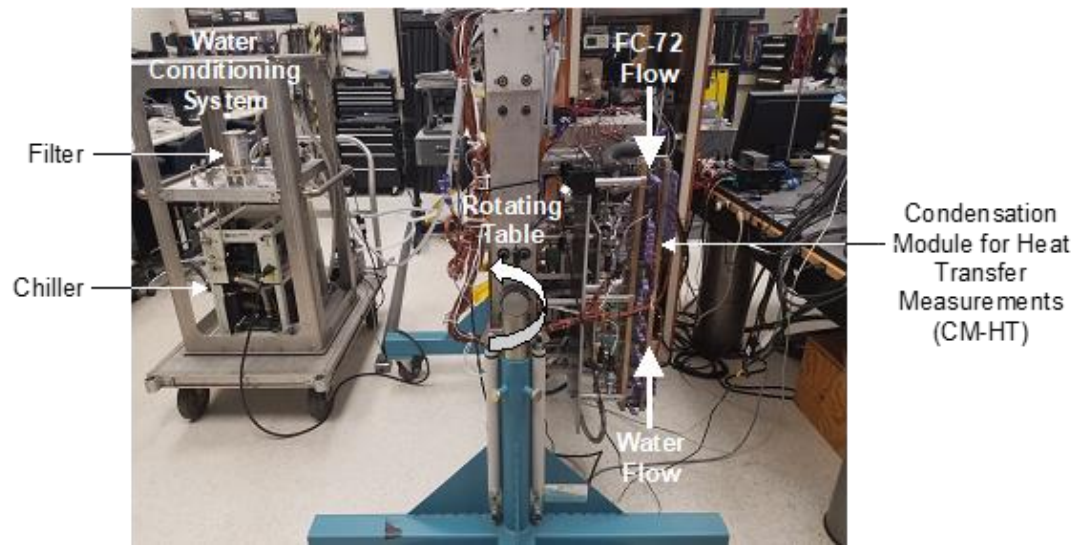
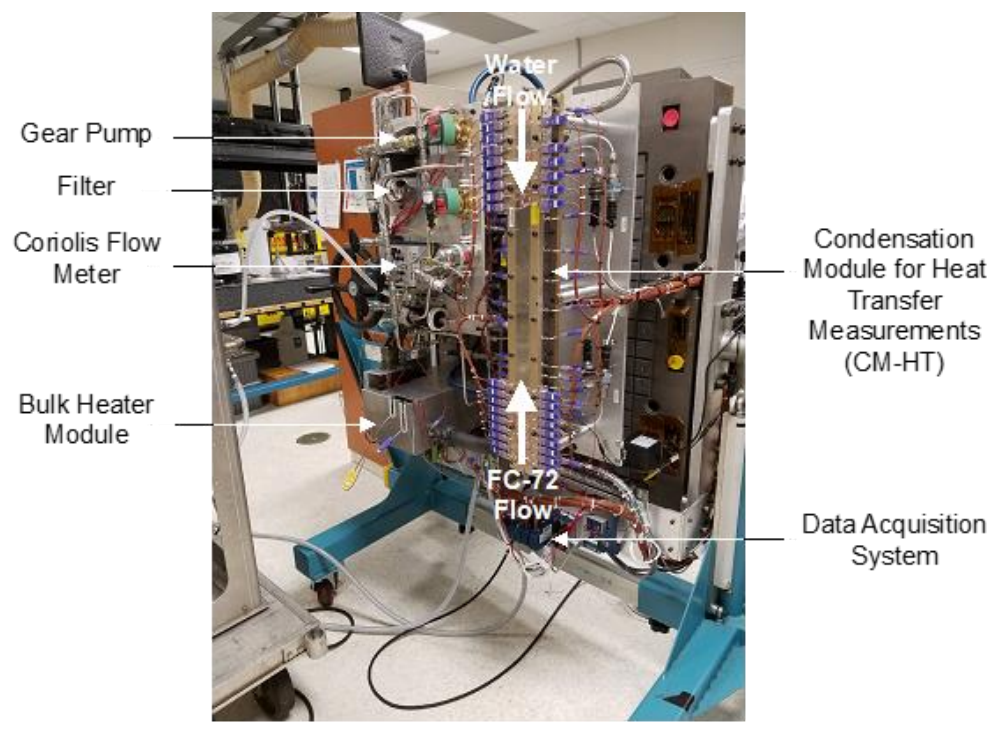


Figure 2.4 (b).

### 2.2.4 Operating Conditions, Operating Procedure, and Measurement Uncertainty

Operating conditions for the current set of tests are selected to match those outlined in NASA's Science Requirements Document for FBCE, intended to allow for characterization of key hardware under relevant operating conditions as well as generation of a database of 1-g results which may be compared to microgravity data. Table 2.4 outlines target operating conditions for the current set of experiments, where, for each FC-72 mass velocity, every combination of water mass velocity, operating pressure, and inlet quality is tested. It should be noted that only results corresponding to the lower pressure level (130 kPa) in table 2.4 are used for analysis of flow regimes and heat transfer results. Additionally, every combination of operating conditions is tested in vertical upflow, vertical downflow, and horizontal flow orientations, allowing investigation of body force effects on flow behavior. Overall, tests conducted across all three orientations include 57 cases in vertical upflow, 57 cases in vertical downflow, and 69 cases in horizontal flow, for a total of 183 data points, encompassing mass velocities of  $G_{FC} = 40.0 - 362.1 \text{ kg/m}^2\text{s}$  and  $G_{H2O} = 64.6 - 388.8 \text{ kg/m}^2\text{s}$ , module FC-72 inlet pressure  $P_{in} = 126.3 - 164.3 \text{ kPa}$ , bulk heater power  $P_{WR_{BH}} = 199.7 - 1578.0 \text{ W}$ , inlet quality  $x_{e,in} = 0.01 - 1.22$ , and exit quality  $x_{e,out} = -0.78 - 0.47$ . It should be noted here that values of inlet and exit quality greater than 1.0 and less than 0 refer to superheated and subcooled conditions, respectively. They are calculated for FC-72 according to the expressions

$$x_{e,in} = \frac{P_{WR_{BH}} - \dot{m}_{FC} c_{p,f,FC} (T_{FC,sat} - T_{BH,in})}{\dot{m}_{FC} h_{fg,FC}}, \quad (2.2)$$

and

$$x_{e,out} = \frac{P_{WR_{BH}} - \dot{m}_{FC} c_{p,f,FC} (T_{FC,sat} - T_{BH,in}) - \dot{m}_{H2O} c_{p,f,H2O} (T_{H2O,out} - T_{H2O,in})}{\dot{m}_{FC} h_{fg,FC}}, \quad (2.3)$$

where  $P_{WR_{BH}}$ ,  $\dot{m}$ ,  $c_p$ , and  $h_{fg}$  are, respectively, the power supplied to FC-72 by the bulk heater, fluid mass flow rate, liquid specific heat, and enthalpy of vaporization. All fluid properties for each phase are evaluated at local pressures.

It should be noted here that for cases with superheated inlet conditions, inlet quality is calculated directly based on measured temperature and pressure at the module inlet. For cases with saturated mixture inlet conditions, Eq. (2.2) is evaluated after adjusting power supplied by the bulk heater  $P_{WR_{BH}}$  to account for heat loss.

Tests are conducted by setting FC-72 flow rate, water flow rate, and bulk heater power to levels necessary to achieve the desired flow rates and inlet quality in the test section. Pressure at the test section inlet is adjusted using the pump and valve on the airside of the accumulator. Multiple minor adjustments to all parameters are necessary, as changes to any one parameter would

alter others. Once desired test conditions are reached, the system is allowed to sit for 3-5 minutes to ensure conditions are steady and no slow transients are present which may affect interpretation of results. After confirming the system is steady, data are collected for an additional period of five minutes: three minutes at a sampling rate of 5 Hz, and two minutes at 200 Hz (with sampling rate changed via a command in the LabView program controlling data acquisition). After completing data collection, tests move to the next desired set of operating conditions. The present study only presents results sampled at 200 Hz, done to allow analysis of frequency composition up to 100 Hz (determined by the Nyquist sampling criterion).

Data collection for all temperature, pressure, flow rate, and power measurements is handled by a cDAQ-9178 data acquisition system with one NI-9205 analog input module and four NI-9214 thermocouple modules, all controlled by LabView. All temperature measurements are made with type-T thermocouples having uncertainty of  $\pm 0.4^\circ\text{C}$ , and pressure measurements using STS absolute pressure transducers with an accuracy of  $\pm 0.1\%$ . Flow rates (and thus mass velocities) are measured using Bronkhorst Cori-Flow Coriolis flow meters with an accuracy of  $\pm 0.2\%$ , and bulk heater power input is calculated from voltage and current data with an accuracy of  $\pm 0.2\text{W}$ . All properties are evaluated at local pressure using data obtained from NIST.

Table 2.4: Target operating conditions for condensation portion of current study.

$G_{FC}$ [ $\text{kg}/\text{m}^2\text{s}$ ]	$G_{H_2O}$ [ $\text{kg}/\text{m}^2\text{s}$ ]	$P_{FC,in}$ [kPa]	$x_{e,in}$
50	130, 260, 390	130, 160	1.0
100	130, 260, 390	130, 160	1.0
100	390	130	0.4, 0.6, 0.8
150	130, 260, 390	130, 160	1.0
150	390	160	0.4, 0.6, 0.8
200	130, 260, 390	130, 160	1.0
200	390	130, 160	0.4, 0.6, 0.8
250	130, 260, 390	130, 160	1.0
300	130, 260, 390	130, 160	1.0
300	390	130, 160	0.4, 0.6, 0.8
325	130, 260, 390	130, 160	1.0
350	390	130, 160	0.4, 0.6, 0.8

### 3. FLOW BOILING

#### 3.1 Impact of Density Wave Oscillations on Flow Boiling System Dynamic Behavior and Stability

Prior to undertaking any detailed analysis and modeling of DWO induced behavior in flow boiling systems, it is first necessary to isolate physically induced oscillatory behavior from that resulting from mechanical sources (i.e. pump, fans, etc.). It is also important to determine relevant ranges of operating conditions for which DWO induced behavior is observed in the current experimental setup.

##### 3.1.1 Analysis of System Dynamics

###### 3.1.1.1 Approach for Determining Influence of Fluid Components

As mentioned in the preceding sections, pressure transducers are placed upstream and downstream of all key fluid components in order to isolate and characterize the contribution of individual components to overall system dynamic performance. As this resulted in an overly large amount of data, however, the current study will focus on five regions found to be of most interest within the system. These are depicted graphically in Fig. 3.1(a), with *Region I* corresponding to pressure drop across the filter, *Region II* pressure at the outlet of the pre-heater, *Region III* pressure drop across the heated length of the FBM ( $L_h$  in Fig. 2.1(b)), *Region IV* pressure drop across the condenser, and *Region V* pressure at the stream-wise location of the accumulator. These locations were selected based on the following rationale:

*Region I:* Pressure drop across the filter includes pressure information acquired at the outlet of the pump (which represents the primary mechanical component within the flow loop), while also providing representative information on the impact of the filter (an important fluid component) within the subcooled portion of the flow loop.

*Region II:* The outlet of the pre-heater represents the first location within the flow loop where, for test cases with saturated inlet conditions, two-phase flow pressure measurements are made within the loop. The pre-heater inlet was observed to exhibit dynamic behavior similar to that at the filter outlet, which is included in Region I.

*Region III:* Pressure drop across the heated length of the flow boiling module is the most critical measurement made in the present study. Improving upon prior work [53], using a larger number

of fast response pressure transducers allows dynamic behavior within the test section in the present study to be compared with that at the outlet of the pre-heater to isolate the effect of boiling within the flow boiling module itself as opposed to behavior introduced by phase change within the pre-heater and propagated upstream.

*Region IV:* Pressure drop across the condenser is comprised of signals from both saturated (condenser inlet) and subcooled (condenser outlet) regions of the flow loop, allowing direct comparison of crucial phenomena in both regions for all operating conditions tested. Additionally, this pressure drop may reflect the influence of mechanical vibrations introduced by the condenser's fans.

*Region V:* The role of the accumulator within the flow loop is to accommodate volume changes introduced by phase change, and as such the height of bellows within the accumulator is expected to fluctuate in response to the system's dynamic behavior. Pressure measurement at the accumulator is expected to provide information on both overall loop dynamic behavior as well as the dynamics associated with response of the accumulator itself.

Adopting the approach successfully utilized in prior work [53], analysis will center on amplitude versus frequency plots generated by performing fast Fourier transforms of transient pressure signals at locations of interest. Sample transient plots will also be presented for specified operating conditions in each region, however, as it is not only important to characterize flow oscillations by finding dominant frequencies and peak amplitudes, but also to understand how these oscillations manifest themselves in the time domain.

Figures 3.1(b) – 3.1(e) provide plots of transient operating conditions for each of the key sets of inlet conditions investigated, depicted here with the test section in vertical upflow orientation. These plots are representative of the transient response of key operating conditions which will be used when comparing flow dynamic behavior at the aforementioned five regions of interest.

In each case, a near step function increase in heat flux applied to the FBM heated walls is followed by an increase in wall temperature asymptotically approaching a constant mean value while the instantaneous value continues to exhibit some fluctuation. The wall temperature used here is  $T_5$  corresponding to the fifth thermocouple along the streamwise direction on the top wall for horizontal flow; relative location of this wall is inconsequential for vertical upflow and vertical downflow orientations. The temperature fluctuations are significantly larger for the cases with

saturated inlet conditions, Figs. 3.1(c) and 3.1(e), than those with subcooled inlet conditions, Figs. 3.1(b) and 3.1(d). Similarly, both mass velocity and inlet quality exhibit significant fluctuations as they approach constant mean values, with higher amplitude fluctuations encountered in the cases with saturated inlet conditions. It is also worth noting that transient plots of inlet quality appear more ‘dense’ than those of mass velocity in each case, which can be attributed to mass velocity being a direct measurement, while quality is calculated according to Eq. (2.1) using several fluctuating parameters. More attention will be paid to the frequency composition of these signals in subsequent sections.

Mean values indicated in the plots were calculated by averaging over the final 30 s for each case. In addition to vertical upflow, subsequent figures will provide amplitude versus frequency plots for horizontal and vertical downflow orientations, both of which correspond to operating conditions similar to those for vertical upflow. The orientation of all measurement locations other than region III (test section) remains unchanged, but changes to test section orientation causes changes to manifest throughout the flow loop so it is reported for associated measurements at all regions of interest. Table 3.1 provides time-averaged operating conditions for each combination of test section orientation and inlet condition to be presented hereafter, with mass velocity, inlet quality, and inlet pressure all associated with the inlet to the heated length of FBM. Heat flux applied to the heated walls of FBM and critical heat flux (CHF) associated with the given inlet conditions are also provided.

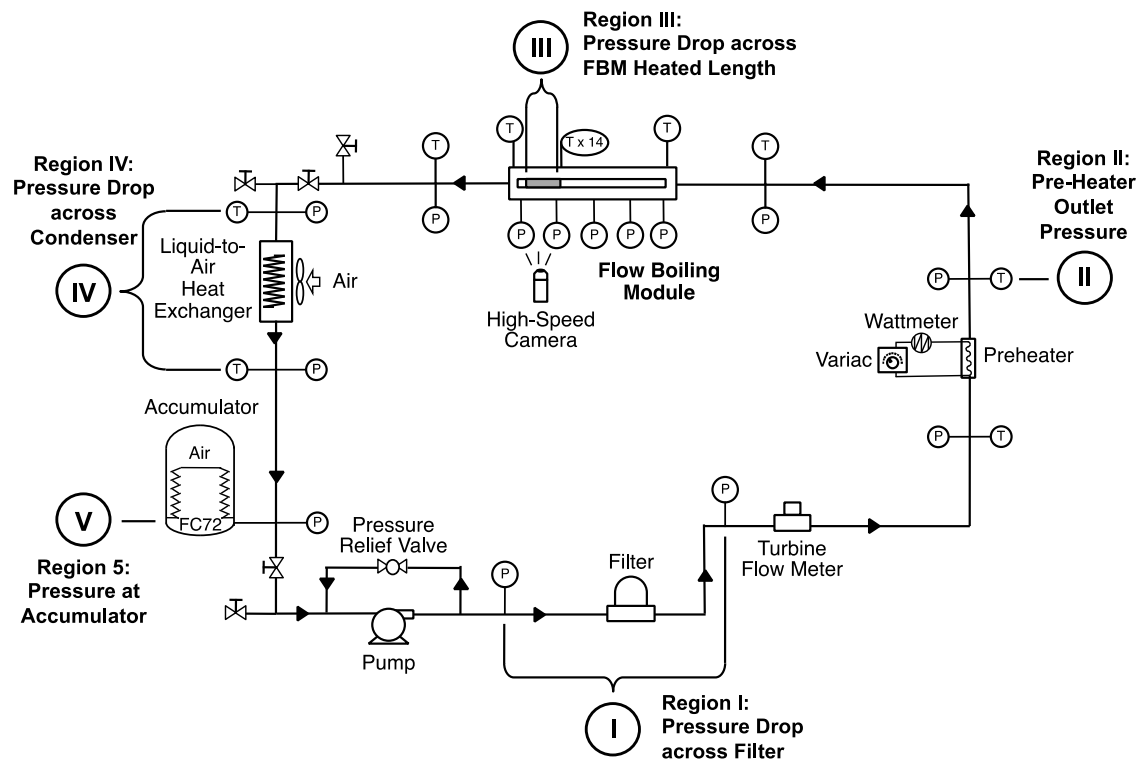


Figure 3.1: (a) Five regions for analysis of dynamic pressure behavior, along with transient records of operating conditions for vertical upflow with (b)  $G \sim 200 \text{ kg/m}^2\text{s}$  and subcooled inlet, (c)  $G \sim 200 \text{ kg/m}^2\text{s}$  and saturated inlet, (d)  $G \sim 800 \text{ kg/m}^2\text{s}$  and subcooled inlet, and (e)  $G \sim 800 \text{ kg/m}^2\text{s}$  and saturated inlet.

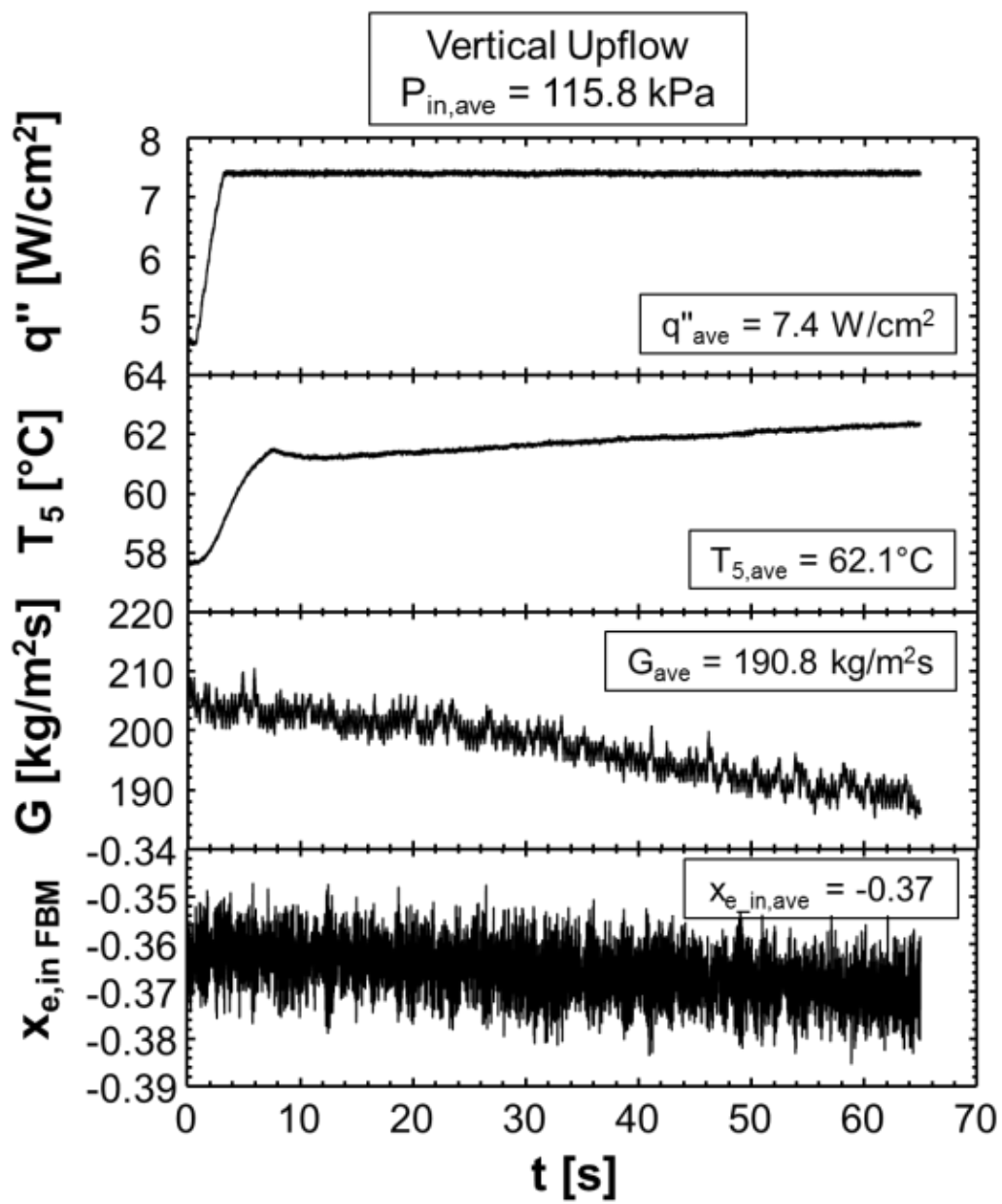


Figure 3.1 (b).

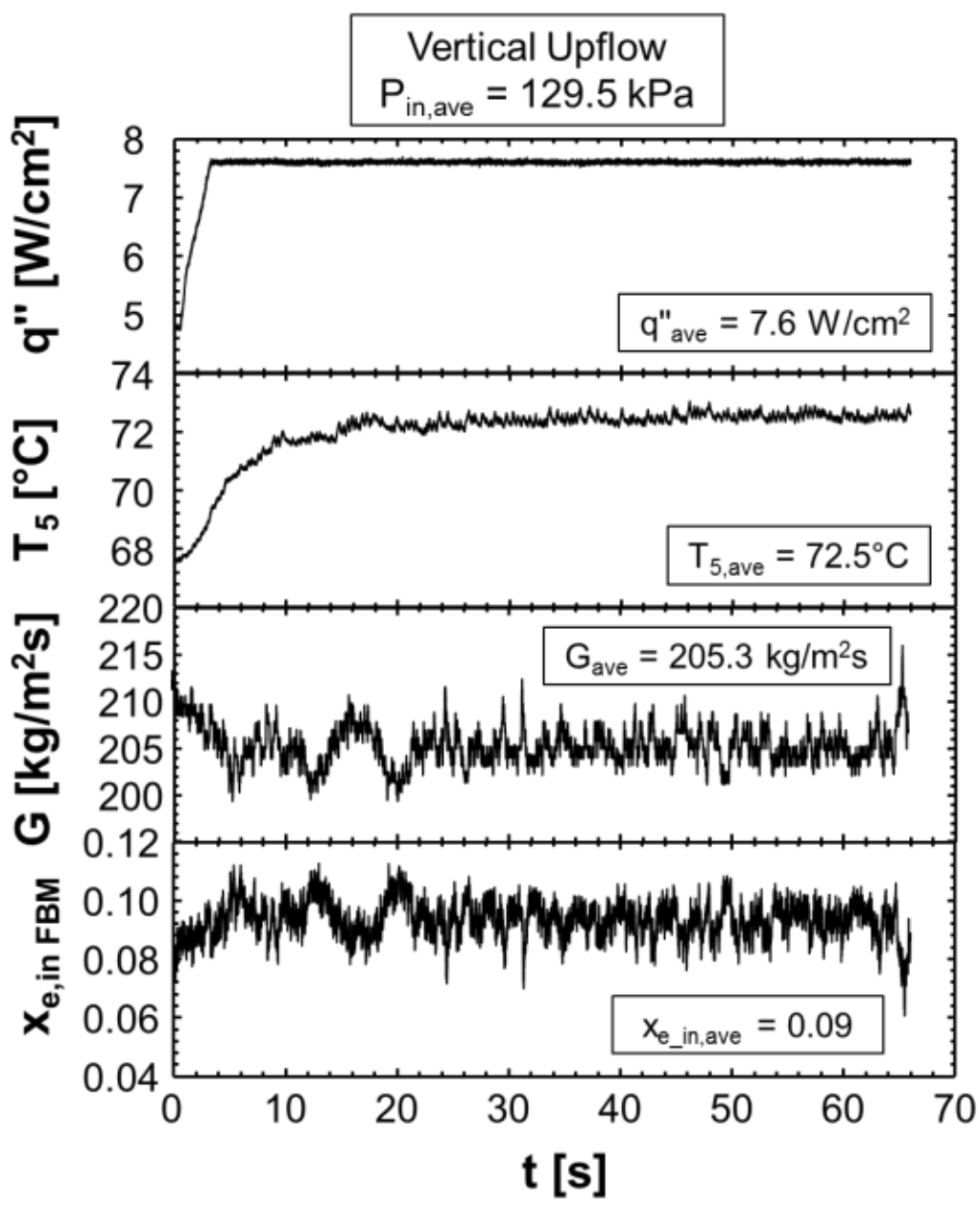


Figure 3.1 (c).

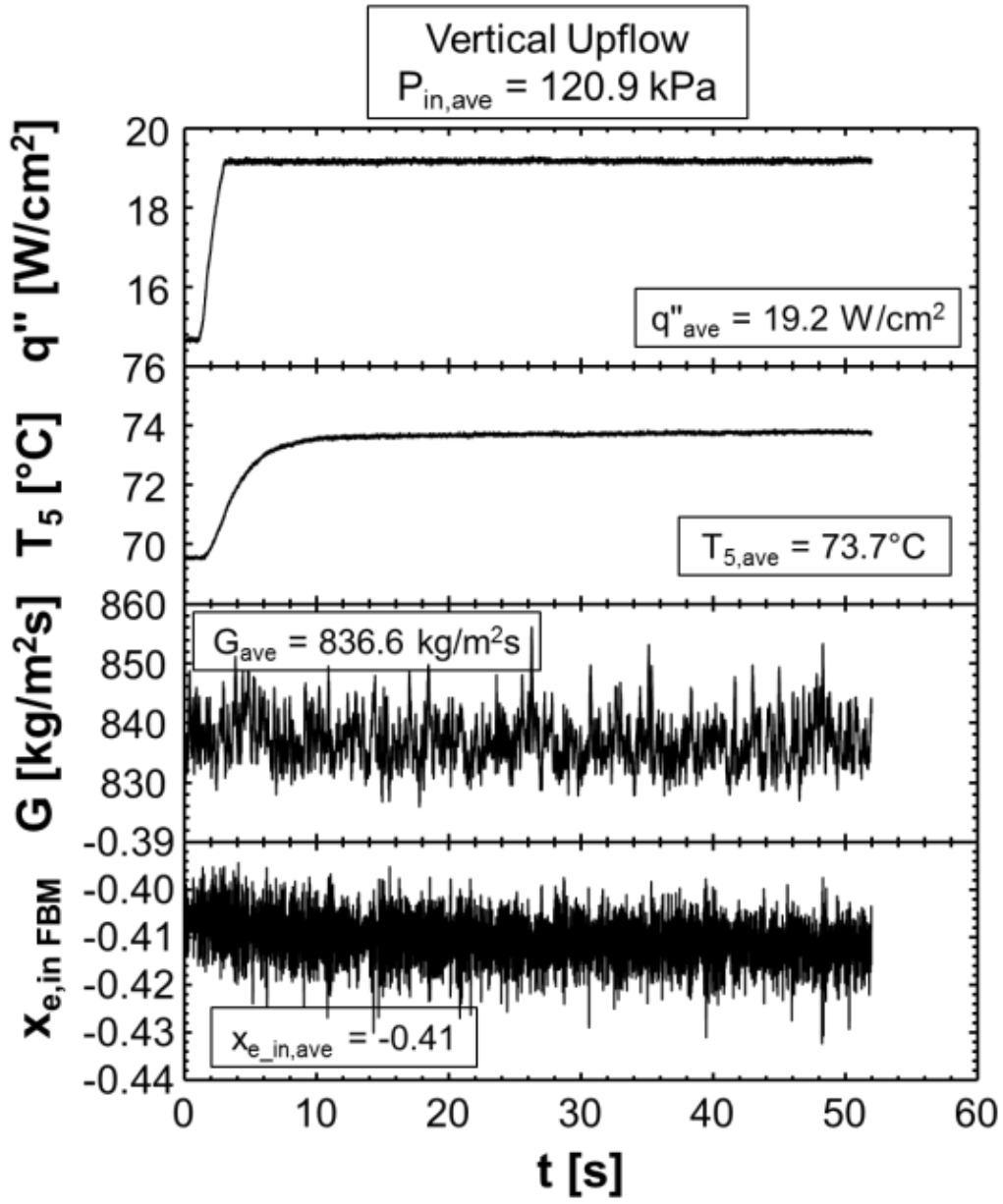


Figure 3.1 (d).

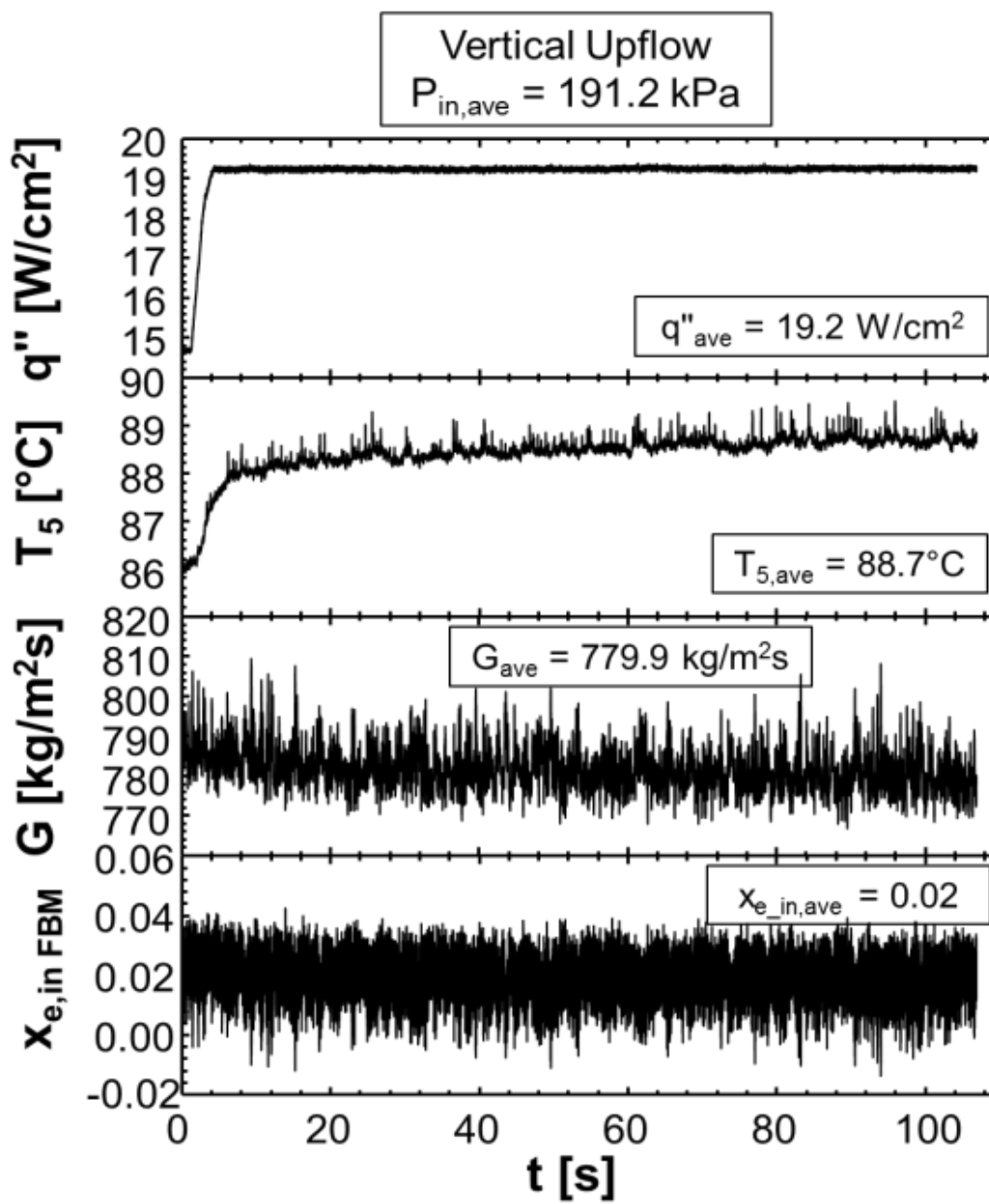


Figure 3.1 (e).

Table 3.1: Key operating conditions for system dynamic analysis cases. Indicated cases correspond to parts (b) – (e) in Figs. 3.1 – 3.7.

Case	Vertical Upflow				
	$G$ [kg/m <sup>2</sup> s]	$x_{e,in}$	$P_{FBM,in}$ [kPa]	$q''_{FBM}$ [W/cm <sup>2</sup> ]	$CHF$ [W/cm <sup>2</sup> ]
(b)	190.8	-0.37	115.8	7.4	22.5
(c)	205.3	0.09	129.5	7.6	19.1
(d)	836.6	-0.41	120.9	19.2	44.6
(e)	779.9	0.02	191.2	19.2	28.9
Case	Vertical Downflow				
	$G$ [kg/m <sup>2</sup> s]	$x_{e,in}$	$P_{FBM,in}$ [kPa]	$q''_{FBM}$ [W/cm <sup>2</sup> ]	$CHF$ [W/cm <sup>2</sup> ]
(b)	203.1	-0.45	127.8	8.0	11.7
(c)	217.6	0.06	106.9	7.4	12.9
(d)	831.7	-0.54	132.5	20.4	25.4
(e)	792.3	0.04	194.6	20.3	28.4
Case	Horizontal Flow				
	$G$ [kg/m <sup>2</sup> s]	$x_{e,in}$	$P_{FBM,in}$ [kPa]	$q''_{FBM}$ [W/cm <sup>2</sup> ]	$CHF$ [W/cm <sup>2</sup> ]
(b)	191.9	-0.52	98.5	7.8	10.7
(c)	214.7	0.08	123.8	6.9	7.8
(d)	845.0	-0.44	108.3	19.5	32.4
(e)	783.6	0.02	183.7	19.4	22.0

### 3.1.1.2 Region I: Filter between Pump and Pre-heater

Immediately upon exiting the pump, the fluid exhibits moderate pressure fluctuations. Figure 3.2(a) depicts transient results for vertical upflow with  $G = 836.6$  kg/m<sup>2</sup>s, which show that pressure drop across the filter oscillates within a 2 – 8 kPa envelope. The fact that the flow exhibits oscillations of similar amplitude both upstream and downstream of the filter is an important conclusion, implying that the filter itself plays little role in influencing system dynamic behavior.

Figures 3.2(b) – 3.2(e) provide amplitude versus frequency plots of the same and show that oscillations are confined primarily to the high-frequency range (with noticeable frequency peaks in the 20-100 Hz range) of the plots. This is indicative of mechanically induced vibrations within

the system, especially as the pump itself is a prime source of vibrations resulting from its internal rotary motion.

Across Figs. 3.2(b) – 3.2(e) amplitudes vary greatly, with some cases (especially vertical upflow in Fig. 3.2(e)) exhibiting significantly higher amplitude oscillations than other cases. Outliers aside, it is clear that Figs. 3.2(d) and 3.2(e) exhibit stronger dynamic behavior than Figs. 3.2(b) and 3.2(c). This trend can be attributed to the increase in mass velocity from  $G \sim 200 \text{ kg/m}^2\text{s}$  for Figs. 3.2(b) and 3.2(c) to  $G \sim 800 \text{ kg/m}^2\text{s}$  for Figs. 3.2(d) and 3.2(e), which comes with an increase in pump work imparted on the fluid and associated increase in magnitude of pump-induced oscillations.

As the fluid continues through the flow loop, it next passes the turbine flow meter. The turbine flow meter used in the flow loop incurred the single largest pressure drop of any component within the loop but, across all sets of operating conditions, was shown to have a negligible impact on dynamic behavior and is therefore omitted from analysis.

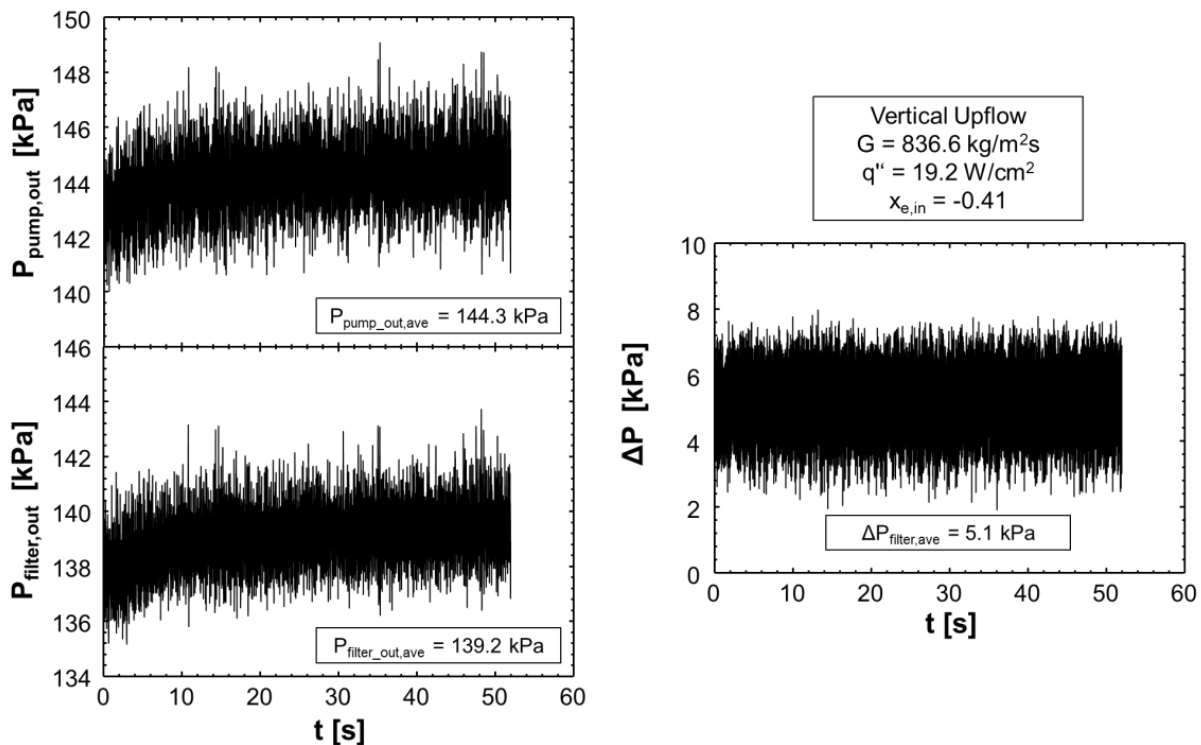


Figure 3.2: (a) Sample plot of transient pressure drop across the filter (region 1), along with amplitude versus frequency plots of the same for vertical upflow, vertical downflow, and horizontal flow with (b)  $G \sim 200 \text{ kg/m}^2\text{s}$  and subcooled inlet, (c)  $G \sim 200 \text{ kg/m}^2\text{s}$  and saturated inlet, (d)  $G \sim 800 \text{ kg/m}^2\text{s}$  and subcooled inlet, and (e)  $G \sim 800 \text{ kg/m}^2\text{s}$  and saturated inlet.

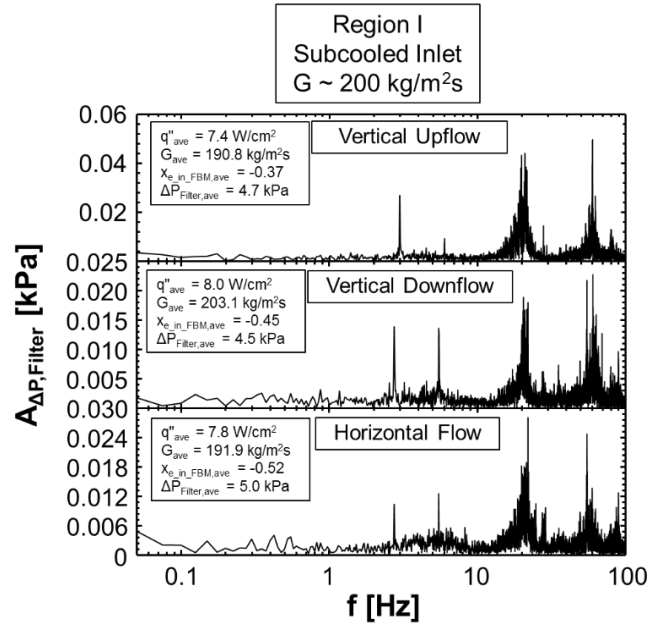


Figure 3.2 (b).

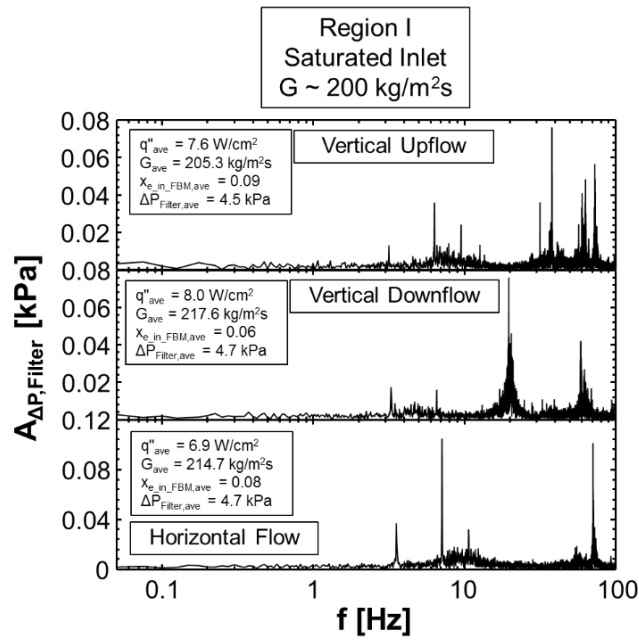


Figure 3.2 (c).

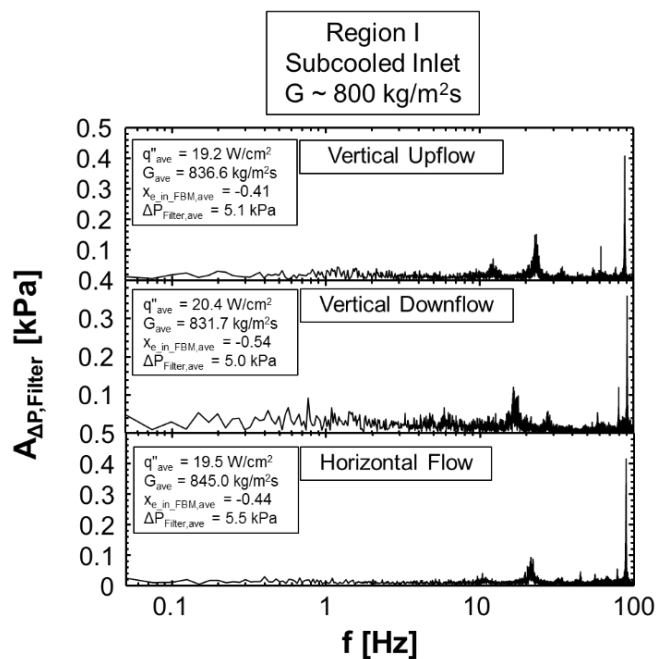


Figure 3.2 (d).

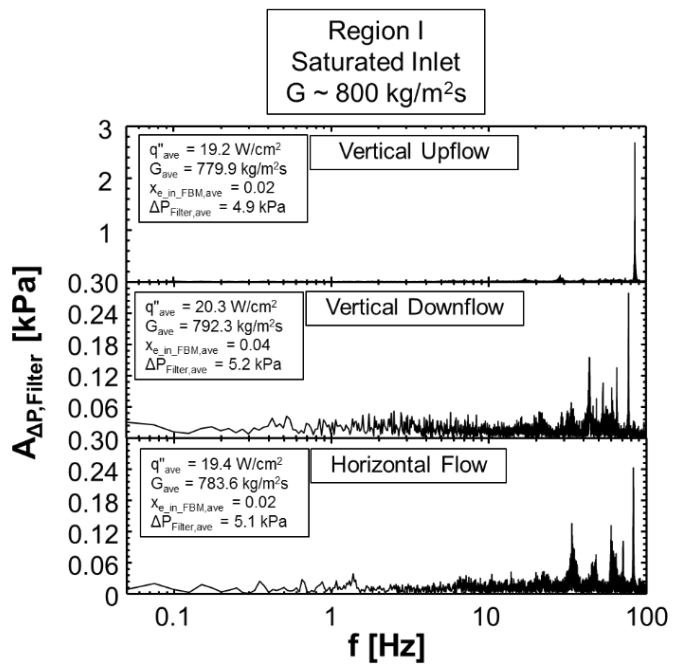


Figure 3.2 (e).

### 3.1.1.3 Region II: Pre-heater Outlet and FBM Inlet

The next component of interest within the flow loop is the pre-heater. Because of miniscule impact of the turbine flow meter on dynamic behavior, frequency composition of the transient pressure signal at the pre-heater inlet is nearly identical to that at the filter outlet for all cases tested.

Figure 3.3(a) clearly depicts, however, for vertical upflow with  $G \sim 800 \text{ kg/m}^2\text{s}$ , that the transient pressure signal at the pre-heater's exit exhibits drastic differences depending on whether the fluid exits the pre-heater in a subcooled or saturated state. While system pressure at the pre-heater's outlet is much higher for the saturated mixture case ( $x_{e,in} = 0.02$ ), the magnitude of pressure oscillations is clearly smaller than for the subcooled case ( $x_{e,in} = -0.41$ ).

Figures 3.3(b) – 3.3(e) also show that the frequency composition is much different for subcooled versus saturated cases. In Figs. 3.3(b) and 3.3(d), corresponding to  $G \sim 200 \text{ kg/m}^2\text{s}$  and  $800 \text{ kg/m}^2\text{s}$ , respectively, with subcooled inlet conditions, it is clear that much of the oscillatory behavior is confined to a range of 5-30 Hz, with some smaller peaks also present in the higher 80-100 Hz range. The only exception is the general upward trend of the plots in Fig. 3.3(b) with decreasing frequency below 1 Hz. This is likely due to the larger time constants associated with loop operation at low flow rates, which can drive gradual changes in system operating conditions that are not always immediately apparent while running experiments.

In Figs. 3.3(c) and 3.3(e), corresponding to saturated inlet conditions, peak frequencies of oscillation are found in the 0.1 – 1 Hz range, and little to no oscillations are seen above 15 Hz. The only exception is the case of vertical downflow in Fig. 3.3(c), which, despite boiling taking place within the pre-heater, continues to exhibit dominant oscillatory modes in the high frequency range similar to those expected for subcooled conditions. It is possible that this behavior is related to the relatively large vertical distance the fluid must travel to reach the inlet of the test section for tests performed in this orientation. In the vertical downflow cases with  $G = 217.6 \text{ kg/m}^2\text{s}$ , low flow inertia allows body force to play a more dominant role, and distribution of bulk flow between liquid and vapor phases becomes less predictable. This potentially provides a continuous liquid path for high-frequency oscillations to propagate not present in the other flow orientations.

Also of note in Figs. 3.3(c) and 3.3(e) is the presence of dominant frequencies in the 0.1 – 5 Hz range. As noted in prior work [53], this behavior is consistent with density wave oscillations, and will be analyzed in greater detail in conjunction with the FBM response.

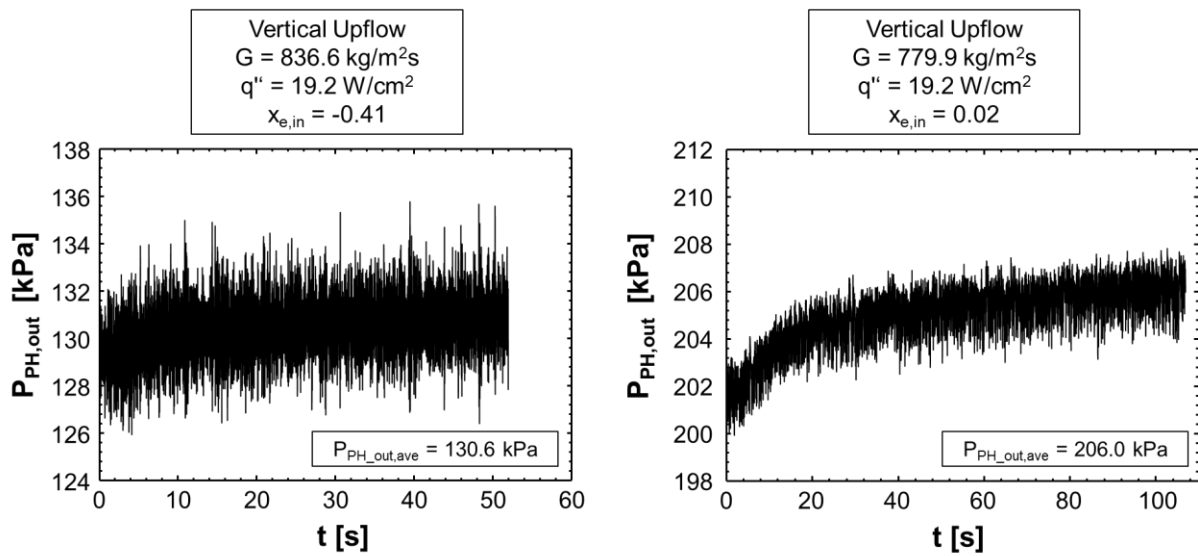


Figure 3.3: (a) Sample plot of transient pre-heater outlet pressure (region II), along with amplitude versus frequency plots of the same for vertical upflow, vertical downflow, and horizontal flow with (b)  $G \sim 200 \text{ kg/m}^2\text{s}$  and subcooled inlet, (c)  $G \sim 200 \text{ kg/m}^2\text{s}$  and  $x_{e,in} \sim 0.10$ , (d)  $G \sim 800 \text{ kg/m}^2\text{s}$  and subcooled inlet, and (e)  $G \sim 800 \text{ kg/m}^2\text{s}$  and  $x_{e,in} \sim 0.05$ .

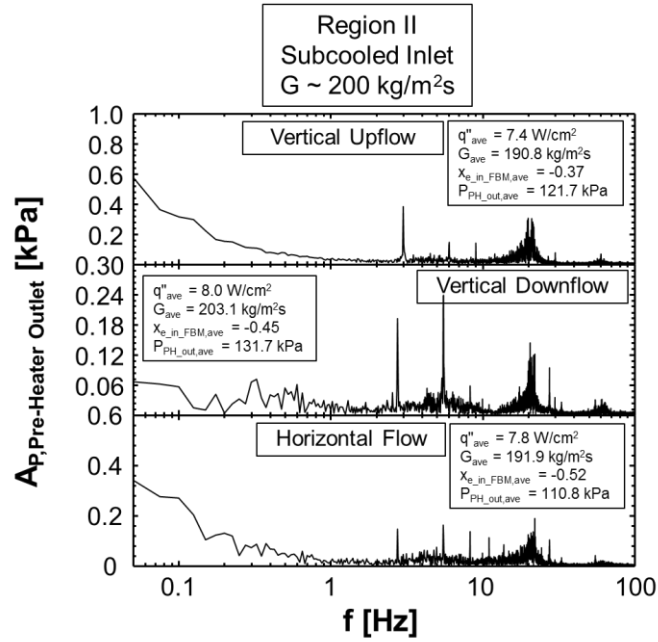


Figure 3.3 (b).

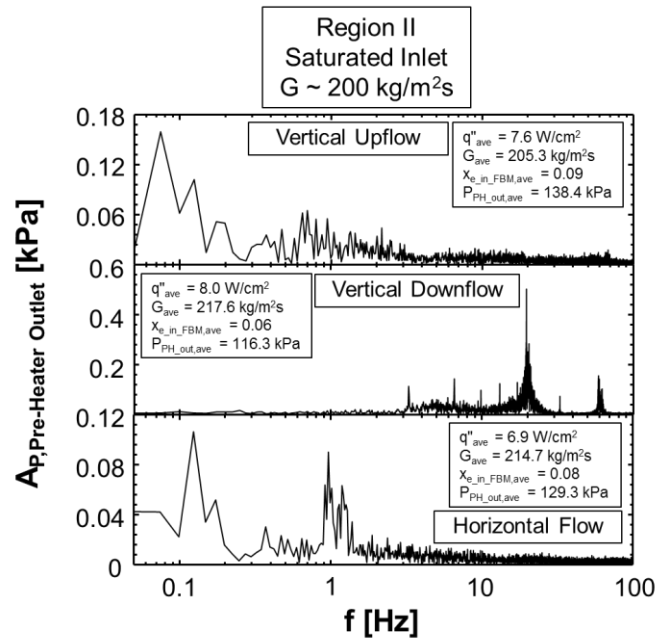


Figure 3.3 (c).

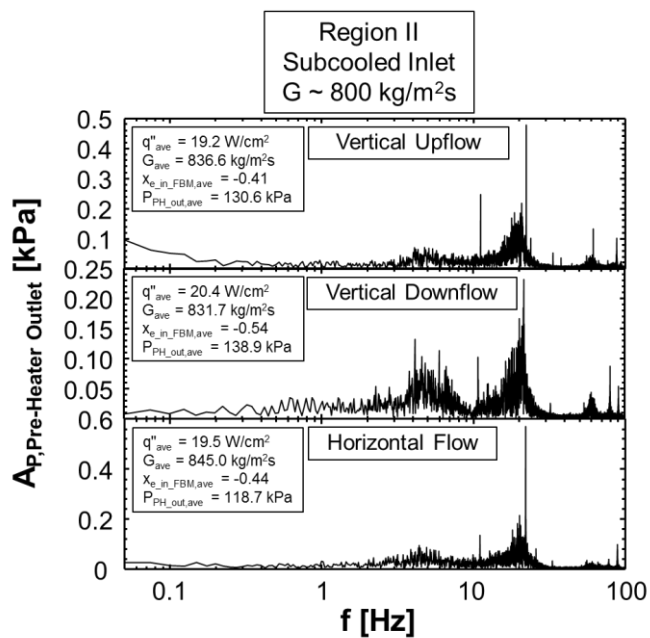


Figure 3.3 (d).

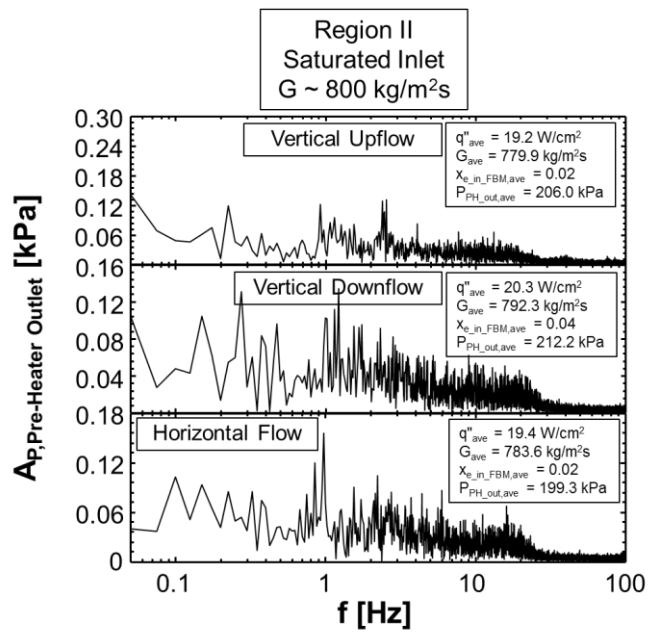


Figure 3.3 (e).

### 3.1.1.4 Region III: Flow Boiling Module (FBM)

Figure 3.4(a) illustrates, for vertical upflow, the significant difference in amplitude of pressure drop oscillations across the heated length of the FBM between cases with subcooled inlet conditions and those with saturated inlet conditions. This runs counter to the trend seen in Fig. 3.3(a), where boiling within the pre-heater was seen to have a stabilizing effect on fluid dynamic behavior. The opposing trends for the FBM and pre-heater can be explained by examining the internal geometry of each: the pre-heater consists of a 12.7-mm i.d. tube coiled multiple times around three cartridge heaters for a total length of 3810 mm, all mounted within a large assembly, while the heated portion of the FBM (described in section 2) possesses a hydraulic diameter of 3.33 mm and a much shorter 114.6-mm heated length. These differences in geometry mean that, even though more power is supplied by the pre-heater, the heat flux applied to the much larger heated area within the pre-heater is lower than that applied to the smaller heated walls within the FBM. In the present study, the highest heat flux achieved within the FBM was  $50.8 \text{ W/cm}^2$ , while heat flux within the pre-heater never exceeded  $0.6 \text{ W/cm}^2$ . The higher heat fluxes applied to the FBM yield more vigorous phase change within the test section, leading to more dynamic flow behavior.

Like Figs. 3.3(b) – 3.3(e), there are appreciable differences in frequency composition of transient pressure signals for subcooled versus saturated inlet conditions. Figures 3.4(b) and 3.4(d), corresponding to subcooled inlet conditions with  $G \sim 200 \text{ kg/m}^2\text{s}$  and  $800 \text{ kg/m}^2\text{s}$ , respectively, again exhibit dominant frequencies in the high frequency range, although amplitudes of oscillation are now much lower and feature fewer sharp peaks. This reduction in amplitude and the ‘smearing’ across the frequency spectrum of upstream well-defined, mechanically induced oscillatory modes is attributed to subcooled boiling along the heated walls within the test section followed by the rapid ‘collapse’ of bubbles back to single-phase liquid as they detach from the wall and enter the bulk, subcooled flow. It should be noted that negative values of time-averaged pressure drop shown for the vertical downflow and horizontal flow orientations with subcooled inlet conditions, Figs. 3.4(b) and 3.4(d), are attributed to difficulties in measuring very small pressure drops coupled with limitations in measurement accuracy of the pressure transducers used.

Figures 3.4(c) and 3.4(e), which correspond to saturated inlet conditions with  $G \sim 200 \text{ kg/m}^2\text{s}$  and  $800 \text{ kg/m}^2\text{s}$ , respectively, exhibit peak frequencies of oscillation in the range of 0.1-5 Hz, similar to those seen in Figs. 3.3(c) and 3.3(e), with the case of vertical downflow with  $G =$

217.6 kg/m<sup>2</sup>s again proving to an exception, likely for the aforementioned reasons. This behavior is consistent with that attributed to Density Wave Oscillations (DWOs) by Boure *et al.* [50], but more thorough investigation is warranted to establish that these low frequency pressure oscillations are indeed due to DWOs.

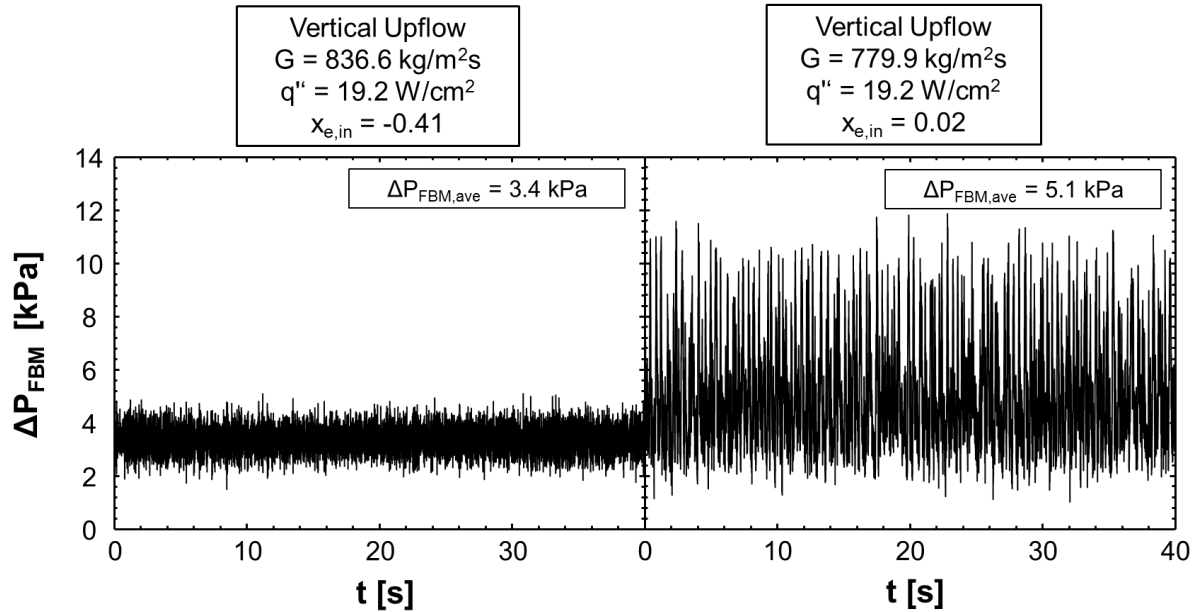


Figure 3.4: (a) Sample plots of transient pressure drop across heated length of FBM (region III), along with amplitude versus frequency plots of the same for vertical upflow, vertical downflow, and horizontal flow with (b)  $G \sim 200 \text{ kg/m}^2\text{s}$  and subcooled inlet, (c)  $G \sim 200 \text{ kg/m}^2\text{s}$  and saturated inlet, (d)  $G \sim 800 \text{ kg/m}^2\text{s}$  and subcooled inlet, and (e)  $G \sim 800 \text{ kg/m}^2\text{s}$  and saturated inlet. Negative values of average pressure drop reported for highly subcooled inlet conditions in vertical downflow and horizontal flow orientations are attributed to difficulties in measuring small pressure drops coupled with limitations in measurement accuracy.

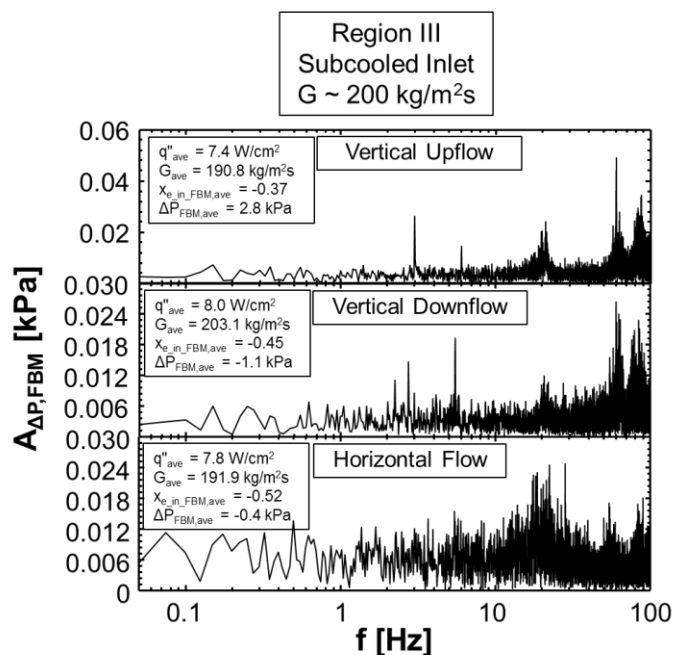


Figure 3.4 (b).

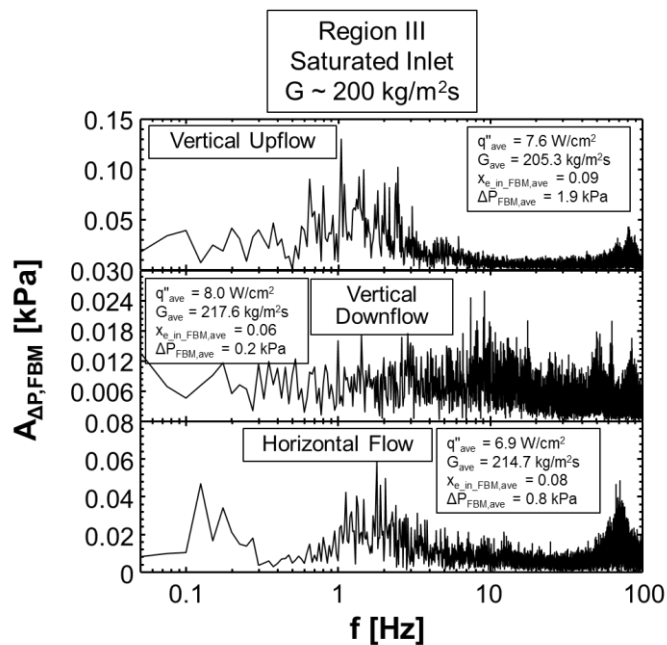


Figure 3.4 (c).

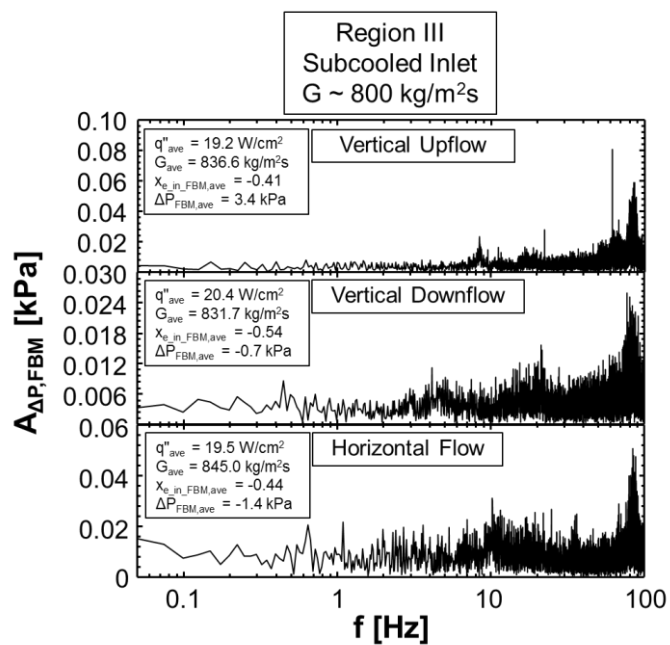


Figure 3.4 (d).

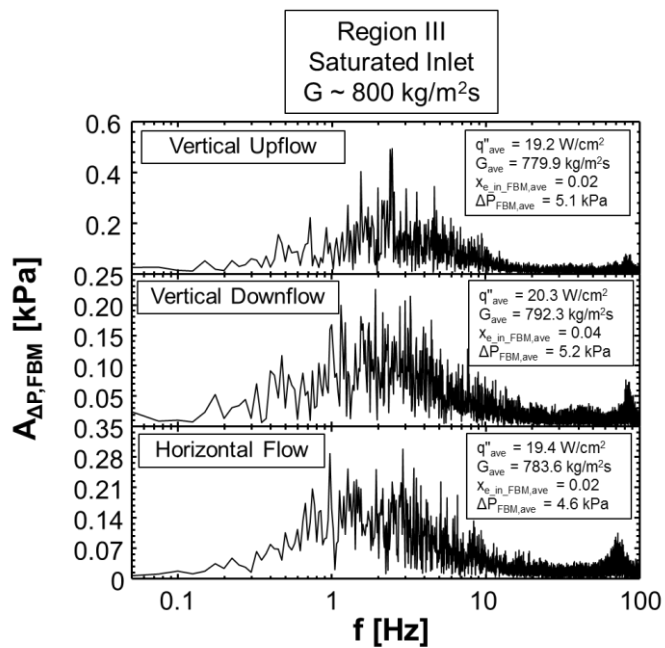


Figure 3.4 (e).

Figures 3.5(a) – (c) provide a clear depiction of the phenomenon described herein as Density Wave Oscillations (DWOs). Figure 3.5(a) presents flow visualization images taken of the heated length of FBM with inlet conditions corresponding to those of Fig. 3.4(e) with vertical upflow orientation. It is difficult to distinguish specific flow features because of finite quality at the inlet to the test section, but it is very clear that at different times the region of interest is alternatively composed of predominantly vapor (images are bright due to high transmission of light) and predominantly liquid (images are dark due to low transmission of light). In particular, there are short time windows where the heated length of FBM is almost entirely occupied by liquid, which are always followed by a period in which liquid content decreases and vapor increases, only for another large liquid region to pass through shortly after.

It is this cyclical passage of High Density Fronts (HDFs) followed by periods of high vapor void fraction (Low Density Fronts) that is termed Density Wave Oscillations in the present study. Figure 3.5(b) helps illustrate this by tabulating the times associated with successive passage of HDFs. By calculating the difference in time between HDFs, single-event frequencies can be calculated ( $f = 1/\Delta t$ ), which are seen to fall perfectly within the frequency range of dominant pressure oscillations depicted in Fig. 3.5(c) (which is taken directly from Fig. 3.4(e)). It should be noted here that time  $t = 0$  s is associated with the onset of image acquisition and has no physical meaning.

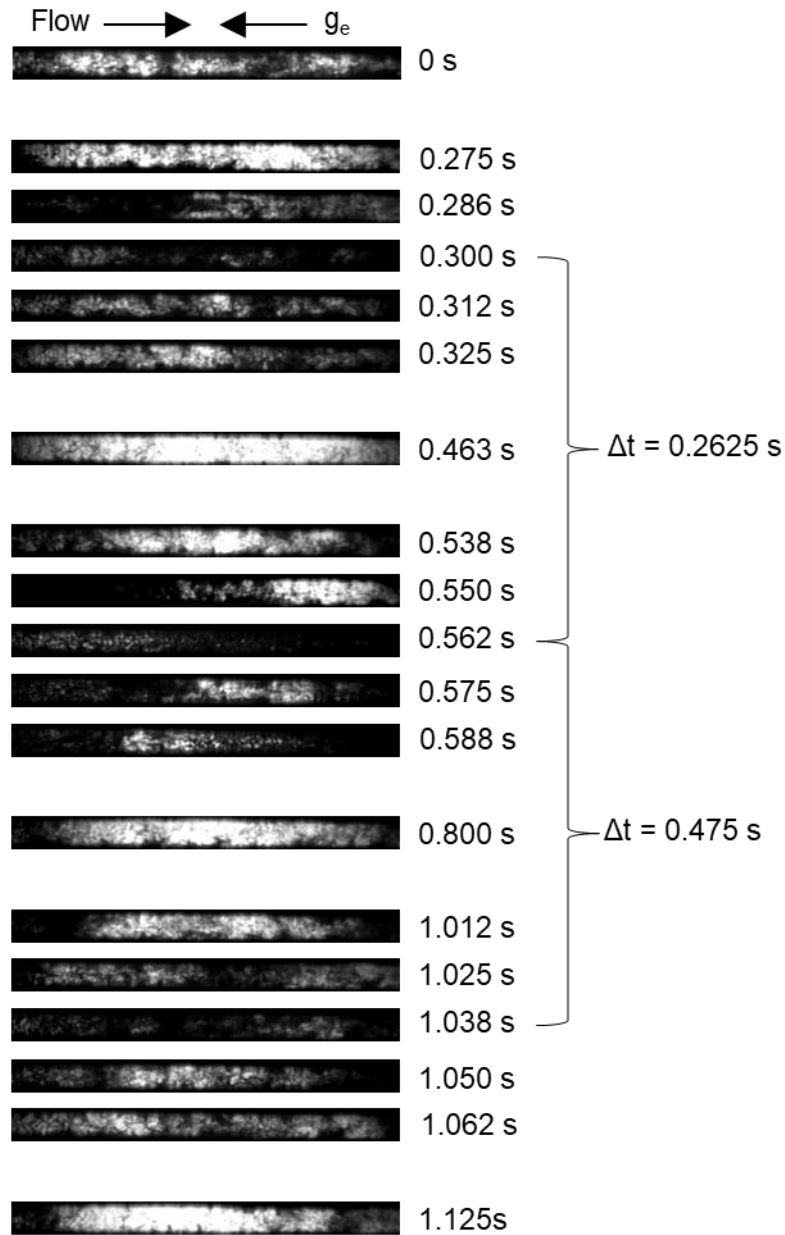


Figure 3.5: (a) Flow visualization images depicting the cycle of low density (bright) and high density (dark) fronts passing through the heated length of FBM in vertical upflow with finite inlet quality, with (b) six consecutive High Density Fronts (HDFs) identified from images and the time between them used to calculate single-event frequencies, which are shown to fall within the range of peak oscillatory behavior in (c).

HDF Occurrence	Time [s]	$\Delta t$ [s]	f [Hz]
1	0.3	-	-
2	0.5625	0.2625	3.81
3	1.0375	0.475	2.11
4	1.225	0.1875	5.33
5	1.825	0.6	1.67
6	2.225	0.4	2.5

Figure 3.5 (b).

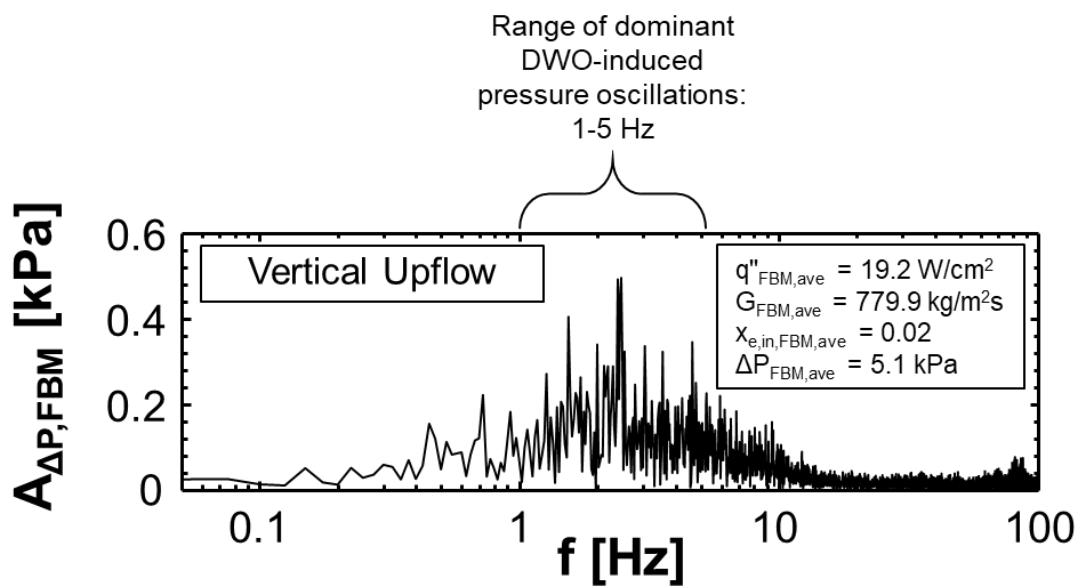


Figure 3.5 (c).

On the analytic side, the attribution of these low-frequency pressure fluctuations to DWOs is further reinforced by the work of Lahey and Podowski [47], who stated that resonant frequency  $f_r$  of a system experiencing DWOs can be expressed as

$$f_r = \frac{1}{2T_{tr}} \sim \frac{U_{FC-72}}{2L_{ts}}, \quad (3.1)$$

where  $T_{tr}$  is the transport time,  $U_{FC-72}$  the velocity of the working fluid, and  $L_{ts}$  the heated length of the test section. In general terms, this equation indicates that the frequency is equal to the inverse of twice the residence time of the disturbance on the heated wall. Here, disturbance propagation speed is approximated by liquid velocity assuming the flow is made of liquid alone. Evaluating this relationship for the conditions represented in Figs. 3.4(c) and 3.4(e) and comparing with experimentally observed dominant frequencies of oscillation yield the values given in Table 3.2. This table shows relatively good agreement for higher mass velocities but significant error for lower mass velocities. Additionally, even for higher mass velocities, the frequency prediction remains static while differences are seen in experimental results for the three orientations. Both trends indicate the inability of Eq. (3.1) to account for body force effects. This error might be related to the inaccuracy of approximating disturbance speed with bulk liquid velocity, and might be corrected by implementing more sophisticated modeling for disturbance propagation speed.

Table 3.2: Predicted and experimental frequencies for DWOs shown in Figs. 3.4(c) and 3.4(e).

Orientation	$G$ [kg/m <sup>2</sup> s]	$x_{e,in}$	$f_{DWO,pred}$ [Hz]	$f_{DWO,exp}$ [Hz]	Error [%]
Vertical Upflow	205.3	0.09	0.57	1.10	48.2%
Vertical Downflow	217.6	0.06	0.57	Unclear	---
Horizontal Flow	214.7	0.08	0.57	1.80	68.3%
Vertical Upflow	787.5	0.02	2.18	2.48	13.8%
Vertical Downflow	792.3	0.04	2.23	1.93	13.5%
Horizontal Flow	783.6	0.02	2.18	0.98 (2.90)*	55.0% (33.0%)*

\* Different values for horizontal flow at the higher mass velocity correspond to two different peaks of nearly identical amplitude

### 3.1.1.5 Region IV: Condenser

Exiting the FBM, the fluid travels to the condenser, where it is converted back to single-phase liquid. Figure 3.6(a) shows transient pressure signals for both the condenser inlet and outlet, illustrating clear differences between the two for the case of saturated flow boiling within the FBM. The pressure at the condenser inlet appears very similar to that at the FBM outlet for saturated flow boiling cases, while the pressure at the condenser outlet resembles that downstream of the pump for all cases. This reinforces the idea introduced in conjunction with Fig. 4, that pressure oscillations in single-phase liquid regions are dominated by high frequency, mechanically induced phenomena, while fluctuations in the two-phase (saturated) regions exhibit negligible influence from mechanical factors and are instead dominated by physical two-phase phenomena, such as DWOs.

Figures 3.6(b) – 3.6(e) reinforce this idea by revealing that pressure oscillations across the condenser are dominated by the sharp, high frequency peaks associated with mechanically induced oscillations. It is unclear whether these oscillations are propagated upstream from the pump (as the flow is subsonic in all cases), or induced by vibrations from the two condenser air fans. Figure 3.6(e), however, illustrates that, for high mass velocity saturated flow boiling cases, DWOs at the inlet become non-negligible when analyzing transient pressure drop results. It is possible that at even higher mass velocities the increased amplitude of DWOs will render them the dominant factor in transient pressure drop fluctuations across the condenser.

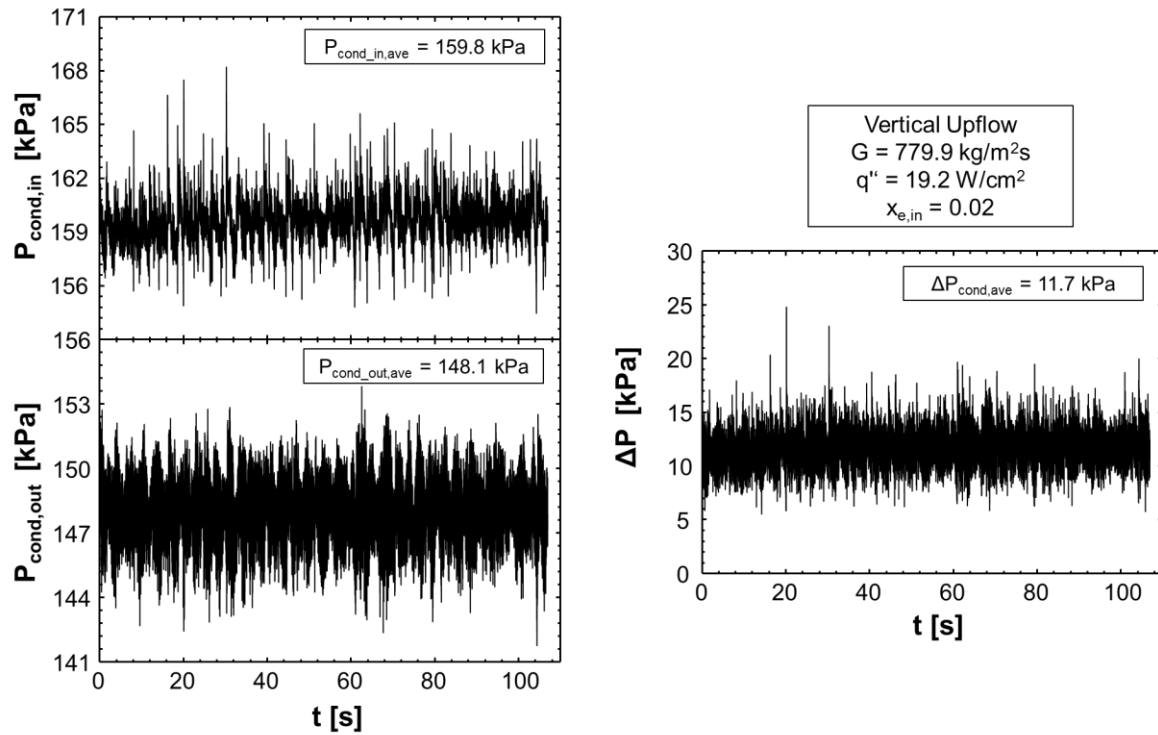


Figure 3.6: (a) Sample plot of transient pressure drop through the condenser (region IV), along with amplitude versus frequency plots of the same for vertical upflow, vertical downflow, and horizontal flow with (b)  $G \sim 200$  kg/m<sup>2</sup>s and subcooled inlet, (c)  $G \sim 200$  kg/m<sup>2</sup>s and saturated inlet, (d)  $G \sim 800$  kg/m<sup>2</sup>s and subcooled inlet, and (e)  $G \sim 800$  kg/m<sup>2</sup>s and saturated inlet.

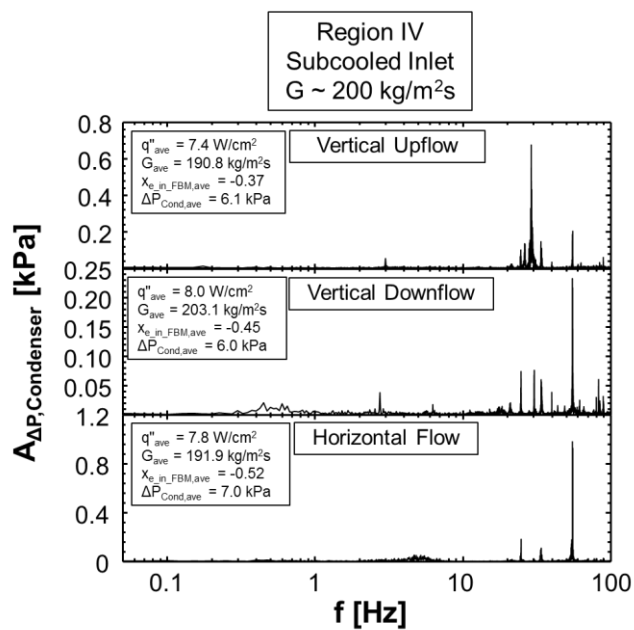


Figure 3.6 (b).

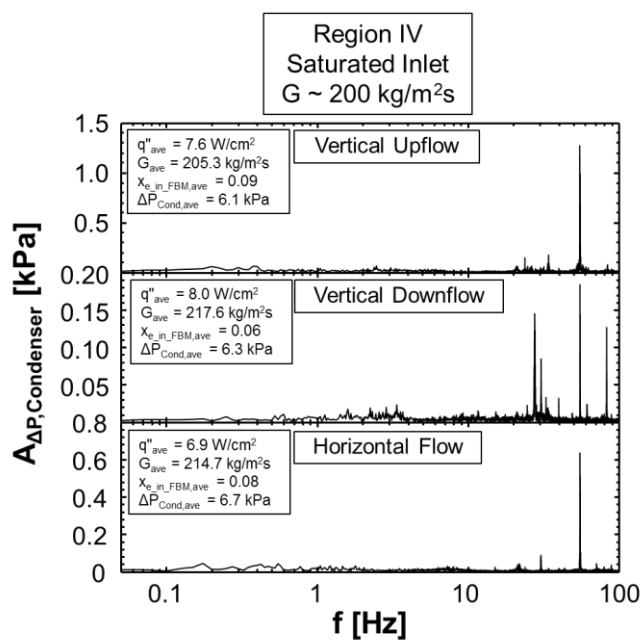


Figure 3.6 (c).

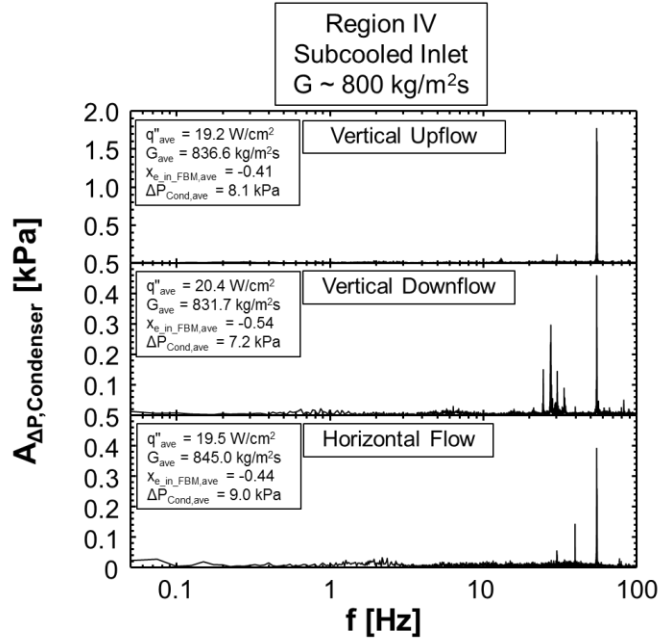


Figure 3.6 (d).

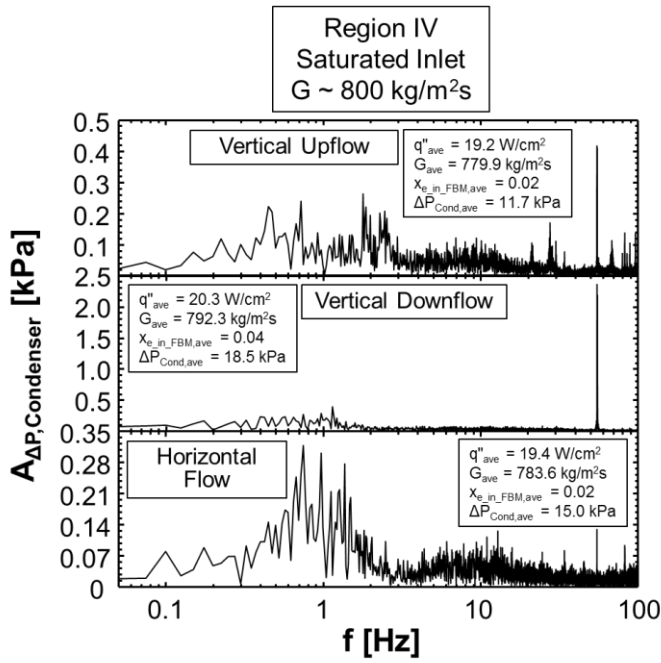


Figure 3.6 (e).

### 3.1.1.6 Region V: Accumulator

After returning to single-phase liquid in the condenser, the fluid makes its way past the accumulator. Figure 3.7(a) shows drastic differences in the pressure measured at the accumulator even for similar operating conditions, with the same flow rate yielding negligible ( $\sim 1$  kPa) pressure fluctuations in the case of subcooled boiling upstream, while more appreciable pressure fluctuations ( $\sim 8$  kPa) are seen for the case of saturated boiling upstream. Figures 3.7(b) – 3.7(e) prove that consistent trends regarding upstream conditions or test section orientation cannot be drawn, with both amplitude and frequency of dominant oscillations varying widely across the parametric ranges evaluated.

The only consistent trend seen across Figs. 3.7(b) – 3.7(e) is the damping of oscillations in the moderate (0.5-10 Hz) range, with oscillations observed only in the high (10-100 Hz) and low ( $< 0.5$  Hz) ranges. This could be due to the internal dynamics of the accumulator itself, as its design necessarily incorporates a mass-spring-damper system with its own mechanical bandwidth.

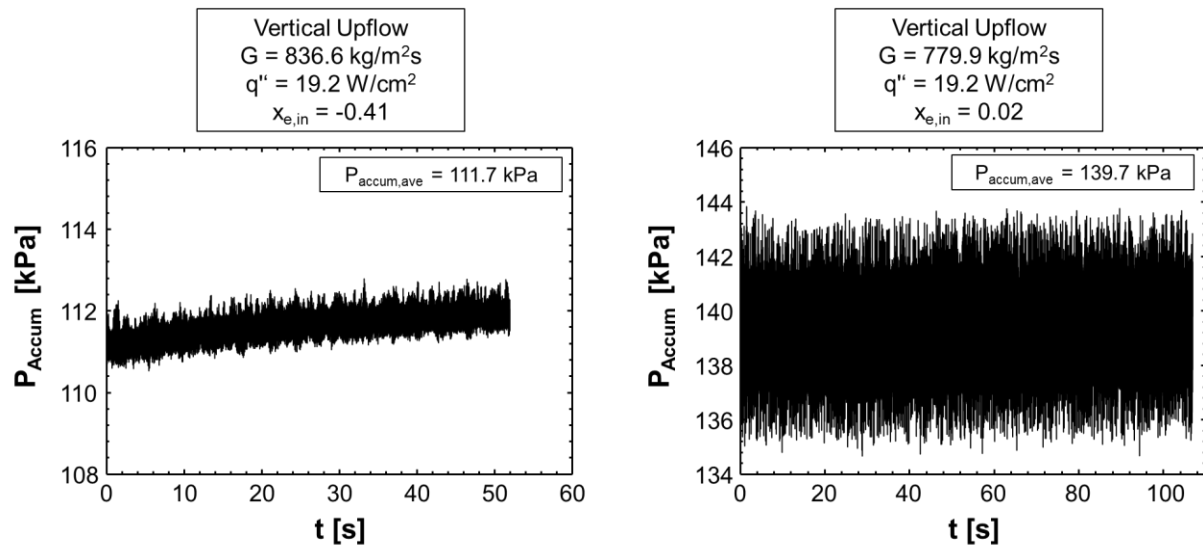


Figure 3.7: Sample plot of accumulator transient pressure (region V), along with amplitude versus frequency plots of the same for vertical upflow, vertical downflow, and horizontal flow with (b)  $G \sim 200 \text{ kg/m}^2\text{s}$  and subcooled inlet, (c)  $G \sim 200 \text{ kg/m}^2\text{s}$  and saturated inlet, (d)  $G \sim 800 \text{ kg/m}^2\text{s}$  and subcooled inlet, and (e)  $G \sim 800 \text{ kg/m}^2\text{s}$  and saturated inlet.

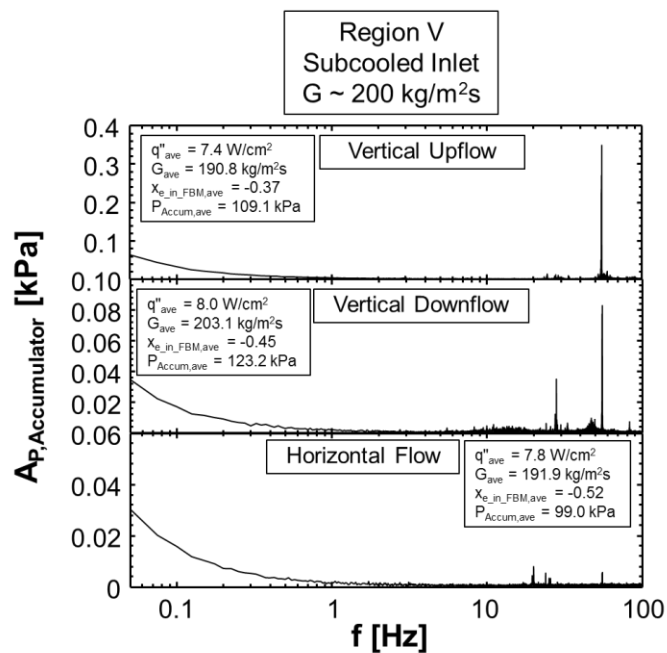


Figure 3.7 (b).

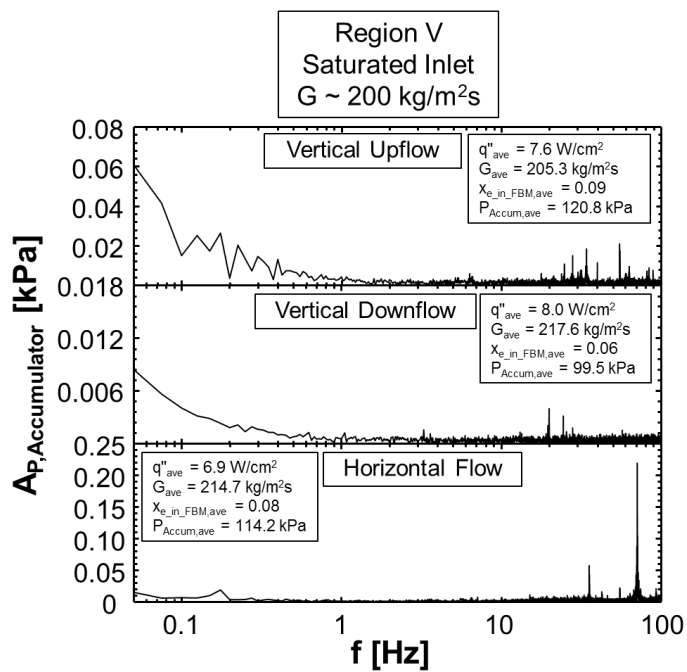


Figure 3.7 (c).

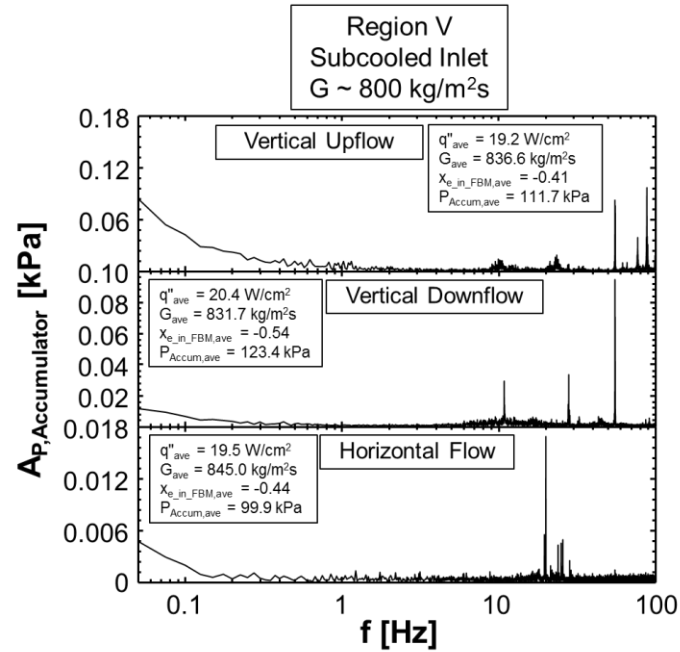


Figure 3.7 (d).

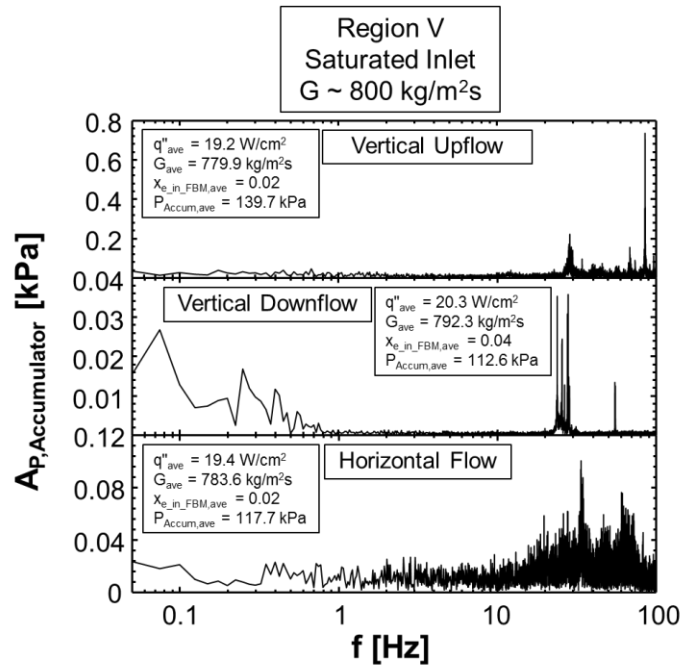


Figure 3.7 (e).

### 3.1.1.7 Overall Outcomes

By analyzing pressure oscillations using high-frequency pressure measurements upstream and downstream of all major fluid components of the flow loop, two key conclusions are drawn which will be of use in subsequent analysis:

- 1) Pressure oscillations within all portions of the flow loop occupied by single-phase liquid are dominated by high frequency mechanically induced phenomena. This includes subcooled flow boiling within the test section, although the process of bubble nucleation, departure, and collapse eliminates the sharp peaks seen elsewhere and distributes oscillations across the high frequency range.
- 2) In cases where saturated flow is introduced by the pre-heater, pressure fluctuations are dominated by behavior characteristic of Density Wave Oscillations (DWOs). Additionally, high frequency pressure oscillations present in the upstream single-phase liquid portion of the flow loop are not present in the portion containing a two-phase mixture, but reappear downstream of the condenser once the fluid has been returned to single-phase liquid.

The second outcome is of particular importance as it allows analysis of dynamic behavior within the two-phase portion of the test loop to focus on physical explanations without fear of mechanically induced phenomena compromising the integrity of results.

## 3.1.2 *Analysis of Flow Boiling Transient Behavior*

### 3.1.2.1 Recap of Trends from Prior Investigation

Previous work by the present author [53] included analysis of parametric trends relating to magnitude of DWOs manifest in transient pressure drop across the heated length of FBM in flows with saturated inlet conditions. Key trends are presented in Fig. 3.8, as the same analysis will not be repeated in the present work, but rather expanded to include the effects of DWOs on other key parameters. It should be noted that the prior study did not address subcooled inlet conditions or dynamic response of regions other than the FBM.

Figure 3.8(a) illustrates that, as mass velocity is increased, the amplitude of pressure oscillations also increases. This trend was observed again in the proceeding section in conjunction with saturated boiling conditions in Figs. 3.4 and 3.6. It should also be noted that there are threshold mass velocities required for DWOs to manifest themselves, which were encountered in the previous study for horizontal flow and vertical downflow orientations, but not for vertical

upflow. In the present study this was seen only with vertical downflow, Fig. 3.4(c). This is likely due to differences in height of the test section for the two studies.

Similarly, Fig. 3.8(b) shows flow dynamic behavior increases as the heat flux is increased. This makes intuitive sense, as more vigorous boiling increases dynamic behavior within the test section.

Finally, Fig. 3.8(c) depicts the inconsistent impact of increasing quality on amplitude of pressure fluctuations. Tests conducted in vertical upflow orientation saw increased pressure fluctuations as inlet quality was increased, while horizontal flow experienced noticeable decreases in fluctuations. Tests performed in vertical downflow orientation were largely unaffected by changes in inlet quality.

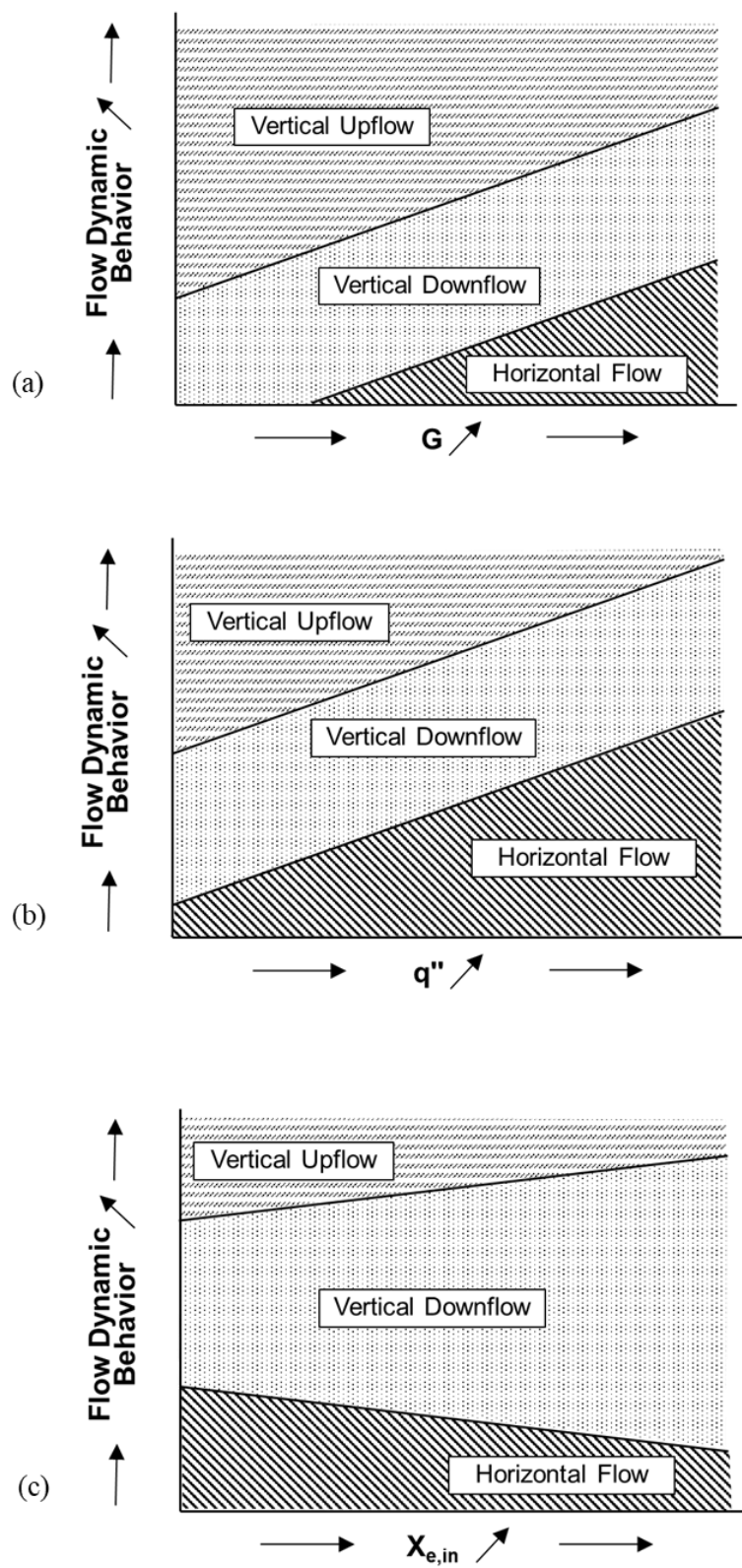


Figure 3.8: Qualitative trends for magnitude of flow boiling dynamic behavior in FBM versus (a) mass velocity, (b) heat flux, and (c) inlet quality.

### 3.1.2.2 Transient Evolution of Key Parameters with Increases in Heat Flux

As outlined in Section 2, tests in the present study were run by using the pump and pre-heater to set a desired flow rate and thermodynamic state at the inlet of the test section prior to applying heat flux to the test section. Heat flux on the heated walls of the FBM was increased in discrete steps, with step size decreasing as CHF was approached, until CHF was achieved and the power supply deactivated to prevent damage to the test section. During this process, no changes were made to pump speed or pre-heater power, allowing system pressure, flowrate, and inlet quality to evolve naturally in response to the boiling taking place along the heated length of the FBM.

Figure 3.9(a) shows the applied heat flux steps, along with the evolution of heated wall temperature, pressure drop over the heated length of the FBM, test section mass velocity, and inlet quality over time for the case of subcooled flow boiling with  $G \sim 400 \text{ kg/m}^2\text{s}$  in vertical upflow orientation. The key feature of this plot is the change in amplitude of pressure drop oscillations between 400 and 600 s along with accompanying decreases in mass velocity and inlet quality. This is due to a transition from *bubbly flow* to *churn flow* as boiling intensity is increased within the test section, clearly seen in associated high speed images. It should also be noted that, as CHF is encountered (just before 1000 s) and power supplied to the heated walls drops to zero, the magnitude of pressure drop oscillations rapidly diminishes, and both mass velocity and inlet quality climb steeply towards their zero heat flux values, clearly demonstrating the strong influence of heat flux on transient flow behavior.

Figure 3.9(b) shows similar plots for vertical upflow with  $G \sim 400 \text{ kg/m}^2\text{s}$ , this time with saturated inlet conditions instead of subcooled. Counter to the case of subcooled flow boiling, which exhibited a clear transition region in the range of 400 - 600 s, saturated flow boiling shows a largely linear change in both amplitude of pressure oscillations and system mass velocity as heat flux is increased within the test section. Inlet quality, while possessing large oscillations in the range of  $x_{e,in} = 0.02 - 0.06$ , shows a generally neutral trend as heat flux within the test section is increased and mass velocity decreases. Similar to Fig. 3.9(a), parameter values quickly return to their zero heat flux values after CHF is encountered and heat flux returned to zero.

Figure 3.9(c) shows a comparison of amplitude versus frequency plots of each parameter of interest for the lowest non-zero heat flux - heat flux 'C' from Figs. 3.9(a) and 3.9(b). Similar to Figs. 3.2 – 3.7, mean values indicated in Fig. 3.9(c) are calculated by averaging over the final

30 s of this heat flux. Immediately apparent is that the oscillations of heat flux are of such low magnitude as to have negligible impact on system dynamics. Temperature fluctuations are confined primarily to the low end of the frequency spectrum, which makes intuitive sense, as the thermal mass of the copper slabs used to create heated walls within the test section acts as a low-pass filter for thermocouple measurements performed within the walls.

It is in the amplitude versus frequency plot of pressure drop across the heated length of the test section where interesting behavior begins to emerge. For the subcooled inlet case, pressure fluctuations are dominated by a high frequency, well defined peak, similar to behavior seen for subcooled inlet cases examined previously in Figs. 3.4(b) and 3.4(d). Pressure fluctuations for the saturated inlet case exhibit behavior consistent with DWOs, with a peak frequency of  $\sim 2$  Hz, and no appreciable oscillations in the high frequency range.

Similar differences can be seen in amplitude versus frequency plots of mass velocity, with oscillations in the subcooled inlet case dominated by a single, sharp peak around 6 Hz, while fluctuations for the saturated inlet are dominated by higher-amplitude peaks distributed across the 0.5 - 2 Hz range. This is due to the influence of DWOs manifest in system mass velocity, which is also seen in the plot for inlet quality fluctuations for saturated inlet conditions. It is very clear that for both saturated and subcooled inlet conditions, frequency composition of inlet quality fluctuations is nearly identical to that for mass velocity fluctuations. This is due to the direct presence of mass flowrate in Eq. (2.1), while pressure fluctuations are only indirectly present in the evaluation of saturation properties.

Finally, Fig. 3.9(d) shows amplitude versus frequency plots for the highest heat flux tested prior to CHF - heat flux 'D' from Figs. 3.9(a) and 3.9(b). Results for the saturated inlet case show behavior attributable to DWOs again clearly dominates results for pressure drop, mass velocity, and inlet quality fluctuations, but now also significantly impacts heated wall temperature fluctuations. This is in itself an important observation as, depending on the amplitude of temperature oscillations, the possibility exists that CHF can be encountered due to heated wall temperature fluctuations exceeding a threshold value.

Parameters shown for the subcooled inlet case in Fig. 3.9(d) exhibit frequency composition similar to their low heat flux counterparts in Fig. 3.9(c), with the exception of subcooled boiling pressure drop fluctuations, which show significant 'smearing' of peaks across the high frequency range. As described when analyzing Figs. 3.4(b) and 3.4(d), this behavior is due to vigorous



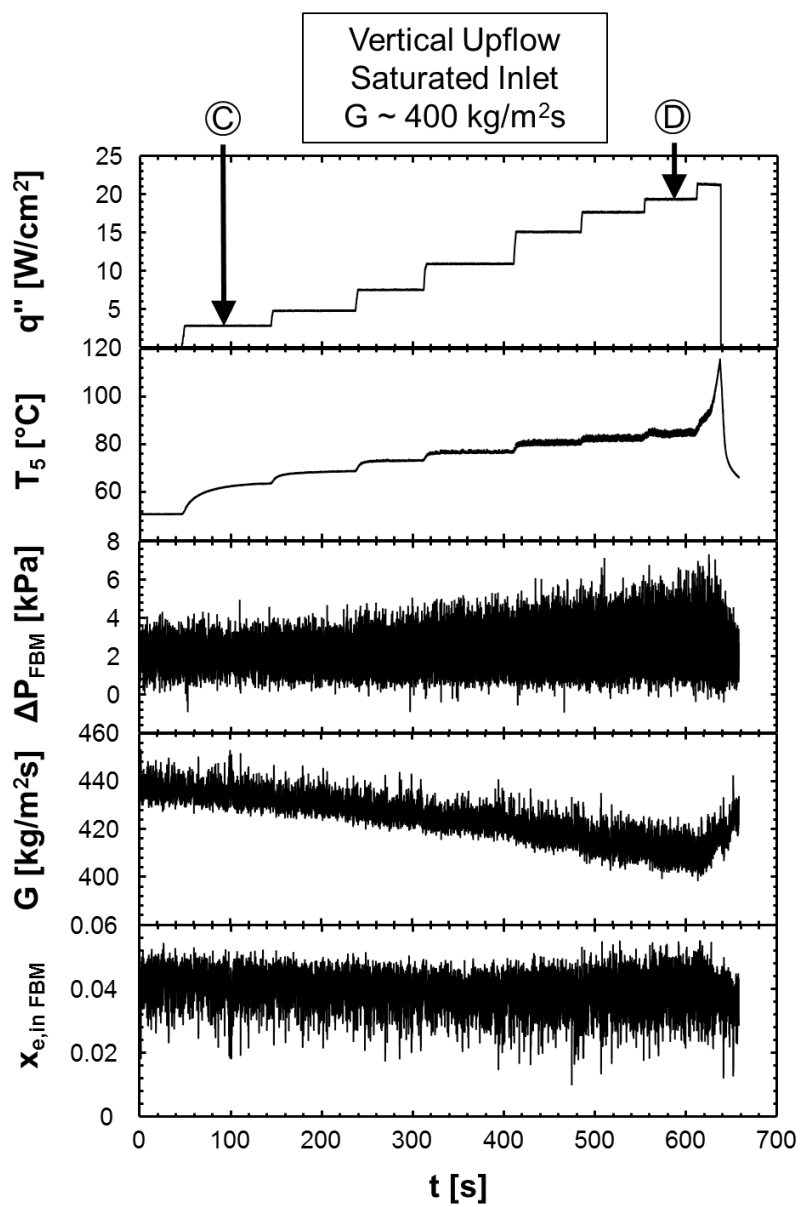


Figure 3.9 (b).

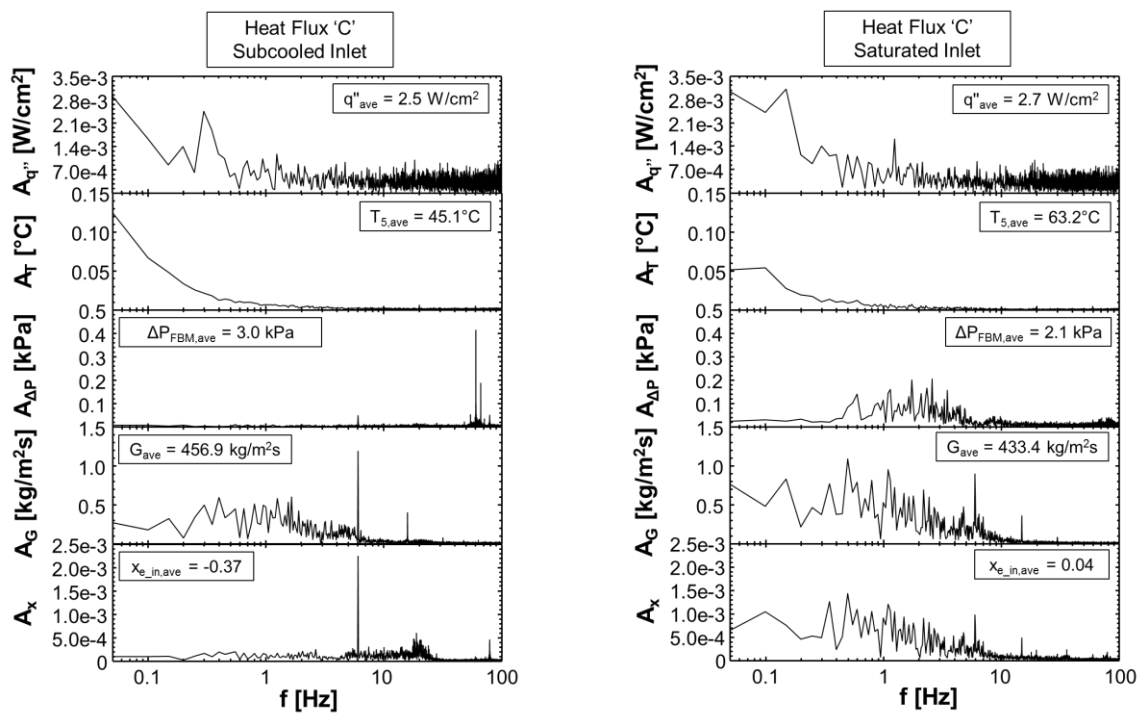


Figure 3.9 (c).

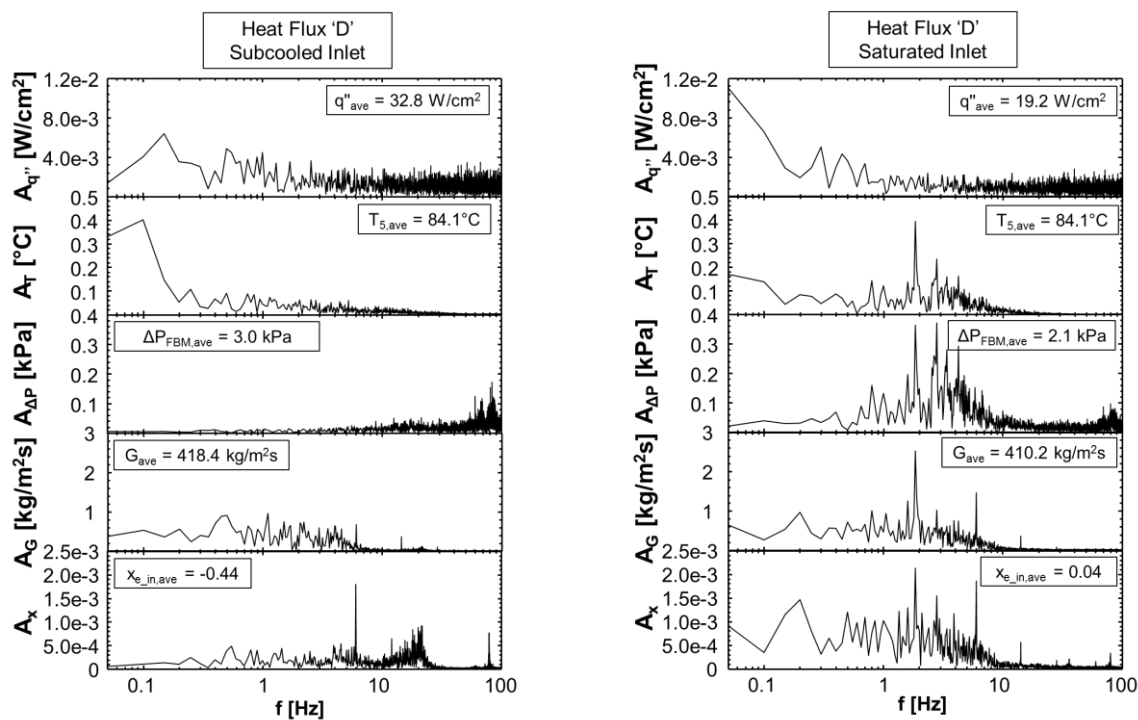


Figure 3.9 (d).

Figures 3.10(a) – 3.10(d) show results for similar operating conditions, now tested in vertical downflow orientation. Immediately apparent is the lack of a well defined transition region in Fig. 3.10(a) similar to that seen in Fig. 3.9(a). This can be attributed to the role of body force acting to stabilize liquid flow in the vertical downflow configuration, while it was destabilizing for vertical upflow. Figure 3.10(b) shows, however, that there is a well defined transition point at  $\sim 400$  s for the saturated inlet case, past which the magnitude of pressure drop fluctuations increases significantly and mass velocity drops sharply. This can be attributed to vapor production within the test section reaching a level where buoyancy force attempting to drive vapor counter to the flow direction begins to have a significant destabilizing effect on the flow. This effect is not seen for the subcooled case in Fig. 3.10(a), as (i) overall flow quality is much lower, and (ii) some vapor produced at the wall condenses back to liquid due to the bulk subcooling present.

Figure 3.10(c), comparing amplitude versus frequency plots for subcooled and saturated inlet cases with low heat flux, exhibits results very similar to those seen for vertical upflow in Fig. 3.9(c), with DWO behavior dominating for the saturated inlet case and higher frequency modes present in the subcooled inlet case.

Similarly, Fig. 3.10(d) reinforces conclusions drawn when analyzing Fig. 3.9(d), namely the presence of significant DWO induced behavior for all parameters (except heat flux) in the saturated inlet case. The presence of large amplitude temperature oscillations for the higher heat flux, saturated inlet case is again particularly worth noting for its potential to initiate CHF. Unlike Fig. 3.9(d), however, DWO induced oscillations in Fig. 3.10(d) show a dominant frequency of  $\sim 1$  Hz. This clear change in frequency with orientation reinforces the need for more sophisticated modeling to predict disturbance transport speed in Eq. (3.1).

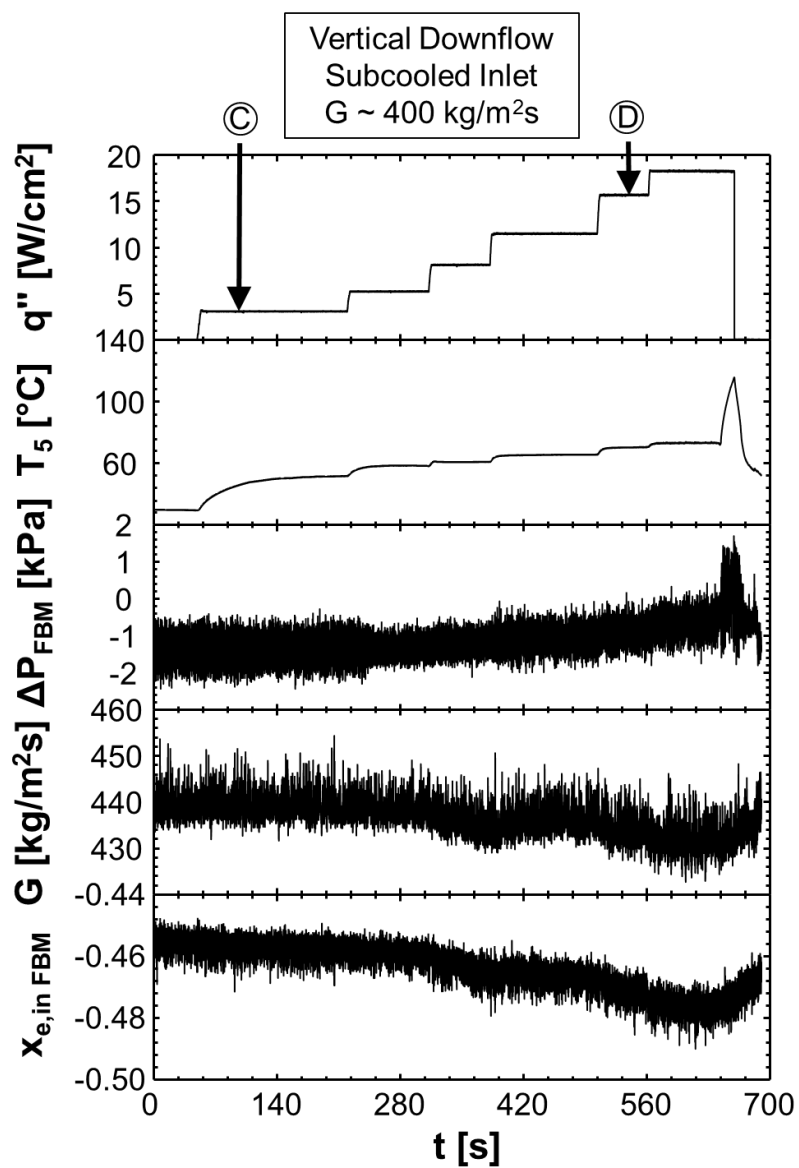


Figure 3.10: Transient results for vertical downflow with (a) highly subcooled and (b) saturated inlet conditions. Fast Fourier transforms of key steady-state parameters corresponding to heat flux levels 'C' and 'D' for each are compared in (c) and (d).

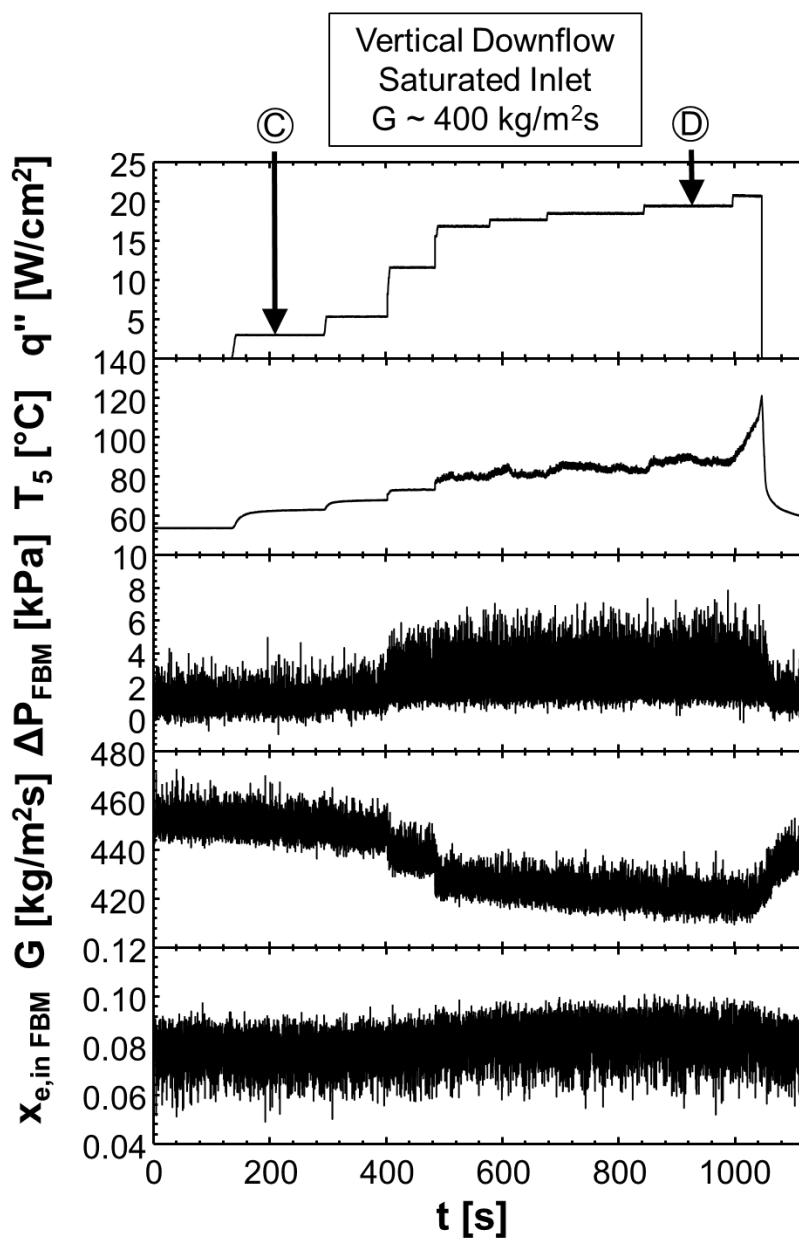


Figure 3.10 (b).

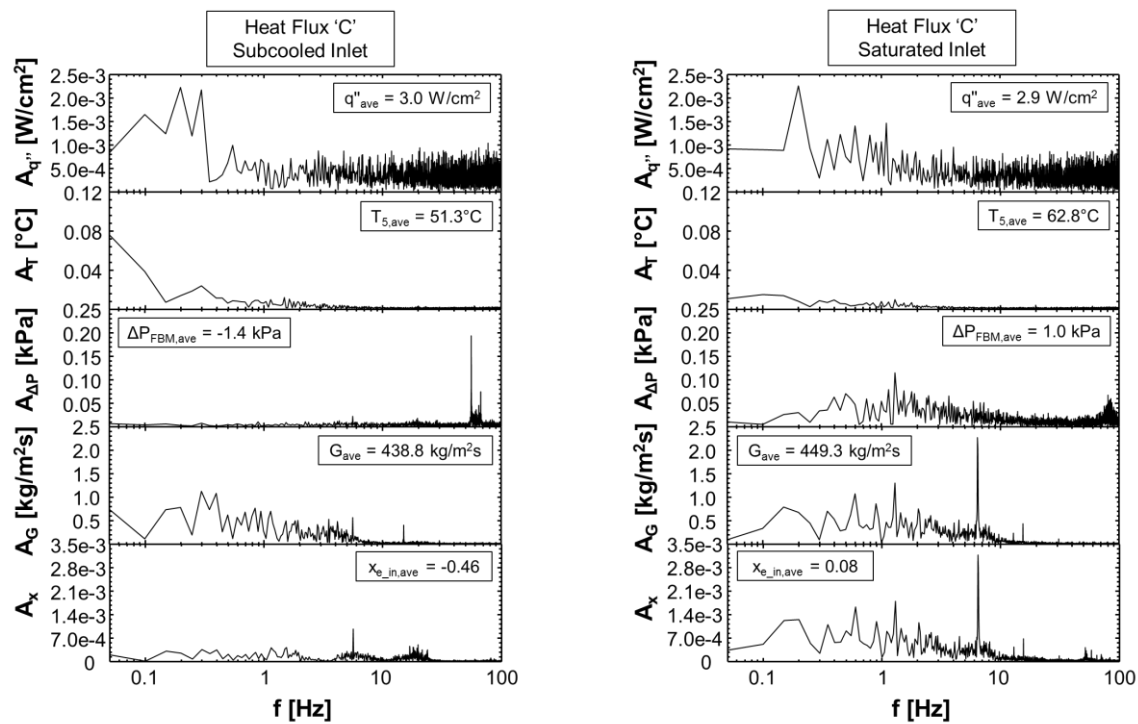


Figure 3.10 (c).

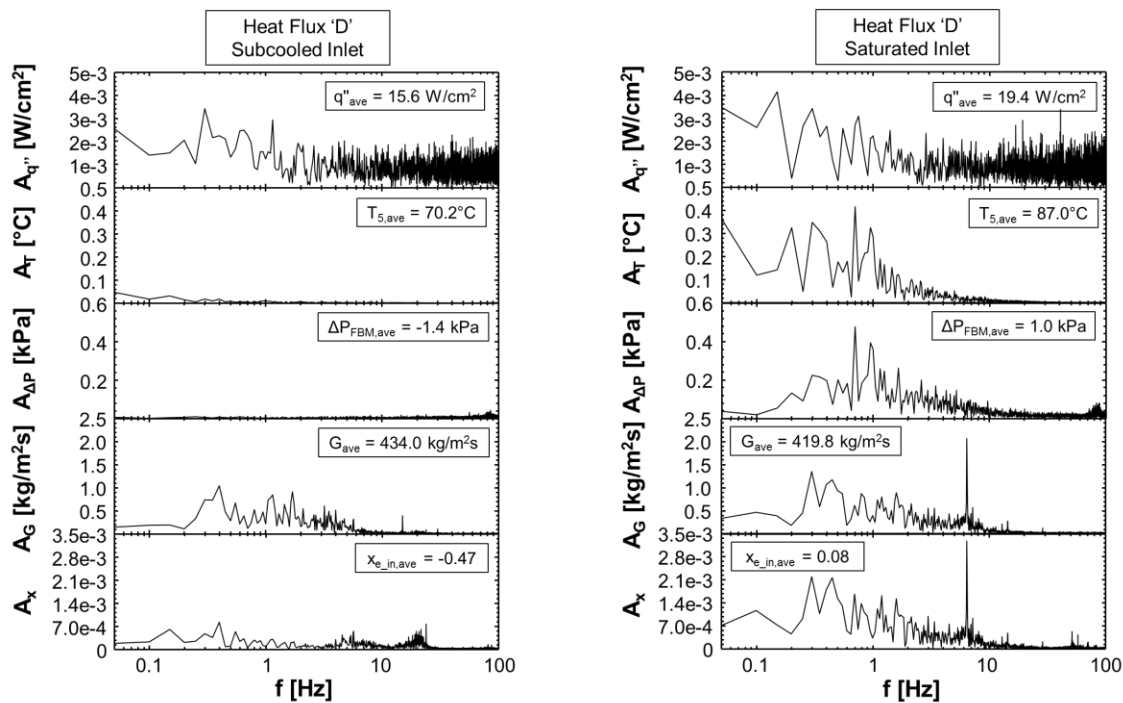


Figure 3.10 (d).

Figures 3.11(a) – 3.11(d) provide similar information for the case of horizontal flow. Immediately noticeable in Fig. 3.11(a) is a clear decrease in pressure drop across the heated length associated with the onset of boiling in the test section, followed by a gradual increase as boiling intensity is increased towards CHF. Mass velocity and inlet quality, however, exhibit only a gradual change in this same region, and do not begin to decrease significantly until heat fluxes close to CHF are applied.

Figure 3.11(b) exhibits higher amplitude oscillations for pressure, mass velocity, and inlet quality than those seen in Fig. 3.11(a), but both are relatively stable compared to their counterparts seen in Figs. 3.9 and 3.10 for vertical upflow and vertical downflow, respectively. This indicates that, within the boiling region of the test section, stability is strongly influenced by the component of body force acting parallel or opposite to flow direction. This notion is reinforced in Figs. 3.11(c) and 3.11(d), which show that, while similar trends regarding the appearance and impact of DWOs seen for vertical upflow and downflow are present in horizontal flow, amplitudes of oscillation are greatly reduced.



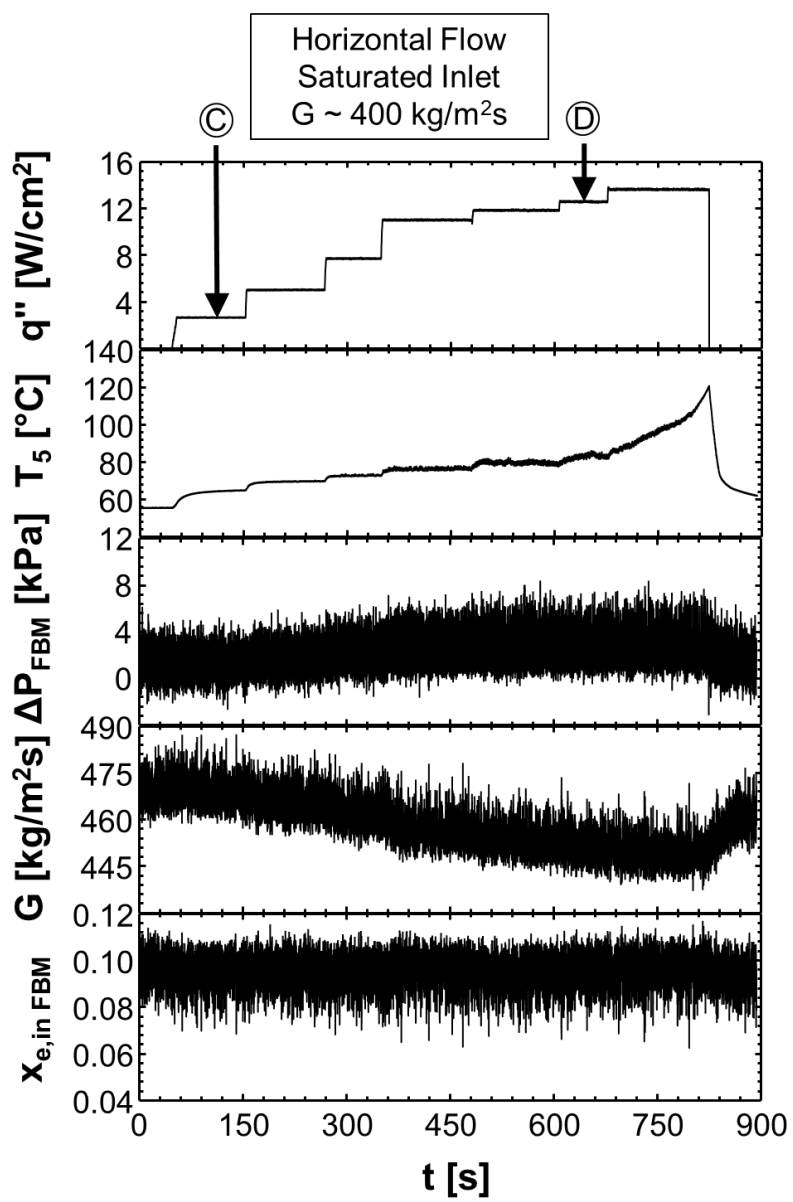


Figure 3.11 (b).

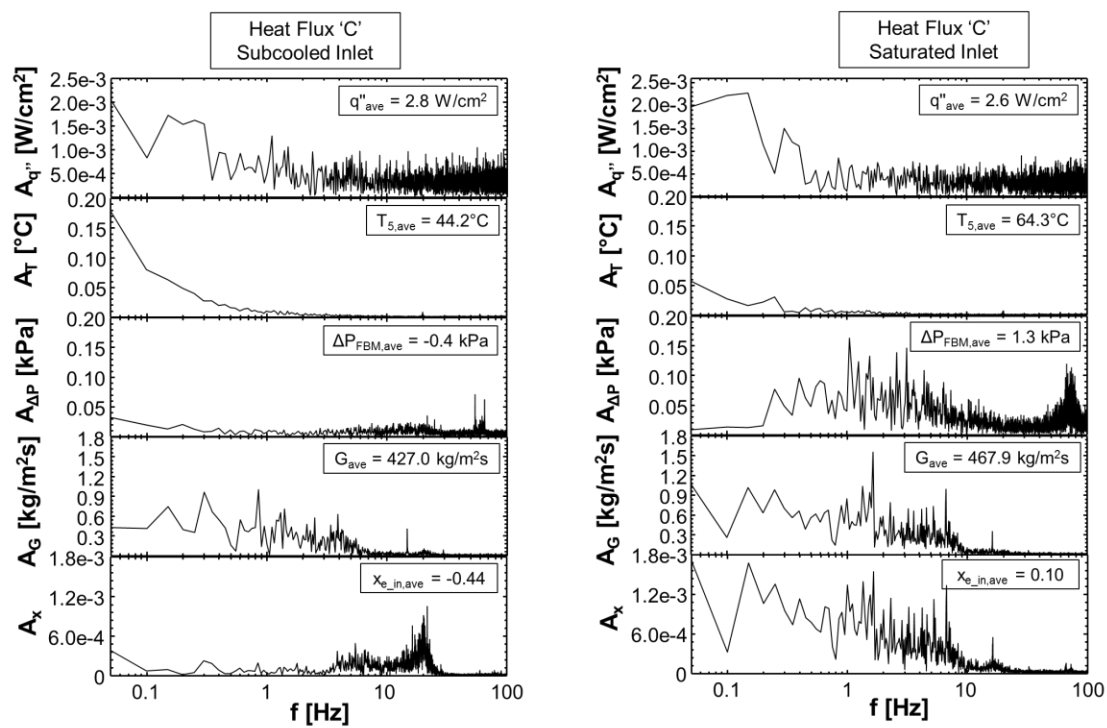


Figure 3.11 (c).

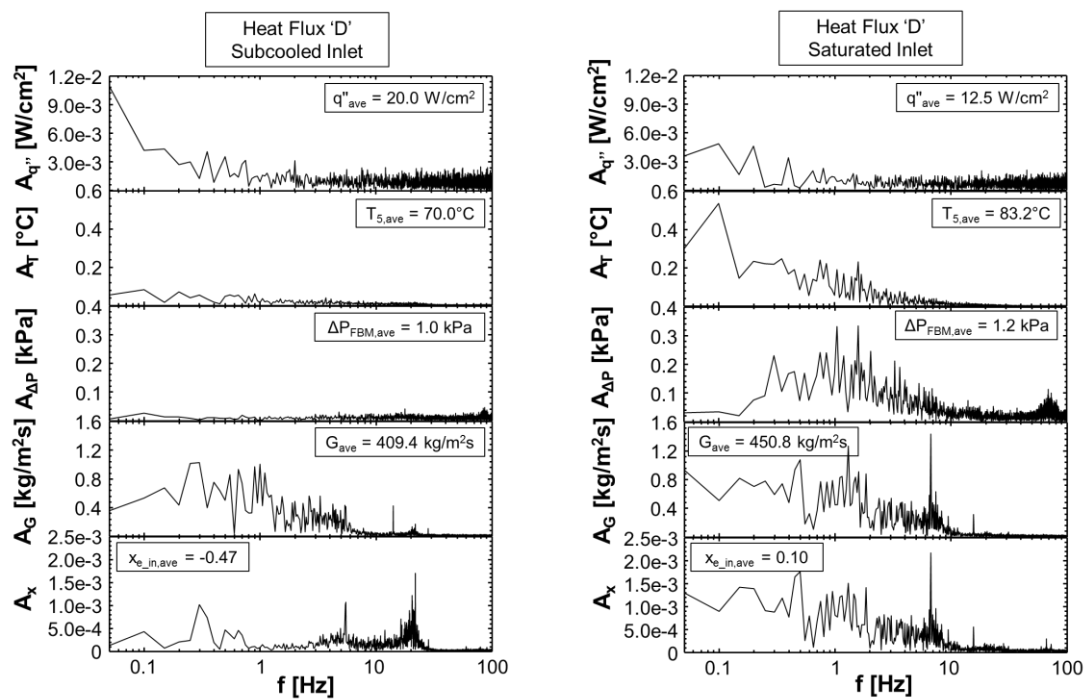


Figure 3.11 (d).

### 3.1.3 *Stability Map Evaluation*

#### 3.1.3.1 Utilization of Stability Maps in Two-phase Flow Analysis

Maps for flow boiling stability have been available in the literature for many decades, but little work has been done to homogenize and evaluate them compared to that done for other simple design tools such as flow regime maps and predictive correlations. In fact, significant variations exist among different maps in terms of coordinates used to evaluate stability and even definition of stability. Some studies were concerned with mathematical instability of governing differential equations, while others demarcated 'stable' and 'unstable' zones of operation in relation to a single type of instability observed within the system in question. Table 3.3 presents information on five prior studies in which stability maps were presented, including working fluid, mass velocity and heat flux ranges, and operating geometry for those empiric in nature, as well as a definition of the concept of 'stability' or 'instability' used in each case. Also listed is similar information for the present study.

Table 3.3: Description of works on which stability maps are based.

Authors	Working Fluid	Hydraulic Diameter [mm]	Mass Velocity [kg/m <sup>2</sup> s]	Heat Flux [kW/m <sup>2</sup> ]	Test Section Configuration	Stability Map Coordinates	Concept of Stability
Ishii and Zuber [37]	Analytic investigation				Single circular mini-channel	$N_{sub}$ vs. $N_{pch}$	<ul style="list-style-type: none"> <li>- Instability identified by existence of low frequency flow oscillations within system.</li> <li>- Evaluated using data of Solberg [79] for flow boiling of water in 5.25-mm diameter tub.</li> </ul>
Lee and Pan [157]	Analytic investigation				Single micro-channel, parallel micro-channels	$N_{sub}$ vs. $N_{pch}$	<ul style="list-style-type: none"> <li>- Cases with no oscillations or with finite amplitude oscillations (termed 'Limit Cycle Oscillations' by the original authors) identified as stable</li> <li>- Instability identified by exponential increase in amplitude of oscillations</li> </ul>
Brutin and Tadriss [38]	n-pentane	0.889	~10 - 2500	15.7 - 125.6	Single micro-channel	$x_{e,out}$ vs. $Re_{f,in}$	<ul style="list-style-type: none"> <li>- Instability identified by large amplitude pressure drop fluctuations</li> <li>- Threshold for amplitude evaluated empirically</li> </ul>
Chang and Pan [58]	Water	0.0863	22 – 110	7.68 – 87.7	15 parallel micro-channels	$N_{sub}$ vs. $N_{pch}$	<ul style="list-style-type: none"> <li>- Parallel channel instability identified by pressure drop fluctuations of <math>\Delta P_{max} - \Delta P_{min} &gt; 6</math> kPa</li> </ul>

Bogojevic <i>et al.</i> [158]	Water	0.194	72.2- 433.3	178-445	40 parallel micro- channels	$q''$ vs. $G$	<ul style="list-style-type: none"> <li>- High-Amplitude, Low Frequency (HALF) oscillations, and Low-Amplitude, High Frequency (LAHF) oscillations</li> <li>- Stability implies absence of both oscillation types</li> </ul>
Present Study	FC-72	3.33	176.5 – 2442.5	0 – 547	Single rectangular channel	$N_{sub}$ vs. $N_{pch}$	<ul style="list-style-type: none"> <li>- Stability implies inexistence of DWOs</li> <li>- Instability based on existence of DWOs</li> </ul>

Figures 3.12(a) and 3.12(b) depict stability maps originally presented by Bogojevic *et al.* [158] and Brutin and Tadrist [38], respectively, with stability boundaries indicated by dashed lines, and data from the present study superimposed over data used in the original studies. Notice that all present data in Fig. 3.12(a) are for vertical upflow orientation with subcooled inlet conditions for which DWOs were not observed. Although all the present data appear to correctly fall into the stable region of the map, it should be noted that this map was designed for a micro-channel heat sink and using water as working fluid. Additionally, the combinations of  $q''$  and  $G$  corresponding to the unstable regions of the map could not be achieved in the present FBM. More importantly, use of dimensional parameters for the map axes precludes generalizing the validity of the map for different working fluids and flow geometries.

As shown in Fig. 3.12(b), the definition of steady state by the map's authors, in which amplitude of pressure oscillations falls below a certain threshold, does not lend itself well to the present data. Note that the present data superimposed in Fig. 3.12(b) correspond to vertical upflow and saturated inlet conditions to conform to the map's positive  $x_e$  range. For the present data shown, DWOs are present and the flow is unstable in the present definition of flow stability. While this map does rely on dimensionless coordinates, it is not able to predict stability behavior of the present study. Additionally, this map cannot be used with negative  $x_e$  values and therefore cannot be assessed for a large fraction of the present data.

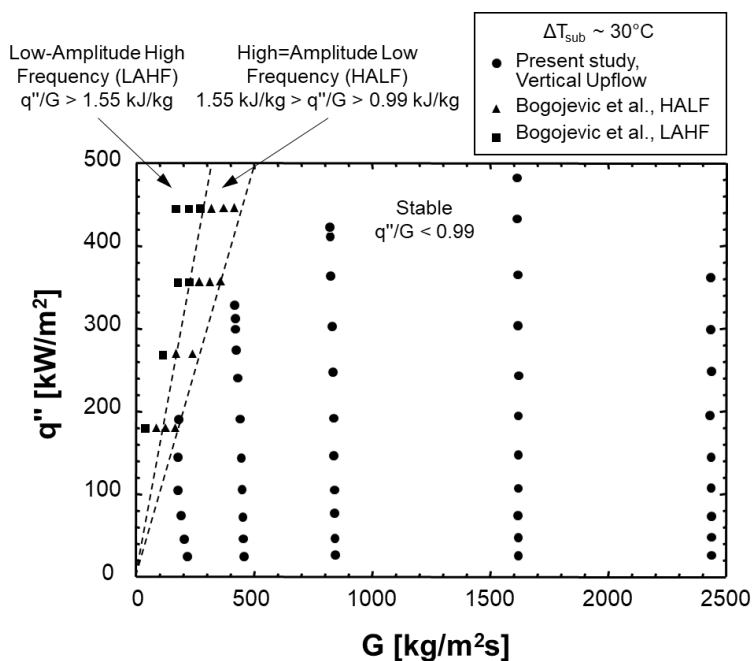


Figure 3.12: Data from the present experiments superimposed on stability maps of (a) Bogojevic *et al.* [158] and (b) Brutin and Tadrict [38].

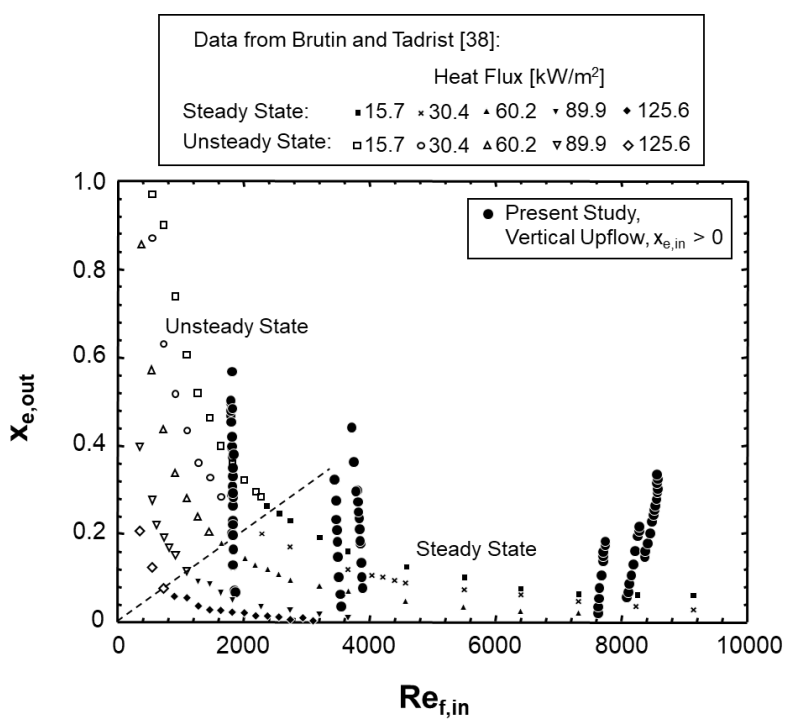


Figure 3.12 (b).

A more common approach to developing stability maps is shown in Figs. 3.13(a) – 3.13(c), where phase change number,

$$N_{pch} = \frac{Q}{\dot{m} h_{fg}} \frac{v_g - v_f}{v_f}, \quad (1.2)$$

and subcooling number,

$$N_{sub} = \frac{h_f - h_m}{h_{fg}} \frac{v_g - v_f}{v_f}, \quad (1.1)$$

are used as  $x$  and  $y$  coordinates, respectively (these terms were initially defined in Eqs. (1.1) and (1.2), and are presented again here to assist in interpretation of plots). By expressing coordinates in terms of dimensionless parameters, these maps allow for better comparison of results across working fluids and geometries.

Figure 3.13(a) shows one of the earliest stability maps presented in literature, created by Ishii and Zuber [37] to evaluate experimental data obtained by Solberg [78]. Ishii and Zuber approached the problem of stability by first generating a two-phase flow model, solving the model numerically for a given set of experimental operating conditions, and defining the transition to instability as a point at which low frequency flow oscillations appear.

Figure 3.13(b) shows the stability map generated by Lee and Pan [157] to detail numeric stability of the solution for flow in a micro-channel. It is worth noting that the 'unstable' region corresponds to conditions where amplitude of oscillations increases exponentially, while the 'stable' region encompasses both flow without oscillations and flow with finite amplitude oscillations (termed 'limit cycle oscillations' by Lee and Pan), of which DWOs are a subset.

Figure 3.13(c) shows the map of Chang and Pan [58], which is based on experimental data obtained for subcooled flow boiling in a micro-channel heat sink. They identified the onset of parallel channel instability as the point at which pressure oscillations within the micro-channel heat sink reach sufficient magnitude to initiate backflow in some channels. They also used data gathered by Qu and Mudawar [57] to validate their stability boundary, making it one of the stronger tools available for prediction of operating conditions for which parallel channel instability will manifest.

Unfortunately, the three stability maps in Fig. 3.13 do not lend themselves well to application using the present data, where physical instabilities are encountered exclusively for saturated inlet

conditions, which correspond to negative values of  $N_{sub}$ . For this reason, expanded stability maps are needed which can encompass test cases corresponding to saturated flow boiling.

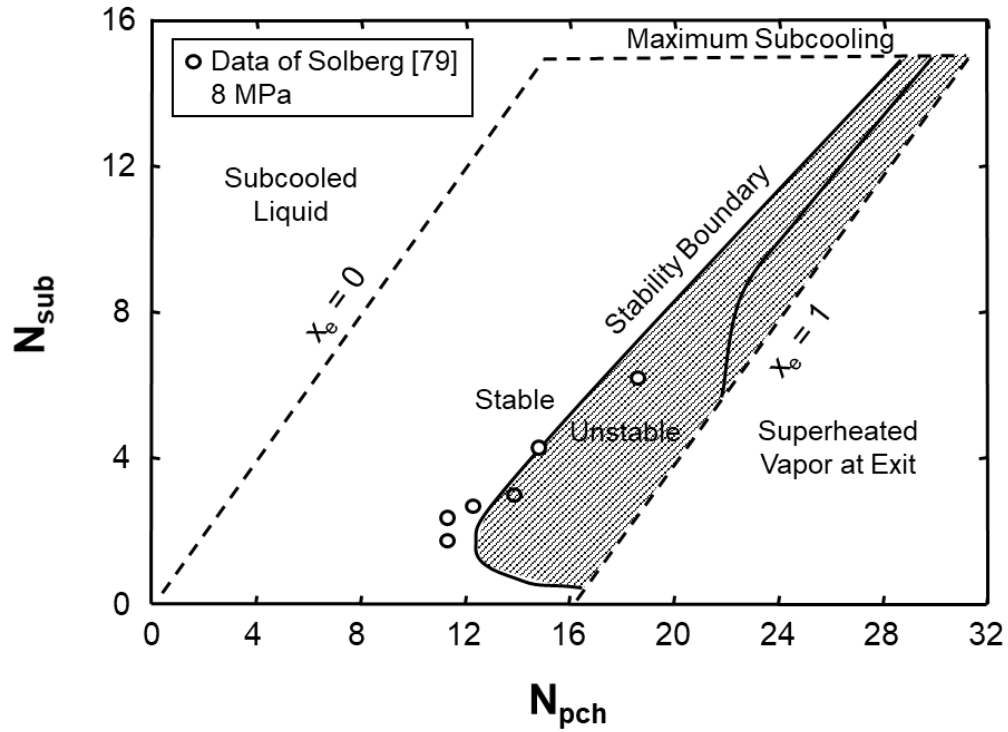


Figure 3.13: Flow boiling stability maps adapted from (a) Ishii and Zuber [37], (b) Lee and Pan [157], and (c) Chang and Pan [58].

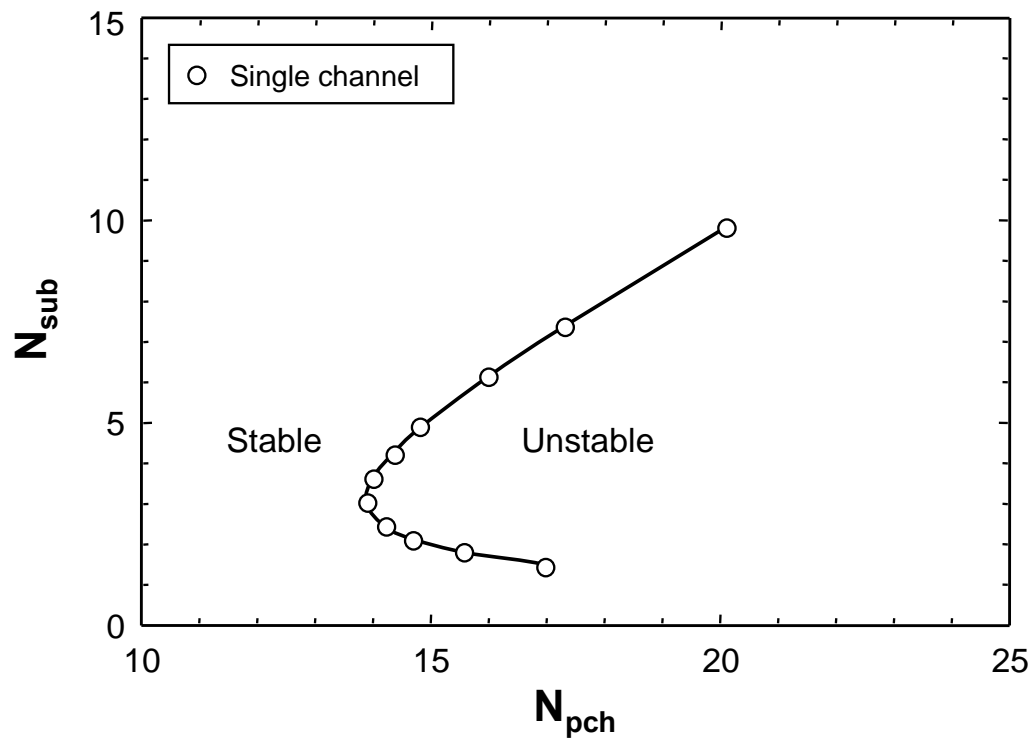


Figure 3.13 (b).

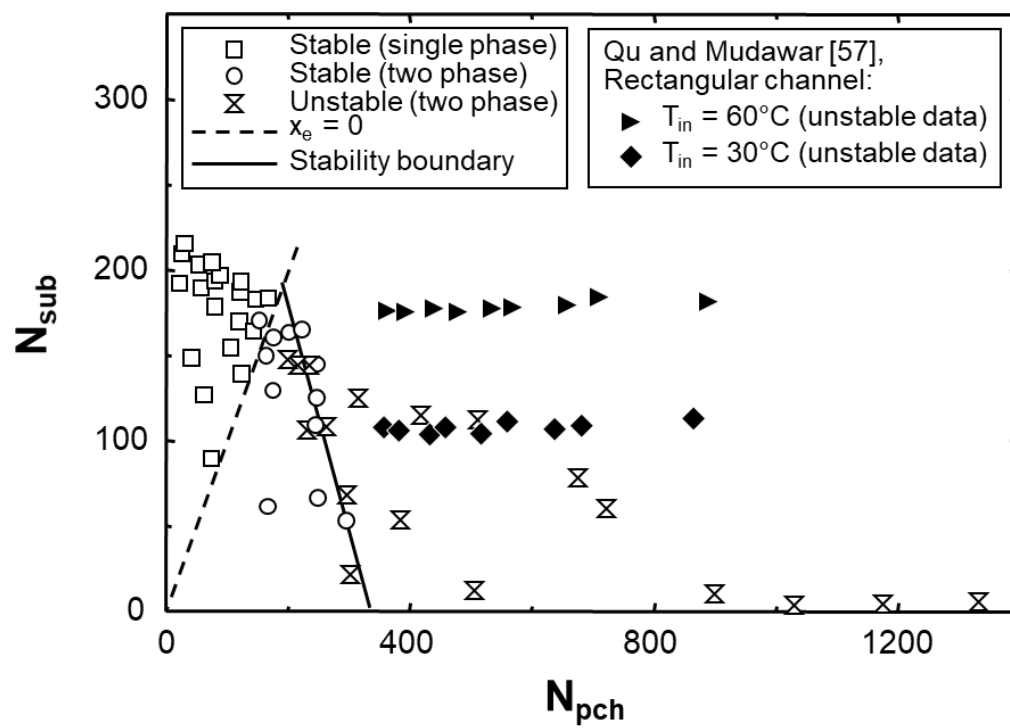


Figure 3.13 (c).

### 3.1.3.2 New Qualitative Stability Maps for Density Wave Oscillations

As mentioned above, stability maps are inherently tied to the concept of stability used by their creators, meaning application of stability maps has little utility unless concepts of 'stability' and 'instability' are clearly defined. In the present study, 'instability' will be defined as conditions under which DWOs are observed within the system, while 'stability' is considered the absence of DWO induced behavior.

Figures 3.14(a), 3.14(b), and 3.14(c) show stability maps for vertical upflow, vertical downflow, and horizontal flow orientations. In each case, there is a clear boundary between subcooled flow boiling (associated with positive values of  $N_{sub}$ ) and saturated flow boiling (associated with negative values of  $N_{sub}$ ). Also, the range of  $N_{pch}$  varies significantly across orientations, with Fig. 3.14(a) showing vertical upflow reaching peak values of  $N_{pch} > 50$ , while Figs. 3.14(b) and 3.14(c) show values of  $N_{pch} < 35$ .

Also indicated on each plot is a qualitative boundary line, summarizing trends seen regarding the existence of DWOs for different operating conditions in each orientation. The boundary line in Fig. 3.14(a) illustrates the fact that DWOs are present for even the lowest mass velocities (*i.e.*, highest phase change numbers) tested in vertical upflow orientation, apparent in the lack of concavity in the boundary line at high values of  $N_{pch}$  (*i.e.*, low values of mass velocity). The boundary line also indicates the necessity of saturated flow conditions for the occurrence of DWOs, evidenced by its position near  $N_{sub} = 0$ .

Figure 3.14(b) shows how, even for saturated inlet conditions, a threshold mass velocity is required for the formation of DWOs in vertical downflow. This is represented by the downward pointing boundary line for high phase change numbers, which represent relatively low mass flowrates present in the denominator of Eq. (1.1). For horizontal flow, Fig. 3.14(c) presents trends similar to those for vertical downflow.

Although all subplots in Fig. 3.14 provide relevant information regarding the existence of DWOs in flow boiling, there is room for improvement in the formulation of stability maps depicting the onset of DWOs. Additional tests involving saturated flow boiling at higher mass velocities would provide valuable information and help extend the range of the stability maps presented. Furthermore, by conducting tests along the boundary between observation and non-observation of DWOs within the FBM for each orientation, the stability boundary could be further refined. Also, by performing similar experiments using different working fluids, predictions could

be better generalized to account for variations in key fluid properties such as latent heat of vaporization, phase density difference, and surface tension.

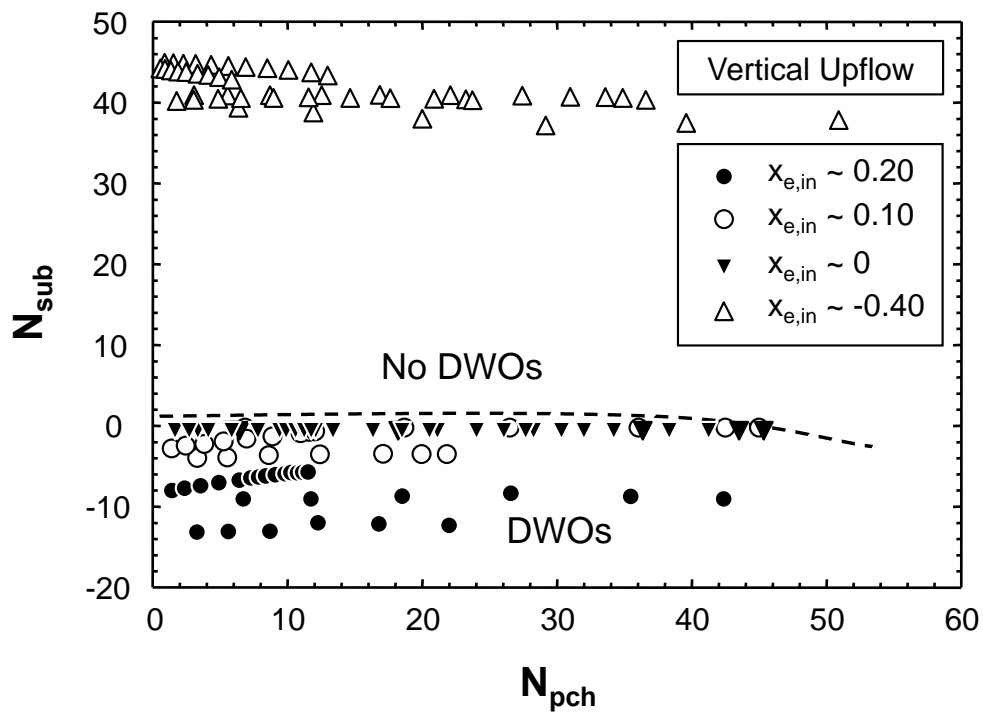


Figure 3.14: Stability maps indicating conditions under which Density Wave Oscillations are present for (a) vertical upflow, (b) vertical downflow, and (c) horizontal flow orientations.

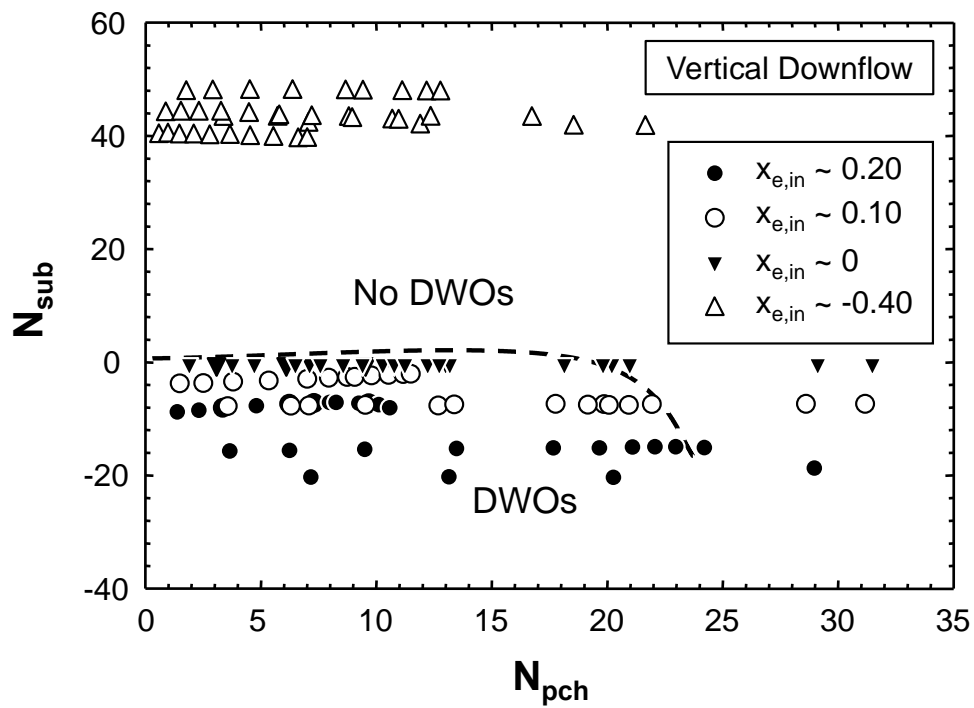


Figure 3.14 (b).

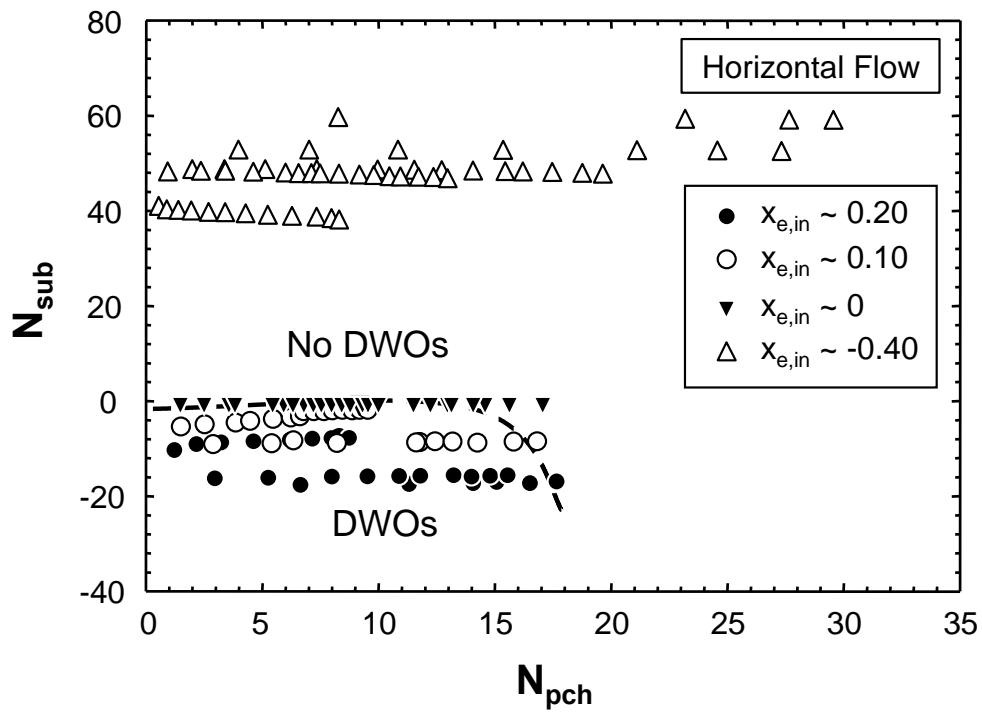


Figure 3.14 (c).

## 3.2 Frequency and Amplitude of Density Wave Oscillations in Vertical Upflow Boiling

### 3.2.1 Analysis of Density Wave Oscillation (DWO) Phenomenon

#### 3.2.1.1 Density Wave Oscillations (DWOs) in Micro-channels versus Mini/macro-channels

In many prior works [49-52] DWOs have been explained as resulting from delay and feedback effects between thermal and hydrodynamic phenomena present within two-phase flows. In micro-channels, the phenomenon leading to DWOs is easily visible, as large values of confinement number,

$$Co = \frac{\sqrt{\frac{\sigma}{g(\rho_f - \rho_g)}}}{D_h}, \quad (3.2)$$

representing the ratio of Taylor Wavelength to channel hydraulic diameter, lead to vapor formation via nucleation on a scale comparable to the hydraulic diameter. This displaces significant amounts of liquid within the channel, and can cause instantaneous mass conservation imbalances between the channel inlet and outlet, leading to a surge of liquid (and associated pressure drop) which ensures continuity is satisfied in time-averaged fashion.

In mini/macro channels (such as in the present FBM), however, vapor generation through nucleation is not of a scale comparable to hydraulic diameter, meaning other explanations must be present for the pressure and flowrate oscillations experimentally detected and associated with DWOs. This also severely limits the applicability of some existing correlations for frequency of oscillatory behavior, such as those recently investigated by Lee *et al.* [61] for pressure oscillations in micro-channel boiling, which depend primarily on the nucleation process and associated surface tension effects.

Classic mini-channel DWO studies, such as the works of Ishii [75], Belblidia and Bratianu [81], and Lahey and Podowski [47], dealt primarily with subcooled flow boiling and attributed low-frequency oscillations in pressure and flowrate resulted from feedback between changes in system pressure and thermophysical properties. In a simple example, an increase in system pressure would lead to a change in position of the Onset of Nucleate Boiling (ONB) point, which would change the pressure-drop characteristics of the system, causing the system pressure to drop, the ONB point to change in the opposite direction, and the process to repeat itself.

These works included extensive analysis, primarily focused on development of full two-phase flow field models (slip flow, drift flux, even homogeneous equilibrium model) and applying classic stability theory to governing equations to determine stability boundaries, leading to the development of stability maps such as that of Ishii and Zuber [37] (developed for use with the experimental data of Solberg [78]).

This classic analysis does not fit well with experimental data observed by the present author in the preceding section (nor a prior study [54]), however, which saw little appreciable oscillatory behavior in the relevant frequency range ( $\sim 0.5 - 10$  Hz) for subcooled flow boiling in the FBM. Indeed, the recent review of Ruspini *et al.* [66] indicated the presence of three ‘types’ of DWOs in the literature: Type 1, due to gravity, Type 2, due to friction, and Type 3, due to momentum. The underlying idea is DWOs could be formed by different combinations of forces/driving behaviors depending on operating conditions and test section geometry, with all eventually yielding oscillations in the low frequency range.

This dependence on operating conditions for both when and how DWOs manifest is more accommodating to experimental conditions such as those in Section 3.1 which do not fit the classical description of DWOs well, but nonetheless exhibit strong signs of oscillatory behavior commonly attributed to DWOs. In keeping with this, the present study will neglect the classic analysis approach and focus on determining the mechanisms behind formation of DWOs by starting from flow visualization images and applying analysis focused on perceived dominant hydrodynamic and thermodynamic effects during the DWO process (*i.e.*, body force, phase change, *etc.*).

### 3.2.2 Analysis of Transient Pressure Signals

As shown in the preceding sections (and prior works [53,54]), a first step in determining the presence and impact of DWOs within a system is analysis of transient pressure results. Having determined conditions for which DWO induced behavior is present in Section 3, the present section will limit analysis to transient pressure signals where DWOs are observed to most clearly illustrate the presence and influence of DWOs within the system.

Figures 3.15(a), 3.15(b), and 3.15(c) provide transient pressure results corresponding to measurement locations at the inlet and outlet of the FBM’s heated length, along with Fourier transforms of each signal, for mass velocities of  $G = 234.2$  kg/m<sup>2</sup>s, 834.1 kg/m<sup>2</sup>s, and 1978.9

kg/m<sup>2</sup>s, respectively, all gathered during year 1 (defined in Section 2). It should be noted that, for each subfigure, two transient plots are provided: one encompassing the entire 20-s period used to perform the fast Fourier transform, and another displaying only the first 3 s of data to better highlight characteristics of each individual curve.

Figure 3.15(a) shows that, for the lowest mass velocity of  $G = 234.2$  kg/m<sup>2</sup>s, both inlet and outlet pressure signals exhibit behavior indicative of DWOs in the 0.5 – 5 Hz frequency range. It is clear, however, that the inlet pressure signal experiences significantly larger fluctuations, and these fluctuations are sharper in nature. The short-duration transient plot clearly displays near-sinusoidal behavior by the outlet pressure, while the inlet pressure seems to be characterized more by sharp departures from a nominal value. This type of oscillatory behavior is periodic in nature but not perfectly sinusoidal, a distinction which will become important in later analysis.

Figure 3.15(b), corresponding to the moderate mass velocity of  $G = 834.1$  kg/m<sup>2</sup>s, shows that as mass velocity is increased larger pressure fluctuations are seen at both inlet and outlet. Similar to Fig. 3.15(a), the outlet pressure behaves in a near-sinusoidal fashion, while the inlet is characterized by sharp departures from a nominal level. This difference in behavior is also clearly manifest in the frequency composition of each signal, with both inlet and outlet pressures exhibiting a peak at ~2 Hz, but with significantly more spread in frequency composition seen in the inlet signal as compared to the outlet signal. Also of interest is the clear presence of a slight phase shift between inlet and outlet pressures when analyzing the short-duration transient plot. Peaks in inlet pressure are followed shortly by peaks in outlet pressure, and troughs in inlet pressure lead to troughs in outlet pressure shortly after. The fact that these two pressure measurement locations do not exhibit in-phase fluctuations indicates the passage of a transient through the heated length of the test section.

Figure 3.15(c) reinforces the trends evident in the first two subfigures by providing similar results for the highest mass velocity case of  $G = 1978.9$  kg/m<sup>2</sup>s. Similar to Fig. 3.15(a), peak frequencies of oscillation for inlet and outlet pressures differ slightly.

Across all three subfigures for the present operating conditions corresponding to finite quality flow within the test section at various pressures and mass velocities DWOs are seen to manifest. Differences are present when comparing inlet and outlet pressure curves for certain cases, however, primarily in frequency of oscillation. This is likely due to some combination of

thermal and hydrodynamic effects taking place within the heated length of the test section, and is indicative of DWOs being characterized by passage of a transient through the system.

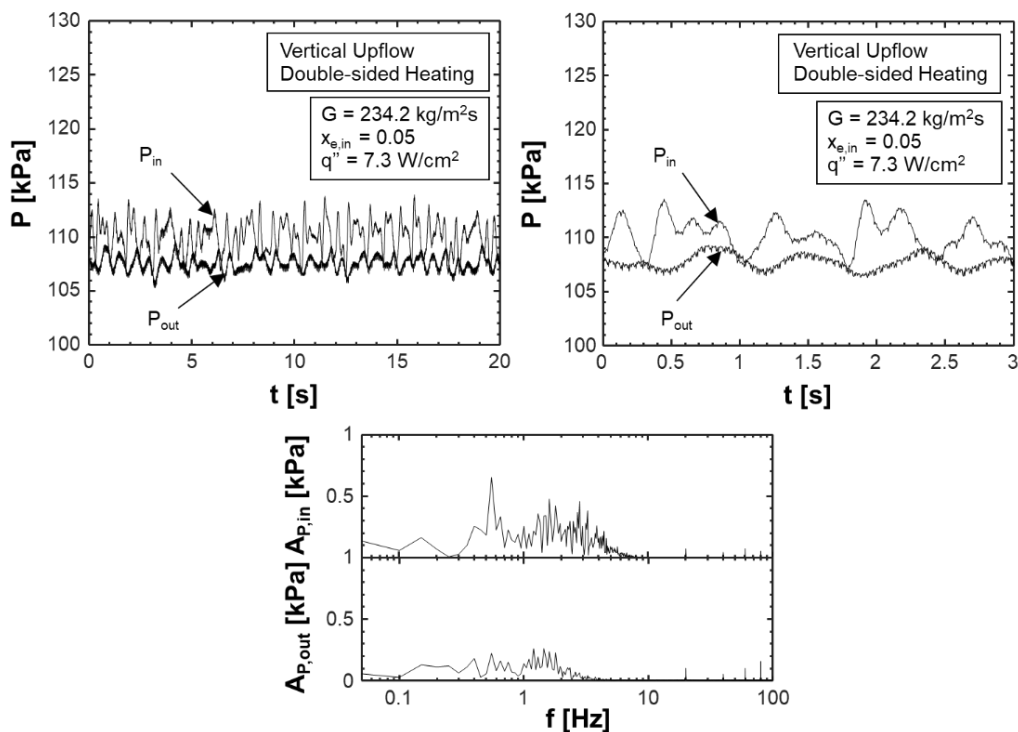


Figure 3.15: Plots of FBM heated length inlet and outlet pressures versus time over 20 s, zoomed in on the first 3 s, and associated fast Fourier transforms over the 20-s period for (a)  $G = 234.2$  kg/m<sup>2</sup>s, (b)  $G = 834.1$  kg/m<sup>2</sup>s, and (c)  $G = 1978.9$  kg/m<sup>2</sup>s,

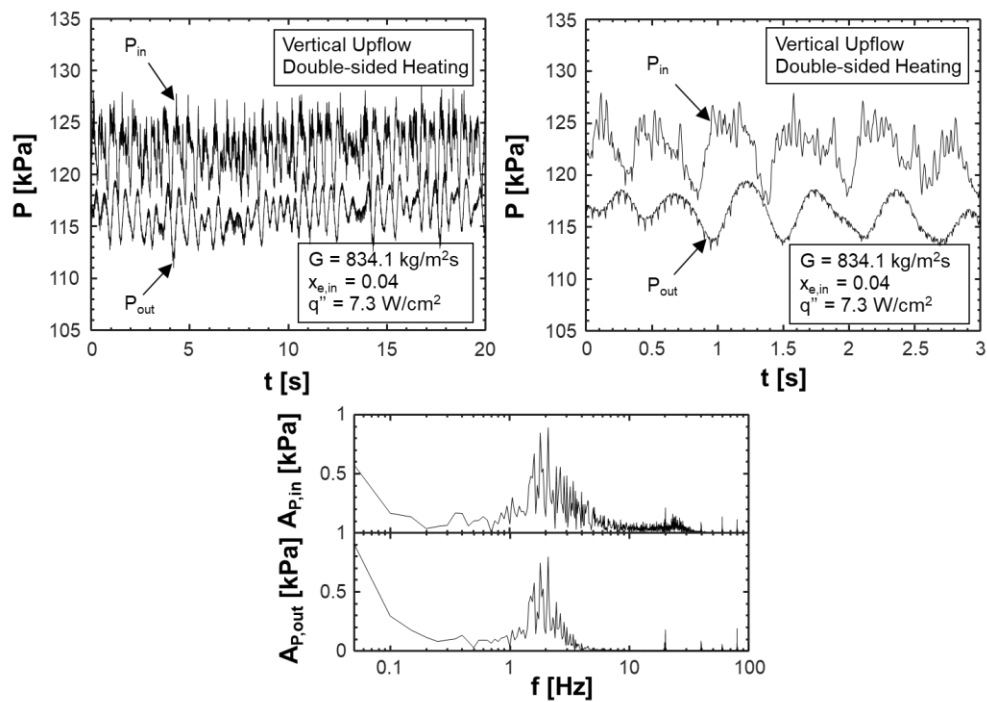


Figure 3.15 (b).

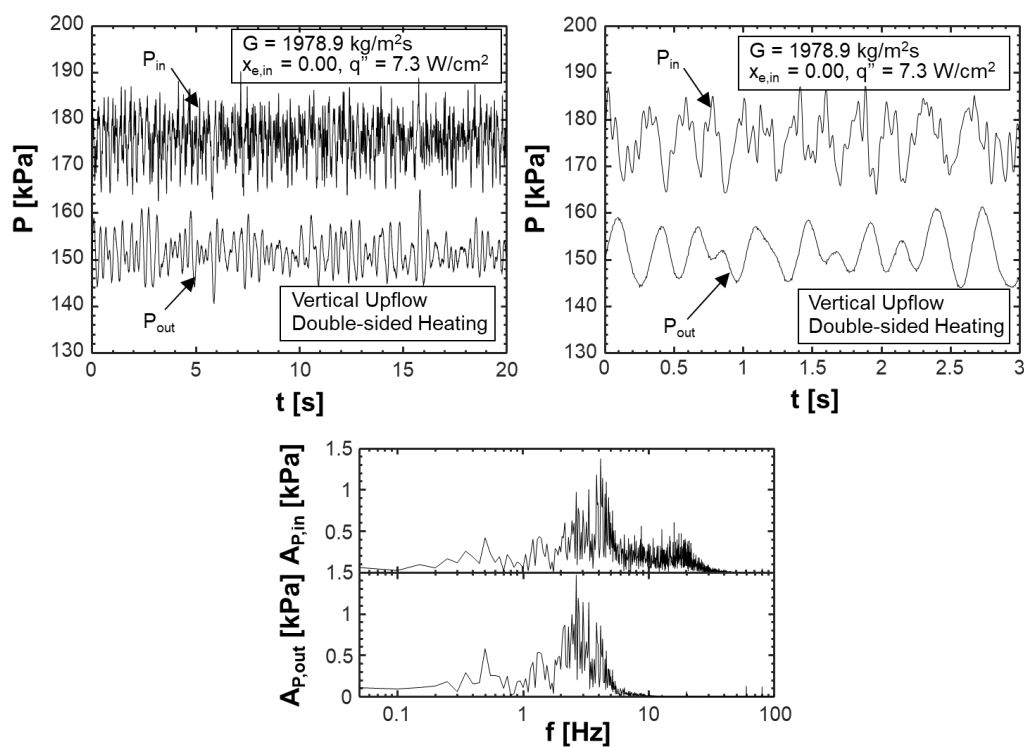


Figure 3.15 (c).

### 3.2.2.1 Flow Visualization Images

Although imaging of two-phase flow with finite quality often yields inferior results to that of subcooled boiling due to the necessity of imaging through a disturbed liquid film (as is the case for annular flow), important conclusions regarding the formation and occurrence of DWOs in the present system may be drawn nonetheless through careful analysis of flow visualization sequences. Although mentioned when discussing experimental methods, it should be noted again that images presented here correspond to the entire 114.6-mm heated length of the FBM and are captured at a rate of 2000 fps with an electronic resolution of 2040 x 174 pixels. Additionally, all images presented within the present section correspond to tests performed during year 1.

Figures 3.16(a) – 3.16(e) depict five sequences of images for a test case corresponding to mass velocity of  $G = 407.8 \text{ kg/m}^2\text{s}$ , inlet quality  $x_{e,in} = 0.03$ , average inlet pressure  $P_{in} = 116.0 \text{ kPa}$ , and heat flux  $q'' = 7.2 \text{ W/cm}^2$ . Each consecutive set of images is separated by 0.005s, and the entire range of images across subfigures 3.16(a) – 3.16(e) corresponds to a single consecutive set of images spanning 0.5 s of real-time.

Figure 3.16(a) illustrates that, for an arbitrary starting point selected within the imaging sequence, flow through the heated length of the test section is nominally annular. However, as time progresses, a point is reached at which flow into the heated length is no longer annular, but is instead largely liquid. This point is indicated in Fig. 3.16(a) with a white arrow. As time advances further, this front (still indicated by a white arrow) is seen to move along the length of the channel, with nucleate boiling now taking place within the liquid as opposed to film evaporation common to annular flow.

Just prior to the transition from Fig. 3.16(a) to 3.16(b), it can be seen that the entire channel length becomes occupied by liquid, with subcooled boiling taking place along the heated walls. At the start of Fig. 3.16(b), however, a pocket of vapor is clearly seen to begin working its way along the channel length, highlighted again by a white arrow. As the front of the vapor pocket moves along the channel length, it begins to lose its crisp boundary, instead devolving back into annular flow, evident from the increased presence of interfacial waves which are a key characteristic of vapor core flow past a liquid film. Annular flow continues to dominate throughout Fig. 3.16(b), similar to the flow conditions present within Fig. 3.16(a).

Just prior to transitioning to Fig. 3.16(c), however, the liquid film in the entrance region begins to show signs of drying out. This continues throughout Fig. 3.16(c), with significantly

reduced liquid content present in the heated length of the channel, and, by the time Fig. 3.16(d) is reached, the heated length becomes almost entirely devoid of liquid.

Halfway through Fig. 3.16(d), however, another liquid wetting front emerges, clearly indicated with white arrows. This high density front advances along the channel length, with nucleate boiling taking place within it similar to the behavior seen in the latter half of Fig. 3.16(a). As the front reaches the end of the heated length increased vapor content causes it to transition away from subcooled boiling of the liquid slug towards annular flow with film boiling as seen in Fig. 3.16(b).

This behavior continues for the first portion of Fig. 3.16(e), until roughly halfway through another vapor (low density) front emerges at the inlet of the channel, clearly indicated with white arrows. This repetition of behavior seen in Fig. 3.16(b) indicates the passage of high density (liquid) and low density (vapor) fronts, with annular flow occupying the interim periods, is a cyclical process.

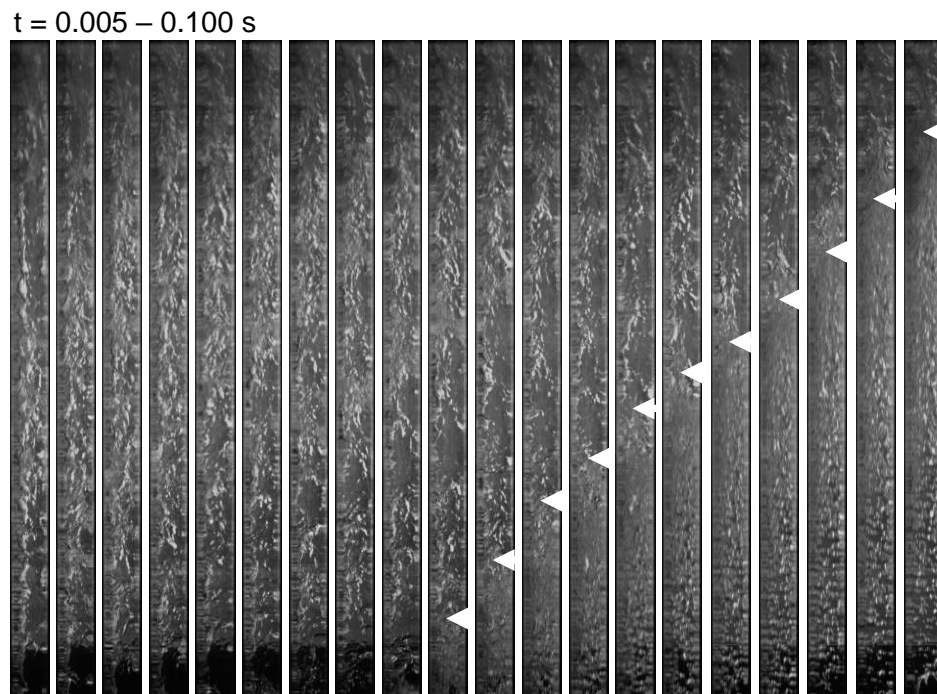


Figure 3.16: Consecutive flow visualization image sequences for vertical upflow boiling with  $G = 407.8 \text{ kg/m}^2\text{s}$ ,  $x_{e,in} = 0.03$ ,  $P_{in} = 116.0 \text{ kPa}$ , and  $q'' = 7.2 \text{ W/cm}^2$ , spanning (a) 0.005 – 0.100s, (b) 0.105-0.200 s, (c) 0.205-0.300 s, (d) 0.30-0.400 s, and (e) 0.405-0.500 s. Time difference between consecutive images is  $\Delta t = 0.005 \text{ s}$ .

$t = 0.105 - 0.200$  s

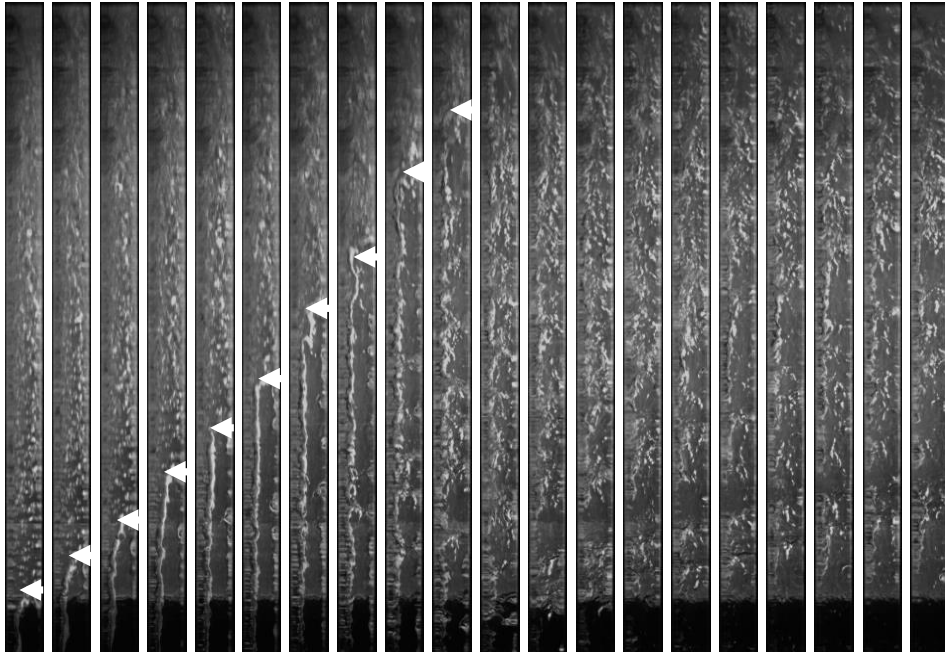


Figure 3.16 (b).

$t = 0.205 - 0.300$  s

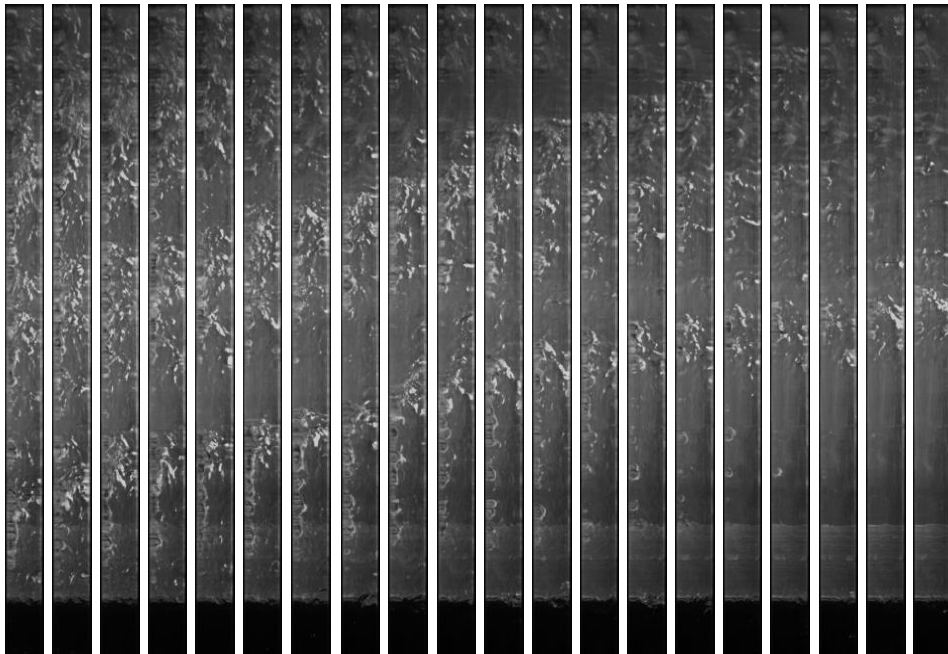


Figure 3.16 (c).

$t = 0.305 - 0.400$  s

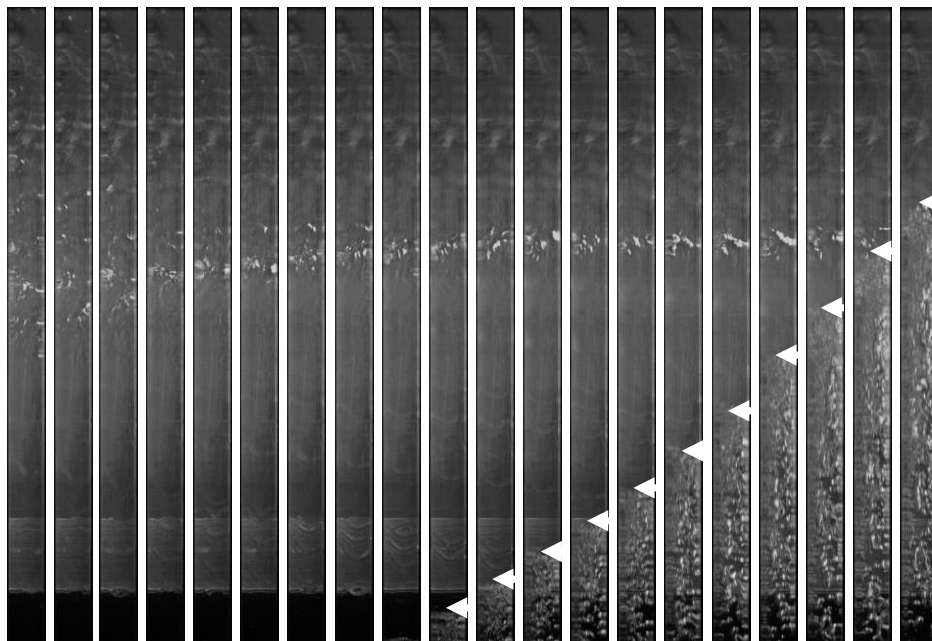


Figure 3.16 (d).

$t = 0.405 - 0.500$  s

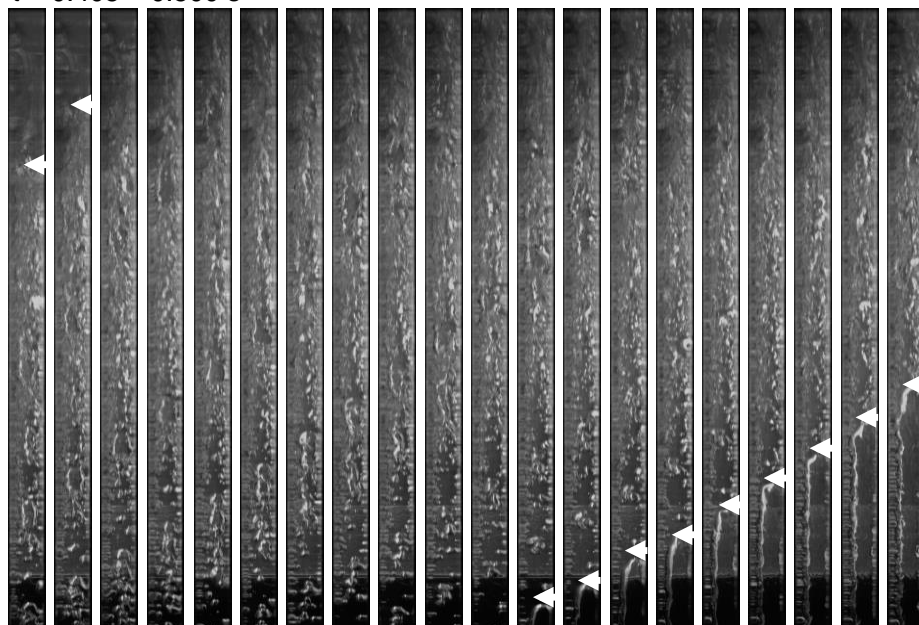


Figure 3.16 (e).

Figures 3.17(a) – 3.17(e), displaying flow visualization image sequences for the higher mass velocity of  $G = 821.6 \text{ kg/m}^2\text{s}$ , inlet quality  $x_{e,in} = 0.06$ , average inlet pressure  $P_{in} = 123.8 \text{ kPa}$ , and heat flux  $q'' = 7.2 \text{ W/cm}^2$ , further reinforces the concept that the passage of high and low density fronts is cyclical in nature. Within each subfigure clear regions of annular flow (characterized by the presence of interfacial waves) give way to the passage of darker colored regions comprised of liquid distributed throughout the cross-sectional area of the channel. These features are clearly identified with white arrows in Fig. 3.17(a).

Figures 3.17(b) and 3.17(c) also show signs of the passage of high density fronts, but these are much smaller in size than those seen in Fig. 3.17(a). Not until Fig. 3.17(d) is another high density front of significant length observed, again marked by white arrows.

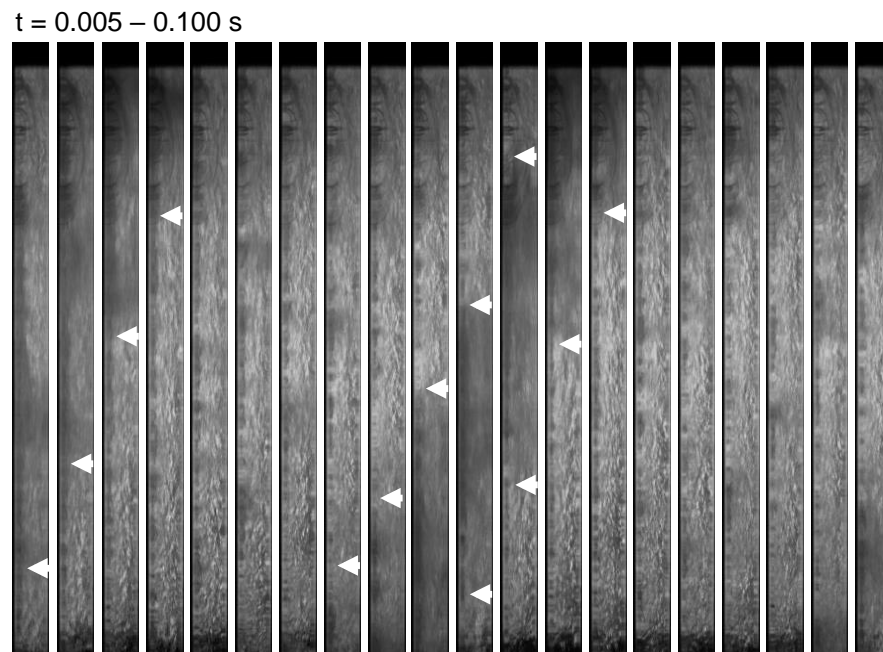


Figure 3.17: Consecutive flow visualization image sequences for vertical upflow boiling with  $G = 821.6 \text{ kg/m}^2\text{s}$ ,  $x_{e,in} = 0.06$ ,  $P_{in} = 123.8 \text{ kPa}$ , and  $q'' = 7.2 \text{ W/cm}^2$ , spanning (a) 0.005 – 0.100s, (b) 0.105-0.200 s, (c) 0.205-0.300 s, (d) 0.30-0.400 s, and (e) 0.405-0.500 s. Time difference between consecutive images is  $\Delta t = 0.005 \text{ s}$ .

$t = 0.105 - 0.200$  s

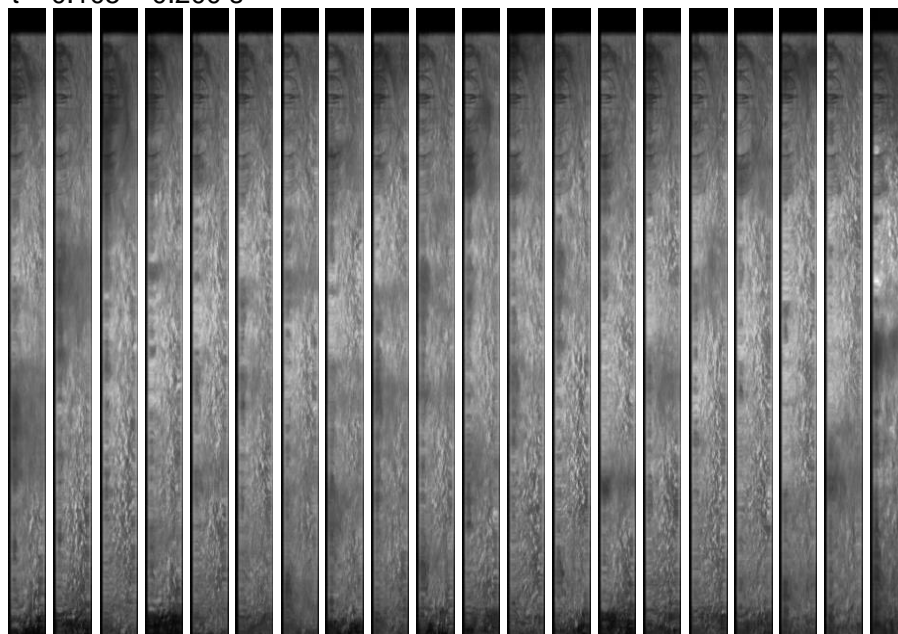


Figure 3.17 (b).

$t = 0.205 - 0.300$  s

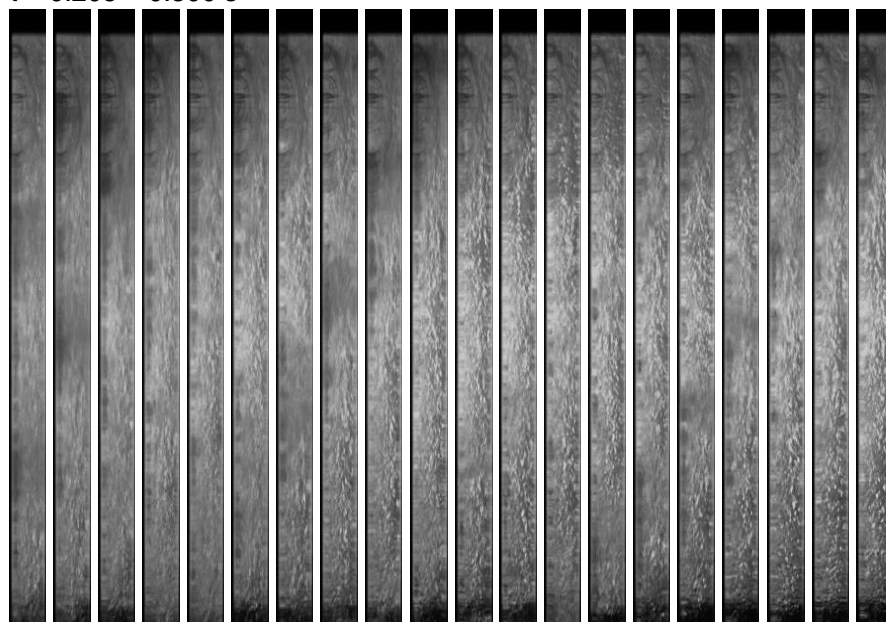


Figure 3.17 (c).

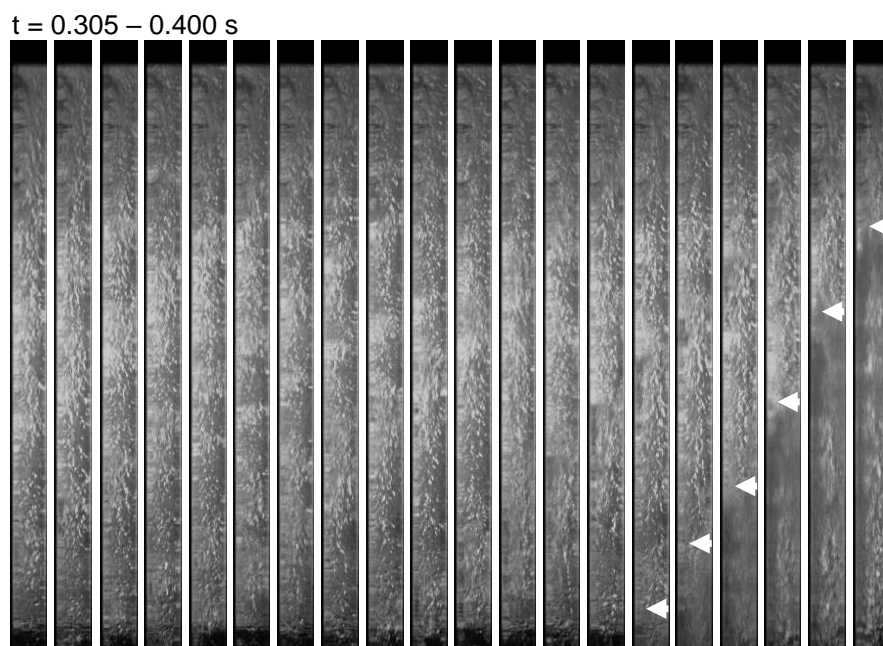


Figure 3.17 (d).

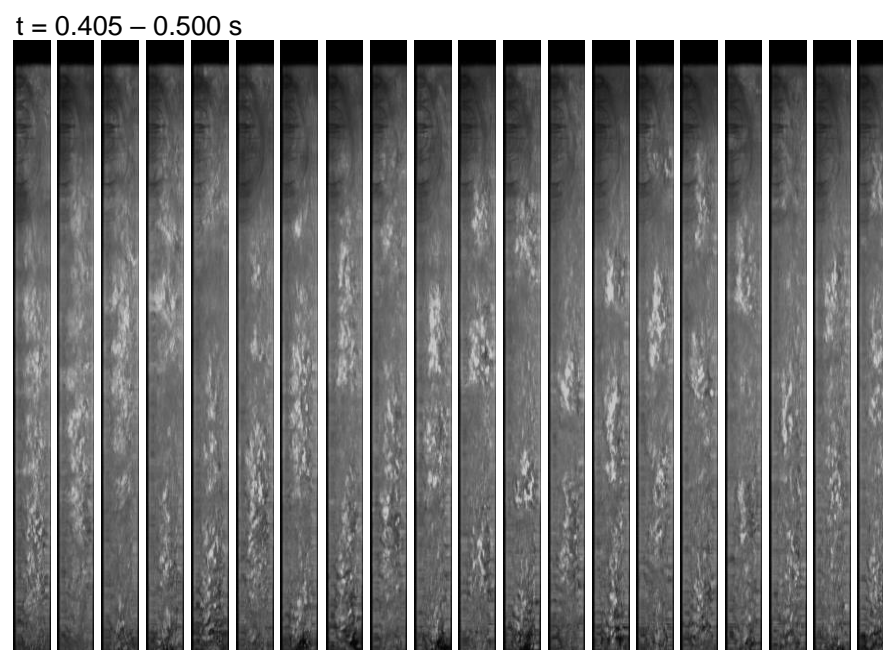


Figure 3.17 (e).

Similarly, Figs. 3.18(a) – 3.18(e) present flow visualization images for the highest mass velocity of  $G = 1636.5 \text{ kg/m}^2\text{s}$ , inlet quality  $x_{e,in} = 0.01$ , average inlet pressure  $P_{in} = 154.6 \text{ kPa}$ , and heat flux  $q'' = 7.2 \text{ W/cm}^2$ , in which alternating passage of high and low density fronts can clearly be seen. Beginning with Fig. 3.18(a), where the front and back of the first two high density fronts are indicated with white arrows, every subfigure shows some indication of alternating high and low density zones.

The possible exception to this is Fig. 3.18(d), which seems to exhibit a largely constant flow composition over its 0.1-s duration. Although flow regimes are more difficult to distinguish here as compared to lower flow velocity cases, annular flow seems to dominate in Fig. 3.18(d), evidenced by the presence of dark, wavy features in the near-wall region. This reinforces the notion that annular, co-current flow is the nominal flow configuration for these cases.

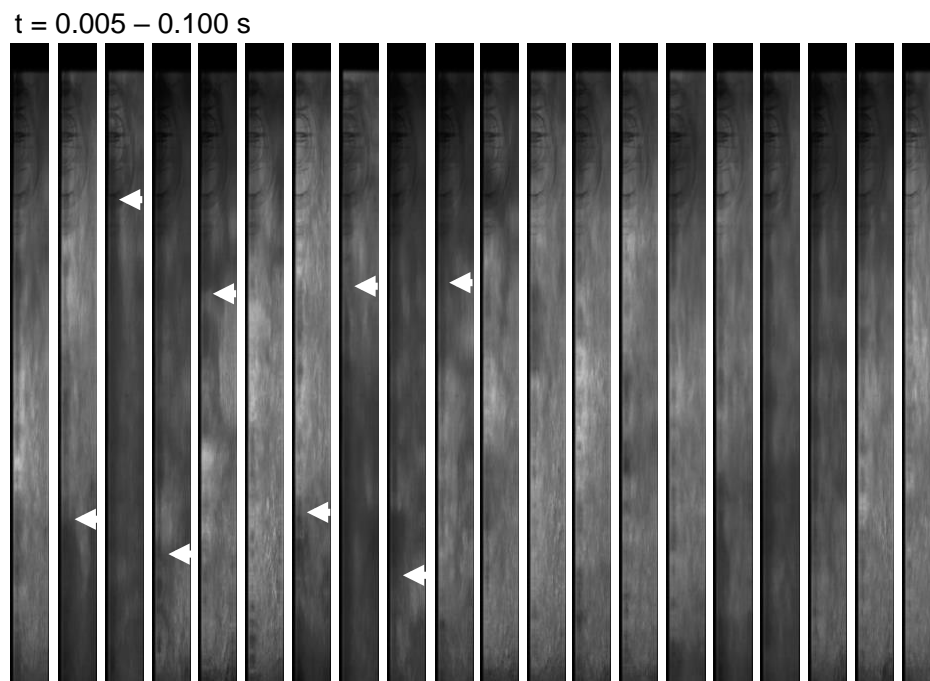


Figure 3.18: Consecutive flow visualization image sequences for vertical upflow boiling with  $G = 1636.5 \text{ kg/m}^2\text{s}$ ,  $x_{e,in} = 0.01$ ,  $P_{in} = 154.6 \text{ kPa}$ , and  $q'' = 7.2 \text{ W/cm}^2$ , spanning (a) 0.005 – 0.100s, (b) 0.105-0.200 s, (c) 0.205-0.300 s, (d) 0.30-0.400 s, and (e) 0.405-0.500 s. Time difference between consecutive images is  $\Delta t = 0.005 \text{ s}$ .

$t = 0.105 - 0.200$  s

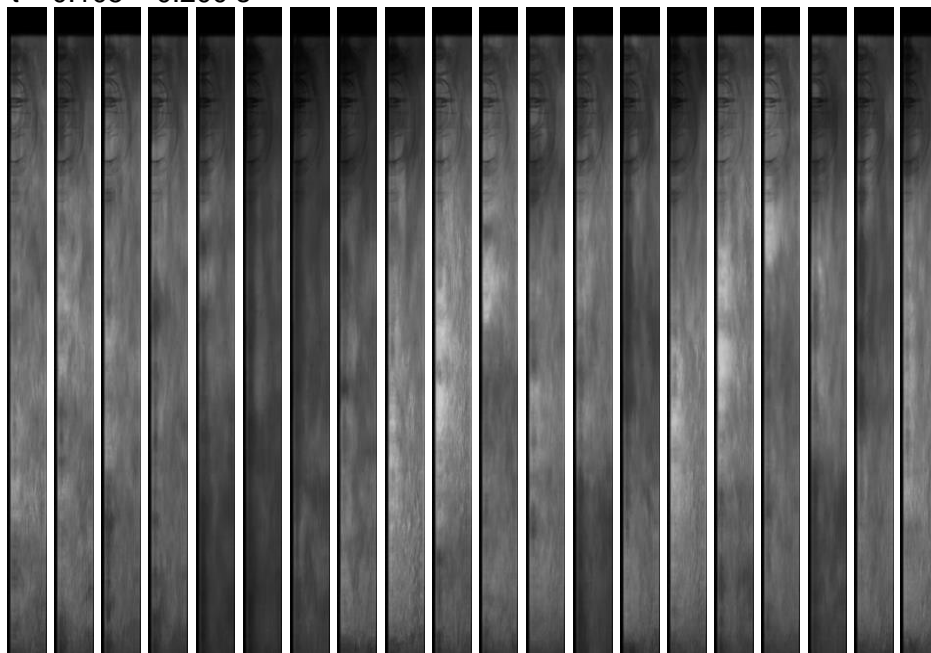


Figure 3.18 (b).

$t = 2.005 - 0.300$  s

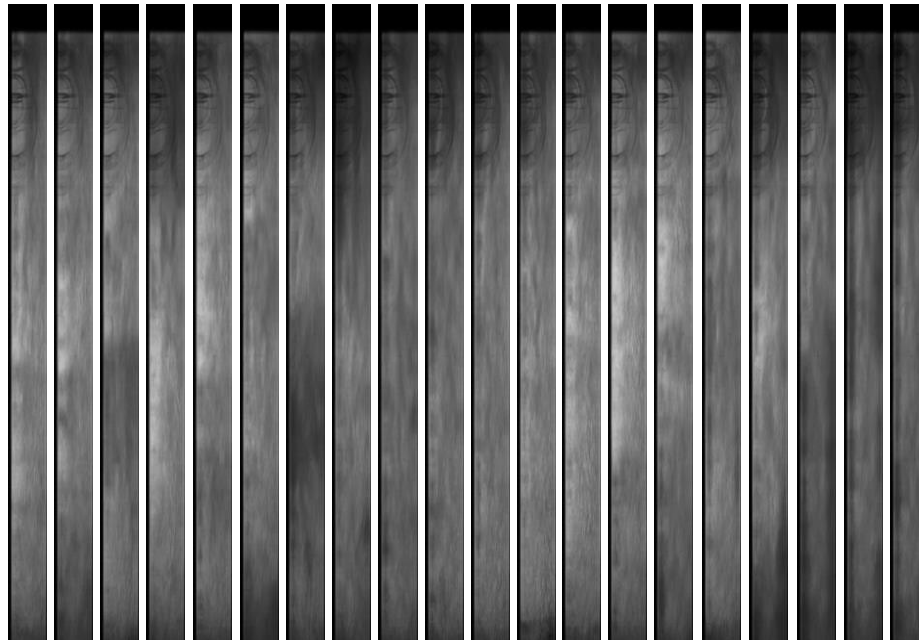


Figure 3.18 (c).

$t = 0.305 - 0.400$  s



Figure 3.18 (d).

$t = 0.405 - 0.500$  s

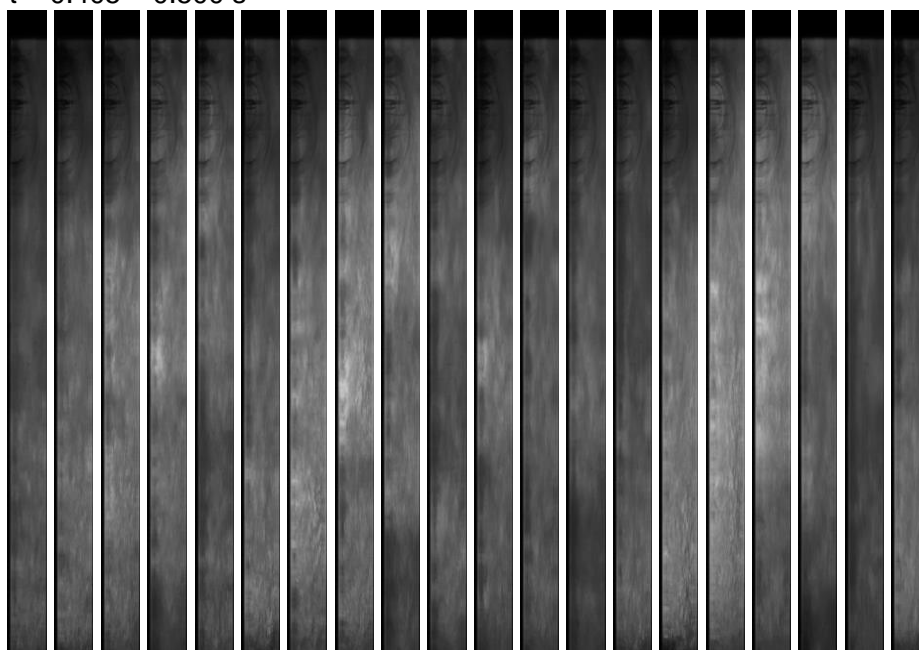


Figure 3.18 (e).

Across Figs. 3.16 – 3.18, flow visualization image sequences indicate the clear presence of cyclical passage of high and low density fronts through the heated length of the test module, with annular flow providing a neutral state between the two. Recalling the clear periodic behavior seen within transient pressure signals in Fig. 3.15, it can be hypothesized that the two phenomena are interrelated, and that the cyclical passage of high and low density fronts are the cause of low frequency oscillatory behavior attributed to DWOs.

All of this information is combined in Figs. 3.19(a) – 3.19(c), which display, respectively, select flow visualization images, a table of single-event frequencies for the cyclical passage of high and low density fronts, and transient pressure results for  $G = 1221.9 \text{ kg/m}^2\text{s}$ , inlet quality of  $x_{e,in} = 0.02$ , average inlet pressure of  $P_{in} = 129.1 \text{ kPa}$ , and heat flux of  $q'' = 7.3 \text{ W/cm}^2$  (in a similar fashion to results displayed in Fig. 3.5). After identifying the passage of high density fronts within high speed flow visualization images as shown in Fig. 3.19(a), single event frequencies can be found, with single event frequency  $f_{SE}$  defined as

$$f_{SE} = \frac{1}{t_{HDF,2} - t_{HDF,1}}, \quad (3.3)$$

where  $t_{HDF,2}$  and  $t_{HDF,1}$  refer to the times (relative within the image sequence) at which the first and second high density fronts (HDFs) are observed passing through the test section, respectively. Some values for single even frequency are tabulated in Fig. 3.19(b).

These values can be compared to the peaks in amplitude versus frequency plots provided for the associated transient pressure curves in Fig. 3.19(c), presented in a fashion identical to that in Fig. 3.15. The peak frequency of oscillation for inlet pressure in this case falls between 3-4 Hz, while for the outlet pressure it is between 2-3 Hz. Tabulated values for  $f_{SE}$  in Fig. 3.19(b) fall within the range of 4-7 Hz, which are slightly higher than the peak frequencies present after taking a Fourier transform of the experimental data, although still very close. The failure to align exactly with the peak frequencies shown in Fig. 3.19(c) can be attributed to the fact that the fast Fourier transform performed to produce the amplitude versus frequency plots shown is conducted over a 20-s period, while the single event frequencies were evaluated over a period of only 0.735 s. High speed imaging was limited to short durations due to data storage limitations, but, were it possible to evaluate single-event frequencies over a similar 20-s period, it is likely the statistical distribution of  $f_{SE}$  would begin to match the amplitude versus frequency plots in Fig. 3.19(c) exactly (similar to the result seen in Section 3). It is expected future experiments may not face these imaging

duration limitations and will help provide full validation that dominant low-frequency pressure oscillations are a direct result of the passage of HDFs.

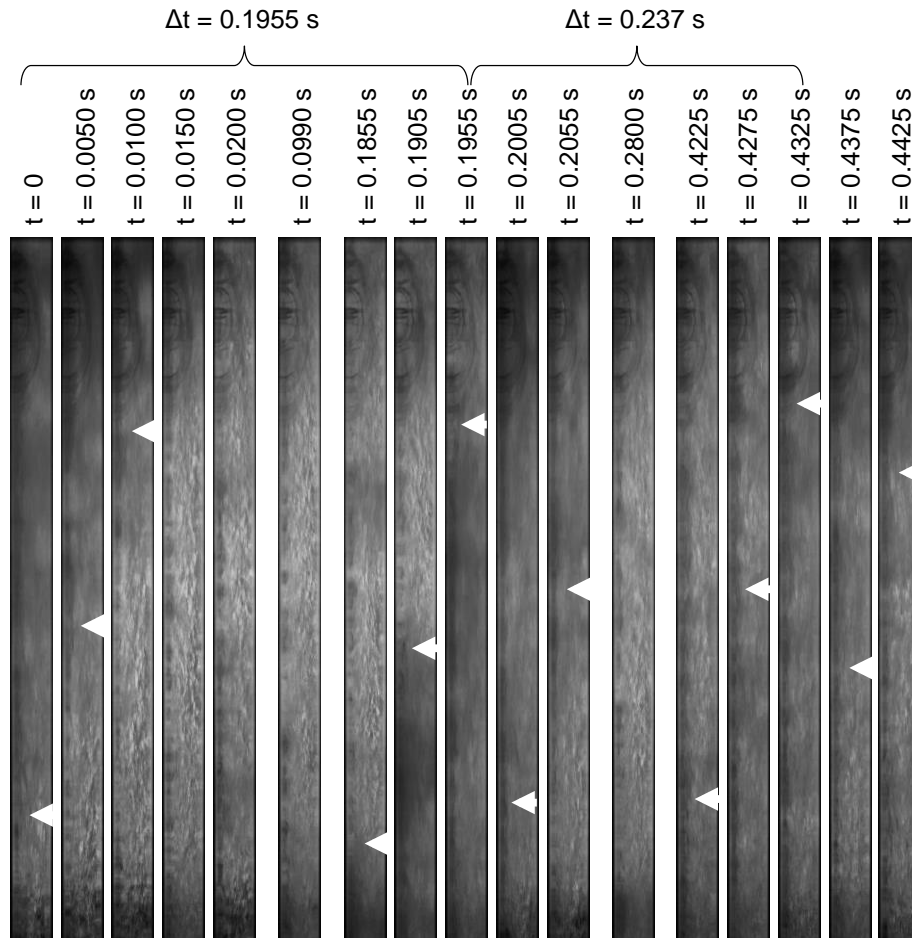


Figure 3.19: (a) Select flow visualization image sequences for  $G = 1221.9 \text{ kg/m}^2\text{s}$ ,  $x_{e,in} = 0.02$ ,  $P_{in} = 129.1 \text{ kPa}$ , and  $q'' = 7.3 \text{ W/cm}^2$  depicting the cycle of low density (bright) fronts and high density (dark) fronts passing through the heated length of the FBM. (b) Tabulated values of single-event frequencies of high density fronts (HDFs) identified from the images and time between HDFs. (c) Transient pressure signals and corresponding fast Fourier transforms confirming the frequencies in (b).

High Frequency Front Occurrence	Time [s]	$\Delta t$ [s]	f [Hz]
1	0.000	-	-
2	0.1955	0.1955	5.11
3	0.4375	0.2420	4.13
4	0.5900	0.1525	6.56
5	0.7350	0.1450	6.90

Figure 3.19 (b).

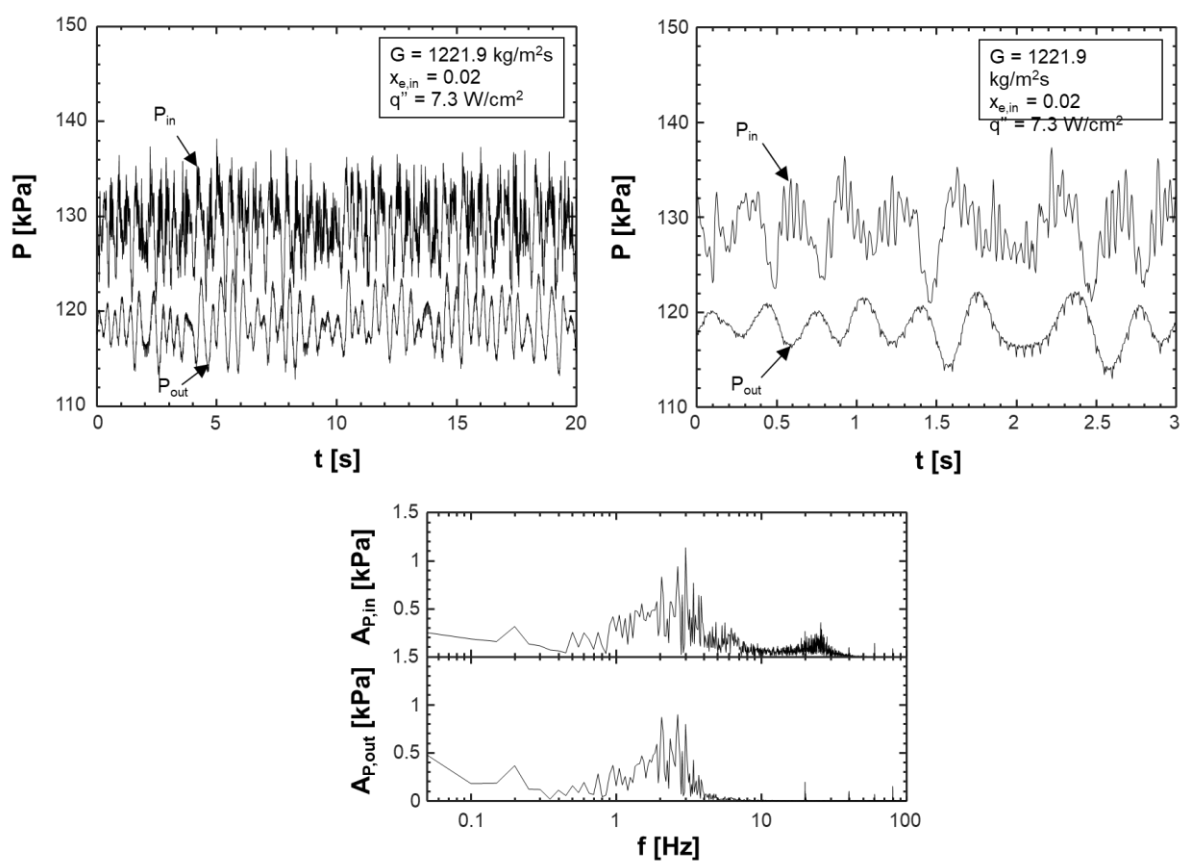


Figure 3.19 (c).

### 3.2.2.2 Explanation of Density Wave Oscillation Phenomenon

Having used both transient pressure results and flow visualization image sequences to describe the characteristics of DWOs within the present system and prove that pressure fluctuations in the low-frequency ( $\sim 0.5 - 10$  Hz) range can be associated with cyclical passage of high and low density fronts (regions comprised of mostly liquid and mostly vapor, respectively), it is now possible to present a comprehensive overview of the DWO process. Before embarking, however, it should again be noted that this analysis applies to mini/macro-channels, and DWO formation and behavior in micro-channels is fundamentally different, something briefly discussed in a recent study by Lee *et al.* [61].

Figure 3.20 provides detailed schematics outlining the process by which DWOs occur in vertical upflow boiling. Figure 3.20(a) depicts the nominal operating state for finite inlet quality vertical upflow boiling. Key features include annular flow with a vapor core and liquid film distributed around the channel circumference. Phase change takes place along the heated length, manifesting as either nucleate boiling within the liquid film or evaporation at the liquid-vapor interface, depending on film thickness and heat flux applied.

Due to the  $\sim 3$  order of magnitude difference in body force acting on the liquid film versus that on the vapor core, as well as the relatively large size of the channel hydraulic diameter compared to the length scales on which surface tension effects are relevant (quantifiable using Eq. (3.2)), significant flow separation effects are able to manifest. Interfacial shear stress, acting due to the fast moving vapor core flowing past the slower liquid film, becomes insufficient to overcome body force effects, and the liquid film reaches an unsustainable thickness for annular co-current flow.

Figure 3.20(b) shows body force effects causing liquid film accumulation in the inlet region of the channel, leading to increased vapor content and reduced liquid content in the downstream portion of the test module. These conditions correspond to the observation of a low density front (LDF) within the heated length. During this period, mass accumulation takes place within the channel, as mass flowrate of low density vapor at the channel outlet is unequal to the combination of liquid and vapor entering the channel. Correspondingly, momentum inflow is greater than outflow, with the difference being stored in the liquid accumulating near the inlet, which begins to gradually advance downstream.

Figure 3.20(c) depicts the motion of this accumulated liquid (high density front, HDF) towards the channel exit. At this point liquid content in the downstream region is at a minimum, a behavior clearly noted in Figs. 3.20(c) and 3.20(d). Additionally, although the HDF is in motion, mass is still accumulating within the channel and net momentum imbalance continues to contribute to its motion. The motion of the HDF itself is extremely complex, as inlet flow to the test section acts as a pseudo-jet impinging on its upstream side, while downstream it is either overtaking flow or being ‘stretched’, depending on relative velocity of the front and the downstream flow. Body force effects also oppose its motion, while it receives assistance from pressure gradient forces. Perhaps most complicated of all is its interaction with the channel wall(s). Ostensibly, shear stress acts to impede motion of the HDF, but the presence of a residual thin liquid film which is ‘re-wet’ (increased in thickness) and accelerated by residual liquid pulled from the front by surface tension forces indicate wall shear stress may play a minor role in comparison to virtual mass force.

Figure 3.20(d) shows the high density front reaching the heated length of the test section, wherein vigorous phase change takes place. In its wake liquid, the liquid film has been reestablished along the channel length, and the same can be seen for the heated length as it reaches the end of the channel. Passage of the HDF from the exit of the channel ensures mass conservation is satisfied, if only in a time-averaged fashion over the duration of the DWO process.

Finally, Fig. 3.20(e) illustrates a return to nominal operating conditions, from which the process may begin again.

It should be noted that the schematics presented in Figs. 3.20(a) – 3.20(e) correspond to operating conditions similar to those in Fig. 4, where clear boundaries between the liquid and vapor phases are present. For higher flow velocities and/or higher inlet qualities, the combination of increased flow velocity, flow acceleration due to increased void fraction, and decreased liquid content are not conducive to clearly defined phase boundaries for LDFs and HDFs, which is instead manifest as distributed regions of low and high density (seen as light and dark fronts in Figs. 3.17-3.19). The mechanisms behind their formation and propagation through the channel, however, remain the same.

It is also worth commenting on the role of body force as a driving mechanism for the formation of DWOs under the present operating conditions. Pressure fluctuations attributable to DWOs have been seen in prior works for multiple orientations in Earth’s gravity [53,] other than vertical upflow, indicating this phenomenon occurs in other orientations due to either other forms

of body force influence (liquid-motion assist in vertical downflow, flow stratification in horizontal flow), or the presence of tubes through which two-phase vertical upflow occurs prior to the test section in these orientations. In a microgravity environment, however, it is possible the present instability mode may not manifest due to the absence of body force. The upcoming Flow Boiling and Condensation Experiment (FBCE) on the International Space Station (ISS) represents possible proof or disproof of this hypothesis.

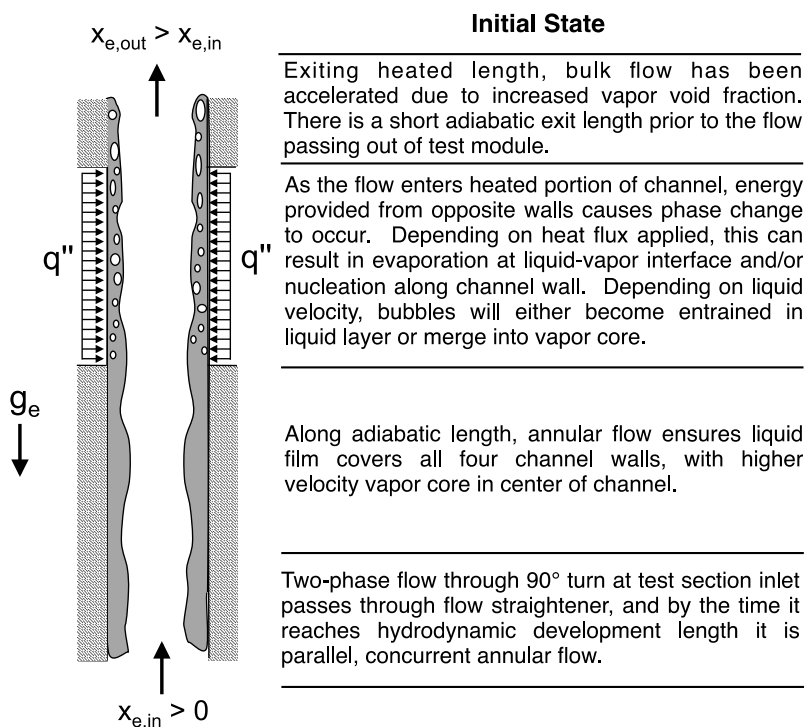


Figure 3.20: Schematics outlining cyclical process behind DWOs, with (a) nominal conditions, (b) liquid accumulation in inlet region, (c) liquid slug/HDF advance, (d) HDF passage through heated lengths, and (e) return to nominal conditions.

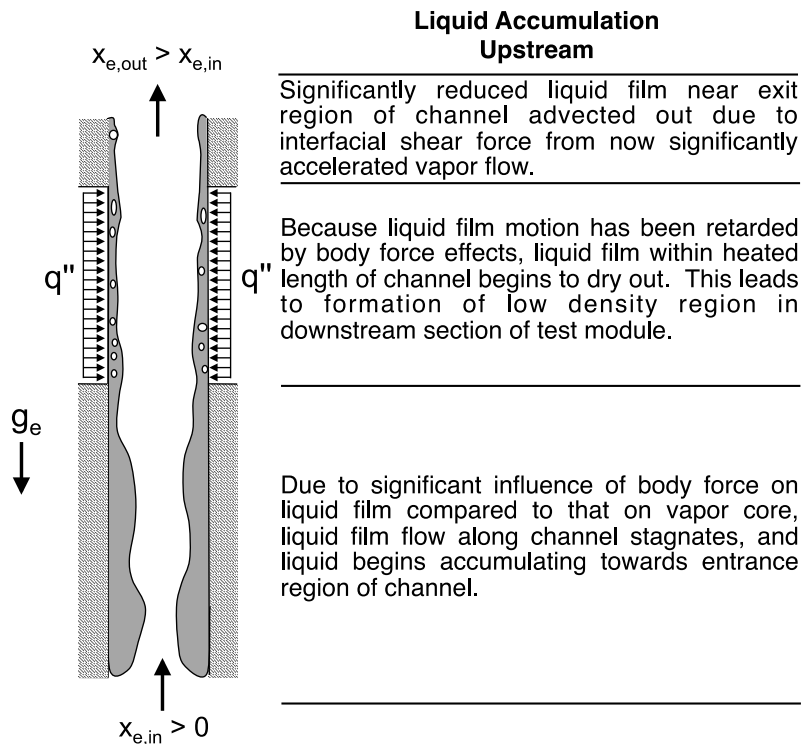


Figure 3.20 (b).

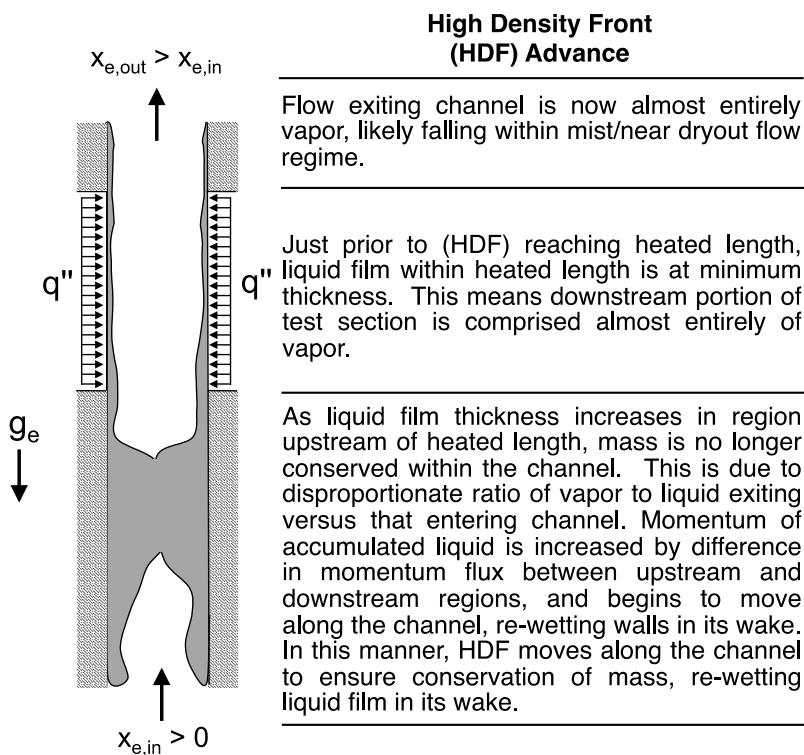


Figure 3.20 (c).

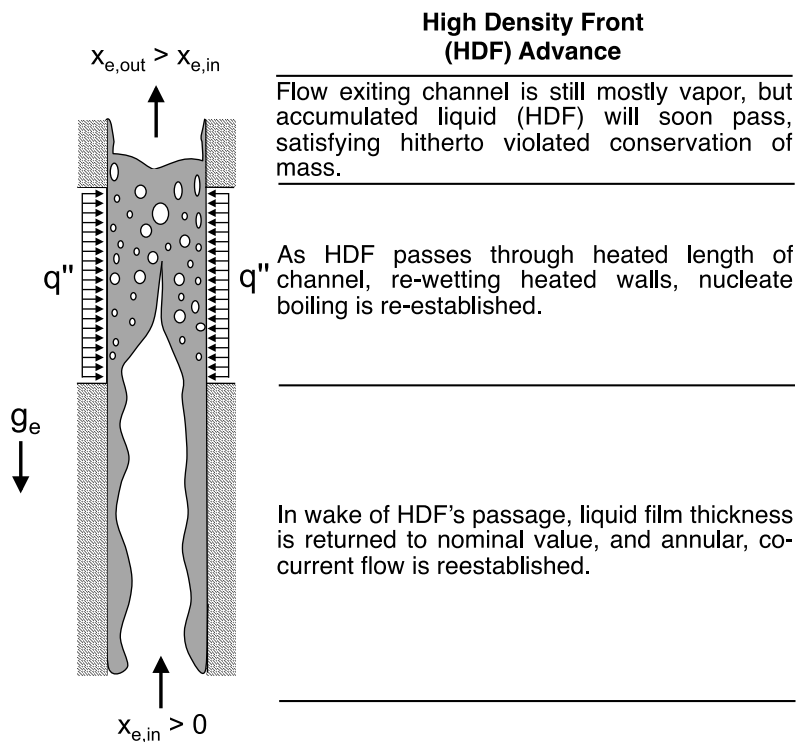


Figure 3.20 (d).

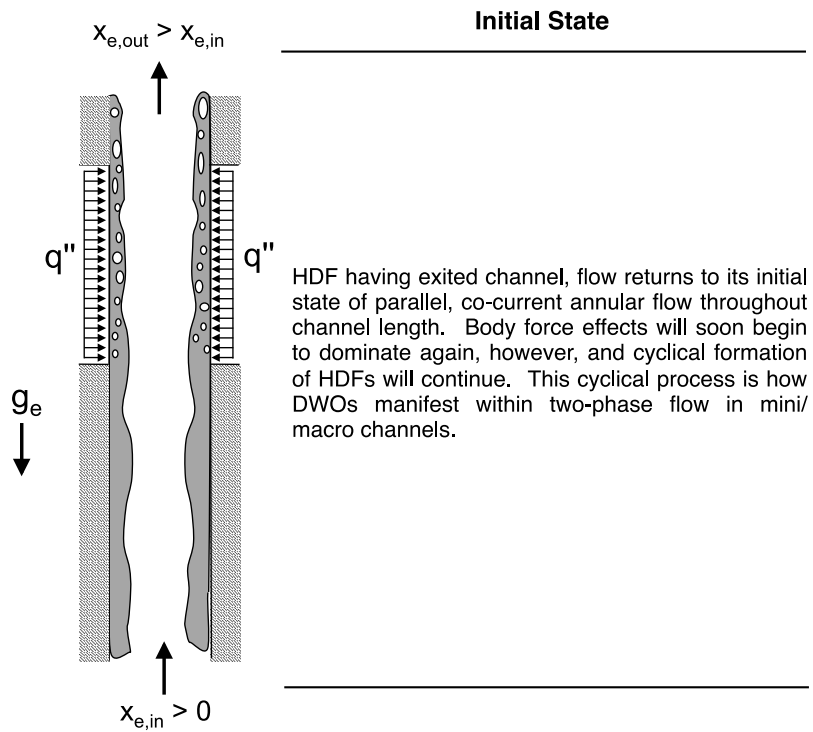


Figure 3.20 (e).

### 3.2.3 Frequency and Amplitude of Density Wave Oscillations

#### 3.2.3.1 Detection Method for Frequency and Amplitude of Oscillation

Having established the process by which DWOs manifest in vertical upflow boiling in mini/macro-channels, analysis can be performed on how frequency and amplitude at which they occur change in response to changes in operating conditions. Prior to this, it is necessary to describe how frequency and amplitude of oscillation are detected.

Figure 3.21(a) shows transient pressure curves for the same case as Fig. 3.15(b), corresponding to operating conditions of  $G = 834.1 \text{ kg/m}^2\text{s}$ ,  $x_{e,in} = 0.04$ ,  $P_{in} = 122.6 \text{ kPa}$ , and  $q'' = 7.3 \text{ W/cm}^2$  observed in year 1. Fast Fourier transforms are performed on these transient pressure signals, with the results shown in Fig. 3.21(b). Peak frequency of oscillation can be found for both inlet and outlet pressure signals by searching for the frequency associated with peak amplitude of oscillation. It should be noted that the search is limited to frequencies in the relevant range ( $\sim 0.1 - 10 \text{ Hz}$ ) to eliminate the false detection of frequencies associated with non-DWO behavior.

For this set of conditions, Fig. 3.21(b) indicates that both inlet and outlet pressures oscillate with a peak frequency of 2.1 Hz, associated with an amplitude of  $\sim 0.9 \text{ kPa}$  on the amplitude versus frequency plots. From the transient curves in Fig. 3.21(a), however, it is clear that pressures oscillate with much higher amplitudes, closer to  $\sim 10 \text{ kPa}$ . This difference is attributed to the combination of two effects. First, as discussed in conjunction with Fig. 3.19, DWOs do not occur at a constant frequency but over a narrow range of frequencies. Second, and more importantly, DWOs are not perfectly sinusoidal in behavior. As was discussed when presenting Fig. 3.15, inlet pressures in particular seem to exhibit sharp periodic departures from a nominal level. This behavior is periodic and can be associated with a frequency, but does not exhibit the type of smoothly continuous behavior associated with trigonometric functions (in other words, the derivatives of inlet pressure fluctuations would be closer to impulse functions than trigonometric functions). Outlet pressure fluctuations seem to exhibit behavior closer to sinusoidal, but are still not perfectly attributable to a single frequency and amplitude. Instead, these fluctuations can be best described using a Fourier series, or a linear combination of sine and cosine functions with associated amplitudes and frequencies, all summing to a single curve within the time domain. The peak frequency detected in Fig. 3.21(b) is simply the frequency most closely associated (containing the most energy) with DWO induced oscillations.

Thus, alternate methodology must be employed to determine the amplitude at which DWO induced pressure fluctuations occur for a given set of operating conditions. To achieve this, fluctuating pressure  $P'$  is isolated, where

$$P' = P - P_{ave}, \quad (3.4)$$

and  $P$  and  $P_{ave}$  are the total and time-averaged pressures, respectively. Figure 3.21(c) shows plots of fluctuating pressure versus time for both inlet and outlet pressures. The fluctuating pressures are plotted over a shortened period of 2 s to better highlight their structure. It is clear that both curves are composed of low-frequency fluctuations with high-frequency oscillations superimposed. This conclusion can also be drawn from analyzing amplitude versus frequency plots in Fig. 3.21(b), which show the majority of fluctuations occur in the 1 – 5 Hz range, but some sharp peaks may be detected in the 10 – 100 Hz range, likely attributable to mechanically induced oscillations [54]. To remove these high-frequency fluctuations and isolate the low frequency behavior attributable to DWOs, a second-order digital Butterworth low-pass filter with a cutoff frequency of 10 Hz is used, with the filter transfer function given by

$$H(z) = \frac{0.02 + 0.04z^{-1} + 0.02z^{-2}}{1.0 - 1.56z^{-1} + 0.64z^{-2}}. \quad (3.5)$$

Numerator and denominator coefficients are truncated here for presentation, but are output with additional significant figures by the python function used to generate them [159].

Filtered pressure fluctuations are identified with dashed lines in Fig. 3.21(c), and clearly illustrate that the high-frequency fluctuations have been removed. Careful analysis also reveals that there is a slight phase shift between the raw and filtered signals, which is characteristic of the filter type used here. This does not, however, impact the amplitude characteristics of the filtered signal.

Using the filtered pressure fluctuation curves, Fig. 3.21(d) illustrates how amplitude of oscillation can be determined by simply halving the difference between maximum and minimum values.

Moving forward, frequency and amplitude of oscillation for DWO induced behavior will be determined for both inlet and outlet pressure signals. These values will then be averaged to present a single characteristic DWO frequency and amplitude for each distinct set of operating conditions.

As discussed when analyzing Fig. 3.15, there can be slight differences in both amplitude and frequency of oscillation as detected at the inlet to the heated length versus the outlet. These differences are taken as being of minimal importance when compared to changes in frequency and amplitude with respect to changes in operating conditions, however, and it is these changes subsequent sections will aim to analyze.

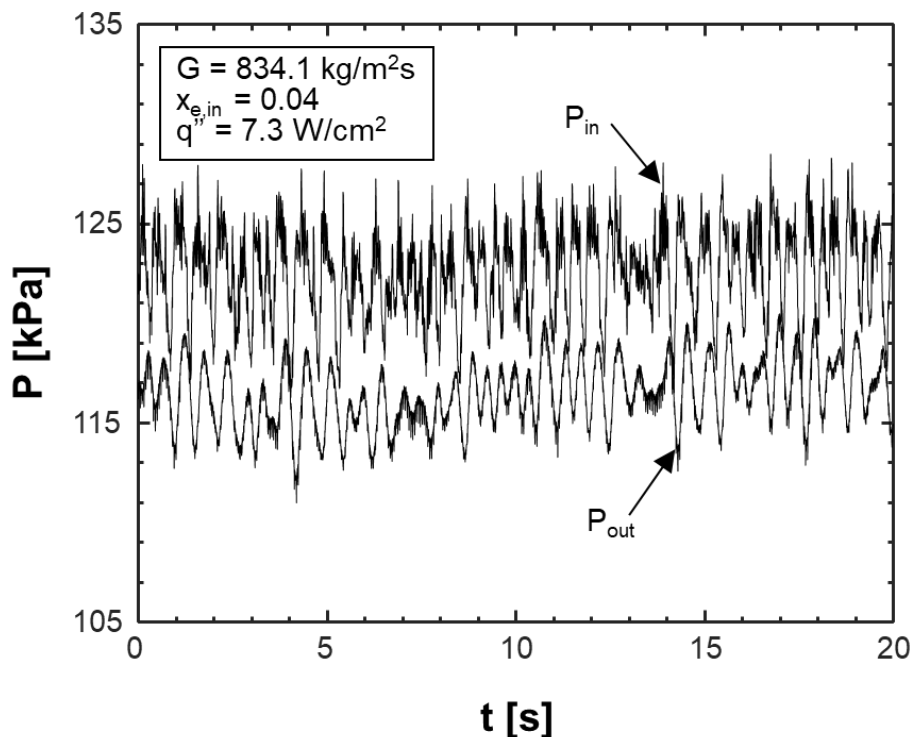


Figure 3.21: Plots showing detection methodology for DWO frequency and amplitude: (a) transient inlet and outlet pressure signals for entire fast Fourier transform (FFT) window, (b) associated FFTs with peak frequencies identified, (c) low-pass filtered pressure signals to isolate DWO behavior, and (d) DWO amplitude detection using filtered signals.

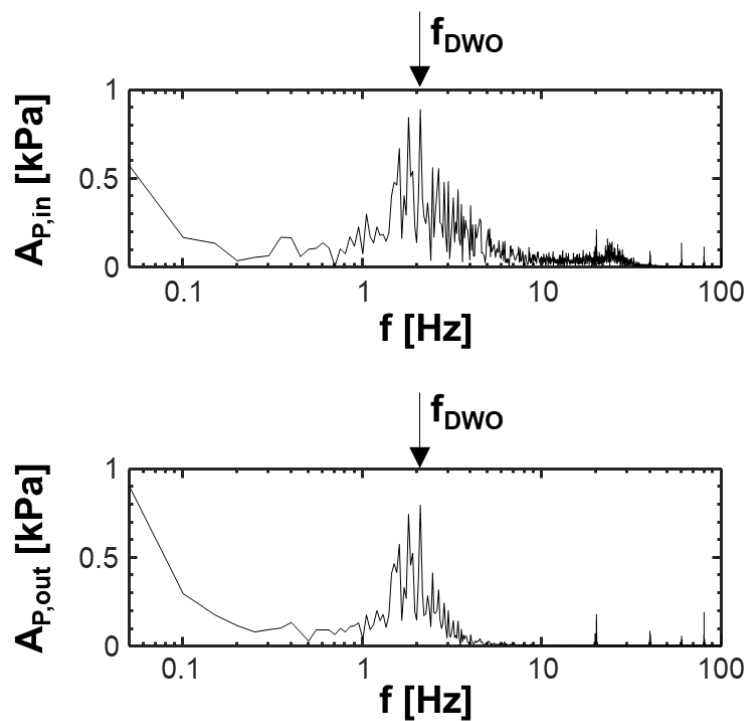


Figure 3.21 (b).

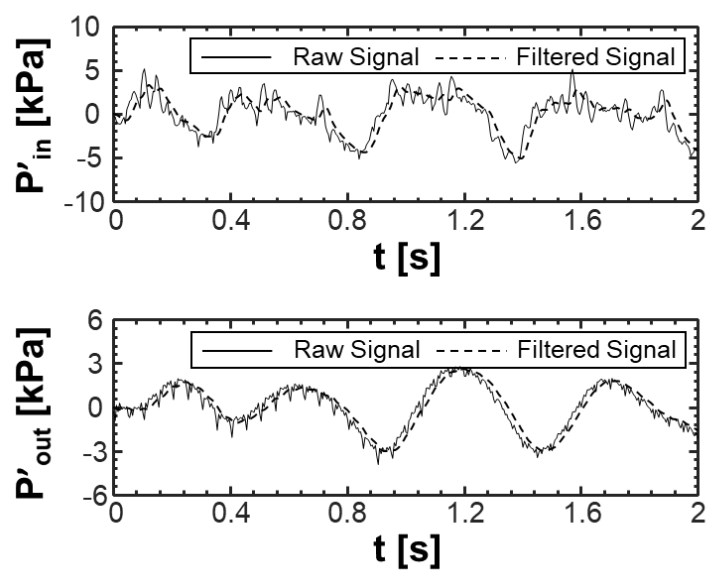


Figure 3.21 (c).

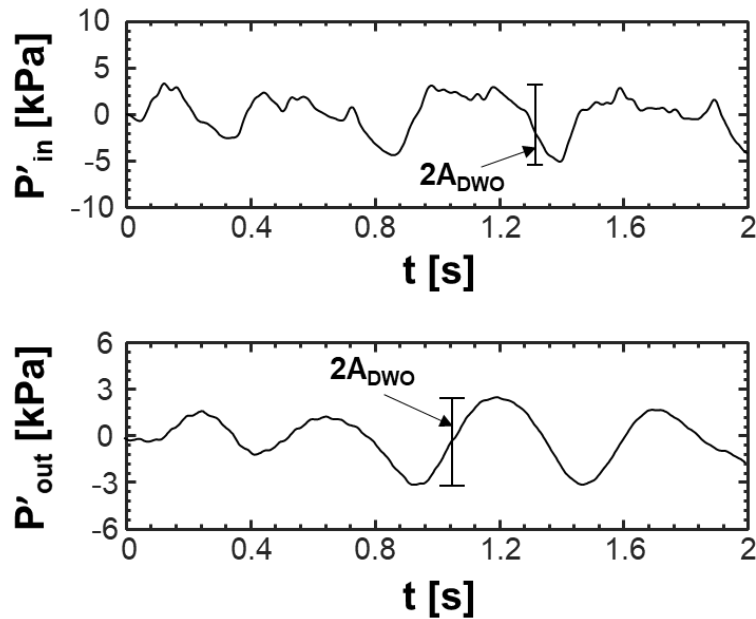


Figure 3.21 (d).

### 3.2.3.2 Frequency and Amplitude of Oscillation in Response to Changes in Mass Velocity, Inlet Quality, and Heat Flux

Figures 3.22(a) – 3.22(d) present plots of DWO frequency versus mass velocity for three different heat flux levels with  $x_{e,in} = 0.00 - 0.04$ ,  $x_{e,in} = 0.07 - 0.13$ ,  $x_{e,in} = 0.19 - 0.25$ , and  $x_{e,in} = 0.30 - 0.40$ , respectively, all gathered in year 1. Across all four plots, frequency of oscillation can be seen to increase with increasing mass velocity, indicating frequency of oscillation shares a direct relationship with flowrate. This is to be expected based on the current understanding of the phenomenon's manifestation, as the description provided along with Fig. 3.20 indicated momentum differences between the channel inlet, here represented by time-averaged mass velocity, and outlet (upstream and downstream of the HDF) are responsible for accelerating the HDF.

For similar reasons there are indications that, for some cases, increases in inlet quality lead to increases in frequency of oscillation. These increases can be attributed to flow acceleration due to increased void fraction leading to higher momentum fluxes (proportional to flow velocity squared), but, due to the fact that overall momentum is conserved for a single mass velocity at multiple qualities, this trend is secondary to that of mass velocity.

Changes in heat flux yield no discernable trend for frequency of oscillation, with each of the three heat flux levels shown exhibiting the peak frequency of oscillation for near-constant values of other operating conditions. This indicates phase change within the test module is of secondary importance to the hydrodynamic phenomenon at play, which is in line with the experimental observation of DWO induced behavior for cases with zero heat flux within the test section. It is likely, however, that phase change within the test section plays some role in the differences between inlet and outlet pressure signals as discussed in relation to Fig. 3.15.

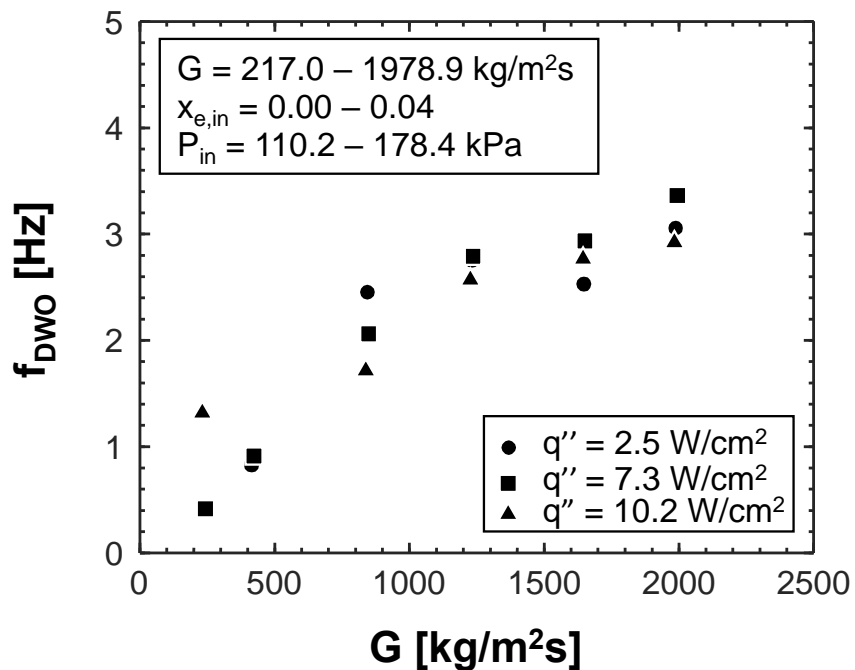


Figure 3.22: Plots of DWO frequency versus mass velocity for three heat flux levels and (a)  $x_{e,in} = 0.00 - 0.04$ , (b)  $x_{e,in} = 0.07 - 0.13$ , (c)  $x_{e,in} = 0.19 - 0.25$ , and (d)  $x_{e,in} = 0.30 - 0.40$ .

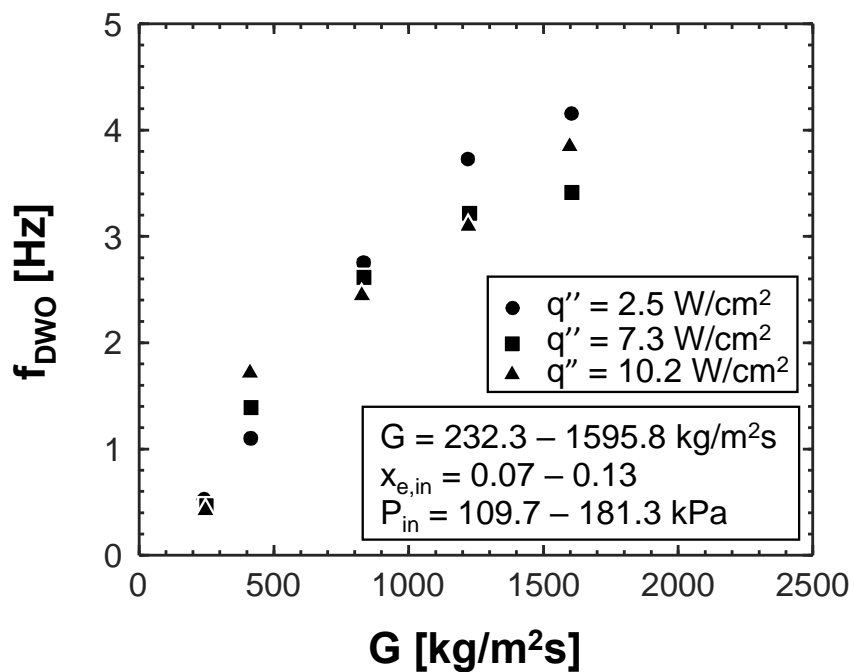


Figure 3.22 (b).

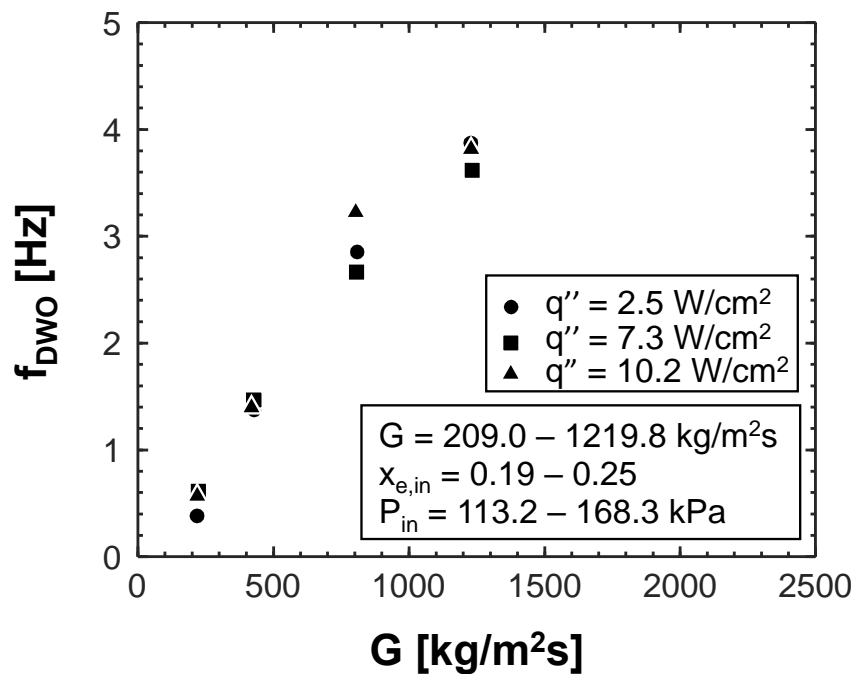


Figure 3.22 (c).

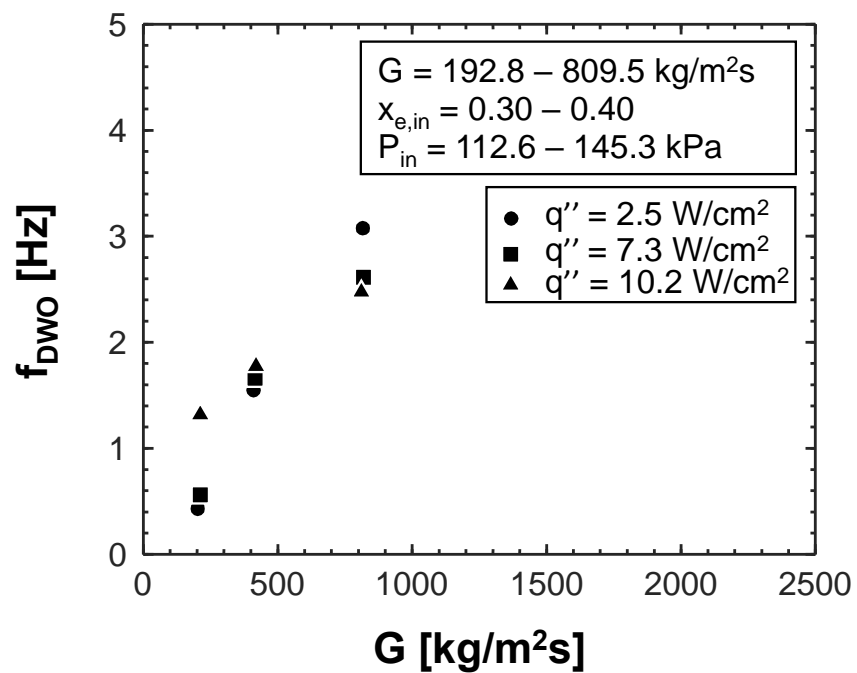


Figure 3.22 (d).

Similarly, Figs. 3.23(a) – 3.23(d) present results for amplitude of DWO induced pressure oscillations versus mass velocity for three different heat flux levels with  $x_{e,in} = 0.00 - 0.04$ ,  $x_{e,in} = 0.07 - 0.13$ ,  $x_{e,in} = 0.19 - 0.25$ , and  $x_{e,in} = 0.30 - 0.40$ , respectively, also gathered in year 1. Across all subfigures, a similar trend of increasing amplitude with increasing mass velocity is present, indicating that both amplitude and frequency of oscillation are heavily tied to mass velocity. A slight increase in amplitude is also seen with increases in inlet quality, although it is of significantly lesser magnitude than that with respect to mass velocity, likely for the reasons mentioned when analyzing similar trends in Fig. 3.22.

Dissimilar to Fig. 3.22, however, is the dependence of amplitude of oscillation on heat flux, with the relative positions of three symbols denoting different heat flux levels indicating (for other operating conditions held nearly constant) higher amplitude oscillations are typically associated with higher values of heat flux. This can likely be attributed to boiling along the heated length during passage of high density fronts impacting the magnitude of pressure oscillations associated with DWOs.

Evident in both Figs. 3.22 and 3.23 is significant variability of results associated with the lowest mass velocity cases. This is likely due to the combined influence of three factors. First, the magnitude of oscillations is lowest for low mass velocity cases, meaning detection of DWO induced behavior becomes more difficult (other sources of fluctuations have a larger contribution to overall transient behavior). Second, all frequencies and amplitudes of oscillation in the present plots are determined using the methodology described in conjunction with Fig. 3.21 for transient pressure signals 20 s in duration. For the lowest mass velocity cases, which commonly exhibit frequencies of oscillation less than 1 Hz in magnitude, this means fewer samples with which to form an average for both frequency and amplitude of oscillation. Finally, for these low mass velocity cases, the ratio of inertia to body forces (commonly assessed using Froude number) is at its minimum, leading to the most irregular flow behavior of all cases analyzed here.

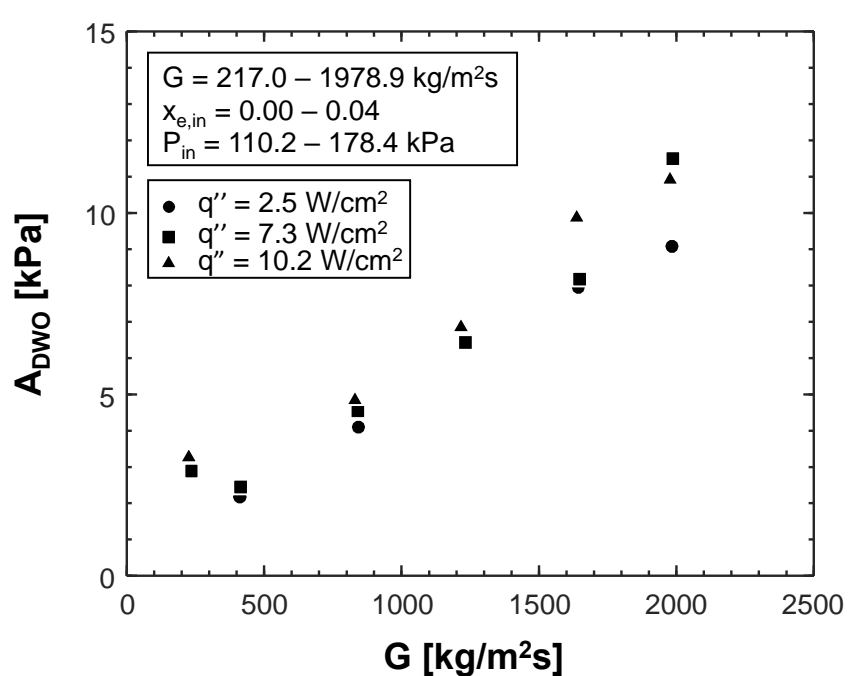


Figure 3.23: Plots of DWO amplitude versus mass velocity for three heat flux levels and (a)  $x_{e,\text{in}} = 0.00 - 0.04$ , (b)  $x_{e,\text{in}} = 0.07 - 0.13$ , (c)  $x_{e,\text{in}} = 0.19 - 0.25$ , and (d)  $x_{e,\text{in}} = 0.30 - 0.40$ .

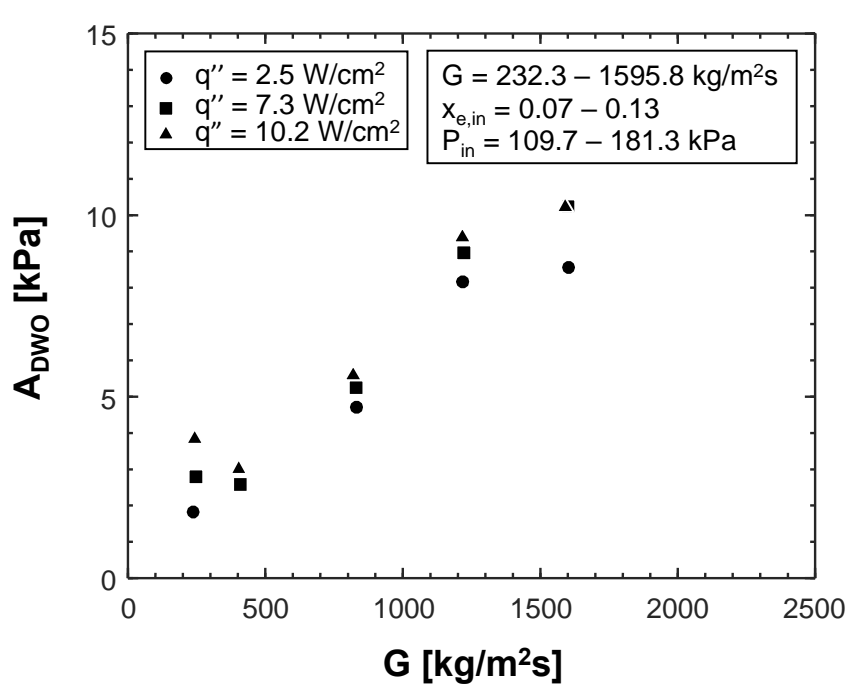


Figure 3.23 (b).

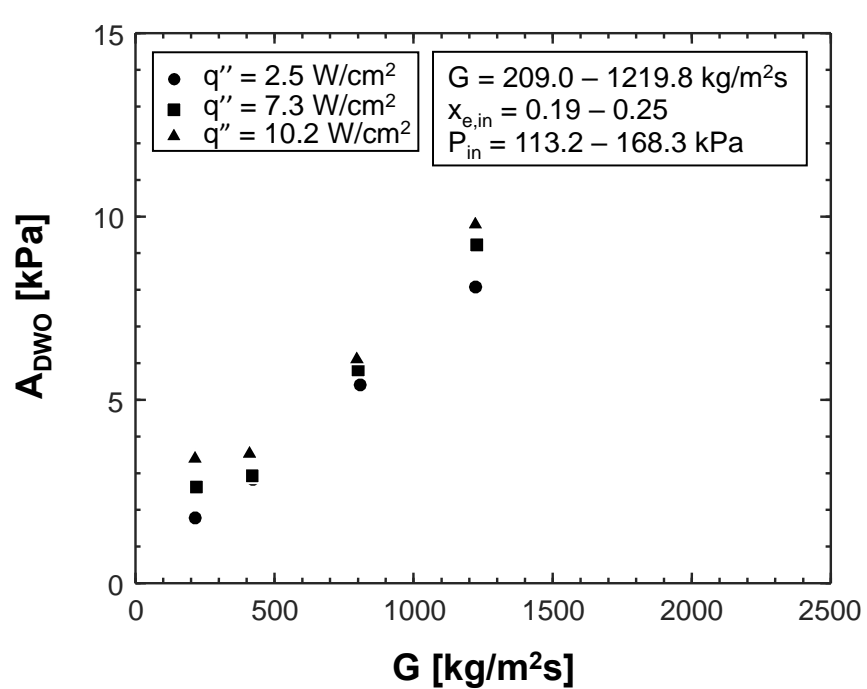


Figure 3.23 (c).

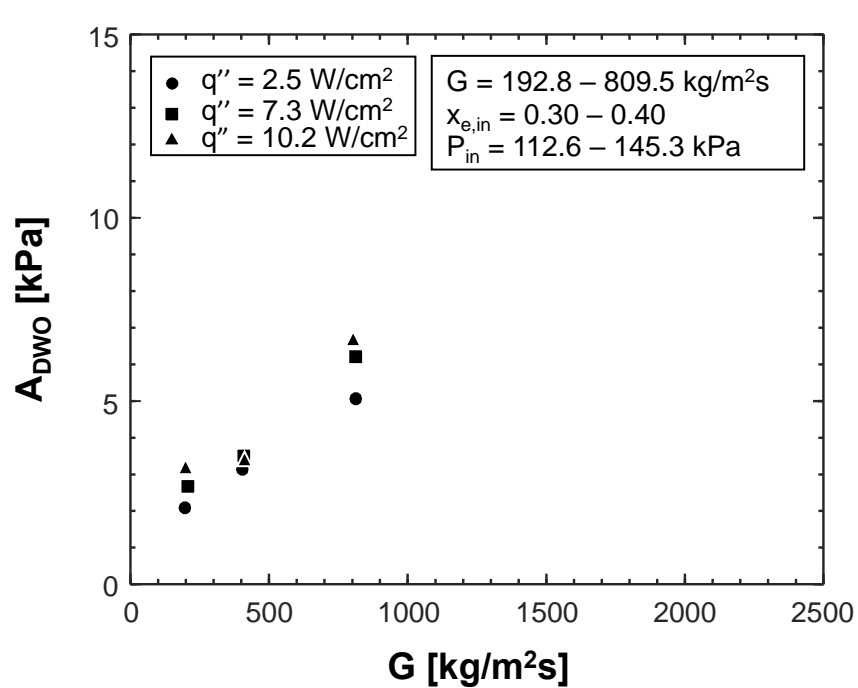


Figure 3.23 (d).

### 3.2.3.3 Frequency and Amplitude of Oscillation in Response to Changes in Relevant Dimensionless Groups

Prior to presenting results, it is necessary to define several relevant dimensionless groups as they will be used hereafter. Liquid Reynolds number,

$$\text{Re}_f = \frac{G(1-x_{e,in})D_h}{\mu_f}, \quad (3.6)$$

where  $G$  is the mass velocity,  $x_{e,in}$  the thermodynamic equilibrium quality at the module inlet,  $D_h$  the hydraulic diameter, and  $\mu_f$  the liquid dynamic viscosity, is a mass fraction weighted ratio of inertial to viscous forces. Liquid Weber number,

$$\text{We}_f = \frac{\rho_f U_{char}^2 D_h}{\sigma}, \quad (3.7)$$

where  $\rho_f$  is the liquid density,  $\sigma$  the surface tension, and characteristic velocity  $U_{char}$  is defined as

$$U_{char} = \frac{G(1-x_{e,in})}{\rho_f}, \quad (3.8)$$

providing a mass fraction weighted ratio of inertial to surface tension forces. Similarly, liquid Froude number,

$$\text{Fr}_f = \frac{\frac{G}{\rho_f}(1-x_{e,in})}{\sqrt{gD_h}}, \quad (3.9)$$

represents a mass fraction weighted ratio of inertia to body forces. It should be noted that these first three dimensionless groups in Eqs. (3.6), (3.7), and (3.9) all contain flow inertia terms in their numerators, and denominators that exhibit little to no change for the current operating conditions ( $\mu_f$  and  $\sigma$  change slightly with operating pressure, while  $g$  and  $D_h$  remain constant).

The final two dimensionless groups, boiling number,  $Bo$ , and phase change number,  $N_{pch}$ , contain both numerators and denominators that change continuously across operating conditions, and provide measures of the relative magnitudes of phase change processes to flow inertia, with phase change number being weighted by phase density differences. Here, they are defined as

$$Bo = \frac{q''}{G h_{fg}} \quad (3.10)$$

and

$$N_{pch} = \frac{Q}{\dot{m} h_{fg}} \frac{v_g - v_f}{v_f}, \quad (1.2)$$

where  $q''$  is the heat flux,  $h_{fg}$  the latent heat of vaporization,  $Q$  the total energy added within FBM,  $\dot{m}$  the mass flowrate, and  $v_g$  and  $v_f$  the vapor and liquid specific volumes, respectively.

Figures 3.25(a) – 3.25(e) show trends for DWO frequency versus each of the respective dimensionless groups mentioned above. It should be noted that data from both 2015 and 2016 experiments are present on these plots, allowing for comparison of data across the two sets of experiments for similar values of the relevant dimensionless groups. Data acquired in 2015 are denoted with circles and those from 2016 with squares.

Figure 3.25(a) shows that, as liquid Reynolds number increases, there is a clear increase in frequency of oscillation for DWO induced pressure fluctuations. This matches well with the trend of increasing frequency with increasing mass velocity seen in Fig. 3.22, as mass velocity is present in the numerator of Eq. (3.6). Frequency values appear to plateau, however, for values of liquid Reynolds number greater than  $\sim 10000$ , indicating some physical limits for frequency at which this phenomenon can occur for the present flow geometry and working fluid.

Similarly, Figs. 3.24(b) and 3.24(c) show increases in frequency for increases in liquid Weber and Froude numbers, respectively, with both also exhibiting diminishing returns past some moderate value. This indicates flow inertia is by far the dominant force at play relative to other hydrodynamic effects.

Figures 3.24(d) and 3.24(e), providing plots of frequency versus boiling and phase change numbers, respectively, exhibit no clear trends with respect to these dimensionless groups. If anything, Fig. 3.24(d) exhibits a slight negative trend, indicating mass velocity (present in the denominator of Eq. (3.10)) continues to the frequency at which DWOs occur. This further reinforces the trend seen in Fig. 3.22, that heat flux level (and the phase change process in general) has little effect on the frequency at which DWOs occur.

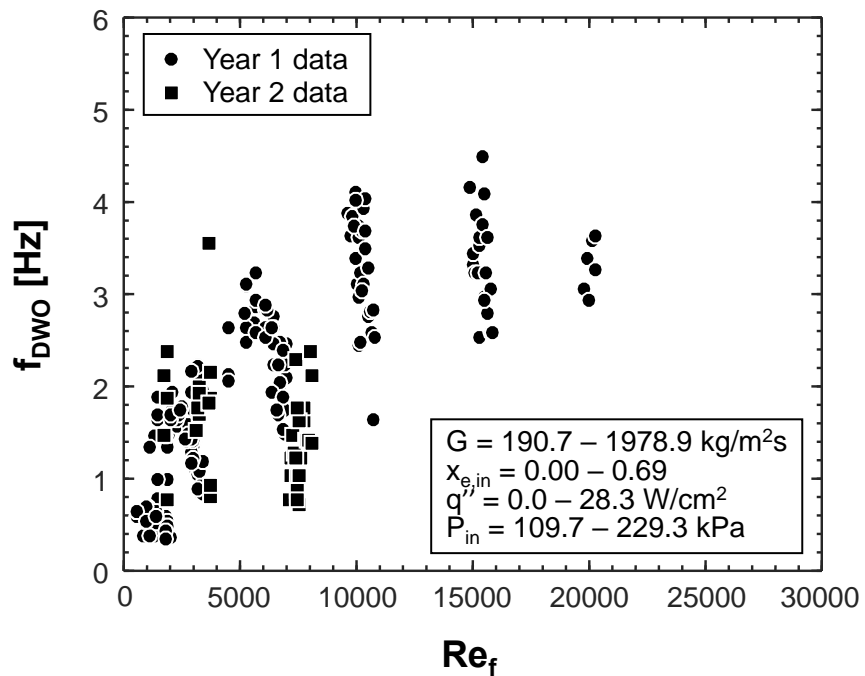


Figure 3.24: Plots of DWO frequency versus (a) liquid Reynolds number,  $Re_f$ , (b) liquid Weber number,  $We_f$ , (c) liquid Froude number,  $Fr_f$ , (d) boiling number,  $Bo$ , and (e) phase change number,  $N_{pch}$ .

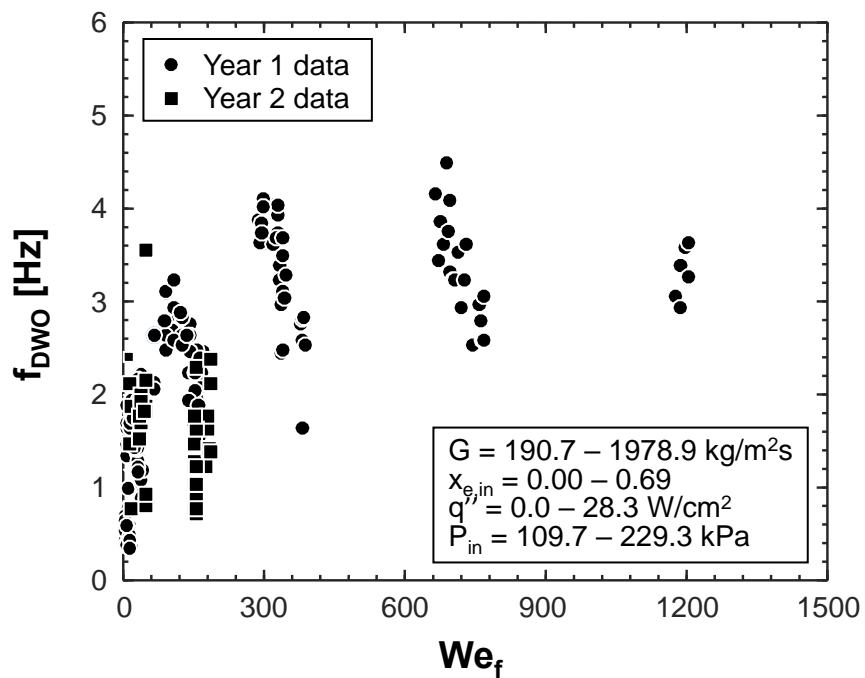


Figure 3.24 (b).

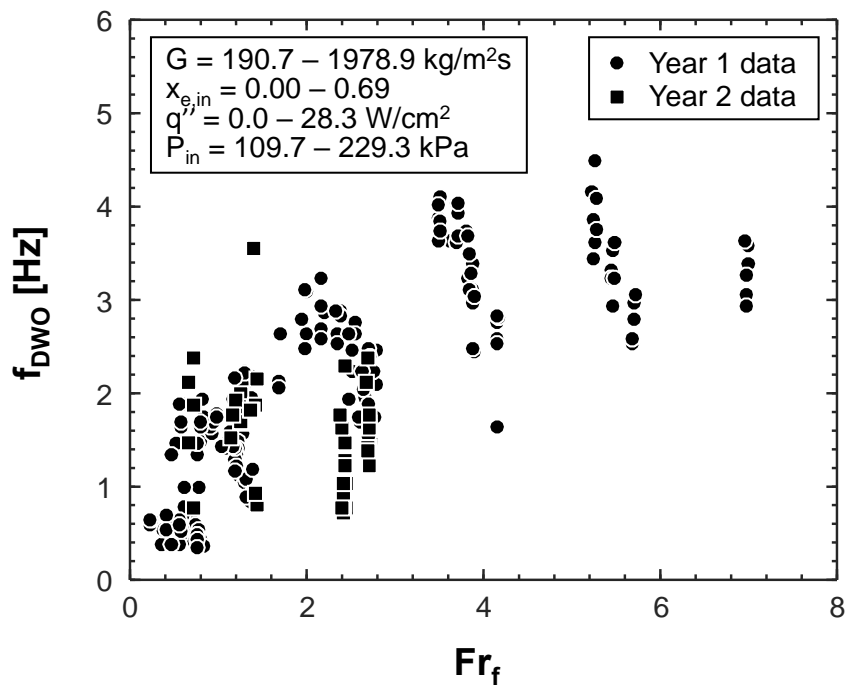


Figure 3.24 (c).

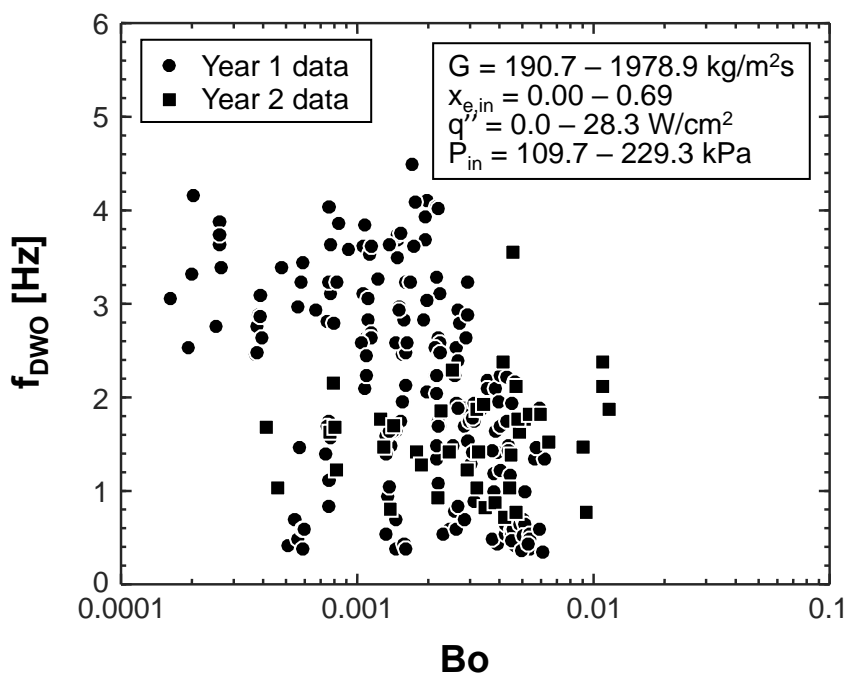


Figure 3.24 (d).

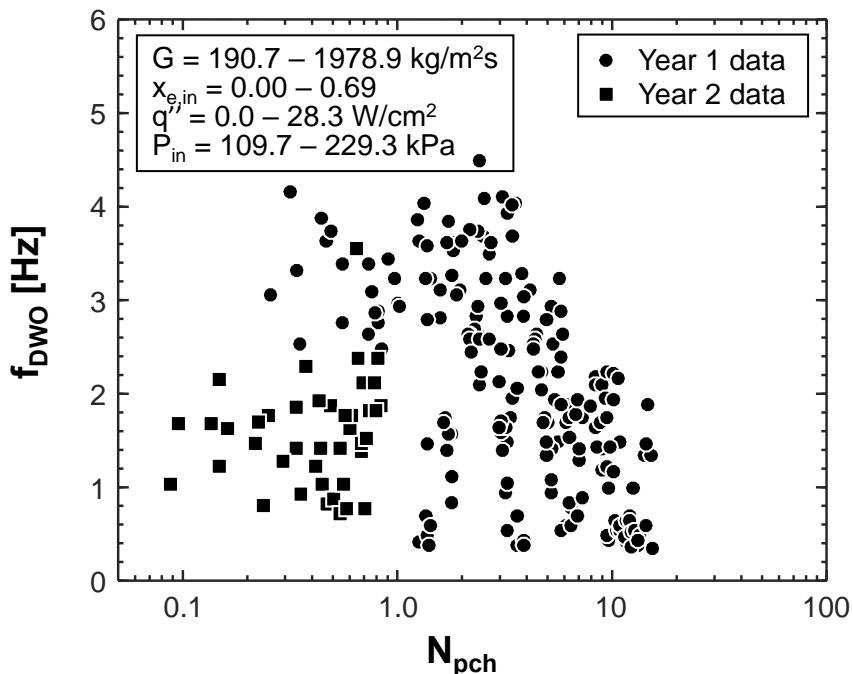


Figure 3.24 (e).

Figures 3.25(a) – 3.25(e) provide similar plots for amplitude of DWO induced oscillations versus relevant dimensionless groups. Similar to the counterparts in Figs. 3.24(a) – 3.24(c), plots of amplitude versus liquid Reynolds, Weber, and Froude numbers exhibit strong positive trends. They also show signs of plateauing in the higher portion of the range for each dimensionless group, but without quite as strong a change in slope, indicating the mechanism(s) limiting frequency of oscillation are also present for amplitude, but without quite as strong an impact.

Figures 3.25(d) and 3.25(e) show plots of amplitude versus boiling and phase change numbers, respectively; neither of which exhibit strong trends. This is somewhat surprising, as Fig. 3.23 clearly showed increases in amplitude of oscillation associated with increases in heat flux, but can likely be explained by the competing influences of phase change (numerator) and flow inertia (denominator) of both dimensionless groups. If anything, slight negative trends are present within these plots, indicating the influence of flow inertia is still the dominant factor here.

Across both Figs. 3.24 and 3.25, it can be seen that frequency and amplitude results from experiments conducted in both year 1 and year 2 of the project show good agreement, with few outliers. This reinforces the idea presented in Section 3.1, that DWO induced oscillatory flow behavior within the test section can be isolated from other fluctuations, and it occurs largely

independent of other hardware within the flow loop, validating it as a physical phenomenon intrinsic to two-phase flows.

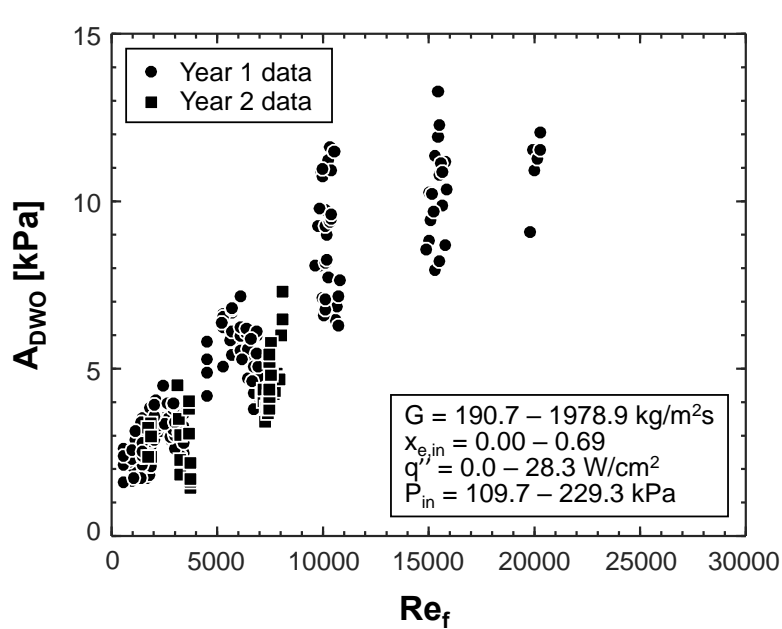


Figure 3.25: Plots of DWO amplitude versus (a) liquid Reynolds number,  $Re_f$ , (b) liquid Weber number,  $We_f$ , (c) liquid Froude number,  $Fr_f$ , (d) boiling number,  $Bo$ , and (e) phase change number,  $N_{pch}$ .

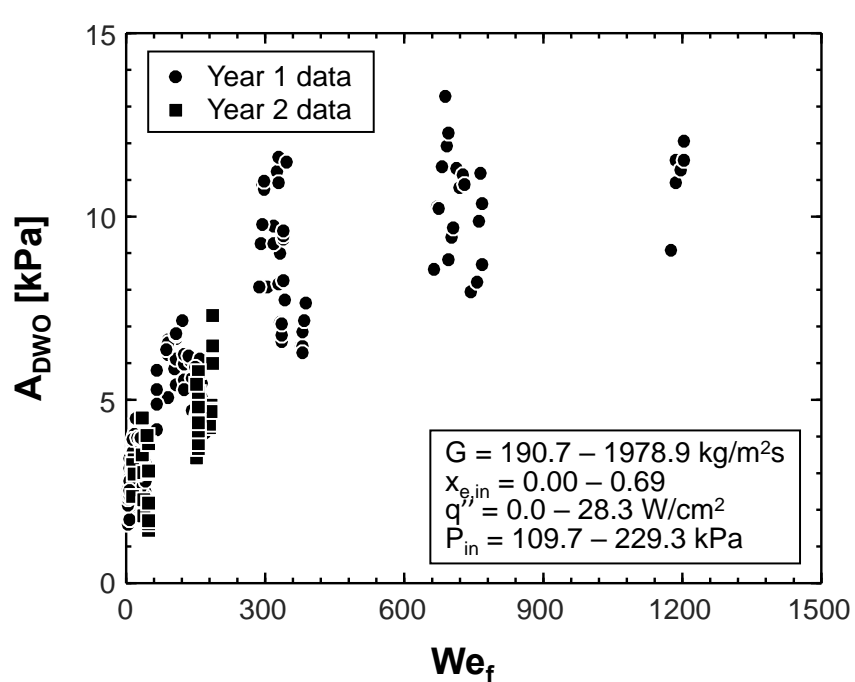


Figure 3.25 (b).

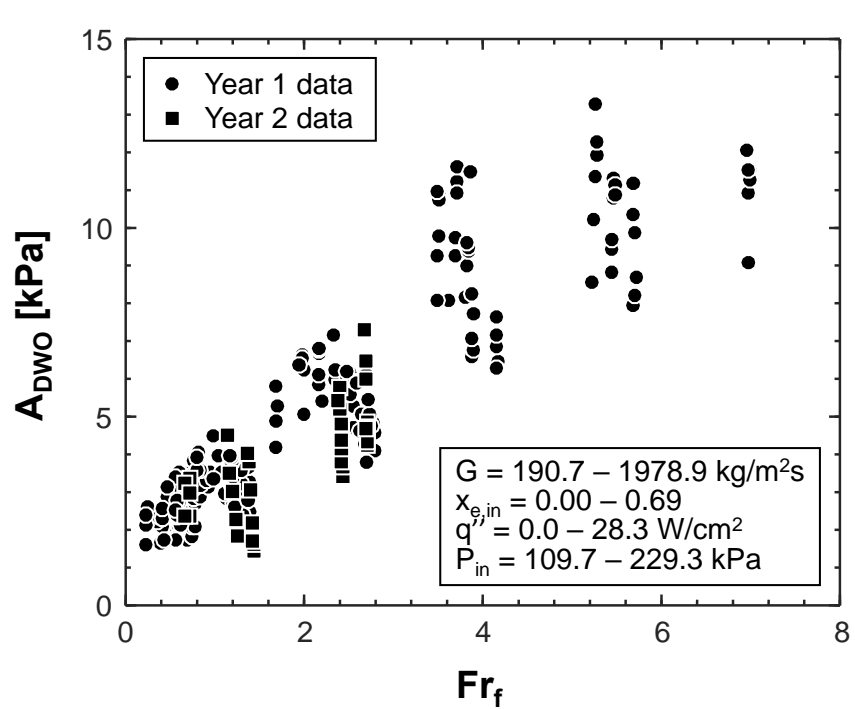


Figure 3.25 (c).

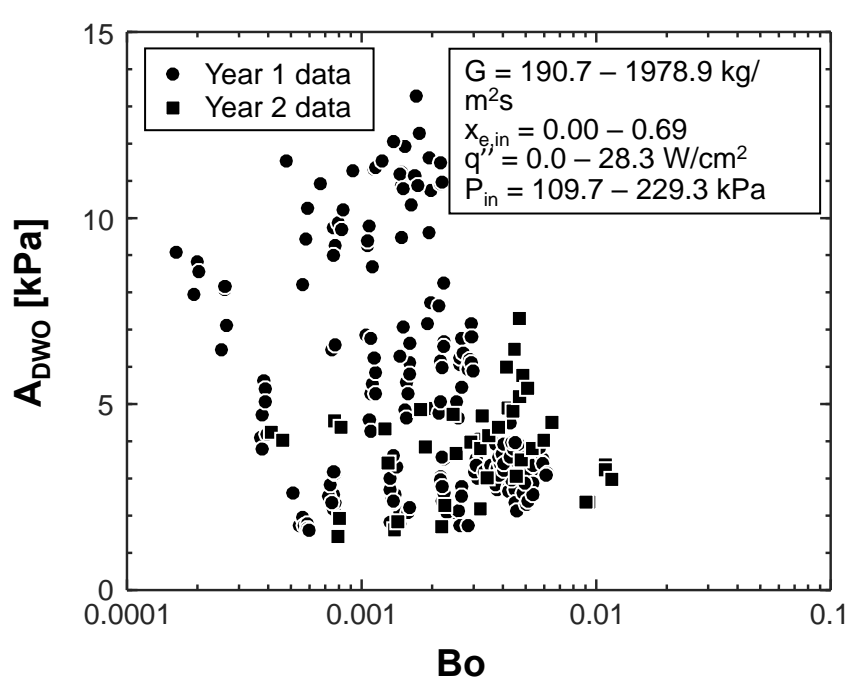


Figure 3.25 (d).

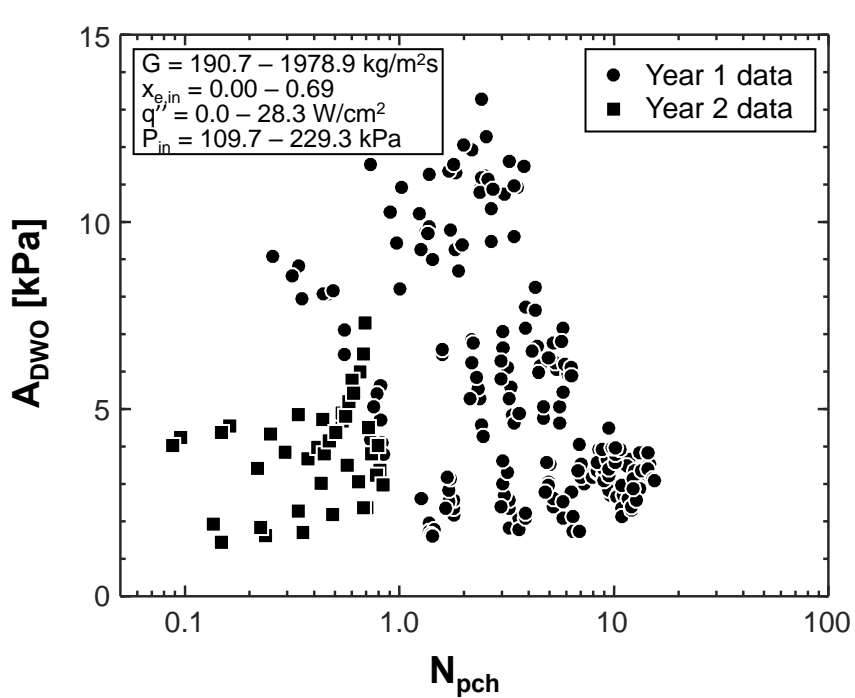


Figure 3.25 (e).

#### 3.2.3.4 Coupling of Frequency and Amplitude of Oscillation

In analyzing Figs. 3.22 – 3.25, it is clear that both frequency and amplitude of DWO induced oscillatory behavior depend primarily on flow inertia. This is in keeping with the DWO process presented schematically in Fig. 3.20, in which flow inertia is directly responsible for advecting the HDF along the channel length.

Figure 3.26, providing a plot of DWO amplitude versus frequency, further reinforces this notion by illustrating the nearly-linear relationship between the two key aspects of DWO behavior. The importance of this in validating physicality of the aforementioned DWO process schematic cannot be understated, and looking forward, coupling of frequency and amplitude of DWO induced oscillatory behavior is a requirement for any predictive tools attempting to predict these key characteristics of DWOs.

It is also worth noting that, across all operating conditions evaluated in this section, the amplitude of pressure fluctuations as a percentage of time-averaged operating pressure is of sufficiently low magnitude (at most 7%) to alleviate any concerns of them posing safety risks to system operation (especially important for development of the FBCE). Magnitudes are sufficient, however, to potentially trigger pre-mature CHF, dryout, or choked flow should operating conditions place a system sufficiently close to these critical points, a concern which should be kept in mind for design of two-phase flow thermal management systems.

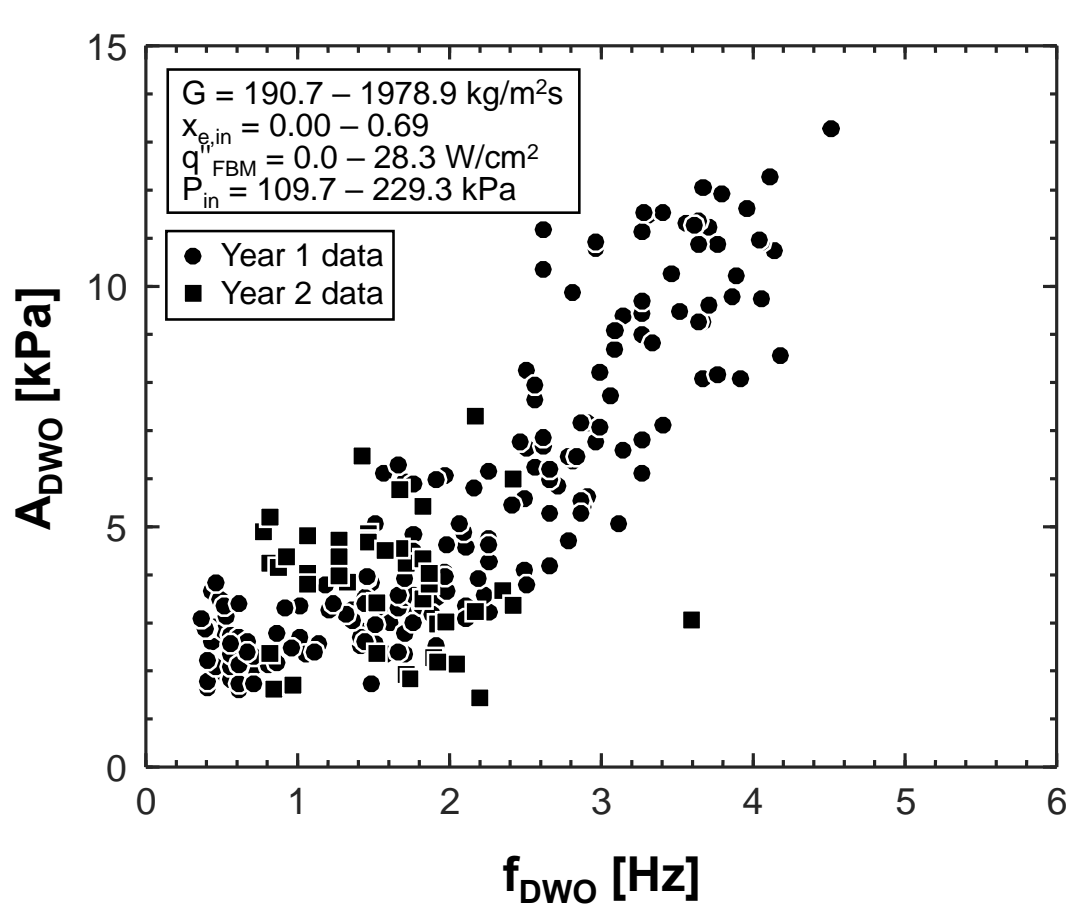


Figure 3.26: Plot of DWO amplitude versus frequency for all data from years 1 and 2 of the study.

### 3.2.4 Utilizing Frequency and Amplitude Information

#### 3.2.4.1 Reconstruction of Experimental Pressure Fluctuations

Having presented flow visualization images and schematics outlining the process by which density wave oscillations occur in mini/macro-channels and analyzed a large experimental database of 236 cases for vertical upflow boiling with DWOs present to gather information on trends, some discussion on utility of gathered data is warranted.

Thus far, all discussion on DWOs has centered on frequency and amplitude of induced oscillatory behavior. As discussed with Fig. 3.21, however, DWOs do not exhibit perfectly sinusoidal behavior, meaning any reconstruction of DWO induced behavior using a single frequency and amplitude is by nature an approximation.

Figures 3.27(a) – 3.27(e) investigate the potential accuracy of such a reconstruction, using inlet pressure signal for the case with mass velocity of  $G = 834.1 \text{ kg/m}^2\text{s}$ , inlet quality of  $x_{e,in} = 0.04$ , average inlet pressure of  $P_{in} = 122.6 \text{ kPa}$ , and heat flux of  $q'' = 7.3 \text{ W/cm}^2$ . Figure 3.27(a) shows the fluctuating pressure signal as well as the reconstructed signal, defined as

$$P'_{rec} = A_{DWO,in} \sin(2\pi f_{DWO,in} t), \quad (3.12)$$

where  $A_{DWO,in}$  and  $f_{DWO,in}$  are the amplitude and frequency of DWO induced oscillatory behavior detected for the inlet pressure signal using the methodology presented in Fig. 3.21, and  $t$  is time.

It is clear from Fig. 3.27(a) that the reconstructed signal does a reasonable job of approximating the original signal. A key limitation, however, is the slow change in phase between the two waveforms over time. At the first trough of the waveforms, the reconstructed signal is slightly ahead of the experimental data, but at the second trough they exhibit an almost exact match. The third trough shows the reconstructed signal lagging slightly behind the experimental data and, by the end of the 2-s window shown here, the two waveforms appear to be  $180^\circ$  out of phase. This is again due to the features of DWOs discussed in Fig. 3.21, specifically that DWO induced behavior is not perfectly sinusoidal in nature and the frequency at which DWOs occur is not constant, falling instead within a narrow range.

For comparison purposes, Figs. 3.27(b) – 3.27(e) provide similar plots of experimental fluctuating pressure alongside 2<sup>nd</sup>, 3<sup>rd</sup>, 4<sup>th</sup>, and 8<sup>th</sup> order Fourier series expansions, respectively. These Fourier series expansions are of the form

$$P'_{\text{FourierSeries}} = \frac{a_0}{2} + \sum_{i=1}^n (a_k \cos(kt) + b_k \sin(kt)), \quad (3.13)$$

where  $n$  is the series order and coefficients  $a$  and  $b$  are determined in Matlab [160]. From these plots it can be qualitatively seen that the reconstructed signal shown in Fig. 3.27(a) and expressed in Eq. (3.12) is superior to the 2<sup>nd</sup> order series expansion, of comparable accuracy to 3<sup>rd</sup> and 4<sup>th</sup> order series, but significantly inferior to the 8<sup>th</sup> order series for the current window of analysis.

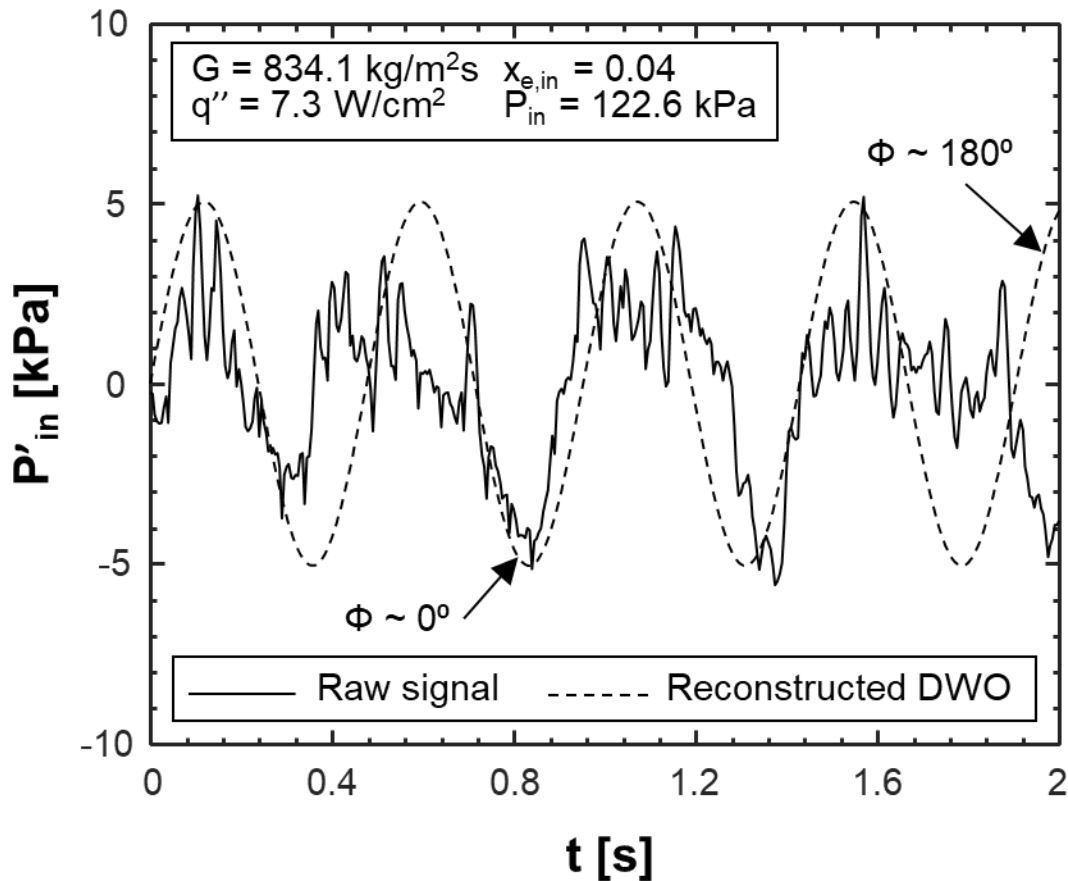


Figure 3.27: Plot of FBM heated length inlet pressure fluctuations along with (a) curve reconstructed from DWO amplitude and frequency, (b) 2<sup>nd</sup> order Fourier series expansion, (c) 3<sup>rd</sup> order Fourier series expansion, (d) 4<sup>th</sup> order Fourier series expansion, and (e) 8<sup>th</sup> order Fourier series expansion.

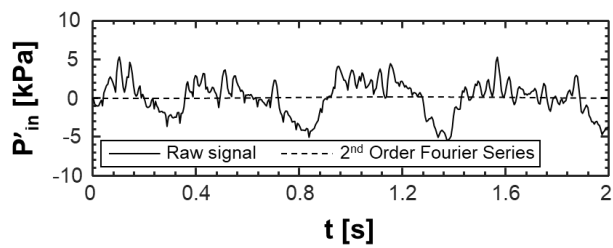


Figure 3.27 (b).

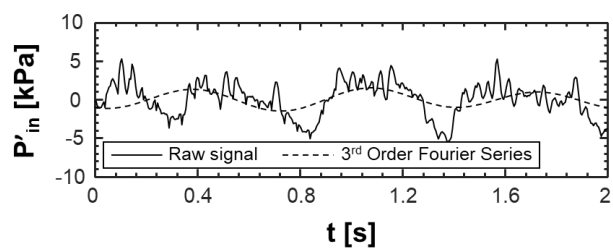


Figure 3.27 (c).

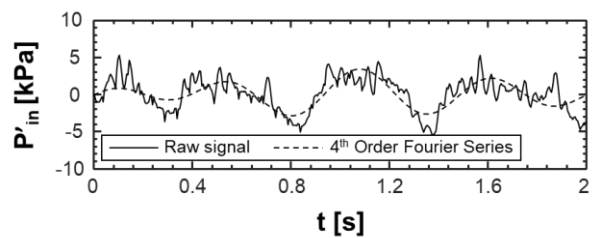


Figure 3.27 (d).

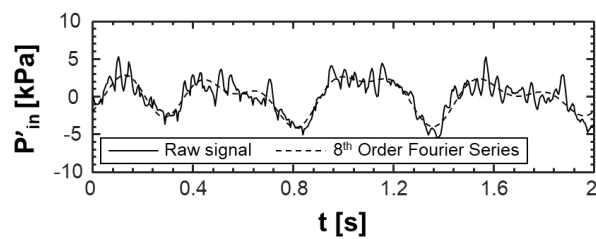


Figure 3.27 (e).

More rigorous evaluation of the agreement between waveforms can be assessed by computing cross correlation coefficients for each respective original and reconstructed signal. The cross correlation coefficient provides a measure of similarity between two waveforms, and is defined as

$$\rho_{cc}(P'_{exp}, P'_{rec}) = \frac{1}{N-1} \sum_{i=1}^N \left[ \left( \frac{P'_{exp,i} - \mu_{P'_{exp}}}{\sigma_{P'_{exp}}} \right) \left( \frac{P'_{rec,i} - \mu_{P'_{rec}}}{\sigma_{P'_{rec}}} \right) \right], \quad (3.14)$$

where  $P'_{exp}$  and  $P'_{rec}$  are the experimental and reconstructed fluctuating pressures,  $N$  is the number of samples in each waveform, and  $\mu$  and  $\sigma$  refer to respective means and standard deviations. Values fall in the range [-1,1], where 1 represents exact match, -1 indicates 180° phase difference, and 0 indicates no correlation between waveforms. It is also possible to think of the cross correlation coefficient as the covariance of the two waveforms divided by the multiplication of their standard deviations, or

$$\rho_{cc}(P'_{exp}, P'_{rec}) = \frac{\text{cov}(P'_{exp}, P'_{rec})}{\sigma_{P'_{exp}} \sigma_{P'_{rec}}}. \quad (3.15)$$

Table 4.1 provides values of cross correlation coefficient for each of the waveform pairs shown in Figs. 3.27(a) – 3.27(e). From these values it is clear that the reconstruction provided in Fig. 3.27(a) is superior to 2<sup>nd</sup> and 3<sup>rd</sup> order Fourier series expansions, but inferior to 4<sup>th</sup> and 8<sup>th</sup> order expansions.

Table 3.4: Cross correlation coefficients for waveform pairs in Fig. 3.27.

Original Signal	Reconstruction	Period for Evaluation [s]	Cross correlation coefficient, $\rho_{cc}$
Experimental inlet fluctuating pressure	2 <sup>nd</sup> order Fourier series expansion	2	0.10
Experimental inlet fluctuating pressure	3 <sup>rd</sup> order Fourier series expansion	2	0.40
<b>Experimental inlet fluctuating pressure</b>	<b>Experimentally detected frequency and amplitude</b>	<b>2</b>	<b>0.48</b>
Experimental inlet fluctuating pressure	4 <sup>th</sup> order Fourier series expansion	2	0.71
Experimental inlet fluctuating pressure	8 <sup>th</sup> order Fourier series expansion	2	0.87

It should be noted here that the cross correlation coefficient does exhibit some dependence on the time period over which the reconstruction is evaluated, especially for very short periods where phase between the two waveforms plays a vital role. Over longer periods these errors average out, and cross correlation coefficients for waveforms reconstructed using experimental amplitude and frequency provide more representative values. Towards this end, Table 3.5 provides values of cross correlation coefficient evaluated on the same 20-s period used for frequency and amplitude detection.

Table 3.5 contains values of cross correlation coefficient  $\rho_{cc}$  evaluated using waveforms reconstructed using information from inlet and outlet oscillations separately as well as averaged values. It can be seen that across the four sets of operating conditions presented herein, cases with similar values for frequency and amplitude of inlet and outlet pressure fluctuations, respectively, yield little difference in reconstruction accuracy when evaluated using local (inlet and outlet) information versus averaged information. However, for the two cases presented here with significant difference between inlet and outlet values of frequency, reconstruction accuracy appears to be significantly different for the two methods of evaluation.

Table 3.5: Cross correlation coefficients for inlet and outlet pressure fluctuations under various operating conditions.

Original Signal	Operating Conditions	Detected Freq. [Hz]	Detected Amp. [kPa]	Average Freq. [Hz]	Average Amp. [kPa]	Period for Evaluation [s]	$\rho_{cc}$ (Individual)	$\rho_{cc}$ (Average)
$P'_{in}$	$G = 834.1 \text{ kg/m}^2\text{s}$ $x_{e,in} = 0.04$	2.1	5.1	2.1	4.6	20	0.24	0.24
$P'_{out}$	$P_{in,ave} = 122.6 \text{ kPa}$ $q'' = 7.3 \text{ W/cm}^2$	2.1	4.1			20	-0.28	-0.28
$P'_{in}$	$G = 1636.5 \text{ kg/m}^2\text{s}$ $x_{e,in} = 0.01$	3.8	9.6	3.0	8.2	20	0.14	-
$P'_{out}$	$P_{in,ave} = 154.6 \text{ kPa}$ $q'' = 7.3 \text{ W/cm}^2$	2.2	6.9			20	-0.35	-0.11
$P'_{in}$	$G = 407.8 \text{ kg/m}^2\text{s}$ $x_{e,in} = 0.03$	0.95	2.8	0.95	2.5	20	-0.33	-0.33
$P'_{out}$	$P_{in,ave} = 116.0 \text{ kPa}$ $q'' = 7.3 \text{ W/cm}^2$	0.95	2.3			20	-0.14	-0.14
$P'_{in}$	$G = 816.1 \text{ kg/m}^2\text{s}$ $x_{e,in} = 0.11$	3.1	6.6	2.5	5.6	20	-0.20	-0.04
$P'_{out}$	$P_{in,ave} = 130.5 \text{ kPa}$ $q'' = 10.2 \text{ W/cm}^2$	1.9	4.6			20	0.08	0.15

Overall, it appears accuracy of reconstruction is far more sensitive to frequency than amplitude. This makes sense, as differences in phase cause multiplicative errors when evaluating the sum in Eq. (3.14), while differences in amplitude only cause additive errors.

Information provided in Table 3.5 indicates values of cross-correlation coefficient for the present reconstruction method fall predominantly in the -0.40 to 0.40 range. This indicates a reasonable degree of fit for the reconstruction method, with major information regarding amplitude and frequency of oscillation captured, but simplifications limiting its ability to fully reconstruct the complex transient waveform. The primary limiting assumptions are:

- (1) DWO induced flow oscillations are perfectly sinusoidal in nature, which has been shown not to be very accurate.
- (2) DWOs occur at constant frequency and amplitude, which has also been shown not to be very accurate.
- (3) The contribution of other induced fluctuations (whether high frequency, mechanically induced phenomena, or low frequency system transients) are negligible to overall system dynamic behavior, which cannot be assumed universally true.

Without addressing these limitations, it is unlikely higher accuracy reconstructions can be performed.

Accuracy of reconstruction is not the key benefit of this method of decomposing DWO induced behavior into single frequency and amplitude, however. Rather, it is the ability to utilize this information to easily characterize DWO induced fluctuations and implement them as boundary conditions and/or model inputs for fully transient two-phase flow simulations.

### 3.2.4.2 Key Trends/Outcomes useful for Future Model Development

Although a key aspect of two-phase flow research for decades (with the first work in the field commonly attributed to Serov [48]), an easily utilized, unified method for dealing with the impact of DWO induced flow oscillations in phase-change thermal management systems is still lacking.

As mentioned in section 3.2.1, many classic studies adopted approaches based on classic stability theory, modeling information propagation within the boiling section of the flow loop to determine unstable conditions for which DWOs would be encountered during subcooled boiling. Studies such as those by Fukuda and Kobori [80] and Lahey and Podowski [47] based their analysis on experimentally observed phenomena and demonstrated some qualitative agreement between stability boundary model and results, but little focus was spent on verifying agreement between experimental and predicted amplitude and frequency of oscillation. Additionally, that their analysis centered on subcooled flow boiling indicates a different forcing function was present for DWOs in their systems compared to that analyzed in the present work, limiting the applicability of their analysis to the current configuration.

More recent work by Schlichting *et al.* [63] accounted for the presence of instability-induced fluctuations within their system model by introducing mass flowrate fluctuations of a specified magnitude. Another study by Alves *et al.* [161] introduced transient phenomena within their analytic model by using transient experimental inlet pressure as a boundary condition. While both studies provide comprehensive analytical models for transient two-phase flow behavior, the lack of a physical constitutive relationship for DWO (or other instability modes) induced oscillatory behavior is a key limitation hindering the utility of their respective models to act as purely predictive design tools.

Development and validation of a model to predict frequency and amplitude of DWO induced fluctuations would prove a valuable constitutive relationship for transient two-phase flow codes due to its ability to more realistically simulate variations in operating pressure and flowrate which then impact important design parameters such as heated wall temperature, heat transfer coefficient, and CHF value through both direct means (*e.g.*, changes to local flow field) and indirect means (*e.g.*, changes to thermophysical properties). Despite the use of a single frequency and amplitude to reconstruct transient experimental results exhibiting less-than-perfect agreement,

a tool capable of predicting peak frequency and amplitude of DWO induced fluctuations would prove a major step forward towards the ability to design around such oscillatory behavior.

Towards this end, the following sections aims to present a new mechanistic model for DWOs capable of predicting frequency of induced oscillatory behavior as well as amplitude of associated pressure fluctuations. This work will draw heavily from key conclusions drawn from analyzing the experimental results presented herein, which are summarized in Table 3.6.

Table 3.6: Key findings from the present section.

Aspect of Study	Key Findings
Manifestation of DWOs	<ul style="list-style-type: none"> <li>• Unlike micro-channels, where surface tension forces are integral in the formation and propagation of DWOs, DWOs in mini/macro-channel flows with finite inlet quality manifest due to flow separation effects.</li> <li>• Manifestation of DWOs in the present geometry is due to a cyclical process of upstream liquid film accumulation and downstream dryout, leading to mass and momentum flux imbalances between channel inlet and outlet, which cause formation and propagation of a liquid slug (HDF) along the channel, re-wetting walls and re-establishing co-current annular flow.</li> </ul>
Frequency of induced oscillations	<ul style="list-style-type: none"> <li>• Average frequency of DWO induced oscillations depends primarily on mass velocity and shows little dependence on heat flux.</li> <li>• Frequency of pressure oscillations occasionally differs between measurement locations upstream and downstream of the heated length, likely due to phase change processes taking place within altering flow characteristics.</li> <li>• DWOs are periodic but not necessarily sinusoidal in nature.</li> <li>• DWOs do not occur at a single constant frequency, with oscillatory behavior instead falling in a narrow frequency band around a peak value.</li> </ul>
Amplitude of induced pressure oscillations	<ul style="list-style-type: none"> <li>• Amplitude of DWO induced pressure oscillations depends primarily on mass velocity, with a lesser dependence on heat flux along the heated length.</li> <li>• Amplitude of DWO induced pressure oscillations also differs slightly between measurement locations upstream and downstream of the heated length, likely due to phase change processes taking place within altering flow characteristics.</li> </ul>
Reconstruction of experimental pressure signals using frequency and amplitude	<ul style="list-style-type: none"> <li>• Reconstruction using peak frequency and average amplitude of oscillation exhibits acceptable agreement when evaluating cross correlation coefficients.</li> <li>• Disagreement stems from (1) continuously changing phase lag between waveforms due to oversimplification associated with using single frequency, and (2) reconstruction lacking high and low frequency information.</li> <li>• Despite limitations, reconstruction is considered more than adequate for use as boundary condition to propagate DWO induced fluctuations into transient two-phase flow models.</li> </ul>

### 3.3 Mechanistic Model to Predict Frequency and Amplitude of Density Wave Oscillations in Vertical Upflow Boiling

#### 3.3.1 *Density Wave Oscillation (DWO) Model Development*

Description of the model development will proceed in three steps: First, schematic presentations of key regions of interest and relevant physical processes occurring therein will be presented to illustrate how key elements of the mechanistic process described in Fig. 3.20 may be quantified. Key assumptions used during modeling will also be discussed here.

Second, a full solution process will be outlined, showing step by step how the model is solved to find parameters of interest (namely frequency and amplitude of DWO induced pressure oscillations). At this point all relevant constitutive relations will be provided, and any additional assumptions employed to ensure stable solutions discussed.

Finally, numeric results for model sub-components will be presented for select sub-cases to show how the model behaves in time as it approaches a solution.

##### 3.3.1.1 Model Setup and Advancement

As shown in Fig. 3.20, the nominal flow condition for cases of interest here is that of annular, co-current flow. The model development will begin by considering flow through a rectangular channel to match the cross section of the FBM; the same model can tackle circular channels as well.

Figure 3.28(a) provides schematics of the entire FBM under nominal conditions for the current investigation. The fluid length is separated into adiabatic and heated (diabatic) lengths, with liquid film thickness constant along the adiabatic length and linearly dependent on position in the heated length due to the application of a uniform, constant heat flux along the heated length. Cross section schematics for both portions of the channel are also provided.

Figure 3.28(a) also establishes three distinct regions for analysis:

- 1) Region 1, Upstream: This section is used to describe flow entering the channel, and is assumed to be steady, with flow field parameters determined by nominal (time-averaged) operating conditions for each test case.
- 2) Region 2, High Density Front (HDF): Shown in Fig. 3.28(a) as a thin region segregating Region 1 (Upstream) from Region 3 (Downstream). It will be discussed in more detail when analyzing Fig. 3.28(b).

- 3) Region 3, Downstream: Flow in the downstream region is initially ( $t = 0$  s) assumed to possess the same mass flow rate as Region 1, with the same quality along the adiabatic length and a linear variation in quality along the heated length. As time advances, however, a separated flow model is solved to update mass and momentum (with conservation of energy also used to account for phase change) in this portion of the channel. This allows the potential for liquid to accumulate in Region 2 should the flow model predict instantaneous mass velocity entering the channel (assumed to be constant) to be greater than that exiting (determined by solution of the separated flow model).

More detail will be provided on Regions 2 and 3 in subsequent figures.

Figure 3.28(b) provides a schematic of Region 2, corresponding to the HDF. A key parameter in this schematic is the length of the HDF,  $l_{HDF}$ , defined as

$$l_{HDF} = \frac{m_{HDF}}{A_c \rho_f}, \quad (3.16)$$

where  $m_{HDF}$  is the mass stored in the HDF,  $A_c$  the cross-sectional area of the channel, and  $\rho_f$  the density of liquid evaluated at the inlet pressure. It should be noted here that, for modeling purposes, the HDF is considered to be composed entirely of liquid, although in reality some amount of vapor is typically present depending on operating conditions.

At the onset of the simulation  $m_{HDF}$  is equal to zero, meaning the length of the HDF is zero and no conservation equations are solved for the Region 2 control-volume. As time is advanced and the separated flow model is solved for Region 3, mass outflow from the channel begins to drop below mass inflow, meaning mass must be stored within the channel. As mentioned when presenting Fig. 3.20, mass storage within the channel is accomplished through liquid phase accumulation in the near-inlet region, here translating to increasing values of  $m_{HDF}$  and  $l_{HDF}$ . Once it possesses finite size and mass, it is possible to solve conservation of momentum for the Region 2 control-volume to find important parameters including HDF velocity,  $u_{HDF}$ , and pressure drop across the HDF,  $DP_{HDF}$ .

Conservation of momentum for the HDF includes terms corresponding to pressure drop, body force, viscous shear, and differences in momentum between Regions 1 and 2 (upstream and HDF) and Regions 2 and 3 (HDF and downstream). The full form of each momentum component

is provided in Table 3.7, along with references for relevant constitutive relations, key assumptions, and related comments. It should be noted here that the relationship used to find wall shear stress acting on the HDF comes from directly evaluating  $m_f \left( du_{HDF} / dy \right)$ , using a linear fit for velocity ranging from  $u = 0$  at the channel wall to  $u = 1.5u_{HDF}$  at the channel centerline (where  $u_{HDF}$  is the average HDF velocity calculated by the model).

Prior to discussing the method by which the model accounts for the motion of the HDF along the channel in time, it is first necessary to provide some discussion on the separated flow model being solved in the downstream portion of the channel, Region 3. Figure 3.28(c) provides schematics of control volumes for both liquid and vapor phases in adiabatic and diabatic portions of the channel, with key force components defined in each, including pressure drop, wall shear stress, interfacial shear stress, body force, and momentum transfer due to phase change. Similar to what was done with the HDF control volume, the full form of all terms can be found in Table 3.8, along with references for relevant constitutive relations, key assumptions, and related comments.

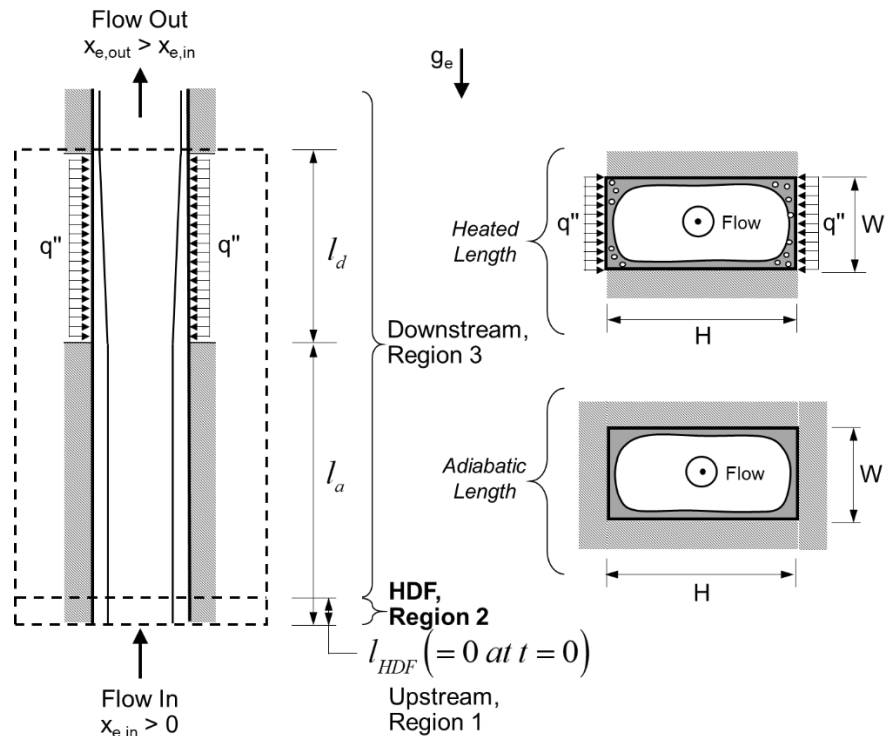


Figure 3.28: (a) General model setup, key characteristics of which are presence of annular flow throughout, segmentation into Upstream Region 1, High Density Front Region 2, and Downstream Region 3, and separate adiabatic and diabatic lengths. (b) Control-volume encompassing HDF Region. (c) Description of force terms in separated flow model used in Downstream Region 3.

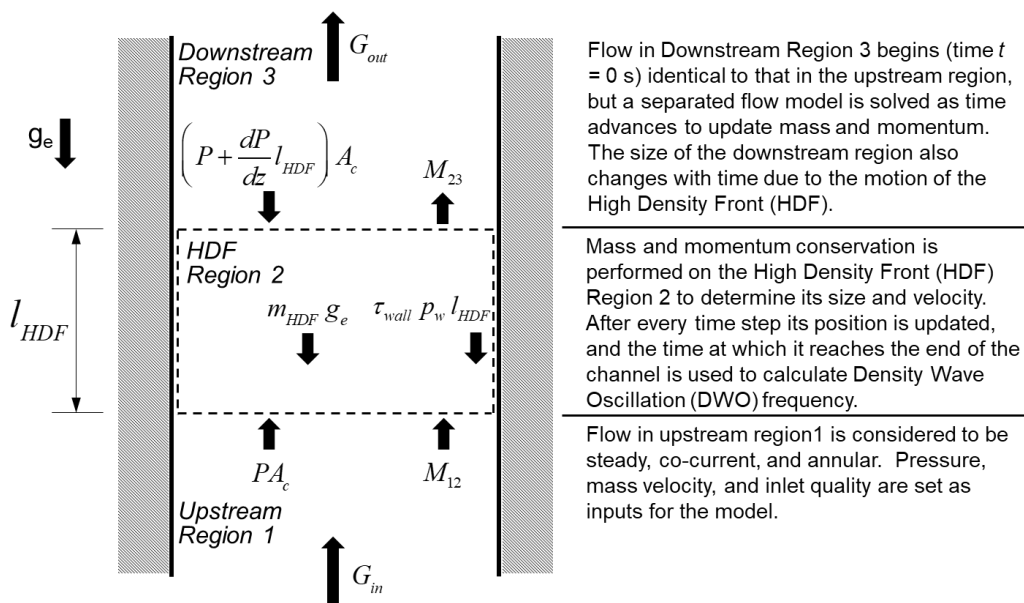


Figure 3.28 (b).

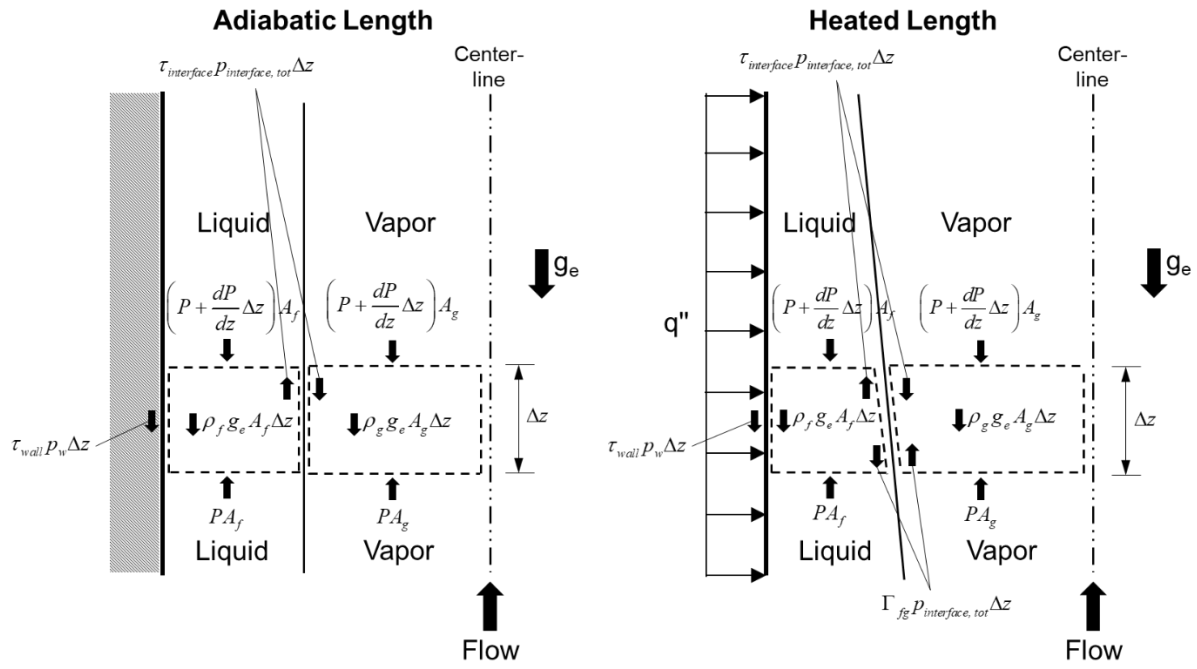


Figure 3.28 (c).

Table 3.7: Relevant assumptions, relations, and references for Region 2 control volume.

Key Assumptions	<p>(1) HDF is entirely composed of liquid</p> <p>(2) HDF initially has no mass, no velocity</p> <p>(3) Neglect interfacial curvature at front and back of HDF (surface tension effects)</p> <p>(4) Neglect virtual mass force effects</p> <p>(5) Neglect loss of liquid from HDF while re-wetting walls</p> <p>(6) Neglect property changes due to local pressure changes</p> <p>(7) Limit relative velocities to <math>\geq 0</math></p>
Constitutive Relations	$M_{12}^n = \rho_g A_{g,tot}^0 (u_g^0 - u_{HDF}^n)^2 + \rho_f A_{f,tot}^0 (u_f^0 - u_{HDF}^n)^2$ $M_{23}^n = \rho_g A_{g,tot}^n (u_g^n - u_{HDF}^n)^2 + \rho_f A_{f,tot}^0 (u_f^n - u_{HDF}^n)^2$ $\tau_{wall}^n = \frac{3\mu_f u_{HDF}^n}{D_H}$ $\Delta P_{HDF}^n = \frac{f_{HDF}^n (1.5G_m)^2 l_{HDF}^n}{2\rho_f D_H} + \rho_f g l_{HDF}^n$ <p>where 0 indicates initial conditions and <math>n</math> current time step</p>
References	<p>Friction factor <math>f_{HDF}</math> is determined using the Colebrook-White equation for turbulent flow [162] with roughness of <math>e = 0.000508 \text{ m}</math> for polished polycarbonate.</p>

Table 3.8: Relevant assumptions, relations, and references for Region 3 control volumes.

Key Assumptions	<p>(1) Flow conditions initially identical to those in Region 1.</p> <p>(2) Neglect property changes due to local pressure differences.</p> <p>(3) Use lumped analysis for region (parameters are not a function of space in Region 3, instantaneous inflow is equal to outflow)</p> <p>(4) Neglect interfacial curvature and associated effects.</p> <p>(5) Flow qualities limited to the range <math>0.01 \leq x_{ave,tot} \leq 0.99</math> to prevent division by zero.</p> <p>(6) Phase momentums are limited to the range <math>0 &lt; M_k &lt; M_{k,1}</math>, where the subscript <math>k</math> indicates each respective phase and 1 refers to their region 1 values.</p>
Constitutive Relations	$\tau_{wall}^n = \frac{\rho_f f_w^n u_f^{n2}}{2}$ $\tau_{interface}^n = \frac{f_i^n \rho_g (u_g^n - u_i^n)^2 + (u_g^n - u_i^n) \frac{q''}{h_{fg}}}{2}$ $\left(\frac{dP}{dz}\right)^n = \left(\frac{dP}{dz}\right)_{2\phi}^n = \left(\frac{dP}{dz}\right)_A^n + \left(\frac{dP}{dz}\right)_G^n + \left(\frac{dP}{dz}\right)_F^n$ $\Gamma_{fg}^n = \frac{q'' u_{interface}^n}{h_{fg}}$
References	<ul style="list-style-type: none"> <li>- Friction factor <math>f_w</math>, is determined using the Colebrook-White equation for turbulent flow [162] with roughness of <math>\varepsilon = 0.000508</math> m for polished polycarbonate.</li> <li>- Interfacial shear stress is determined by the Wallis relation [163].</li> <li>- Frictional pressure drop is calculated using the Homogeneous Equilibrium Model with the mixture viscosity model of Akers <i>et al.</i> [164].</li> </ul>

Having defined the relevant physical processes in play, Fig. 3.29(a) illustrates how they come together to form an overall system with the goal of finding the size and velocity of the HDF at any given instant in time. Starting with Region 3, conservation of momentum is updated at each time step, with values used to calculate new phase velocities. These velocities are then used to calculate the overall mass velocity in the downstream region at each instant in time.

This information is then used to update the mass stored in Region 2, the HDF. After this conservation of momentum is performed on Region 2 to find the updated velocity of the HDF, which can be multiplied by the time step  $\Delta t$  to find the updated  $z$ -location of the HDF at time  $n$ .

Figure 3.29(b) illustrates this process by providing system schematics at four different times. Similar to the schematic presented in Fig. 3.28(a), Fig. 3.29(b) shows that the model begins with Region 3 covering the entire downstream portion of the channel, and the HDF (Region 2) possessing zero thickness. As time advances, the HDF grows in length (due to mass accumulating within) and travels along the length of the channel, causing Region 3 to decrease in length. It should be noted that everything upstream of the HDF is assumed to follow the behavior of Region 1, which physically corresponds to passage of the HDF serving to re-wet the liquid film and re-establish annular, co-current flow throughout (as seen in Fig. 3.16).

As the HDF continues to travel along the channel length, Fig. 3.29(b) shows the adiabatic length eventually going to zero, and the model concludes when the HDF reaches the end of the channel. At this point, the total time taken for the HDF to accumulate mass and travel to the end of the channel is defined here as the period of Density Wave Oscillation (DWO), allowing a frequency to be calculated as

$$f_{DWO} = \frac{1}{t_{HDF \text{ exits channel}}}. \quad (3.17)$$

Similarly, amplitude of DWO induced pressure oscillations may be calculated at the same instant by taking one-half the difference between maximum total two-phase and frictional HDF pressure drops, or

$$A_{DWO} = \frac{\Delta P_{2\phi, \max}^0 - \Delta P_{HDF, \max \text{ frictional}}^n}{2}, \quad (3.18)$$

where maximum two-phase pressure drop is calculated at time  $t = 0$  s for the entire channel and maximum HDF pressure drop is calculated at the final time-step. These terms reflect the difference in pressure drop in the channel under nominal operating conditions ( $\Delta P_{2f}$ ), evaluated at time  $t = 0$

s in the model when conditions in Region 3 are identical to those in Region 1, and when the HDF is passing through the heated length ( $DP_{HDF}$ ), evaluated at time  $t = t_{final}$  when the HDF is at its maximum length and is passing from the channel. Relations used for the calculation of each pressure drop term will be provided when discussing the full solution procedure in the following section. It should be noted, however, that selection of the relationship for two-phase pressure drop was performed using extensive analysis on accuracy of two-phase frictional pressure drop correlations presented in a prior study [53].

The general idea behind this formulation is that channel pressure drop characteristics change in response to the alternating passage of two-phase annular flow and a single-phase slug, meaning just as the frequency at which DWOs are observed is related to the time required for the downstream region to cycle through annular two-phase flow, dryout, single-phase liquid (HDF), and return to annular two-phase flow, the magnitude of associated pressure oscillations are tied to the changes in pressure drop encountered while cycling from a maximum pressure drop regime (annular two-phase flow) to a minimal pressure drop regime (single-phase liquid).

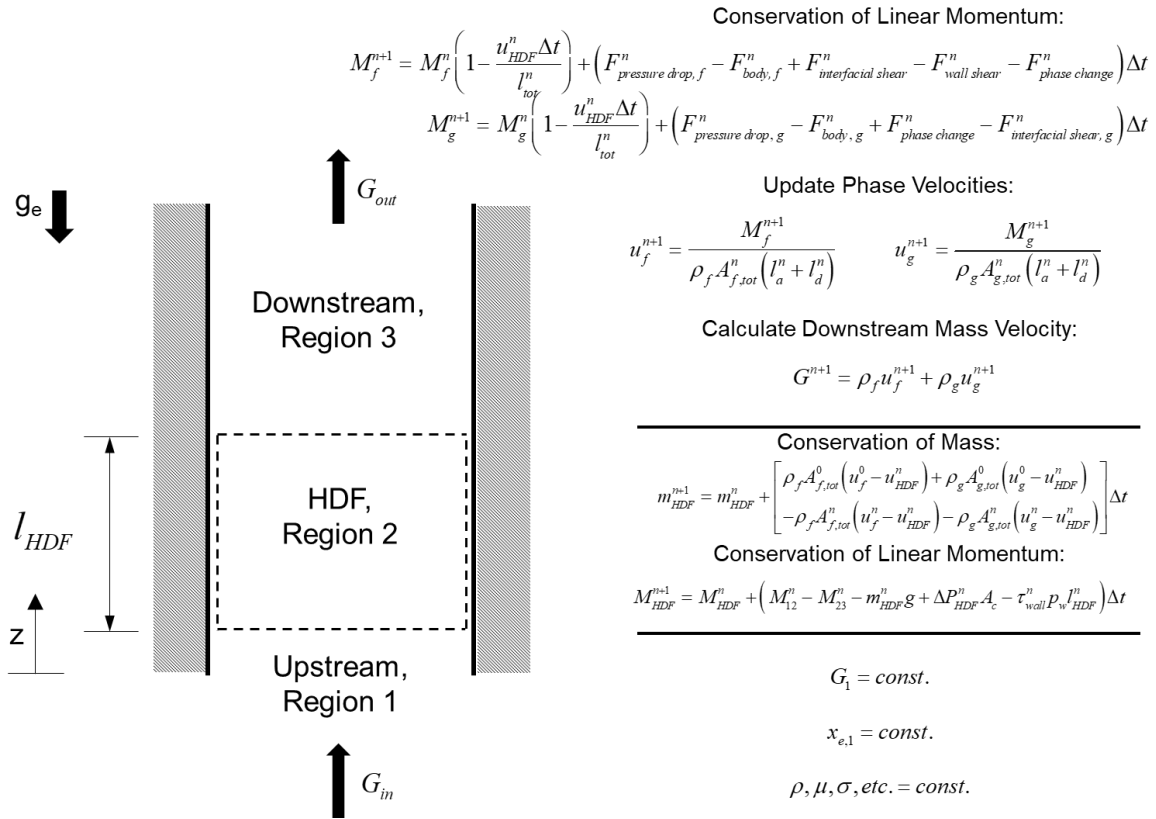


Figure 3.29: (a) Depiction of primary solution equations for each region of the DWO model, and (b) evolution of model control volumes with time.



### 3.3.1.2 Full Solution Procedure

Figure 3.30 provides a flow chart for solution of the current model, and a full list of relationships necessary for replicating the model may be found in Table 3.9 (with each row corresponding to the indicated step in Fig. 3.30). Important geometric parameters defined in Table 3.9 include length  $l$ , flow cross-sectional area  $A$  occupied by each phase, perimeter  $p$  (including diabatic, interfacial, and wetted variants), and vapor-core radius  $r_g$  (calculated assuming a circular shape). Key subscripts used when describing these and other parameters this section include  $a$  for adiabatic,  $d$  for diabatic,  $tot$  for total (indicated the parameter is evaluated along the entire length of Region 3),  $z$  to indicate streamwise position (primarily used when evaluating two-phase pressure drop by marching along the channel length),  $2\phi$  to indicate two-phase,  $w$  for wetted, and *interface* for interfacial terms. Key subscripts on force terms include *wall shear* for wall shear stress, *interfacial shear* for interfacial shear stress, *pressure drop*, for pressure drop evaluated for phase  $k$  ( $k = f$  or  $k = g$ ), *phase change* for momentum transfer due to phase change, and *body*, for body force evaluated for phase  $k$ .

Figure 3.30 indicates the model starts by collecting relevant input parameters, including test section geometry and flow-field conditions for Region 1 (namely pressure  $P_{in}$ , quality  $x_{e,in}$ , heat flux along the heated length  $q''$ , and mass velocity  $G_{in}$ ). All relevant fluid properties are calculated at the prescribed inlet pressure  $P_{in}$ , and assumed to remain constant during model advancement. This is a reasonable assumption, as analysis of experimental amplitude of DWO induced pressure fluctuations in the preceding section revealed they do not exceed 7% of time-averaged pressure in magnitude, meaning any accompanying property fluctuations will be minimal.

Model inputs for Region 1 are used to calculate initial values of all important flow-field parameters in Region 3, including adiabatic and diabatic length average qualities  $x_{ave,a}$  and  $x_{ave,d}$ , respectively, phase velocities  $u_f$  and  $u_g$ , phase flow areas  $A_f$  and  $A_g$ , phase momentums  $M_f$  and  $M_g$  and phase mass velocities  $G_f$  and  $G_g$ .

A key parameter in calculating flow-field variables is void fraction  $\alpha$ , which due to its difficulty to measure experimentally is approximated here using the Zivi void fraction correlation [165], defined as

$$\alpha_{Zivi} = \left( 1 + \left( \frac{1-x}{x} \right) \left( \frac{\rho_g}{\rho_f} \right)^{2/3} \right)^{-1}, \quad (3.19)$$

where  $x$  is flow quality evaluated over the region of interest.

Having initialized all relevant parameters in Region 3, force terms outlined in Fig. 3.28(c) may be calculated, and momentum updated for Region 3. It is important to note that the equation handling conservation of momentum for Region 3 includes a term to account for changing length of the control volume due to HDF motion along the channel.

Updated momentum values are then used to find updated phase velocities in Region 3, which in turn allow calculation of overall mass velocity in Region 3 at the current time step. This value is used along with the known, constant value of mass velocity entering the channel (Region 1) to update conservation of mass for the HDF (Region 2).

It is important to note here that conservation of momentum for the HDF is not solved (meaning it is assumed to remain at rest) until it has accumulated mass equal to 0.0005 kg (0.5 g). This is intended to avoid false prediction of extremely high accelerations in the initial time steps.

After updating mass and momentum for the HDF (Region 2), updates for velocity and stream-wise location of the HDF may also be made. As long as the HDF has not reached the end of the channel, the model continues to run by first updating important flow field parameters, advancing to the next time step, and repeating the process.

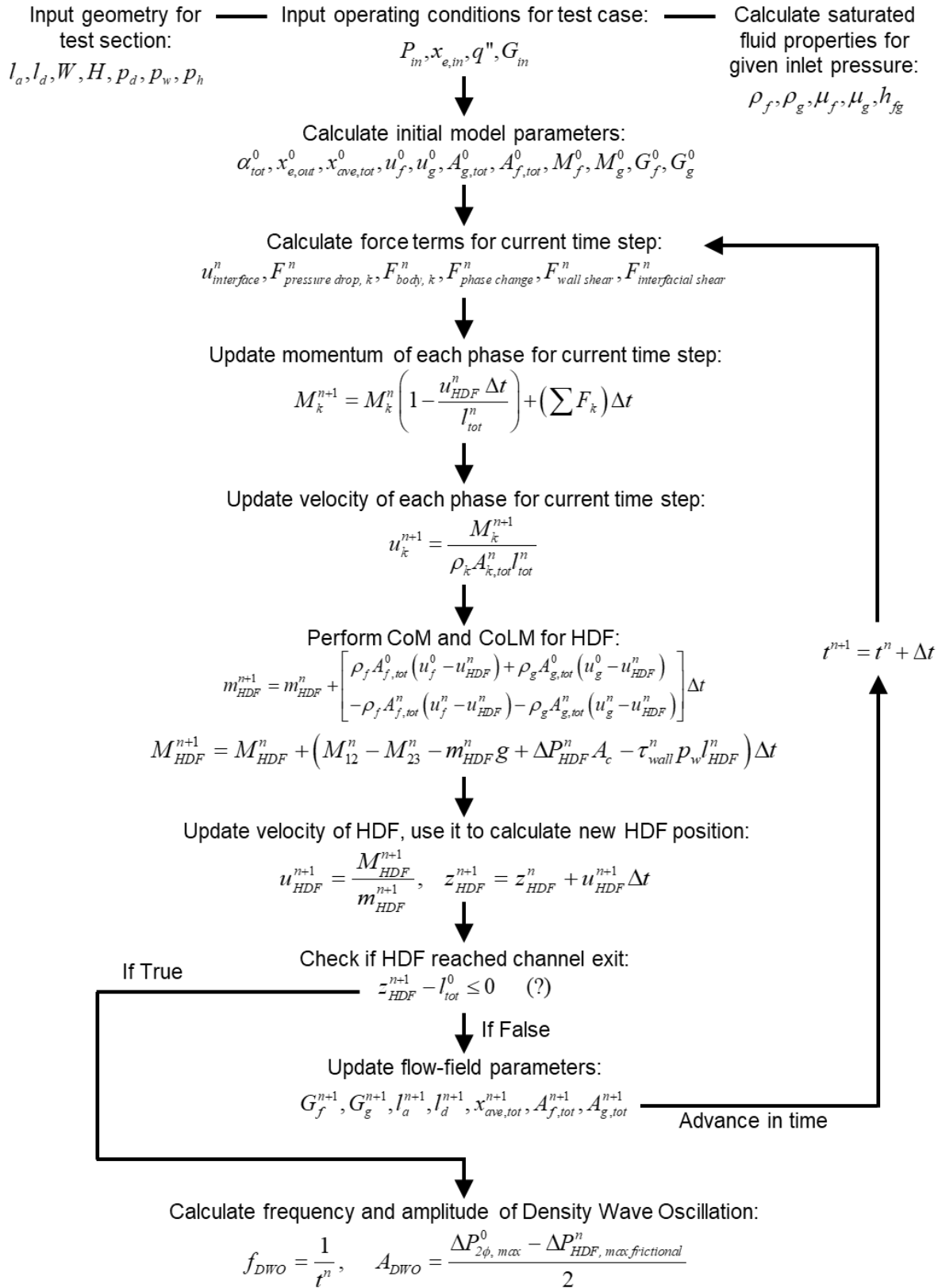


Figure 3.30: Flow chart for model solution.

Table 3.9: Model relationships associated with each respective step in the model solution procedure outlined in Fig. 3.29.

<p>Calculate initial model parameters</p>	$\alpha_{Zivi}(x_e) = \left( 1 + \left( \frac{1-x_e}{x_e} \right) \left( \frac{\rho_g}{\rho_f} \right)^{2/3} \right)^{-1}, \quad x_{e,out}^0 = x_{e,in}^0 + \frac{q^n p_H l_d}{G_{in} A_c h_{fg}}, \quad x_{ave,a}^0 = x_{e,in}^0, \quad x_{ave,d}^0 = \frac{x_{e,in}^0 + x_{e,out}^0}{2},$ $x_{ave,tot}^0 = \frac{x_{ave,a}^0 l_a^0 + x_{ave,d}^0 l_d^0}{l_a^0 + l_d^0}, \quad \alpha_{tot}^0 = \alpha_{Zivi}(x_{ave,tot}^0), \quad A_{g,tot}^0 = A_c \alpha_{tot}^0,$ $A_{f,tot}^0 = A_c - A_{g,tot}^0, \quad \alpha_{in}^0 = \alpha_{Zivi}(x_{e,in}^0), \quad l_{tot}^0 = l_a^0 + l_d^0, \quad r_g^0 = \sqrt{\frac{A_{g,tot}^0}{\pi}},$ $p_{interface,tot}^0 = 2\pi \sqrt{\frac{A_{g,tot}^0}{\pi}}, \quad u_g^0 = \frac{G_{in} x_{e,in}^0}{\rho_g \alpha_{in}^0}, \quad u_f^0 = \frac{G_{in} (1-x_{e,in}^0)}{\rho_f (1-\alpha_{in}^0)},$ $M_f^0 = \rho_f u_f^0 A_{f,tot}^0 l_{tot}^0, \quad M_g^0 = \rho_g u_g^0 A_{g,tot}^0 l_{tot}^0$
<p>Force terms for current time step</p>	$u_{interface}^n = \frac{u_f^n \rho_f + u_g^n \rho_g}{\rho_f + \rho_g}, \quad F_{pressure\ drop, k}^n = - \left( \sum_{z=0}^{l_{tot}^n} \left( \frac{dP}{dz} \right)_{2\phi, z}^n \Delta z \right) A_{k,tot}^n, \quad F_{body, k}^n = \rho_k g A_{k,tot}^n l_{tot}^n,$ $F_{phase\ change}^n = \left( \frac{q^n p_d l_d^n}{h_{fg}} \right) u_{interface}^n, \quad F_{wall\ shear}^n = \frac{\rho_f f_w^n u_f^{n2} p_w l_{tot}^n}{2},$ $F_{interfacial\ shear}^n = \frac{f_i^n \rho_g (u_g^n - u_{interface}^n)^2 p_{interface, tot}^n l_{tot}^n + (u_g^n - u_{interface}^n) \frac{q^n p_d l_d^n}{h_{fg}}}{2},$ $f_w^n = \frac{64}{Re_f^n} \text{ for } Re_f^n \leq 2300$ $\frac{1}{\sqrt{f_w^n}} = -2 \log \left( \frac{e}{3.7 D_H} + \frac{2.51}{Re_f^n \sqrt{f_w^n}} \right) \text{ for } Re_f^n > 2300$ $Re_f^n = \frac{r_f u_f^n D_H}{m_f}$ $f_i^n = \frac{16}{Re_c^n} \text{ for } Re_c^n \leq 2000$ $f_i^n = \frac{0.079}{(Re_c^n)^{0.25}} \text{ for } 2000 < Re_c^n \leq 20000$ $f_i^n = \frac{0.046}{(Re_c^n)^{0.2}} \text{ for } 20000 < Re_c^n$ $Re_c^n = \frac{\rho_g (u_g^n - u_{interface}^n) r_g^n}{\mu_g}$

Table 3.9: Continued.

<p>Force terms for current time step (continued)</p>	$\left(\frac{dP}{dz}\right)_{2\phi,z}^n = \left(\frac{dP}{dz}\right)_{A,z}^n + \left(\frac{dP}{dz}\right)_{F,z}^n + \left(\frac{dP}{dz}\right)_{G,z}^n,$ $\alpha_z = \left(1 + \frac{1-x_z}{x_z} \frac{\rho_g}{\rho_f}\right)^{-1},$ $-\left(\frac{dP}{dz}\right)_{A,z}^n = G^{n2} \frac{d}{dz} \left[ \frac{v_g x_z^2}{\alpha_z} + \frac{v_f (1-x_z)^2}{1-\alpha_z} \right],$ $-\left(\frac{dP}{dz}\right)_{G,z}^n = (\alpha_z \rho_g + (1-\alpha_z) \rho_f) g$ $-\left(\frac{dP}{dz}\right)_{F,z}^n = \left[ \frac{2f_{2\phi,z}^n v_f G^{n2}}{D_H} \right] \left( 1 + x_z \frac{v_g - v_f}{v_f} \right),$ $f_{2\phi,z}^n = \frac{16}{\text{Re}_{2\phi,z}^n}, \quad \text{Re}_{2\phi,z}^n < 2000$ $f_{2\phi,z}^n = \frac{0.079}{(\text{Re}_{2\phi,z}^n)^{0.25}}, \quad 2000 \leq \text{Re}_{2\phi,z}^n < 20000$ $f_{2\phi,z}^n = \frac{0.046}{(\text{Re}_{2\phi,z}^n)^{0.2}}, \quad 20000 \leq \text{Re}_{2\phi,z}^n$ $\text{Re}_{2\phi,z}^n = \frac{G^n D_H}{\mu_{2\phi,z}}, \quad \mu_{2\phi,z} = \frac{\mu_f}{(1-x_z) + x_z \left( \frac{v_g}{v_f} \right)^{0.5}}$
<p>Update phase momentum and velocity</p>	$M_f^{n+1} = M_f^n \left( 1 - \frac{u_{HDF}^n \Delta t}{l_{tot}^n} \right) + \left( F_{pressure\ drop, f}^n - F_{body, f}^n - F_{phase\ change}^n - F_{wall\ shear}^n + F_{interfacial\ shear}^n \right) \Delta t,$ $M_g^{n+1} = M_g^n \left( 1 - \frac{u_{HDF}^n \Delta t}{l_{tot}^n} \right) + \left( F_{pressure\ drop, g}^n - F_{body, g}^n + F_{phase\ change}^n - F_{interfacial\ shear}^n \right) \Delta t,$ $u_f^{n+1} = \frac{M_f^{n+1}}{\rho_f A_{f,tot}^n l_{tot}^n}, \quad u_g^{n+1} = \frac{M_g^{n+1}}{\rho_g A_{g,tot}^n l_{tot}^n}$

Table 3.9: Continued.

Update mass, momentum , velocity, length, and position of HDF	$m_{HDF}^{n+1} = m_{HDF}^n + \left[ \rho_f A_{f,tot}^0 (u_f^0 - u_{HDF}^n) + \rho_g A_{g,tot}^0 (u_g^0 - u_{HDF}^n) - \rho_f A_{f,tot}^n (u_f^n - u_{HDF}^n) - \rho_g A_{g,tot}^n (u_g^n - u_{HDF}^n) \right] \Delta t,$ $M_{HDF}^{n+1} = M_{HDF}^n + \left( \begin{aligned} & r_g A_{g,tot}^0 (u_g^0 - u_{HDF}^n)^2 + r_f A_{f,tot}^0 (u_f^0 - u_{HDF}^n)^2 - r_g A_{g,tot}^n (u_g^n - u_{HDF}^n)^2 \\ & - r_f A_{f,tot}^n (u_f^n - u_{HDF}^n)^2 - m_{HDF}^{n+1} g + DP_{HDF}^n A_c - \frac{3m_f u_{DWO}^n P_F l_{HDF}^n}{D_H} \end{aligned} \right) Dt,$ $DP_{HDF}^n = \frac{f_{HDF}^n (1.5G_{in})^2 l_{HDF}^n}{2r_f D_H} + r_f g l_{DWO}^n, l_{HDF}^{n+1} = \frac{m_{HDF}^{n+1}}{r_f A_c}, u_{HDF}^{n+1} = \frac{M_{HDF}^{n+1}}{m_{HDF}^{n+1}}, z_{HDF}^{n+1} = z_{HDF}^n + u_{HDF}^{n+1} Dt,$ $f_{HDF}^n = \frac{64}{Re_{HDF}^n} \text{ for } Re_{HDF}^n \leq 2300$ $\frac{1}{\sqrt{f_{HDF}^n}} = -2 \log \left( \frac{e}{3.7 D_H} + \frac{2.51}{Re_{HDF}^n \sqrt{f_{HDF}^n}} \right) \text{ for } Re_{HDF}^n > 2300$ $Re_{HDF}^n = \frac{G_{in} D_H}{m_f}$
---	---

Table 3.9 Continued.

<p>Update flow-field parameters if HDF has not reached channel exit</p>	$G^{n+1} = G_f^{n+1} + G_g^{n+1} = \frac{\rho_f u_f^{n+1} A_{f,tot}^n + \rho_g u_g^{n+1} A_{g,tot}^n}{A_c}, \quad x_{f,in}^{n+1} = \frac{r_g u_g^{n+1} A_{g,tot}^n}{G^{n+1} A_c},$ <p>if <math>z_{HDF}^{n+1} &lt; l_a^0</math>:</p> $l_a^{n+1} = l_a^0 - z_{HDF}^{n+1}, \quad x_{ave,a}^{n+1} = \frac{\frac{1}{2} x_{f,in}^{n+1} (u_g^{n+1} + u_f^{n+1}) \Delta t - \frac{1}{2} x_{ave,a}^n (u_g^{n+1} + u_f^{n+1}) \Delta t + x_{ave,a}^n l_a^{n+1}}{l_a^{n+1}}$ $x_{ave,d}^{n+1} = \frac{\frac{1}{2} x_{ave,a}^n (u_g^{n+1} + u_f^{n+1}) \Delta t - \frac{1}{2} x_{ave,d}^n (u_g^{n+1} + u_f^{n+1}) \Delta t + x_{ave,d}^n l_d^{n+1} + \frac{q'' p_d l_d^{n+1} \Delta t}{l_d^{n+1} A_{d,f}^n \rho_f h_{fg}}}{l_d^{n+1}}$ <p>if <math>z_{HDF}^{n+1} \geq l_a^0</math>:</p> $l_a^{n+1} = 0, \quad l_d^{n+1} = l_d^n - (z_{HDF}^{n+1} - l_a^0), \quad x_{ave,a}^{n+1} = 0,$ $x_{ave,d}^{n+1} = \frac{\frac{1}{2} x_{f,in}^{n+1} (u_g^{n+1} + u_f^{n+1}) \Delta t - \frac{1}{2} x_{ave,d}^n (u_g^{n+1} + u_f^{n+1}) \Delta t + x_{ave,d}^n l_d^{n+1} + \frac{q'' p_d l_d^{n+1} \Delta t}{l_d^{n+1} A_{d,f}^n \rho_f h_{fg}}}{l_d^{n+1}}$ <p><u>Then:</u></p> $x_{ave,tot}^{n+1} = \frac{x_{ave,a}^{n+1} l_a^{n+1} + x_{ave,d}^{n+1} l_d^{n+1}}{l_a^{n+1} + l_d^{n+1}}, \quad a_d^{n+1} = a_{Zivi} (x_{ave,d}^{n+1}), \quad A_{d,f}^{n+1} = (1 - a_d^{n+1}) A_c, \quad a_{tot}^{n+1} = a_{Zivi} (x_{ave,tot}^{n+1}),$ $A_{g,tot}^{n+1} = a_{tot}^{n+1} A_c, \quad A_{f,tot}^{n+1} = (1 - a_{tot}^{n+1}) A_c, \quad r_g^{n+1} = \sqrt{\frac{A_{g,tot}^{n+1}}{\rho}}, \quad p_{interface,tot}^{n+1} = 2\pi \sqrt{\frac{A_{g,tot}^{n+1}}{\pi}}$
<p>If HDF has reached channel exit, calculate associated amplitude and frequency</p>	$f_{DWO} = \frac{1}{l^n}, \quad A_{DWO} = \frac{\Delta P_{2\phi, max}^0 - \Delta P_{HDF, max frictional}^n}{2}$

A particular challenge in the development of the present model is updating flow quality in the downstream portion of the channel. Quality is used to find void fraction (via Eq. (3.19)), which is in turn used to calculate flow areas and interfacial perimeter to be used in conservation of momentum. This makes it a critical component of the model, one which must be treated with care.

Beginning with values from the previous time step, quality in Region 3 is updated through linear superposition of four key effects along each portion of the channel length (adiabatic and diabatic):

- 1) Preservation of average quality for each length from the previous time step.
- 2) Inflow of a new flow quality  $x_{f,in}^{n+1}$  to the initial length (adiabatic while  $z_{HDF}^{n+1} < l_a^0$ , diabatic after) calculated based on updated phase velocities and advected into length at the mean of the two phase velocities. Similarly, if  $z_{HDF}^{n+1} < l_a^0$ , there is inflow of adiabatic length average quality  $x_{a,ave}^n$  into the diabatic length at the same velocity.
- 3) Outflow of old average quality for each length at the same average velocity. Outflow from the adiabatic length is inflow to the diabatic length, and outflow from the diabatic length exits the channel.
- 4) Phase change along the heated length of the channel.

Altogether this provides the following relationships for updated qualities along the adiabatic and diabatic lengths, respectively, of

$$x_{ave,a}^{n+1} = \frac{\frac{1}{2} x_{f,in}^{n+1} (u_g^{n+1} + u_f^{n+1}) \Delta t - \frac{1}{2} x_{ave,a}^n (u_g^{n+1} + u_f^{n+1}) \Delta t + x_{ave,a}^n l_a^{n+1}}{l_a^{n+1}} \quad (3.20)$$

and 
$$x_{ave,d}^{n+1} = \frac{\frac{1}{2} x_{ave,a}^n (u_g^{n+1} + u_f^{n+1}) \Delta t - \frac{1}{2} x_{ave,d}^n (u_g^{n+1} + u_f^{n+1}) \Delta t + x_{ave,d}^n l_d^{n+1} + \frac{q'' P_d l_d^{n+1} \Delta t}{l_d^{n+1} A_{d,f}^n \rho_f h_{fg}}}{l_d^{n+1}}, \quad (3.21)$$

with channel average quality then calculated as

$$x_{ave,tot}^{n+1} = \frac{x_{ave,a}^{n+1} l_a^{n+1} + x_{ave,d}^{n+1} l_d^{n+1}}{l_a^{n+1} + l_d^{n+1}}. \quad (3.22)$$

After the HDF passes through the entire adiabatic length ( $z_{HDF}^{n+1} \geq l_a^0$ ), the adiabatic length quality is set to zero (as it no longer affects the solution; in reality the adiabatic length is now composed

partially by the HDF, with the remainder experiencing flow conditions identical to those in Region 1) and only the diabatic length quality is solved for.

This solution process continues until the HDF reaches the end of the channel ( $z_{HDF}^{n+1} \geq l_a^0 + l_d^0$ ), at which point frequency and amplitude of pressure fluctuations associated with its passage may be calculated.

### 3.3.1.3 Investigation of Model Sub-component Trends

Having established all key relations used in model development and outlined the solution procedure, plots of these values versus time can be analyzed to determine physical validity of the model as a whole. Towards this end, Fig. 3.31 provides plots of important model components for Region 3 versus time for the case of mass velocity  $G = 835.9 \text{ kg/m}^2\text{s}$ , inlet pressure  $P_{in} = 122 \text{ kPa}$ , inlet quality  $x_{e,in} = 0.04$ , and FBM heat flux  $q'' = 2.5 \text{ W/cm}^2$ . It should be noted here that all model predictions shown hereafter were generated using a time step of  $\Delta t = 0.0001 \text{ s}$ .

Figures 3.31(a) and 3.31(b) show plots of liquid and vapor phase momentum components versus time, along with the summation of these values (which is multiplied by  $\Delta t$  at each time step to update momentum for each phase). A key point to note is the dominance of body force over the initial  $\sim 0.05 \text{ s}$  for the liquid phase, acting to drive the summation of force terms negative (thus reducing liquid phase momentum).

For the vapor phase in Fig. 3.31(b), interfacial shear is the dominant negative term, but overall vapor phase momentum is seen to increase due to the role of two-phase pressure drop.

In both Fig. 3.31(a) and 3.31(b) momentum balance components are seen to decrease in amplitude as time increases. This is due to the motion of the HDF (Region 2) overtaking much of the channel length, causing the magnitude of force terms plotted in Figs. 3.31(a) and 3.31(b) to decrease.

Figure 3.31(c) provides a plot of momentum versus time, illustrating how inlet (Region 1) momentum, Region 3 liquid and vapor momentum, as well as total momentum in Region 3 change versus time. At the outset, momentum in Region 3 is equal to that in Region 1 and is primarily composed of liquid phase momentum. Liquid phase momentum is quickly reduced, however, (due primarily to the influence of body force seen in Fig. 3.31(a)), with total momentum in Region 3 becoming equal to that of vapor momentum around the 0.1 s mark.

Figure 3.31(d) illustrates how phase velocities in Region 3 change over the same period, with liquid velocity dropping to near-zero along with its momentum in Fig. 3.31(c), while vapor velocity decreases initially then seems to reach a steady value.

However, even though vapor velocity levels out, vapor mass velocity continues increasing with time, illustrated in Fig. 3.31(e). This is due to the increase in channel average quality with time, giving the vapor phase a significantly larger flow area compared to that of the liquid. Figure 3.31(f) shows channel average flow quality versus time, and provides an important physical validation for the model: namely, that average flow quality in the region downstream of the HDF (Region 3) becomes near-unity just prior to the passage of the HDF out of the channel (indicating dryout has occurred downstream of the HDF). This was seen in flow visualization images analyzed in Section 3.2, and that the model predicts this provides an important intermediate verification of the model's validity.

Figure 3.31(g) illustrates the changes in phase flow areas corresponding to the continuously increasing channel average quality seen in Fig. 3.31(f). Two key features of this plot are (1) that the summation of phase areas is always equal to the total cross-sectional area of the channel, shown here with a solid line, and (2) even though liquid phase momentum becomes near-zero around 0.1s (seen in Fig. 3.31(c)), there is still a small amount of liquid content in the downstream region which is slowly removed via phase change and very slow advection (evidenced by the very low value of liquid phase mass velocity in Fig. 3.31(e)).

Finally, Fig. 3.31(h) shows how both adiabatic and heated (diabatic) lengths change versus time. Initially the HDF is unmoving, and only once its minimum mass condition (described in the preceding section) is met does it depart. The change in adiabatic length within Region 3 versus time illustrates the initial acceleration of the HDF (evidenced by the non-linear change in  $l_a$  versus time), which eventually gives way to a more linear HDF velocity (seen in the lesser inflection in change of  $l_d$  versus time).

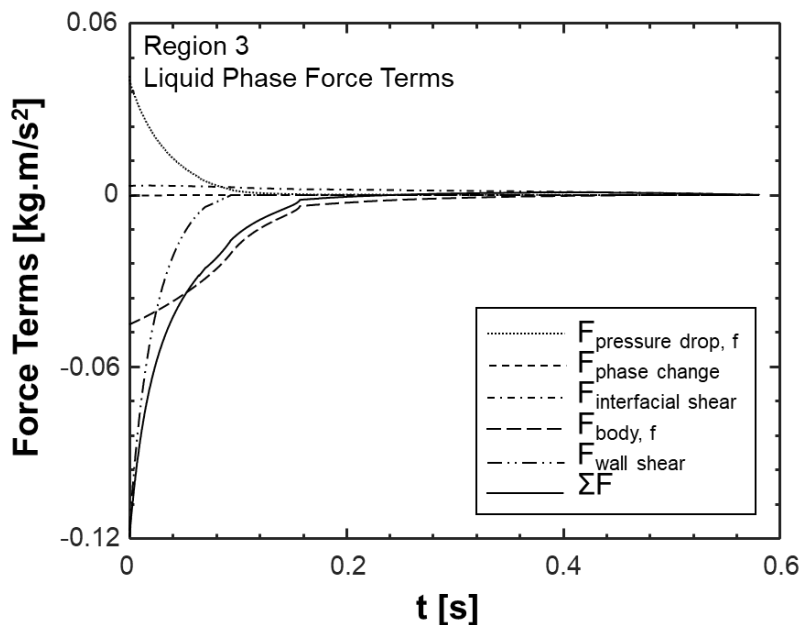


Figure 3.31: Plots of Region 3 model subcomponent predictions versus time: (a) SFM force terms for liquid phase and (b) vapor phase, (c) phase momentum terms, (d) phase velocities, (e) mass velocities, (f) average quality, (g), phase cross-sectional areas, and (h) flow lengths, all for the case with mass velocity  $G = 835.9 \text{ kg/m}^2 \text{ s}$ , inlet pressure  $P_{in} = 122 \text{ kPa}$ , inlet quality  $x_{e,in} = 0.04$ , and FBM heat flux  $q'' = 2.5 \text{ W/cm}^2$ .

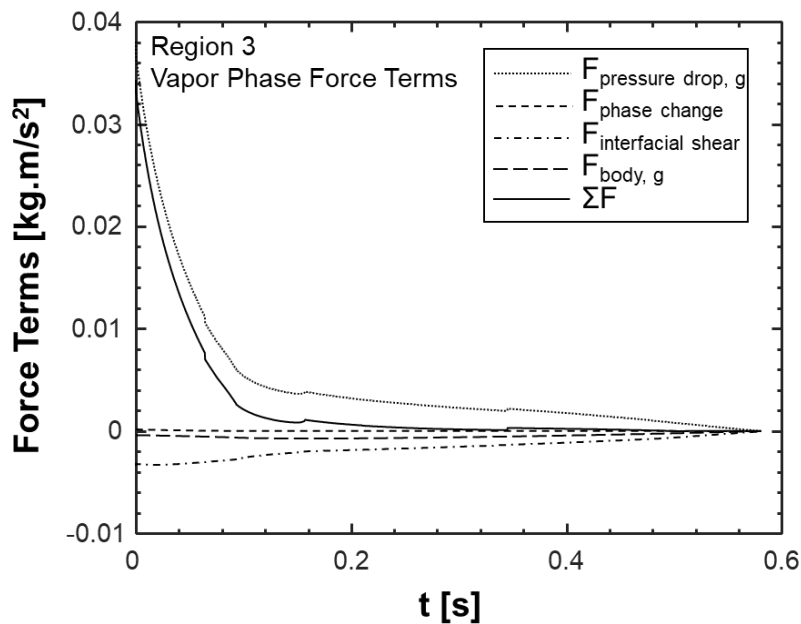


Figure 3.31 (b).

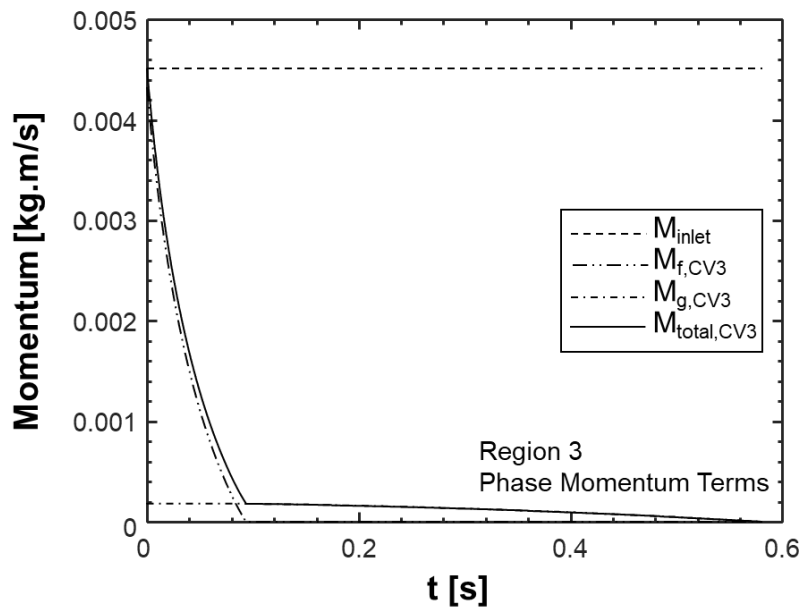


Figure 3.31 (c).

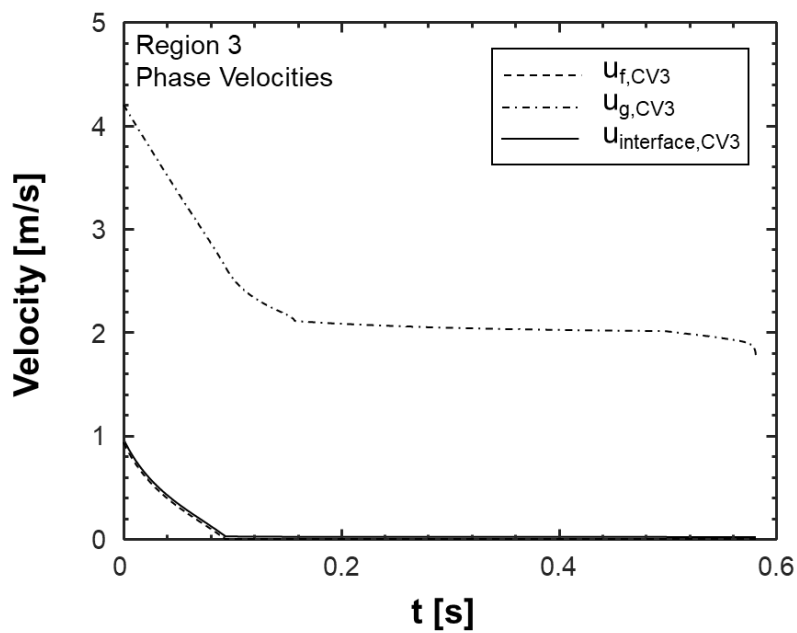


Figure 3.31 (d).

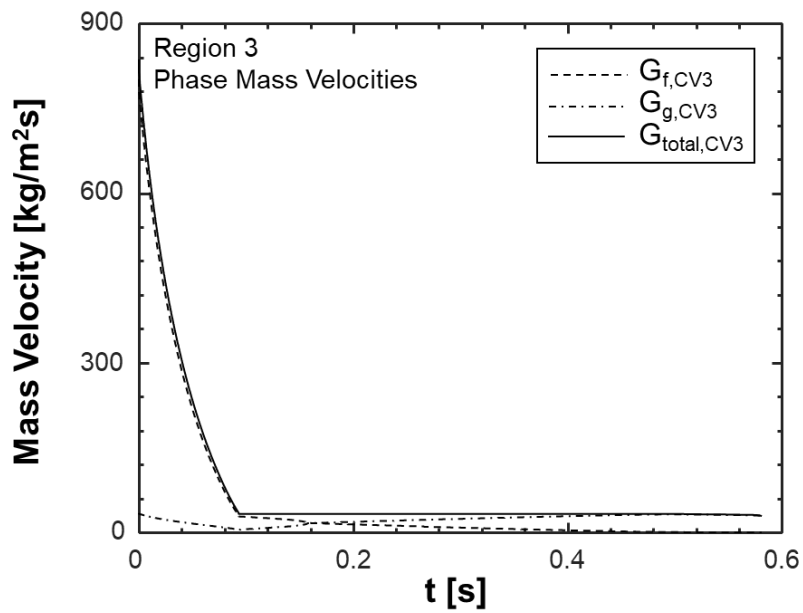


Figure 3.31 (e).

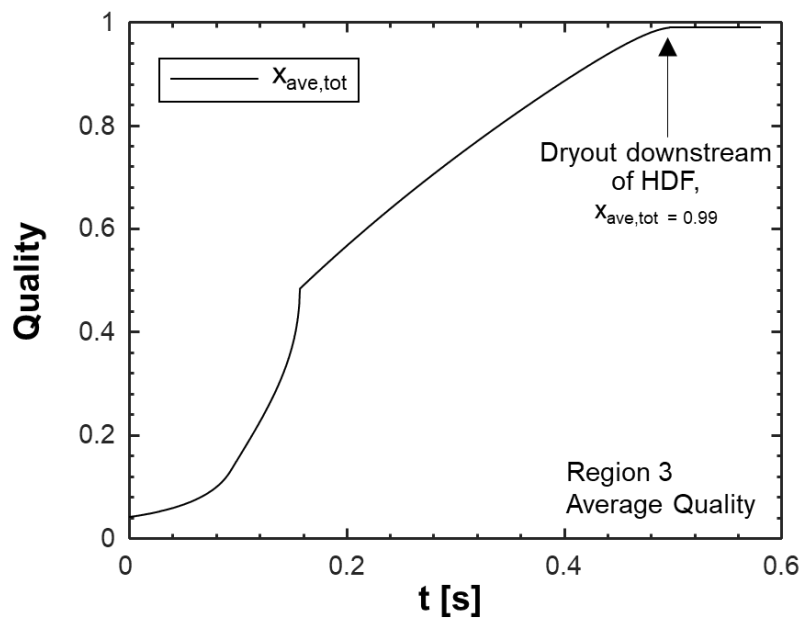


Figure 3.31 (f).

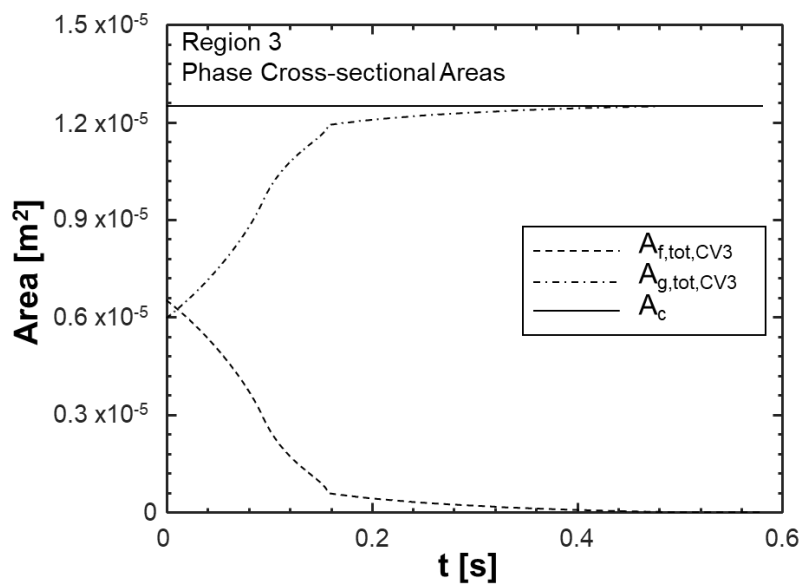


Figure 3.31 (g).

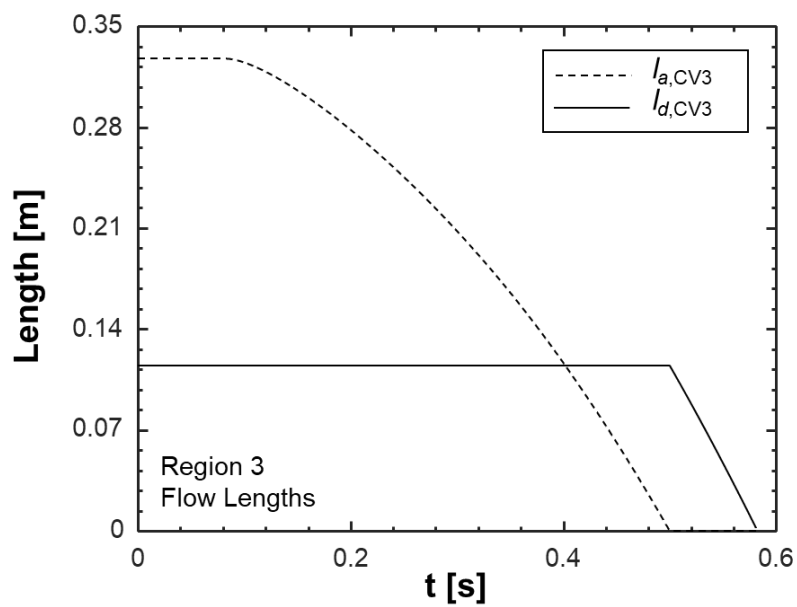


Figure 3.31 (h).

Similar to Fig. 3.31, Fig. 3.32 provides plots of important Region 2 (HDF) model sub-components for the same case as Fig. 3.31. Figure 3.32(a) begins by providing plots of relative phase velocities between the HDF (Region 2) and the upstream (Region 1) and downstream (Region 3) portions of the channel. As mentioned when discussing Fig. 3.28, these velocities are limited to values  $\geq 0$ .

Figure 3.32(a) shows how, prior to the HDF's departure, relative velocities between the Regions 1 and 2 remain constant, while those between Regions 3 and 2 decrease due to the decreasing phase velocities within Region 3 (seen in Fig. 3.31(d)). After the HDF departs, relative velocities between Regions 1 and 2 also begin to decrease due to the motion of the HDF relative to the fixed velocities in the inlet region.

Figure 3.32(b) indicates how mass accumulates within the HDF due to the differences in relative velocities between Regions 1 and 2 and Regions 2 and 3. Mass increases quickly at first due to differences in relative liquid phase velocities, but as these go to zero in Fig. 3.32(a) and only relative vapor velocities are present the rate of mass accumulation slows significantly.

Figure 3.32(c) shows the evolution of force terms acting on the HDF versus time. It is clear that pressure drop and body force dominate, with the difference in momentum fluxes between Regions 1 and 2 and Regions 2 and 3 playing a significantly role immediately after the HDF departs which decreases over time (as relative velocities decrease, shown in Fig. 3.32(a)).

Figure 3.32(d) shows the cumulative effect of these components in the form of a plot for the HDF's momentum versus time, which is used along with the mass shown in Fig. 3.32(b) to calculate the HDF's velocity, shown in Fig. 3.32(e).

Finally, Fig. 3.32(f) illustrates how the position of the HDF approaches the end of the channel, while the length of the HDF is simultaneously changing. It is clear that, for the current case, the maximum length of the HDF is  $\sim 0.08$  m, which seems to be a physical value when comparing with the size of HDFs seen in prior flow visualization images.

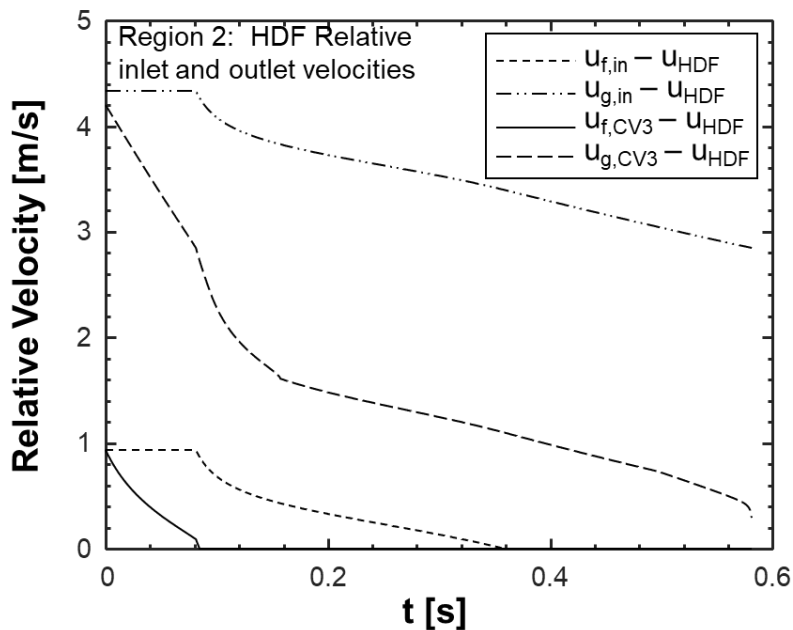


Figure 3.32: Plots of Region 2 (HDF) model subcomponents predictions versus time: (a) relative velocities entering and exiting HDF, (b) mass accumulation within HDF, (c) HDF momentum balance components, (d) HDF momentum, (e) HDF velocity, and (f) HDF length and position, all for the case of mass velocity  $G = 835.9 \text{ kg/m}^2\text{s}$ , inlet pressure  $P_{in} = 122 \text{ kPa}$ , inlet quality  $x_{e,in} = 0.04$ , and FBM heat flux  $q'' = 2.5 \text{ W/cm}^2$ :

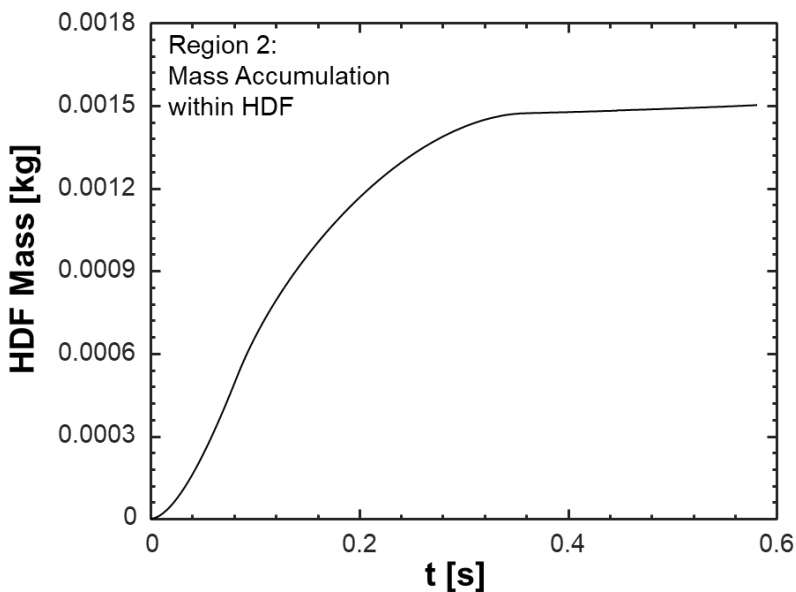


Figure 3.32 (b).

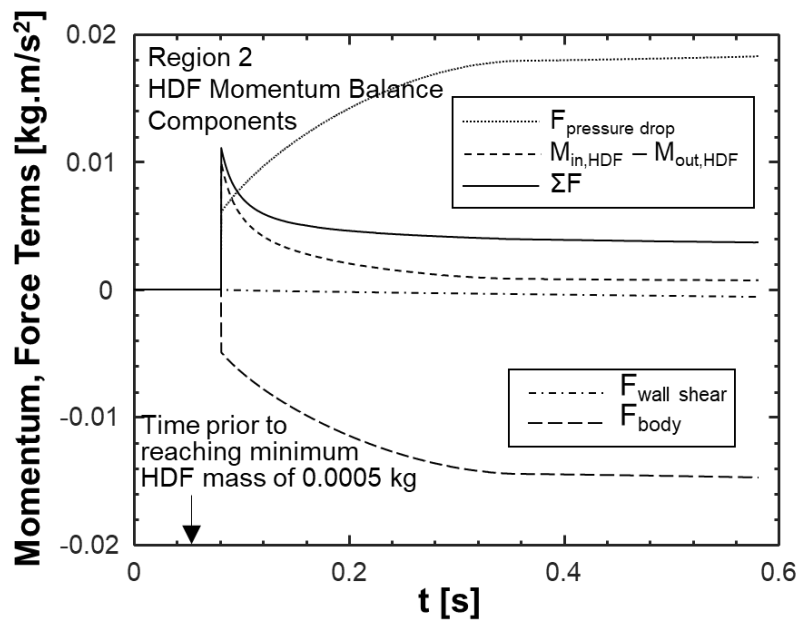


Figure 3.32 (c).

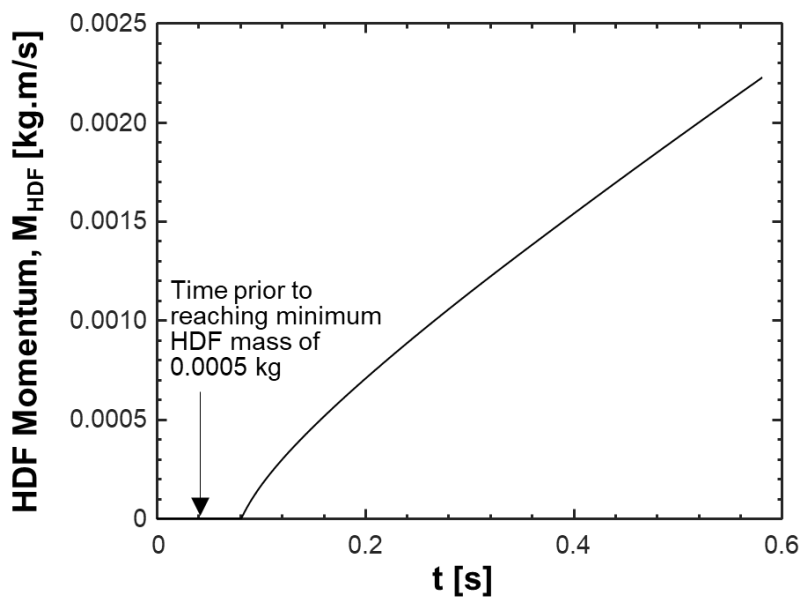


Figure 3.32 (d).

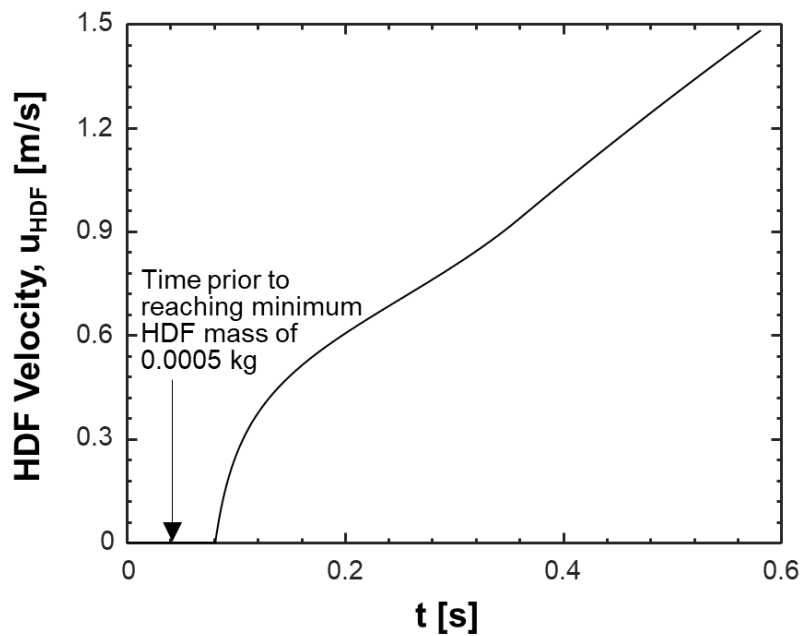


Figure 3.32 (e).

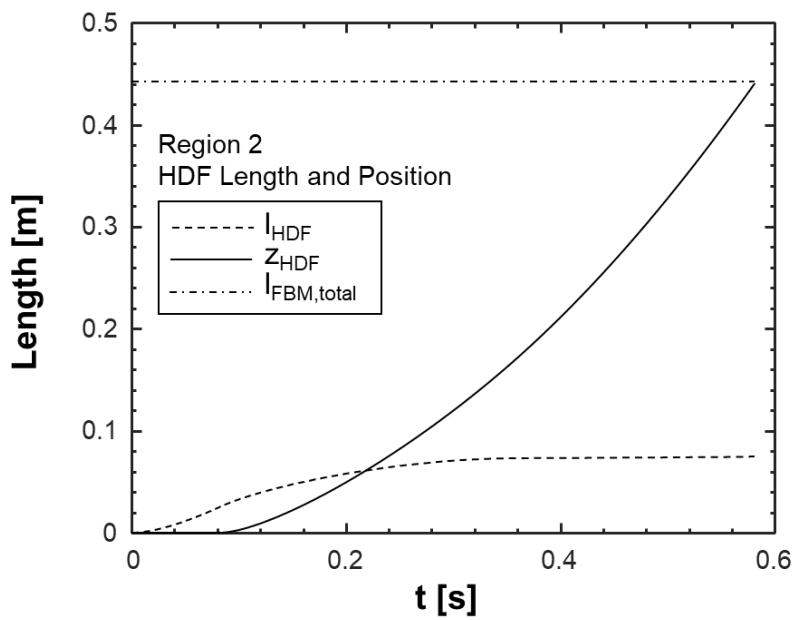


Figure 3.32 (f).

To reinforce this idea, Fig. 3.33 provides flow visualization images covering the 0.1146 m heated length of FBM for three different sets of operating conditions, allowing for estimation of the length of the HDF in each case.

The first case in Fig. 3.33 shows three images for the case of  $G = 406.6 \text{ kg/m}^2\text{s}$ , inlet pressure  $P_{in} = 117.1 \text{ kPa}$ , inlet quality  $x_{e,in} = 0.07$ , and FBM heat flux  $q'' = 7.3 \text{ W/cm}^2$ . The first image indicates the presence of dryout in the downstream portion of the FBM heated length just prior to the arrival of the HDF (indicated with a white arrow), the second shows the body of the HDF occupying the majority of the heated length, and the third image shows a return to annular flow in the wake of the HDF (all of which serve to further validate assumptions made while modeling the behavior of Regions 1, 2, and 3).

As the height of the FBM is known to be 5 mm, it was possible to import the image into the 2-D drafting software Draftsight, use channel height as a reference dimension, and determine the length of the HDF. It should be noted that the exact beginning and end of the HDF are not clearly defined in images, so the lengths measured using this technique should not be considered as exact.

The second and third cases in Fig. 3.33 provide similar plots for cases of  $G = 1177.8 \text{ kg/m}^2\text{s}$ , inlet pressure  $P_{in} = 133.6 \text{ kPa}$ , inlet quality  $x_{e,in} = 0.05$ , and FBM heat flux  $q'' = 7.3 \text{ W/cm}^2$ , and  $G = 1978.9 \text{ kg/m}^2\text{s}$ , inlet pressure  $P_{in} = 175.8 \text{ kPa}$ , inlet quality  $x_{e,in} = 0.00$ , and FBM heat flux  $q'' = 7.3 \text{ W/cm}^2$ , respectively. Two features of these subfigures are of significance to the ongoing analysis. First, the HDFs identified no longer appear to be composed of continuous liquid phase as in the first case, but rather liquid distributed within vapor to the point it is unclear which should be considered the continuous phase. The second feature is the significant length of the HDF in the third case, indicating it is longer than the entire 0.1146-m heated length of FBM.

It is important to recall the definition of  $l_{HDF}$  in the model as being mass of the HDF divided by the density of liquid times the cross-sectional area of the channel, thus implying the assumption that the HDF is composed entirely of liquid. Flow visualization images reveal that this is not the case, especially at higher velocities, where it appears up to ~50% of the HDF (by volume) can be composed of vapor phase. Thus, although the length of the HDF may increase, it is likely the mass stored within the HDF decreases as mass velocity is increased, matching the trend predicted by the model as discussed later.

Having fully outlined model construction, provided all relevant model relations and solution technique, as well as investigated sub-component trends to provide important intermediate validation of model physics, it is now possible to discuss model results for prediction of frequency and amplitude of DWO induced pressure oscillations.

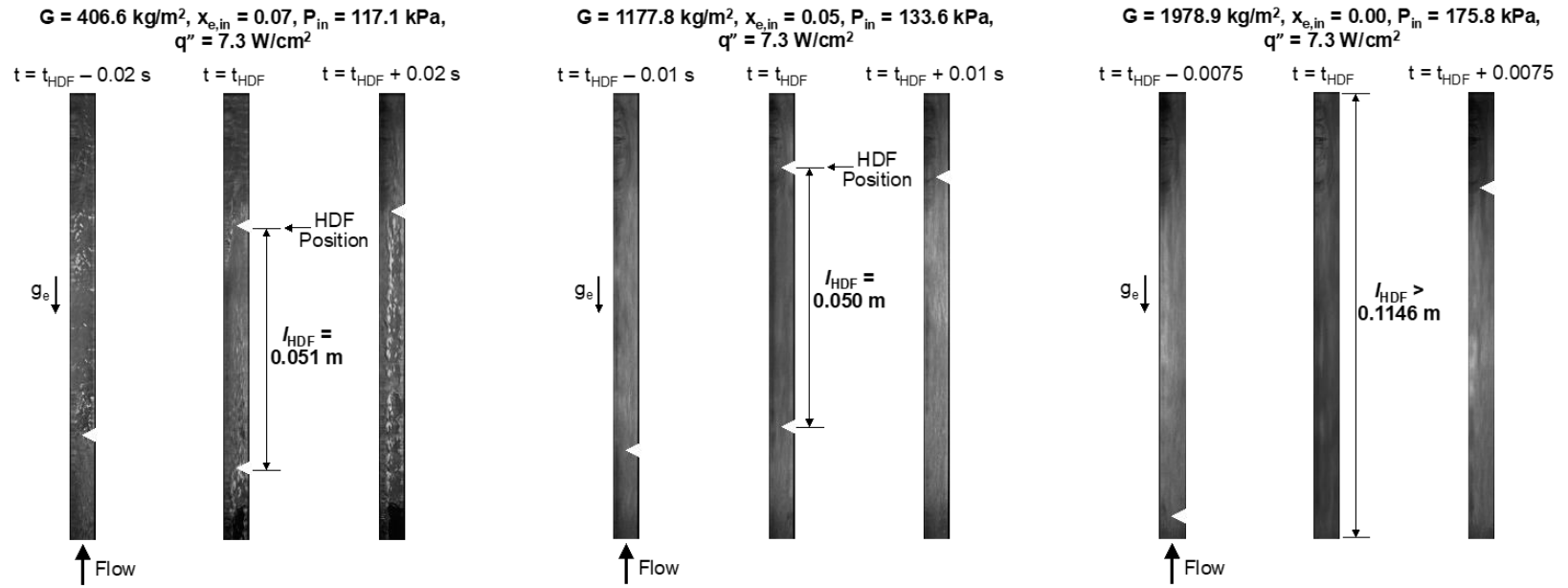


Figure 3.33: Measurements of HDF length for three different sets of operating conditions.

### 3.3.2 DWO Model Evaluation

Prior to comparing model predictions with associated experimental results, it was necessary to first determine exact experimental values for frequency and amplitude of DWO induced pressure oscillations. This was a major focus of the preceding section (Section 3.2), which should be consulted if any questions on methodology arise.

#### 3.3.2.1 Parametric Trends of Model Predictions

Prior to evaluating the entire 236 point database to determine overall performance statistics for the model, response to changes in key operating conditions (such as mass velocity, inlet quality, and heat flux) were first assessed to determine physical validity of model parametric trends. Experimental results shown here were all gathered in year 1.

Figure 3.34 provides plots of both amplitude and frequency versus changes in mass velocity (Figs. 3.34(a) and 3.34(b)), inlet quality (Figs. 3.34(c) and 3.34(d)), and heat flux (Figs. 3.34(e) and 3.34(f)). Model simulations run to create these plots involved holding all inputs other than the parameter of interest constant. Experimental data points were selected which mirrored the model conditions as closely as possible, although it was not possible to hold all experimental parameters other than the one of interest exactly constant.

Figure 3.34(a) indicates the model predicts a linear increase in frequency of oscillation as mass velocity increases, a trend that is largely mirrored by the experimental data points. A slight difference in trend is present for three highest mass velocity data points, deviating slightly from the linear relationship seen prior to that point, but this is likely attributable to the significant increase in operating pressure for these points, along with changes in inlet quality (which will be seen to have an impact on frequency of oscillation in Fig. 3.34(c)).

Figure 3.34(b) illustrates the model is able to very accurately capture the trend of exponentially increasing amplitude of DWO induced pressure oscillations as mass velocity is increased. Experimental and analytic values exhibit a nearly exact match in trend, indicating the dependence of amplitude on mass velocity is being captured adequately by the current model.

Figure 3.34(c) demonstrates how values of frequency change for changes in inlet quality to the test section (quality in Region 1 of the model). As inlet quality initially increases from a near-zero value frequency of oscillation also increases, until a peak value is reached near the  $x_{e,in} = 0.45$  point, past which frequency is seen to decrease. This trend can be explained in terms

of Region 1 phase velocities: for a constant mass flow rate in Region 1, as inlet quality is increased from zero both vapor and liquid phase velocities are increased to provide the same mass flow rate. This causes larger momentum flux differences across the HDF as dryout begins to occur in Region 3, leading to higher acceleration values for the HDF. However, as quality continues to increase, decreasing liquid content within the channel causes formation of the HDF to take longer, thus decreasing the frequency of oscillation despite increased HDF velocity.

Figure 3.34(d) demonstrates a slight decline in amplitude of induced pressure fluctuations as inlet quality is increased prior to a near-linear increase. The experimental data mirrors this closely, with the exception of the final point, which shows significant deviation from the trend. Similar to the discussion accompanying Fig. 3.34(a), this is likely attributable to changes in pressure and/or mass velocity present in the experimental data not recreated in the model predictions.

Figure 3.34(e) presents trends for frequency of oscillation versus heat flux applied to the heated length of FBM. The model predicts a neutral relationship between frequency and heat flux, which is largely identical to that of experimental results. Experimental results do indicate some fluctuations in frequency values, but again, these are likely attributable to small changes in other operating conditions indicated by the insets.

Finally, Fig. 3.34(f) provides results for amplitude versus heat flux indicating a linear increase in amplitude of oscillation is expected for increases in heat flux. The experimental data matches well with the predicted values, indicating the effect of heat flux is well captured by the model.

Overall, Fig. 3.34 verifies that model trends for changes in mass velocity, inlet quality, and heat flux are physical in nature and match well with experimental results. This serves to further signify the model is capable of capturing the key physical processes governing the manifestation of DWOs in vertical upflow with finite inlet quality.

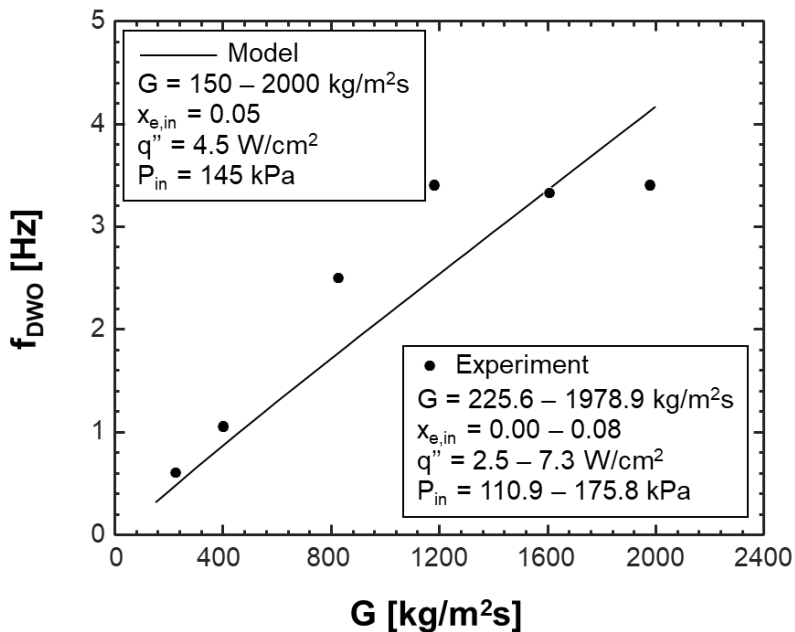


Figure 3.34: Comparison of parametric trends for model predictions and experimental results: (a) DWO frequency versus mass velocity, (b) DWO amplitude versus mass velocity, (c) frequency versus inlet quality, (d) amplitude versus inlet quality, (e) frequency versus heat flux, and (f) amplitude versus heat flux.

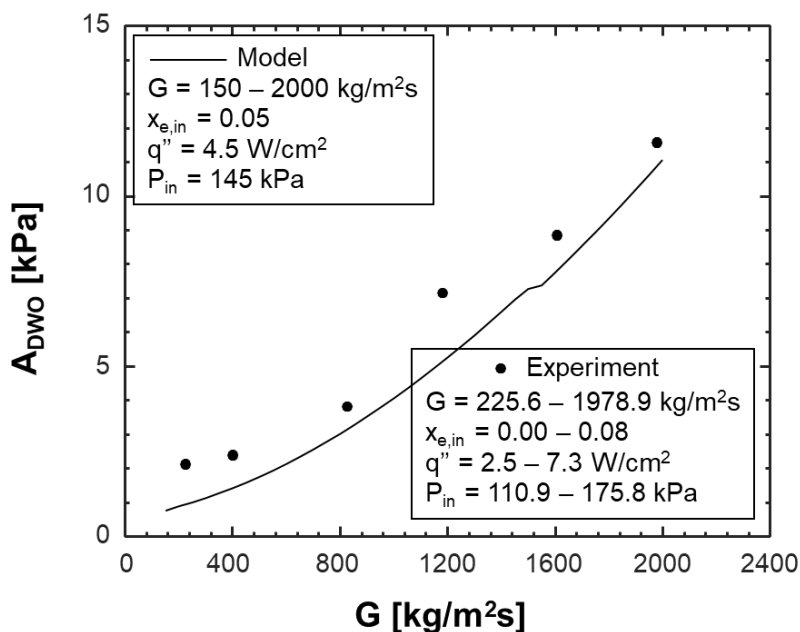


Figure 3.34 (b).

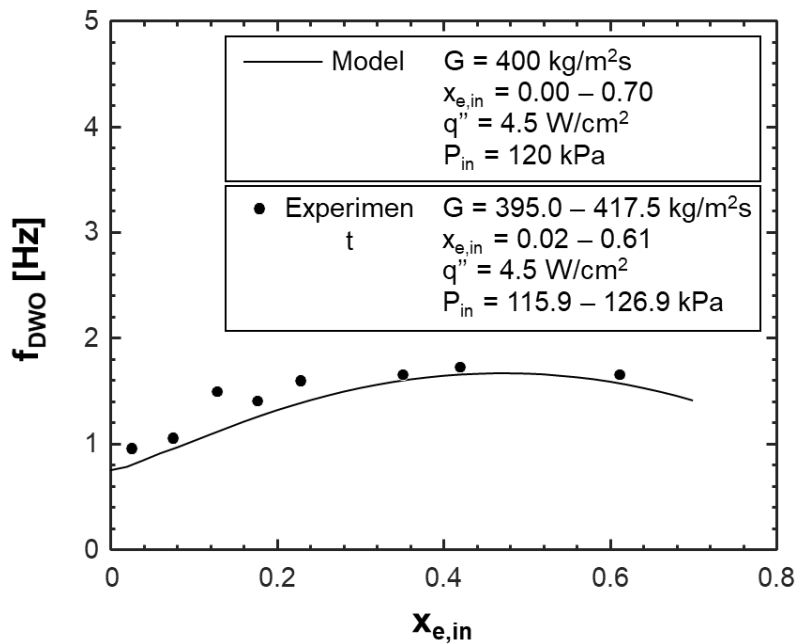


Figure 3.34 (c).

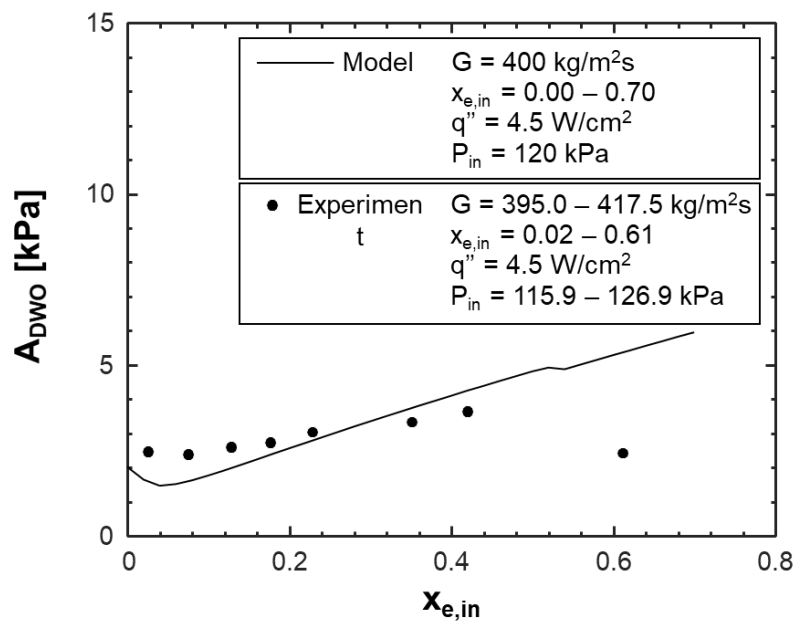


Figure 3.34 (d).

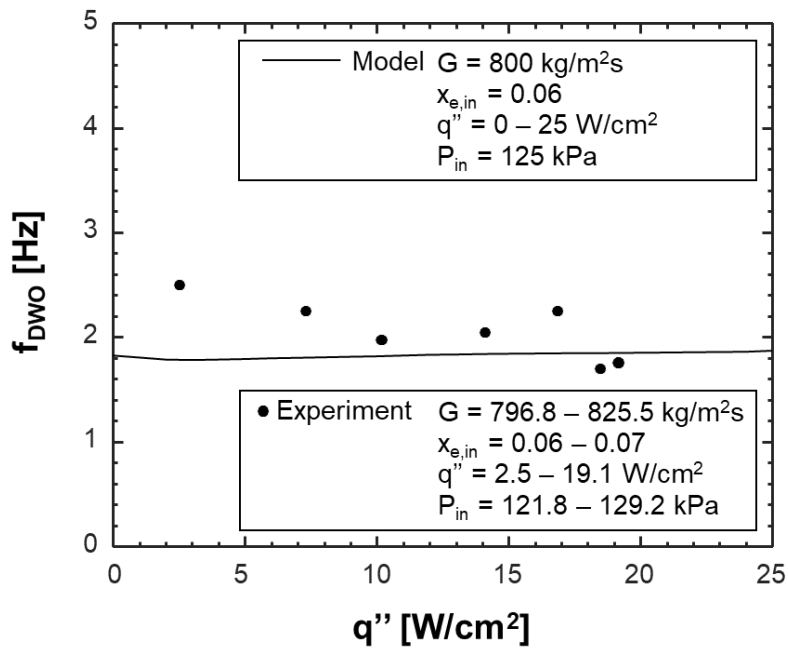


Figure 3.34 (e).

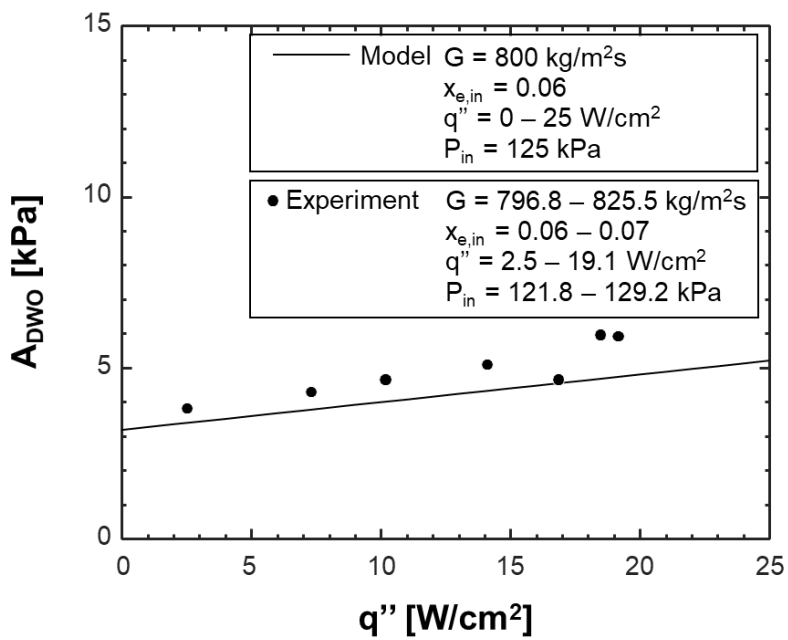


Figure 3.34 (f).

### 3.3.2.2 Model Evaluation using Experimental Database

As discussed in Section 2, a database of 236 operating conditions for which DWO induced behavior was observed in vertical upflow was constructed, spanning two separate years of testing. Experimental trends encountered while analyzing this database were discussed extensively in Section 3.2, and in the present study operating conditions for all 236 points were used to generate model predictions for frequency and amplitude of DWO induced pressure oscillations which were then compared with experimentally measured values to determine the overall predictive capabilities of the model.

Figure 3.35 provides plots of predicted frequency versus experimental frequency of DWO induced pressure oscillations for identical sets of operating conditions. The database was subdivided into low and high mass velocity cases (Figs. 3.35(a) and 3.35(b)), low and high inlet quality cases (Figs. 3.35(c) and 3.35(d)), and low and high heat flux cases (Figs. 3.35(e) and 3.35(f)) to determine how the model handles different ranges of operating conditions. Additionally, Fig. 3.35(g) provides overall results for the entire range of operating conditions present in the database.

Key statistics presented in these plots are Mean Absolute Error (MAE), defined as

$$MAE = \frac{1}{N} \sum \frac{|f_{DWO,pred} - f_{DWO,exp}|}{f_{DWO,exp}} \times 100\%, \quad (3.23)$$

where  $N$  is the total number of samples, and  $f_{DWO,pred}$  and  $f_{DWO,exp}$  refer to model-predicted and experimental values of frequency, respectively. Additionally, parameters  $q$  and  $z$  refer to the number of predictions falling within 30% and 50% of the experimental value, respectively.

Figures 3.35(a) and 3.35(b) illustrate the model's ability to accurately predict frequency of oscillation for both low and high mass velocity cases, although with slightly ( $\sim 7.9\%$ ) higher accuracy for high flow rate cases. In general, the highest variability in prediction accuracy is seen for low frequency predictions (corresponding primarily to the lowest flow rate cases). As discussed in Section 3.2, experimental detection of peak frequency of oscillation is most difficult for low mass velocity cases due to lower amplitude peaks on frequency versus amplitude plots (leading to a higher 'signal-to-noise' ratio, meaning DWO induced oscillations are harder to isolate from other fluctuations), meaning some error associated with prediction of frequency for low mass velocity cases may be attributable more to measurement limitations in those cases rather than model validity.

Figures 3.35(c) and 3.35(d) provide similar plots for low and high inlet quality cases, respectively. Results indicate slightly ( $\sim 9.6\%$ ) better predictive accuracy is possible for lower values of flow quality, but it is worth noting that high quality cases were only possible for low mass velocities due to operating pressure limitations [53,54], meaning the degradation in predictive accuracy for high qualities cannot be solely attributed to the model's ability to account for changes in inlet quality.

Figures 3.35(e) and 3.35(f) provides plots for low and high heat fluxes, respectively, which indicate little change in predictive accuracy for changes in heat flux.

Overall, Fig. 3.35(g) demonstrates that, for a wide range of operating conditions including tests conducted using two separate experimental facilities (although maintaining the same test module), an overall MAE of 29.6% was achieved when comparing model predictions to experimental results. Further, values of  $q = 71.6\%$  and  $z = 85.2\%$  indicate the model does an excellent job of capturing overall trends for the entire range of operating conditions present in the current dataset.

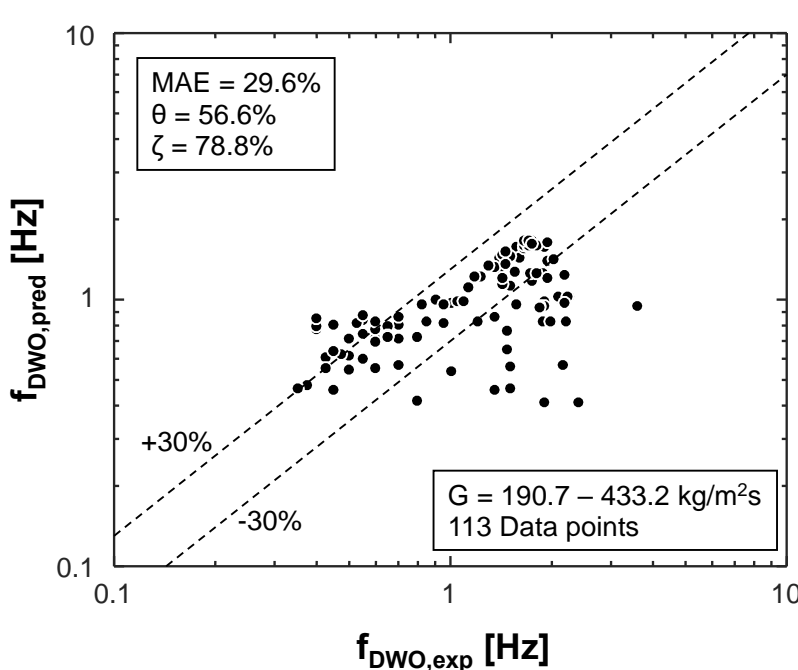


Figure 3.35: Plots of DWO frequency predicted by the model versus experimentally determined values for (a) low mass flux, (b) high mass flux, (c) low inlet quality, (d) high inlet quality, (e) low heat flux, (f) high heat flux, and (g) overall range of parameters.

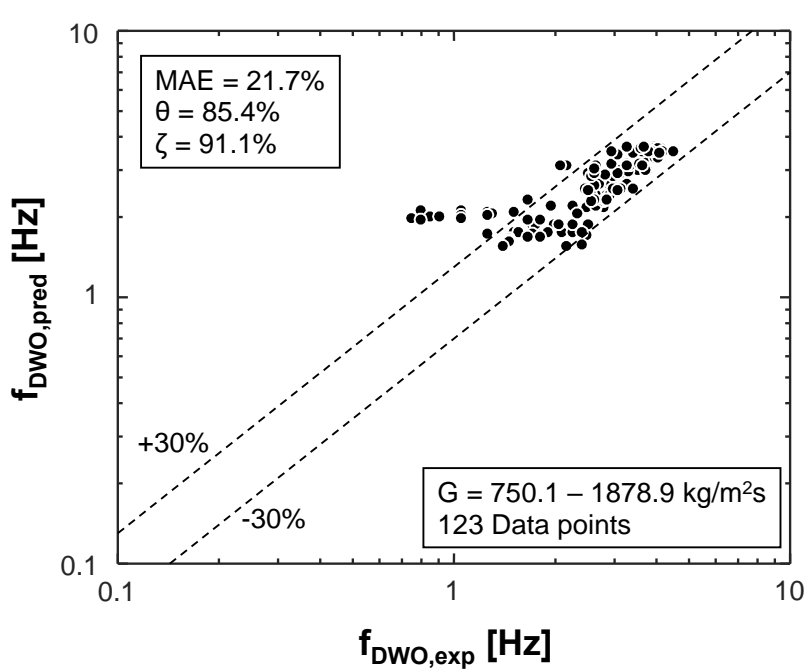


Figure 3.35 (b).

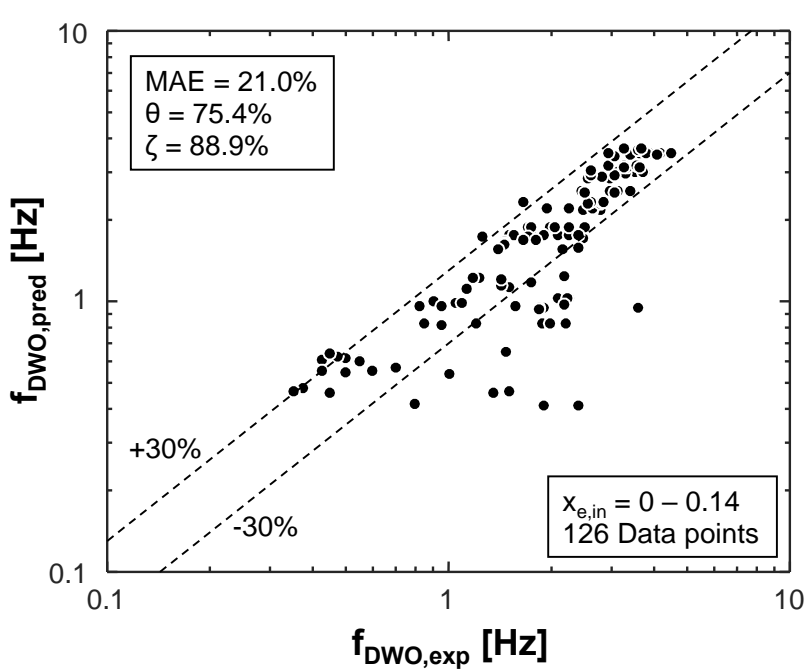


Figure 3.35 (c).

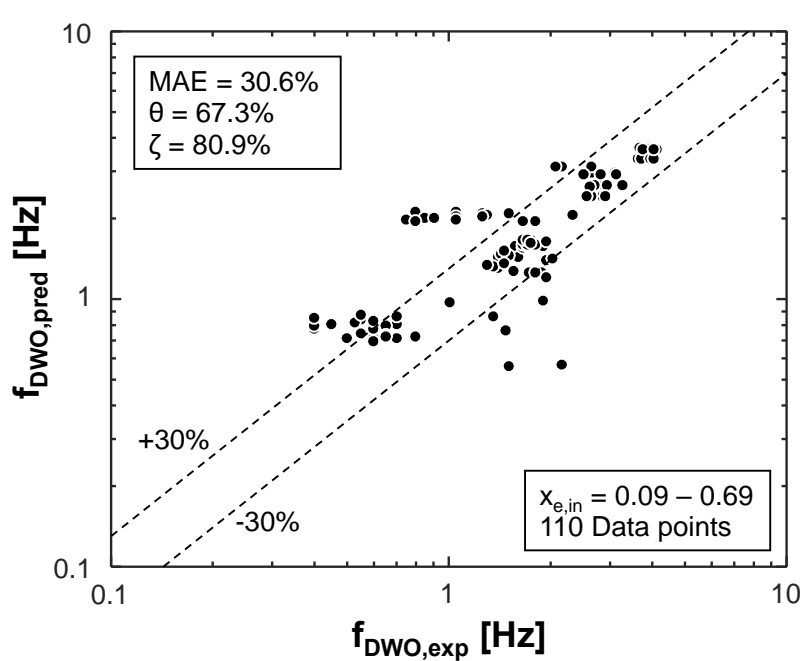


Figure 3.35 (d).

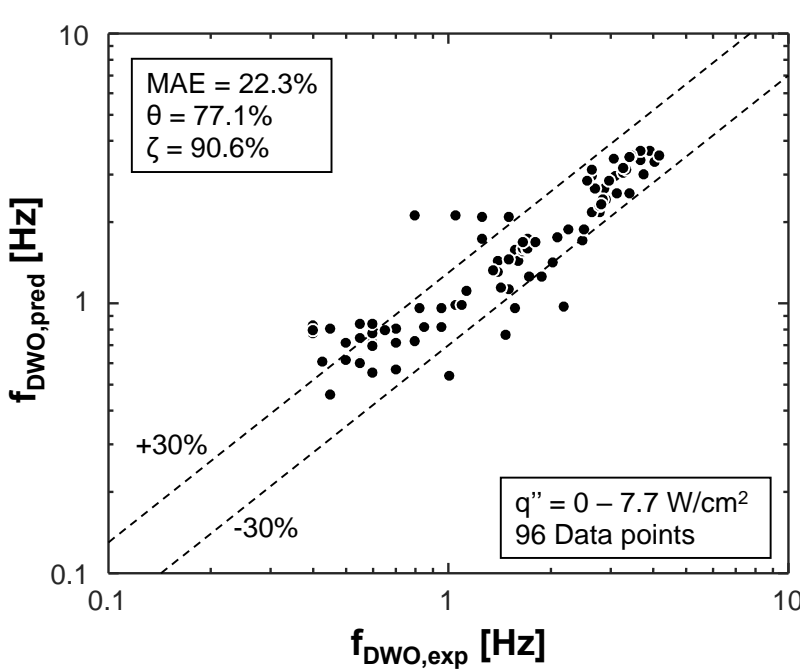


Figure 3.35 (e).

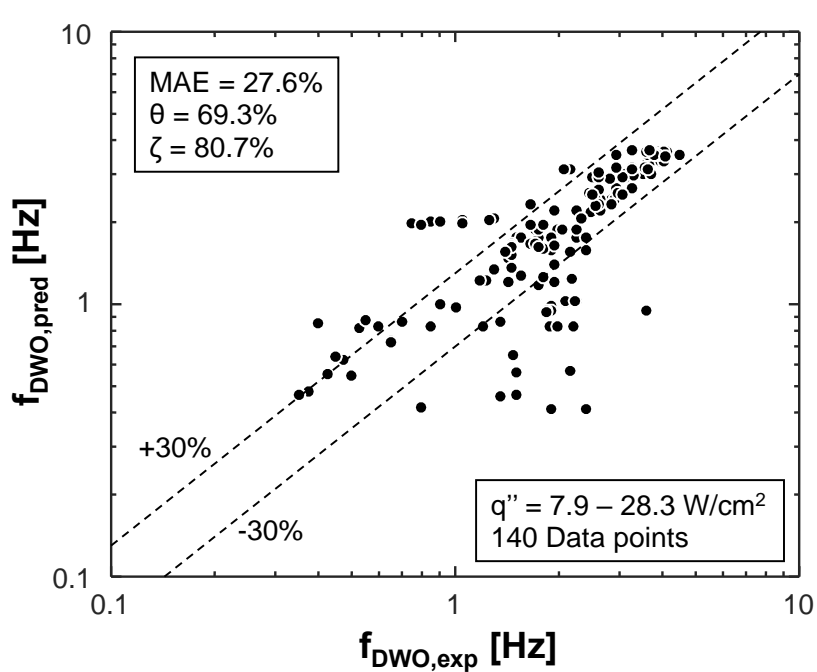


Figure 3.35 (f).

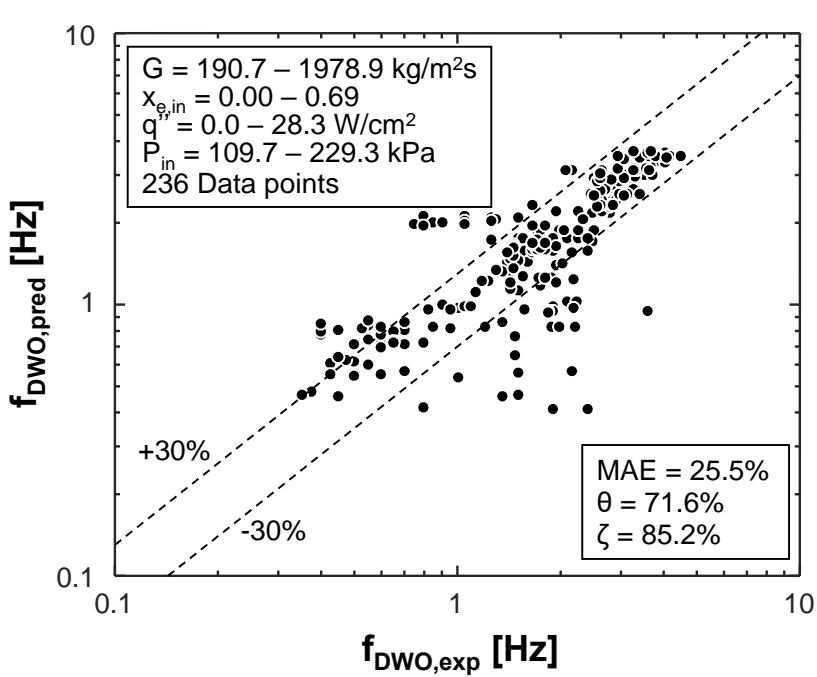


Figure 3.35 (g).

Similarly, Fig. 3.36 provides plots of predicted versus experimental amplitude of DWO induced pressure oscillations. Values of MAE are also presented (calculated by substituting amplitudes for frequencies in Eq. (3.23)), along with values of  $q$  and  $z$ .

Figures 3.36(a) and 3.36(b) show results for amplitude prediction corresponding to low and high mass velocities, respectively, which indicate the model offers significantly more accurate predictions for higher mass velocities. The primary source of inaccuracy for these two subfigures is found for low mass velocities, where the model significantly underpredicts amplitude of DWO induced pressure oscillations. This is likely due to the influence of virtual mass force and other effects not captured by the model which play a more significant role on HDF motion at lower mass velocities. These limitations will be discussed further in a subsequent section.

Figures 3.36(c) and 3.36(d) demonstrate nearly identical predictive accuracy is achieved for both high and low ranges of inlet qualities. Similarly, Figs. 3.36(e) and 3.36(f) illustrate near-identical MAE values for both low and high ranges of mass flux.

Overall, Fig. 3.36(g) illustrates the model provides an overall MAE of 31.7% on predictions of amplitude of DWO induced pressure oscillations for the current database. Additionally, similar to the conclusion drawn when analyzing Fig. 3.35 (g),  $q = 50.8\%$  and  $z = 83.9\%$  indicate the model does an excellent job of matching general experimental trends present within the database.

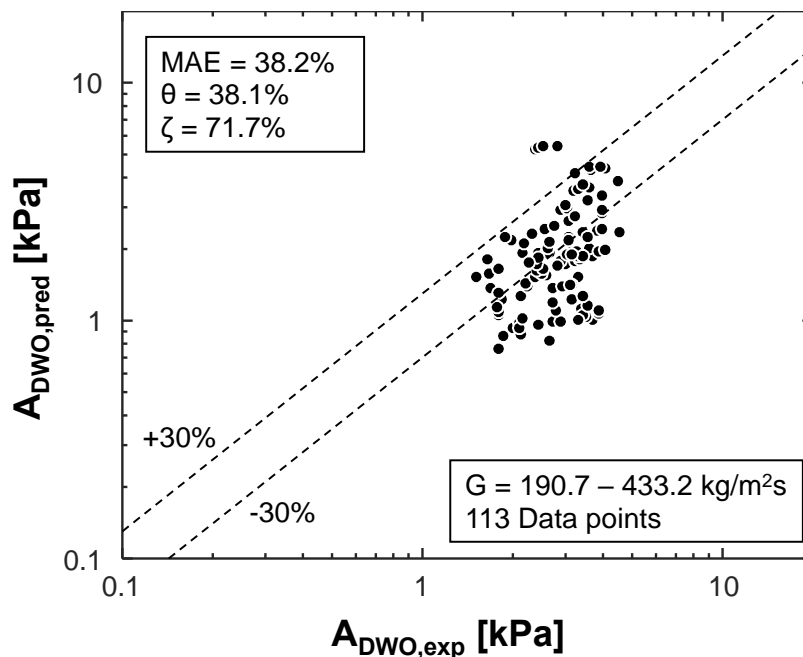


Figure 3.36: Plots of DWO amplitude predicted by the model versus experimentally determined values for (a) low mass flux, (b) high mass flux, (c) low inlet quality, (d) high inlet quality, (e) low heat flux, (f) high heat flux, and (g) overall range of parameters.

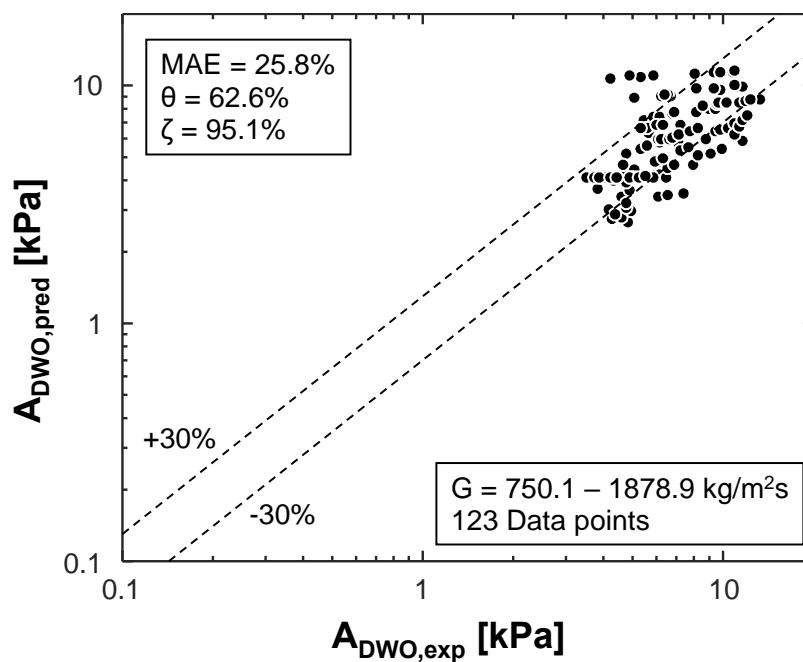


Figure 3.36 (b).

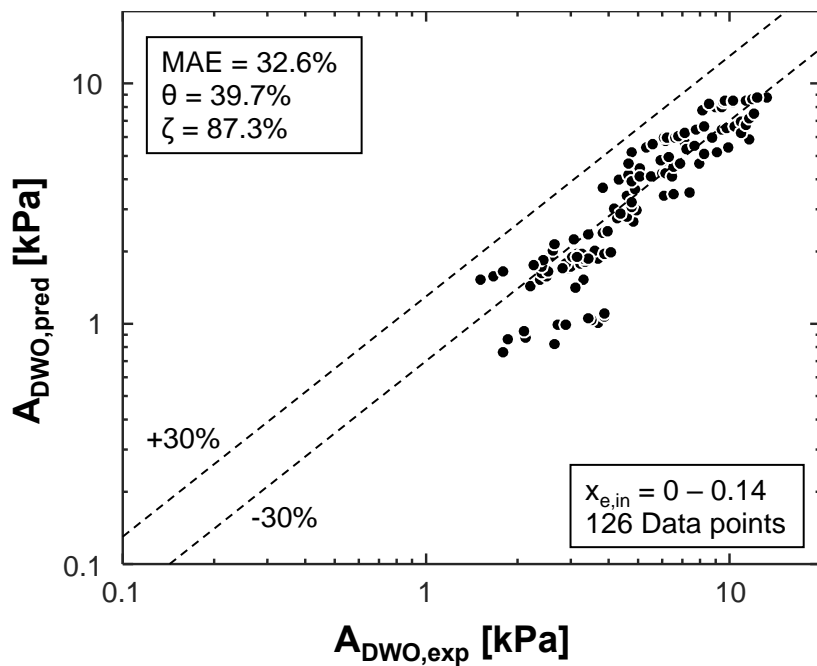


Figure 3.36 (c).

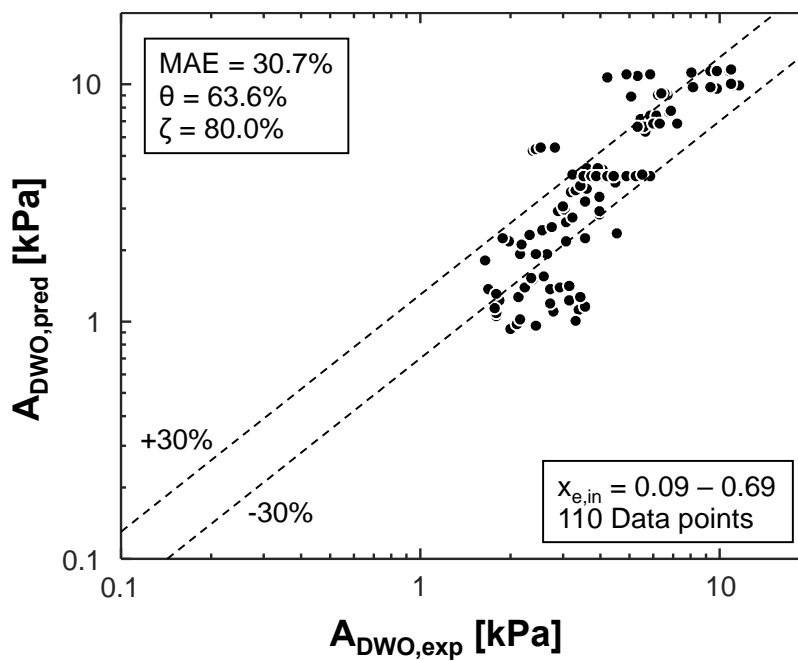


Figure 3.36 (d).

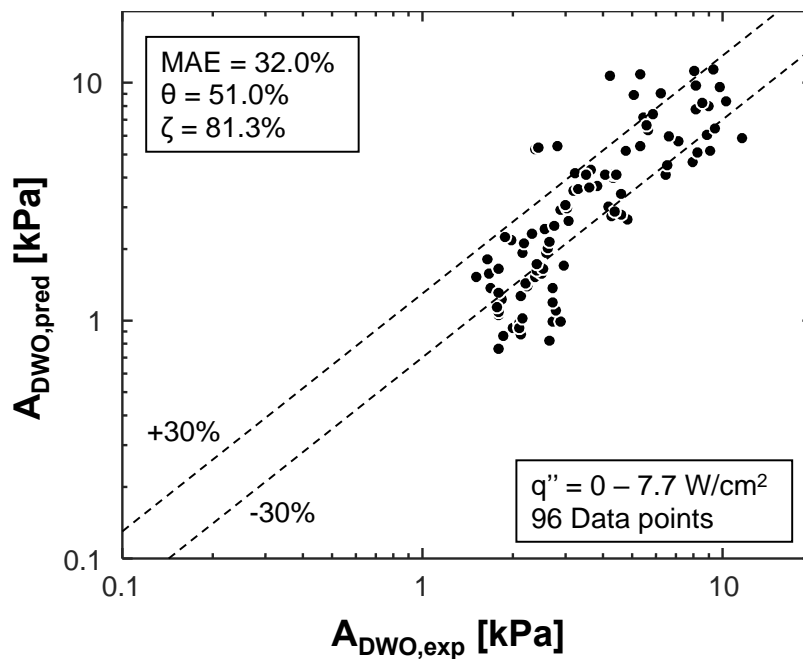


Figure 3.36 (e).

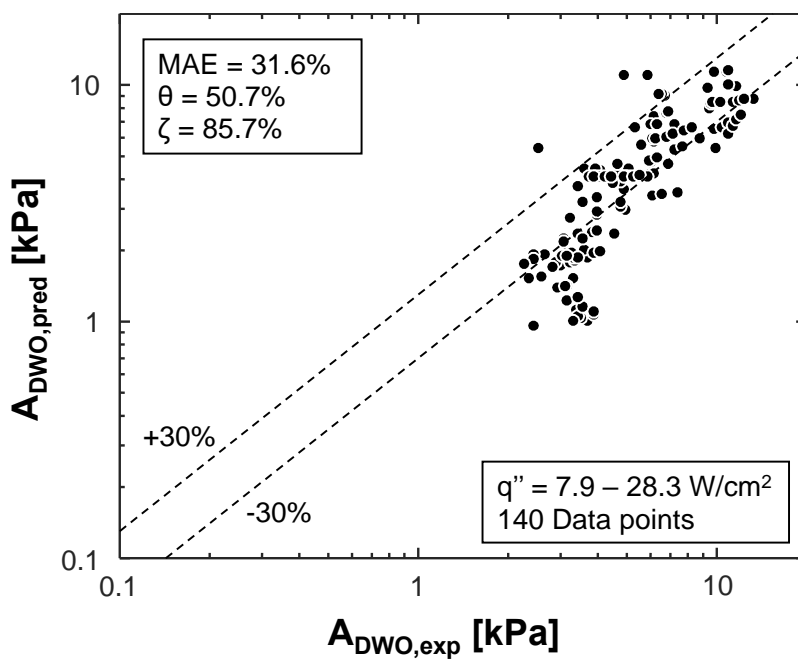


Figure 3.36 (f).

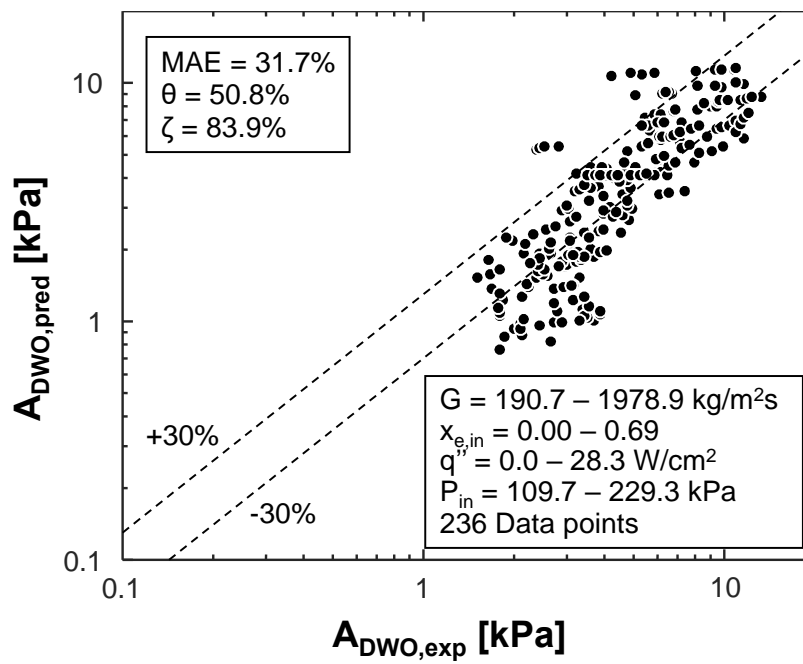


Figure 3.36 (g).

### 3.3.2.3 Parametric Extensions using Model Predictions

Having validated that the model provides good predictive accuracy and is capable of capturing key physical trends within the experimental dataset used for validation, an interesting continuation for analysis of the DWO phenomenon is to analyze parametric trends for changes in key operating conditions for which experimental data is not available.

Towards this end, Fig. 3.37 provides plots containing predictions of frequency and amplitude of DWO induced pressure oscillations for changes in local acceleration (Figs. 3.37 (a) and 3.37 (b) for frequency and amplitude, respectively), heated length (Figs. 3.37 (c) and 3.37 (d)), adiabatic length (Figs. 3.37 (e) and 3.37 (f)) and working fluid (Figs. 3.37 (g) and 3.37 (h)).

Starting with Fig. 3.37 (a), values of frequency of oscillation are seen to only vary slightly for changes in local acceleration. This is an interesting outcome, as the mechanistic description of the DWO process used to develop the model depends heavily on the role of body force, but is not necessarily invalid. It may be that only the orders of magnitude *difference* in body forces acting on liquid and vapor phases is required to incite the present instability mode, and that the magnitude of body force itself plays a minor role in determining the frequency at which the oscillations occur. It is still believed, however, that in the total absence of local acceleration this instability mode would not manifest – upcoming testing of the Flow Boiling and Condensation Experiment (FBCE) on the International Space Station (ISS) provides an excellent opportunity to test this hypothesis.

Amplitude of oscillation, however, shows significant dependence on body force, with higher values of local acceleration leading to much larger amplitudes of DWO induced pressure oscillations. This represents an important conclusion for potential applications of two-phase flow thermal management systems in applications experiencing hyper-gravity, where avoidance and/or mitigation of this instability mode may become important.

Figures 3.37 (c) and 3.37 (d) show predictions of frequency and amplitude of oscillation for changes in heated length of the test section indicating that frequency decreases and amplitude increases as diabatic length increases. This makes intuitive sense, as increases channel length leads to longer travel time for HDFs (leading to lower frequencies), while the same leads to increased two-phase flow pressure drop.

Similarly, Figs. 3.37 (e) and 3.37 (f) show plots of frequency and amplitude of DWO induced pressure oscillations for changes in adiabatic length of the channel. Trends identical to

those seen when analyzing Figs. 3.37 (c) and 3.37 (d) are present, although slopes of respective trendlines are slightly different due to the constant heat input in Figs. 3.37 (e) and 3.37 (f).

Finally, Figs. 3.37 (g) and 3.37 (h) provide predictions for frequency and amplitude of oscillation (respectively) versus mass velocity for four different working fluids. Immediately apparent in each subfigure is the similarity between results for FC-72, R134a, and HFE 7100, and the distinct differences for results generated using water as the working fluid.

Model predictions using water as the working fluid indicate both frequency and amplitude of DWO induced pressure oscillations will be several times larger than those using the other three working fluids. In particular, the extremely high amplitude of pressure oscillations associated with water flow at high mass velocities has the potential to significantly impact system safety considerations. It is likely that the high latent heat and surface tension of water as compared to other fluids evaluated here are responsible for these differences.

Across all subfigures in Fig. 3.37, it should be noted that predictions do not account for other factors present when designing and conducting flow boiling tests (*e.g.*, the presence of dryout and/or CHF for large heated lengths, onset of choked flow for high mass velocity flow of water through the present test section, *etc.*), and are simply intended to help inform future tests. Based on results shown here, conduction of tests with similar operating conditions using FC-72 in microgravity as well as Earth-based tests using water as the working fluid are of particular interest.

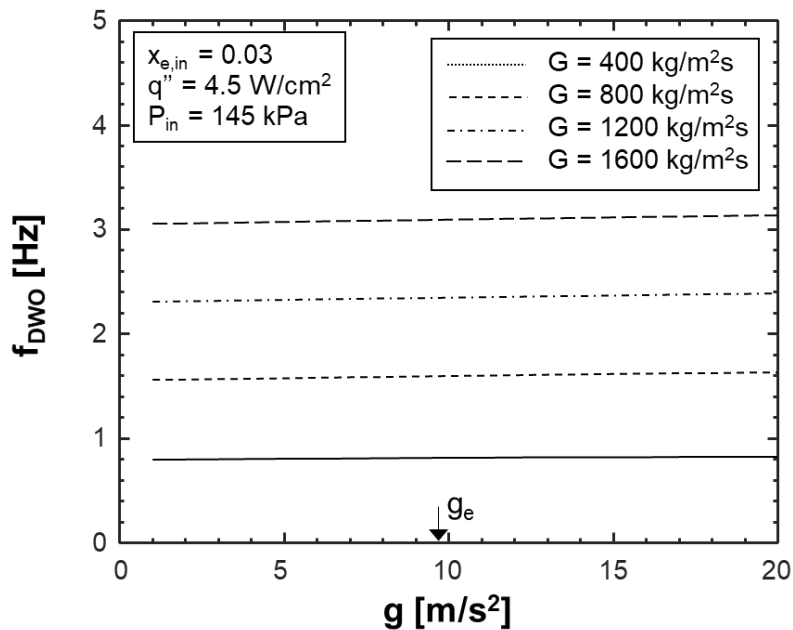


Figure 3.37: Plot presenting model predictions for parametric changes to operating environment and test section geometry: (a) DWO frequency versus local acceleration (gravity), (b) DWO amplitude versus local acceleration, (c) frequency versus heated length, (d) amplitude versus heated length, (e) frequency versus adiabatic length, (f) amplitude versus adiabatic length, (g) frequency versus mass velocity for different working fluids, and (h) amplitude versus mass velocity for different working fluids.

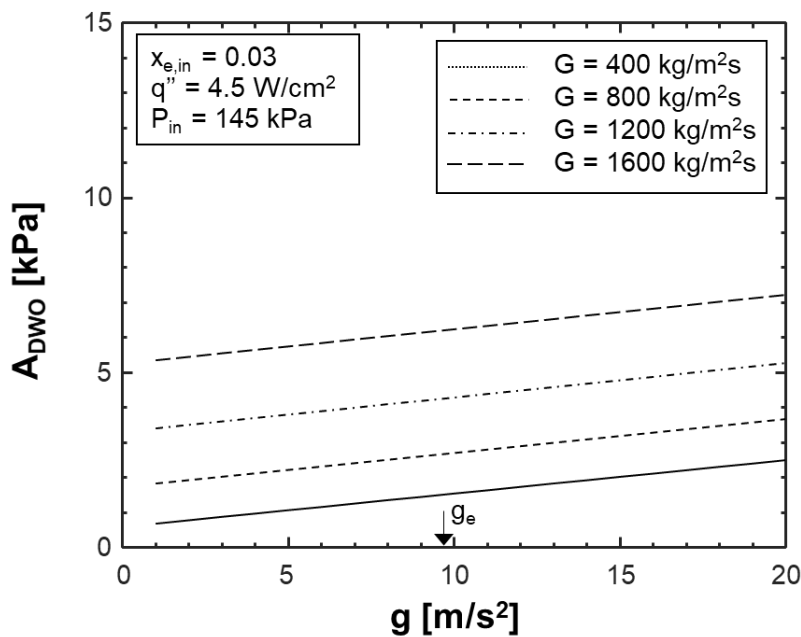


Figure 3.37 (b).

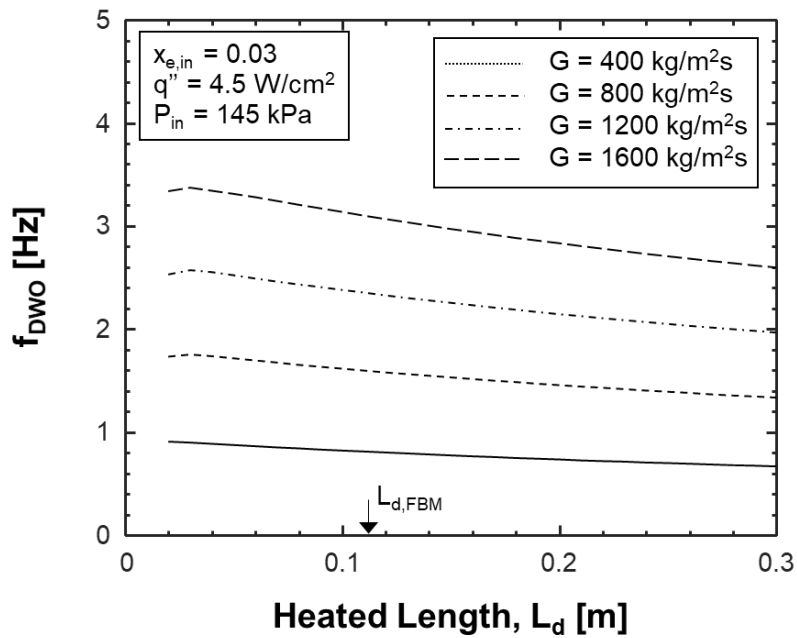


Figure 3.37 (c).

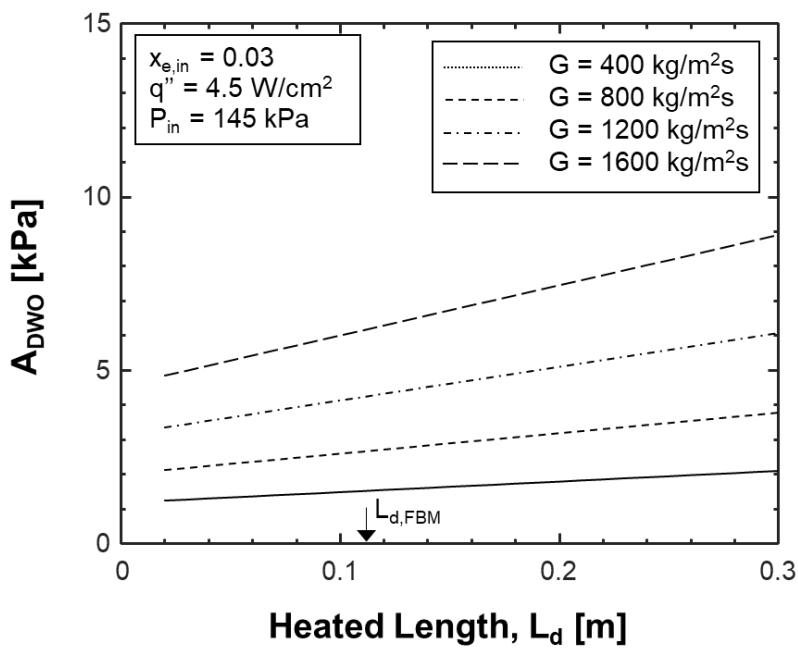


Figure 3.37 (d).

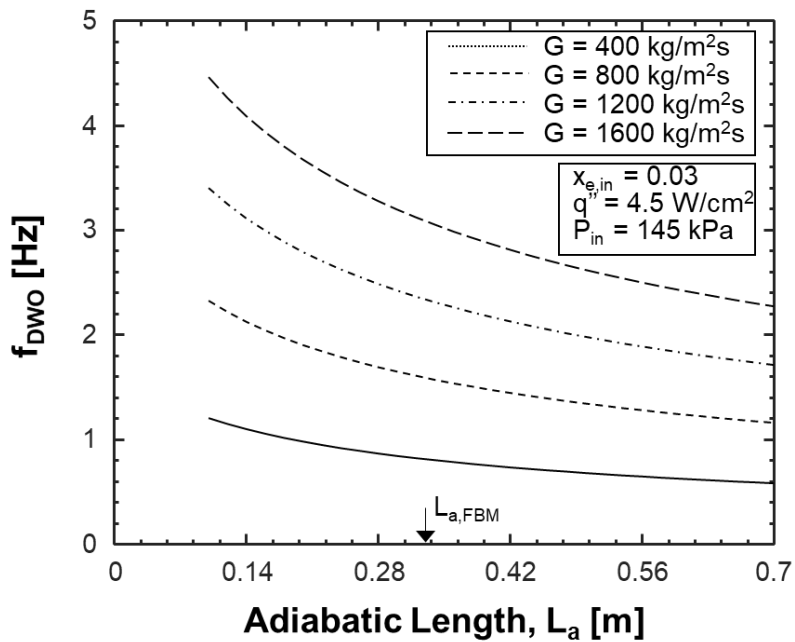


Figure 3.37 (e).

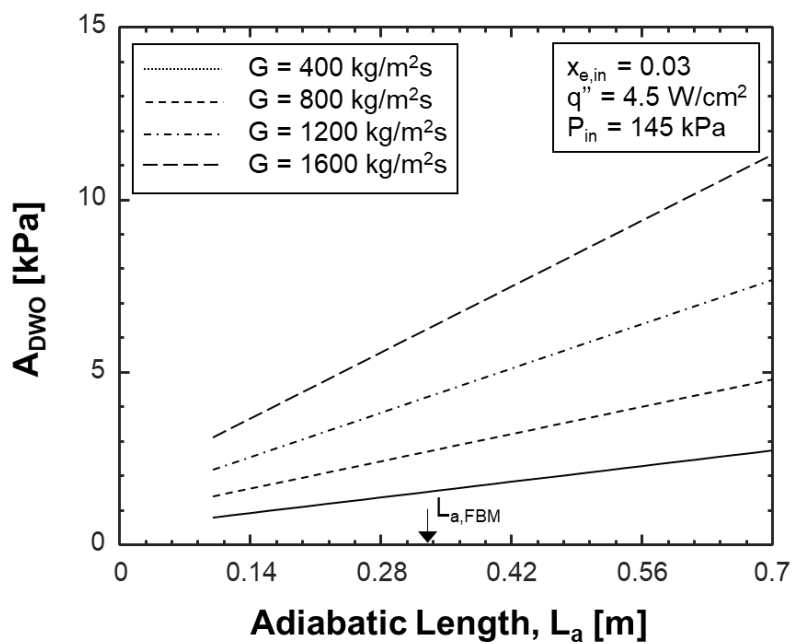


Figure 3.37 (f).

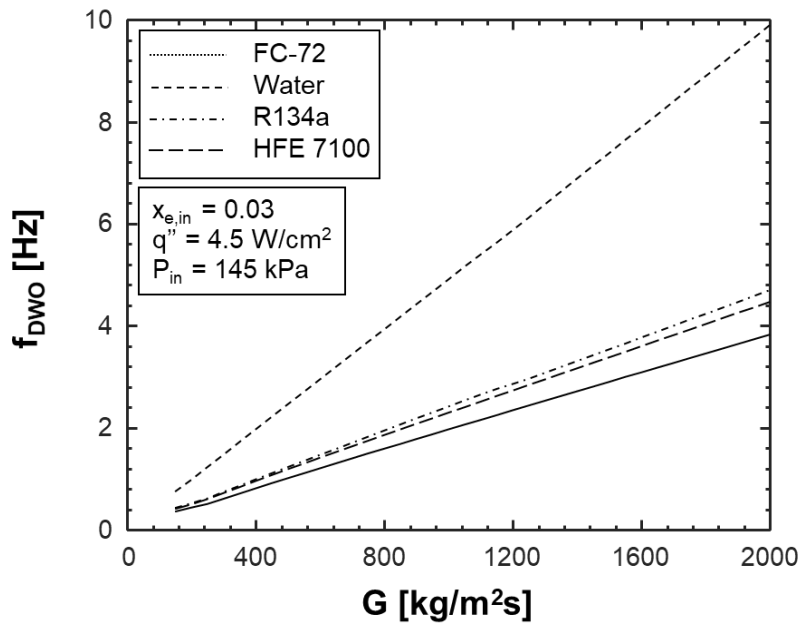


Figure 3.37 (g).

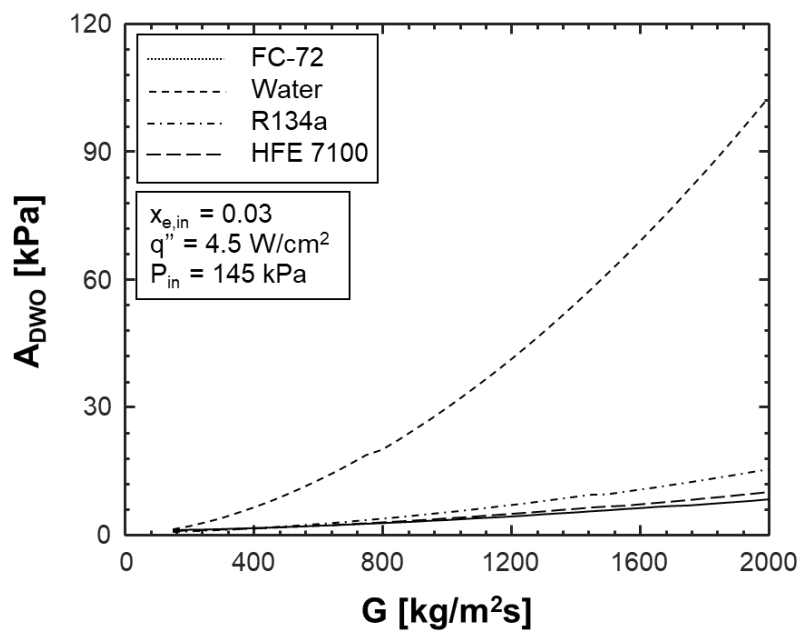


Figure 3.37 (h).

### 3.3.2.4 Discussion of Model Limitations and Focus for Future Work

The model developed in the current study has been shown to be a powerful tool for predicting frequency and amplitude of DWO induced pressure oscillations, capable of accurately capturing physical trends across a wide range of operating conditions and offering high predictive accuracy. Despite this, there is room for improvement which could alleviate some shortcomings in its current formulation, primarily in the formulation of conservation of momentum for the HDF (Region 2).

As discussed alongside Fig. 3.28 (b), conservation of momentum for Region 2 (HDF) includes the difference in momentum flux across the control-volume, pressure drop across the control-volume, viscous shear stress, and body force components. One key effect is missing, however, which is the influence of virtual mass force. Virtual mass force governs momentum interactions associated with the passage of the HDF re-wetting liquid film along the channel's walls, something that is neglected in the present model.

Similarly, boiling taking place within the HDF as it passes through the heated length of the channel is neglected, although it is possible it might play a role in creating differences in frequency and amplitude of oscillations sometimes observed between heated length inlet and outlet.

The final major limitation in the current model deals with the shape of the HDF itself. As the model is currently formulated, the HDF is treated as a slug of liquid advancing along the channel at a constant velocity. In reality, however, it is likely the HDF has a much higher velocity near the channel centerline, a near-zero velocity near the wall, and possibly a slight negative velocity near the wall at the trailing edge where surface tension forces are pulling liquid away to re-establish the liquid film along the wall. These effects lead the HDF to become elongated as it traverses the channel, even as it loses mass in the process (due to re-wetting of the liquid film), leading to the trend seen in Fig. 3.33 of increasing length and decreasing liquid composition of HDFs as mass velocity increases.

In order to better inform modeling of these phenomena, future experiments should include time-syncing of flow visualization results and transient pressure measurements to allow for instantaneous comparison of numeric and imaging results. Additionally, images captured spanning the entire length of FBM (adiabatic and diabatic lengths) could help validate modeling of mechanisms governing formation and propagation of HDFs through the channel. Finally, use of sophisticated measurement techniques such as particle image velocimetry (PIV) and laser

Doppler velocimetry (LDV) to gather liquid velocity measurements both in and directly behind the HDF would allow for detailed validation of any future models seeking to develop detailed wall-normal velocity profiles within the HDF and include virtual mass force effects.

## 4. FLOW CONDENSATION

### 4.1 Flow Condensation Pressure Oscillations at Different Orientations

#### 4.1.1 *Transient Pressure Results and Existence of Key Oscillatory Modes*

As mentioned in section 1, literature investigating transient aspects of flow boiling is more prolific than that for flow condensation, leaving significant questions regarding formation and characteristics of instabilities and oscillations in condensing systems. Towards this end, the present work will begin with investigation of the presence of oscillatory modes within condensing flows.

##### 4.1.1.1 Observation of Oscillatory Modes within CM-HT

Figures 4.1(a) – 4.1(c) present CM-HT inlet and outlet pressure results plotted over a 20-s period, a shortened 3-s window (to better highlight curve characteristics), and associated fast Fourier transform results (with transform performed over the 20-s period) in vertical upflow, vertical downflow, and horizontal flow orientations, respectively. Each plot corresponds to similar superheated FC-72 inlet conditions with FC-72 mass velocity  $G_{FC} \sim 300 \text{ kg/m}^2\text{s}$ , cooling water mass velocity  $G_{H2O} \sim 129 \text{ kg/m}^2\text{s}$ , FC-72 module inlet pressure  $P_{in,ave} \sim 130 \text{ kPa}$ , FC-72 module inlet quality  $x_{e,in} \sim 1.05$ , and exit quality  $x_{e,out} \sim 0.45$ .

Immediately apparent when comparing subfigures is the range of oscillatory behavior exhibited for each case. Figure 4.1(a) shows vertical upflow condensation experiencing almost no oscillations (evident from both transient plots and the lack of peaks in FFT results). Meanwhile, vertical downflow, Fig. 4.1(b), and horizontal flow, Fig. 4.1(c), clearly show the presence of oscillatory modes in their respective frequency response plots, with most oscillatory behavior observed in the 1-10 Hz frequency range.

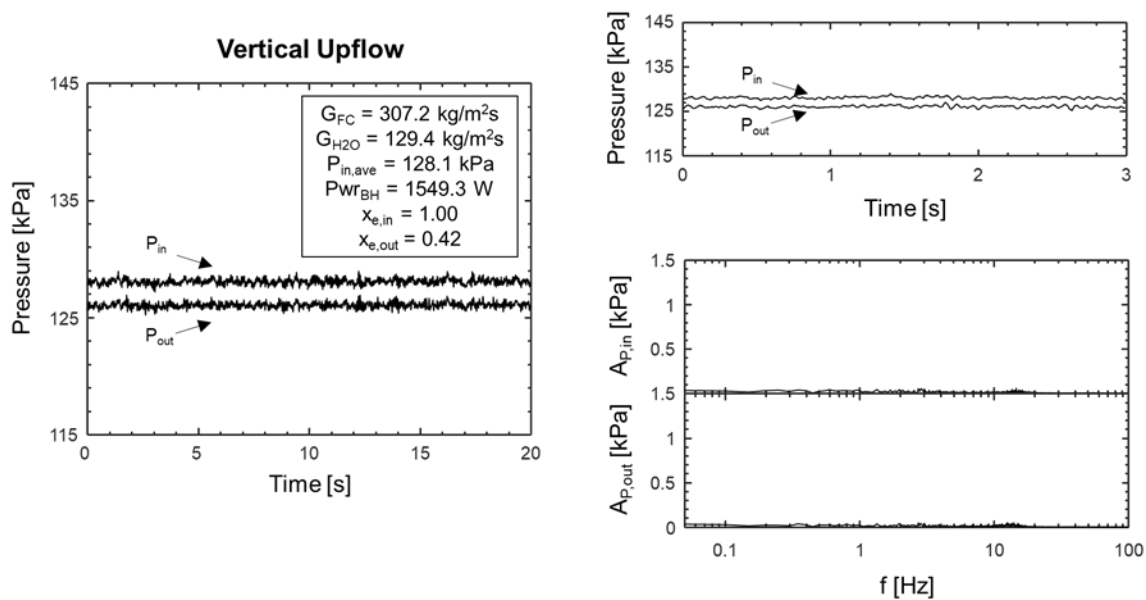


Figure 4.1: Transient CM-HT inlet and outlet pressure curves over 20-s and 3-s periods, along with associated fast Fourier transforms taken over the 20-s period for (a) vertical upflow, (b) vertical downflow, and (c) horizontal flow orientations with superheated vapor inlet.

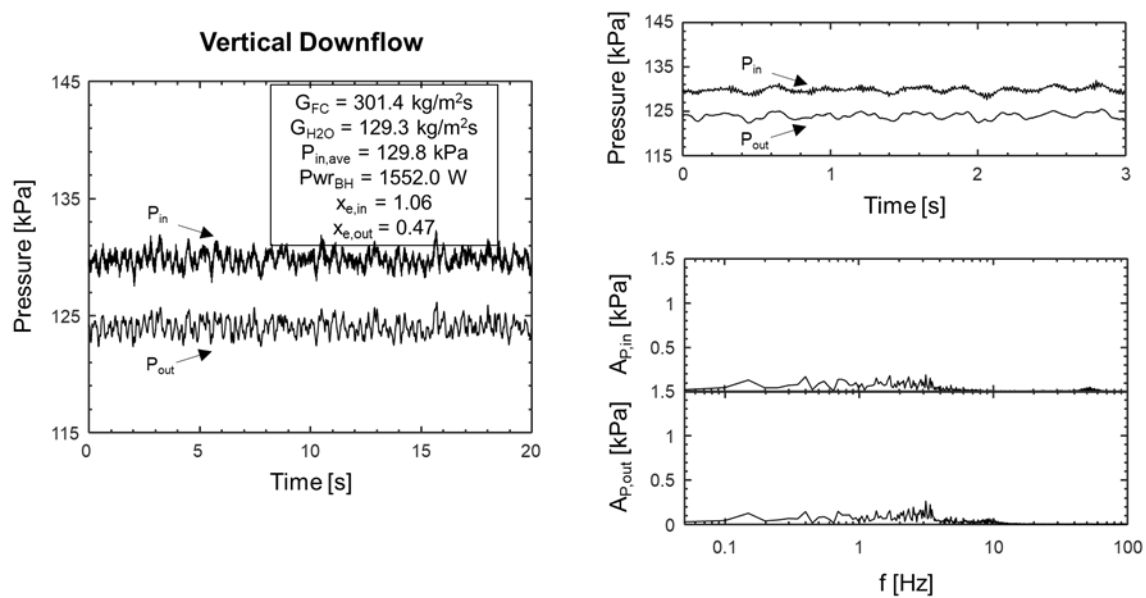


Figure 4.1 (b).

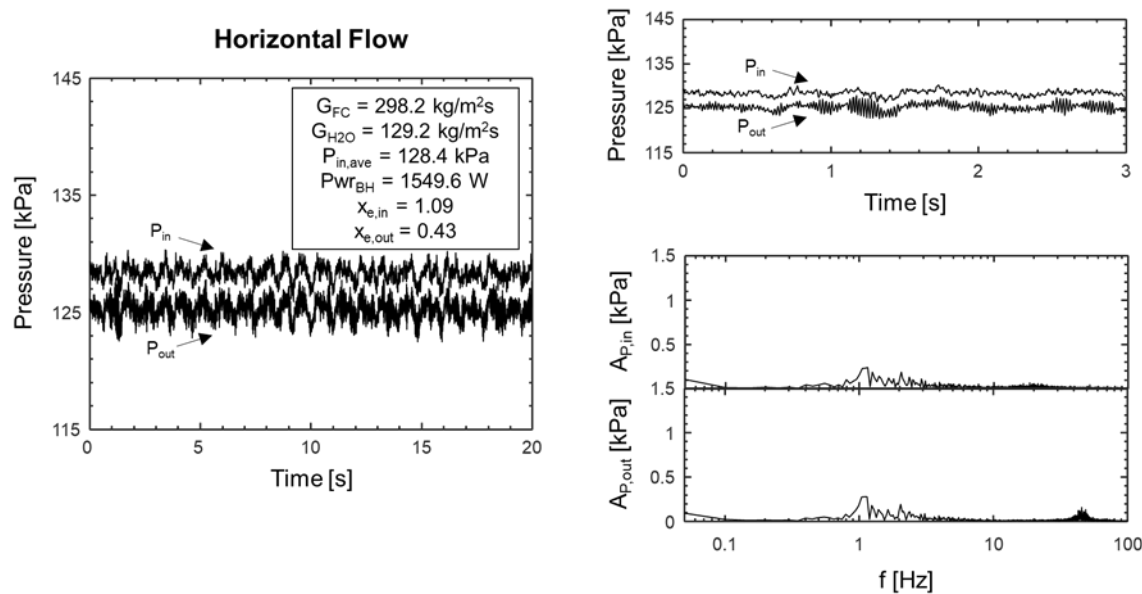


Figure 4.1 (c).

Figures 4.2(a) – 4.2(c) show similar results, this time for saturated rather than superheated FC-72 inlet conditions, with  $G_{FC} \sim 200 \text{ kg/m}^2\text{s}$ ,  $G_{H2O} \sim 388 \text{ kg/m}^2\text{s}$ ,  $P_{in,ave} \sim 130 \text{ kPa}$ ,  $x_{e,in} \sim 0.15$ , and  $x_{e,out} \sim -0.25$ . Results for vertical upflow, Fig. 4.2(a), now exhibit large amplitude oscillations, with successively lower amplitude oscillatory behavior observed for vertical downflow, Fig. 4.2(b), and horizontal flow, Fig. 4.2(c). Oscillations present in the vertical upflow are concentrated around 10 Hz, while those in vertical downflow and horizontal flow are present primarily near 1 Hz, with secondary peaks present near 10 Hz.

Figures 4.1(a) – 4.1(c) and 4.2(a) – 4.2(c) combine to illustrate two key points. First, well defined oscillatory modes are present within flow condensation for certain operating conditions, and second, these oscillatory modes (and even the existence of these modes) vary depending on operating conditions. Prior to undertaking parametric analysis to better characterize these phenomena, however, it is necessary to determine whether these oscillations are physical in nature (arising from inherent aspects of two-phase flow and/or condensation), or a manifestation of mechanically induced behavior propagated from another point within the flow loop.

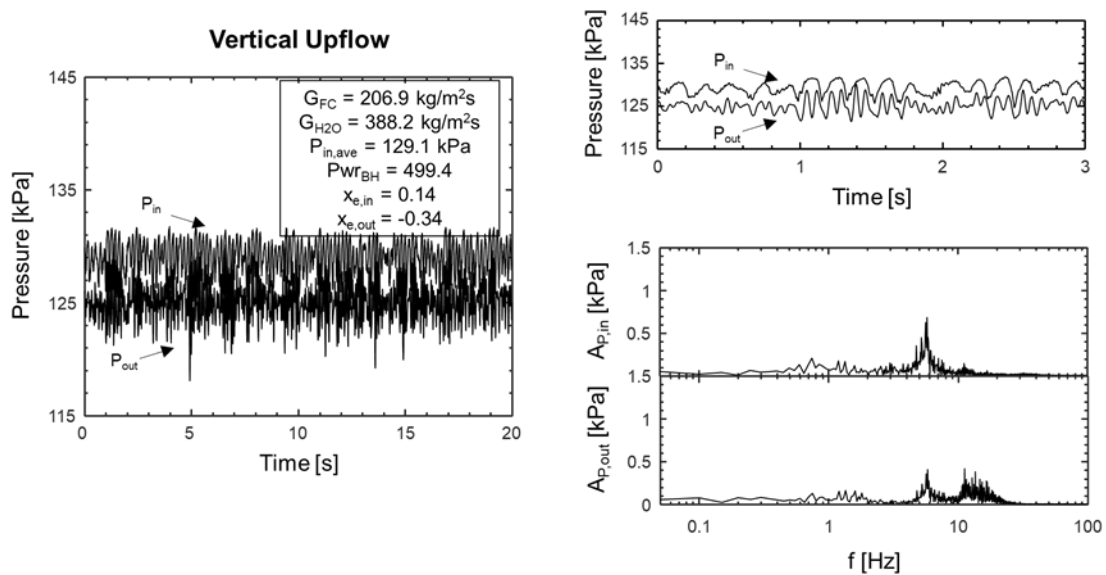


Figure 4.2: Transient CM-HT inlet and outlet pressure curves over 20-s and 3-s periods along with associated fast Fourier transforms taken over the 20-s period for (a) vertical upflow, (b) vertical downflow, and (c) horizontal flow orientations with saturated mixture inlet.

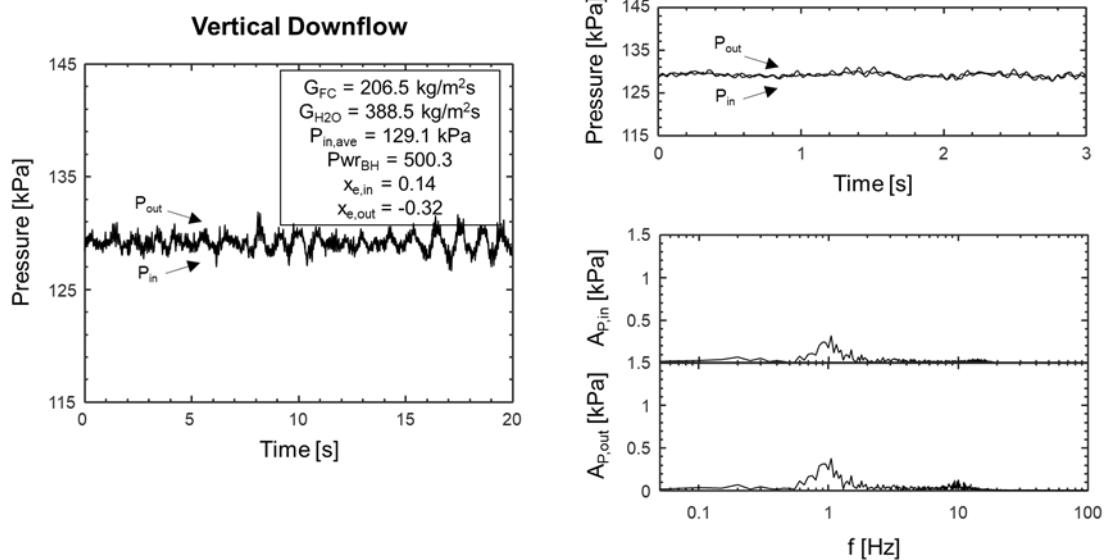


Figure 4.2 (b).

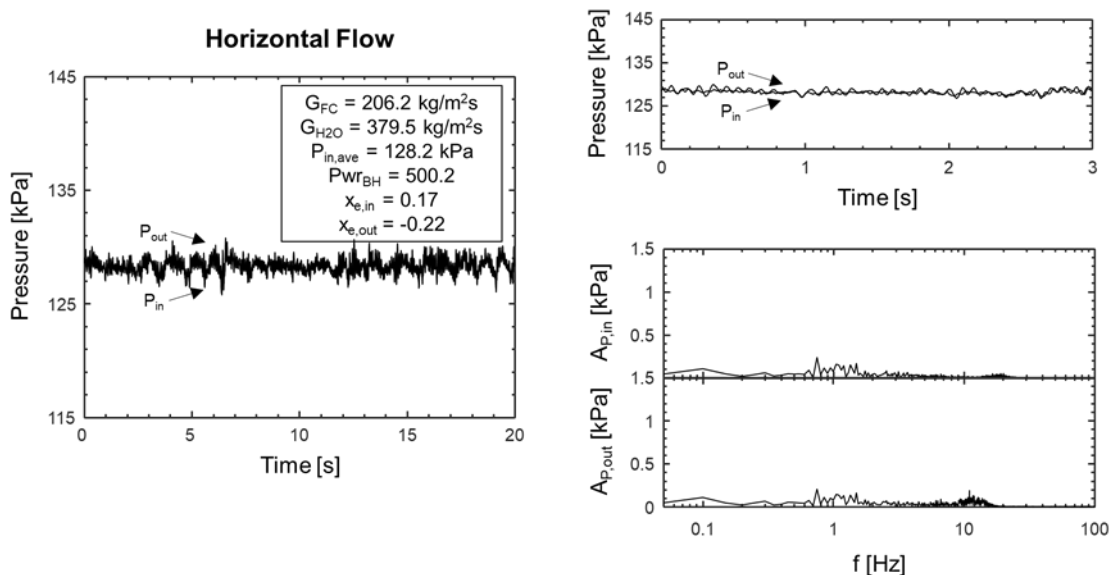


Figure 4.2 (c).

Towards this end, Figs. 4.3(a) – 4.3(d) provide transient plots and frequency response curves for pump inlet and outlet pressures, bulk heater power input, CM-HT water inlet and outlet pressures, and CM-HT FC-72 inlet and outlet pressures, respectively. The case shown here corresponds to vertical upflow with  $G_{FC} = 206.1 \text{ kg/m}^2\text{s}$ ,  $G_{H2O} = 388.1 \text{ kg/m}^2\text{s}$ ,  $P_{in,ave} = 129.1 \text{ kPa}$ ,  $x_{e,in} = 1.27$ , and  $x_{e,out} = 0.15$ . The goal of these plots is to characterize oscillatory behavior induced by key active mechanical components within the loop, and compare it to that observed within the region of interest (FC-72 flow through CM-HT) to determine if oscillatory behavior within the test section is impacted by mechanical components within the loop. This is similar to analysis performed at length for flow boiling in a prior work [84].

Figure 4.3(a) shows clear presence of significant oscillations for both pump inlet (suction-side) and outlet pressures, with difficulty distinguishing between the two due to small magnitude pressure change across the pump and high oscillatory amplitude for each signal. Performing FFT's on each signal reveals the majority of oscillatory modes are found in the high-frequency range (20–100 Hz), with clear dominant peaks for both inlet and outlet pressure signals at  $\sim 90 \text{ Hz}$ . The fact these modes are very sharp is indicative of mechanical, pump-induced oscillatory behavior [83].

Figure 4.3(b) illustrates the square-wave nature of power input through the bulk heater while the system operates in constant-temperature mode (with a PID controller pulsing power input to achieve a desired bulk heater temperature). This mode of operation is only used for a subset

operating conditions tested (those for which superheated inlet conditions are desired), but, due to its oscillatory nature, it is reasonable to speculate on whether flow dynamic behavior is impacted. The frequency response plot shown in Fig. 4.3(b) indicates peak frequencies are present in the low-frequency range of the spectrum (0.1–1 Hz), with clear peaks decreasing in amplitude as frequency increases. This is expected based on the known decomposition of square waves [87].

Figure 4.3(c) provides plots of CM-HT waterside inlet and outlet pressures. Although the water conditioning loop is separate from the primary (FC-72) flow loop, presence of strong oscillatory modes within the water loop could potentially cause vibrations within the test module that could be picked up within the FC-72 pressure signal. This is not the case for the current setup, however, as Fig. 4.3(c) clearly shows near-zero oscillatory behavior present within the waterside of the system.

Finally, Fig. 4.3(d) provides transient and associated frequency composition plots of FC-72 pressure at the inlet and outlet of CM-HT, with difficulty distinguishing between the two again due to small magnitude change and relatively high amplitude oscillations. These plots show presence of a low-amplitude oscillatory mode over a narrow frequency band centered on ~10 Hz. This is clearly different from oscillatory modes observed at other locations throughout the loop, indicating oscillatory behavior observed within the FC-72 side of the test section may be considered independent of other oscillatory modes introduced in the system.

This conclusion is reinforced by the fact that dominant oscillatory modes are only observed within the test section for certain combinations of operating conditions, while behavior across the pump, bulk heater, and water loop remains largely constant regardless of operating conditions. The dependence of existence of peak oscillatory modes within the test section on operating conditions is discussed further in the following subsection.

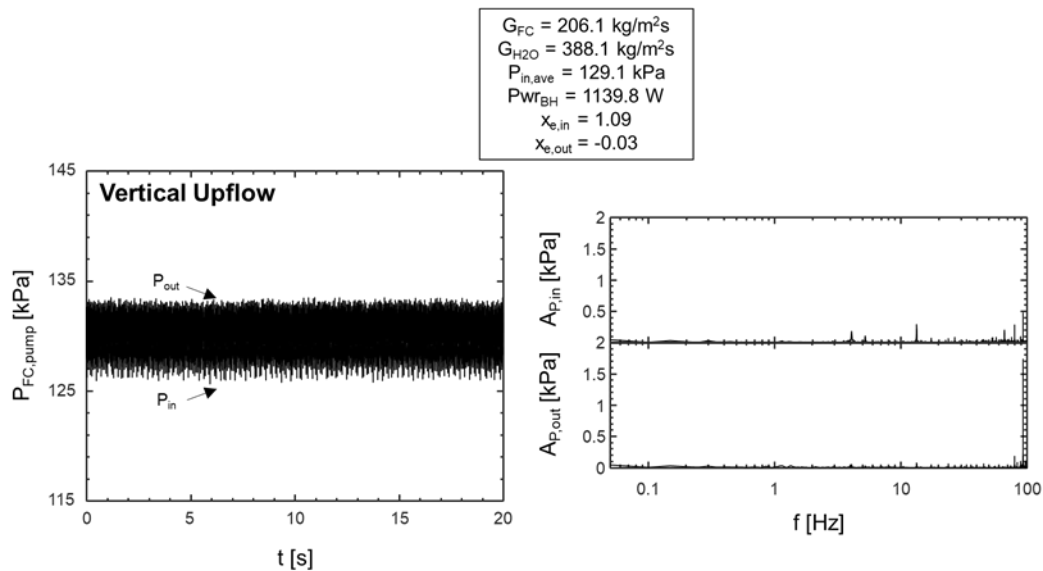


Figure 4.3: Sample transient plots and associated fast Fourier transforms for (a) FC-72 pump inlet and outlet pressures, (b) bulk heater power input, (c) CM-HT water inlet and outlet pressures, and (d) CM-HT FC-72 inlet and outlet pressures.

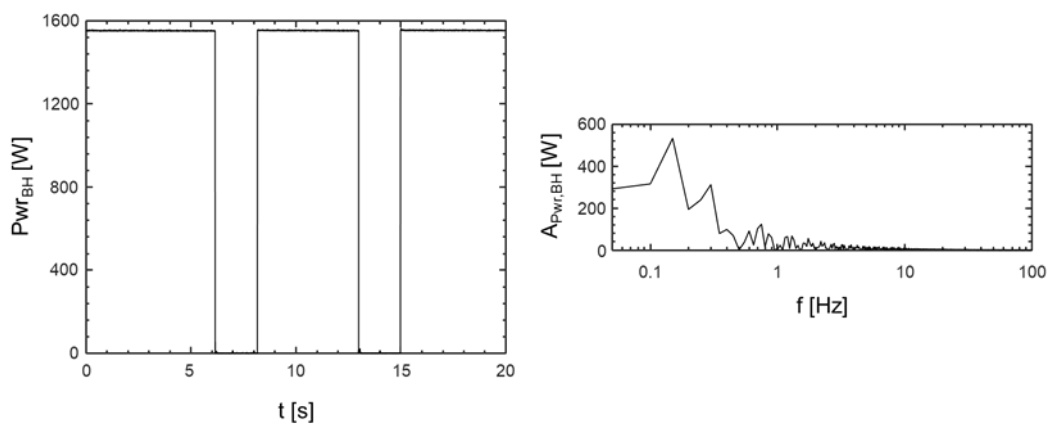


Figure 4.3 (b).

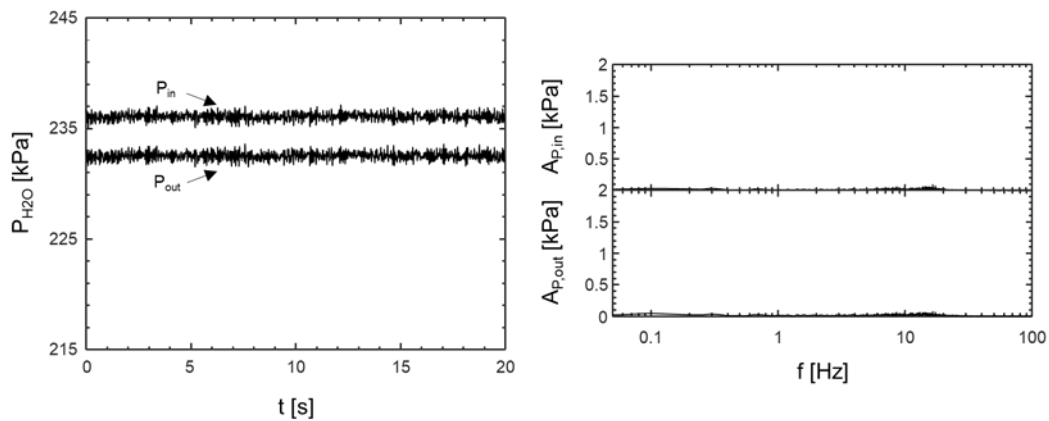


Figure 4.3 (c).

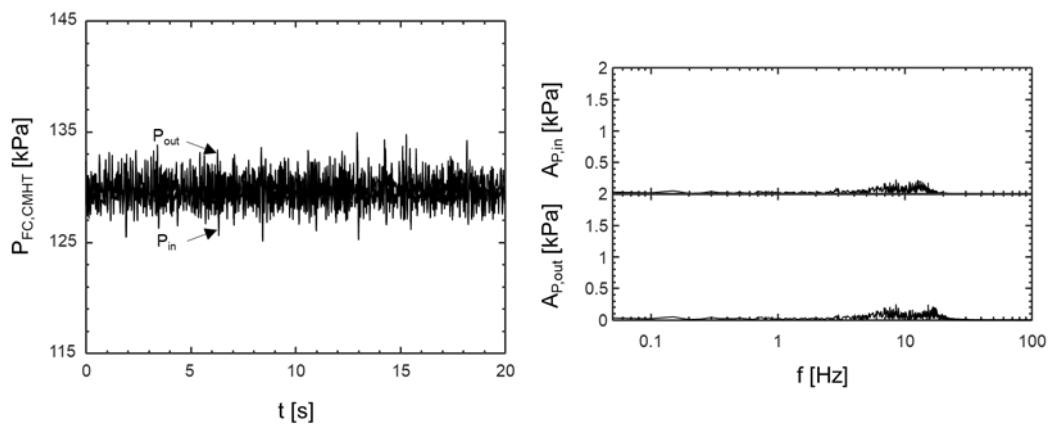


Figure 4.3 (d).

#### 4.1.1.2 Existence of Peak Oscillatory Mode within CM-HT

In order to evaluate parametric trends regarding the presence of a clearly defined peak oscillatory mode within the test section, it is first necessary to set criteria determining whether a peak oscillatory mode is in fact present. Then, once a peak oscillatory mode has been identified, some measure of its intensity should be provided for comparison with oscillatory modes present under other operating conditions.

Figures 4.4(a) – 4.4(c) depict the process by which these two key pieces of information are determined for three sets of operating conditions, all in vertical upflow. First, fast Fourier transforms are performed on test module FC-72 inlet and outlet pressure signals to determine frequency composition of any oscillations present (only results corresponding to inlet pressure signals are shown in the present plot). Frequency response curves are then passed through a 10 Hz low-pass filter to help smoothen results and provide a continuous response curve. The low-pass filter used is a second-order Butterworth digital filter with transfer function

$$H(z) = \frac{0.02 + 0.04z^{-1} + 0.02z^{-2}}{1.0 - 1.56z^{-1} + 0.64z^{-2}}, \quad (4.1)$$

where  $z$  is the digital domain variable. Coefficients shown here are truncated for presentation but preserved with additional significant figures by the python script used to generate them [159].

The low pass filter applied here is intended to allow for determination of the  $Q$  Factor (or  $Q$ , for short) of peaks present in the frequency response of each signal. Prior to this calculation, however, it is necessary to determine if any peaks are present within the frequency response. This is done by checking whether the maximum value of the frequency response satisfies two conditions:

- 1) The difference between the maximum and mean amplitude values on the frequency response plot is greater than 0.1,

$$DA_{max,mean} = \max(A_p) - \text{mean}(A_p) > 0.1. \quad (4.2)$$

- 2) The ratio of maximum to mean amplitude values is greater than 2,

$$A_{max} / A_{mean} = \frac{\max(A_p)}{\text{mean}(A_p)} > 2. \quad (4.3)$$

This set of criteria determines (1) that the max value of the frequency response is sufficiently greater than the mean value (with the value here determined by inspection of the entire dataset),

and (2) that the ratio of max value to mean value is sufficiently high, so the satisfaction of both criteria ensures the presence of a true peak in the frequency response.

It should be noted that the second criterion listed above is not used to exclude any cases in the present dataset, but may be important for application to other datasets where significant variations in noise (possibly due to mechanical vibrations from outside sources [166]) are present.

Once it has been determined whether a true peak exists in the frequency response curve (e.g., Figs. 4.4(a) and 4.4(b), but not Fig. 4.4(c)), the sharpness of the peak may be determined by calculating its  $Q$  Factor. This is done by determining the frequency at which the peak occurs and dividing it by the full width half maximum (amplitude) frequency range, or

$$Q = \frac{f_{A=\max(A)}}{\Delta f_{A=1/2\max(A)}} = \frac{f_{peak}}{\Delta f_{FWHM}}, \quad (4.4)$$

In physical terms,  $Q$  Factor represents the concentration of oscillatory energy about a single frequency value. Figure 4.4(a) exhibits a very sharp peak at 5.5 Hz, and the associated  $Q$  Factor of 5.79 indicates that the energy associated with this oscillatory mode is concentrated in a narrow band about that peak. Figure 4.4(b), meanwhile, exhibits a dominant oscillatory mode that is distributed over a wide frequency range, reflected in a  $Q$  Factor of 1.03. Figure 4.4(c) exhibits no clear peak in its frequency response plot, and is assigned a  $Q$  Factor of 0 (indicating an approximately flat frequency response and the nonexistence of a dominant oscillatory mode).

It should be noted that all values of  $Q$  presented hereafter are calculated for both inlet and outlet FC-72 pressure signals then averaged, providing a single  $Q$  value for each set of operating conditions.

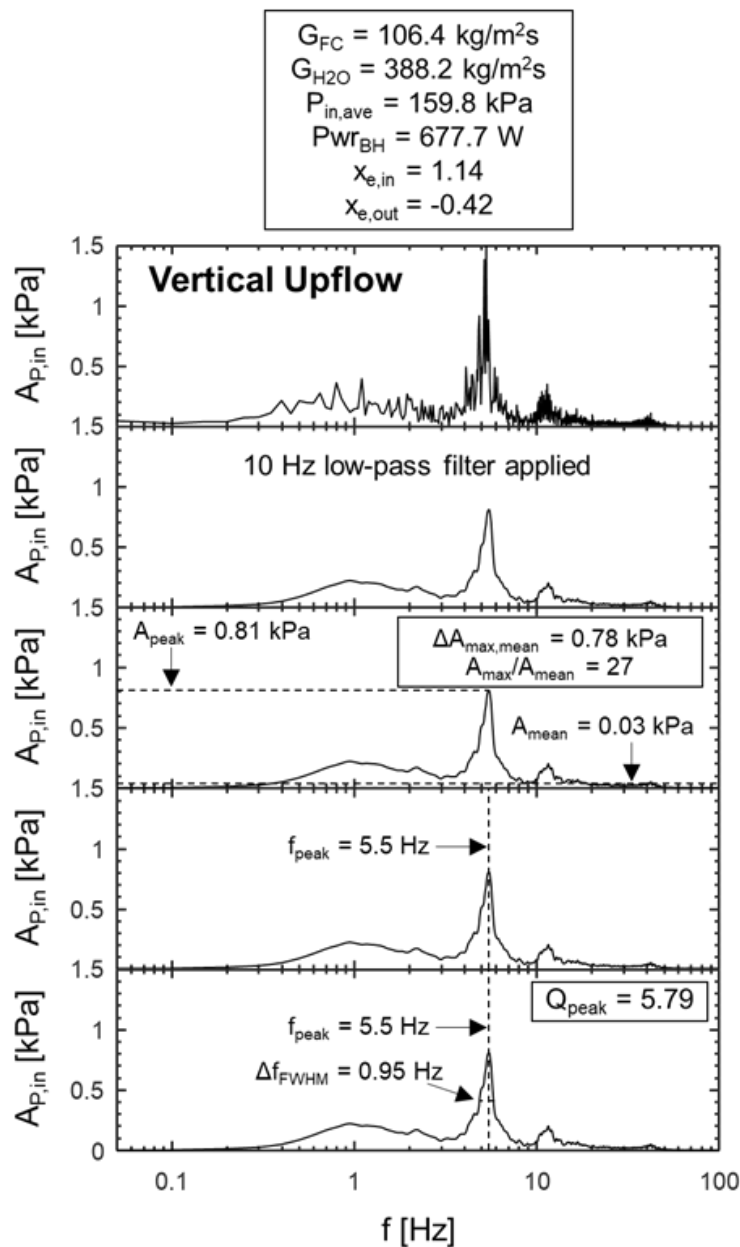


Figure 4.4: Process of determining  $Q$  Factor for peak frequency of oscillation by taking fast Fourier transform of 20-s duration inlet pressure signal, applying 10-Hz low pass filter to FFT curve, determining if a true peak exists, identifying the frequency associated with the peak, and determining the associated  $Q$  Factor for cases with (a) high  $Q$ , (b) moderate  $Q$ , and (c) no peak.

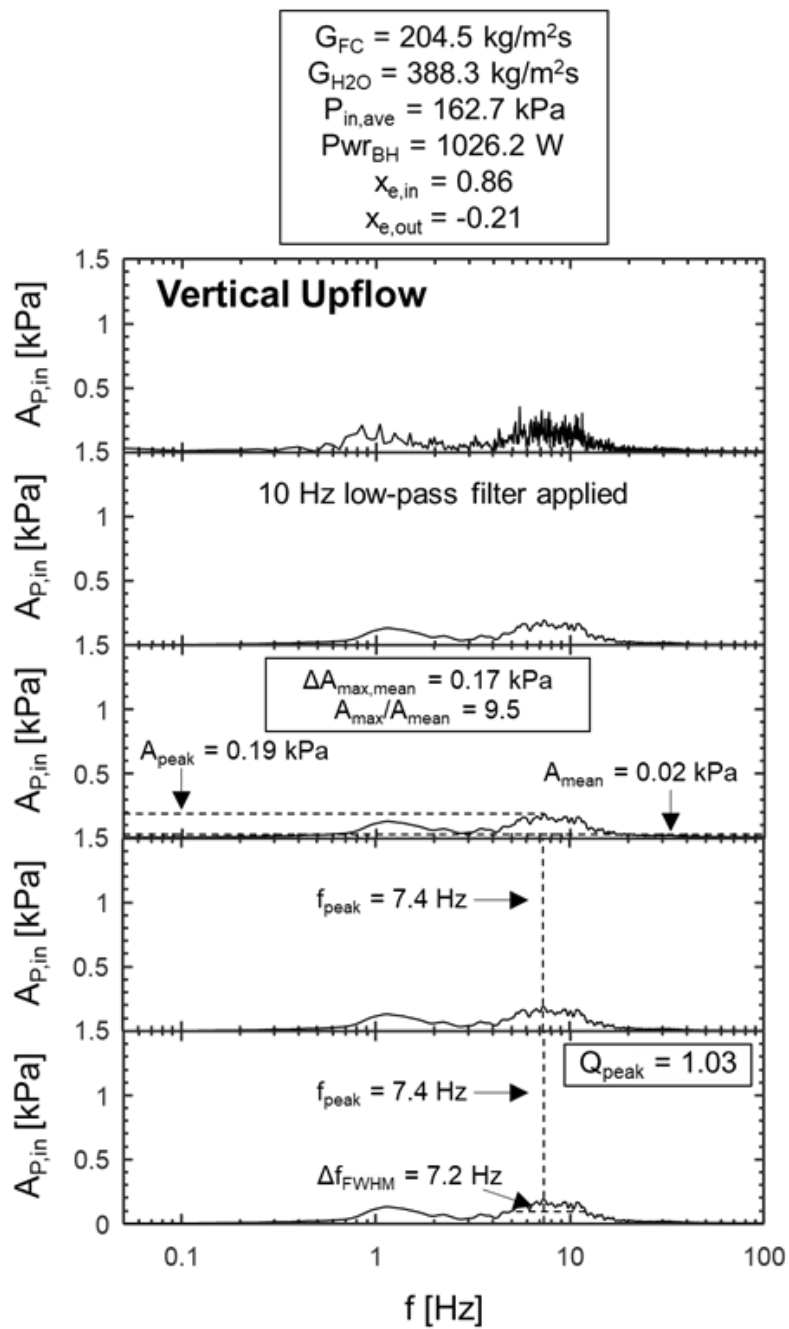


Figure 4.4 (b).

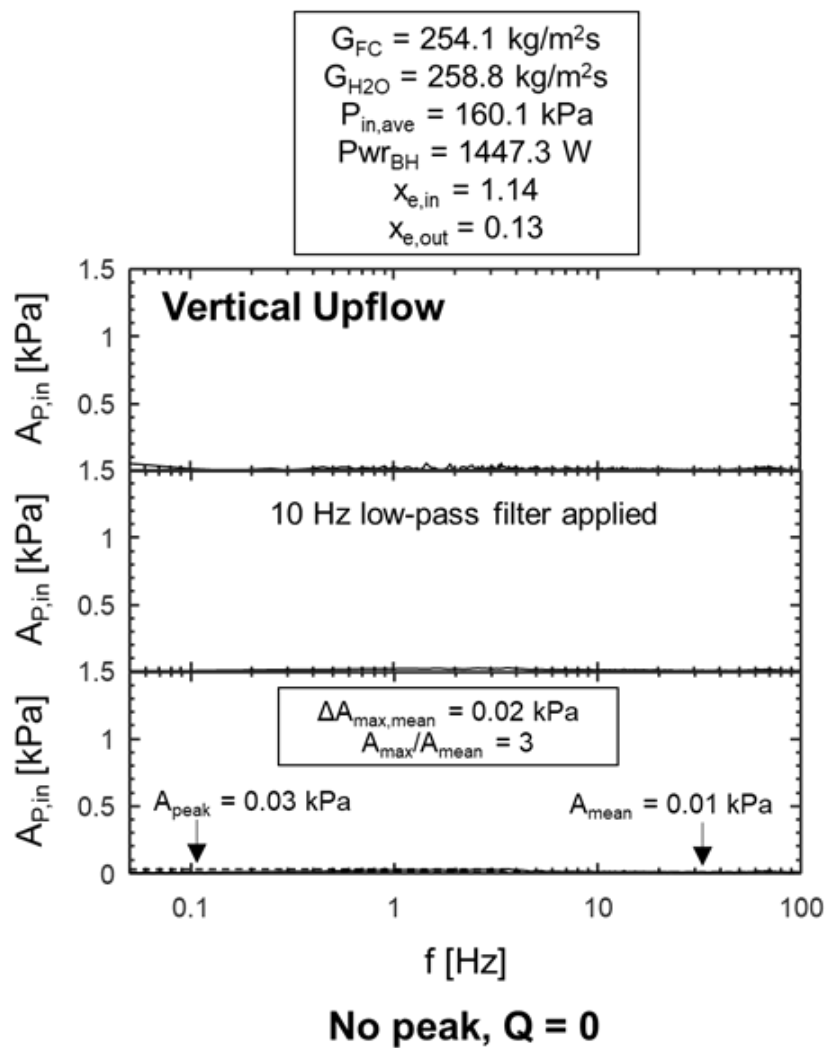


Figure 4.4 (c).

Having presented a methodology by which the existence of a dominant oscillatory mode may be determined and its intensity characterized, it is possible to undertake a parametric evaluation of the influence of different key operating conditions on formation of dominant oscillatory modes. Figures 4.5(a) – 4.5(c) present plots of  $Q$  Factor versus FC-72 mass velocity, inlet quality, exit quality, and (time-averaged) inlet pressure for vertical upflow, vertical downflow, and horizontal flow orientations, respectively.

Figure 4.5(a) shows  $Q$  Factor decreasing as both mass velocity and exit quality are increased. These trends indicate vertical upflow condensation exhibits less pronounced oscillatory behavior (meaning a clearly defined oscillatory mode is not present) as mass velocity is increased and as liquid content at the exit of the channel is reduced. This makes intuitive sense, as body force acts to destabilize the liquid film in vertical upflow orientation, with increased mass velocity (increased liquid inertia and interfacial shear) as well as reduced liquid content acting to reduce the influence of body force on hydrodynamic behavior. No discernible trends are present for variations in inlet quality and inlet pressure.

Figure 4.5(b) shows similar plots for results obtained in vertical downflow orientation. Counter to that seen for vertical upflow, results here indicate increased oscillatory behavior as mass velocity is increased in vertical downflow orientation. Similar to vertical upflow, values of  $Q$  Factor also decrease for increases in channel exit quality, despite the fact the majority of downflow cases with no peak oscillatory mode ( $Q = 0$ ) occur for cases with negative exit quality. Similar to vertical upflow, little or no trends are present for variations in inlet quality and operating pressure.

Figure 4.5(c), presenting results obtained during horizontal flow condensation, exhibits no appreciable trend in values of  $Q$  for changes in mass velocity, inlet quality, exit quality, or operating pressure.

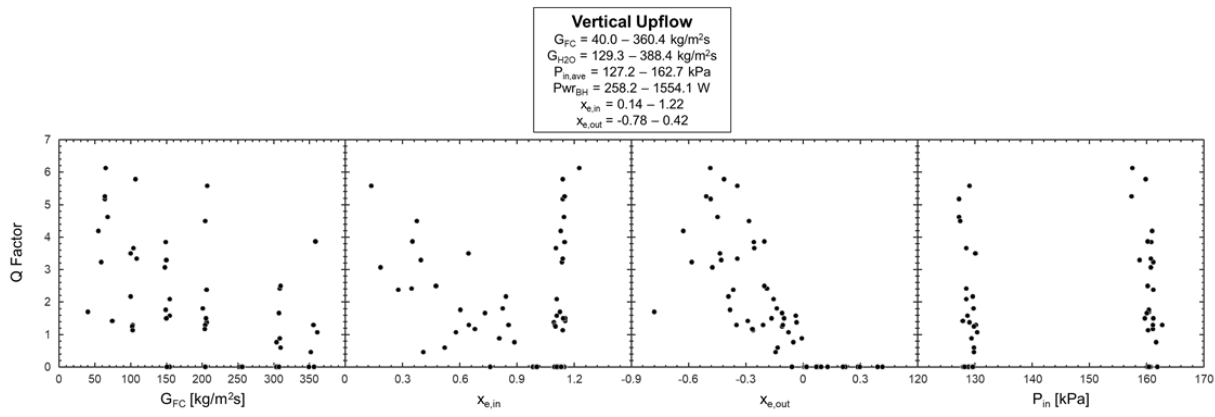


Figure 4.5: Plots of  $Q$  Factor versus FC-72 mass velocity, inlet quality, exit quality, and inlet pressure, for all cases in (a) vertical upflow, (b) vertical downflow, and (c) horizontal flow orientations.

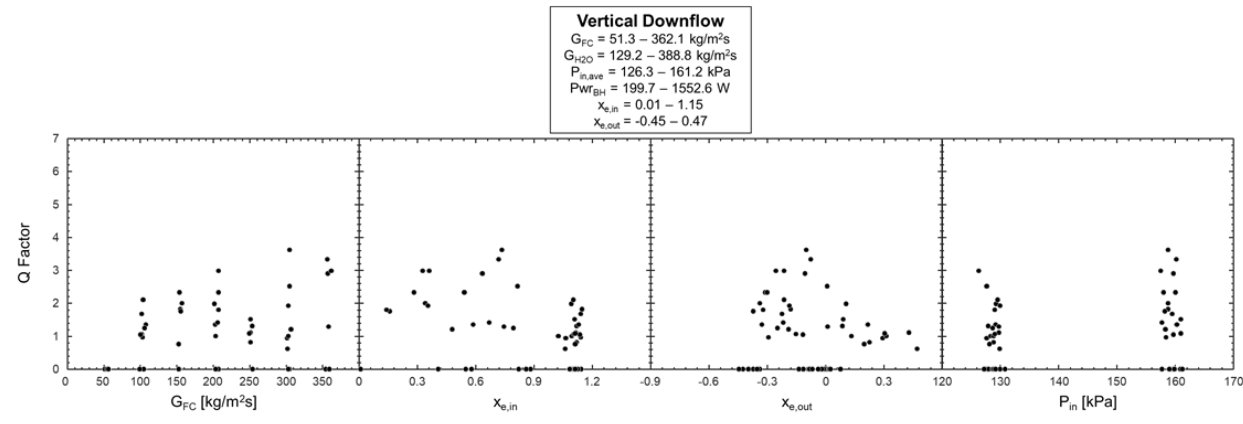


Figure 4.5 (b).

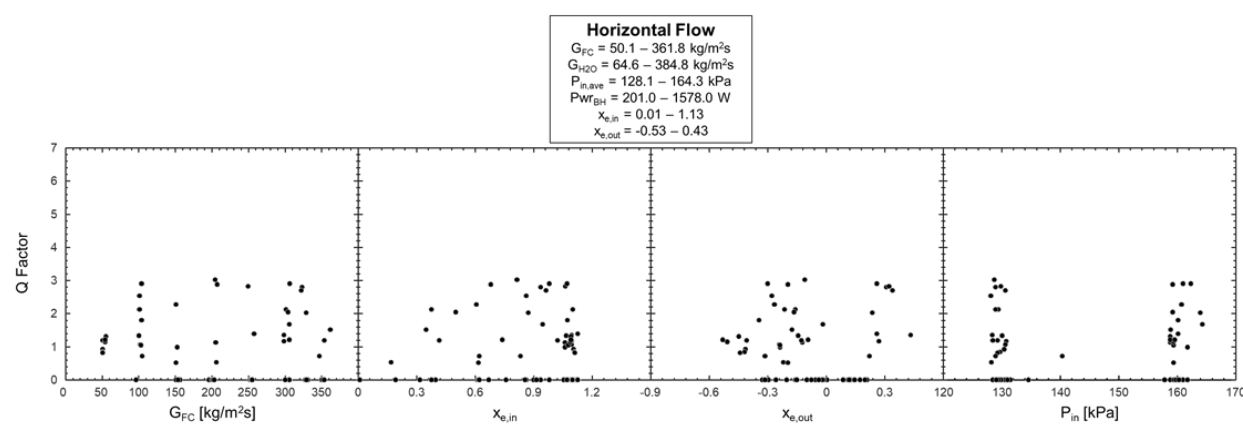


Figure 4.5 (c).

Analyzing trends across all subfigures in Fig. 4.5, body force has a significant effect on the manifestation of oscillatory behavior in flow condensation, and one which is compounded by changes to key operating parameters. To better understand physical phenomena influencing dynamic behavior,  $Q$  Factor will be plotted versus several relevant dimensionless groups. These include inlet vapor Reynolds number,  $Re_{g,in}$ , defined as

$$Re_{g,in} = \frac{G_{FC} x_{e,in} D_h}{\mu_g}, \quad (4.5)$$

where  $D_h$  is the channel hydraulic diameter and  $\mu_g$  the dynamic viscosity of vapor, inlet vapor Weber number,  $We_{g,in}$ , defined as

$$We_{g,in} = \frac{r_g \left( G_{FC} x_{e,in} U_g \right)^2 D_h}{\sigma}, \quad (4.6)$$

where  $\rho_g$  is vapor density,  $v_g$  vapor specific volume, and  $\sigma$  surface tension, and inlet vapor Froude number,  $Fr_{g,in}$ , defined as

$$Fr_{g,in} = \frac{v_g G_{FC} x_{e,in}}{\sqrt{g D_h}}, \quad (4.7)$$

where  $g$  is Earth's gravitational constant. Similar values are also defined in terms of channel exit and liquid properties, defined as

$$Re_{f,out} = \frac{G_{FC} (1 - x_{e,out}) D_h}{m_f}, \quad (4.8)$$

$$We_{f,out} = \frac{\rho_f \left( G_{FC} (1 - x_{e,out}) v_f \right)^2 D_h}{\sigma}, \quad (4.9)$$

and

$$Fr_{f,out} = \frac{U_f G_{FC} (1 - x_{e,out})}{\sqrt{g D_h}}, \quad (4.10)$$

for exit liquid Reynolds number, Weber number, and Froude number, respectively. It should be noted that properties used in the calculation of all dimensionless groups are evaluated at time-averaged inlet pressure for each case and the value of  $g$  remained constant for all orientations (no sign changes).

Similar to Figs. 4.5(a) – 4.5(c), Figs. 4.6(a) – 4.6(c) provide plots of  $Q$  versus each of the dimensionless groups presented in Eqs. (4.5) – (4.10) for vertical upflow, vertical downflow, and horizontal flow orientations, respectively. Figure 4.6(a) shows quadratic decreases in  $Q$  for

changes in dimensionless groups based on inlet parameters, while those based on outlet parameters exhibit linear decreases. The general decreasing trend is consistent with that seen for mass velocity in Fig. 4.5(a), as mass velocity is present in the numerator of every dimensionless group here. The difference in slope between dimensionless groups based on inlet and outlet parameters, however, indicates the intensity of oscillatory modes in vertical upflow condensation is more strongly tied to inlet conditions than exit.

Figure 4.6(b) provides similar plots for vertical downflow. Dimensionless groups based on inlet parameters exhibit no clear trends, while those based on exit parameters show linear increases in  $Q$  as Reynolds, Weber, and Froude numbers are increased.

Figure 4.6(c) indicates results for the horizontal orientation again exhibit no appreciable trends for any of the parameters evaluated here. It is worth noting, however, that tests conducted in horizontal orientation exhibit the lowest  $Q$  values as well as the highest percentage of  $Q = 0$  cases (46% versus 39% for vertical downflow and 28% for vertical upflow), indicating it is the most stable orientation. Vertical upflow, meanwhile, can be seen to exhibit the highest  $Q$  values of the three orientations, with vertical downflow falling between the two.

Overall, Figs. 4.5(a) – 4.5(c) and 4.6(a) – 4.6(c) indicate that, for vertical upflow and downflow orientations, mass velocity is the key parameter governing existence of a dominant oscillatory mode. In vertical upflow increases in mass velocity exhibit a stabilizing effect of the flow, while in vertical downflow increases in mass velocity destabilize the flow. Further, trends regarding  $Q$  Factor (interpreted here as a measure of the intensity of a dominant oscillatory mode) depend strongly on channel inlet and vapor parameters for vertical upflow and channel exit and liquid parameters for vertical downflow. This is a key outcome, as it implies different physical processes govern flow dynamics in vertical upflow and downflow orientations.

$Q$  Factor alone is insufficient to fully characterize flow dynamic behavior, however, as it does not include information regarding differences in amplitude and frequency of oscillations. Thus, moving forward, only cases with non-zero  $Q$  will be considered, and amplitude and frequency at which they exhibit peak oscillations will be analyzed.

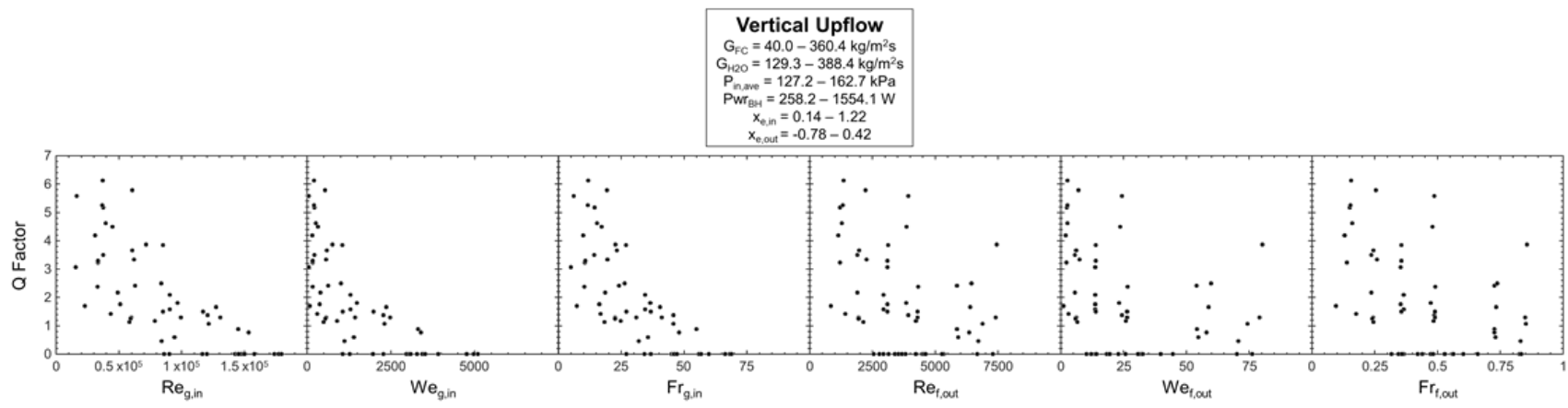


Figure 4.6: Plots of  $Q$  Factor versus FC-72 inlet vapor Reynolds, Weber, and Froude numbers, and exit liquid Reynolds, Weber, and Froude numbers, for all cases in (a) vertical upflow, (b) vertical downflow, and (c) horizontal flow orientations.

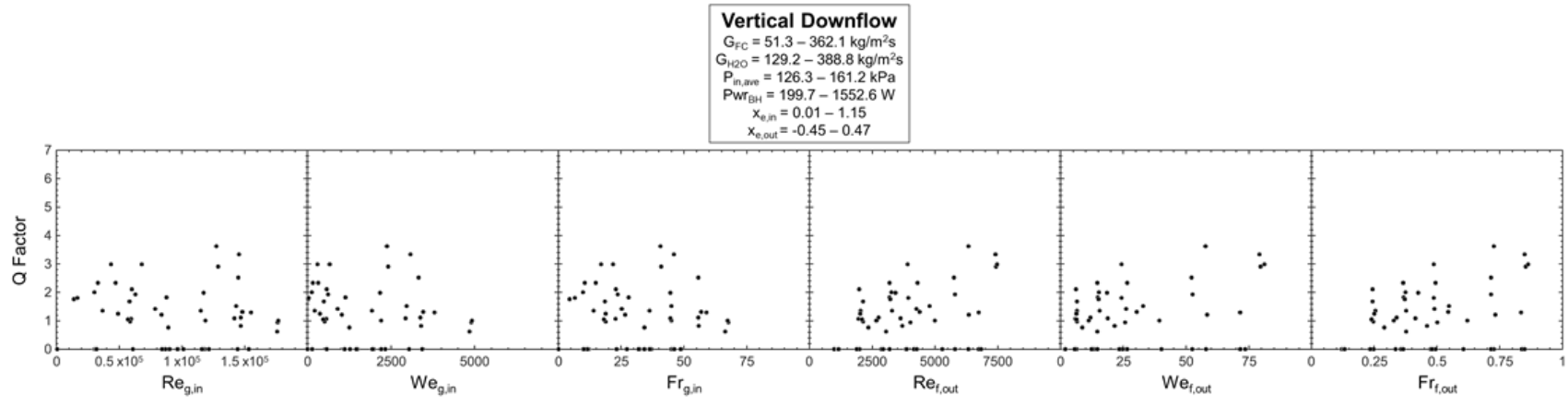


Figure 4.6 (b).

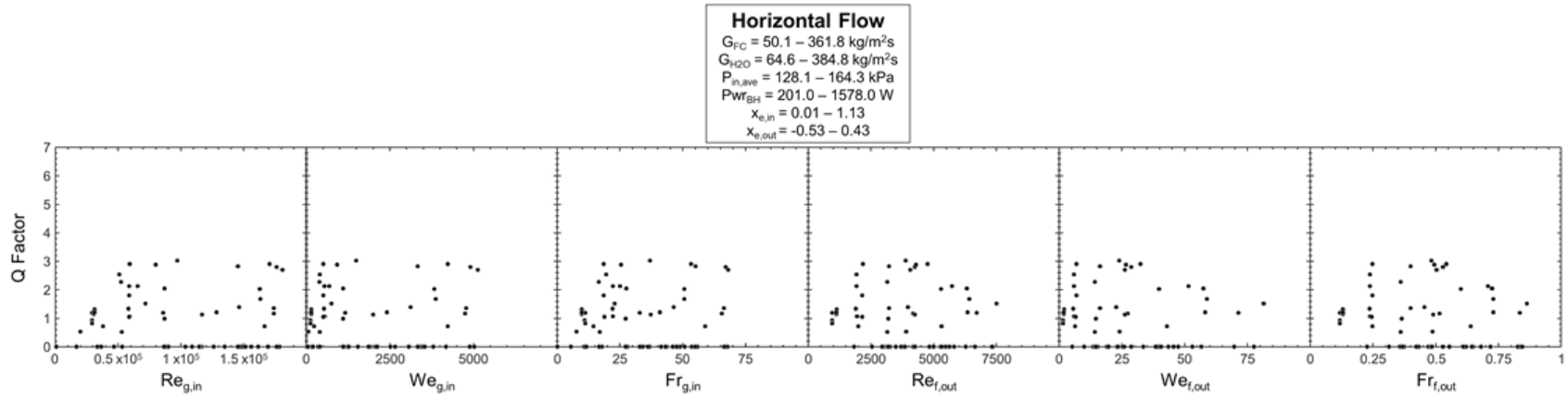


Figure 4.6 (c).

#### 4.1.2 Characterization of Dominant Oscillatory Mode

Prior to analyzing trends regarding amplitude and frequency of peak oscillatory modes, it is first necessary to discuss detection of peak frequency and amplitude of oscillation. Figures 4.7(a) and 4.7(b) present the process used step-by-step. Figure 4.7(a) provides plots of CM-HT inlet and outlet pressure measurements for a case in vertical upflow with  $G_{FC} = 106.4 \text{ kg/m}^2\text{s}$ ,  $G_{H2O} = 388.2 \text{ kg/m}^2\text{s}$ ,  $P_{in,ave} = 159.8 \text{ kPa}$ ,  $x_{e,in} = 1.14$ , and  $x_{e,out} = -0.42$ . Figure 4.7(b) shows associated fast Fourier transform results (frequency response plots) for each signal, again calculated over the 20-s period as indicated in previous sections.

Frequency response plots in Fig. 4.7(b) have peak frequency (frequency value associated with maximum amplitude on the response plot) labeled, as well as a vertical dashed line drawn at 30 Hz. This is done to indicate filter cutoff frequency used to filter transient pressure curves prior to amplitude detection as shown in Fig. 4.7(c), applied to fluctuating pressure signals (zero mean) defined as

$$P' = P - P_{ave}, \quad (4.11)$$

where  $P'$  is the fluctuating component of pressure,  $P$  is instantaneous pressure, and  $P_{ave}$  is average pressure over the 20-s period under evaluation.

The concept behind application of a low pass filter (applied as a second order Butterworth filter function, similar to that provided in Eq. (4.1) although with different filter coefficients placing cutoff frequency at 30 Hz) is isolation of the oscillatory amplitude attributable to relevant physical (peak) oscillatory mode and elimination of any high-frequency sources which may be present. It is necessary to place filter cutoff frequency at such a high value due to the necessity of capturing peak frequencies for certain combinations of operating conditions which yield them at relatively high frequencies ( $\sim 20 \text{ Hz}$ ), something which will be discussed in subsequent sections.

After filtering transient pressure signals, Fig. 4.7(d) provides an example of detection of oscillatory amplitude, defined as half the maximum pressure value minus the minimum pressure value evaluated over the same 20-s period on which fast Fourier transforms are performed and shown in Fig. 4.7(a) (Figs. 4.7(c) and 4.7(d) only include 3 s of transient data to better highlight curve characteristics). It is important to note here that all cases evaluated in the current study correspond to steady-state operating conditions, meaning all fluctuations are about a constant,

time-averaged value, and the system is not undergoing any transient changes in operating conditions.

After detecting values of peak frequency and amplitude of oscillation for both inlet and outlet signals, these values are averaged to provide a single peak frequency and amplitude of oscillation for each set of operating conditions.

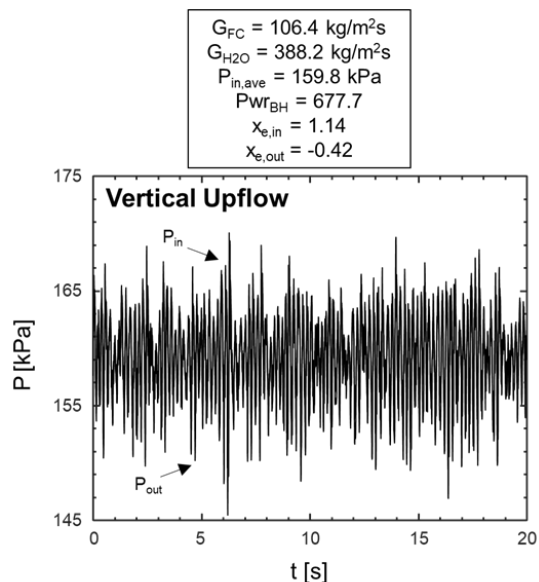


Figure 4.7: Plots showing detection methodology for peak frequency and amplitude of oscillation: (a) transient FC-72 inlet and outlet pressure signals for entire fast Fourier transform window, (b) associated FFTs with peak frequencies identified, as well as filter frequency (used in later steps) identified, (c) low-pass filtered pressure signals, and (d) amplitude detection using filtered signals.

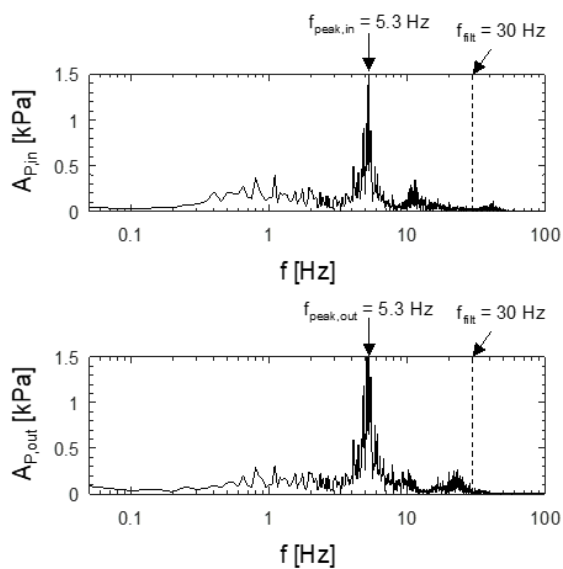


Figure 4.7 (b).

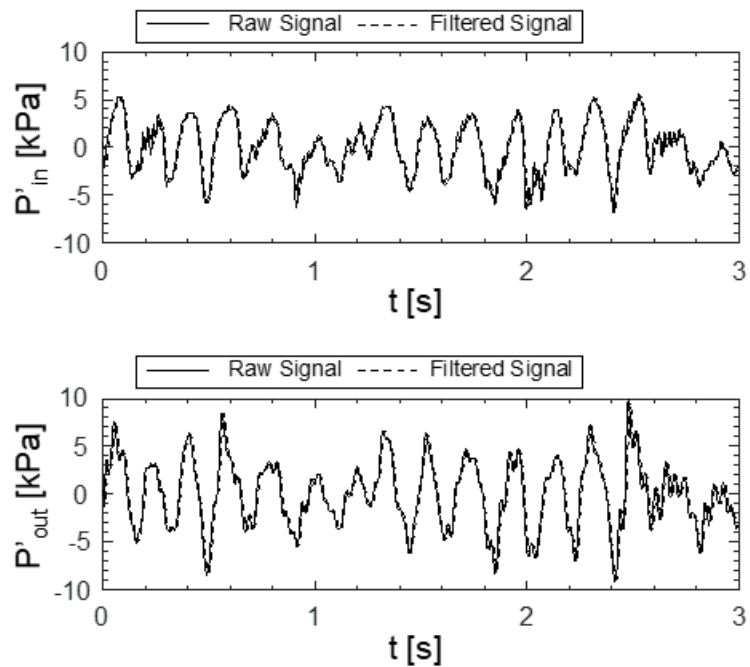


Figure 4.7 (c).

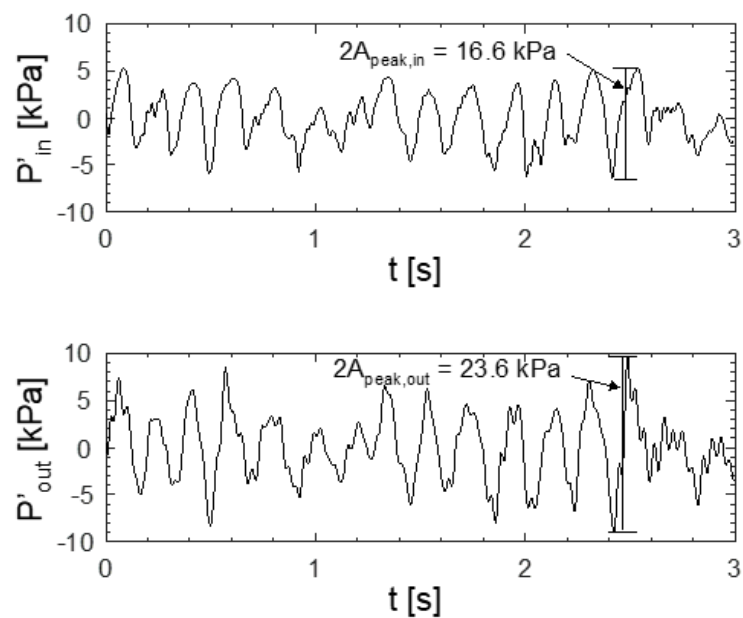


Figure 4.7 (d).

#### 4.1.2.1 Peak Frequency of Oscillation

Having described how peak frequency of oscillation is determined for each flow condensation case exhibiting a dominant oscillatory mode, it is possible to evaluate key physical factors governing changes in peak frequency across operating conditions. Figures 4.8(a) – 4.8(c) provide plots of peak frequency of oscillation versus FC-72 mass velocity, inlet quality, exit quality, and time-averaged inlet pressure for vertical upflow, vertical downflow, and horizontal flow, respectively (similar to Fig. 4.5 for  $Q$  Factor).

Figure 4.8(a) shows peak frequency values increasing slightly as mass velocity is increased. Changes in inlet quality appear to have little relationship to changes in frequency, although as exit quality increases frequency is seen to increase as well. Recalling the trend seen in Fig. 4.5(a) which showed  $Q$  values decreasing as exit quality increased, Fig. 4.8(a) implies frequency of peak oscillatory mode increases as the intensity of the oscillatory mode dies out. Inlet pressure appears to have no effect on peak frequency of oscillation.

Figure 4.8(b) provides similar plots for results obtained in vertical downflow orientation. Immediately noticeable when comparing results to those obtained for vertical upflow is the significant reduction in peak frequency of oscillation compared to those seen in vertical upflow (with most cases exhibiting  $f_{peak} = 1 - 5$  Hz in vertical downflow compared to  $f_{peak} = 5 - 15$  Hz in vertical upflow). This indicates that at minimum the oscillatory mode observed here is strongly dependent on body force, and possibly that different mechanisms are responsible for oscillatory behavior observed in vertical upflow and downflow orientations (reinforcing the conclusion drawn analyzing respective trends for  $Q$ ).

Analysis of individual plots in Fig. 4.8(b) again indicates a positive correlation between increases in mass velocity and increases in frequency of oscillation. Trends regarding inlet quality, exit quality, and inlet pressure are largely nonexistent. The presence of three outlier high-frequency measurements seen for high mass velocity, high pressure cases may represent a transition towards a new oscillatory mode for operating conditions not investigated in the current study, but, as sample size for these cases is small, time will not be spent speculating on factors responsible for their presence.

Finally, Fig. 4.8(c) shows only low frequency oscillations are detected for horizontal flow cases, with no appreciable trends present. This reinforces the idea presented when analyzing Figs.

4.5 and 4.6, that oscillations in horizontal flow are of minimal impact compared to those in vertical upflow and downflow orientations.

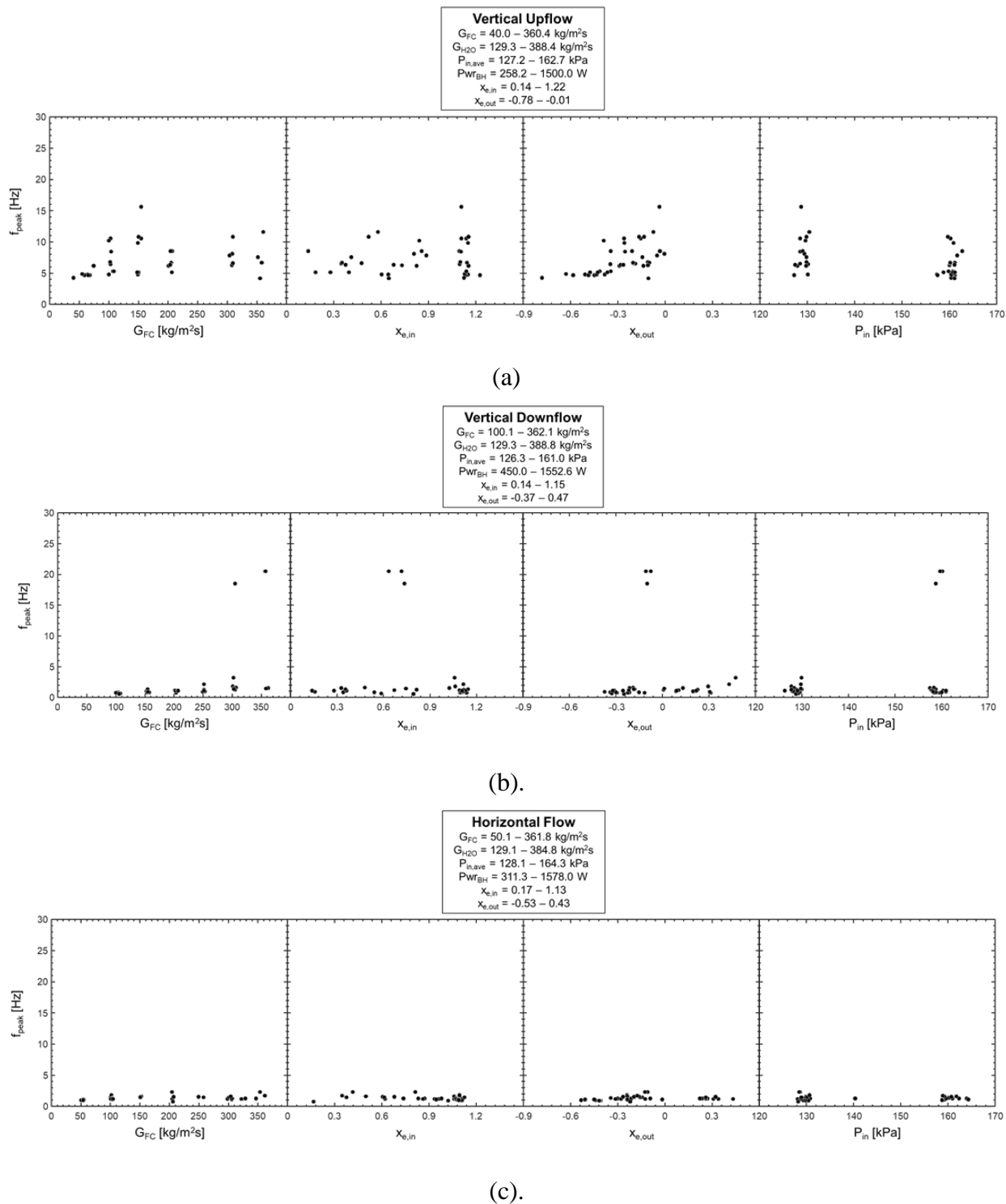


Figure 4.8: Plots of peak frequency of oscillation versus FC-72 mass velocity, inlet quality, exit quality, and inlet pressure, for all cases in (a) vertical upflow, (b) vertical downflow, and (c) horizontal flow orientations.

Figures 4.9(a) – 4.9(c) provide plots of peak frequency versus the same relevant dimensionless groups used in Fig. 4.6 for each orientation tested. Figure 4.9(a) shows that for vertical upflow peak frequency of oscillation is closely tied to increases in Reynolds, Weber, and Froude numbers calculated based on inlet conditions and vapor properties (see Eqs. (4.5) – (4.7)). Lack of correlation between peak frequency and dimensionless groups calculated based on channel exit conditions and liquid properties reinforces the idea presented when analyzing Fig. 4.6(a), that oscillatory behavior in vertical upflow orientation is closely tied to vapor flow at the test module inlet.

Figure 4.9(b) provides similar plots for vertical downflow orientation indicating slight positive relationships between peak frequency and dimensionless groups based on both inlet-vapor parameters and exit-liquid parameters. This is an intriguing result, as only parameters based on outlet conditions and liquid properties were shown to govern existence of a peak oscillatory mode in Fig. 4.6(b). Having eliminated cases with no clear oscillatory mode, Fig. 4.9(b) indicates peak frequency of oscillation is controlled by a combination of liquid and vapor behavior.

Figure 4.9(c) again shows little correlation between changes in operating conditions and differences in peak frequency of oscillation, further differentiating oscillatory behavior observed in horizontal orientation from that in vertical upflow and downflow orientations.

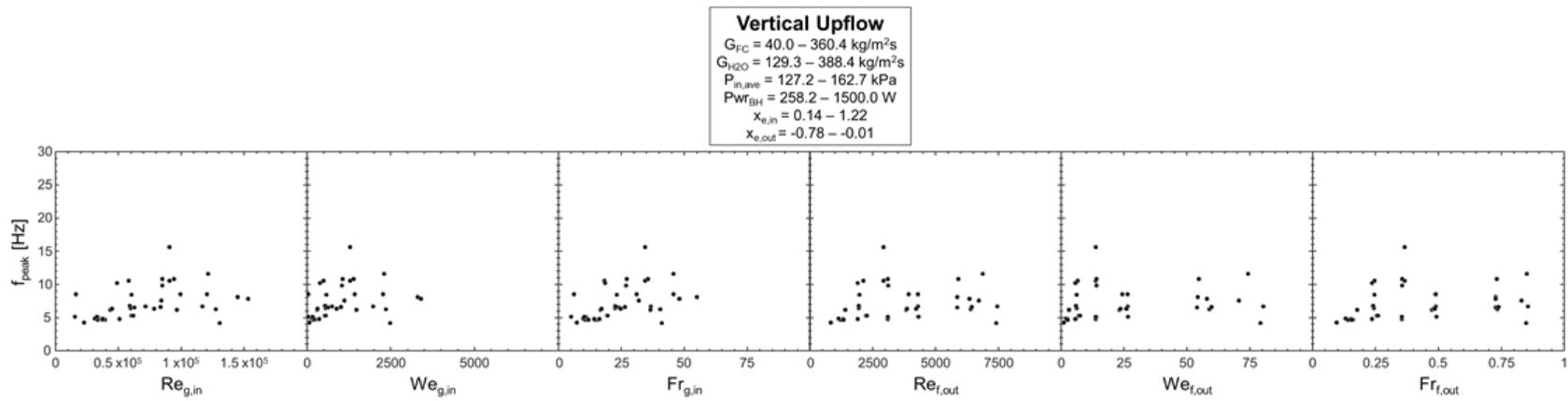


Figure 4.9: Plots of peak frequency of oscillation versus FC-72 inlet vapor Reynolds, Weber, and Froude numbers, and exit liquid Reynolds, Weber, and Froude numbers, for all cases in (a) vertical upflow, (b) vertical downflow, and (c) horizontal flow orientations.

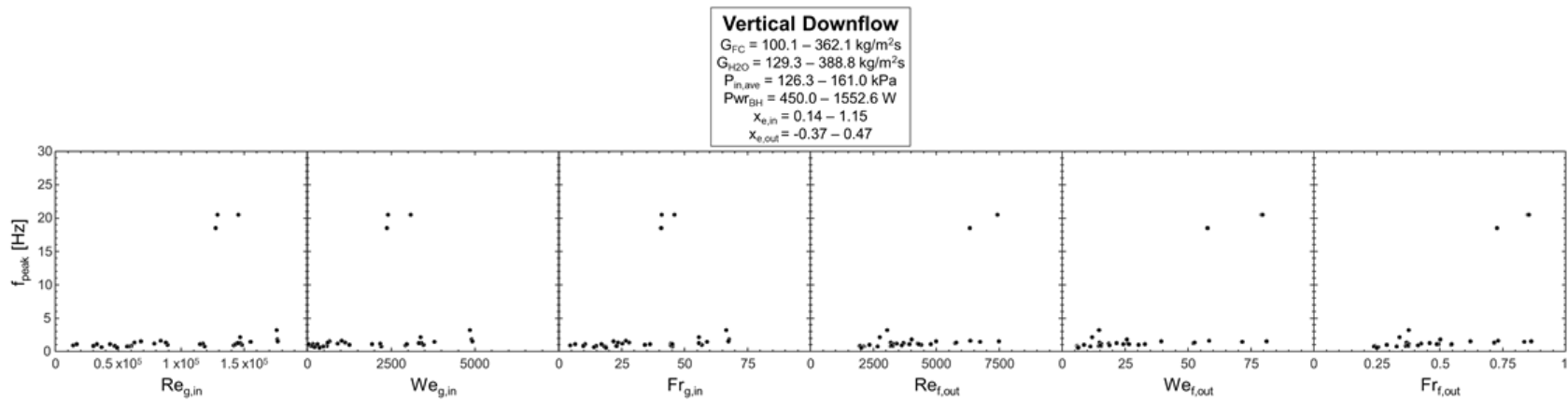


Figure 4.9 (b).

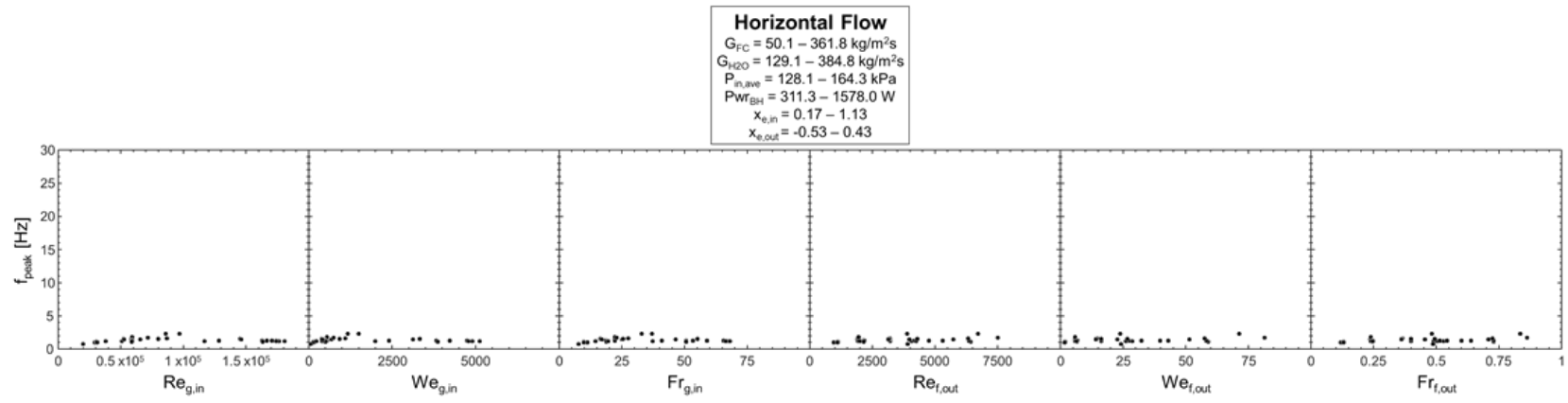


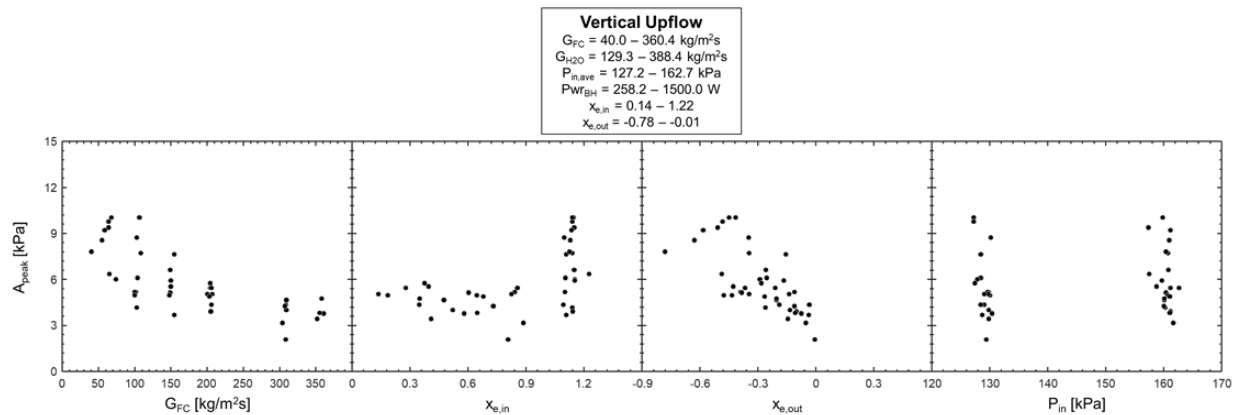
Figure 4.9 (c).

#### 4.1.2.2 Peak Amplitude of Oscillation

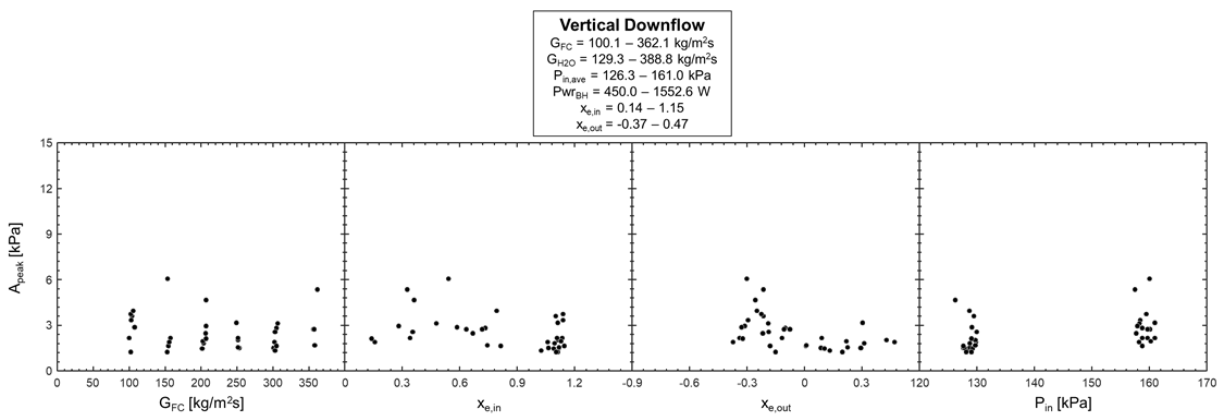
Similar to Figs. 4.5 and 4.8, Figs. 4.10(a) – 4.10(c) provide plots of amplitude versus FC-72 mass velocity, inlet quality, exit quality, and time-averaged inlet pressure for vertical upflow, vertical downflow, and horizontal flow, respectively. Figure 4.10(a) shows that amplitude of oscillation for cases in vertical upflow decreases as mass velocity increases, reflecting the trend for  $Q$  Factor seen in Fig. 4.5(a). -The highest amplitude cases are all observable for inlet qualities greater than  $x_{e,in} = 1.0$ , although there is not a smooth trend observable in the plot. This is likely due to a change in flow regime along the condensation length associated with higher qualities and low flowrates. Amplitude of oscillation shows a strong dependence on exit quality, decreasing as exit quality increases. This matches well with the trend seen in Fig. 4.5(a), which indicated intensity of the oscillatory mode decreased as exit quality increased. Little variation in amplitude is seen for changes in inlet pressure, indicating mass velocity and exit quality are primarily responsible for governing amplitude of oscillation in vertical upflow.

Figure 4.10(b) provides similar plots for vertical downflow orientation. Little variation in amplitude of peak oscillatory mode is seen for changes in FC-72 mass velocity, inlet quality, and inlet pressure, but as exit quality is increased amplitude is seen to decrease. This is likely due to reduced liquid content associated with higher exit quality cases leading to lower intensity (amplitude) pressure oscillations, and reflects a similar trend seen when analyzing changes in  $Q$  value in Fig. 4.5(b).

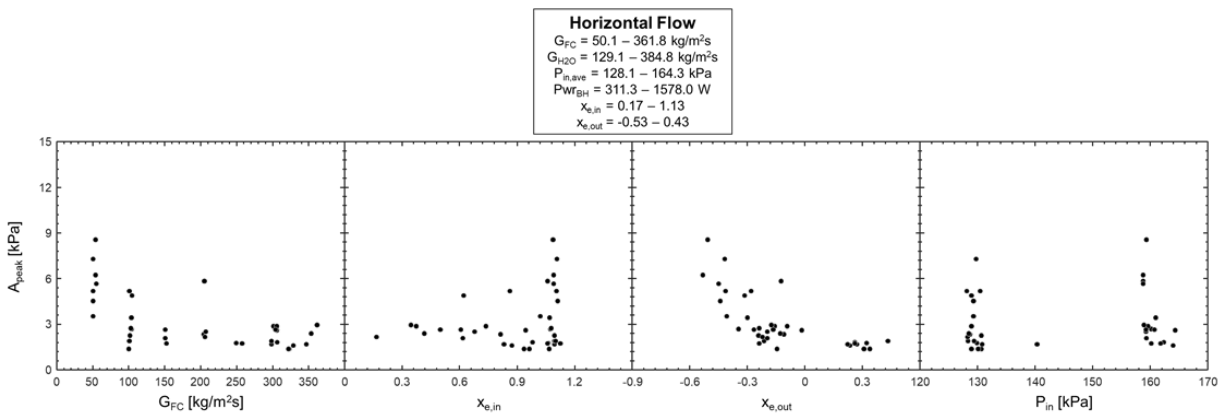
Figure 4.10(c) provides the first evidence of trends associated with pressure oscillations observed in horizontal orientation, with increases in mass velocity and exit quality leading to clear reductions in amplitude of oscillation, while increases in inlet quality lead to increases in amplitude of oscillation.



(a).



(b).



(c).

Figure 4.10: Plots of peak amplitude of oscillation versus FC-72 mass velocity, inlet quality, exit quality, and inlet pressure, for all cases in (a) vertical upflow, (b) vertical downflow, and (c) horizontal flow orientations.

Figures 4.11(a) – 4.11(c) conclude analysis of amplitude trends by providing plots of amplitude of peak oscillatory mode versus relevant dimensionless groups defined in Eqs. (4.5) – (4.10) for each orientation. Figure 4.11(a), corresponding to tests run in vertical upflow, shows amplitude decreasing for increases in each dimensionless group, although trends for groups based on inlet conditions and vapor properties are more linear than those based on exit conditions and liquid properties.

Figure 4.11(b), corresponding to cases run in vertical downflow orientation, shows amplitude of peak oscillatory mode decreasing for increases in dimensionless groups based on inlet conditions and vapor properties, while no clear trend is present for those based on exit conditions and liquid properties. This is counter to what was seen for both  $Q$  Factor and frequency, both of which exhibited stronger dependence on exit conditions and liquid properties for vertical downflow cases.

Finally, Fig. 4.11(c) illustrates asymptotic decreases in amplitude of peak oscillatory mode for increases in all dimensionless groups shown. This reinforces the trend first observed in Fig. 4.10(c), that mass velocity of condensing flow is the key parameter governing changes in amplitude of oscillation for horizontal flow, with other parameters playing a smaller role.

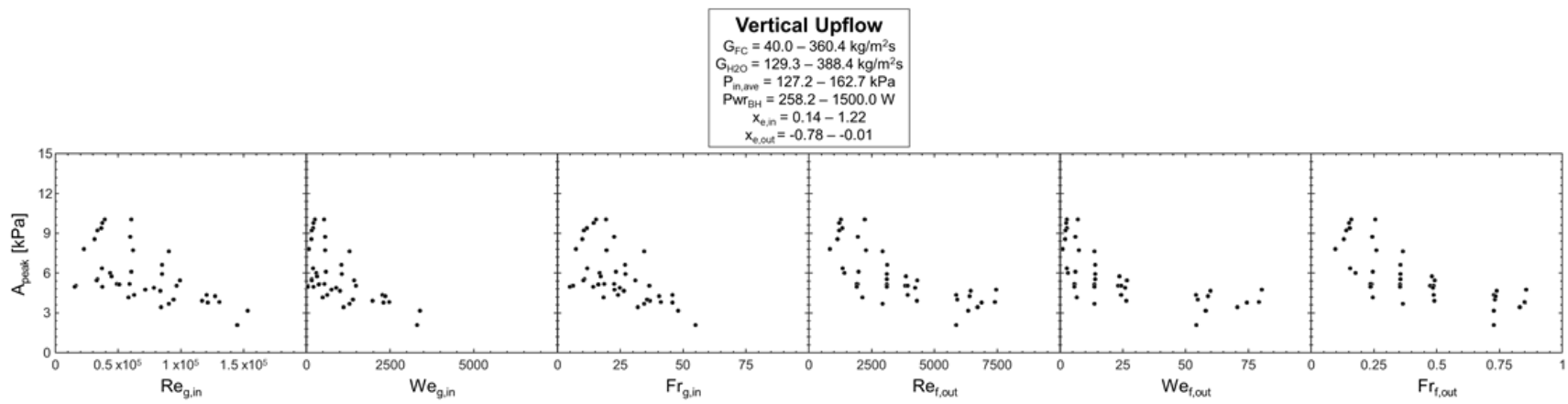


Figure 4.11: Plots of peak amplitude of oscillation versus FC-72 inlet vapor Reynolds, Weber, and Froude numbers, and exit liquid Reynolds, Weber, and Froude numbers, for all cases in (a) vertical upflow, (b) vertical downflow, and (c) horizontal flow orientations.

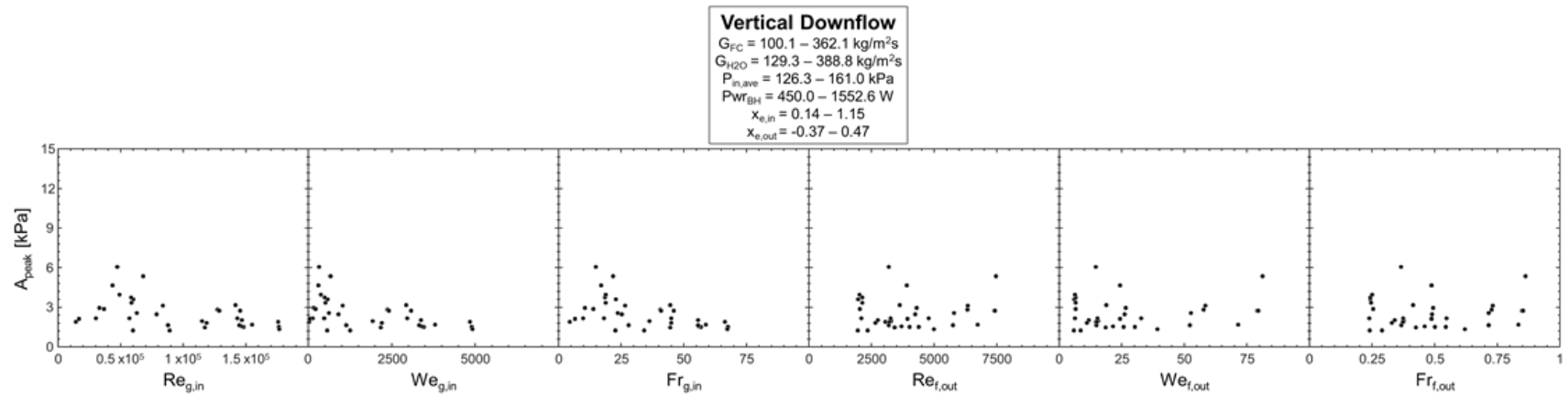


Figure 4.11 (b).

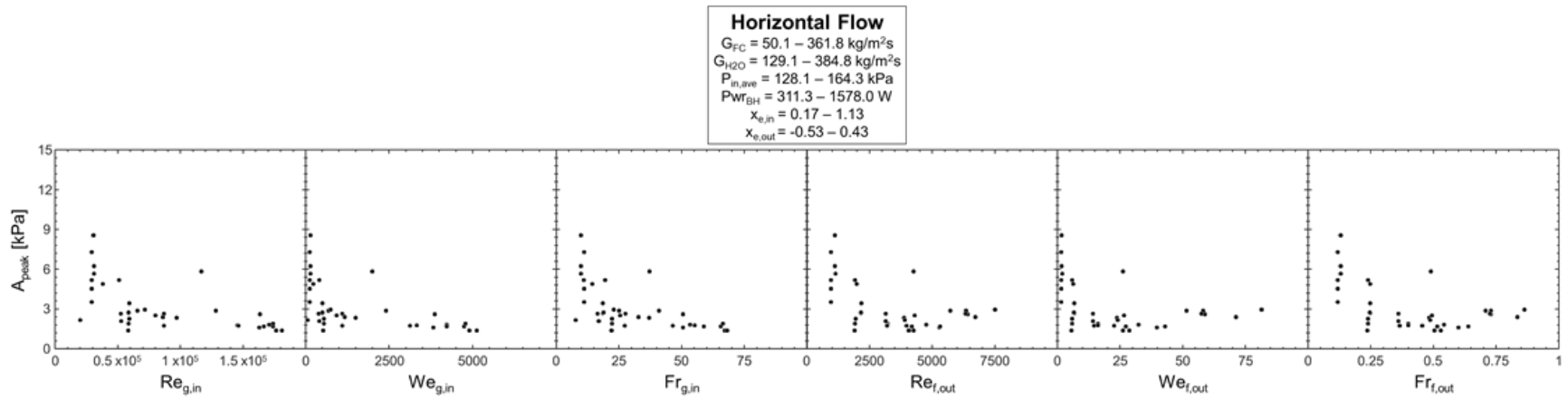


Figure 4.11 (c).

Across the three orientations shown in Figs. 4.10 and 4.11 it is notable that vertical downflow exhibits the lowest amplitude oscillations (on average), with low mass velocity cases in horizontal flow providing higher amplitudes than any encountered in vertical downflow, and vertical upflow clearly exhibiting the highest amplitudes of oscillation (on average) for the three orientations. This is reflected in evaluation of peak amplitude ratio for each orientation, defined as

$$\text{Peak Amplitude Ratio} = \max \left( \frac{A_{peak}}{P_{in,ave}} \right) \times 100\%, \quad (4.12)$$

which exhibits values of 7.9% for vertical upflow, 3.8% for vertical downflow, and 5.6% for horizontal flow.

Although this contradicts the conclusion drawn from analysis of  $Q$  Factor and peak frequency that horizontal flow exhibits the most stable behavior, it is not entirely unexpected due to the role of body force in stabilizing liquid film motion during vertical downflow condensation. It also matches reasonably well with the observations of Soliman and Berenson [101], who saw values of peak amplitude ratio less than 10% for vertical upflow and less than 5% for vertical downflow and horizontal flow orientations.

Having shown that different parameters affect characteristics of oscillatory behavior differently, it is important to recognize the inability of a single parameter to fully characterize oscillatory motion. Only by analyzing trends related to  $Q$  Factor (governing the ‘intensity’ of the oscillatory mode), frequency (the rate at which it occurs in time), and amplitude (the degree to which it changes local flow characteristics) together may a full picture of factors governing oscillatory behavior in flow condensation be obtained.

#### 4.1.2.3 Impact of Oscillatory Modes

It is possible to discuss relative impact of oscillatory modes by analyzing their  $Q$  Factors, frequencies, and amplitudes together. An oscillatory mode with high values of all three can be said to (1) be well described by a single frequency and amplitude (due to high  $Q$ ), and (2) exert a relatively large influence on system behavior and performance (due to high frequency and amplitude leading to rapidly changing local pressures). The opposite is true for cases with low values of all three parameters.

Figures 4.12(a) – 4.12(c) provide plots of peak frequency versus  $Q$  Factor, amplitude of peak oscillatory mode versus  $Q$  Factor, and frequency versus amplitude, respectively, for all orientations tested. Figure 4.12(a) shows much wider ranges of both  $Q$  Factor and peak frequency are encountered in vertical upflow orientation compared to vertical downflow (neglecting outlying cases) and horizontal flows. Additionally, a small decrease in frequency is apparent for vertical upflow as  $Q$  increases, indicating lower frequency oscillatory modes may be more well defined. No clear trends are present for vertical downflow and horizontal flow orientations.

Figure 4.12(b) indicates that, for both vertical upflow and downflow orientations, higher values of  $Q$  are seen for cases with higher amplitude oscillations. This makes intuitive sense based on how  $Q$  Factor is calculated, as higher amplitude peaks on the frequency response will lead to higher  $Q$  values as well as higher amplitude oscillations observed in pressure signals. The fact that higher  $Q$  leads to higher amplitude in these two cases does not have to be true (*e.g.*, multiple lower and/or distributed peaks could lead to high amplitude with low  $Q$ ), however, and that it indicates oscillatory behavior observed in pressure curves is the result of a single physical mechanism. The lack of observable trend for horizontal flow, meanwhile, further reinforces the idea that no single, clear mechanism is present behind oscillations observed in this orientation.

Figure 4.12(c) shows plots of peak frequency versus amplitude for all three orientations. Vertical upflow once again exhibits the most dynamic (meaning large frequencies and amplitudes of oscillation) behavior, but the lack of trends for each plot indicates factors governing frequency of oscillation are independent from those determining amplitude. This is an important conclusion, as it indicates fundamentally different instability mode from that recently analyzed for flow boiling [53-56].

Overall, trends for key parameters characterizing oscillatory behavior exhibit clear differences for near-identical operating conditions (flow rate, pressure, quality) depending on orientation. Table 4.1 provides a summary of trends for each combination of key parameter and orientation, as well as general observations about oscillatory behavior observed in each orientation.

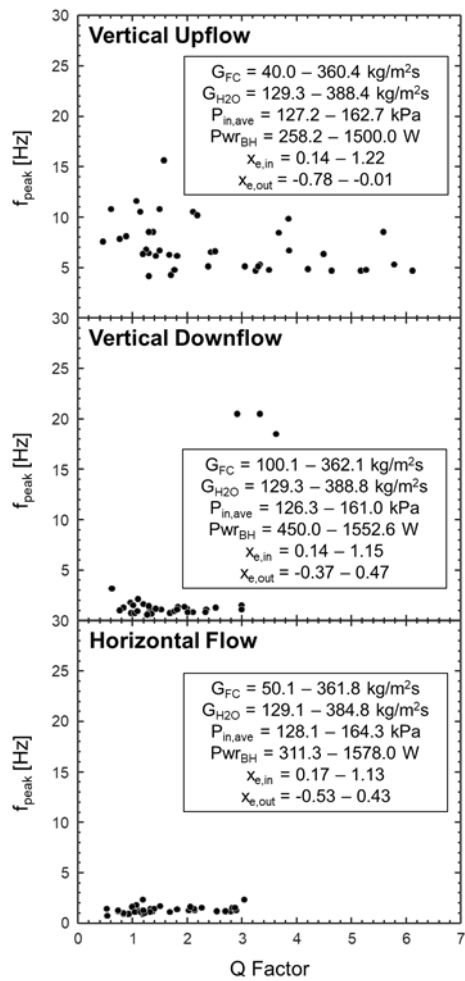


Figure 4.12: Plots of (a) peak frequency of oscillation versus  $Q$  factor, (b) amplitude of peak oscillation versus  $Q$  factor, and (c) peak frequency versus peak amplitude for vertical upflow, vertical downflow, and horizontal flow orientations.

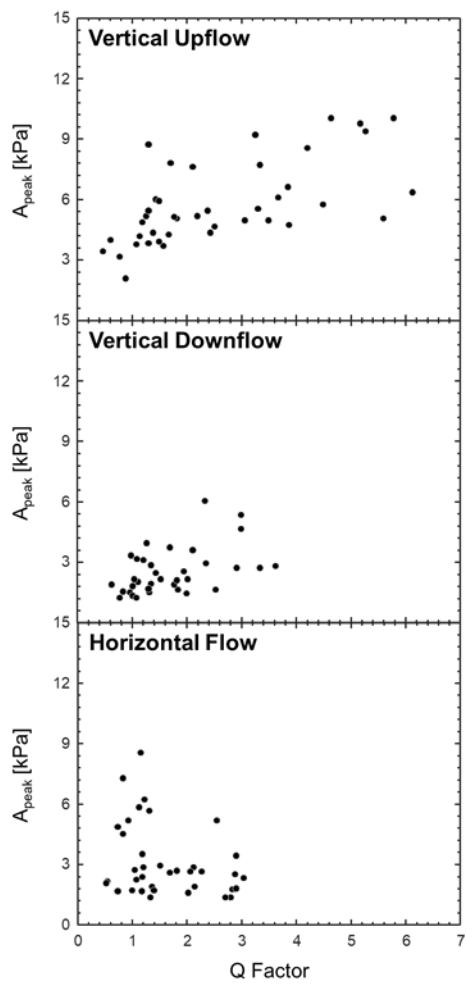


Figure 4.12 (b).

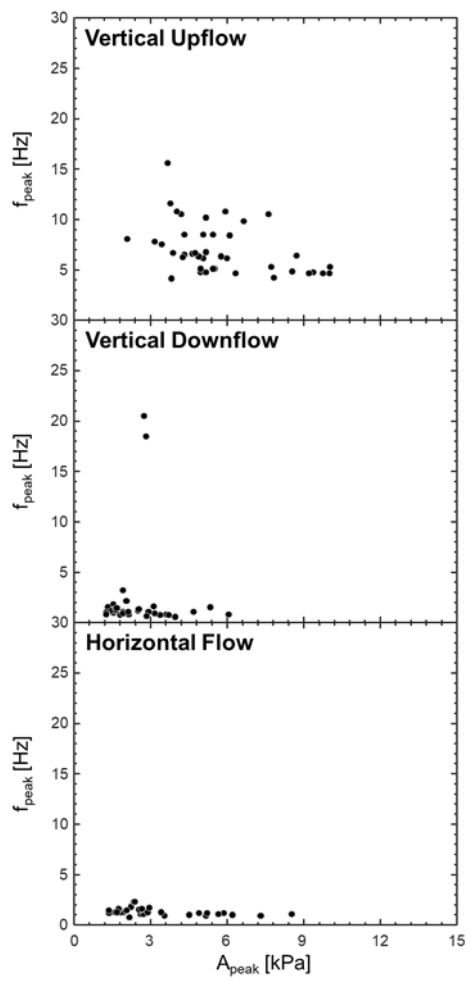


Figure 4.12 (c).

Table 4.1: Summary of trends governing oscillatory behavior in each orientation.

Parameter	Vertical Upflow	Vertical Downflow	Horizontal Flow
$Q$	<ul style="list-style-type: none"> <li>Decreases with increasing <math>G_{FC}</math>, <math>x_{e,in}</math></li> <li>Strong dependence on inlet vapor conditions, weak dependence on exit liquid conditions</li> </ul>	<ul style="list-style-type: none"> <li>Increases with increasing <math>G_{FC}</math></li> <li>Only exhibits dependence on exit liquid conditions</li> </ul>	<ul style="list-style-type: none"> <li>No clear trends</li> <li>Lowest <math>Q</math> values and highest percentage of <math>Q = 0</math> cases of three orientations</li> </ul>
$f_{peak}$	<ul style="list-style-type: none"> <li>Increases with increasing <math>G_{FC}</math></li> <li>Only exhibits dependence on inlet vapor conditions</li> </ul>	<ul style="list-style-type: none"> <li>Increases with increasing <math>G_{FC}</math></li> <li>Shows slight correlation with inlet vapor and exit liquid parameters</li> </ul>	<ul style="list-style-type: none"> <li>No clear trends</li> <li>Lowest frequency values observed among three orientations</li> </ul>
$A_{peak}$	<ul style="list-style-type: none"> <li>Decreases with increasing <math>G_{FC}</math>, may increase with <math>x_{e,in}</math></li> <li>Dependence on both inlet vapor and exit liquid parameters</li> </ul>	<ul style="list-style-type: none"> <li>Decreases with increasing <math>x_{e,out}</math></li> <li>Only exhibits dependence on inlet vapor parameters</li> <li>Lowest amplitude oscillations of three orientations</li> </ul>	<ul style="list-style-type: none"> <li>Decreases with increasing <math>G_{FC}</math></li> <li>Strong dependence on both inlet vapor and exit liquid parameters</li> </ul>
General Observations	<ul style="list-style-type: none"> <li>Highest percentage of cases exhibiting dominant oscillatory mode, 72%</li> <li>Highest peak amplitude ratio, 7.9%</li> <li>Highest average frequency values</li> <li>Overall, most dynamic orientation</li> </ul>	<ul style="list-style-type: none"> <li>61% of cases exhibiting dominant oscillatory mode</li> <li>Lowest peak amplitude ratio, 3.8%</li> <li>Overall, appreciable dynamic behavior observed, but at low amplitude</li> </ul>	<ul style="list-style-type: none"> <li>Lowest percentage of cases exhibiting dominant oscillatory mode, 54%</li> <li>Moderate peak amplitude ratio, 5.6%</li> <li>Overall, least dynamic behavior observed</li> </ul>

#### 4.1.3 Relationship to Observed Interfacial Behavior

Although analysis of experimental pressure data clearly shows the presence of oscillatory modes in flow condensation, evaluation of their characteristics is incomplete without some

commentary on physical mechanisms leading to their formation. Although flow visualization images captured correspond to external flow condensation (as discussed in Section 2) and all results analyzed thus far have been for internal flow, it is expected that key behavior at the interface between liquid film and vapor flow will be similar for the two configurations. Differences in liquid film and interfacial behavior have been discussed in previous work as the key feature influenced by body force which may lead to differences in condensation behavior [136,137], and it will be analyzed in that context again here.

Figure 4.13 presents flow visualization image sequences captured using the condensation module for flow visualization (CM-FV) corresponding to horizontal flow with  $G_{FC} = 82.9 \text{ kg/m}^2\text{s}$ ,  $G_{H2O} = 696.8 \text{ kg/m}^2\text{s}$ ,  $P_{FC,in} = 123.1 \text{ kPa}$ , and  $x_{e,in} = 1.15$ , with consecutive images in each sequence separated by 0.0075 s. Figures 4.13(a) – 4.13(c) correspond to imaging locations centered near the inlet ( $z = 28 \text{ mm}$ ), at the center of the channel ( $z = 294 \text{ mm}$ ), and at the channel exit ( $z = 560 \text{ mm}$ ), respectively.

Figure 4.13(a) shows that, for the case with slightly superheated inlet conditions, a thin liquid film covers the stainless-steel tube (condensation surface) in the upstream portion of the channel. This film shows clear signs of interfacial waves, formed by flow of vapor in the annulus past liquid. Also important to note is the slight increase in thickness of the liquid film towards the bottom of the stainless steel tube, illustrating gravity's influence on film behavior in horizontal flow, something which becomes more noticeable in later subfigures.

Figure 4.13(b) provides similar image sequences, this time captured at the center of the channel. It is apparent that by the time flow reaches the middle of the channel significantly more vapor has condensed into liquid than seen in Fig. 4.13(a). Due to this liquid buildup and the tendency of body force to drive stratification in horizontal flow (with liquid occupying the bottom of the channel and vapor the top), the liquid film initially formed on the inner stainless steel tube has begun to drop from the tube and occupy the bottom surface of the annulus. Images in Fig. 4.13(b) clearly show bridging between liquid on the bottom of the inner tube (condensing surface) and the liquid now flowing along the bottom wall of the annulus. Interfacial waves are also clearly visible along both liquid films, indicating the presence of high-velocity vapor flowing between the two.

Figure 4.13(c) continues this analysis by providing images captured at the outlet of the channel. Liquid content present in the channel has further increased by this point, with the majority

of liquid present at the bottom wall of the annulus, along which large waves appear and flow towards the channel exit.

Across all subfigures shown in Fig. 4.13, it is apparent that flow dynamic behavior (seen here as interfacial waves, bridging, and film breakup effects) increases as liquid content within the channel increases. Orientation effects in horizontal flow drive stratification of liquid and vapor phases, which leads to the production of interfacial waves, but does not significantly disturb the motion of either liquid or vapor phase, something which is not the case for flow in other orientations.

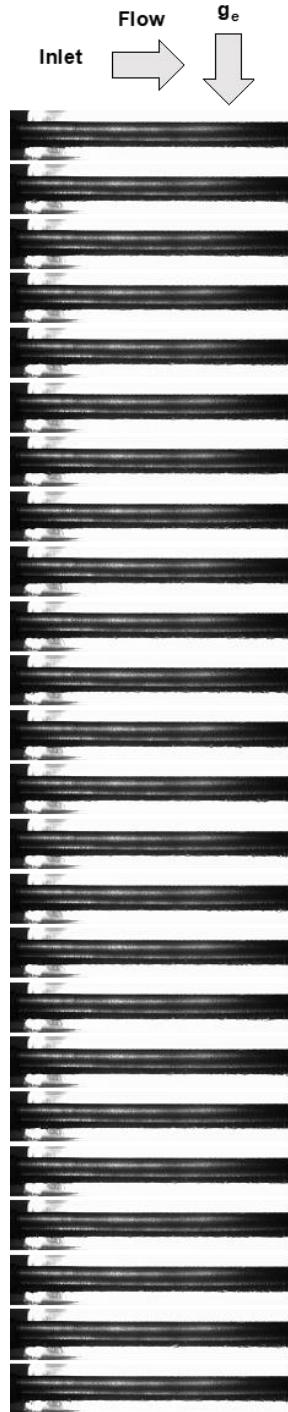


Figure 4.13: Sequential images of horizontal flow with  $G_{FC} = 82.9 \text{ kg/m}^2\text{s}$ ,  $G_{H_2O} = 696.8 \text{ kg/m}^2\text{s}$ ,  $P_{FC,in} = 123.1 \text{ kPa}$ ,  $P_{WRBH} = 1361.9$ , and  $x_{e,in} = 1.15$ , centered (a) near the inlet ( $z = 28 \text{ mm}$ ), (b) at the middle of the channel ( $z = 294 \text{ mm}$ ), and (c) near the exit ( $z = 560 \text{ mm}$ ), with individual images in each sequence separated by  $0.0075 \text{ s}$ .

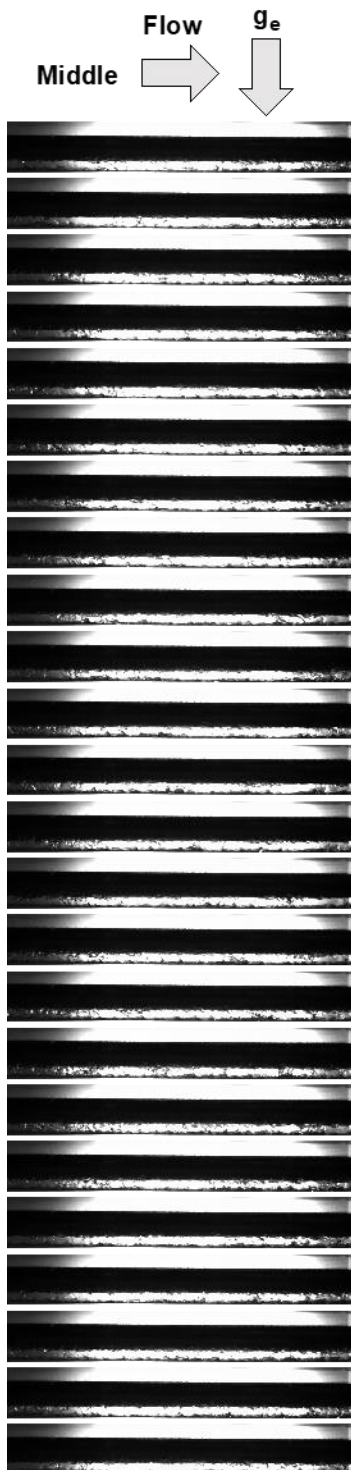


Figure 4.13 (b).

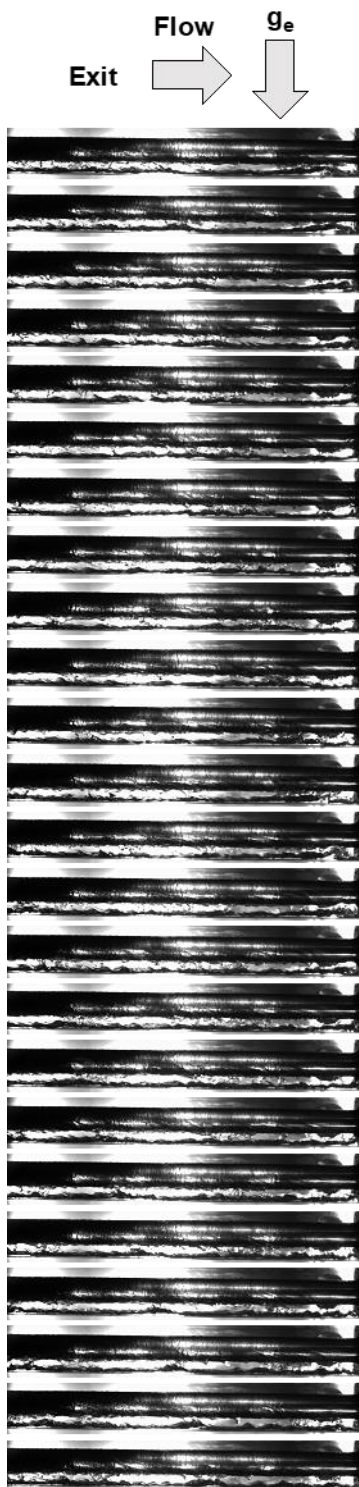


Figure 4.13 (c).

Figure 4.14 provides image sequences for vertical downflow condensation captured at the center ( $z = 294$  mm) of the channel, corresponding to conditions of (a)  $G_{FC} = 34.6$  kg/m<sup>2</sup>s,  $G_{H_2O} = 926.1$  kg/m<sup>2</sup>s,  $P_{FC,in} = 130.1$  kPa, and  $x_{e,in} = 1.10$ , (b)  $G_{FC} = 33.6$  kg/m<sup>2</sup>s,  $G_{H_2O} = 931.8$  kg/m<sup>2</sup>s,  $P_{FC,in} = 130.5$  kPa, and  $x_{e,in} = 0.68$ , and (c)  $G_{FC} = 34.2$  kg/m<sup>2</sup>s,  $G_{H_2O} = 934.7$  kg/m<sup>2</sup>s,  $P_{FC,in} = 130.0$  kPa, and  $x_{e,in} = 0.38$ . The key difference to note across subfigures is the value of inlet quality, decreasing from  $x_{e,in} = 1.10$  in (a), to  $x_{e,in} = 0.68$  in (b), and  $x_{e,in} = 0.38$  in (c). Consecutive images are again separated by 0.0075 s.

Figure 4.14(a) shows that, for the case with superheated vapor at the inlet of the channel, little liquid is seen along the stainless-steel tube (condensation surface) at the channel midpoint. What little liquid is present shows signs of interfacial waves, although significantly fewer than were seen in Fig. 4.13 for horizontal flow.

Figure 4.14(b), corresponding to saturated mixture inlet conditions with high quality (low liquid content), exhibits more noticeable interfacial behavior at the channel midpoint due to the larger amount of liquid present within the system. Also important to note is the presence of a small number of liquid droplets entrained in the vapor flow in this case (difficult to observe due to focus of the imaging configuration on capturing interfacial behavior), indicating the increased liquid content within the channel is leading to more dynamic film behavior. It is expected that for higher mass velocities this dynamic behavior would be increased.

Significantly different features are present in Fig. 4.14(c), corresponding to the lowest inlet quality conditions shown here. Immediately noticeable is the presence of a transition to bulk liquid flow roughly three quarters of the way down the images. Liquid film accumulated along the condensing length is seen to impinge on this solid liquid surface, leading to vapor entrainment within the liquid. Vapor motion within the liquid appears to be largely neutral, likely due to buoyancy force opposing bulk fluid inertia for this entrained vapor.

Although the sharp transition from annular flow condensation along the tube to bulk liquid flow is likely an artifact of the external flow configuration used for CM-FV, and is not expected for internal flow analyzed in CM-HT, the key features of (1) liquid film breakup and droplet impingement, and (2) impact of liquid waves on the solid liquid surface may explain much of the dynamic behavior observed for vertical downflow cases in the preceding sections. The second feature agrees well with the idea proposed by Soliman and Berenson, that pressure fluctuations

observed in horizontal and vertical downflow orientations are due to waves striking the vapor-liquid interface [101].

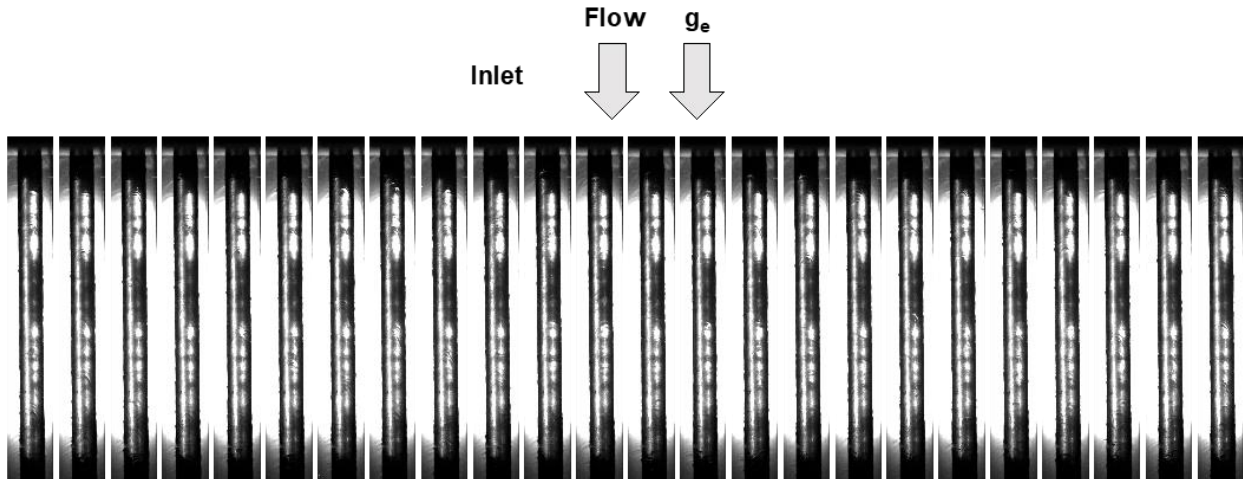


Figure 4.14: Sequential images of vertical downflow at the middle region (centered at  $z = 294$  mm) with (a)  $G_{FC} = 34.6$  kg/m<sup>2</sup>s,  $G_{H_2O} = 926.1$  kg/m<sup>2</sup>s,  $P_{FC,in} = 130.1$  kPa,  $P_{WRBH} = 570.3$  W, and  $x_{e,in} = 1.10$ , (b)  $G_{FC} = 33.5$  kg/m<sup>2</sup>s,  $G_{H_2O} = 931.8$  kg/m<sup>2</sup>s,  $P_{FC,in} = 130.5$  kPa,  $P_{WRBH} = 416.7$  W, and  $x_{e,in} = 0.68$ , and (c)  $G_{FC} = 34.2$  kg/m<sup>2</sup>s,  $G_{H_2O} = 934.7$  kg/m<sup>2</sup>s,  $P_{FC,in} = 130.0$  kPa,  $P_{WRBH} = 323.4$  W, and  $x_{e,in} = 0.38$ , with individual images in each sequence separated by 0.0075 s.

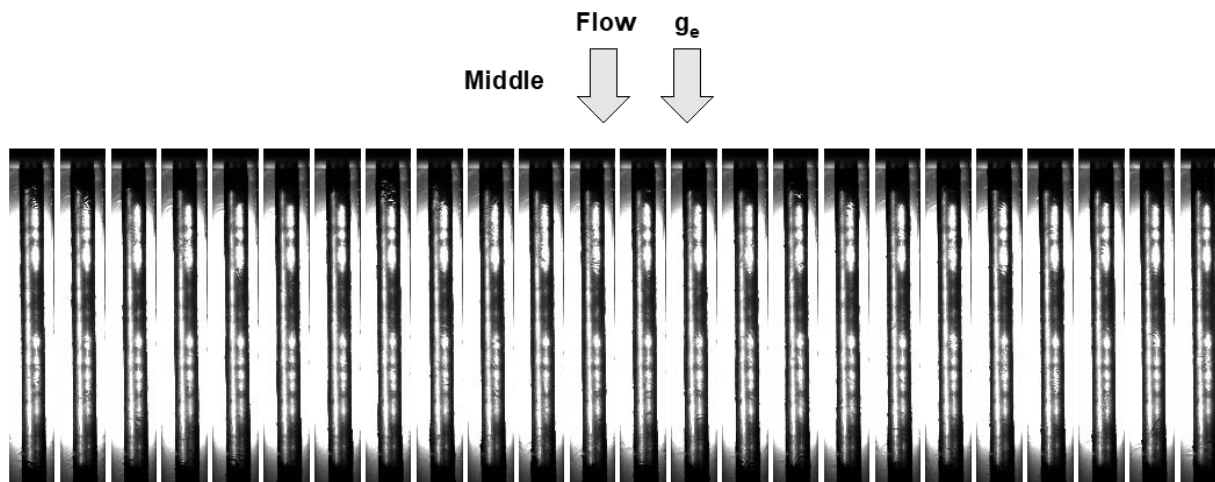


Figure 4.14 (b).

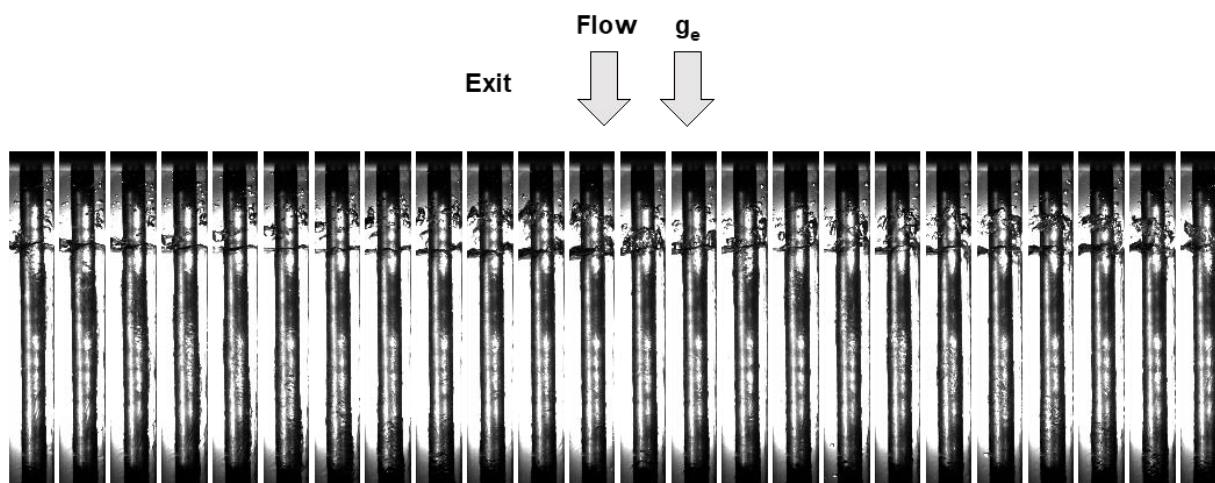


Figure 4.14 (c).

Flow visualization images corresponding to vertical upflow orientation were not captured using CM-FV due to time constraints on testing, but to present representative behavior for similar operating conditions, Fig. 4.15 has been adapted from the work of Park and Mudawar [93]. Their work involved investigation of vertical upflow condensation using FC-72 as working fluid in a smooth circular tube with comparable hydraulic diameter and condensation length to that used in the present study. Their original experimental work should be consulted for additional details.

Subfigures in Fig. 4.15 correspond to cases with slightly superheated inlet conditions and (a)  $G_{FC} = 13.32 \text{ kg/m}^2\text{s}$  and  $G_{H_2O} = 6.09 \text{ kg/m}^2\text{s}$ , (b)  $G_{FC} = 53.29 \text{ kg/m}^2\text{s}$  and  $G_{H_2O} = 73.36 \text{ kg/m}^2\text{s}$ , and (c)  $G_{FC} = 106.45 \text{ kg/m}^2\text{s}$  and  $G_{H_2O} = 97.79 \text{ kg/m}^2\text{s}$ , captured at distances of  $z = 190 \text{ mm}$ ,  $z =$

190 mm, and  $z = 952$  mm from the start of the condensation length, respectively. They primarily serve to characterize the impact of increasing mass velocity on liquid film behavior in vertical upflow orientation. This includes *falling film* behavior for very low mass velocities (where body force is much stronger than flow inertia, causing the liquid film to move counter to bulk flow and resulting in significant breakup and entrainment effects), *flooding* at moderate mass velocities (where liquid film is largely stationary), and *climbing film* at high mass velocities (where interfacial shear provided by the fast-moving vapor core is sufficient to overcome body force and advect the liquid film along the channel).

The key takeaway across these three subfigures is the role of increased mass velocity acting to stabilize liquid film behavior in vertical upflow orientation. This matches well with trends seen in sections 4.1.1 and 4.1.2, which indicated a strong dependence of flow stability on increased mass velocity in vertical upflow orientation.

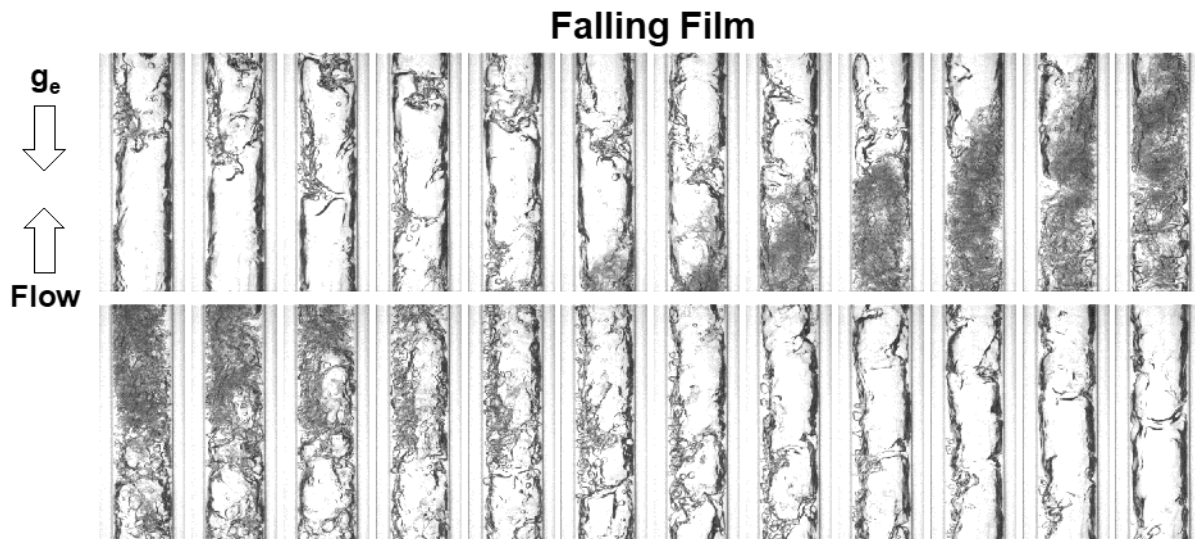


Figure 4.15: Sequential images of (a) falling film in inlet region (centered at  $z = 190$  mm) with  $G_{FC} = 13.32$  kg/m<sup>2</sup>s and  $G_{H_2O} = 6.09$  kg/m<sup>2</sup>s, (b) flooding in inlet region with  $G_{FC} = 53.29$  kg/m<sup>2</sup>s and  $G_{H_2O} = 73.36$  kg/m<sup>2</sup>s, and (c) climbing film in outer region (centered at  $z = 952$  mm) with  $G_{FC} = 106.45$  kg/m<sup>2</sup>s and  $G_{H_2O} = 97.79$  kg/m<sup>2</sup>s, with individual images in each sequence separated by 0.0125 s. Adapted from [93].

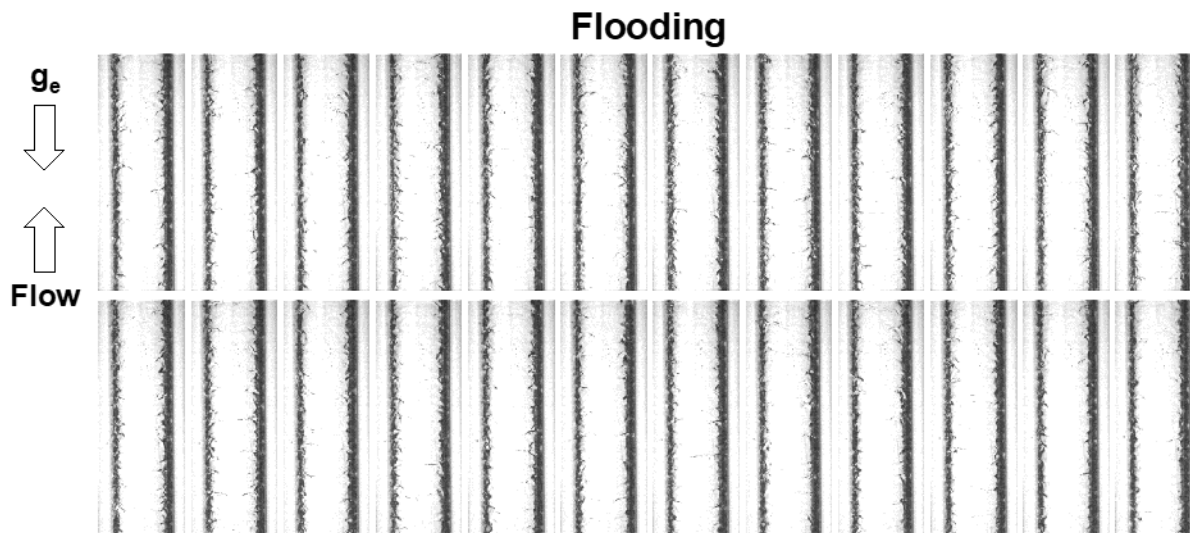


Figure 4.15 (b).

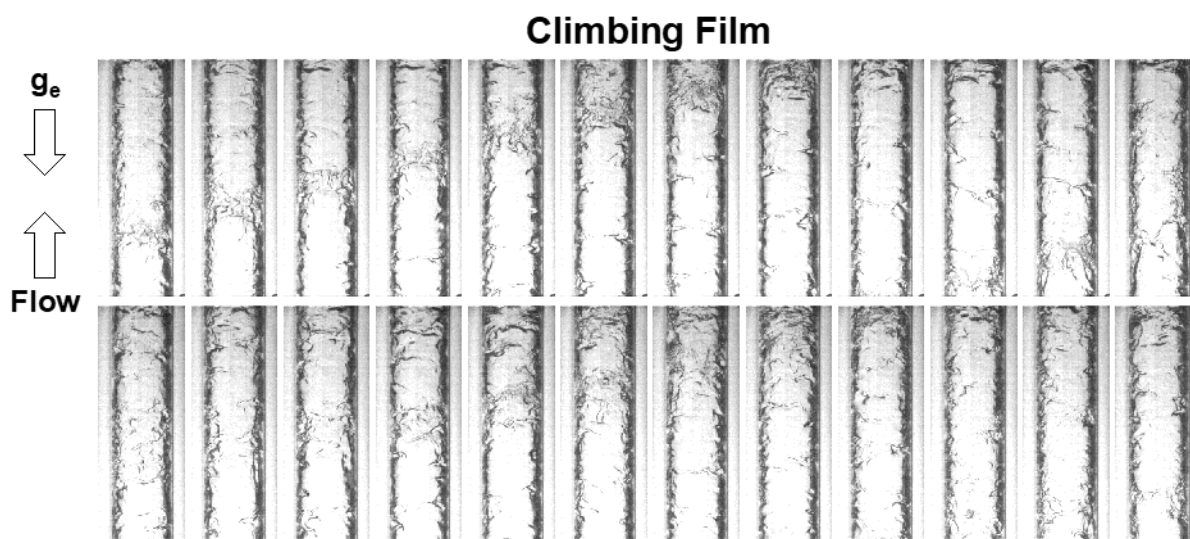


Figure 4.15 (c).

Across all three orientations, agreement between parametric trends evaluated in Sections 4.1.1 and 4.1.2 and conclusions drawn from qualitative analysis of corresponding flow visualization image sequences reveals a strong correlation between measured pressure oscillatory modes and observed liquid film behavior. Future work centering on a more thorough parametric

analysis of flow visualization image sequences and simultaneous pressure measurements may lead to establishment of a physical basis for observed oscillatory modes in each orientation.

Important to note at this point is a departure from one of the core ideas proposed by Soliman and Berenson [101], that oscillatory behavior observed in vertical downflow and horizontal flow orientations is due to the same mechanism (wave impact on the liquid-vapor interface). Based on differences observed in parametric trends for  $Q$ ,  $f_{peak}$ , and  $A_{peak}$ , as well as differences in liquid film behavior seen in flow visualization image sequences, it is not clear that oscillatory modes in these two orientations are due to the same mechanism. In fact, analysis performed here indicates the existence of distinct oscillatory modes for each of the three orientations investigated.

## 4.2 Identification of Condensation Flow Regime at Different Orientations using Temperature and Pressure Measurements

### 4.2.1 Condensate Liquid Distribution

As mentioned in the introduction, condensation flow regimes describe distribution of liquid and vapor phases within the condensation length, with transition criteria and associated regime maps available in the literature providing guidelines for what distribution may be expected for different ranges of operating conditions. Prior to analyzing the specifics of liquid film distribution for commonly defined flow regimes (*i.e.*, circumferentially uniform *annular* flow or liquid pooling near the bottom in *stratified* flow), it is useful to first discuss qualitative changes in flow behavior in response to competing influences of body force and flow inertia in different orientations. As a good summary of this has been provided in section 4.1.3, it will not be replicated here.

#### 4.2.1.1 Summary of Qualitative Trends for Condensate Liquid Behavior

In all flow visualization image sequences presented in the preceding subsection, the dominant competing effects were seen to be those of flow inertia (related to liquid flowrate) and body force (differing based on channel orientation). Figure 4.16 presents schematics summarizing the effects competing influences of body force and flow inertia have on liquid distribution within the condensation length.

Figure 4.16(a) provides a schematic for vertical upflow condensation. The left-hand figure shows how, at any given axial location along the condensation length, liquid film distribution is expected to be circumferentially symmetric. This is due to body force acting directly opposite to

fluid motion, meaning while it affects liquid motion as it travels through the channel, it does not bias liquid to any particular location along the tube circumference.

The schematics in Fig. 4.16(a) illustrating axial flow characteristics (to the right of the axial cut discussed in the previous paragraph) illustrate how body force impacts transport behavior within the channel. At high mass flows, interfacial shear provided by the fast-moving vapor core is sufficient to advect liquid along the channel, and annular co-current flow (*climbing film*) is established. At low mass velocities, however, film motion may stagnate or even move counter to the direction of vapor flow, meaning periodic effects such as film breakup and droplet entrainment become important for liquid transport through the condensation channel. Flow regimes encountered for low mass velocities include *flooding*, *oscillating film*, and *falling film*.

Figure 4.16(b) provides similar schematics for vertical downflow condensation. Similar to Fig. 4.16(a), the circumferential distribution of liquid is seen to be axisymmetric due to body force acting parallel to flow direction. Dissimilar from Fig. 4.16(a), however, is the fact that no appreciable differences in film motion are seen for low versus high mass flowrates. By acting in the same direction as fluid motion, body force has a stabilizing effect on liquid film motion, ensuring *annular co-current* flow for all operating conditions.

Figure 4.16(c) uses an additional schematic for circumferential distribution to highlight how flow rate affects liquid distribution in horizontal flow condensation. For high mass flows, liquid film spreads evenly around the channel circumference, leading to *annular co-current* flow similar to that seen in vertical downflow orientation. At low mass flowrates body force drives liquid film to accumulate in the bottom of the channel, leading to flow regimes including *stratified*, *stratified wavy*, and *plug* flow regimes.

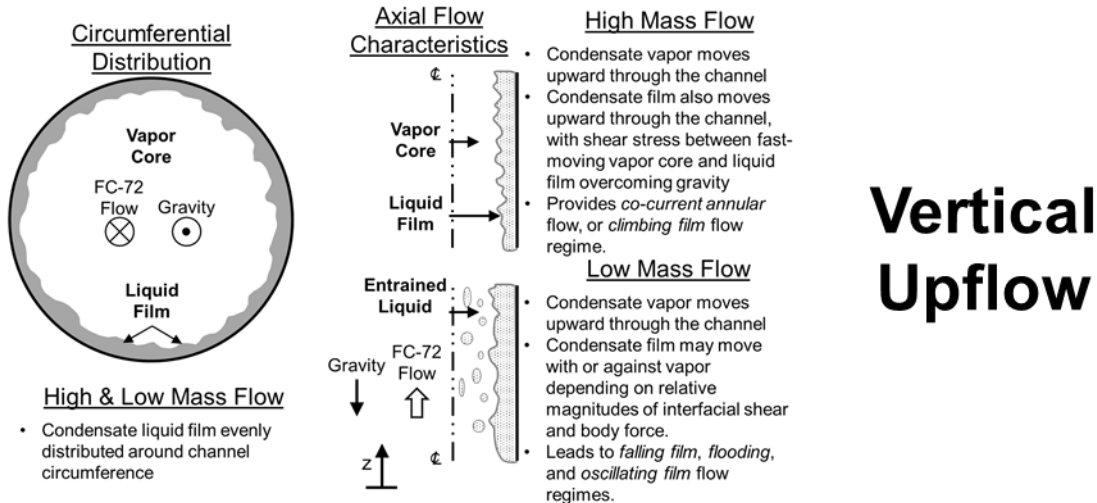


Figure 4.16: Schematics of liquid film circumferential distribution and axial flow characteristics for (a) vertical upflow, (b) vertical downflow, and (c) horizontal flow orientations.

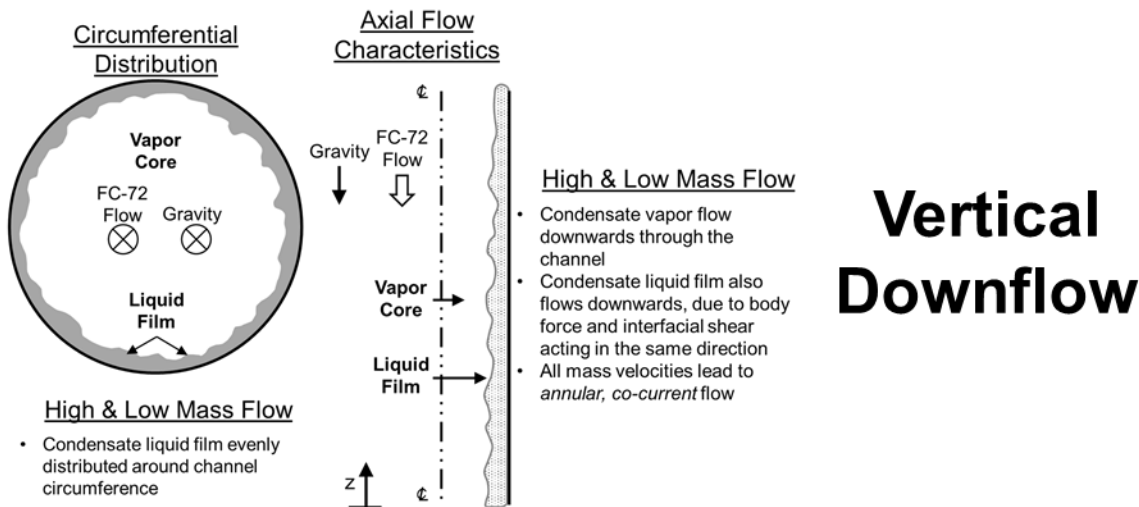
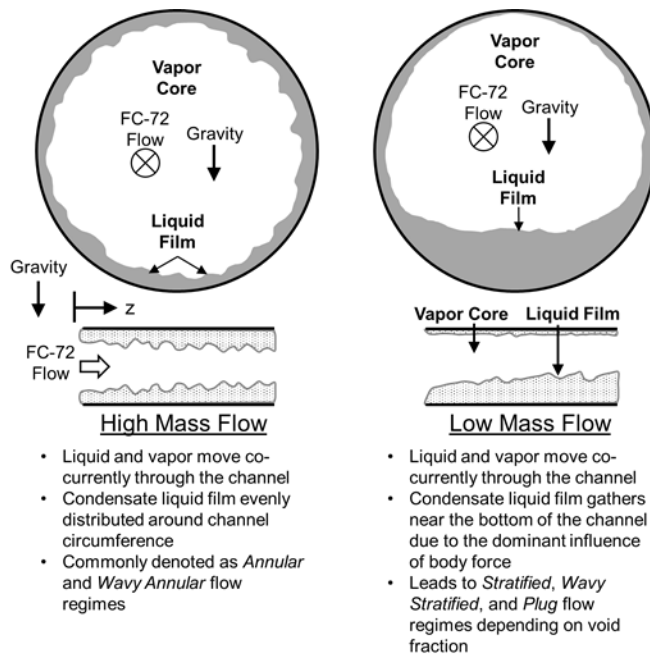


Figure 4.16 (b).



## Horizontal Flow

Figure 4.16 (c).

### 4.2.1.2 Utility of a new Method for Flow Regime Identification

Information discussed in the preceding subsection represents common knowledge for flow regimes in condensing flows, reaffirmed by numerous researchers over many decades of image analysis and modeling work. There is no disputing the role of flow regime on condensation heat transfer, and a number of researchers have proposed methods for predicting condensation heat transfer which depend on knowing/predicting flow regime within the condensation length [167-170].

Practically, this has translated to a need for system designers to validate two separate classes of design tools: one for determining condensation flow regime and one for determining condensation heat transfer coefficient (pressure drop applies here as well). The difficulty stems from the lack of visual access to liquid flow in condensing systems, necessitating construction of a second test section (as done in the current work) or complicated additions to standard condensation heat exchangers (often affecting heat transfer) to allow image capture. To overcome this limitation, the present work aims to present a new method for determining liquid film distribution and motion in condensing systems based entirely on temperature and pressure measurements.

#### 4.2.2 Flow Regime Identification

Work on flow regime identification using temperature and pressure measurements was split into two areas of focus. The first is to determine whether liquid and vapor motion in vertical orientations is co-current (commonly *co-current annular* flow or *climbing film* flow regime) or counter-current (leading to *flooding*, *oscillating film*, and *falling film* regimes). The second involves detection whether flow in horizontal orientations is stratified (*stratified flow*, *wavy-stratified flow*, *plug flow*) or axisymmetric (*annular flow*, *slug flow*).

##### 4.2.2.1 Co-current and Counter-current Flows

Conservation of mass is an important concept to keep in mind when attempting to determine whether vertical flow is co-current or counter-current. As discussed in conjunction with Fig. 4.16, low mass velocity cases in vertical upflow orientation lead liquid film to move counter to vapor motion or remain largely static. In both cases some other mechanism is needed to remove accumulating liquid phase from the condensation length, otherwise the channel would become filled entirely with liquid and condensation would no longer take place. This mechanism may be glimpsed in Fig. 4.15, which shows falling film giving way to the passage of a large liquid front, likely formed by falling film liquid accumulating in the entrance of the channel then departing. This ensures mass flow into the channel balances with that out of the channel in a time-averaged fashion.

Although less noticeable than for *falling film*, other counter-current regimes such as *oscillating film* and *flooding* also rely on periodic transport of liquid phase out of the condensation length to ensure mass conservation. As mass velocity is increased and flow within the channel exhibits *climbing film* behavior, this periodic mechanism is no longer necessary as both liquid and vapor move along the channel together.

As discussed at great length in prior works dealing with boiling in a vertical channel, this periodic motion of liquid through the channel is observable in both pressure and temperature measurements [53-56]. Based on this, plots of temperature and pressure versus time for different operating conditions in vertical upflow and vertical downflow (used for comparison purposes, as downflow condensation is expected to always be co-current and annular) were used as a starting point for analysis.

Figure 5.17(a)-(d) provide plots of temperature and pressure versus time, captured over the last 100 s of each respective steady-state data acquisition period. Temperature measurements displayed correspond to the first, third, fifth, seventh, ninth, and eleventh axial measurement stations within CM-HT (see the schematic in Fig. 2.3(a) for details on exact positions). Each curve represents an average of three circumferentially spaced thermocouple measurements on the tube wall at each axial location, as indicated by the schematic inset in Fig. 4.17(a).

Figures 4.17(a) and 4.17(b) correspond to vertical upflow with superheated vapor inlet conditions with  $G_{FC} = 303.3 \text{ kg/m}^2\text{s}$  and  $G_{FC} = 63.1 \text{ kg/m}^2\text{s}$ , respectively. Immediately apparent is the significant difference in pressure oscillatory behavior between the high and low flowrate cases. Figure 4.17(a) illustrates minimal pressure fluctuations are present for high mass velocities (where *co-current annular* flow is expected), while Fig. 4.17(b) showcases pressure changes on the order of 20 kPa (for conditions where *falling film* flow is expected).

Comparison of temperature fluctuations for the two sets of operating conditions shown in Figs. 4.17(a) and 4.17(b) yields fewer concrete conclusions than for inlet and exit pressures, with no clear differences in amplitude of fluctuations. It is worth noting that stainless steel wall temperature values are decreased for the case with low FC-72 mass velocity, a fact which will become important in subsequent figures.

Figures 4.17(c) and 4.17(d) show similar plots corresponding to vertical downflow condensation with mass velocities of  $G_{FC} = 301.9 \text{ kg/m}^2\text{s}$  and  $G_{FC} = 53.8 \text{ kg/m}^2\text{s}$ , respectively. Amplitudes of pressure fluctuations for both cases are significantly smaller than those observed in Fig. 4.17(b), with Fig. 4.17(d) in particular exhibiting minimal pressure fluctuations. This is attributable to the low FC-72 flow rate in Fig. 4.17(d) allowing gravity to dominate flow behavior. Comparison of temperature fluctuations across Figs. 4.17(c) and 4.17(d) again reveal no clear trends.



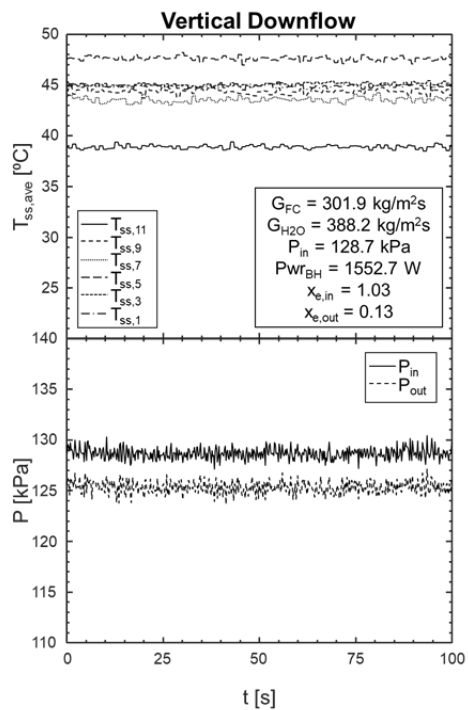


Figure 4.17 (c).

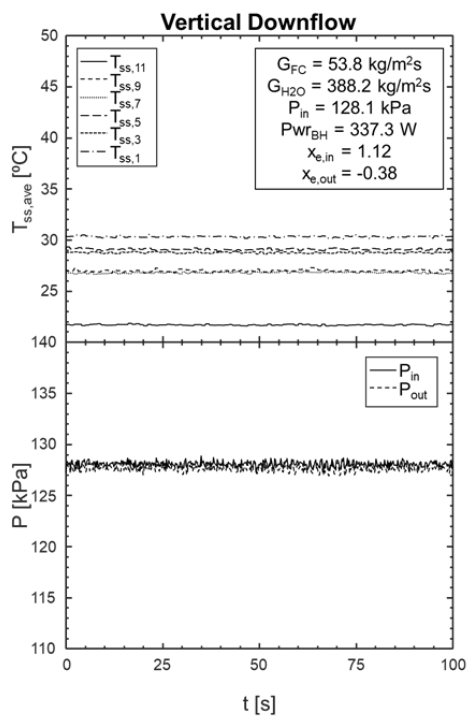


Figure 4.17 (d).

Continuing the present analysis to fully determine conditions for which vertical flows exhibit counter-current and co-current regimes, Fig. 4.18 presents *scaled temperature and pressure fluctuations*. These are calculated according to the relationships

$$\text{scaled temperature fluctuation} = \frac{T'}{T_{ave}} \times 100\% = \frac{0.5(\max(T_{0-n}) - \min(T_{0-n}))}{\text{mean}(T_{0-n})} \times 100\%, \quad (4.13)$$

and

$$\text{scaled pressure fluctuation} = \frac{P'}{P_{ave}} \times 100\% = \frac{0.5(\max(P_{0-n}) - \min(P_{0-n}))}{\text{mean}(P_{0-n})} \times 100\%, \quad (4.14)$$

where  $T_{0-n}$  represents instantaneous temperature measurements in degrees Celsius spanning time  $t_0$  to  $t_n$ , and  $P$  may refer to inlet or exit pressure (in kPa) depending on the subscript used.

Figure 4.18(a) provides plots of scaled temperature fluctuations averaged along the channel length versus mass velocity for cases with superheated inlet conditions in both vertical upflow (top plot) and vertical downflow (bottom plot). It should be noted here that channel length averaged values are calculated by using area-weighted averaging of all eleven local values for each set of operating conditions, and that vertical lines depicting boundaries between counter-current flow, co-current flow, and the transition between are intended only to apply to vertical upflow results: vertical downflow exhibits *co-current annular* flow for all operating conditions shown here.

A clear convergence in values of scaled temperature fluctuations is seen for vertical upflow in Fig. 4.18(a) as mass velocity is increased, with mass velocities in the range  $G_{FC} > 125 \text{ kg/m}^2\text{s}$  exhibiting no appreciable changes as mass velocity is changed, while those below  $G_{FC} = 125 \text{ kg/m}^2\text{s}$  increase significantly. Vertical downflow results in the bottom plot yield no clear trends, with  $G_{FC} \sim 100 \text{ kg/m}^2\text{s}$  cases deviating from others for unclear reasons.

Similar plots of channel length average scaled temperature fluctuations for cases with saturated mixture inlet conditions are shown in Fig. 4.18(b). The top plot (again corresponding to vertical upflow) presents a convergence in values for high mass velocity cases as was seen for upflow in Fig. 4.18(a), only this time values do not converge until somewhere between  $G_{FC} = 200 - 300 \text{ kg/m}^2\text{s}$ . This is likely attributable to increased liquid content present in the channel for cases with saturated inlet conditions requiring higher flowrates to move out of counter-current flow regimes and into *co-current annular* flow.

Vertical downflow results in Fig. 4.18(b) depict two clear modes of oscillatory behavior exist for cases with saturated mixture inlet conditions. At the lowest mass velocity of  $G_{FC} \sim 100$

kg/m<sup>2</sup>s scaled temperature fluctuations are at a maximum amplitude of ~3.5%, but for the higher flowrate of  $G_{FC} \sim 200$  kg/m<sup>2</sup>s values drop from ~3.5% to 1% as inlet quality increases from  $x_{e,in} \sim 0.4$  to  $x_{e,in} \sim 0.8$ . Higher values of mass flowrate all show scaled temperature fluctuations of ~1%, which is in line with ‘converged’ values in the other three plots from Figs. 4.18(a) and 4.18(b). It is believed this large difference between low and high flowrate cases is attributable to the presence of large interfacial waves on the liquid film, something discussed extensively for a variety of falling film and gravity driven flow configurations [171-177].

Figure 4.18(c) shows scaled pressure fluctuations for both vertical upflow and vertical downflow orientations with superheated vapor inlet conditions, with the top plot corresponding to inlet pressure data and the bottom plot to exit pressure. These provide the strongest evidence of a transition between counter-current and co-current regimes, with scaled pressure fluctuations 4-5 times higher for low flowrates (6-8%) in vertical upflow orientation than high flowrates (1-2%), indicating counter-current regimes are present for lower mass velocities. Scaled pressure fluctuations in vertical downflow orientation stay within the 1-2% range for all flowrates tested, and vertical upflow results are seen to converge to identical values for flowrates above  $G_{FC} \sim 225$  kg/m<sup>2</sup>s, strongly suggesting *co-current annular* flow (*climbing film* in upflow) is present for both orientations. At moderate mass velocities in the range  $G_{FC} \sim 100 - 200$  kg/m<sup>2</sup>s flow appears to be transitioning from counter-current to co-current (evidenced by scaled pressure fluctuations) leading these cases to be labeled ‘transition’ in Fig. 4.18(c). The fact scaled pressure fluctuations for these operating conditions have not yet converged to the 1-2% range seen for vertical downflow means some oscillatory behavior is likely still present, but likely only in the form of *flooding* flow regime as opposed to the *falling film* flow regime seen for the lowest mass velocity cases.

Finally, Fig. 4.18(d) provides plots of scaled pressure fluctuations versus mass velocity for both vertical upflow and downflow cases with saturated mixture inlet conditions. Values for the two orientations are seen to converge as mass velocity is increased, but without the clear demarcations visible as for cases with superheated vapor inlet seen in Fig. 4.18(c).

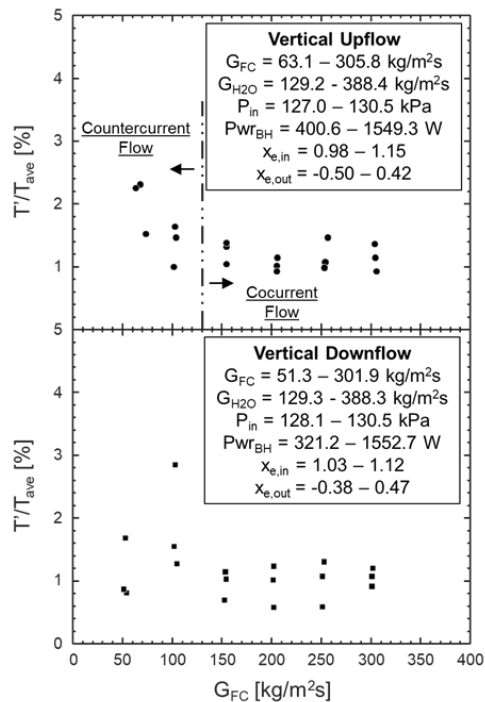


Figure 4.18: Plots of scaled temperature fluctuations versus mass velocity for (a) superheated vapor and (b) two-phase mixture inlet conditions, and scaled pressure fluctuations at channel inlet and outlet for (c) superheated vapor and (d) two-phase mixture inlet conditions.

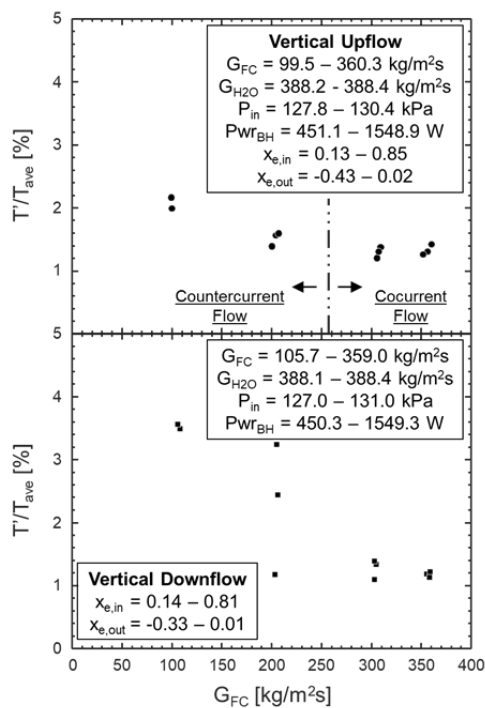


Figure 4.18 (b).

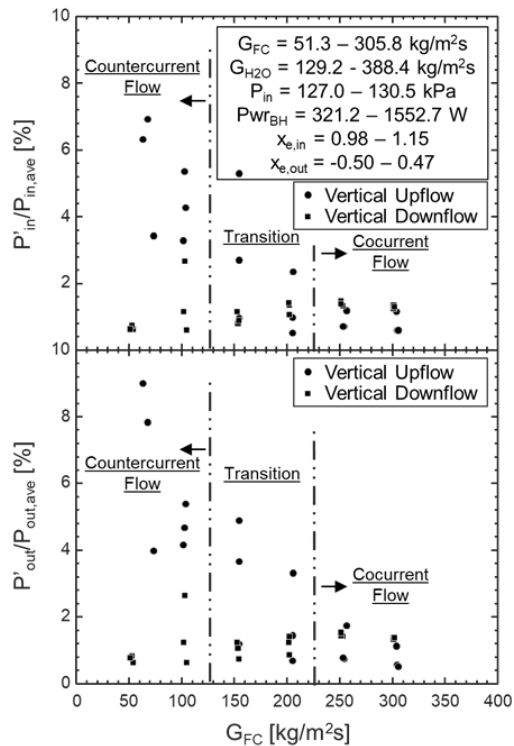


Figure 4.18 (c).

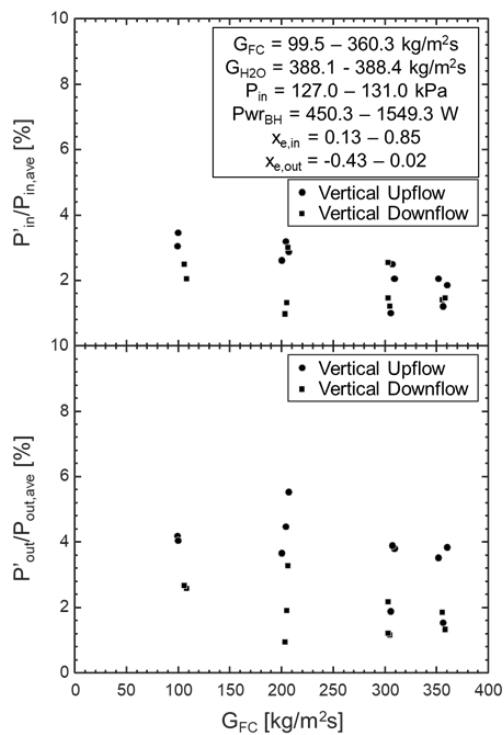


Figure 4.18 (d).

In summary for the present subsection, analysis of transient temperature and pressure results revealed the clear presence of significant oscillatory behavior in vertical upflow for mass velocities  $G_{FC} < 125 \text{ kg/m}^2\text{s}$  due to counter-current flow behavior (*falling film* flow regime). For mass velocities  $G_{FC} > 225 \text{ kg/m}^2\text{s}$  both temperature and pressure results reveal scaled fluctuations converge between vertical upflow and downflow orientations, leading to the conclusion *co-current annular* flow is present for these operating conditions (*climbing film* flow regime in upflow). Mass velocities in the range  $G_{FC} \sim 125 - 225 \text{ kg/m}^2\text{s}$  were labeled as transitional due to a lack of significant oscillatory behavior in vertical upflow, but still enough to prevent convergence with vertical downflow data. These points are likely experiencing some combination of *oscillating film* and *flooding* flow regimes.

It should also be noted it is possible amplitude of scaled fluctuating parameters may be similar for low flowrate cases (experiencing counter-current flow) and very high flowrate cases (experiencing dynamic film behavior). Detection of flow regime is still possible by determining whether an increase in flowrate leads to a decrease in oscillatory behavior (indicating flow is counter-current, approaching co-current) or an increase in oscillatory behavior (indicating flow is already co-current). The reverse will also be true if a small decrease in flowrate is used as a test.

#### 4.2.2.2 Stratified and Axisymmetric Horizontal Flows

Having presented a method for distinguishing between co-current and counter-current vertical flows, as well as the significant influence of interfacial waves on heat transfer in gravity-dominated downward flows, we finally discuss the detection of stratified and axisymmetric flows in horizontal orientation. Recalling trends discussed when analyzing Fig. 4.13, increases in mass velocity are seen to lead to a ‘spreading’ of liquid film around the channel circumference. At low mass velocities condensed liquid is expected to pool in the bottom of the condensation channel while hot vapor remains exposed to the top surface (leading to *stratified*, *wavy-stratified*, or *plug* flow regimes), behavior which should lead to clear gradients in circumferential temperature.

Towards this end Fig. 4.19 provides plots of local stainless-steel wall temperatures,  $T_{SS}$ , and water temperatures,  $T_{H2O}$ , averaged over the steady-state data acquisition period at all eleven axial measurement locations. Values of standard deviation  $\sigma_{SS}$  and  $\sigma_{H2O}$  for each respective set of local temperature measurements are also calculated and plotted versus position along the

condensation length in the bottom subplots. These values are calculated according to the relationships

$$\sigma_{SS} = \sqrt{\frac{1}{N-1} \sum_{n=1}^N (T_{SS,n} - \bar{T}_{SS})^2} \quad (4.15)$$

for stainless-steel temperatures, and

$$\sigma_{H_2O} = \sqrt{\frac{1}{N-1} \sum_{n=1}^N (T_{H_2O,n} - \bar{T}_{H_2O})^2} \quad (4.16)$$

for water. As described in Fig. 2.3(a), CM-HT contains three stainless-steel surface temperature measurements (spaced  $120^\circ$  apart) and two water temperature measurements (spaced  $180^\circ$  apart) at each axial location, meaning  $N = 3$  for  $\sigma_{SS}$  and  $N = 2$  for  $\sigma_{H_2O}$ , and  $\bar{T}$  is the average of these local values. The only exception to this is the first axial measurement station for stainless-steel wall temperatures where one of the three thermocouples has been omitted due to systematic errors resulting from instrumentation.

Figure 4.19(a) provides plots of temperatures and standard deviations between associated measurements for vertical upflow, vertical downflow, and horizontal flow orientations, all with superheated vapor inlet conditions and  $G_{FC} \sim 300 \text{ kg/m}^2\text{s}$ . All three orientations show some local variations in values of standard deviation between circumferentially spaced temperature measurements, but no systematic bias, with all standard deviations falling within  $0\text{-}3^\circ\text{C}$ .

Figure 4.19(b) shows similar results for all three orientations again with  $G_{FC} \sim 300 \text{ kg/m}^2\text{s}$ , this time corresponding to inlet qualities of  $x_{e,in} \sim 0.80$ . Results again indicate little difference in deviation between circumferentially spaced measurements for different operating conditions.

This trend changes in Fig. 4.19(c), however, which provides temperature results for all three orientations with  $G_{FC} \sim 100 \text{ kg/m}^2\text{s}$  and superheated vapor inlet conditions. Vertical upflow and vertical downflow results in Fig. 4.19(c) again appear similar to one another, but horizontal flow results show significant deviation by one of the three thermocouples at all axial stations, with maximum values of standard deviation reached in the downstream region of the channel. This behavior is indicative of stratified flow conditions with two thermocouples at circumferential locations covered by subcooled liquid, while the third location remains exposed to hot vapor (with a thin intervening liquid film). The final measurement location shows all three temperature measurements collapsed back to a single value, and it can be inferred that complete condensation

has been achieved by this point along the channel length (exit quality for the case is given as  $x_{e,out} = -0.25$  indicating subcooled liquid conditions at the exit).

It is worth noting here that differences in water temperatures remain largely constant for both cases where no clear circumferential gradients are present (Figs. 4.19(a), 4.19(b), and the vertical orientations in 4.19(c)) as well as for horizontal flow in Fig. 4.19(c) where gradients are clearly visible for stainless-steel temperatures. This indicates water temperatures are insufficient to determine condensate liquid distribution (wall temperatures must be used); however, water temperatures are measured at the sides and not the top of the flow channel in the current tests, meaning it is possible different water measurement locations might show some signs of stratification.

Figure 4.19(d) rounds out the picture by providing temperature information for all three orientations with  $G_{FC} \sim 100 \text{ kg/m}^2\text{s}$  and  $x_{e,in} \sim 0.80$ . Results again show no appreciable trends for vertical upflow and downflow orientations, while horizontal flow again shows a clear divergence of values in the up- and mid-stream regions indicating the presence of stratified flow.

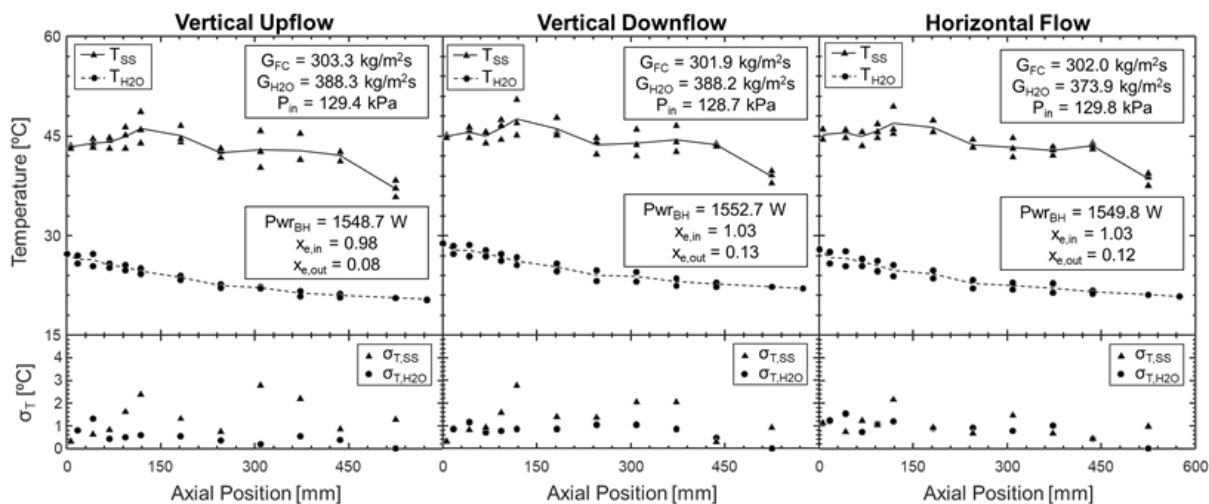


Figure 4.19: Plots of stainless steel ( $T_{ss}$ ) and water ( $T_{H2O}$ ) temperature measurements at all axial locations as well as standard deviation between respective measurements in all three orientations for (a)  $G_{FC} \sim 300 \text{ kg/m}^2\text{s}$  and  $x_{e,in} \sim 1.00$ , (b)  $G_{FC} \sim 300 \text{ kg/m}^2\text{s}$  and  $x_{e,in} \sim 0.80$ , (c)  $G_{FC} \sim 100 \text{ kg/m}^2\text{s}$  and  $x_{e,in} \sim 1.10$ , and (d)  $G_{FC} \sim 100 \text{ kg/m}^2\text{s}$  and  $x_{e,in} \sim 0.80$ .

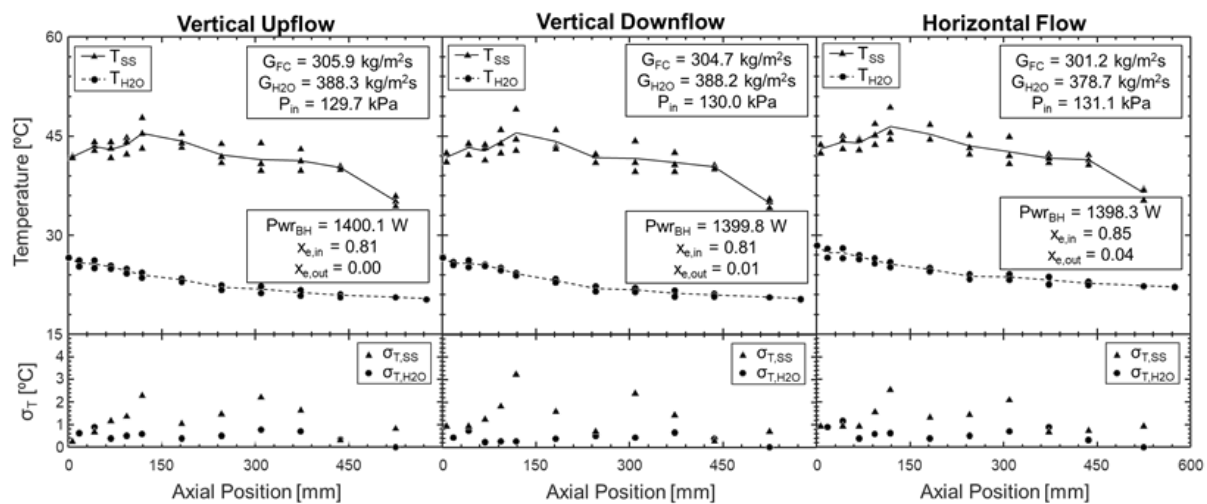


Figure 4.19 (b).

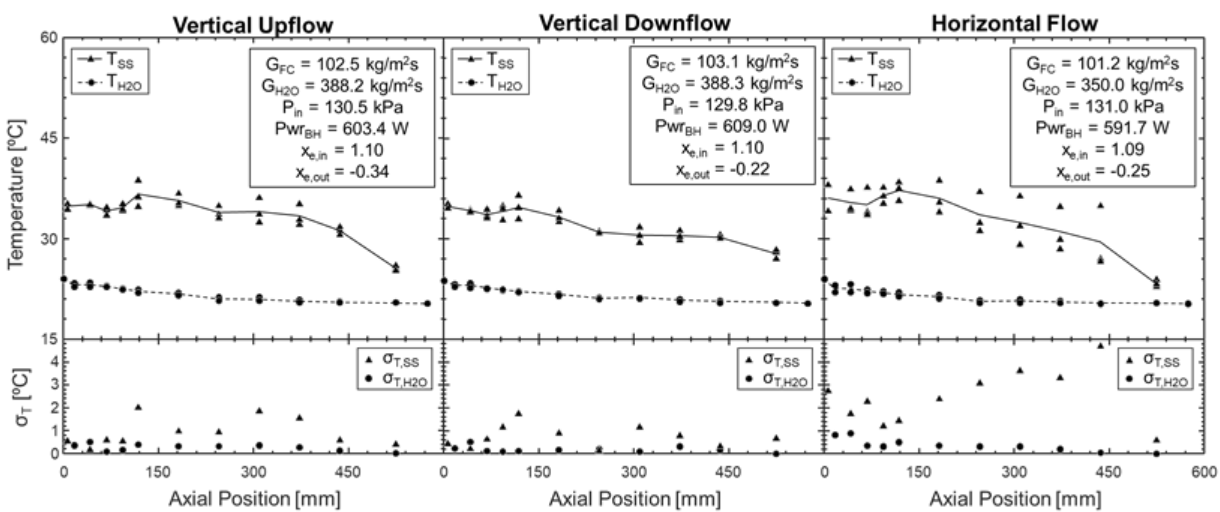


Figure 4.19 (c).

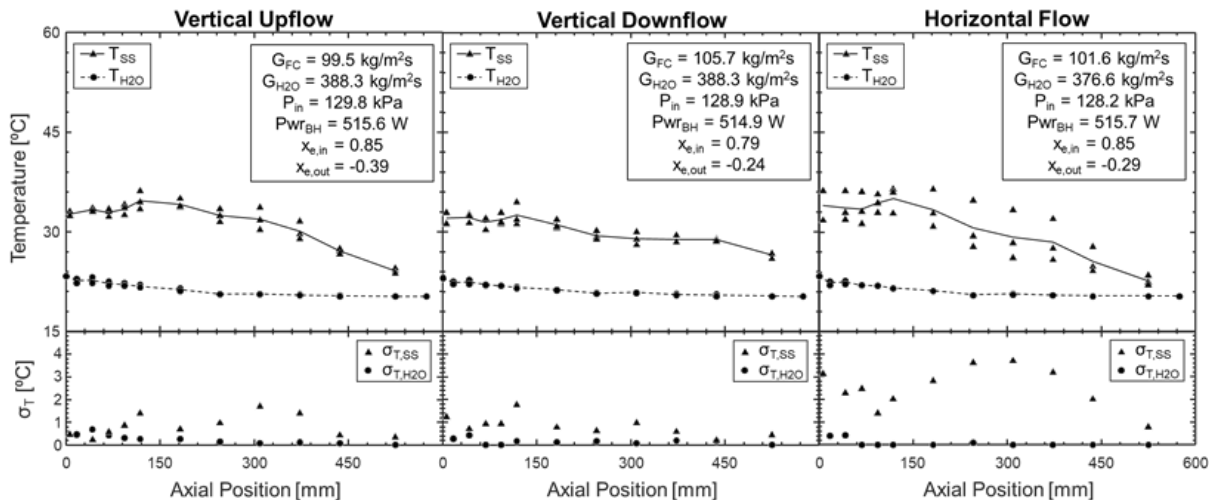


Figure 4.19 (d).

Figure 4.20 summarizes trends from Fig. 4.19 by plotting channel length averaged values of stainless-steel wall temperature standard deviations versus mass velocity for all cases in the dataset. Immediately apparent are the high standard deviation values for horizontal flow at low mass velocities, commonly 4-5 times higher in magnitude than their vertical upflow and downflow counterparts. As mass velocity increases, standard deviation values for horizontal flow are seen to decrease, approaching convergence with upflow and downflow near  $G_{FC} \sim 200 \text{ kg/m}^2\text{s}$  and exhibiting no noticeable differences from these orientations by  $G_{FC} \sim 350 \text{ kg/m}^2\text{s}$ . Based on this a clear transition point from stratified flows (*stratified*, *wavy-stratified*, and *plug* flow regimes) to axisymmetric flows (*annular*, *wavy-annular*, and *slug* flow regimes) is identified at  $G_{FC} \sim 175 \text{ kg/m}^2\text{s}$  and marked with a vertical dashed line. Similar to the note when discussing demarcations on Fig. 4.18, this line should only be taken to apply to horizontal flow cases (vertical upflow and downflow are seen to be axisymmetric for all operating conditions), and is meant to reflect the general transition from stratified to axisymmetric flow (which is a smooth process and not a step function).

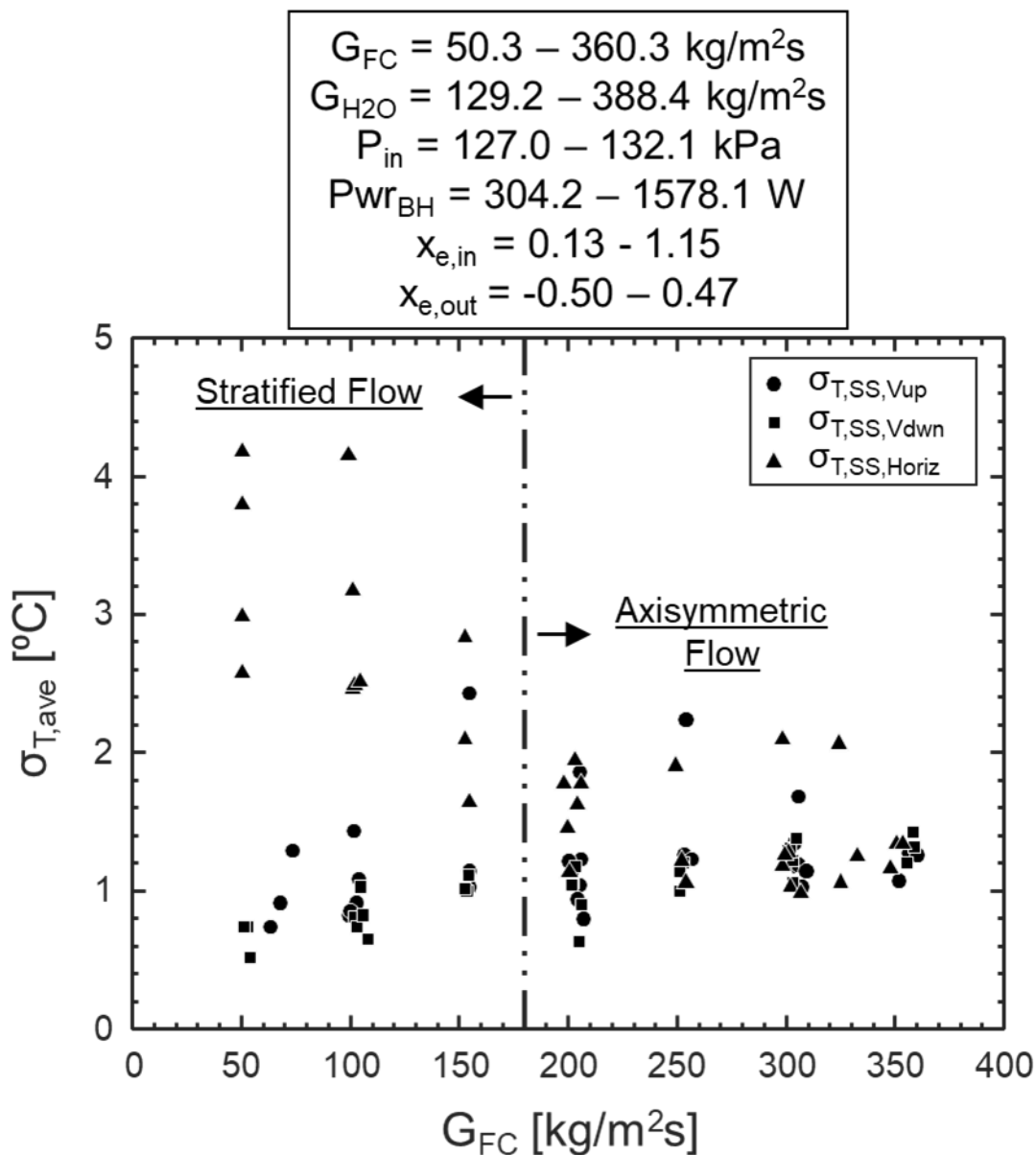


Figure 4.20: Standard deviation between circumferential stainless-steel wall temperature measurements versus mass velocity for all three orientations. Values show signs of convergence by  $G \sim 200 \text{ kg/m}^2\text{s}$ , indicating this is the mass velocity at which horizontal flow transitions from *stratified* to *annular* flow in the current test section.

#### 4.2.2.3 Summary of New Method for Identifying Condensation Flow Regime

The preceding subsections provide a new methodology for determining (1) whether flow in vertical orientations is co-current or counter-current and (2) whether flow in horizontal

orientations is stratified or axisymmetric. Table 4.2 summarizes key points of the approach for each and provides guidelines for utilization in other experimental systems.

It is worth noting that all analysis in the present section assumes uniform flow of cooling water through the module annulus. Thermocouple insertion and routing paths through the annulus may lead to asymmetry depending on module design, and these effects should be considered when applying the present methodology to different test sections.

Table 4.2: Summary of flow regime identification approach in each orientation.

Orientation	Co-current vs. Counter-current Flow	Stratified vs. Axisymmetric Flow	General Notes
<i>Vertical Upflow</i>	<ul style="list-style-type: none"> <li>• Calculate scaled temperature and pressure fluctuations</li> <li>• If values decrease for increased mass velocities, flow is counter-current (<i>falling film, oscillating film, flooding</i> flow regimes)</li> <li>• If values remain constant for changes in mass velocity, flow is co-current (<i>co-current annular, slug</i> flow regimes)</li> </ul>	<ul style="list-style-type: none"> <li>• Flow is axisymmetric for all operating conditions due to the role of body force acting opposite to flow (thus not creating any bias for circumferential film distribution)</li> </ul>	<ul style="list-style-type: none"> <li>• Ability to detect appreciable temperature and pressure fluctuations depends on thermal mass of condensation surface, magnitude of condensation length</li> <li>• May have difficulty applying co-current / counter-current test to data collected in short micro-channel heat sinks</li> </ul>
<i>Vertical Downflow</i>	<ul style="list-style-type: none"> <li>• Flow is co-current for all mass velocities due to role of body force aiding liquid film motion</li> <li>• Large values of scaled temperature fluctuations may be present for low mass velocities due to dominance of interfacial waves on film heat transfer</li> </ul>	<ul style="list-style-type: none"> <li>• Flow is axisymmetric for all operating conditions due to the role of body force acting parallel to flow direction</li> </ul>	<ul style="list-style-type: none"> <li>• Additional investigation on the transition between interfacial wave and vapor shear dominated heat transfer regimes necessary</li> </ul>

Table 4.2 Continued.

<p><i>Horizontal Flow</i></p>	<ul style="list-style-type: none"> <li>• Flow is co-current for all mass velocities</li> </ul>	<ul style="list-style-type: none"> <li>• Necessary to have multiple circumferentially spaced condensation surface temperature measurements (with at least 2 spaced 180° apart along the body force vector)</li> <li>• Calculate standard deviation between all circumferentially spaced temperature measurements</li> <li>• If values decrease as mass velocity is increased, flow is stratified (<i>stratified, wavy-stratified, plug</i> flow regimes)</li> <li>• If values remain neutral or increase slightly as mass velocity increases, flow is axisymmetric (<i>annular, wavy-annular, slug</i> flow regimes)</li> </ul>	<ul style="list-style-type: none"> <li>• Similar to the note for vertical upflow, ability to detect circumferential temperature gradients depends on thermal mass of condensation surface</li> <li>• May also be difficult to implement for micro-channel heat sinks</li> </ul>
<p><i>Inclined Channels (Extension)</i></p>	<ul style="list-style-type: none"> <li>• Depending on channel inclination and test section geometry it may be necessary to test if flow is co-current</li> <li>• Same approach as described for vertical upflow should be adopted</li> </ul>	<ul style="list-style-type: none"> <li>• Depending on channel inclination and test section geometry it may be necessary to test if flow is stratified</li> <li>• Same approach as described for horizontal flow should be adopted</li> </ul>	<ul style="list-style-type: none"> <li>• Testing of inclined channels necessary to determine utility of criteria as a function of orientation angle</li> </ul>

### 4.2.3 Comparison of Results with Flow Regime Maps

Having provided classification of flow regime observed using temperature and pressure measurements in the previous section, it is now useful to compare identified regimes with those predicted by transition criteria commonly used in literature. These are typically analytically formulated to capture key physics and empirically closed based on data used by respective authors. Comparison of results thus serves two purposes: (1) to validate that flow regimes identified using the new methodology are qualitatively in line with common predictions, and (2) to assess the ability of predictive tools to accurately capture the experimental flow regime trends presented in Section 4.2.2.

#### 4.2.3.1 Vertical Upflow Condensation Regime Map

Flow regime maps for vertical upflow condensation are rarely found due to the undesirable role of body force destabilizing liquid film motion in this orientation leading designers to give preference to other orientations (primarily vertical downflow and horizontal flow). As mentioned in Section 1, however, significant work on modeling flow regime transitions in vertical upflow was done by Wallis [110]. He introduced a parameter  $C$  used for classifying flow regimes, defined as

$$C = \sqrt{j_g^*} + \sqrt{j_f^*}, \quad (4.17)$$

where  $j_g^*$  and  $j_f^*$  are dimensionless superficial velocities of vapor and liquid, respectively. These are in turn defined as

$$j_g^* = \frac{j_g}{\sqrt{gD_i(\rho_f - \rho_g)/\rho_g}} \quad (4.18)$$

and

$$j_f^* = \frac{j_f}{\sqrt{gD_i(\rho_f - \rho_g)/\rho_f}}, \quad (4.19)$$

where  $D_i$  is the diameter of the condensation tube and  $j_g$  and  $j_f$  are vapor and liquid superficial velocities, respectively, defined as

$$j_g = \frac{x_e G_{FC}}{\rho_g} \quad (4.20)$$

and

$$j_f = \frac{(1-x_e)G_{FC}}{\rho_f}. \quad (4.21)$$

Specifying different values of  $C$  as representing different flow regimes allows transition criteria to be expressed in terms of relevant influences of body force, phase inertia, and phase mass fraction within the condensation length. These parameters have been shown throughout the study to be the dominant factors governing flow regime in vertical upflow condensation.

A recent study by Park and Mudawar [93] adapted Wallis' original methodology for use in predicting flow regime during vertical upflow condensation of FC-72 in a smooth tube with inner diameter  $D_i = 11.89$  mm, comparable to the 7.12-mm value of the current test section. Due to this similarity their transition criteria are evaluated in the present study, given as  $C = 0.85$  for the transition from *falling film* to *oscillating film*,  $C = 1.0$  for *oscillating film* to *flooding*, and  $C = 1.21$  for *flooding* to *climbing film*.

The flow regime map of Park and Mudawar [93] is shown in Fig. 4.21(a), with data from the current experiments evaluated using the transition criteria indicated (meaning symbols shown are predicted based on local operating conditions). It should be noted here that experimental values presented correspond to locally calculated quality values at all 11 axial measurement locations along the channel length and fluid properties evaluated at the channel inlet pressure. Locations with qualities  $x_e > 0.99$  and  $x_e < 0.01$  are assigned values of 0.99 and 0.01, respectively, to avoid dividing by zero in calculations. Full details on calculation of local quality values is outside the scope of the present section and may be found in section 4.3.

Figure 4.21(b) provides a plot of  $C$  versus FC-72 mass velocity for all vertical upflow cases. This plot is intended to highlight how predictions of flow regime change as mass velocity is increased, with low mass velocity cases predicted to exhibit mostly *falling film*, *oscillating film*, and *flooding* behavior, while higher mass velocity cases transition to predominantly climbing film flow regime.

Figure 4.21(c) re-plots this information, now expressing only a channel average flow regime instead of the local values shown in Figs. 4.21(a) and 4.21(b). Channel-length average flow regime is calculated by determining an area-weighted value of  $C$  for each test case (just as area weighted scaled fluctuating parameters and standard deviations were calculated in Sections 4.2.1 and 4.2.2) and evaluating the given transition criteria based on that average value.

Also shown in Fig. 4.21(c) are the transition boundaries originally created as a part of Fig. 4.18. These highlight the regimes as identified from experimental temperature and pressure data, allowing for easy comparison with those predicted by the map of Park and Mudawar.

Comparison of results is provided in Table 4.3 and indicate that the map of Park and Mudawar does a good job of capturing trends observed experimentally. At low mass velocities where counter-current flow is expected, their map predicts 4/8 cases to be *falling film* flow regime, and 7/8 cases to be something other than *climbing film* (*co-current annular* flow).

For moderate mass velocities where flow is expected to transition between counter-current and co-current flow, the map of Park and Mudawar predicts 1 *oscillating film*, 1 *flooding*, and 7 *climbing film* cases. This indicates their transition criteria are generally reflective of experimental results, with potentially a slightly early transition to climbing film flow regime compared to what is observed.

Finally, for high mass velocities their map correctly identifies all 12 experimentally identified co-current flow cases as *climbing film* flow regime.

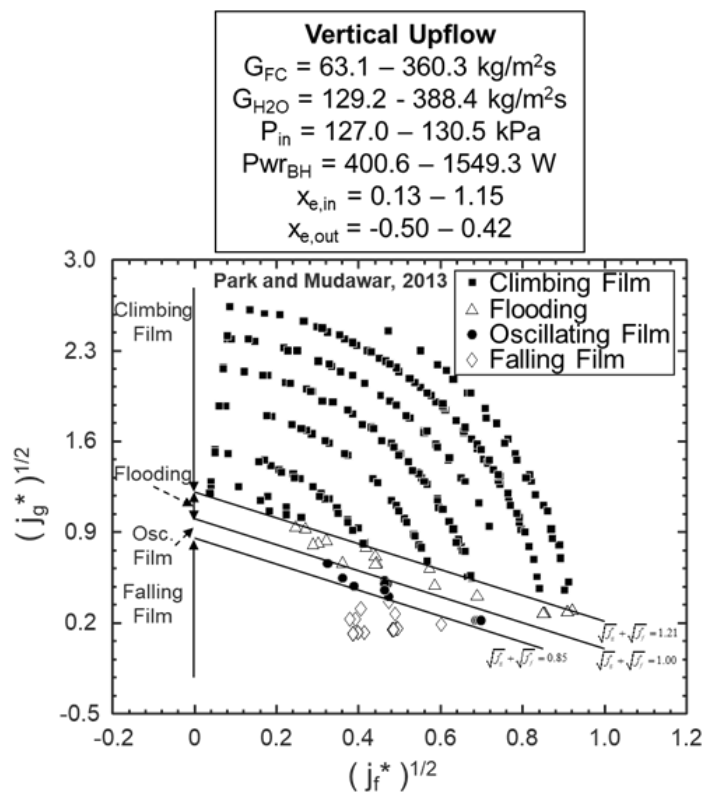


Figure 4.21: (a) Vertical upflow condensation regime map of Park and Mudawar [93] providing predictions of flow regime for all local measurements in the current dataset, along with (b) predicted flow regime versus mass velocity and (c) channel length-average predicted flow regime versus mass velocity.

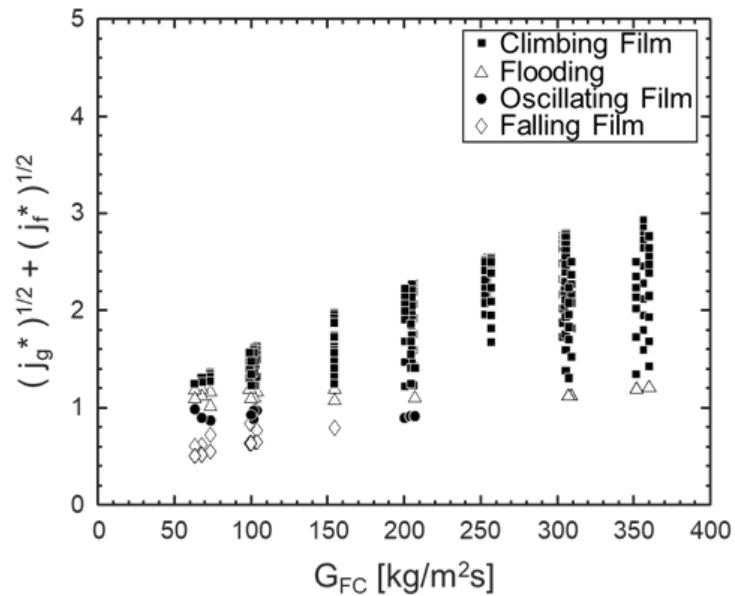


Figure 4.21 (b).

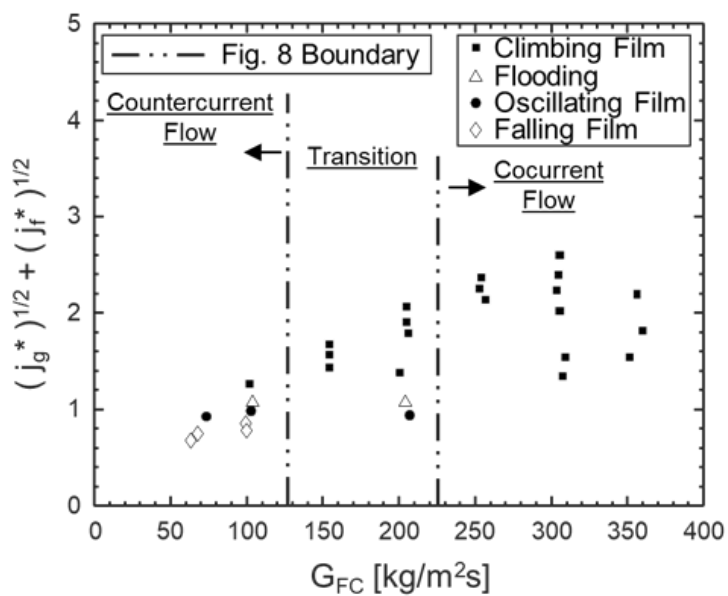


Figure 4.21 (c).

Table 4.3: Summary of flow regime identification approach in vertical upflow.

Experimentally Identified Flow Regime	Number of Experimentally Determined Cases	Predictions by Park and Mudawar [35]	Percent Correct
<b>Counter-current Flow</b> ( <i>falling film</i> flow regimes)	8	4 falling film, 2 oscillating film, 1 flooding, 1 climbing film	50% (87.5%)
<b>Transition</b> ( <i>oscillating film, flooding</i> flow regimes)	9	1 oscillating film, 1 flooding, 7 climbing film	22.2%
<b>Co-current Flow</b> ( <i>climbing film</i> flow regime)	12	12 climbing film	100%

#### 4.2.3.2 Horizontal Flow Condensation Regime Maps

Compared to the limited options available for prediction of vertical upflow condensation flow regime, a prolific number of maps have been created for horizontal flow. Figure 4.22 provides evaluation of four of the numerous available, selected due to their compatibility with the present experiment work and their presence in the overall condensation literature. Results for each map are also summarized in Table 4.4, similar to that done in Table 4.3 for Fig. 4.21.

Figure 4.22(a) starts by presenting the map of Park *et al.* [94], created based on flow of FC-72 through a smooth circular tube. Their approach follows that originally outlined by Soliman [115,116] and expresses transition criteria in terms of modified Weber number  $We^*$  and the Lockhart-Martinelli parameter  $X_{tt}$ . These parameters are defined according to the relationships

$$We^* = 2.45 Re_g^{0.64} \left( \frac{\mu_g^2}{\rho_g \sigma D} \right)^{0.3} / \phi_g^{0.4} \text{ for } Re_f \leq 1250, \quad (4.22a)$$

$$\text{and } We^* = 0.85 Re_g^{0.79} \left( \frac{\mu_g^2}{\rho_g \sigma D} \right)^{0.3} \left[ \left( \frac{\mu_g}{\mu_f} \right)^2 \left( \frac{\rho_f}{\rho_g} \right) \right]^{0.084} \left( \frac{X_{tt}}{\phi_g^{2.55}} \right)^{0.157} \text{ for } Re_f > 1250, \quad (4.22b)$$

where

$$Re_g = x_e G_{FC} D / \mu_g, \quad (4.23)$$

$$Re_f = G_{FC} (1 - x_e) D / \mu_f, \quad (4.24)$$

$$X_{tt} = \left( \frac{1-x_e}{x_e} \right)^{0.9} \left( \frac{\rho_g}{\rho_f} \right)^{0.5} \left( \frac{\mu_f}{\mu_g} \right)^{0.1}, \quad (4.25)$$

and

$$\phi_g = 1 + 1.09 X_{tt}^{0.039}. \quad (4.26)$$

Using these dimensionless groups originally presented by Soliman [115,116], Park *et al.* [94] defined their flow regime transition criteria as

$$\textit{Stratified: } We^* < 6.03, \quad (4.27a)$$

$$\textit{Stratified to wavy stratified: } 6.03 \leq We^* < 19.39, \quad (4.27b)$$

$$\textit{Wavy stratified to wavy-annular with gravity influence: } 19.39 \leq We^* < 25.46, \quad (4.27c)$$

$$\textit{Wavy-annular without gravity influence: } We^* \geq 25.46. \quad (4.27d)$$

Figure 4.22(b) shows the predictions of Park *et al.*'s map (presented as 'channel average' flow regimes as was done in Fig. 4.21(c) for vertical upflow) as a function of mass velocity. For low FC-72 mass velocities, all cases are predicted to be either *stratified* or *wavy stratified* flow regime which matches well with the experimentally identified stratified flow boundary.

For higher mass velocity cases their map predicts a majority of cases will exhibit *annular flow* with a smaller number (primarily those cases with saturated mixture inlet conditions) still exhibiting *stratified flow* behavior.

Figure 4.22(c) presents the map of Kim *et al.* [96] which relies on the same dimensionless groups proposed by Soliman [115,116]. Their work dealt with condensation of FC-72 inside a micro-channel heat sink, however, and they expressed their transition criteria as

$$\textit{Smooth-annular to wavy-annular: } We^* = 90 X_{tt}^{0.5}, \quad (4.28a)$$

$$\textit{Wavy-annular to transition: } We^* = 24 X_{tt}^{0.41}, \quad (4.28b)$$

$$\textit{Transition to slug: } We^* = 7 X_{tt}^{0.2}. \quad (4.28c)$$

Immediately apparent is that unlike the map of Park *et al.* [94], Kim *et al.* [96] expressed their transition criteria as a function of both  $We^*$  and  $X_{tt}$ . Due to the definition of  $X_{tt}$  in Eq. (4.25) showing a dependence on local fluid quality (as well as a combination of material properties), expressing regime transition criteria in terms of  $X_{tt}$  allows included effects of liquid content within

the channel to be accounted for (*i.e.*, allowing differentiation between cases with low and high inlet qualities).

One added complexity when interpreting the map of Kim *et al.* is its lack of stratified flow regimes. Due to the original experimental work being micro-channel condensation and surface tension effects playing a dominant role in small-diameter channels, operating conditions which would provide stratified flow in larger diameter tubes are predicted to yield slug flow here. For the sake of the current analysis, cases where flow regime is predicted to be *slug flow* using the map of Kim *et al.* will be treated as representing stratified flow. This is not a bad assumption, as the original map is intended to show a transition from inertia dominated regimes (*i.e.*, *annular flow*) to non-inertia dominated regimes (surface tension dominated in microchannels, gravity dominated in mini/macro-channels). It still represents an assumption, however, and care should be taken when utilizing this map for non-micro-channel flows.

Figure 4.22(d) shows how predictions of channel average flow regime using the map of Kim *et al.* [96] change as mass velocity increases. For low mass velocity cases, most test cases are predicted to exhibit slug or transition flow, matching well with the experimental assessment of flow regime. For higher mass velocity cases, predictions are primarily of smooth-annular and wavy-annular flow, again matching well with experimental results outlined in Section 4.2.2. Similar to the map of Park *et al.* discussed above, however, is the prediction of non-inertia-dominated flow regimes for high mass velocities with saturated mixture inlet conditions.

The map of Breber *et al.* [113] is shown in Fig. 4.22(e). This map is one of the most commonly utilized flow regimes maps available for horizontal flow condensation and uses dimensionless superficial vapor velocity  $j_g^*$  and Lockhart-Martinelli parameter  $X_{tt}$  as its coordinates. They defined their transition criteria as

$$\text{Annular flow: } j_g^* > 1.5, X_{tt} < 1.0, \quad (4.29a)$$

$$\text{Wavy or stratified flow: } j_g^* < 0.5, X_{tt} < 1.0, \quad (4.29b)$$

$$\text{Slug flow: } j_g^* < 1.5, X_{tt} > 1.5, \quad (4.29c)$$

$$\text{Bubbly flow: } j_g^* > 1.5, X_{tt} > 1.5, \quad (4.29d)$$

with transition regimes between those explicitly defined above.

Investigation of flow regimes predicted using the map of Breber *et al.* [113] versus FC-72 mass velocity in Fig. 4.22(f) shows that, for low mass velocities, predicted regimes include *slug*

*flow, wavy-stratified flow, stratified-annular transition, stratified-slug transition*, and even one case of *annular flow*. For high mass velocities, all but one case show *annular flow* and *slug flow* are predicted, however, both of which are axisymmetric regimes and match well with the experimentally identified behavior.

The final flow regime map presented is that of Song *et al.* [122] shown in Fig. 4.22(g), which has only recently become available in literature. Similar to other authors they use the Lockhart-Martinelli parameter  $X_{tt}$  as one of their dimensionless groups, but for the other group they define a new parameter  $S_2$  as

$$S_2 = Fr_g Bd^{-0.15} Ca_f^{-0.1} (1 + Bo^{0.25}), \quad (4.30)$$

where vapor Froude number  $Fr_g$ , Bond number  $Bd$ , liquid Capillary number  $Ca_f$ , and modified Boiling number  $Bo$  are defined as

$$Fr_g = \frac{G^2}{\rho_g (\rho_f - \rho_g) gD}, \quad (4.31)$$

$$Bd = \frac{(\rho_f - \rho_g) gD^2}{\sigma}, \quad (4.32)$$

$$Ca_f = \frac{\mu_f G}{\rho_f \sigma}, \quad (4.33)$$

and 
$$Bo = \frac{Q_{cond}}{G_{FC} h_{fg}}. \quad (4.34)$$

They define their transition criteria as

$$\text{Wavy-stratified flow: } S_2 < (20 + X_{tt})^{0.86}, \quad (4.35a)$$

and if *wavy-stratified flow* is not present:

$$\text{Plug flow to slug flow: } S_2 = 2.45 X_{tt}^{2.29}, \quad (4.35b)$$

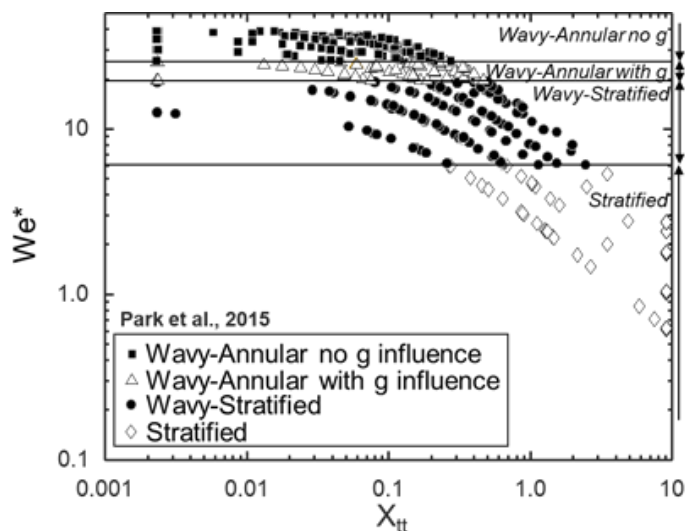
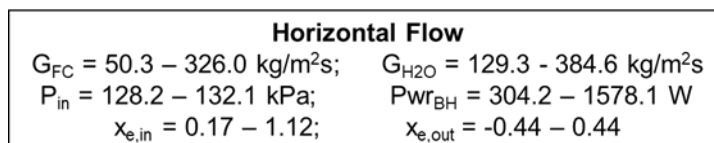
$$\text{Slug flow to transition flow: } S_2 = 21.45 X_{tt}^{1.71}, \quad (4.35c)$$

$$\text{Transition flow to wavy-annular flow: } S_2 = 83.4 X_{tt}^{1.62}, \quad (4.35d)$$

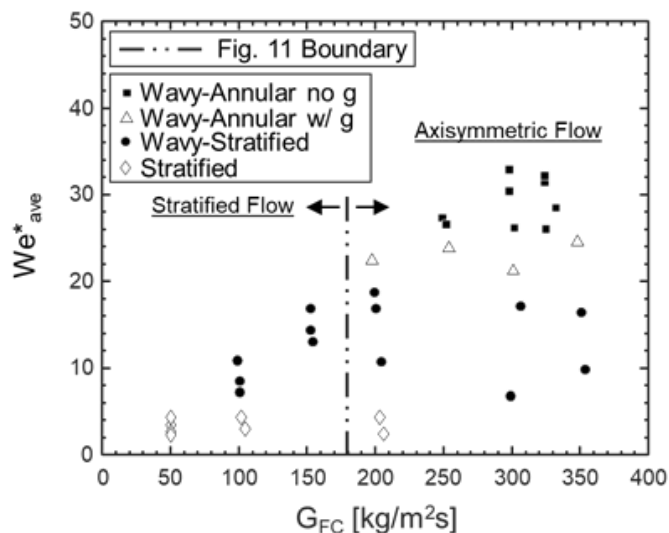
and 
$$\text{Wavy-annular flow to smooth-annular flow: } S_2 = 360.6 X_{tt}^{1.52}. \quad (4.35e)$$

Figure 4.22(h) shows the flow regime map of Song *et al.* [122] does an excellent job of predicting *wavy-stratified flow* for low mass velocities, as was seen when analyzing the

experimental data. For high mass velocities, a mixture of *slug*, *plug*, *transition*, *wavy-annular*, and *smooth-annular* flow regimes is predicted, with the majority of cases predicted to be *smooth-annular*. Overall, the map of Song *et al.* does the best job of capturing experimental results out of all the maps presented here, evidenced by a 100% accuracy classifying stratified flow cases and 72.7% accuracy for axisymmetric flow shown in Table 4.4.



(a).



(b).

Figure 4.22: Flow regime map of (a) Park *et al.* [94] used to evaluate current dataset, with (b) identified flow regimes across the range of mass velocities tested. Similar plots for flow regime maps of Kim *et al.* [96] (c), (d), Breber *et al.* [113] (e), (f), and Song *et al.* [122] (g), (h).

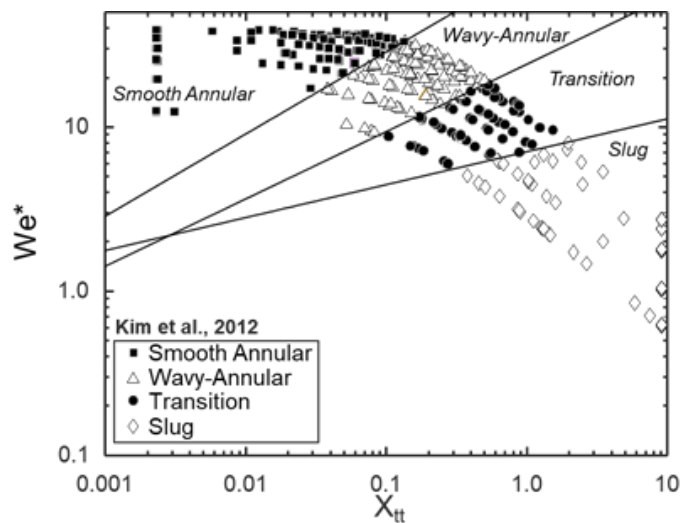


Figure 4.22 (c).

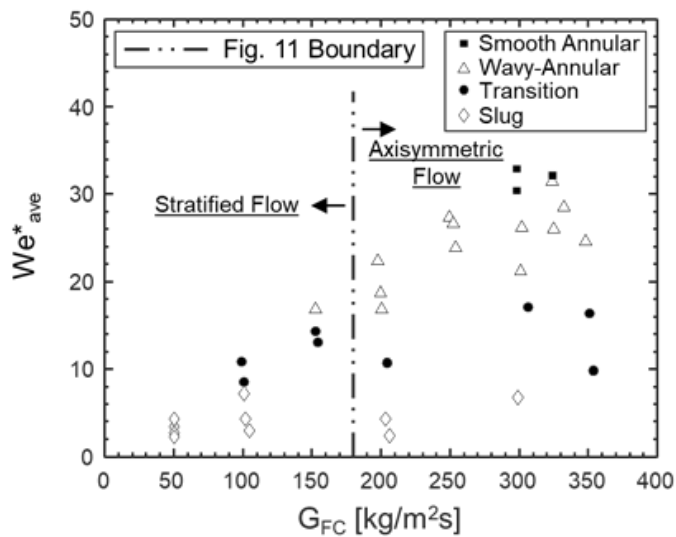


Figure 4.22 (d).

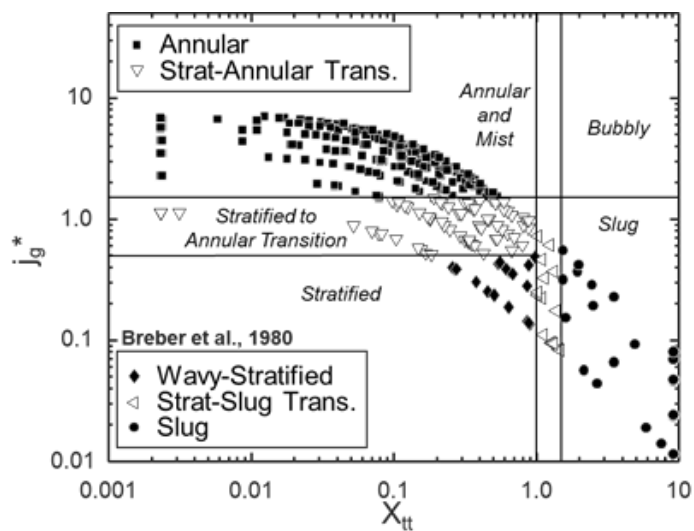


Figure 4.22 (e).

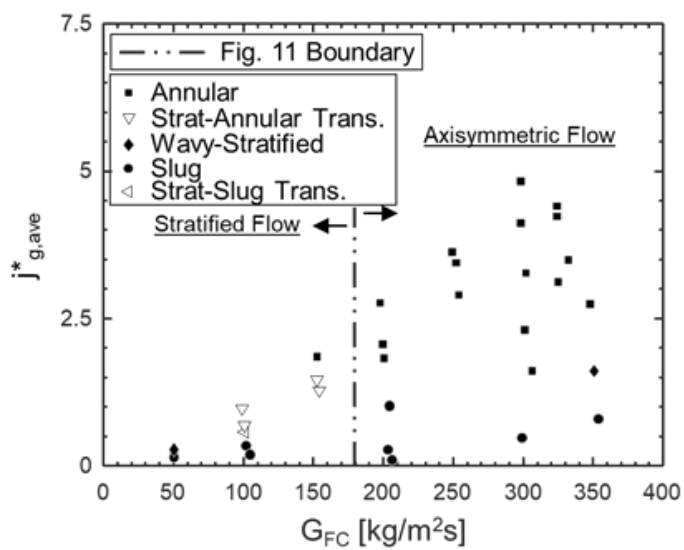


Figure 4.22 (f).

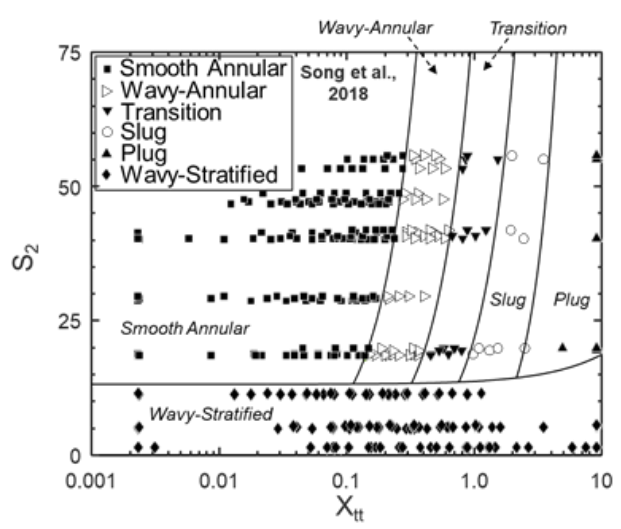


Figure 4.22 (g).

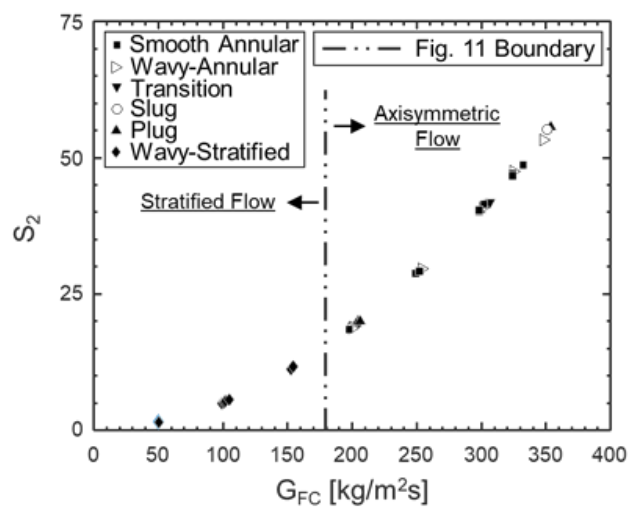


Figure 4.22 (h).

Table 4.4: Summary of flow regime identification approach in horizontal flow.

Experimentally Identified Flow Regime	Number of Experimentally Determined Cases	Predictions by Park <i>et al.</i> [36]	Percent Correct	Predictions by Kim <i>et al.</i> [40]	Percent Correct	Predictions by Breber <i>et al.</i> [51]	Percent Correct	Predictions by Song <i>et al.</i> [60]	Percent Correct
<b>Stratified Flow</b> ( <i>stratified, wavy-stratified, plug</i> flow regimes)	12	6 stratified, 6 wavy-stratified	100%	7 slug, 4 transition, 1 wavy-annular	91.7%	5 slug, 1 wavy-stratified, 4 strat-annular transition, 1 annular, 1 strat-slug	50.0%	12 wavy-stratified	100%
<b>Axisymmetric Flow</b> ( <i>annular, wavy-annular, slug</i> flow regimes)	22	2 stratified, 7 wavy-stratified, 4 wavy-annular w/ g, 9 wavy-annular no g	59.1%	3 slug, 4 transition, 12 wavy-annular, 3 smooth annular	68.2%	5 slug, 1 bubbly, 16 annular	100%	6 wavy-annular, 9 smooth annular, 5 plug, 1 slug, 1 transition	72.7%

### 4.3 Flow Condensation Heat Transfer in a Smooth Tube at Different Orientations: Experimental Results and Predictive Models

#### 4.3.1 Data Selection and Heat Transfer Reduction

Many researchers develop condensation heat transfer models which treat heat transfer mechanisms differently depending on condensation flow regime [167-169]. The necessity of accurately predicting flow regime and understanding its impact on condensation heat transfer behavior is discussed at length in section 4.2 of the current work, and as such will not be presented again here. For the sake of the current section, it is sufficient to note that cases identified as exhibiting stratified flow (horizontal flow with  $G_{FC} < 200 \text{ kg/m}^2\text{s}$ ) have been excluded from the current analysis. Low mass velocity cases in vertical upflow orientation should also be interpreted carefully, as they have been shown to exhibit counter-current flow characteristics.

##### 4.3.1.1 Condensation Heat Transfer Coefficient Calculation

As mentioned when describing the test section (CM-HT) in section 2.2, thermocouples are included at 11 axial locations along the condensation length for measuring heat transfer. Each measurement location contains three thermocouples brazed to the outer surface of the stainless-steel tube (spaced  $120^\circ$  apart) and two thermocouples inserted into the water flow (spaced  $180^\circ$  apart). The first step in heat transfer data reduction is to average the two water temperatures and three stainless-steel temperatures at each axial location to provide a single representative temperature for water and stainless-steel at all 11 measurement points. As shown in Fig. 4(a), this allows a 1-D, radial energy balance to be performed to calculate condensation heat transfer coefficient (with the assumption of axisymmetric behavior at all axial locations).

It should be noted that significant effort was spent analyzing standard deviation between local measurements conducted at each axial location in section 4.2, as these values were used to identify the transition from stratified to annular flow for cases in horizontal orientation. Stratified horizontal flow condensation lead to significant differences between stainless-steel temperature measurements at the same axial location (as discussed in the preceding subsection), meaning that taking an average of the three values is an oversimplification of heat transfer behavior. Because of this horizontal flow cases with mass velocities  $G_{FC} \sim 50 \text{ kg/m}^2\text{s}$  and  $G_{FC} \sim 100 \text{ kg/m}^2\text{s}$  have been omitted from the current analysis.

The next step in data reduction is to curve fit all 13 water temperature measurements (inlet temperature, exit temperature, and 11 averaged temperatures along the condensation length). This was done using a third order polynomial. Second, third, fourth, and fifth order polynomials were investigated, with second order seen to over-constrain heat flux to a linear variation along the channel length (as condensation heat flux is manifest in the rate of change of water temperatures), while fourth and fifth order polynomials provided similar results to third order but were seen to introduce nonphysical trends in select cases due to overfitting of experimental data. Third order polynomials have also been used in several prior works with great success [92-94,98,131].

Having curve fit water temperatures, it is possible to calculate local incremental energy transfer  $dq_{cond}$ . This is equal to the rate of change of water temperature at the measurement location (evaluated by taking the derivative of the water temperature curve fit), and in the present work is evaluated over a 1 mm distance  $\Delta z$ . Formally,

$$\Delta q_{cond,n} = \dot{m}_{H_2O} c_{p,f,H_2O} \left[ \frac{dT_{H_2O,fit}}{dz} \right]_n \Delta z, \quad (4.36)$$

where  $\dot{m}_{H_2O}$  is water mass flowrate,  $c_{p,f,H_2O}$  is water specific heat, and  $n$  indicates the streamwise location where calculations are taking place ( $n$  ranges from 1 to 11). It should be noted here that all fluid properties are evaluated at local pressures assuming a linear variation between inlet and exit values for both water and FC-72 streams.

This local condensation energy transfer may be applied to the broader area surrounding measurement points in order to calculate total energy transferred from condensate (FC-72) to coolant (water). This may be used to update local FC-72 flow quality along the channel length according to the relationship

$$x_{e,n+1} = x_{e,n} - \Delta x_e = x_{e,n} - \frac{Q_{cond,n}}{\dot{m}_{FC} h_{fg,FC}} = x_{e,n} - \frac{\dot{m}_{H_2O} c_{p,f,H_2O} (T_{H_2O,n} - T_{H_2O,n+1})}{\dot{m}_{FC} h_{fg,FC}}, \quad (4.37)$$

where  $Q_{cond,n}$  refers to the total condensation energy transferred between locations  $n$  and  $n+1$ . Local flow quality is not used in calculation of condensation heat transfer coefficient but becomes important when interpreting local heat transfer trends as well as when calculating channel-average heat transfer coefficient in later analysis.

Once local incremental energy transfer has been calculated based on water temperature change, it is possible to calculate stainless-steel inner surface temperature through a basic

conduction network diagram as shown in Fig. 4.23(a) (making the assumption of steady, radial conduction). This leads to an expression for inner stainless-steel temperature of

$$T_{ss,i,n} = T_{ss,o,n} + \Delta q_{cond,n} R_{conduction,n} = T_{ss,o,n} + \left[ \dot{m}_{H_2O} c_{p,f,H_2O} (\Delta T_{H_2O,n}) \right] \left[ \frac{\ln\left(\frac{D_o}{D_i}\right)}{2\pi k_{ss} \Delta z} \right], \quad (4.38)$$

where  $R_{conduction,n}$  is the conduction thermal resistance at location n,  $\Delta T_{H_2O,n}$  is the water temperature derivative as evaluated in Eq. (4.36),  $D_o$  and  $D_i$  are outer and inner stainless-steel tube diameters, and  $k_{ss}$  is the thermal conductivity of stainless-steel. Values for each of the parameters used in calculating  $R_{conduction,n}$  are provided in Fig. 4.23 (a).

Once inner stainless-steel wall temperature has been calculated, condensation heat transfer coefficient is defined as

$$h_{cond,n} = \frac{\Delta q_{cond,n}}{\pi D_i \Delta z (T_{FC,sat,n} - T_{ss,i,n})}, \quad (4.39)$$

where saturation temperature  $T_{FC,sat,n}$  is evaluated at the local condensate pressure (again using an assumed linear variation between measured inlet and exit pressures).

It is worth discussing here the use of  $T_{FC,sat}$  to calculate condensation heat transfer coefficient in the portion of the channel where bulk flow is expected to be superheated (i.e., mixed mean temperature is above saturation temperature at the local pressure). In many cases present in the current dataset (corresponding to slightly superheated inlet conditions) this is the case for the first 1-3 measurement locations along the channel length.

Figure 4.23(b) provides a schematic of local temperature variation in the radial direction, moving from the adiabatic condition where water meets the polycarbonate wall, across the water and up to the stainless-steel wall, through the stainless-steel wall, across the condensate liquid film, and into the condensate vapor core. It is a fact of the condensation process that, regardless of the amount of superheat present in the vapor core, the interface between liquid and vapor phases will always be maintained at saturation temperature for the local pressure. Because of this the present study uses  $T_{FC,sat}$  to calculate condensation heat transfer coefficient at all locations within the condensation length regardless of local superheat (and after the flow has fully condensed heat transfer coefficient is no longer calculated). There are arguments to be made in favor of using local temperature within the superheated region, but regardless of which temperature is chosen, it

is imperative that it be clearly stated so values of local heat transfer coefficient may be compared across works.

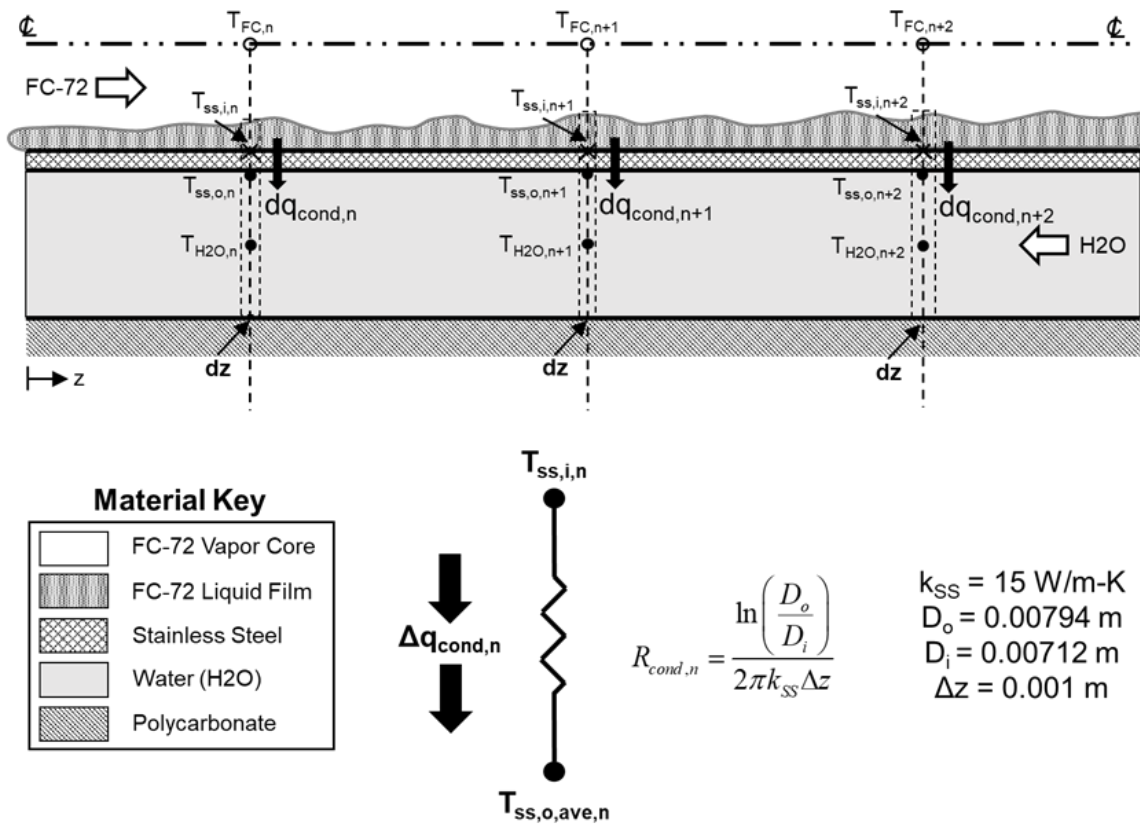


Figure 4.23: (a) Schematics for heat transfer coefficient data reduction methodology used here, along with (b) schematic illustrating the importance of capturing radial temperature variations present along the condensation length.

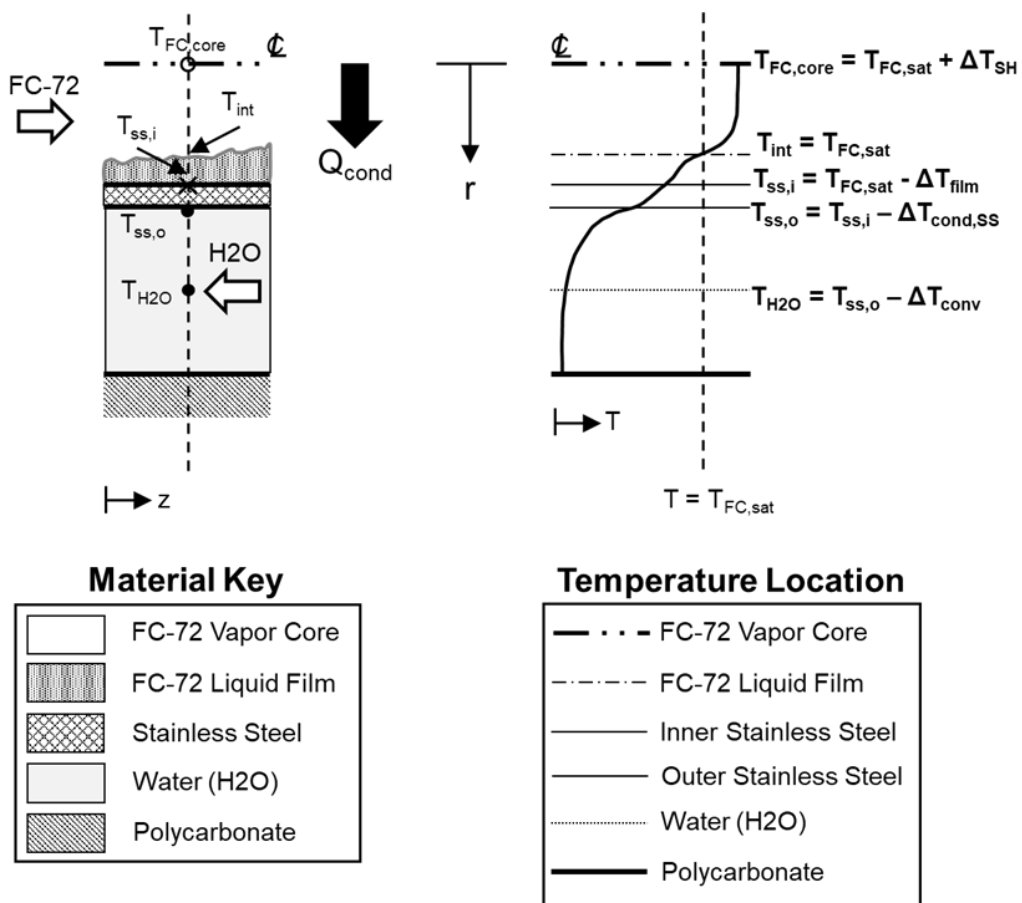


Figure 4.23 (b).

Figure 4.24 presents sample plots showing calculation of condensation heat transfer coefficient for a single test case corresponding to vertical downflow with  $G_{FC} = 301.9 \text{ kg/m}^2\text{s}$ ,  $G_{H_2O} = 388.2 \text{ kg/m}^2\text{s}$ ,  $P_{in} = 128.7 \text{ kPa}$ ,  $P_{WRBH} = 1552.7 \text{ W}$ ,  $x_{e,in} = 1.03$ , and  $x_{e,out} = 0.13$ . Figure 4.24(a) shows plots of experimental inlet and exit pressures for both FC-72 (condensate) and water (coolant), along with linear fits used to approximate pressure at intermediate locations.

Figure 4.24(b) provides local temperature measurements for FC-72 (with saturation temperature evaluated at local pressure), stainless-steel, and water, with stainless-steel and water temperatures corresponding to averages of circumferentially spaced local measurements as discussed previously. Water temperature curve fit is also shown along with its associated  $R^2$  value.  $R^2$  values for the set of cases used here are always above 0.9, and commonly in the range  $R^2 = 0.97 - 0.99$ , indicating water temperatures are well fit by the third order polynomials used.

Calculated inner stainless-steel wall temperature is also shown here, differing by 2-3°C in the inlet region and near-identical to outer wall temperatures in the exit region (due to a decrease in heat transfer as liquid film thickens in the exit region).

Local FC-72 temperature is plotted along with saturation temperature at the local pressure along the condensation length (with local temperature calculated based on sensible heat change in the upstream, superheated region). It is clear a small difference in values is visible near the first measurement point, after which the bulk flow becomes saturated ( $1.00 < x_{e,n} < 0$ ).

Figure 4.24(c) provides values of local condensation heat transfer coefficient, calculated using temperature values shown in Fig. 4.24(b) and Eq. (4.39). Values calculated using local FC-72 temperature in the superheated region are plotted separately from those calculated using  $T_{FC,sat}$  at all locations. This is done to highlight the small difference in values incurred in the inlet region of the channel (where bulk flow is expected to be superheated) and zero difference along the remainder of the channel length.

Overall, condensation heat transfer coefficient is seen to be high in the inlet region (where liquid film is thinnest), decline along the channel length as liquid content increases, and approach a low value in the exit region as flow transitions to single-phase liquid. Investigation of condensation heat transfer parametric trends will be performed in the following section, but first it is necessary to provide additional detail on uncertainty analysis for the present data.

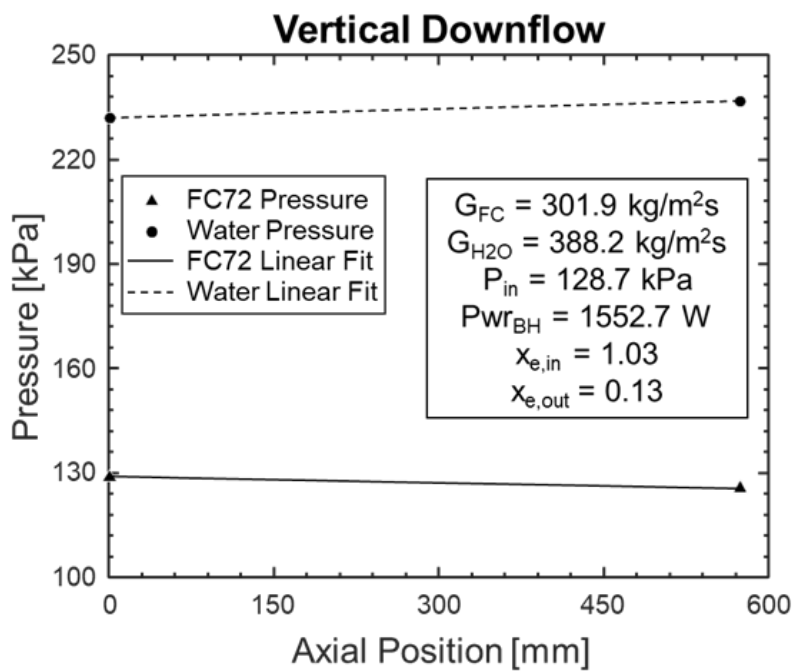


Figure 4.24: Values of (a) local pressure and (b) local temperature used to calculate local heat transfer coefficient values shown in (c). Includes comparison between use of local superheated vapor temperature and interface (saturation) temperature to calculate heat transfer coefficient values.

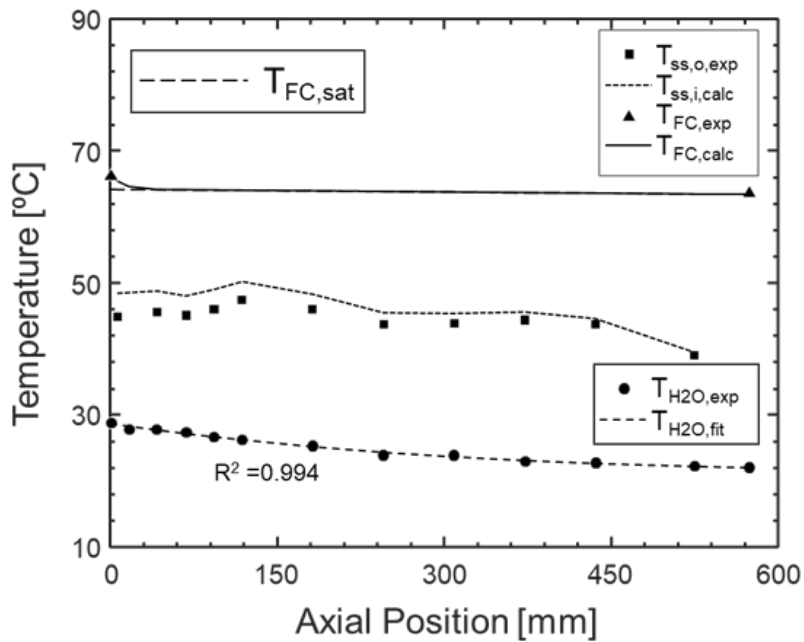


Figure 4.24 (b).

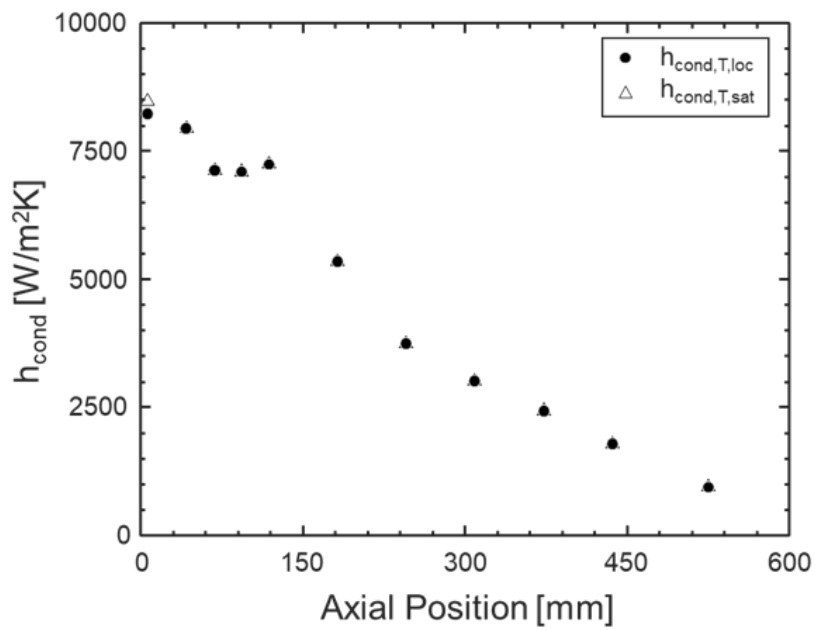


Figure 4.24 (c).

#### 4.3.1.2 Condensation Heat Transfer Coefficient Uncertainty Analysis

To calculate uncertainty associated with condensation heat transfer coefficients it is necessary to recall that Eqs. (4.39) and (4.36) combine to define heat transfer coefficient as

$$h_{cond,n} = \frac{\Delta q_{cond,n}}{\pi D_i \Delta z (T_{FC,sat,n} - T_{ss,i,n})} = \frac{\dot{m}_{H_2O} c_{p,f,H_2O} \left[ \frac{dT_{H_2O,fit}}{dz} \right]_n \Delta z}{\pi D_i \Delta z (T_{FC,sat,n} - T_{ss,i,n})}. \quad (4.40)$$

While performing heat transfer data reduction the water temperature curve fit derivative is evaluated locally about each measurement point, but to approximate uncertainty associated with this derivative it is more appropriate to treat this derivative as a change in water temperature across a larger  $\Delta z$  centered on each measurement location (meaning values of  $\Delta z$  are small in the upstream region and large in the downstream region). This leads to a relationship of the form

$$h_{cond,n} = \frac{\dot{m}_{H_2O} c_{p,f,H_2O} (T_{H_2O,n+1} - T_{H_2O,n})}{\pi D_i \Delta z_n (T_{FC,sat,n} - T_{ss,i,n})}, \quad (4.41)$$

which has uncertainty values associated with measurement of water mass flowrate  $\dot{m}_{H_2O}$ , water temperatures  $T_{H_2O,n+1}$  and  $T_{H_2O,n}$ , FC-72 saturation temperature evaluated at local pressure  $T_{FC,sat,n}$ , and stainless-steel wall temperature  $T_{ss,i,n}$ . Tube inner diameter  $D_i$  and thermocouple spacing  $\Delta z_n$  are assumed to be exact quantities (as they were measured precisely after fabrication), as is specific heat of cooling water  $c_{p,f,H_2O}$ . Uncertainty for local condensation heat transfer coefficient may then be calculated as

$$\left[ \frac{U_h}{h_{cond,n}} \right]^2 = \left[ \frac{U_{\dot{m}}}{\dot{m}_{H_2O}} \right]^2 + 2 \left[ \frac{U_{T,H_2O}}{T_{H_2O,n+1} - T_{H_2O,n}} \right]^2 + \left[ \frac{U_{T,FC,sat}}{T_{FC,sat,n} - T_{ss,i,n}} \right]^2 + \left[ \frac{U_{T,ss}}{T_{FC,sat,n} - T_{ss,i,n}} \right]^2, \quad (4.42)$$

where  $U_h$ ,  $U_{\dot{m}}$ ,  $U_{T,H_2O}$ ,  $U_{T,FC,sat}$ , and  $U_{T,ss}$  are the uncertainties of local condensation heat transfer coefficient, water mass flowrate, water temperature measurements, calculated FC-72 saturation temperature at the local pressure, and stainless-steel wall temperature measurements, respectively.  $U_h$  is the parameter being solved for, but all other uncertainties are defined as  $U_{\dot{m}} = 0.002\dot{m}_{H_2O}$ ,  $U_{T,H_2O} = 0.1^\circ\text{C}$ ,  $U_{T,FC,sat} = 0.2^\circ\text{C}$ , and  $U_{T,ss} = 0.3^\circ\text{C}$ . Water and stainless-steel wall temperatures are measured using type-T thermocouples with manufacturer stated uncertainties of  $\pm 0.4^\circ\text{C}$  (as mentioned in section 2.2), but these sensors went through extensive calibration in NASA Glenn Research Center's calibration lab prior to use, and post-calibration uncertainties are reflected in the values provided above.

Equation (4.42) was evaluated for every set of operating conditions tested, and Figure 4.25(a) provides local uncertainty results for a subset of data corresponding to all cases with superheated (or near-superheated) inlet conditions. Local values calculated for each set of operating conditions were averaged (over all operating conditions) at each axial measurement location, providing representative values of uncertainty as a function of position along the channel length.

It is clear uncertainty is low in the upstream region, with values for each of the three orientations falling near 25%. This gradually increases for successive measurement points until the sixth measurement station, where spacing between successive temperature measurements becomes larger and uncertainty drops. Near the exit of the channel, however, uncertainty increases significantly, approaching values of 100% for the final three measurement locations.

All variation in local uncertainty values may be explained by the dominant contribution of water temperature measurement on overall uncertainty value. The denominator of the second term on the right-hand side of Eq. (4.42),  $T_{H2O,n+1} - T_{H2O,n}$ , is often on the same order of magnitude as measurement uncertainty for each thermocouple ( $\sim 0.1 - 1^\circ\text{C}$ ), meaning that term is the primary source of uncertainty in condensation heat transfer coefficient calculation. Recalling the plot of water temperatures versus position in Fig. 4.24(b), water temperatures change relatively rapidly in the upstream region, meaning the difference in successive values is high and their contribution is low. Temperatures change more slowly near the FC-72 exit, but spacing between points is increased, resulting in the drop in uncertainty near the sixth measurement station. Near the FC-72 exit (and water inlet), however, there are near-zero changes in water temperature, resulting in the high uncertainty values shown in Fig. 4.25(a).

These trends regarding uncertainty of local measurements should be kept in mind when analyzing local heat transfer trends in the following section but are not the only calculated uncertainties to keep in mind. The parameter most frequently of interest when analyzing condensing systems is channel average heat transfer coefficient  $h_{cond,ave}$ , defined analytically as

$$h_{cond,ave} = \frac{1}{L_{cond}} \int_0^{L_{cond}} h(z) dz, \quad (4.43)$$

where the condensation length  $L_{cond}$  is defined as the portion of the channel with quality  $1.00 < x_{e,loc} < 0$ . In the present scheme, average condensation heat transfer coefficient is calculated numerically according to the relationship

$$h_{cond,ave} = \frac{1}{L_{cond}} \sum_{i=1}^{n_{cond}} h_{cond,n} \Delta z_n, \quad (4.44)$$

where  $\Delta z_n$  is the local distance centered between consecutive measurement points along the condensation length and  $n_{cond}$  is the number of measurement locations with local qualities  $1.00 < x_{e,loc} < 0$  for each test case. It should be noted that  $n_{cond}$  as well as the physical locations of  $n_{cond}$  shift depending on whether inlet conditions are slightly superheated or saturated mix.

Propagating uncertainty associated with local condensation heat transfer coefficients  $h_{cond,n}$  through Eq. (4.44) is done by evaluating the expression

$$\frac{U_{h,ave}}{h_{cond,ave}} = \frac{1}{L_{cond}} \left( \sum_{i=1}^{n_{cond}} E_{cond,i}^2 \Delta z_i^2 \right)^{1/2}, \quad (4.45)$$

where  $E_{cond,i}$  is the absolute error associated with each local heat transfer coefficient measurement (relative value as shown in Fig. 4.25(a) multiplied by local heat transfer coefficient value).

For the same cases as plotted in Fig. 4.25(a), Fig. 4.25(b) displays uncertainty of average heat transfer coefficient plotted versus FC-72 mass velocity for all three orientations tested. Uncertainty reaches its maximum value of ~25% for low mass velocity cases, decreasing to ~5% for higher mass velocity cases. This is again due to the role of water temperature measurement dominating heat transfer coefficient uncertainty: Cases with high  $G_{FC}$  have larger associated condensation heat transfer, leading to larger temperature gradients on the water side which reduce uncertainty.

At each FC-72 mass velocity results for three different water mass velocities are shown. In each case the highest measurement uncertainty is associated with the highest water mass velocity, as these cases have the smallest water temperature change along the heated length. This would indicate low water flowrate cases as desirable, but as will be seen when analyzing heat transfer results, low uncertainty must be balanced with the need for water-independent heat transfer measurement (requiring high water heat transfer coefficients and thus high water flowrates).

Moving forward, heat transfer results will be presented without error-bars, as these unnecessarily crowd figures and make interpretation difficult. Thus, it is important to use the information presented in this subsection when analyzing heat transfer results presented hereafter. Low-uncertainty results (channel-averaged results, local results at the channel inlet) may be

interpreted with confidence, while high-uncertainty results (local results at the channel exit) should only be interpreted with care.

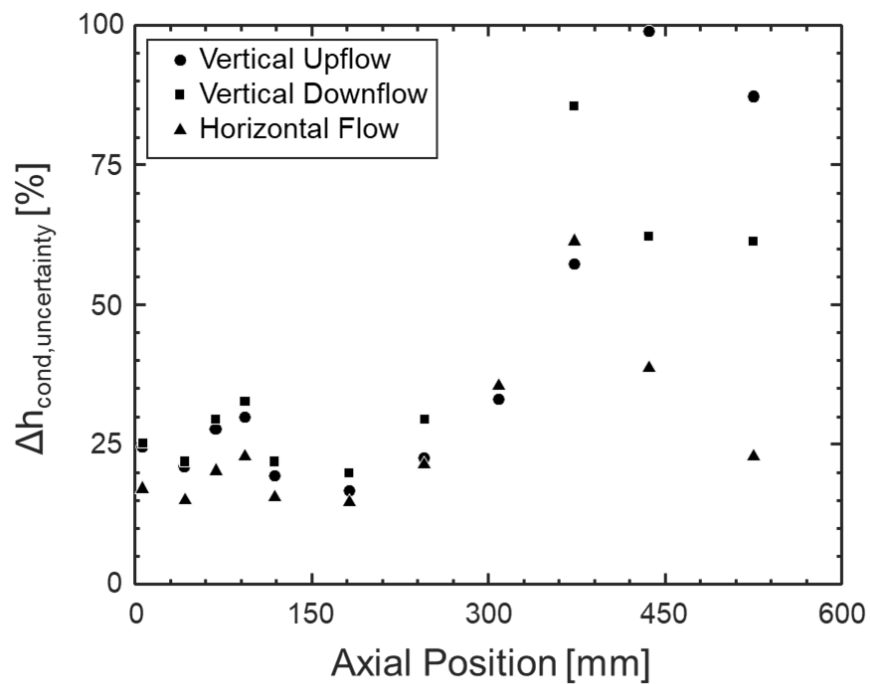


Figure 4.25: Uncertainty of (a) local heat transfer coefficient calculations averaged over all cases with superheated vapor inlet conditions (inset in Fig. 6 (b)) versus measurement position, and (b) uncertainty of channel length average heat transfer coefficient values versus FC-72 mass velocity.

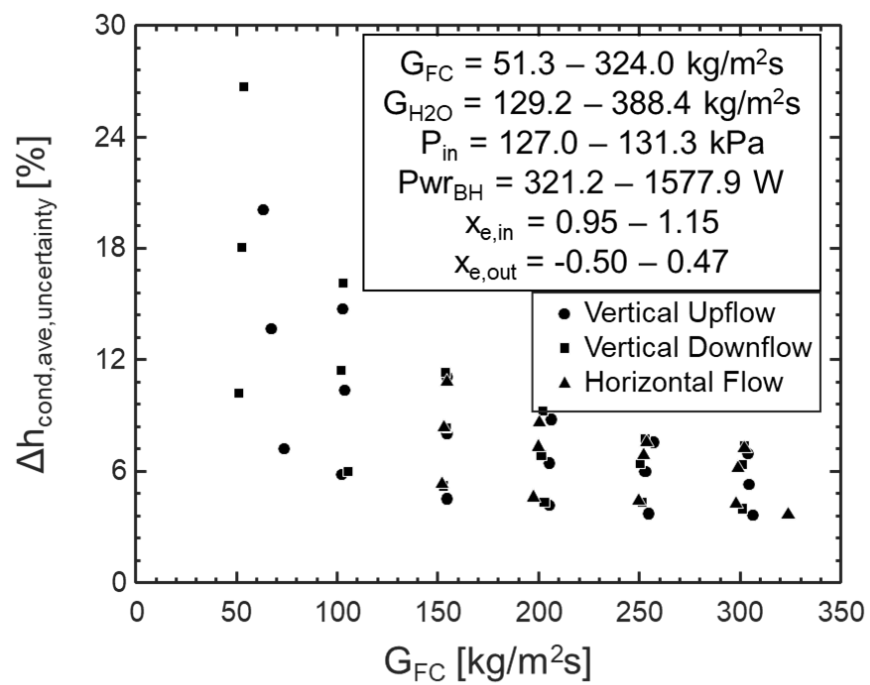


Figure 4.25 (b).

### 4.3.2 Heat Transfer Results

Having provided details on condensation heat transfer coefficient data reduction and uncertainty analysis, it is now time to investigate condensation heat transfer coefficient trends.

#### 4.3.2.1 Local Results

Figure 4.26 provides plots of local heat transfer coefficient versus axial position along the condensation length for each orientation. Figure 4.26(a) shows plots corresponding to all mass velocity cases with superheated vapor inlet conditions, Fig. 4.26(b) provides plots of high mass velocity ( $G_{FC} \sim 300 \text{ kg/m}^2\text{s}$ ) with multiple inlet qualities, and Fig. 4.26(c) low mass velocity ( $G_{FC} \sim 100 \text{ kg/m}^2\text{s}$ ) with multiple inlet qualities. There is no horizontal data in Fig. 4.26(c) due to the omission of low flowrate horizontal cases (as discussed in the preceding section). It should also be noted that all cases presented in Fig. 4.26 correspond to the highest water mass velocity.

Figure 4.26(a) shows that, for all orientations and flowrates, condensation heat transfer is at its maximum value in the upstream region of the channel. The liquid film here is at its thinnest which leads to highly efficient condensation heat transfer. Towards the channel exit significant liquid film thickening has occurred which leads to decreased condensation heat transfer. For some of the lower flowrate cases full condensation is achieved prior to the channel exit, and heat transfer coefficient for locations past this point are not calculated.

Figure 4.26(b) provides similar results, now for a single mass velocity  $G_{FC} \sim 300 \text{ kg/m}^2\text{s}$  with different curves on the same plots representing changes in channel inlet quality (corresponding to target values of  $x_{e,in} \sim 1.00, 0.80, 0.60,$  and  $0.40$ ). Local heat transfer coefficient values in each orientation are seen to be highest for the highest quality cases and decrease as inlet quality decreases. This result makes sense intuitively as lower inlet quality cases possess thicker liquid films which reduce local condensation heat transfer coefficient.

Figure 4.26(c) shows results for low mass velocity ( $G_{FC} \sim 100 \text{ kg/m}^2\text{s}$ ) with multiple inlet qualities. Differences between inlet qualities is significantly reduced compared to that seen in Fig. 4.26(b) for high mass velocity cases. This indicates inlet quality has a secondary effect on condensation heat transfer coefficient, with mass velocity playing a dominant role.

Across Figs. 4.26(a), 4.26(b), and 4.26(c), the influence of orientation is most noticeable at low mass velocities. For cases with  $G_{FC} \sim 50$  and  $100 \text{ kg/m}^2\text{s}$ , vertical upflow is seen to exhibit higher local heat transfer coefficient values than vertical downflow. This can be attributed to the

presence of a counter-current flow regime in upflow condensation for these operating conditions (as discussed in Fig. 4.16) leading to significant liquid film breakup and periodic transport of liquid through the condensation length. Vertical downflow cases for these operating conditions are expected to exhibit a smooth liquid film along the entire condensation length with liquid transport primarily due to body force. Although a more stable operating condition (in terms of mass velocity and pressure fluctuations), this configuration is seen to yield lower overall heat transfer coefficient values.

For higher mass velocity cases, results across the three orientations become similar. The only exceptions are heat transfer coefficient values calculated at the first (upstream) measurement location for horizontal flow, which is noticeably higher than its vertical upflow and downflow counterparts. In the downstream region behavior becomes near identical to that for upflow and downflow orientations, however, meaning this upstream enhancement is a localized phenomenon. It should also be noted that this difference for horizontal flow falls within the uncertainty band outlined in Fig. 4.25(a), meaning it should not be interpreted as a physical phenomenon.

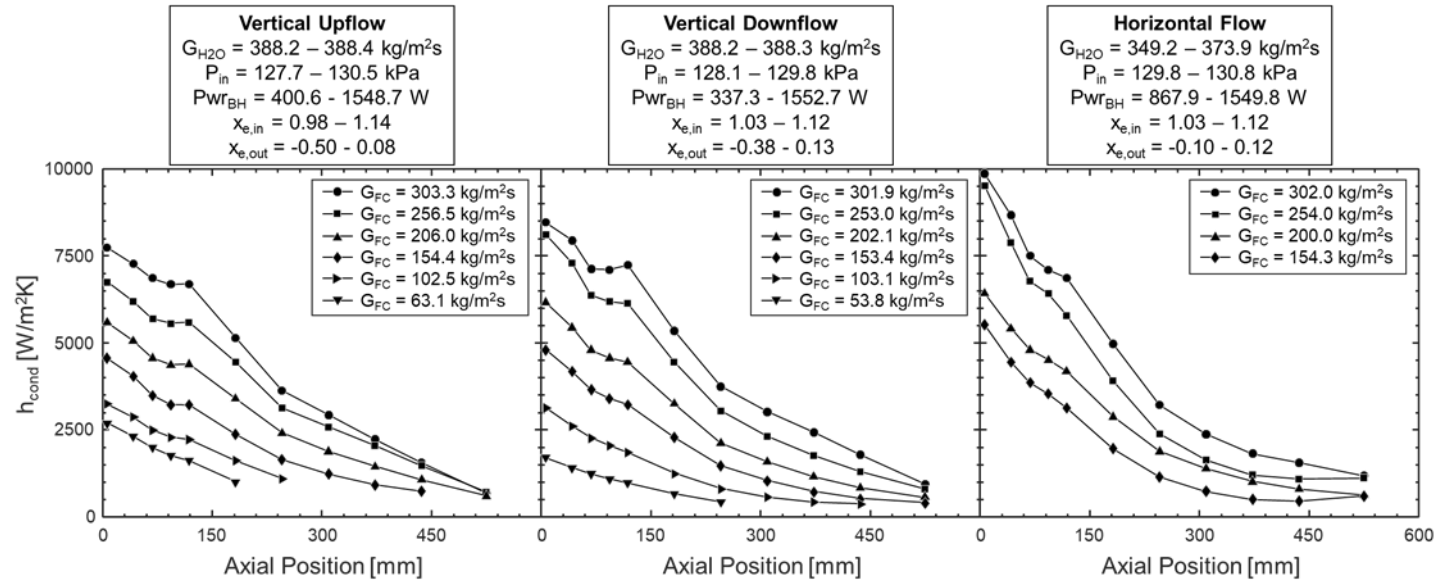


Figure 4.26: Evaluation of heat transfer coefficient versus axial location for all three orientations with (a) multiple flowrates and  $x_{e,in} \sim 1.05$ , (b) multiple inlet qualities and  $G_{FC} \sim 300 \text{ kg/m}^2\text{s}$ , and (c) multiple inlet qualities and  $G_{FC} \sim 100 \text{ kg/m}^2\text{s}$ .

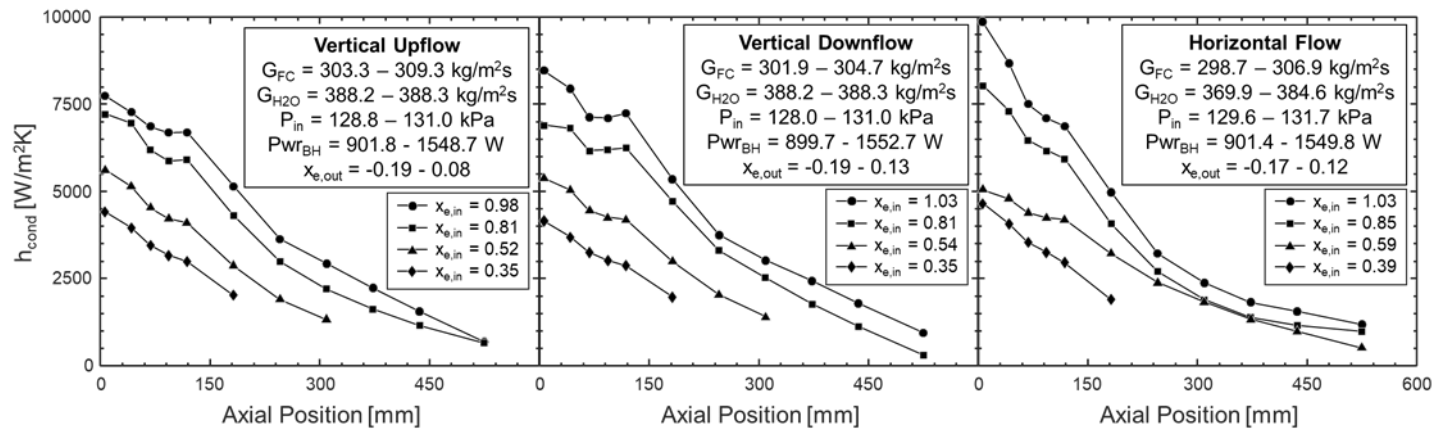


Figure 4.26 (b).

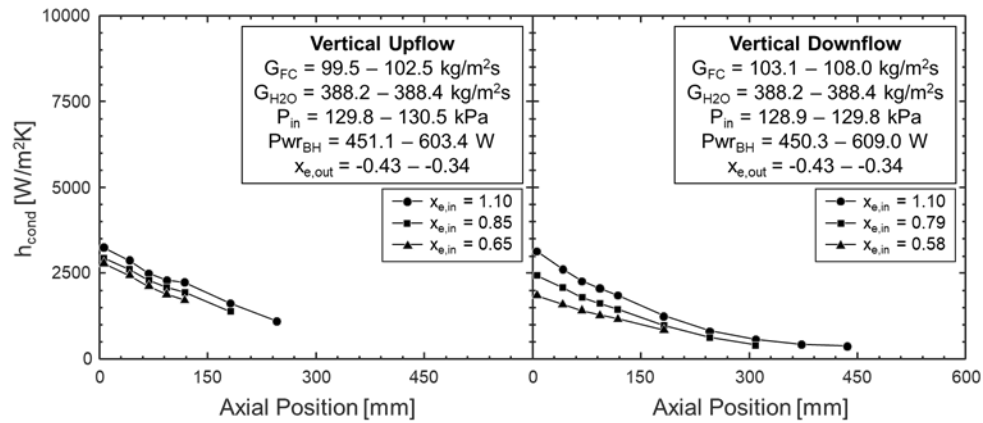


Figure 4.26 (c).

Figure 4.27 again provides plots of local condensation heat transfer coefficient, this time plotted versus local quality (as calculated by Eq. (4.37), corresponding to quality at each of the 11 measurement locations). Only locations with qualities in the range  $1.00 < x_{e,n} < 0$  are shown in the present plots. Figures 4.27(a), 4.27(b), and 4.27(c) correspond to vertical upflow, vertical downflow, and horizontal flow orientations, respectively. Each subplot within the subfigures shows results for multiple mass velocities with inlet qualities of  $x_{e,in} \sim 1.00$ ,  $x_{e,in} \sim 0.80$ , and  $x_{e,in} \sim 0.50$ , moving from left to right.

Figure 4.27(a) clearly shows values of heat transfer coefficient decreasing as local quality decreases, similar to the conclusion drawn when analyzing Fig. 4.26. Additionally, the trend of decreased heat transfer coefficient for decreasing mass velocity is again present, although only noticeable at high local qualities. As local quality decreases differences between mass velocities are reduced, with heat transfer coefficient values corresponding to near-zero qualities exhibiting almost no differences across the full mass velocity range.

As discussed when comparing Figs. 4.26(b) and 4.26(c), differences in heat transfer coefficient for different mass velocities are most pronounced for high local qualities. This is likely due to the dominant role of interfacial shear (provided by the fast-moving vapor core) for these regions where the liquid film is thinnest. As liquid film thickness increases liquid inertia becomes more appreciable and interfacial shear stress plays a less influence role in advecting the liquid film, leading to smaller differences in heat transfer coefficient for different mass velocities.

It is also important to recall when analyzing differences in heat transfer coefficient for the low quality region that these measurements often correspond to the exit region of the channel, which Fig. 4.25(a) showed possessing significant uncertainty. Thus, these results should be interpreted with caution in the present study.

Across all three orientations shown in Fig. 4.27, differences in orientation are again most visible for low mass velocity cases, with vertical upflow cases exhibiting higher heat transfer coefficient values compared to vertical downflow counterparts. For higher mass velocity cases all three orientations yield similar values for local condensation heat transfer coefficient as a function of local quality.

It should be noted that comparison of heat transfer coefficient values for fixed orientation, mass velocity, and local quality, but with differing inlet quality (moving horizontally across Fig. 4.26(a), 4.26(b), or 4.26(c)), indicates differences in value. Practically, this indicates a dependence

of heat transfer coefficient on the axial location where the measurement was made: In a purely theoretical case this should not be true, but practical considerations (i.e. change in local pressure with position, change in wall temperature due to changes in cooling water temperature, differences in uncertainty with position as discussed in Fig. 4.25) mean values may exhibit slight differences.

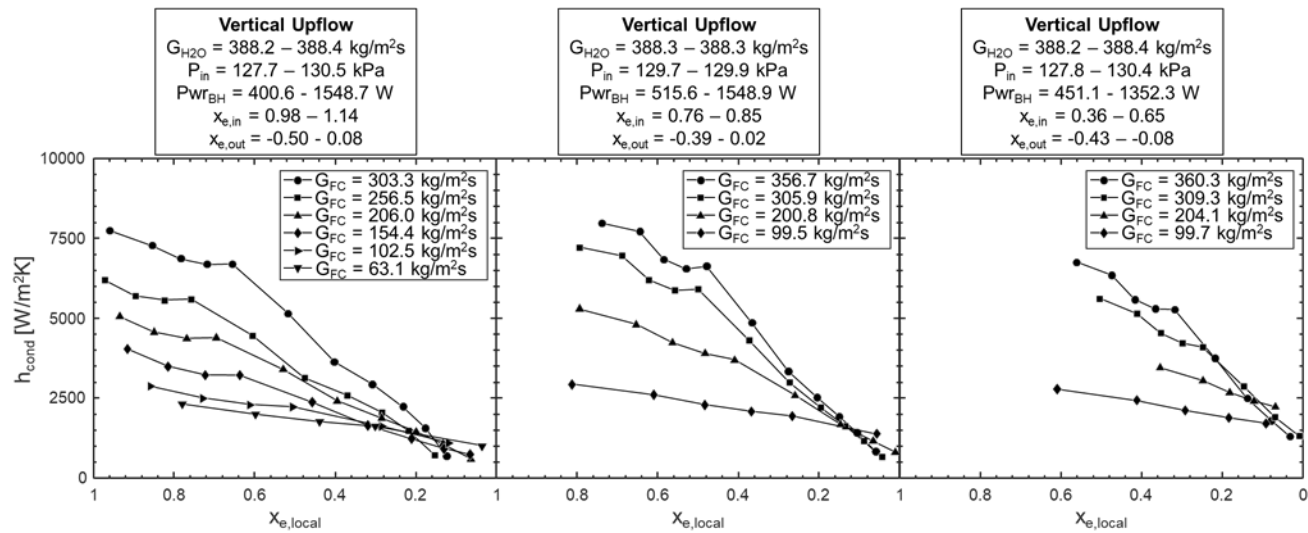


Figure 4.27: Evaluation of heat transfer coefficient versus local quality for multiple mass velocities with (from left to right)  $x_{e,in} > 1.00$ ,  $x_{e,in} \sim 0.80$ , and  $x_{e,in} \sim 0.60$ , in (a) vertical upflow, (b) vertical downflow, and (c) horizontal flow orientations.

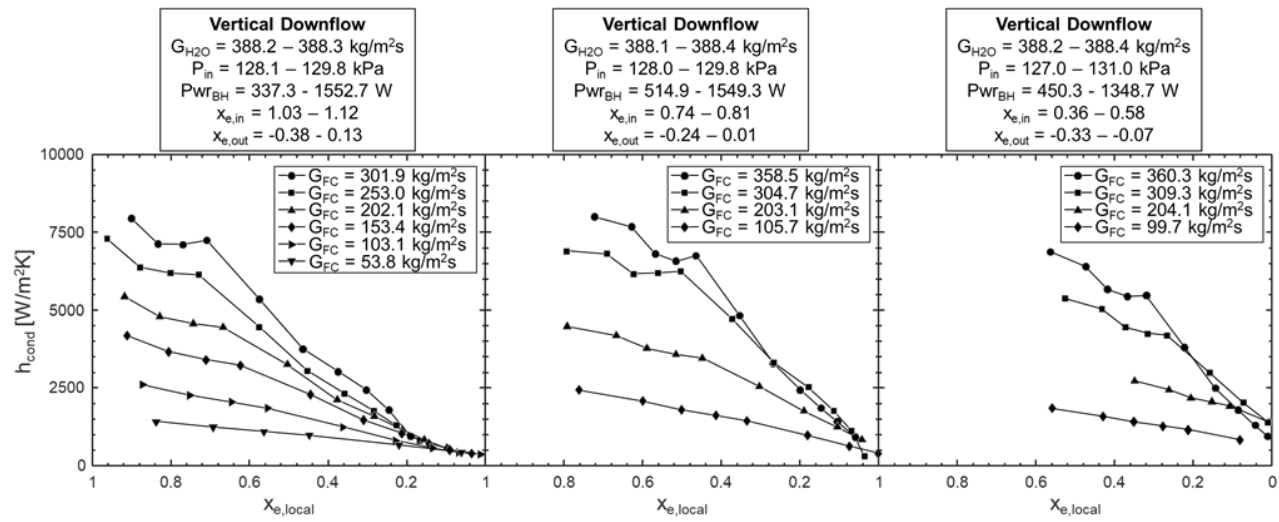


Figure 4.27 (b).

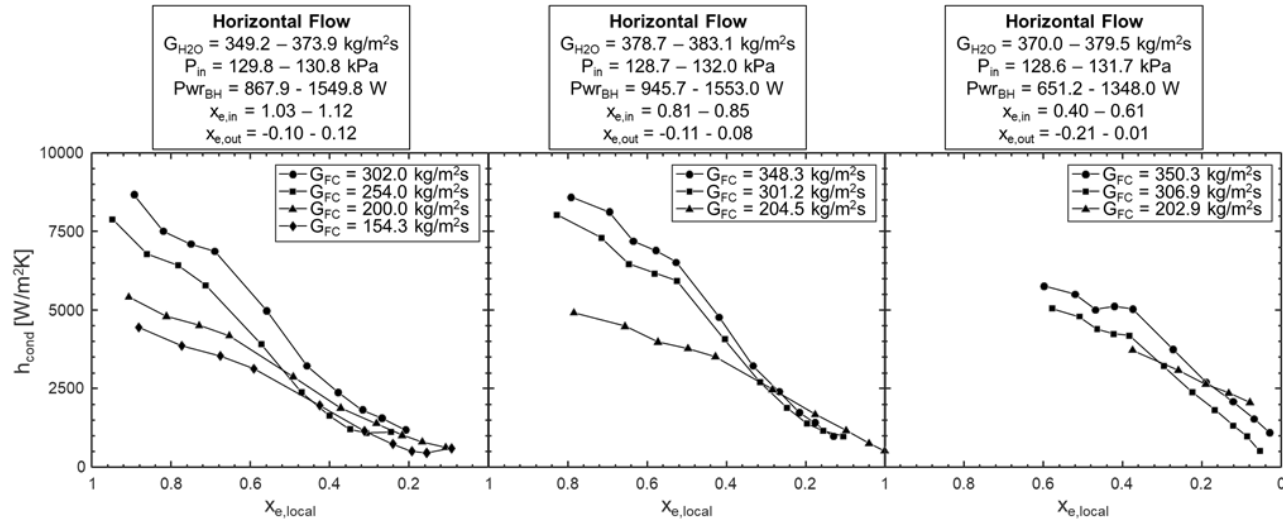


Figure 4.27 (c).

#### 4.3.2.2 Channel-average Results

Prior to discussing parametric trends for channel-averaged condensation heat transfer coefficient, it is first necessary to comment on the impact of water mass velocity on overall condensation within the test section. Figure 4.28 provides plots of channel averaged heat transfer coefficient (left, calculated using Eq. (4.44)) and total condensation heat transfer (right) versus cooling water mass velocity  $G_{H2O}$ . All results prior to this point have corresponded to maximum cooling water mass velocity of  $G_{H2O} \sim 388 \text{ kg/m}^2\text{s}$ , but three different water flowrates were tested (as outlined in Table 2.3) to determine ability of the current test section to offer condensation heat transfer results independent of cooling water flowrate. If water flowrate is high enough heat transfer coefficient on the condensate side will become the limiting thermal resistance and heat transfer results will not change for increase in water flowrate.

Figure 4.28(a) shows that, for vertical upflow condensation, cases with low condensate (FC-72) mass velocity exhibit little-to-no changes in condensation heat transfer for changes in cooling water mass velocity. As condensate mass velocity increases, however, channel average heat transfer coefficient and total condensation heat transfer are seen to decrease and increase, respectively, for increases in cooling water mass velocity. Moderate values of  $G_{FC}$  appear to plateau between  $G_{H2O} \sim 260 - 390 \text{ kg/m}^2\text{s}$ , but high values of  $G_{FC}$  exhibit changes in heat transfer all the way through peak values of  $G_{H2O}$ . This decrease in heat transfer coefficient is likely attributable to a lowering of the stainless-steel wall temperature by faster water flow.

Similar conclusions may be drawn when analyzing results for vertical downflow and horizontal flow orientations in Figs. 4.28 (b) and (c), respectively. Based on this, data presented for the remainder of this section will correspond only to cases with (i)  $G_{H2O} \sim 390 \text{ kg/m}^2\text{s}$ , (ii)  $G_{H2O} \sim 260 \text{ kg/m}^2\text{s}$  with  $G_{FC} \leq 150 \text{ kg/m}^2\text{s}$ , and (iii)  $G_{H2O} \sim 130 \text{ kg/m}^2\text{s}$  with  $G_{FC} \leq 100 \text{ kg/m}^2\text{s}$ , done to ensure heat transfer results are water-side independent (or as close as possible using the current dataset). It is expected the final ISS experiment test matrix will include cases with higher water mass velocity ( $G_{H2O} \sim 520 \text{ kg/m}^2\text{s}$ ), done to help further ensure water-side independence of condensation results.

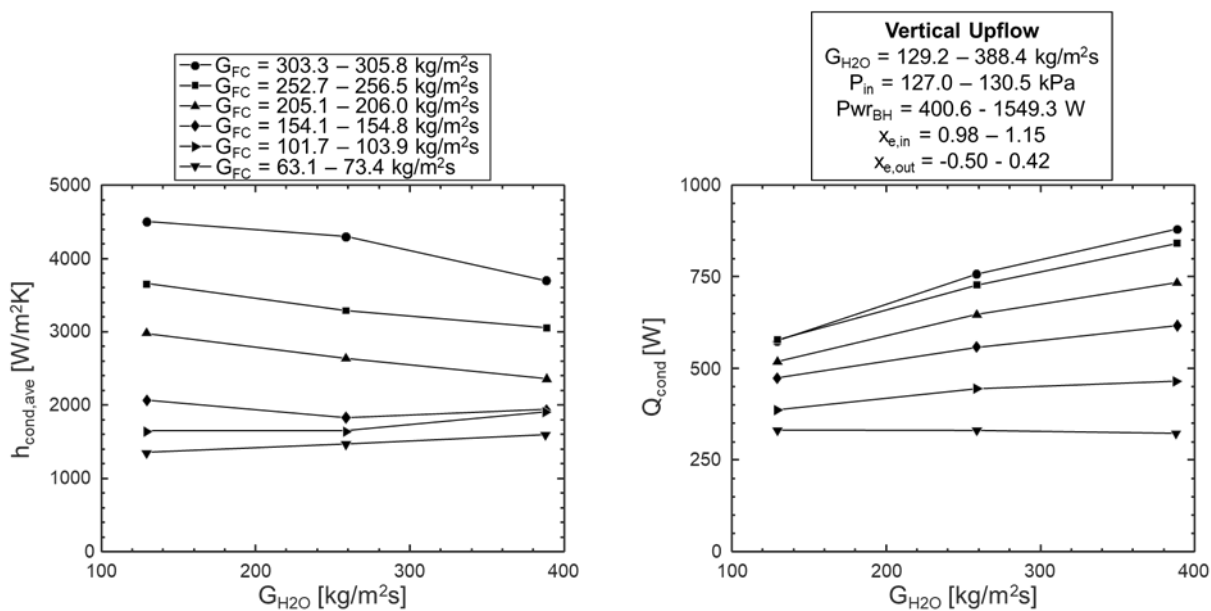


Figure 4.28: Plots of channel-average condensation heat transfer coefficient and total condensation energy transfer versus cooling water mass velocity for (a) vertical upflow, (b) vertical downflow, and (c) horizontal flow orientations.

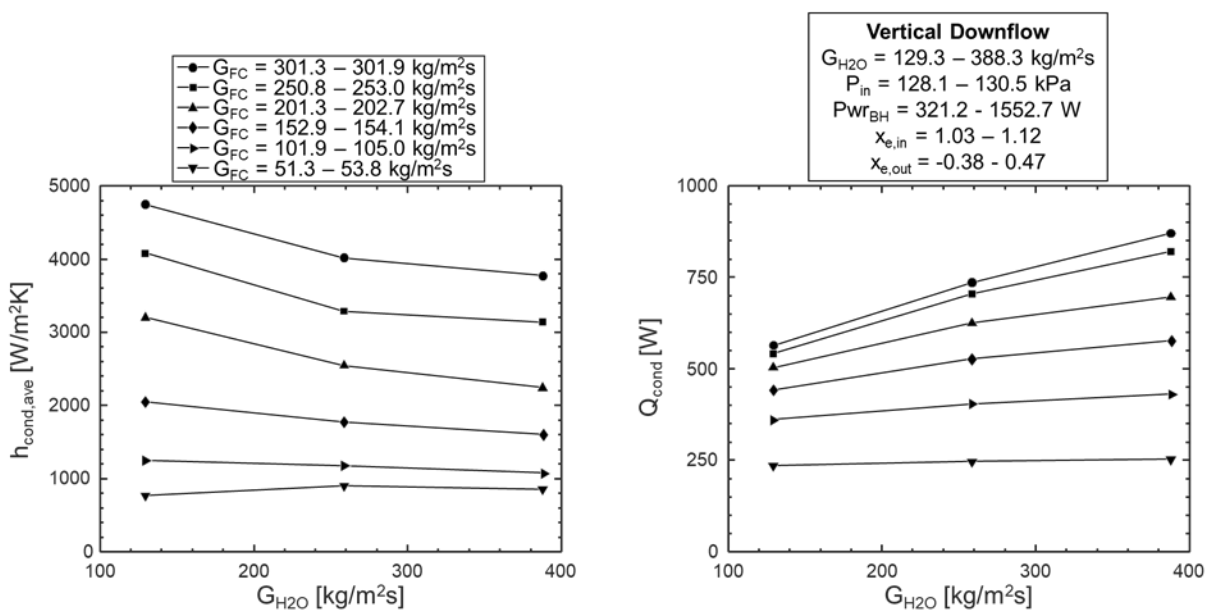


Figure 4.28 (b).

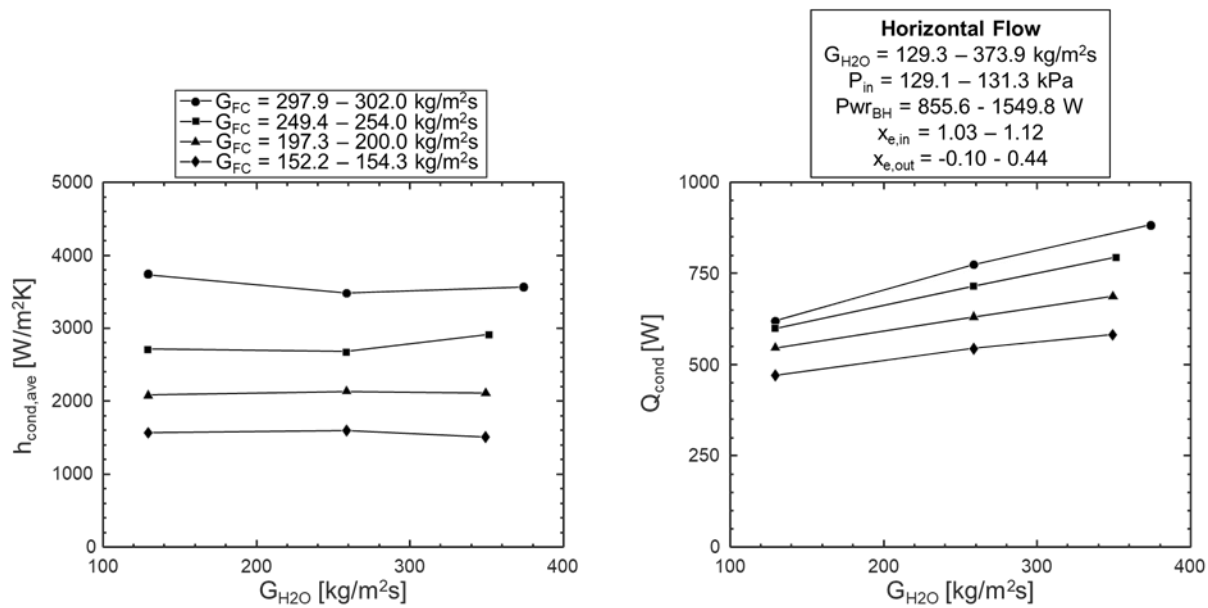


Figure 4.29 (c).

Figure 4.29 provides plots of average heat transfer coefficient (using the water-independent subset of data) versus FC-72 mass velocity for each orientation tested. Separate curves on each plot correspond to different water mass velocities tested, and the fact these curves collapse well verifies the subset outlined in the preceding paragraph is composed of water-independent condensation results.

Comparison between Figs. 4.29(a) and 4.29(b), corresponding to vertical upflow and downflow orientations, reinforces the trend first discussed alongside Fig. 4.26, that at low FC-72 mass velocities upflow heat transfer is higher than downflow. As mass velocity increases, however, values of channel-length average heat transfer coefficient become similar for all three orientations (including horizontal flow in Fig. 4.29(c)).

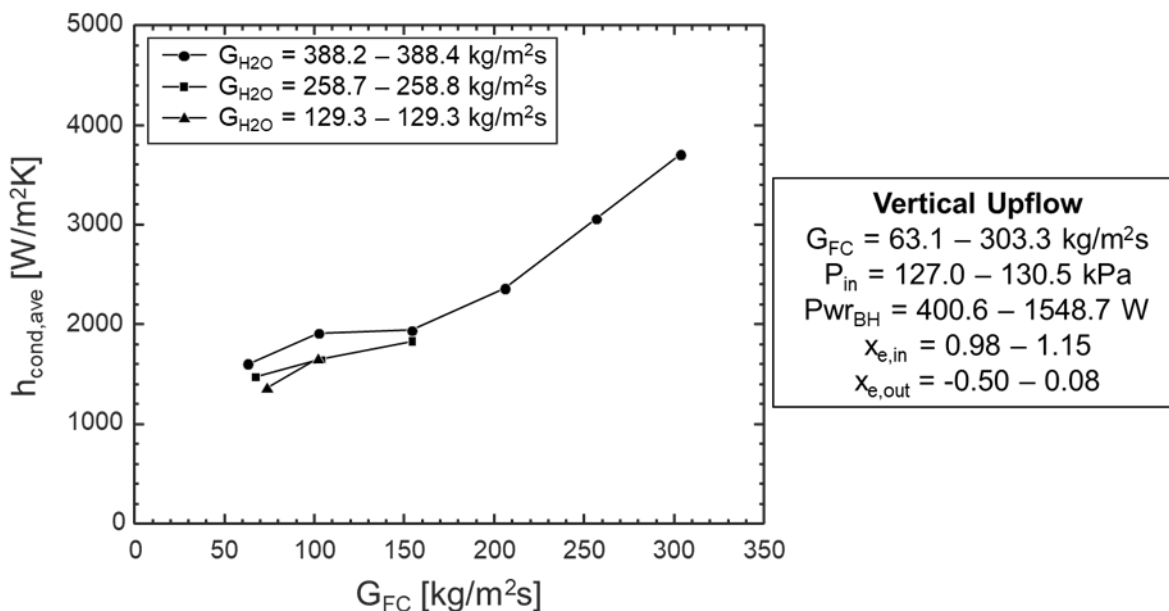


Figure 4.29: Evaluation of condensation length average heat transfer coefficient versus FC-72 mass velocity for (a) vertical upflow, (b) vertical downflow, and (c) horizontal flow orientations.

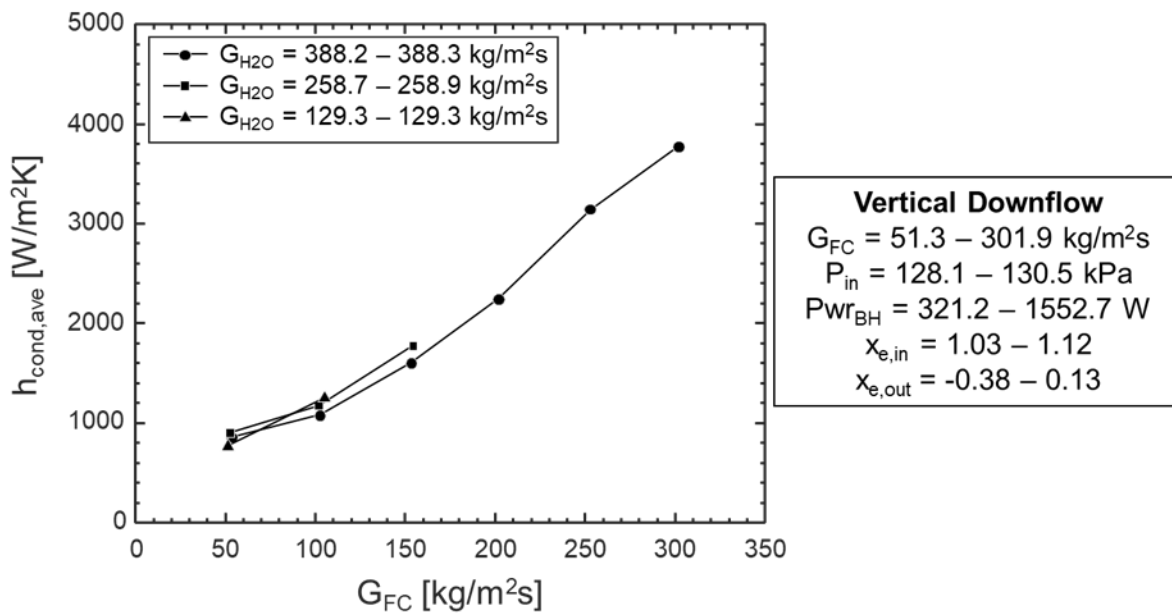


Figure 4.29 (b).

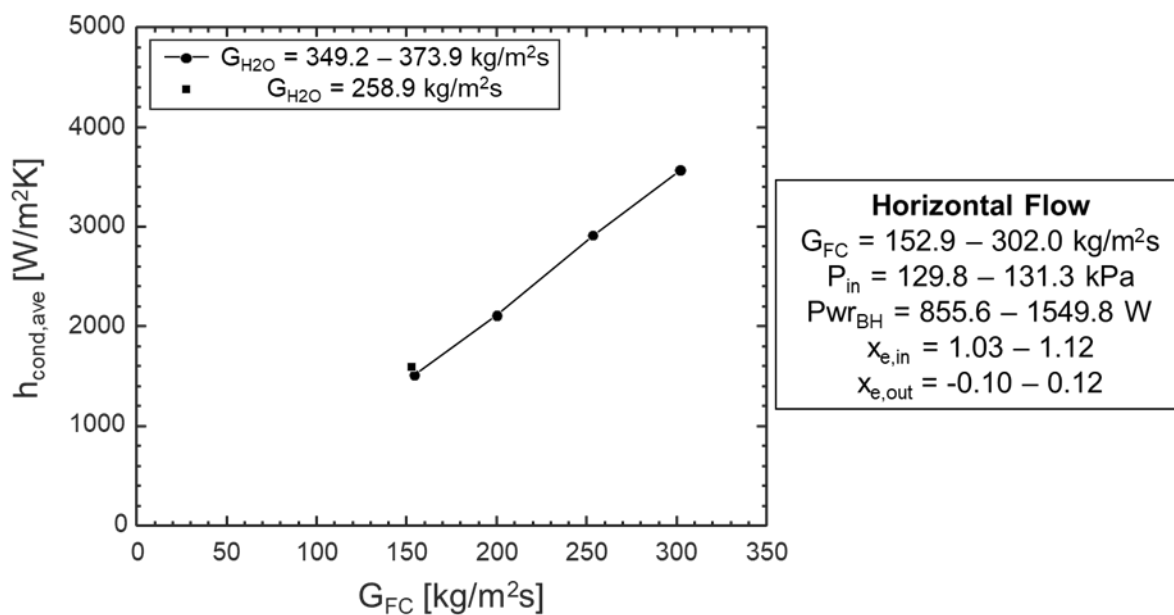


Figure 4.29 (c).

Figure 4.30 provides similar plots for each orientation, this time of channel average heat transfer coefficient versus FC-72 inlet quality for each case. Curves on each plot represent similar values of FC-72 mass velocity, and only the highest water mass velocity of  $G_{H2O} \sim 390 \text{ kg/m}^2\text{s}$  is represented in this figure.

Trends related to changes in inlet quality are not as straightforward to interpret as those for FC-72 mass velocity. In the majority of cases, increasing inlet quality from a low value towards  $x_{e,in} = 1.00$  results in increased heat transfer coefficient (seen for most FC-72 mass velocities in Fig. 4.30(a) and 4.30(b) corresponding to vertical upflow and downflow). Above  $x_{e,in} = 1.00$ , however, average heat transfer coefficient is seen to decrease for increasing  $x_{e,in}$ . This is likely due to using only points with  $1.00 < x_{e,loc} < 0$  when calculating channel-average heat transfer coefficient, which results in some upstream measurement locations being neglected when calculating channel average heat transfer coefficient for cases with superheated vapor inlet conditions.

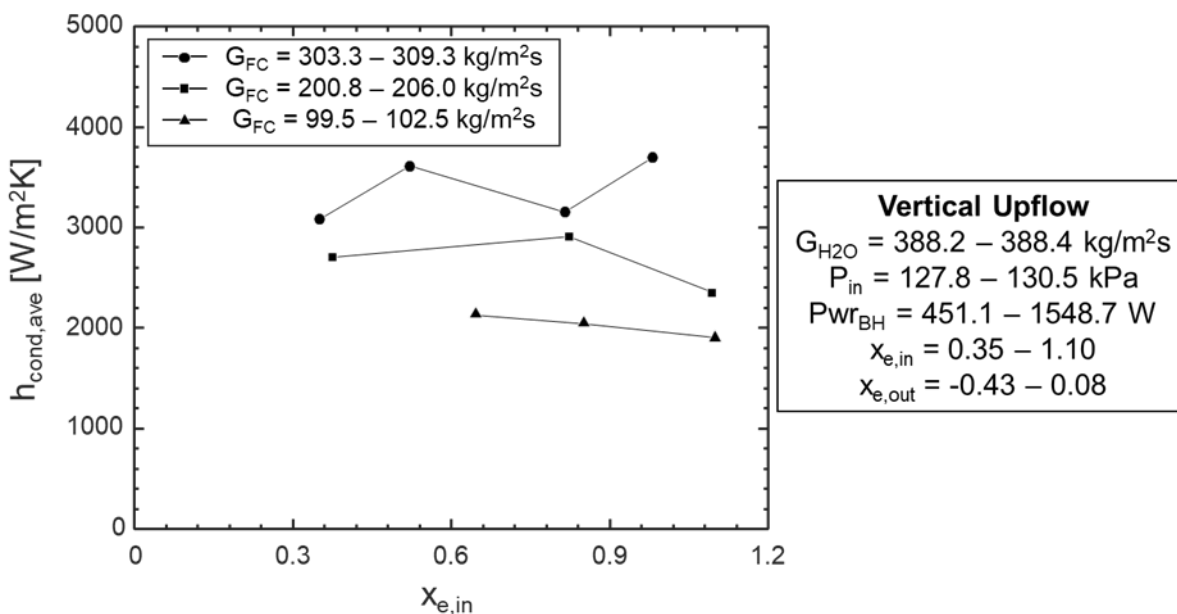


Figure 4.30: Evaluation of condensation length average heat transfer coefficient versus FC-72 inlet quality for (a) vertical upflow, (b) vertical downflow, and (c) horizontal flow orientations.

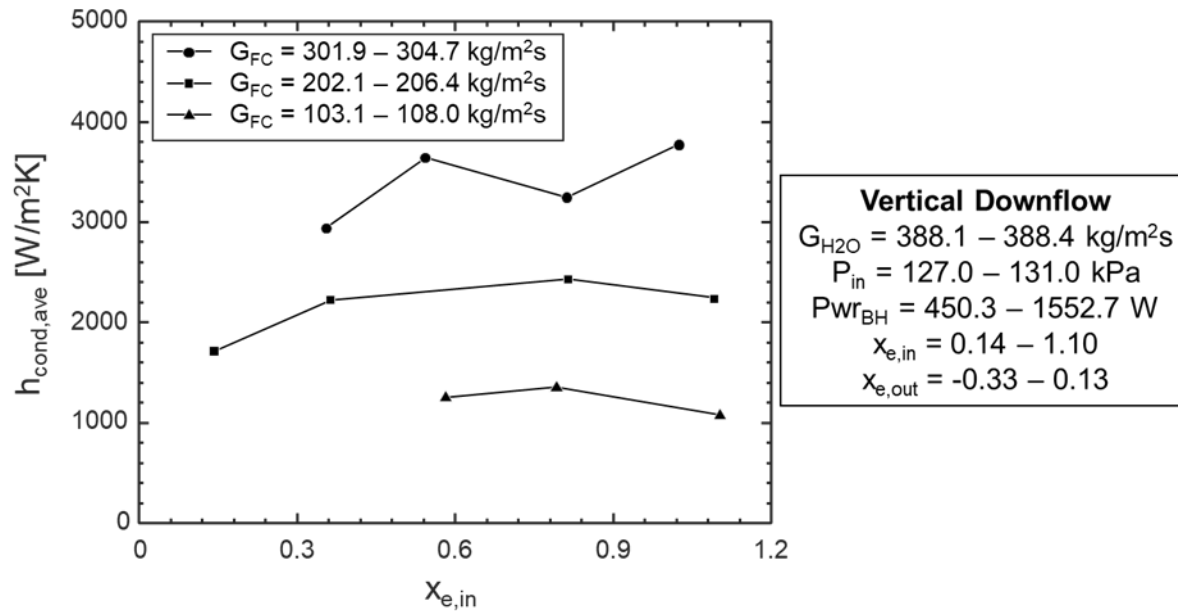


Figure 4.30 (b).

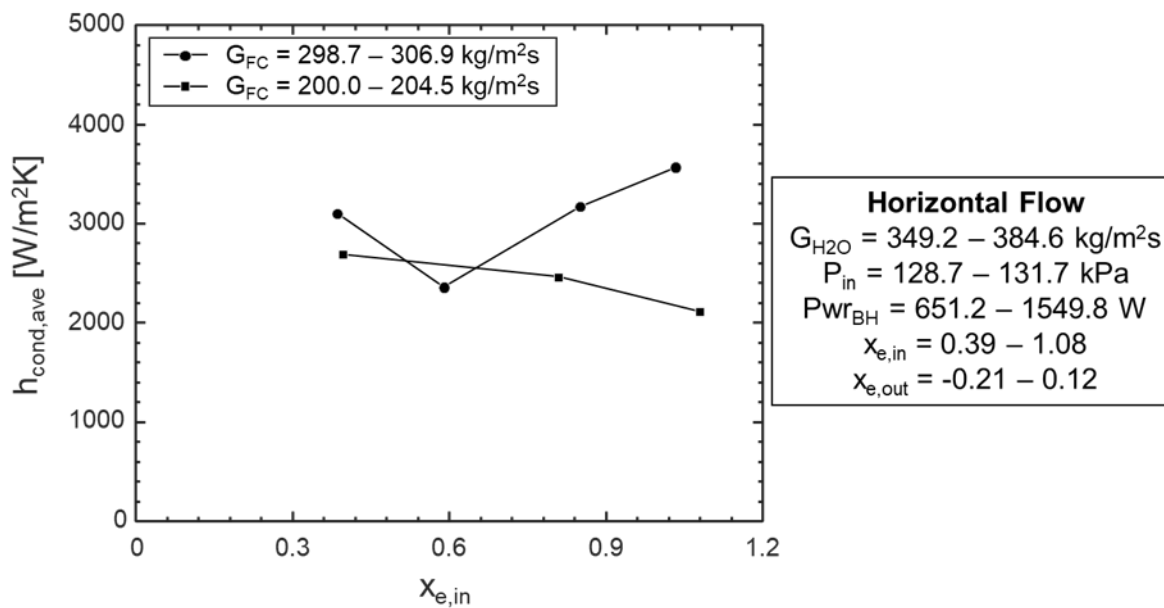


Figure 4.30 (c).

Across Figs. 4.26-4.30 (presenting both local and channel averaged values for condensation heat transfer coefficient), mass velocity (flow inertia) is seen to be the dominant parameter affecting values of condensation heat transfer coefficient. Higher flow inertia is seen to lead to higher condensation rate in all cases. Flow quality is also seen to influence condensation heat transfer coefficient, with lower quality cases/locations (meaning more liquid is present) exhibiting lower heat transfer rate due to reduced interfacial area and lower temperature gradient between vapor condensate and tube surface (due to the presence of thick liquid film).

When comparing heat transfer results across the three orientations investigated heat transfer behavior is seen to be near-identical for high mass velocity cases, while at low mass velocities heat transfer behavior differs significantly between orientations. These orientation effects are investigated in more detail in the following subsection.

#### 4.3.2.3 Influence of Body Force

As discussed in the introduction, conducting flow condensation tests at multiple orientations in Earth's gravity is one method for investigating the influence of body force on flow condensation heat transfer. This 1-g data will be analyzed alongside microgravity data to be collected on the ISS by the Flow Boiling and Condensation Experiment (FBCE) to provide a more complete analysis of body force effects, but for now important conclusions may still be drawn from analysis of 1-g data.

Figure 4.31(a) provides a plot of channel average heat transfer coefficient versus mass velocity for all three orientations. At low mass velocities (for which horizontal cases are omitted due to their non-axisymmetric nature) clear differences are seen between vertical upflow and downflow orientations, with upflow exhibiting higher heat transfer coefficient values. In a recent study by O'Neill *et al.* [137] a similar plot was provided for condensation of FC-72 in a larger tube ( $D_i = 11.89$  mm,  $L_{cond} = 807.7$  mm). Differences in condensation heat transfer across orientations was again most pronounced at low mass velocities, but in their work vertical downflow was seen to exhibit peak condensation heat transfer coefficient while the present study clearly shows vertical upflow exhibiting the highest values of heat transfer coefficient.

Additionally, values of heat transfer coefficient for the three orientations are seen to converge at a lower mass velocity ( $G_{FC} \sim 200$  kg/m<sup>2</sup>s) in the present study as opposed to the value of  $G_{FC} \sim 400$  kg/m<sup>2</sup>s seen in the prior work [137]. These differences are likely due to the

heightened influence of surface tension in the present test section, which possesses a hydraulic diameter of  $D_i = 7.12$  mm.

Figure 4.31 (b) plots ratios of vertical upflow to downflow and horizontal to downflow heat transfer coefficients for each mass velocity. For the present test section vertical upflow is seen to exhibit heat transfer coefficient nearly double that of vertical downflow, with values converging near  $G_{FC} \sim 200$  kg/m<sup>2</sup>s (as mentioned when analyzing Fig. 4.31 (a)). Horizontal flow values, only included for cases with  $G_{FC} \geq 150$  kg/m<sup>2</sup>s, are seen to be near identical to vertical downflow values at the outset. It is expected results for lower mass velocities (where stratified flow is present) would diverge.

It should be noted here that the mass velocity for which vertical upflow and downflow results begin to converge,  $G_{FC} \sim 200$  kg/m<sup>2</sup>s, is very close to the transition to co-current annular vertical upflow established in section 4.2. Similarly, horizontal flow condensation heat transfer is seen to converge with vertical downflow at  $G_{FC} \sim 150$  kg/m<sup>2</sup>s, which is near the transition point between stratified and axisymmetric flow outlined in section 4.2.

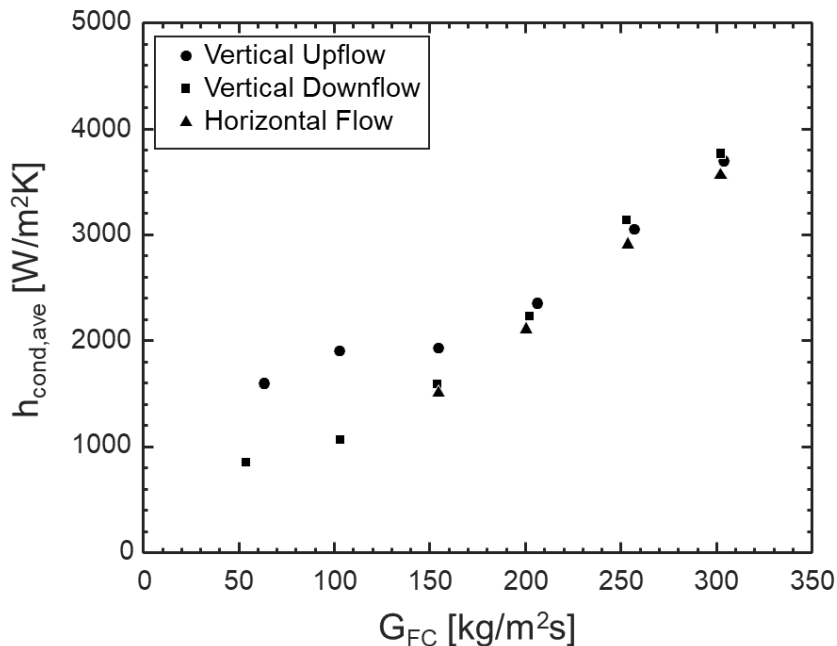


Figure 4.31: (a) Average condensation heat transfer coefficient versus mass velocity for three water flowrates in all three orientations, and (b) ratio of Vertical Upflow and Horizontal Flow (respectively) to Vertical Downflow average heat transfer coefficient, showing the effect of increases in mass velocity on converging values.

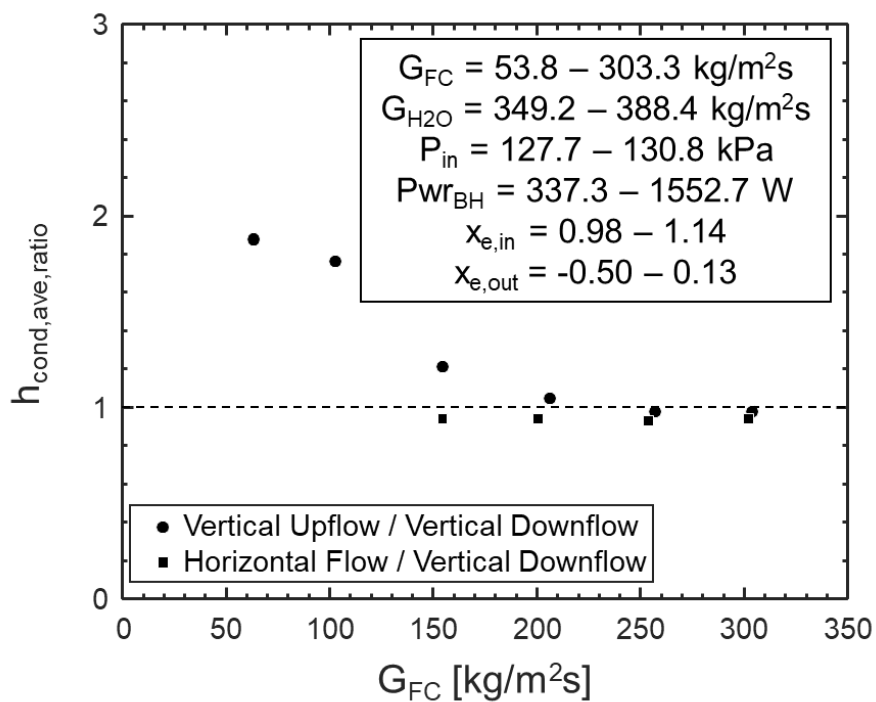


Figure 4.31 (b).

Physically, this means cases with annular, co-current flow exhibit body force independent heat transfer. The prior study by O'Neill *et al.* [137] developed a set of mechanistic criteria for determining mass velocity required for body force independent heat transfer as a function of relevant dimensionless groups. Two are used, one assessing the influence of body force parallel (or opposite) to flow direction, and the other determining the impact of body force perpendicular to flow direction (*i.e.*, leading to stratification at low mass velocities in horizontal flow). The first, dealing with the influence of body force parallel to flow, is of the form

$$|Fr| = \frac{0.235}{a Re_c^n}, \quad (4.46)$$

where  $Fr$  is Froude number,  $Re_c$  is vapor core Reynolds number, and  $a$  and  $n$  are constants. These are defined as (respectively)

$$Fr = \frac{\rho_g}{\rho_f} \frac{(\bar{u}_g - u_i)^2}{g \sin(\theta) D_F}, \quad (4.47)$$

$$Re_c = \frac{\rho_g (\bar{u}_g - u_i) (D_h - 2\delta)}{\mu_g}, \quad (4.48)$$

$$a = 16, n = -1 \text{ for } 0 \leq Re_c < 2000$$

$$a = 0.079, n = -0.25 \text{ for } 2000 \leq Re_c < 20,000 \quad (4.49)$$

$$a = 0.046, n = -0.20 \text{ for } 20,000 \leq Re_c$$

where  $\bar{u}_g$  is mean vapor velocity,  $u_i$  is interfacial velocity,  $g$  is Earth's gravitational constant,  $D_F$  is film diameter,  $\theta$  is test section orientation,  $\delta$  is film thickness, and constants defined by Eq. (4.49) are according to Shah and London [83].

The second criterion, dealing with the influence of body force perpendicular to flow direction, is defined as

$$\frac{|Bo|}{We^2} = 5.12 \times 10^{-5}, \quad (4.50)$$

where  $Bo$  is Bond number and  $We$  is Weber number, defined as

$$Bo = \frac{(\rho_f - \rho_g) g \cos(\theta) L_{char}^2}{\sigma}, \quad (4.51)$$

and

$$We = \frac{(\rho_f^* \rho_g^*) (\bar{u}_g - \bar{u}_f)^2 L_{char}}{(\rho_f^* + \rho_g^*) \sigma}. \quad (4.52)$$

In these equations  $\bar{u}_f$  is mean liquid velocity,  $\rho_f^*$  and  $\rho_g^*$  are modified liquid and vapor densities, and  $L_{char}$  is a characteristic length scale which cancels in Eq. (4.50).

Values on the right hand side of Eq.'s (4.46) and (4.50) are transition points (with criteria values less than the RHS indicating gravity independent heat transfer) determined using the original dataset. For full details on the development of these criteria and how they may be evaluated the original reference should be consulted [137].

Figures 4.32(a) and 4.32(b) provide plots of these dimensionless criteria (for Eq.'s (4.46) and (4.50), respectively) plotted versus mass velocity using operating conditions for the present study. The bold parameters in each inset are those actually used by the criteria (mass velocity, pressure for properties calculation, and exit quality limited to values  $x_{e,out} \geq 0.15$  due to formulation of the criteria [137]).

Figure 4.32(a) shows that, for vertical upflow and downflow data, gravity independence is predicted by  $G_{FC} \sim 125 \text{ kg/m}^2\text{s}$ . This is slightly less than the  $G_{FC} \sim 200 \text{ kg/m}^2\text{s}$  observed in the present experiments. For horizontal flow, Fig. 4.32 (b) does not predict gravity independence until  $G_{FC} \sim 300 \text{ kg/m}^2\text{s}$ , which is higher than the  $G_{FC} \sim 150 \text{ kg/m}^2\text{s}$  observed experimentally.

In both cases predictions are slightly off from experimentally observed convergence points in Fig. 4.31. Despite this Figs. 4.32(a) and 4.32(b) do a good job of capturing experimental trends of convergence towards gravity independence and provide a good qualitative measure of gravity independence for the present dataset. It is expected that future work re-evaluating these gravity independence criteria on a more generalized dataset (including data for different working fluids and test sections) may provide more robust predictions of gravity independence.

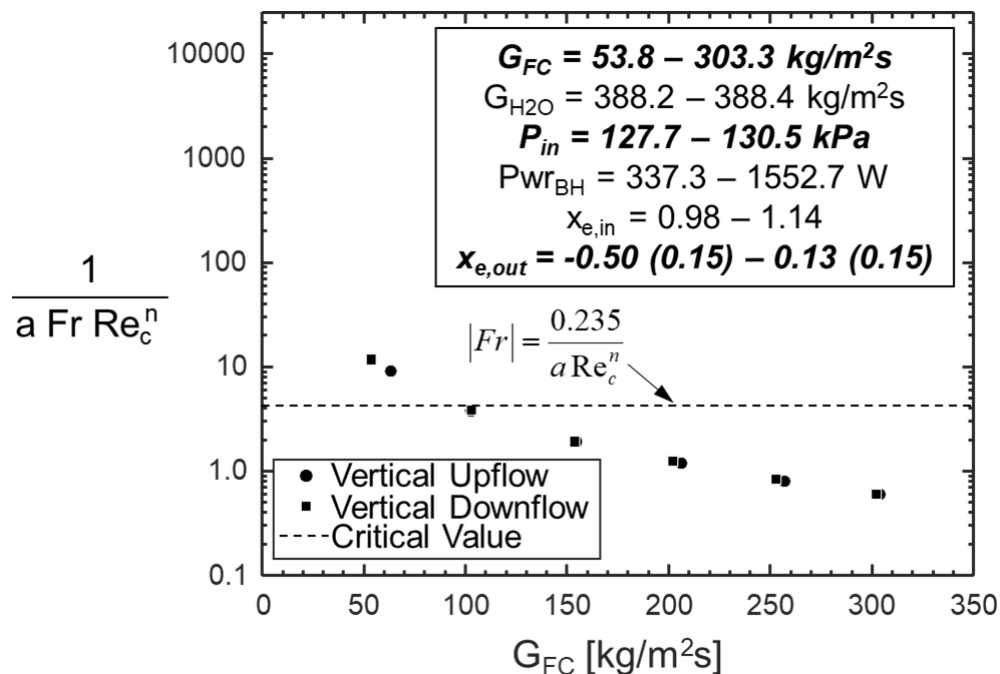


Figure 4.32: Evaluation of gravity independence criteria developed by O'Neill et al. [137] using the current data. Subfigures correspond to the influence of body force acting (a) parallel or opposite to flow direction and (b) perpendicular to flow direction.

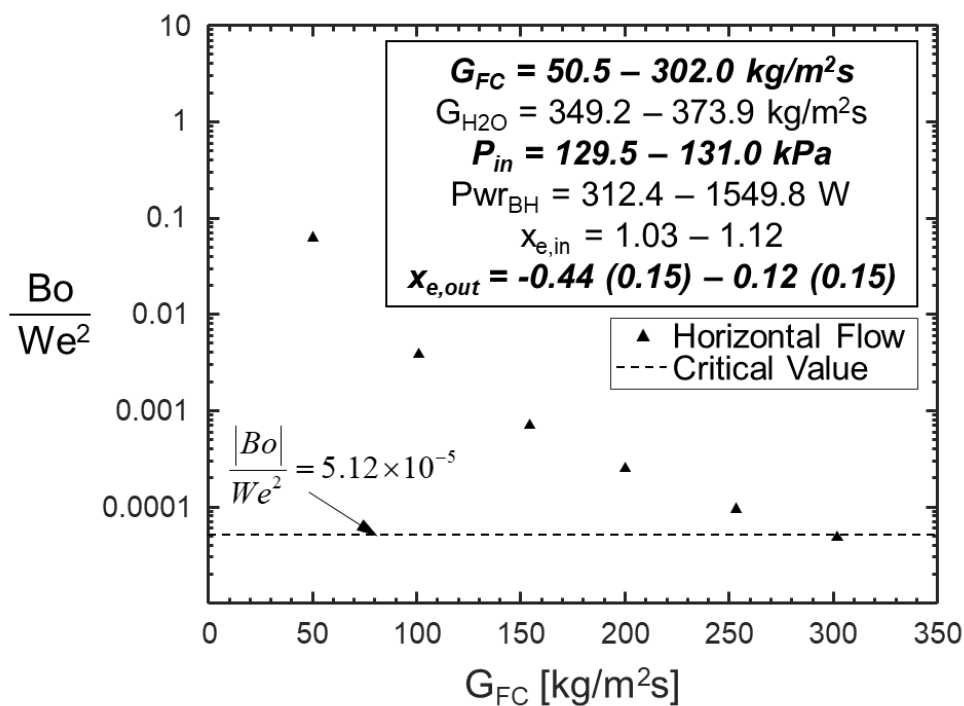


Figure 4.32 (b).

### 4.3.3 *Evaluation of Predictive Models*

Having presented experimental results for flow condensation heat transfer coefficient in vertical upflow, vertical downflow, and horizontal flow orientations, it is now possible to use the data to evaluate common predictive models present in literature. Before beginning evaluation, it should be noted that only experimental cases using the highest water mass velocity ( $G_{H_2O} \sim 390$  kg/m<sup>2</sup>s) are presented here to ensure water-independent (or as close as possible) heat transfer results are used.

Analysis in this section will be segmented based on channel orientation, as different tools are recommended for different flow orientations.

#### 4.3.3.1 Separated Flow Model (SFM) Predictions for Vertical Downflow

Originally developed by Kim and Mudawar [141] for prediction of flow condensation in parallel micro-channel heat sinks, the Separated Flow Model (SFM) for annular condensation has since been adapted and used in several studies investigating flow condensation in single circular tubes similar to the current test geometry [92,131,137]. Table 4.5 provides a full list of model equations as formulated for flow in mini-channels at variable orientation, and details on solution procedure may be found in the original work [141].

Table 4.5: Annular flow model relations [141].

*Mass conservation*

$$\frac{dm_f}{dz} - G_{fg} = 0; \quad \frac{dm_g}{dz} + G_{fg} = 0; \quad \dot{m}_f = r_f \int_0^d u_f \rho (D-2y) dy; \quad \dot{m}_g = r_g \bar{u}_g \rho (D-2d)^2/4; \quad G_{fg} = q_w'' \rho D/h_{fg}$$

*Momentum conservation for liquid film*

$$t = m_f \left( 1 + \frac{e_m}{n_f} \right) \frac{du_f}{dy} = \left( -\frac{dp}{dz} \right) \frac{A_{f,*}}{P_{f,y}} + \frac{t_i P_{f,d} + G_{fg} u_i}{P_{f,y}} \quad (\text{Horizontal Flow})$$

$$= \left( -\frac{dp}{dz} + r_f g \right) \frac{A_{f,*}}{P_{f,y}} + \frac{t_i P_{f,d} + G_{fg} u_i}{P_{f,y}} \quad (\text{Vertical Downflow})$$

$$= \left( -\frac{dp}{dz} - r_f g \right) \frac{A_{f,*}}{P_{f,y}} + \frac{t_i P_{f,d} + G_{fg} u_i}{P_{f,y}} \quad (\text{Vertical Upflow})$$

□

$$A_{f,*} = \frac{\rho}{4}(D-2y)^2 - \frac{\rho}{4}(D-2d)^2, \quad P_{f,y} = \rho(D-2y), \quad P_{f,d} = \rho(D-2d)$$

*Velocity profile across film*

$$u_f(y) = \frac{d}{m_f} \left( -\frac{dP}{dz} \right) \int_0^{y/d} \frac{A_{f,*}}{P_{f,y}} \left( 1 + \frac{e_m}{n_f} \right)^{-1} d \left( \frac{y}{d} \right) + \frac{d}{m_f} \left( t_i P_{f,d} + G_{fg} u_i \right) \int_0^{y/d} \frac{1}{P_{f,y}} \left( 1 + \frac{e_m}{n_f} \right)^{-1} d \left( \frac{y}{d} \right) \quad (\text{Horizontal Flow})$$

$$= \frac{d}{m_f} \left( -\frac{dP}{dz} + r_f g \right) \int_0^{y/d} \frac{A_{f,*}}{P_{f,y}} \left( 1 + \frac{e_m}{n_f} \right)^{-1} d \left( \frac{y}{d} \right) + \frac{d}{m_f} \left( t_i P_{f,d} + G_{fg} u_i \right) \int_0^{y/d} \frac{1}{P_{f,y}} \left( 1 + \frac{e_m}{n_f} \right)^{-1} d \left( \frac{y}{d} \right) \quad (\text{Vertical Downflow})$$

$$= \frac{d}{m_f} \left( -\frac{dP}{dz} - r_f g \right) \int_0^{y/d} \frac{A_{f,*}}{P_{f,y}} \left( 1 + \frac{e_m}{n_f} \right)^{-1} d \left( \frac{y}{d} \right) + \frac{d}{m_f} \left( t_i P_{f,d} + G_{fg} u_i \right) \int_0^{y/d} \frac{1}{P_{f,y}} \left( 1 + \frac{e_m}{n_f} \right)^{-1} d \left( \frac{y}{d} \right) \quad (\text{Vertical Upflow})$$

$$\frac{u}{u_i} = u_f(d)$$

□

Table 4.5 Continued.

*Pressure gradient*

$$\frac{dP}{dz} = \frac{\frac{\mu_f \dot{m}_f}{\rho_f \delta^2} - (\tau_i P_{f,\delta} + \Gamma_{fg} u_i) \int_0^1 \left[ P_{f,y} \int_0^{y/\delta} \frac{1}{P_{f,y}} \left( 1 + \frac{\varepsilon_m}{v_f} \right)^{-1} d\left(\frac{y}{\delta}\right) \right] d\left(\frac{y}{\delta}\right)}{\int_0^1 \left[ P_{f,y} \int_0^{y/\delta} \frac{A_{f,*}}{P_{f,y}} \left( 1 + \frac{\varepsilon_m}{v_f} \right)^{-1} d\left(\frac{y}{\delta}\right) \right] d\left(\frac{y}{\delta}\right)} \quad (\text{Horizontal Flow})$$

$$= -\rho_f g + \frac{\frac{\mu_f \dot{m}_f}{\rho_f \delta^2} - (\tau_i P_{f,\delta} + \Gamma_{fg} u_i) \int_0^1 \left[ P_{f,y} \int_0^{y/\delta} \frac{1}{P_{f,y}} \left( 1 + \frac{\varepsilon_m}{v_f} \right)^{-1} d\left(\frac{y}{\delta}\right) \right] d\left(\frac{y}{\delta}\right)}{\int_0^1 \left[ P_{f,y} \int_0^{y/\delta} \frac{A_{f,*}}{P_{f,y}} \left( 1 + \frac{\varepsilon_m}{v_f} \right)^{-1} d\left(\frac{y}{\delta}\right) \right] d\left(\frac{y}{\delta}\right)} \quad (\text{Vertical Downflow})$$

$$= \rho_f g + \frac{\frac{\mu_f \dot{m}_f}{\rho_f \delta^2} - (\tau_i P_{f,\delta} + \Gamma_{fg} u_i) \int_0^1 \left[ P_{f,y} \int_0^{y/\delta} \frac{1}{P_{f,y}} \left( 1 + \frac{\varepsilon_m}{v_f} \right)^{-1} d\left(\frac{y}{\delta}\right) \right] d\left(\frac{y}{\delta}\right)}{\int_0^1 \left[ P_{f,y} \int_0^{y/\delta} \frac{A_{f,*}}{P_{f,y}} \left( 1 + \frac{\varepsilon_m}{v_f} \right)^{-1} d\left(\frac{y}{\delta}\right) \right] d\left(\frac{y}{\delta}\right)} \quad (\text{Vertical Upflow})$$

*Momentum conservation for vapor core*

$$t_i = \frac{1}{P_{f,d}} \left[ A_g \left( -\frac{dP}{dz} \right) - \frac{d(r_g \bar{u}_g^2 A_g)}{dz} - G_{fg} u_i \right] \quad (\text{Horizontal Flow})$$

$$= \frac{1}{P_{f,d}} \left[ A_g \left( -\frac{dP}{dz} + r_f g \right) - \frac{d(r_g \bar{u}_g^2 A_g)}{dz} - G_{fg} u_i \right] \quad (\text{Vertical Downflow})$$

$$= \frac{1}{P_{f,d}} \left[ A_g \left( -\frac{dP}{dz} - r_f g \right) - \frac{d(r_g \bar{u}_g^2 A_g)}{dz} - G_{fg} u_i \right] \quad (\text{Vertical Upflow})$$

$$\frac{A_g}{\bar{u}_g} = \rho (D - 2d)^2 / 4$$

*Interfacial shear stress relation [163,178]*

$$t_i = \frac{1}{2} f_i r_g (\bar{u}_g - u_i)^2 + \frac{(\bar{u}_g - u_i) G_{fg}}{2P_{f,d}}$$

$$f_i = 16/Re_c \text{ for } Re_c < 2,000; \quad f_i = 0.079 Re_c^{-0.25} \text{ for } 2,000 \leq Re_c < 20,000,$$

$$f_i = 0.046 Re_c^{-0.2} \text{ for } Re_c \geq 20,000; \quad Re_c = r_g (\bar{u}_g - u_i) (D - 2d) / m_g$$

Table 4.5 Continued.

*Eddy momentum diffusivity* [141]

$$\frac{\varepsilon_m}{\nu_f} = -\frac{1}{2} + \frac{1}{2} \sqrt{1 + 4K^2 y^{+2} \left[ 1 - \exp\left(-\sqrt{1 - \frac{y^+}{\delta^+}} \frac{y^+}{A^+}\right) \right]^2 \left(1 - \frac{y^+}{\delta^+}\right)^{0.1} \frac{\tau}{\tau_w}}; \quad K = 0.4; \quad A^+ = 26 \left(1 + 30.18 \mu_f \rho_f^{-0.5} \tau_w^{-1.5} \frac{dP}{dz}\right)^{-1}$$

*Turbulent Prandtl number* [175]

$$Pr_T = 1.4 \exp\left(-15 \frac{y^+}{d^+}\right) + 0.66; \quad d^+ = du^*/n_f$$

*Heat transfer coefficient*

$$h = \frac{q_w''}{T_{sat} - T_w} = \frac{\Gamma_f c_{p,f} u^*}{T_d^+} = \frac{\Gamma_f c_{p,f} u^*}{\int_0^{d^+} \frac{q_w''}{q_w''} \left[ \frac{1}{Pr_f} + \frac{1}{Pr_T} \frac{e_m}{n_f} \right] dy^+} = \frac{\Gamma_f c_{p,f} u^*}{\int_0^{d^+} \frac{D}{D - 2d^+} \left[ \frac{1}{Pr_f} + \frac{1}{Pr_T} \frac{e_m}{n_f} \right] dy^+}$$

Although capable of providing predictions for flow at any orientation, as currently constructed the model provides best predictions for vertical downflow condensation. Figure 4.33 provides six plots comparing local condensation heat transfer coefficient to predictions ((a) – (f)), as well as a plot (Fig. 4.33(g)) providing ratio of predicted to experimental channel-average heat transfer coefficient values for all 17 test cases used.

Figure 4.33(a) shows that, for high  $G_{FC}$  and slightly superheated inlet conditions, the SFM under-predicts heat transfer coefficient in the upstream portion of the channel, although downstream results show closer agreement. Successive decreases in  $G_{FC}$  in Figs. 4.33(b) and 4.33(c) lead to closer agreement in both upstream and downstream portions of the channel.

Figure 4.33(d) provides results for high  $G_{FC}$  with two-phase mixture inlet conditions. Heat transfer coefficient is again underpredicted in the upstream portion of the channel, but to a lesser degree than that seen in Fig. 4.33(a) corresponding to superheated vapor at the channel inlet. Similar to the trend seen for Figs. 4.33(b) and 4.33(c), decreases in  $G_{FC}$  for Figs. 4.33(e) and 4.33(f) lead to closer agreement between predicted and experimental heat transfer coefficient values.

Ratios of predicted to experimental channel-average heat transfer coefficient values in Fig. 4.33(g) are plotted versus liquid only Reynolds number,  $Re_{fo}$ , and turbulent-turbulent Martinelli parameter,  $X_{tt}$ , defined as

$$Re_{fo} = \frac{G_{FC} D_i}{\mu_f}, \quad (4.53)$$

and

$$X_{tt} = \left( \frac{1-x}{x} \right)^{0.9} \left( \frac{\rho_g}{\rho_f} \right)^{0.5} \left( \frac{\mu_f}{\mu_g} \right)^{0.1}, \quad (4.54)$$

respectively. These two dimensionless groups were selected as they both commonly appear in correlations for condensation heat transfer coefficient and allow assessment of predictive ability for differences in flow inertia (Reynolds) and liquid content within the channel (Martinelli parameter).

Accuracy statistics used for evaluating each correlation are Mean Absolute Error, defined as

$$MAE = \frac{1}{N} \sum_{n=1}^N \left| \frac{h_{pred,n} - h_{exp,n}}{h_{exp,n}} \right|, \quad (4.55)$$

multiplied by 100 and expressed as a percent, as well as  $\theta$  and  $\zeta$ , the percent of predictions falling within 30% and 50% of the experimental value, respectively.

Figure 4.33(g) indicates that the SFM provides accurate predictions of condensation heat transfer coefficient for the current data set, evidenced by MAE of 31.2%,  $\theta = 41.2\%$ , and  $\zeta = 94.1\%$ . No clear trends with respect to changes in liquid content ( $X_{tt}$ ) are evident, but predictions clearly become less accurate as  $Re_{fo}$  is increased. Before over-analyzing this trend, it should be recalled that Fig. 4.28(b) indicated vertical downflow condensation results for the highest  $G_{FC}$  cases were not entirely water-side independent, and higher water flowrates may lead to slightly lower values of heat transfer coefficient (bring predictions into closer agreement with experimental values). It is expected altering the test matrix to include higher  $G_{H2O}$  cases for the ISS experiment will allow this to be tested.

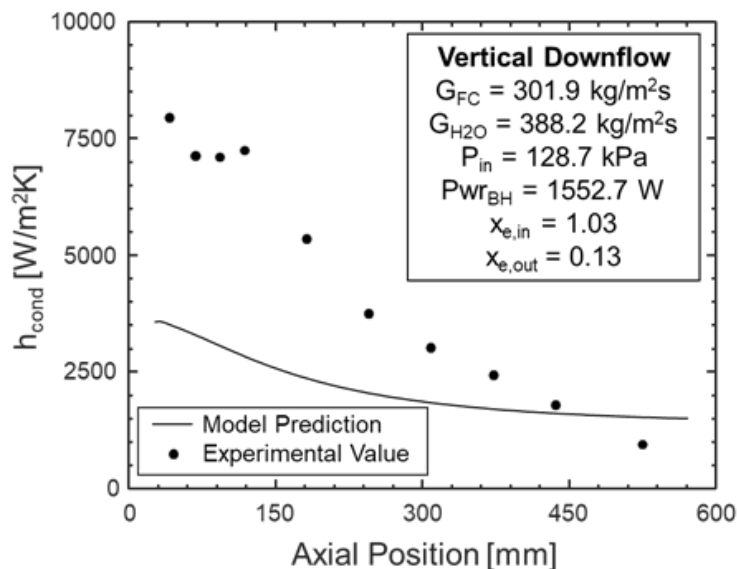


Figure 4.33: Separated flow model local heat transfer predictions for vertical downflow with (a), (b), (c) superheated vapor inlet and descending mass velocity, (d), (e), (f) two-phase inlet and descending mass velocity, and (g) overall performance of SFM channel-average heat transfer predictions.

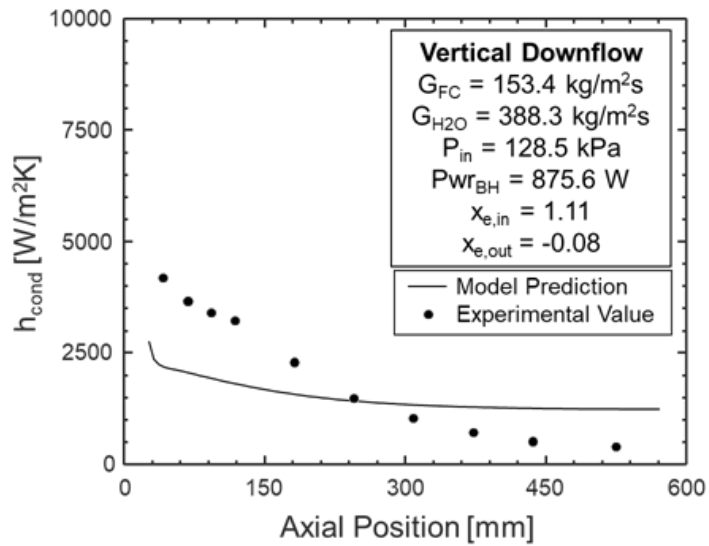


Figure 4.33 (b).

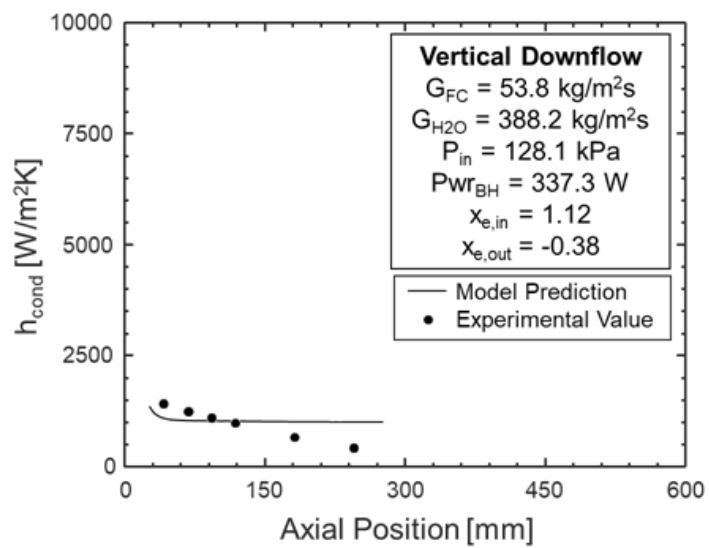


Figure 4.33 (c).

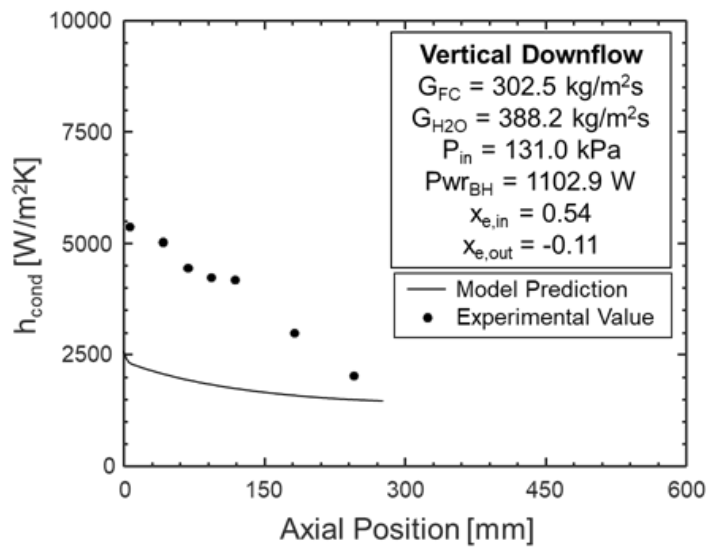


Figure 4.33 (d).

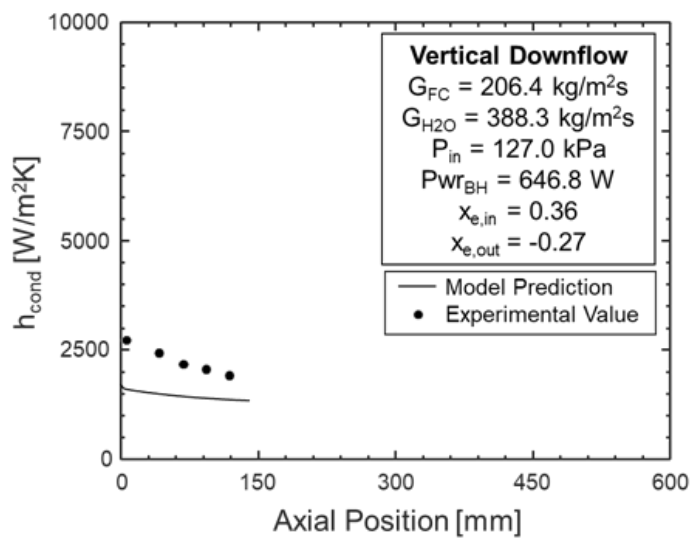


Figure 4.33 (e).

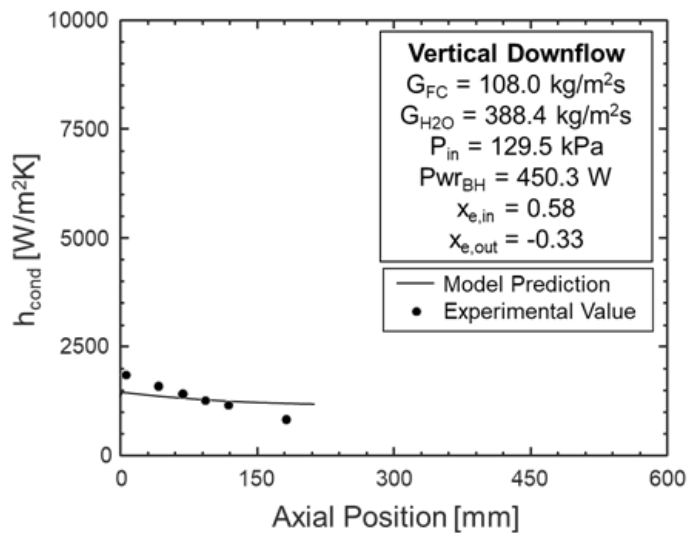


Figure 4.33 (f).

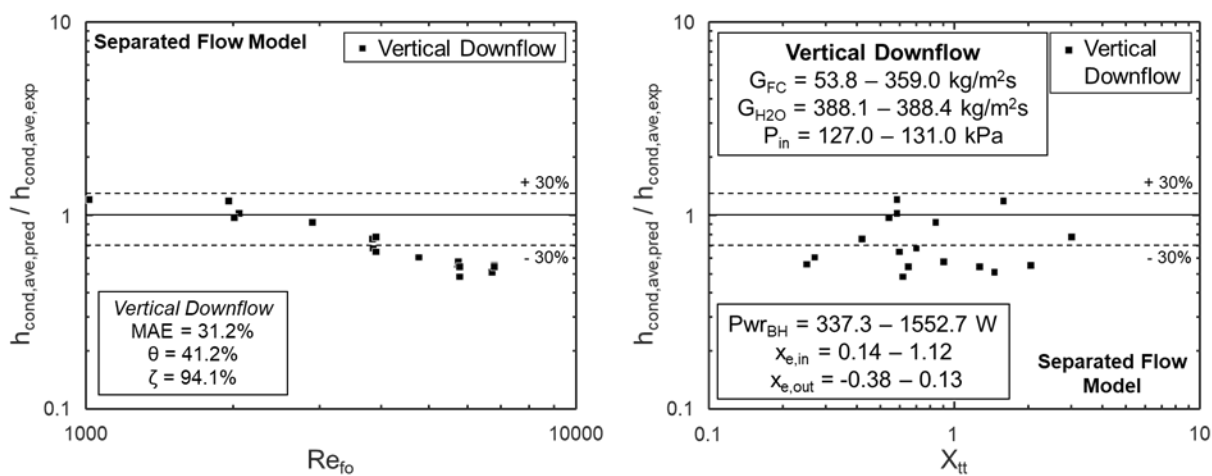


Figure 4.33 (g).

#### 4.3.3.2 Common Correlations for Horizontal Flow

While the Separated Flow Model provided the most accurate predictions of vertical downflow condensation for the current dataset, common semi-empirical correlations were found to give sufficiently accurate predictions for horizontal flow. Several of these are evaluated here, and suggestions made on which should be used for similar applications.

Similar to that done by Kim and Mudawar in their review [179], correlations used here have been split into those intended for use with macro-channels and those for mini/micro-channels (indicating prevalence of confinement effects). Macro-channel correlations include those by Akers and Rosson [180], Cavallini and Zecchin [181], Shah [182], Haraguchi *et al.* [183], Dobson and Chato [89], Moser *et al.* [184], and the updated Shah correlation [168]. Mini/micro-channel correlations include those by Wang *et al.* [119], Koyama *et al.* [186], Huang *et al.* [187], Bohdal *et al.* [188], Park *et al.* [189], and Kim and Mudawar [156]. Full forms of all correlations are provided in Table 4.6, along with information on the experimental work and performance evaluated using the current dataset.

Table 4.6: Condensation heat transfer coefficient correlations evaluated.

Author(s)	Equation	Remarks	MAE (%) <i>Horizontal</i> <i>l</i>	$\theta$ (%) <i>Horizontal</i> <i>l</i>	$\zeta$ (%) <i>Horizontal</i> <i>l</i>
Recommended for macro-channels					
Akers and Rosson [164]	$\frac{h_p D_h}{k_f} = 0.026 \text{Pr}_f^{1/3} \left\{ G \left[ (1-x) + x \left( \frac{\rho_f}{\rho_g} \right)^{0.5} \right] \frac{D_h}{\mu_f} \right\}^{0.8}$	D = 19.05 mm R12, propane $\text{Re}_g \left( \frac{\mu_g}{\mu_f} \right) \left( \frac{\rho_f}{\rho_g} \right)^{0.5} > 20,000$ $\text{Re}_f > 5000$	61.3	0	7.1
Cavallini and Zecchin [181]	$\frac{h_p D_h}{k_f} = 0.05 \text{Re}_f^{0.8} \text{Pr}_f^{0.33} \left[ 1 + \left( \frac{\rho_f}{\rho_g} \right)^{0.5} \left( \frac{x}{1-x} \right) \right]^{0.8}$	R12, R22, R113 $7000 \leq \text{Re}_{fo} \leq 53,000$	26.1	64.3	92.9
Shah (1979) [182]	$\frac{h_p D_h}{k_f} = 0.023 \text{Re}_{fo}^{0.8} \text{Pr}_f^{0.4} \left[ (1-x)^{0.8} + \frac{3.8x^{0.76} (1-x)^{0.04}}{P_R^{0.38}} \right]$	D = 7 – 40 mm Water, R11, R12, R22, R113, methanol, ethanol, benzene, toluene, trichloroethylene	34.1	35.7	85.7
Haraguchi et al. [183]	$\frac{h_p D_h}{k_f} = 0.0152 \text{Re}_f^{0.77} \frac{\phi_g}{X_{tt}} (1 + 0.6 \text{Pr}_f^{0.8})$ $X_{tt} = \left( \frac{\mu_f}{\mu_g} \right)^{0.1} \left( \frac{1-x}{x} \right)^{0.9} \left( \frac{v_f}{v_g} \right)^{0.5}$ $\phi_g = 1 + 0.5 \left[ \frac{G}{\sqrt{g \rho_g (\rho_f - \rho_g) D_h}} \right]^{0.75} X_{tt}^{0.35}$	D = 8.4 mm R22, R123, R134a	36.2	42.9	78.6
Dobson and Chato [89]	$\frac{h_p D_h}{k_f} = 0.023 \text{Re}_f^{0.8} \text{Pr}_f^{0.4} \left( 1 + \frac{2.22}{X_{tt}^{0.89}} \right)$	D = 3.14 – 7.04 mm R12, R22, R134a, R32/R125	24.1	71.4	100
Moser et al. [184] (Friedel [185])	$\frac{h_p D_h}{k_f} = \frac{0.0994 C_1 \text{Re}_f^{C_2} \text{Re}_{eq}^{1+0.875 C_1} \text{Pr}_f^{0.815}}{\left[ 1.58 \ln(\text{Re}_{eq}) - 3.28 \right] \left[ 2.58 \ln(\text{Re}_{eq}) + 13.7 \text{Pr}_f^{2/3} - 19.1 \right]}$ $C_1 = 0.126 \text{Pr}_f^{-0.448}$ $C_2 = -0.113 \text{Pr}_f^{-0.563}$ $\text{Re}_{eq} = \phi_{fo, \text{Friedel}}^{8/7} \text{Re}_{fo}$	D = 3.14 – 20 mm R11, R12, R125, R22, R134a, R410a	39.5	21.4	78.6

Table 4.6 Continued.

<p>Shah (2009) [168]</p>	$j_g = \frac{xG}{\sqrt{gD\rho_g(\rho_f - \rho_g)}}, Z_{Shah} = \left(\frac{1}{x} - 1\right)^{0.8} P_R^{0.4}$ <p>For Vertical and Inclined Tubes:</p> <p>if <math>j_g \geq \frac{1}{2.4Z_{shah} + 0.73}</math>:</p> $\frac{h_p D_h}{k_f} = 0.023 Re_{\rho}^{0.8} Pr_f^{0.4} \left(\frac{\mu_f}{14\mu_g}\right)^n \left[ (1-x)^{0.8} + \frac{3.8x^{0.76}(1-x)^{0.04}}{P_R^{0.38}} \right]$ <p>where <math>n = 0.0058 + 0.557 P_R</math>          else if <math>j_g \leq 0.89 - 0.93 \exp(-0.087 Z_{shah}^{-1.17})</math>:</p> $\frac{h_p D_h}{k_f} = 1.32 \frac{D_h}{k_f} Re_f^{0.6} \left[ \frac{\rho_f(\rho_f - \rho_g) g k_f^3}{\mu_f^3} \right]^{1/4}$ <p>else:</p> $\frac{h_p D_h}{k_f} = 0.023 Re_{\rho}^{0.8} Pr_f^{0.4} \left(\frac{\mu_f}{14\mu_g}\right)^n \left[ (1-x)^{0.8} + \frac{3.8x^{0.76}(1-x)^{0.04}}{P_R^{0.38}} \right] + 1.32 \frac{D_h}{k_f} Re_f^{0.6} \left[ \frac{\rho_f(\rho_f - \rho_g) g k_f^3}{\mu_f^3} \right]^{1/4}$ <p>For Horizontal Tubes:</p> <p>if <math>j_g \geq 0.98(Z_{shah} + 0.263)^{-0.62}</math>:</p> $\frac{h_p D_h}{k_f} = 0.023 Re_{\rho}^{0.8} Pr_f^{0.4} \left(\frac{\mu_f}{14\mu_g}\right)^n \left[ (1-x)^{0.8} + \frac{3.8x^{0.76}(1-x)^{0.04}}{P_R^{0.38}} \right]$ <p>where <math>n = 0.0058 + 0.557 P_R</math>          else:</p> $\frac{h_p D_h}{k_f} = 0.023 Re_{\rho}^{0.8} Pr_f^{0.4} \left(\frac{\mu_f}{14\mu_g}\right)^n \left[ (1-x)^{0.8} + \frac{3.8x^{0.76}(1-x)^{0.04}}{P_R^{0.38}} \right] + 1.32 \frac{D_h}{k_f} Re_f^{0.6} \left[ \frac{\rho_f(\rho_f - \rho_g) g k_f^3}{\mu_f^3} \right]^{1/4}$	<p><math>D_h = 2 - 49</math> mm                  Water, R11, R12, R22, R113, R123, R134a,                  benzene, R32, R125, R404A, R410A,                  R507, propylene, propane, isobutane,                  R142b, R502, methanol, ethanol, toluene,                  Dowtherm 209.</p>	<p>24.7</p>	<p>57.1</p>	<p>100</p>
<p>Recommended for mini/micro-channels</p>					
<p>Wang et al. [119]</p>	$\frac{h_{tp} D_h}{k_f} = 0.0274 Re_f^{0.6792} Pr_f^{0.2208} \frac{\phi_g}{X_{tt}}$ $\phi_g^2 = 1.376 + 8X_{tt}^{1.665}$	<p><math>D_h = 1.46</math> mm, Multi-channel R134a</p>	<p>24.2</p>	<p>64.3</p>	<p>100</p>
<p>Koyama et al. [186]</p>	$\frac{h_{tp} D_h}{k_f} = 0.0152(1 + 0.6 Pr_f^{0.8}) Re_f^{0.77} \frac{\phi_g}{X_{tt}}$ $\phi_g^2 = 1 + 21[1 - \exp(-0.319 D_h)] X_{tt} + X_{tt}^2$	<p><math>D_h = 0.80</math> and <math>1.11</math> mm, Multi-channel R134a</p>	<p>62.0</p>	<p>0</p>	<p>7.1</p>
<p>Huang et al. [187]</p>	$\frac{h_{tp} D_h}{k_f} = 0.0152(-0.33 + 0.83 Pr_f^{0.8}) Re_f^{0.77} \frac{\phi_g}{X_{tt}}$ $\phi_g = \phi_{g, Haraguchi}$	<p><math>D = 1.6</math> and <math>4.18</math> mm R410A, R410A/oil</p>	<p>38.8</p>	<p>35.7</p>	<p>78.6</p>

Table 4.6 Continued.

Bohdal et al. [188]	$\frac{h_p D_h}{k_f} = 25.084 \text{Re}_f^{0.258} \text{Pr}_f^{-0.495} P_R^{-0.288} \left( \frac{x}{1-x} \right)^{0.266}$	<p>D = 0.31 – 3.30 mm R134a, R404a</p>	58.5	0	21.4
Park et al. [189]	$\frac{h_p D_h}{k_f} = 0.0055 \text{Pr}_f^{1.37} \text{Re}_f^{0.7} \frac{\phi_g}{X_u}$ $\phi_g^2 = 1 + 13.17 \left( \frac{\rho_g}{\rho_f} \right)^{0.17} \left[ 1 - \exp \left( -0.6 \sqrt{\frac{g(\rho_f - \rho_g) D_h^2}{\sigma}} \right) \right] X_u + X_u^2$	<p>D<sub>h</sub> = 1.45 mm, Multi-channel R134a, R236fa, R1234ze(E)</p>	53.4	0	35.7

Table 4.6 Continued.

Kim and Mudawar [156]	<p>for <math>We^* &gt; 7X_{tt}^{0.2}</math> :</p> $\frac{h_p D_h}{k_f} = 0.048 Re_f^{0.69} Pr_f^{0.34} \frac{\phi_g}{X_{tt}}$ <p>for <math>We^* \leq 7X_{tt}^{0.2}</math> :</p> $\frac{h_p D_h}{k_f} = \left[ \left( 0.048 Re_f^{0.69} Pr_f^{0.34} \frac{\phi_g}{X_{tt}} \right)^2 + \left( 3.2 \times 10^{-7} Re_f^{-0.38} Su_{go}^{1.39} \right)^2 \right]^{0.5}$ <p>where <math>X_{tt} = \left( \frac{\mu_f}{\mu_g} \right)^{0.1} \left( \frac{1-x}{x} \right)^{0.9} \left( \frac{\rho_g}{\rho_f} \right)^{0.5}</math></p> $\phi_g^2 = 1 + CX + X^2, X^2 = \frac{(dP/dz)_f}{(dP/dz)_g}$ $-\left( \frac{dP}{dz} \right)_f = \frac{2f_f v_f G^2 (1-x)^2}{D_h}, -\left( \frac{dP}{dz} \right)_g = \frac{2f_g v_g G^2 x^2}{D_h}$ <p><math>f_k = 16 Re_k^{-1}</math> for <math>Re_k &lt; 2000</math></p> <p><math>f_k = 0.079 Re_k^{-0.25}</math> for <math>2000 \leq Re_k &lt; 20,000</math></p> <p><math>f_k = 0.046 Re_k^{-0.2}</math> for <math>Re_k \geq 20,000</math></p> <p>where subscript k denotes f or g for liquid or vapor phases, respectively</p> <p><math>Re_f \geq 2000, Re_g \geq 2000</math> (tt); <math>C = 0.39 Re_{fo}^{0.03} Su_{go}^{0.10} \left( \frac{\rho_f}{\rho_g} \right)^{0.35}</math></p> <p><math>Re_f \geq 2000, Re_g &lt; 2000</math> (tv); <math>C = 8.7 \times 10^{-4} Re_{fo}^{0.17} Su_{go}^{0.50} \left( \frac{\rho_f}{\rho_g} \right)^{0.14}</math></p> <p><math>Re_f &lt; 2000, Re_g \geq 2000</math> (vt); <math>C = 0.0015 Re_{fo}^{0.59} Su_{go}^{0.19} \left( \frac{\rho_f}{\rho_g} \right)^{0.36}</math></p> <p><math>Re_f &lt; 2000, Re_g &lt; 2000</math> (vv); <math>C = 3.5 \times 10^{-5} Re_{fo}^{0.44} Su_{go}^{0.50} \left( \frac{\rho_f}{\rho_g} \right)^{0.48}</math></p>	<p><math>D_h = 0.424 - 6.22</math> mm  R12, R123, R1234yf, R1234ze (E), R134a,  R22, R236fa, R245fa, R32, R404A, R410A,  R600a, FC72, methane, CO<sub>2</sub></p>	39.5	21.4	85.7
-----------------------	--	---	------	------	------

Similar to Fig. 4.33(g), Figure 4.34 provides plots of the ratio of predicted to experimental heat transfer coefficient versus  $Re_{fo}$  and  $X_{tt}$ . Figure 4.34(a), providing results for the correlation of Akers and Rosson [180], indicates the correlation under-predicts experimental heat transfer values for all operating conditions tested here.

Figure 4.34(b) shows results are much better using the correlation of Cavallini and Zecchin [181], with horizontal flow exhibiting MAE of 26.1%. Their correlation appears to predict results with higher accuracy for high flow inertia and low liquid content cases.

Figure 4.34(c) presents similar results for the original Shah correlation [182]. Cases with low liquid content (low values of  $X_{tt}$ ) again yield more accurate predictions.

These trends continue to manifest in Fig. 4.34(d), which shows the correlation of Haraguchi *et al.* [183] performing significantly better for high flowrates and low liquid content within the channel.

The correlation of Dobson and Chato [89], shown in Fig. 4.34(e), remains relatively accurate for all flowrates tested in the current dataset, but again struggles to accurately predict results in cases with low flow quality (high  $X_{tt}$ ). Similar results are seen for both the correlations of Moser *et al.* [184] and the modified Shah correlation [168], shown in Figs. 4.34(f) and 4.34(g), respectively.

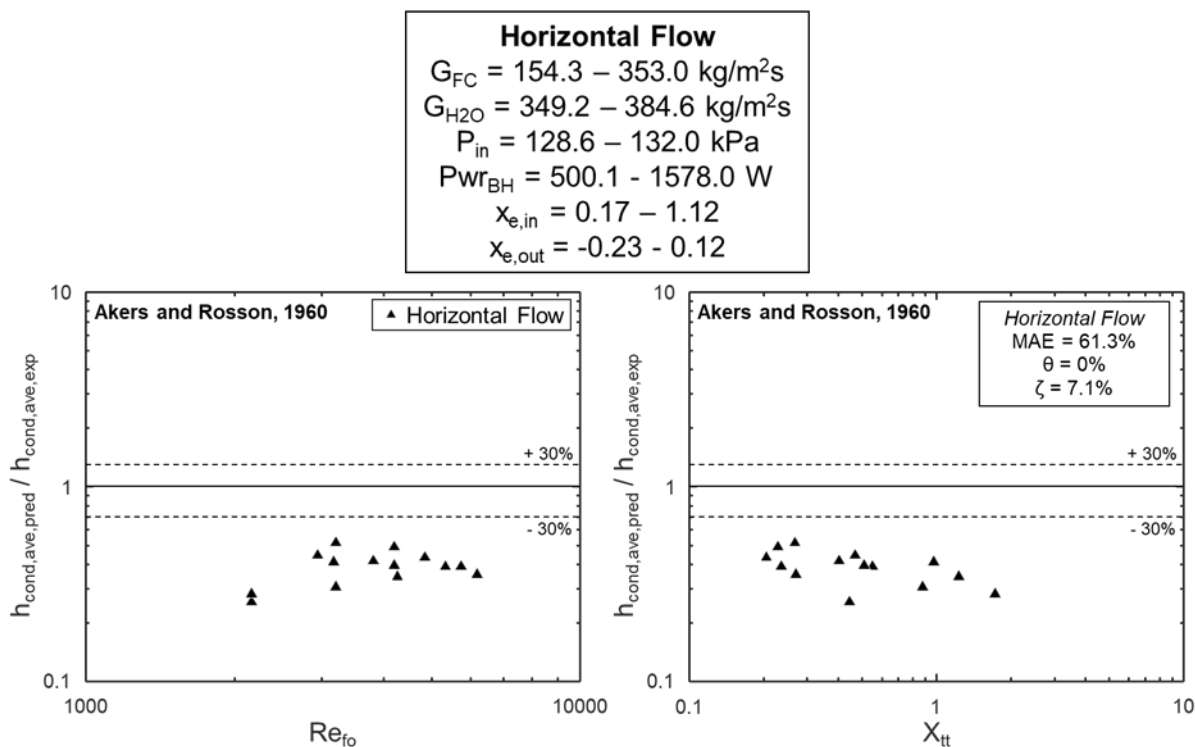


Figure 4.34: Ratio of experimental to predicted heat channel average heat transfer coefficient versus liquid-only Reynolds number and  $X_{tt}$ , with heat transfer coefficient values predicted by correlations of (a) Akers and Rosson [180], (b) Cavallini and Zecchin [181], (c) Shah [182], (d) Haraguchi et al. [183], (e) Dobson and Chato [89], (f) Moser et al. [184], and (g) the updated Shah correlation [168]. Correlations shown here are recommended for use with macro-channels.

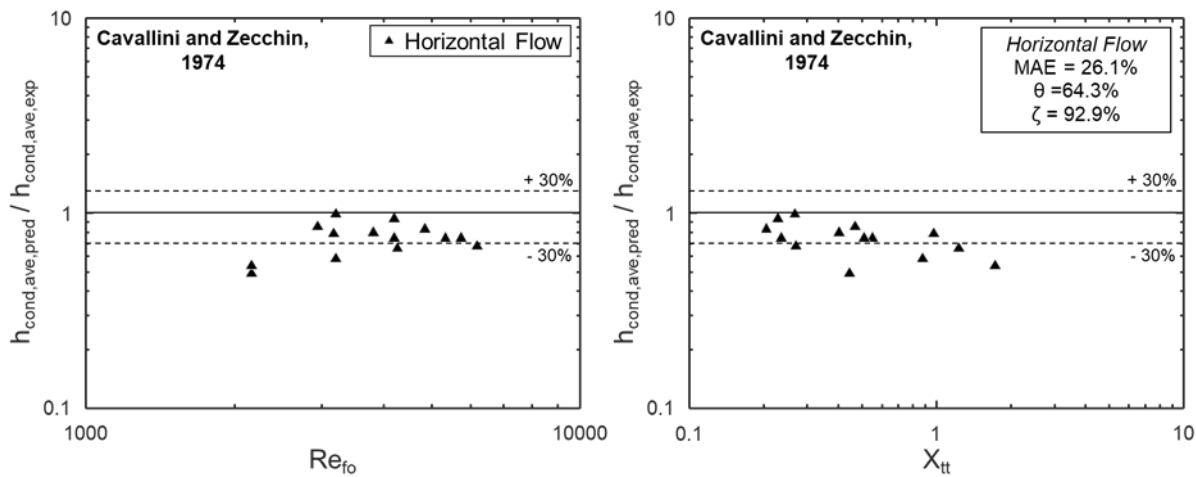


Figure 4.34 (b).

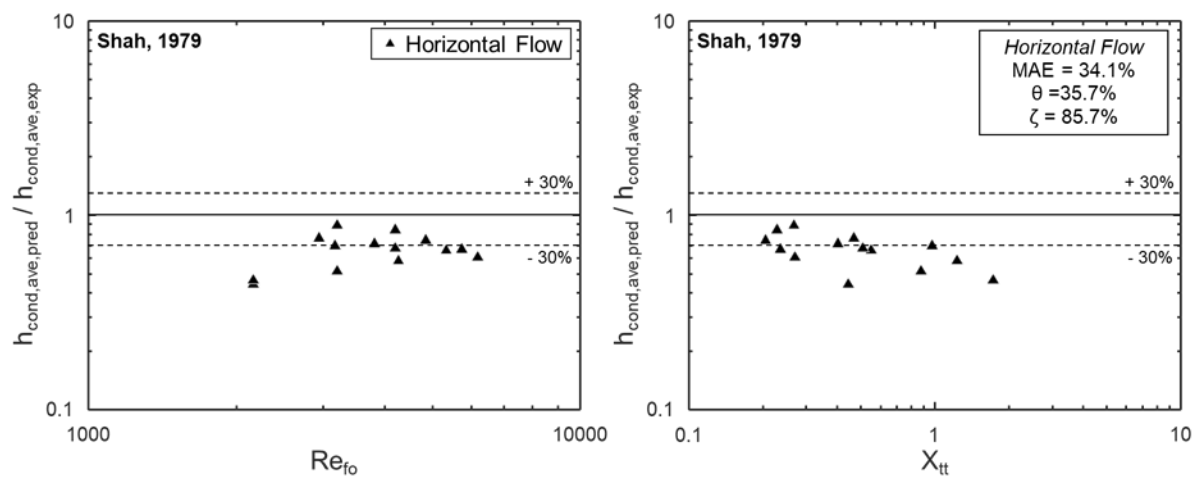


Figure 4.34 (c).

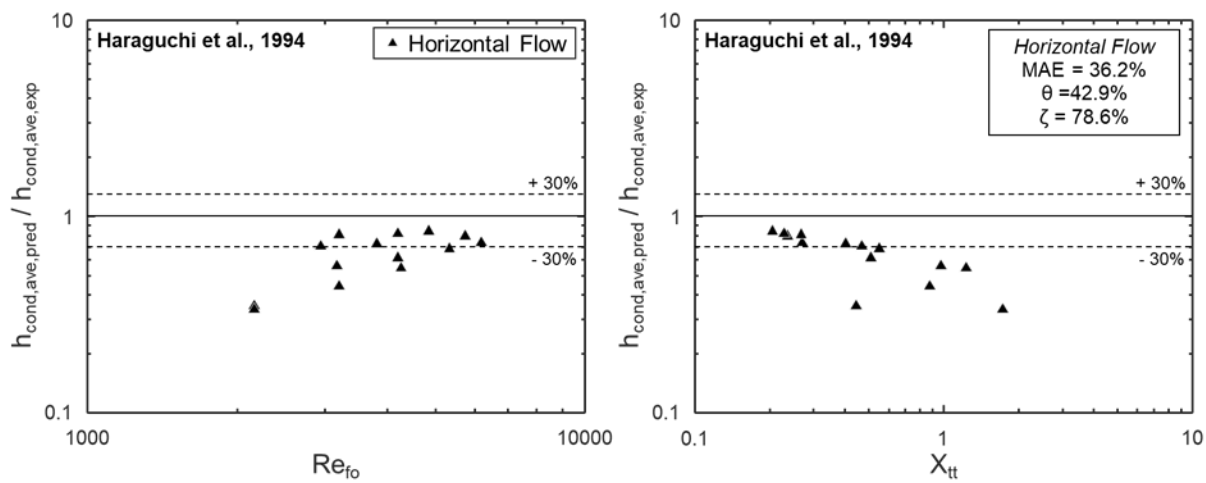


Figure 4.34 (d).

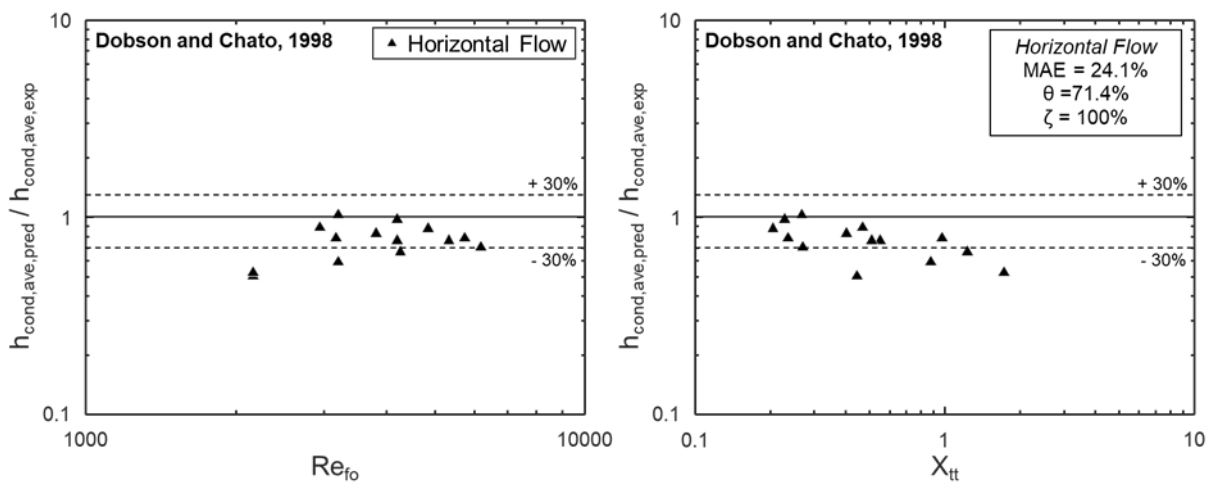


Figure 4.34 (e).

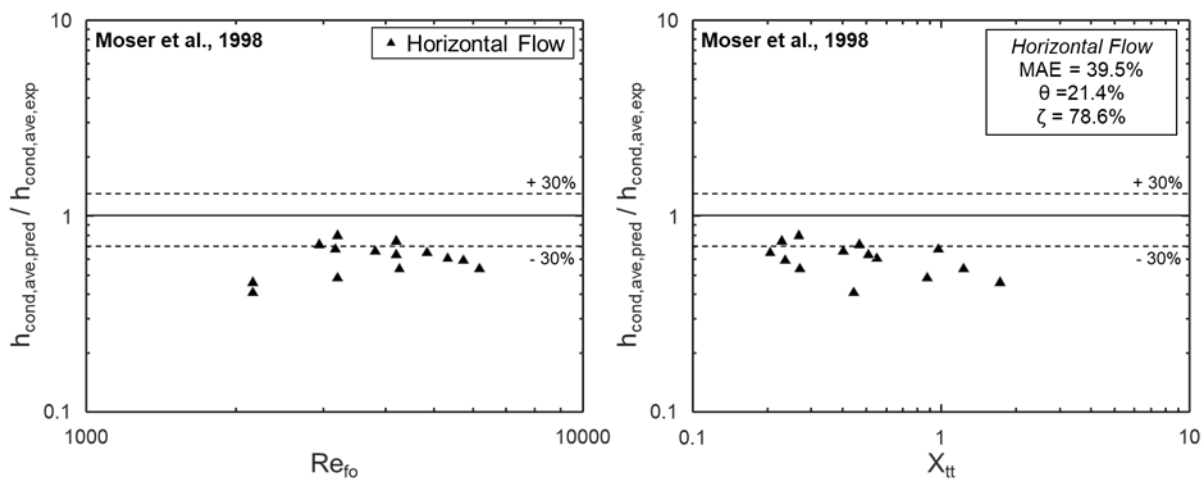


Figure 4.34 (f).

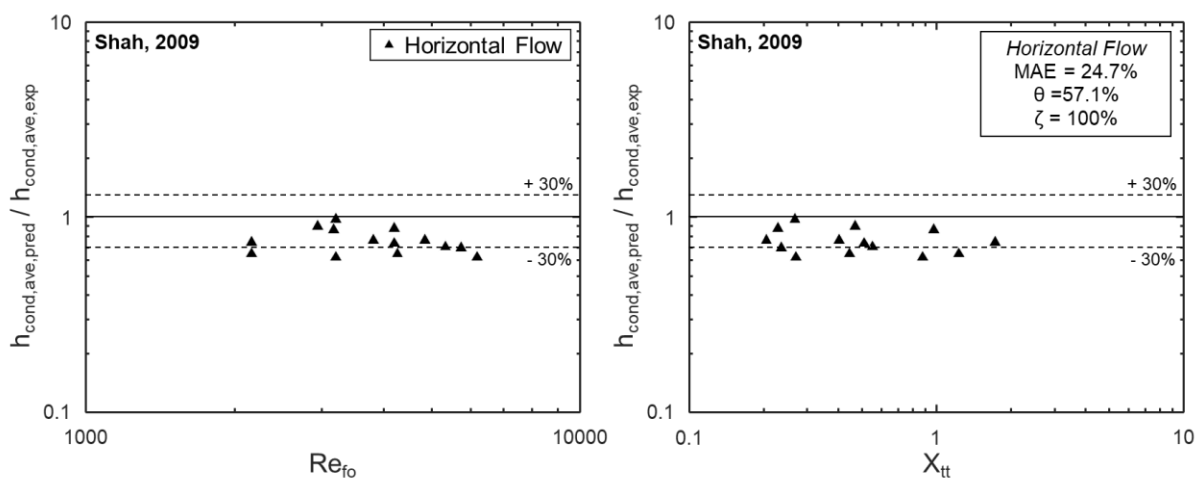


Figure 4.34 (g).

Figure 4.35 provides similar results using correlations intended for mini/micro-channel flows. Figure 4.35(a), corresponding to the correlation of Wang *et al.* [119], offers one of the highest predictive accuracy of any correlation tested here with MAE of 24.2%. Predictive accuracy is similar for all flowrates tested but decreases slightly for higher liquid content.

Figure 4.35(b) shows the correlation of Koyama *et al.* [186] underpredicting results for all cases tested here. The correlation of Huang *et al.* [187], shown in Fig. 4.35 (c), underpredicts heat transfer coefficient for low flowrates and high liquid content, but offers reasonable predictions for high flowrates and low liquid content within the channel.

Figures 4.35(d) and 4.35(e) both significantly under predict results for all operating conditions investigated here. Figure 4.35(d), corresponding to the correlation of Bohdal *et al.* [188], seems to offer better predictions for lower ranges of Reynolds number, dissimilar to what is seen for most correlations investigated here.

Finally, Fig. 4.35(f) provides results from the universal correlation developed by Kim and Mudawar [156]. Their correlation offers reasonable predictive results for all flowrates tested, but underpredicts condensation heat transfer coefficient for higher liquid content cases.

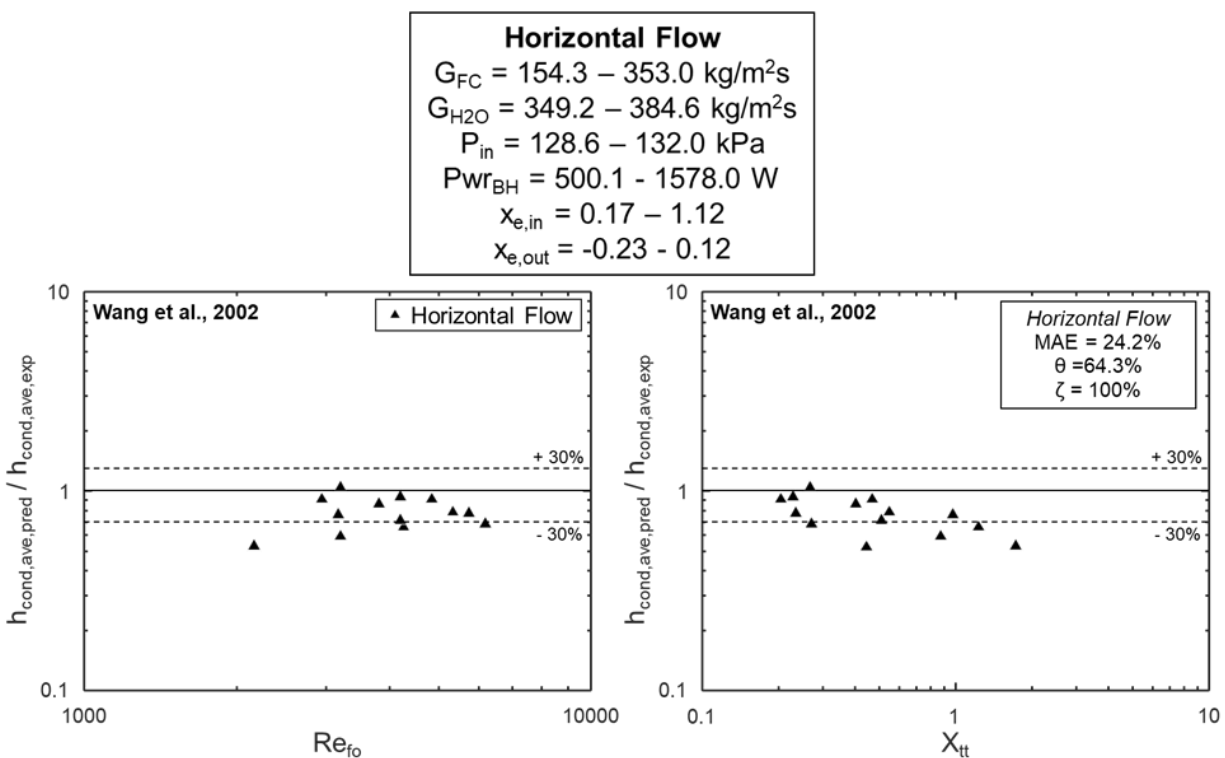


Figure 4.35: Ratio of experimental to predicted heat channel average heat transfer coefficient versus liquid-only Reynolds number and  $X_{tt}$ , with heat transfer coefficient values predicted by correlations of (a) Wang et al. [119], (b) Koyama et al. [186], (c) Huang et al. [187], (d) Bohdal et al. [188], (e) Park et al. [189], and (f) Kim and Mudawar [56]. Correlations shown here are recommended for use with mini/micro-channels.

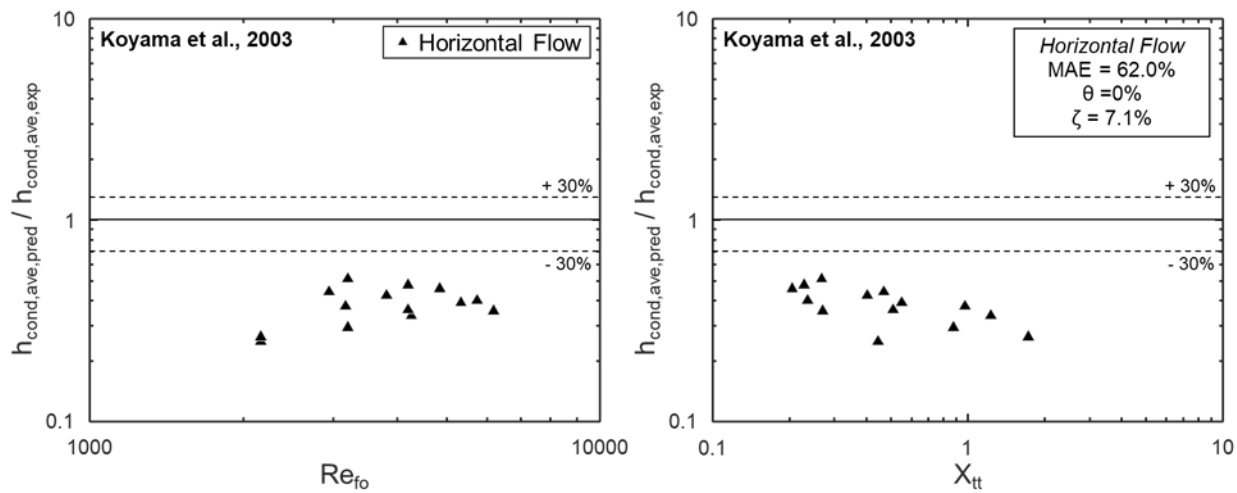


Figure 4.35 (b).

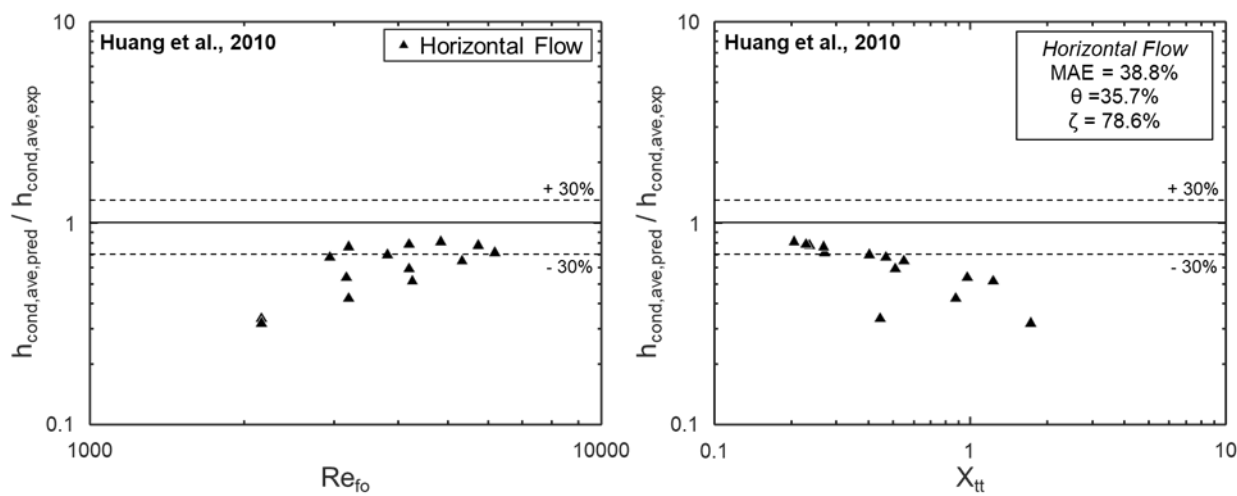


Figure 4.35 (c).

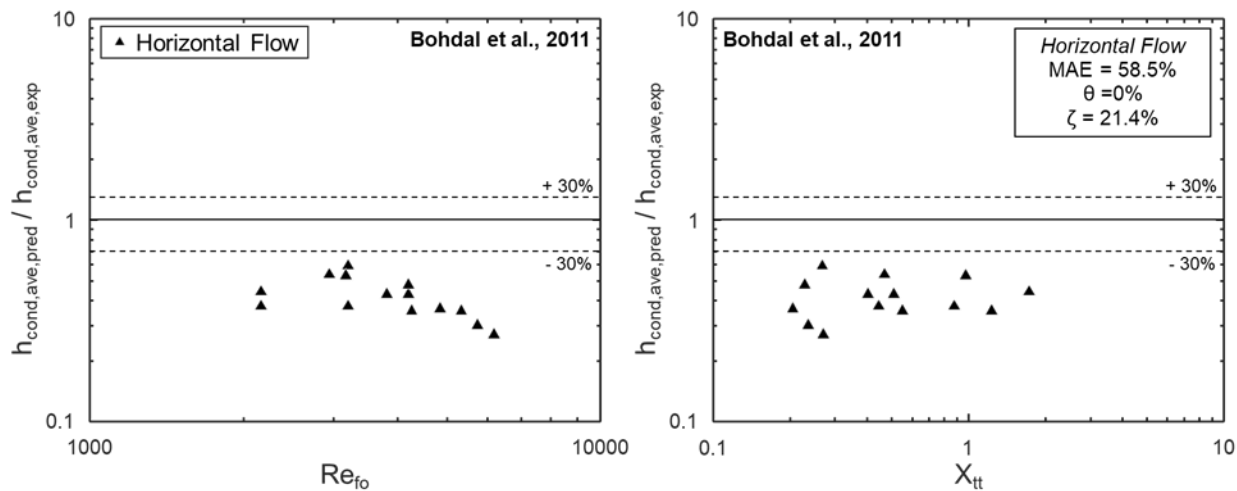


Figure 4.35 (d).

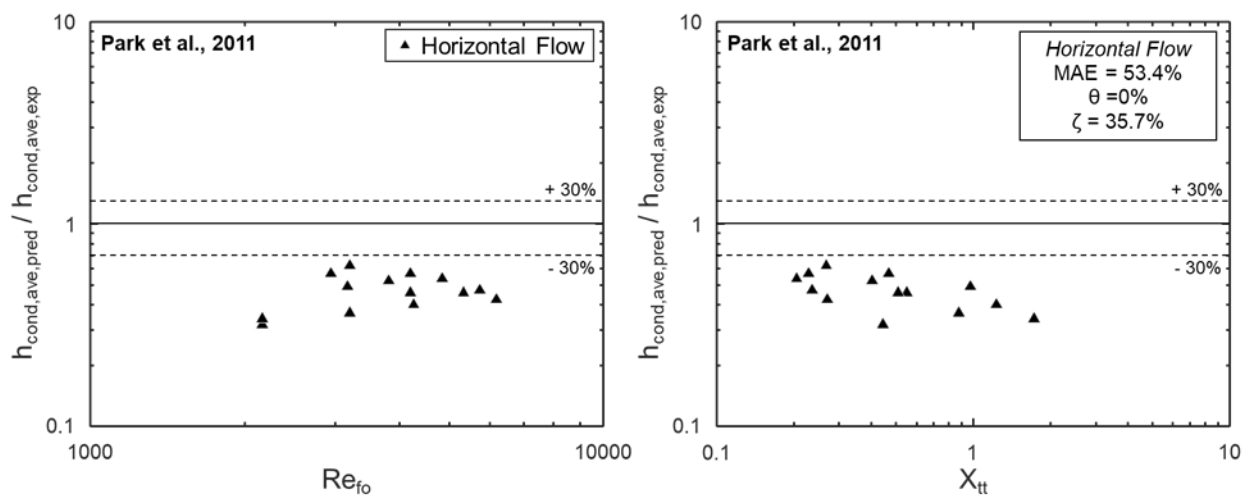


Figure 4.35 (e).

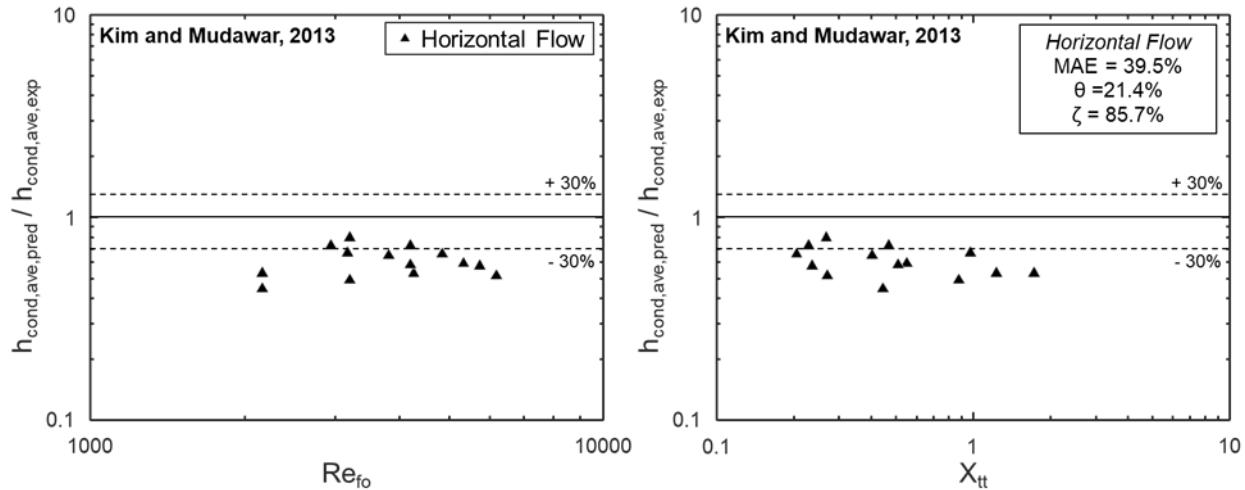


Figure 4.35 (f).

Across all correlations investigated here several key trends may be seen:

- (1) The correlations of Shah [168], Wang *et al.* [119], and Dobson and Chato [89] offer the greatest predictive accuracy for the current dataset, with MAEs of 24.7%, 24.2%, and 24.1%, respectively.
- (2) Most correlations predict results with higher accuracy for high flowrate cases.
- (3) Almost every correlation struggles to accurately predict condensation heat transfer for low flow qualities (high liquid content). It is likely that most correlations shown here do not perform well due to an absence of low-quality datapoints for the datasets used in their original formulation.

#### 4.3.3.3 Challenges with Predicting Vertical Upflow

Due to the role of body force destabilizing flow in vertical upflow condensation, this orientation is far less frequently adopted than vertical downflow and horizontal configurations. Difficulty in establishing co-current flow found in other orientations leads to significantly different heat transfer mechanisms in vertical upflow condensation, meaning many common semi-empirical and mechanistic design tools struggle to accurately capture heat transfer behavior in vertical upflow condensation, particularly in cases with high liquid content and low flow inertia.

Because of these limitations in predictive tools and the rare nature of condensers operating in vertical upflow orientation, the current experimental results will not be compared to any

commonly available predictive tools. Should design of a condenser in vertical upflow orientation be necessary, adoption of a micro-channel heat sink is recommended, as these are less susceptible to orientation effects (due to the dominant role of surface tension) and have many associated predictive tools which may be used with higher accuracy.

## 5. CONCLUSIONS

### 5.1 Flow Boiling

#### 5.1.1 *DWO Existence and Impact on System Stability*

This portion of the study presented dynamic results for flow boiling of FC-72 in a rectangular channel subjected to heating from two opposite sides. Tests were executed for a range of mass velocities for subcooled and saturated inlet conditions in vertical upflow, vertical downflow, and horizontal flow orientations. High frequency pressure measurements made throughout the flow loop were used to assess the influence of individual loop components on the dynamic behavior of the working fluid. By isolating the influence of mechanically induced flow disturbances, physical instability modes were identified and analyzed, primarily within the test section itself. Several stability maps were then presented, with pros and cons of each discussed. Key findings from this study are as follows:

- 1) Analysis of flow dynamic behavior throughout the flow loop revealed that fluctuations within the single-phase liquid regions of the loop are dominated by mechanically induced oscillations, primarily from rotary motion of the pump and vibrations from air fans mounted on the condenser.
- 2) Within the two-phase region of the flow loop, pressure fluctuations exhibited characteristics commonly associated with Density Wave Oscillations (DWOs). Flow visualization images were utilized to show that pressure fluctuations representative of DWOs are associated with cyclical passage of High Density and Low Density Fronts through the measurement region. A simple method for prediction of characteristic frequency was put forward, and shown to provide moderately good capability, but future work to include the influence of body force on prediction of DWO frequency is needed.
- 3) Within the test section, cases involving saturated flow boiling displayed strong influence of DWOs on not only pressure, but also key parameters such as heated wall temperature, mass flowrate, and inlet quality. Under conditions where amplitude of DWOs is large, this indicates a capacity for stability considerations to impact cooling system design.

- 4) Several stability maps commonly found in the literature were presented and shown to have limited applicability to the present data. Three new stability maps were also presented that provide qualitative information regarding the conditions for which DWOs form in vertical upflow, vertical downflow, and horizontal flow orientations.

#### 5.1.2 *Frequency and Amplitude of DWOs in Vertical Upflow Boiling*

This portion of the study investigated mechanisms behind the occurrence of Density Wave Oscillations (DWOs) and the characteristics of these oscillations in vertical upflow boiling of FC-72 within a single mini-channel. Based on conclusions from prior work [53], only conditions for which DWOs were observed within the test module were analyzed, providing a total of 236 data points spanning two separate sets of testing. Sequences of flow visualization images were presented to provide a mechanistic understanding of the DWO process, followed by schematics detailing this information. A methodology for detecting frequency and amplitude of oscillation was detailed and utilized to provide information regarding trends for frequency and amplitude of DWO induced pressure oscillations with respect to key operating parameters such as mass velocity, inlet quality, and heat flux, as well as relevant dimensionless groups. Some analysis regarding the validity of reconstructing transient pressure signals using a single frequency and amplitude was also included, along with discussion on the utility of a predictive tool capable of determining frequency and amplitude for given operating conditions. Key findings from this study are as follows:

- (1) Analysis of flow visualization results reveals the dominant, low-frequency oscillatory mode within the current system can be related to the cyclical passage of high and low density fronts through the test module, a process itself attributable to flow separation effects.
- (2) Trends for frequency and amplitude of oscillation remain consistent across the two sets of experiments presented herein, and indicate mass velocity is the dominant factor in determining both frequency and amplitude of DWO induced pressure oscillations.
- (3) DWO induced pressure oscillation amplitude was seen to be at most 7% of time-averaged inlet pressure, indicating there is little safety risk associated with the present operating conditions (important for FBCE operation on the ISS).

- (4) Reconstruction of transient pressure fluctuations using a single frequency and amplitude yielded moderate agreement with original transient waveforms, with key limitations being the insufficiency of a single frequency to describe DWO induced behavior and lost low and high frequency information.
- (5) Although imperfect for recreating experimental pressure results, a predictive model for frequency and amplitude of DWO induced fluctuations capable of serving as a constitutive relationship for advanced transient two-phase flow simulations would prove valuable.

### 5.1.3 *Mechanistic Model to Predict Frequency and Amplitude of DWOs in Vertical Upflow Boiling*

This portion of the study presented a new mechanistic model for Density Wave Oscillations for vertical upflow boiling with finite inlet quality capable of predicting frequency and amplitude of DWO induced pressure oscillations. Experimental data were analyzed and used as the basis to formulate a mechanistic description of the process by which DWOs occur within the present setup. Counter to many prior investigations which refer to DWOs as forming due to feedback effects between flow rate, pressure drop, and flow enthalpy changes causing the location of the bulk boiling boundary to fluctuate, DWOs as observed in the present work were determined to occur due to the presence of separated flow allowing for the accumulation of liquid in the channel inlet. This liquid accumulation forms a High Density Front (HDF) that departs and travels along the channel, re-wetting the liquid film and re-establishing annular, co-current flow throughout.

This cyclical process of HDF formation and passage through the channel was modeled by subdividing the channel into three key control volumes and evaluating conservation equations for each. Model subcomponents were investigated and showed the model to exhibit physically valid trends, as did parametric evaluation of frequency and amplitude predictions. Model predictions were validated using database of 236 points where DWOs were observed experimentally and results showed the model possessing good predictive capabilities, evidenced by a Mean Absolute Error (MAE) of 25.5% when predicting frequency and 31.7% when predicting amplitude. Key findings from this study are as follows:

- (1) Analysis of experimental results revealed that dominant low-frequency pressure oscillations observed in a majority of vertical upflow cases with finite inlet quality are associated with the cyclical passage of High Density Fronts (HDFs) through the test section.
- (2) A physical explanation for mechanisms leading to the formation and passage of HDFs through the test section was presented, centering on the orders of magnitude difference in body forces acting on liquid and vapor phases while in a separated flow regime.
- (3) A mechanistic model for DWOs was developed by analyzing the process behind formation and motion of HDFs through the test section. The model is capable of predicting frequency and amplitude of DWO induced pressure oscillations, and was shown to accurately capture physical trends for a wide parametric range. Predictive accuracy of the model was evaluated using a 236-point dataset and shown to be satisfactory.
- (4) The model was used to investigate potential parametric variations not possible with current experimental facilities, and led to two key features of interest for future studies: whether this phenomenon will manifest in the absence of gravity, and that use of water as a working fluid could potentially yield pressure fluctuations of significantly higher amplitude.
- (5) Limitations of the current modeling work were discussed, with the key takeaway being the need for more detailed treatment of HDF hydrodynamics.

## **5.2 Flow Condensation**

### *5.2.1 Condensation Pressure Oscillations at Different Orientations*

This portion of the study examined pressure oscillations observed during flow condensation through a smooth circular tube in vertical upflow, vertical downflow, and horizontal flow orientations. Analysis of instantaneous pressure signals measured at module inlet and outlet locations revealed the presence of dominant oscillatory modes in the moderate (1 – 20 Hz) frequency range whose intensity exhibited dependence on operating conditions including flow rate, quality, and orientation. Investigation of oscillatory phenomena at other locations within the flow loop revealed modes detected within the test section could be considered independent of modes introduced at other locations, allowing analysis to proceed considering oscillatory behavior observed in the test section to be physical in nature.

Three key parameters were defined and evaluated to describe observed oscillatory behavior:  $Q$  Factor (governing existence and intensity of oscillatory modes), frequency, and amplitude. Parametric trends for each were evaluated across a range of relevant operating conditions and interpreted using relevant dimensionless groups. These showed a strong dependence of oscillatory characteristics on orientation. Important qualitative conclusions are summarized in Table 4.2.

Finally, flow visualization images sequences for vertical upflow, vertical downflow, and horizontal flow orientations were presented, and used to provide commentary on the effects of liquid mass accumulation, inlet quality, and mass velocity in addition to orientation on observed dynamic behavior.

Key conclusions from this study are:

- 1) Flow condensation exhibits a wide range of oscillatory behavior depending on operating conditions and flow orientation. This behavior is seen to be independent of mechanical sources within the flow loop, indicating it is physical in nature.
- 2) Parametric evaluation of  $Q$  Factor, peak frequency, and amplitude of peak oscillatory mode reveal changes to key operating conditions including mass velocity, inlet quality, and exit quality affect these parameters differently depending on flow orientation. Across the three orientations investigated here, vertical upflow is seen to exhibit the most dynamic behavior, with vertical downflow exhibiting less, and horizontal flow showing the least oscillatory behavior.
- 3) For the most extreme case investigated here, amplitude of oscillation is seen to be 7.9% of time-averaged inlet pressure, indicating pressure oscillations are of sufficiently low magnitude to not impact system safety.
- 4) Analysis of flow visualization image sequences indicates liquid film behavior in each orientation reflecting conclusions drawn regarding overall dynamic behavior. More thorough analysis of interfacial behavior and liquid film dynamics in future work may provide a physical basis for modeling of dominant oscillatory modes in flow condensation.

### 5.2.2 *Identification of Condensation Flow Regime Using Temperature and Pressure Measurements*

The portion of the present study investigated condensation flow regime in a smooth circular tube. Flow behavior as a function of condensate mass velocity in vertical upflow, vertical

downflow, and horizontal flow orientations was assessed through flow visualization images. Qualitative trends were used as a starting point for development of a new methodology using temperature and pressure measurements to determine whether upflow condensation exhibited co-current or counter-current flow behavior (referring to liquid and vapor phases). Similarly, circumferentially spaced temperature measurements were used in horizontal flow to determine whether flow exhibited stratified or axisymmetric characteristics. The influence of interfacial waves on temperature fluctuations observed in vertical downflow condensation at low mass velocities was also discussed.

Experimentally determined flow regime boundaries were compared with results predicted by several popular flow regime maps for both vertical upflow and horizontal flow orientations. Assessments of their performances are provided in Tables 4.3 and 4.4 for upflow and horizontal orientations, respectively.

Key conclusions from this study are:

- (1) Condensation flow regimes in vertical upflow may be grouped into those exhibiting co-current flow (*climbing film*) and those exhibiting counter-current flow (*flooding, oscillating film, falling film*). Similarly, horizontal flow regimes may be grouped as stratified (*stratified, wavy-stratified, plug*) and axisymmetric (*annular, slug, bubbly*).
- (2) Liquid film behavior in vertical upflow condensation may be accurately determined as co-current or counter-current based on observed magnitudes of temperature and pressure fluctuations. If these fluctuations maintain the same amplitude or increase slightly as mass velocity is increased, flow is co-current. If they decrease as mass velocity increases, flow is counter-current.
- (3) Liquid film distribution in horizontal flow condensation may be determined to be stratified or axisymmetric based on observed magnitudes of standard deviation between circumferentially spaced temperature measurements. If these values maintain the same magnitude or increase slightly as mass velocity is increase, flow is axisymmetric. If they decrease as mass velocity increases, flow is stratified.
- (4) Comparison of identified flow regimes with those predicted by popular flow regime maps yield reasonable agreement across all maps investigated here. For vertical upflow, the map of Park and Mudawar [93] is capable of accurately predicting condensation flow regime. In horizontal flow the map of Song *et al.* [122] does the best job predicting flow regime.

### 5.2.3 Flow Condensation Heat Transfer

The final portion of the present study dealt with flow condensation of dielectric FC-72 in a smooth circular tube at different orientations in Earth's gravity. Calculation of both local and channel average condensation heat transfer coefficient values was performed for a subset of the dataset corresponding to axisymmetric flow conditions. Uncertainty analysis was also presented for calculated values of condensation heat transfer coefficient, showing channel average values possess low uncertainty (~ 5% - 25 %), but local measurements near the channel outlet may possess high uncertainties (~ 25% - 100 %).

Parametric analysis of both local and averaged condensation heat transfer coefficient values reveal mass velocity is the dominant parameter governing changes in heat transfer coefficient value (increases in mass velocity yield increased heat transfer coefficient assuming all other operating conditions are held constant). Flow quality also influences heat transfer coefficient, with higher liquid content (lower quality) leading to lower values of condensation heat transfer coefficient.

Channel orientation was also seen to influence condensation heat transfer, particularly at low mass velocities. At low mass velocities vertical upflow is seen to exhibit highest values of heat transfer coefficient, while as mass velocity is increased results for all three orientations begin to converge. Gravity independence criteria developed by O'Neill *et al.* [137] are evaluated using the present dataset and are seen to give reasonable estimation of gravity independence point.

Comparison of experimental heat transfer results in vertical downflow orientation with SFM predictions yielded good agreement, particularly for low mass velocity cases. For horizontal flow, evaluation of correlations commonly found in literature revealed the majority of correlations slightly under predict heat transfer in the current dataset, and particularly struggle with low flow quality cases. The correlations of Shah [168], Wang *et al.* [119], and Dobson and Chato [89] were seen to offer the best predictive performance across all three orientations.

Key conclusions from this study are:

- (1) Identification of condensation flow regime using temperature and pressure based methods presented in section 4.2 prior to heat transfer data reduction is crucial for eliminating non-axisymmetric cases from the dataset and identifying countercurrent flow cases for later analysis.

- (2) Uncertainty analysis for heat transfer coefficient calculations revealed channel average heat transfer coefficient values are calculated with uncertainties of  $\pm 3.6\%$  to  $\pm 26.7\%$  (depending on operating conditions). Local heat transfer coefficient values in the channel exit region may have significantly higher uncertainties, however, and trends for this portion of the channel should be analyzed with caution.
- (3) Mass velocity is seen to be the dominant parameter governing changes in condensation heat transfer coefficient. Liquid content plays a secondary role, and orientation (body force) is also seen to have an influence, particularly at low flowrates.
- (4) Separated Flow Model (outlined in Table 4.5) predictions for vertical downflow condensation heat transfer yield reasonable agreement with experimental results, evidenced by an overall MAE of 31.2% on the current dataset.
- (5) Assessment of correlations for heat transfer coefficient in horizontal flow reveal the majority do a reasonable job of predicting heat transfer coefficient. Most correlations struggle to predict heat transfer in cases with high liquid content (low quality) and the majority of inaccuracies come from these cases. Best predictive results are found for the correlations of Shah [168], Wang *et al.* [119], and Dobson and Chato [89], with MAEs of 24.7%, 24.2%, and 24.1%, respectively.

Future experiments on the International Space Station (ISS) involving tests at similar operating conditions using a test section with the same diameter and condensation length will provide a microgravity dataset for comparison with the current 1-g results. It is expected these results will greatly further understanding of the role of body force on the condensation heat transfer process.

## REFERENCES

- [1] I. Mudawar, Assessment of high-heat-flux thermal management schemes, *IEEE Trans. - CPMT* 24 (2001) 122-141.
- [2] C.L. Tien, K.S. Chung, Entrainment limits in heat pipes, *AIAA J.* 17 (1979) 643-646.
- [3] T.J. LaClair, I. Mudawar, Thermal transients in a capillary evaporator prior to the initiation of boiling, *Int. J. Heat Mass Transfer* 43 (2000) 3937-3952.
- [4] M. Shafahi, V. Bianco, H. Vafai, O. Manco, An investigation of the thermal performance of cylindrical heat pipes using nanofluids, *Int. J. Heat Mass Transfer* 53 (2010) 376-383.
- [5] P.J. Marto, V.J. Lepere, Pool boiling heat transfer from enhanced surfaces to dielectric fluids, *J. Heat Transfer* 104 (1982) 292-299.
- [6] I. Mudawar, T.M. Anderson, Parametric investigation into the effects of pressure, subcooling, surface augmentation and choice of coolant on pool boiling in the design of cooling systems for high-power density chips, *J. Electronic Packaging* 112 (1990) 375-382.
- [7] S.J. Reed, I. Mudawar, Elimination of boiling incipience temperature drop in highly wetting fluids using spherical contact with a flat surface, *Int. J. Heat Mass Transfer* 42 (1999) 2439-2454.
- [8] J.A. Shmerler, I. Mudawar, Local heat transfer coefficient in wavy free-falling turbulent liquid films undergoing uniform sensible heating, *Int. J. Heat Mass Transfer* 31 (1988) 67-77.
- [9] I. Mudawar, R.A. Houpt, Mass and momentum transport in smooth falling liquid films laminarized at relatively high Reynolds numbers, *Int. J. Heat Mass Transfer* 36 (1993) 3437-3448.
- [10] C.O. Gersey, I. Mudawar, Effects of heater length and orientation on the trigger mechanism for near-saturated flow boiling CHF - I. Photographic and statistical characterization of the near-wall interfacial features, *Int. J. Heat Mass Transfer* 38 (1995) 629-642.
- [11] S.M. Ghiaasiaan, *Two-phase flow, boiling and condensation in conventional and miniature systems*, Cambridge University Press, New York, 2008.
- [12] W. Qu, I. Mudawar, Thermal design methodology for high-heat-flux single-phase and two-phase micro-channel heat sinks, *Proc. I-THERM 2002*, San Diego, California, pp. 347-359.

- [13] S. Mukherjee, I. Mudawar, Smart pumpless loop for micro-channel electronic cooling using flat and enhanced surfaces, *IEEE Trans. – CPMT* 26 (2003) 99-109.
- [14] S. Mukherjee, I. Mudawar, Pumpless loop for narrow channel and micro-channel boiling from vertical surfaces, *J. Electronic Packaging* 125 (2003) 431-441.
- [15] J. Lee, I. Mudawar, Critical heat flux for subcooled flow boiling in micro-channel heat sinks, *Int. J. Heat Mass Transfer* 52 (2009) 3341-3352.
- [16] J. Lee, I. Mudawar, Fluid flow and heat transfer characteristics of low temperature two-phase micro-channel heat sinks – part 1: Experimental methods and flow visualization results, *Int. J. Heat Mass Transfer* 51 (2008) 4315-4326.
- [17] M. Monde, T. Inoue, Critical heat flux in saturated forced convective boiling on a heated disk with multiple impinging jets, *J. Heat Transfer* 113 (1991) 722-727.
- [18] D.C. Wadsworth, I. Mudawar, Enhancement of single-phase heat transfer and critical heat flux from an ultra-high-flux simulated microelectronic heat source to a rectangular impinging jet of dielectric liquid, *J. Heat Transfer* 114 (1992) 764-768.
- [19] M.E. Johns, I. Mudawar, I., An ultra-high power two-phase jet-impingement avionic clamshell module, *J. Electronic Packaging* 118 (1996) 264-270.
- [20] I. Mudawar, Recent advances in high-flux, two-phase thermal management, *J. Thermal Sci. Eng. Appl.* 5 (2013) 021012.
- [21] W.P. Klinzing, J.C. Rozzi, I. Mudawar, Film and transition boiling correlations for quenching of hot surfaces with water sprays, *J. Heat Treating* 9 (1992) 91-103.
- [22] D.D. Hall, I. Mudawar, Optimization of quench history of aluminum parts for superior mechanical properties, *Int. J. Heat Mass Transfer* 39 (1996) 85-95.
- [23] L. Lin, R. Ponnappan, Heat transfer characteristics of spray cooling in a closed loop, *Int. J. Heat Mass Transfer* 46 (2003) 3737-3746.
- [24] J.D. Bernardin, I. Mudawar, A Leidenfrost point model for impinging droplets and sprays, *J. Heat Transfer* 126 (2004) 272-278.
- [25] M. Visaria, I. Mudawar, Effects of high subcooling on two-phase spray cooling and critical heat flux, *Int. J. Heat Mass Transfer* 51 (2008) 5269-5278.
- [26] I. Mudawar, D. Bharathan, K. Kelly, S. Narumanchi, Two-phase spray cooling of hybrid vehicle electronics, *IEEE Trans. – CPMT* 32 (2009) 501-512.

- [27] M. Visaria, I. Mudawar, Application of two-phase spray cooling for thermal management of electronic devices, *IEEE Trans. – CPMT* 32 (2009) 784-793.
- [28] I. Mudawar, Two-phase micro-channel heat sinks: theory, applications and limitations, *J. Electronic Packaging* 133 (2011) 041002-2.
- [29] M.K. Sung, I. Mudawar, Experimental and numerical investigation of single-phase heat transfer using a hybrid jet impingement/micro-channel cooling scheme, *Int. J. Heat Mass Transfer* 49 (2006) 682-694.
- [30] M.K. Sung, I. Mudawar, Single-phase hybrid micro-channel/jet impingement cooling, *Int. J. Heat Mass Transfer* 51 (2008) 4342-4352.
- [31] M.K. Sung, I. Mudawar, Single-phase and two-phase heat transfer characteristics of low temperature hybrid micro-channel/micro-jet impingement cooling module, *Int. J. Heat Mass Transfer* 51 (2008) 3882-3895.
- [32] S. Lee, I. Mudawar, M.M. Hasan, Thermal analysis of hybrid single-phase, two-phase and heat pump thermal control system (TCS) for future spacecraft, *Appl. Therm. Eng.* 100 (2016) 190-214.
- [33] F.P. Chiramonte, J.A. Joshi, Workshop on critical issues in microgravity fluids, transport, and reaction processes in advanced human support technology – final report, NASA TM-2004-212940, 2004.
- [34] The National Academies, Recapturing a future for space exploration: life and physical sciences research for a new era, National Academies Press, Washington, DC, 2011.
- [35] H. Zhang, I. Mudawar, M.M. Hasan, Flow boiling CHF in microgravity, *Int. J. Heat Mass Transfer* 48 (2005) 3107-3118.
- [36] H. Zhang, I. Mudawar, M.M. Hasan, Application of flow boiling for thermal management of electronics in microgravity and reduce-gravity space systems, *IEEE Trans. – CPMT* 32 (2009) 466-477.
- [37] M. Ishii, N. Zuber, Thermally induced flow instabilities in two-phase mixtures, *Proc. 4th Int. Heat Transfer Conf. on Heat Transfer* (1970), Paris, vol. 5, paper B5.11.
- [38] D. Brutin, L. Tadrist, Pressure drop and heat transfer analysis of flow boiling in a minichannel: influence of the inlet condition on two-phase flow stability, *Int. J. Heat Mass Transfer* 47 (2004) 2365-2377.

- [39] G. Wang, P. Cheng, A.E. Bergles, Effects of inlet/outlet configurations on flow boiling instability in parallel microchannels, *Int. J. Heat Mass Transfer* 51 (2008) 2267-2281.
- [40] R.H. Whittle, R. Forgan, A correlation for the minima in the pressure drop versus flow-rate curves for sub-cooled water flowing in narrow heated channels, *Nucl. Eng. Des.* 6 (1967) 89-99.
- [41] J.E. Kennedy, G.M. Roach Jr., M.F. Dowling, S.I. Abdel-Khalik, S.M. Ghiaasiaan, S.M. Jeter, Z.H. Quershi, The onset of flow instability in uniformly heated horizontal microchannels, *J. Heat Transfer* 122 (2000) 118-125.
- [42] J. Wang, Y. Huang, Y. Wang, Visualized study on specific points on demand curves and flow patterns in a single-side heated narrow rectangular channel, *Int. J. Heat Fluid Flow* 32 (2011) 982-992.
- [43] J. Lee, H. Chae, S.H. Chang, Flow instability during subcooled boiling for a downward flow at low pressure in a vertical narrow rectangular channel, *Int. J. Heat Mass Transfer* 67 (2013) 1170-1180.
- [44] M. Ledinegg, Instability of flow during natural and forced circulation, *Die Wärme* 61 (1938) 891-898.
- [45] P. Saha, M. Ishii, N. Zuber, An experimental investigation of the thermally induced flow oscillations in two-phase systems, *J. Heat Transfer* 98 (1976) 616-622.
- [46] M. Ozawa, S. Nakanishi, S. Ishigai, Y. Mizuta, H. Tarui, Flow instabilities in boiling channels: Part 1, Pressure drop oscillations, *Bull. JSME* 22 (1979) 1113-1118.
- [47] R.T. Lahey Jr., M.Z. Podowski, On the analysis of various instabilities in two-phase flow, *Multiphase Sci. Tech.* 4 (1989) 183-370.
- [48] E.P. Serov, The operation of once-through boiler in variable regimes, *Trudy, Moscow Energ. Inst.* 11 (1953)
- [49] G. Yadigaroglu, A.E. Bergles, Fundamental and higher-mode density-wave oscillations in two-phase systems, *J. Heat Transfer* 94 (1972) 189-195.
- [50] J.A. Boure, A.E. Bergles, L.S. Tong, Review of two-phase flow instability, *Nucl. Eng. Des.* 25 (1973) 165-192.
- [51] D.F. Delmastro, A. Clausse, J. Converti, The influence of gravity on the stability of boiling flows, *Nucl. Eng. Des.* 127 (1991) 129-139.

- [52] C.W. Shin, H.C. NO, Experimental study for pressure drop and flow instability of two-phase flow in the PCHE-type steam generator for SMRs, *Nucl. Eng. Des.* 318 (2017) 109-118.
- [53] L.E. O'Neill, C.R. Kharangate, I. Mudawar, Time-averaged and transient pressure drop for flow boiling with saturated inlet conditions, *Int. J. Heat Mass Transfer* 103 (2016) 133-153.
- [54] L.E. O'Neill, I. Mudawar, M.M. Hasan, H.K. Nahra, R. Balasubramaniam, N.R. Hall, A. Lokey, J.R. Mackey, Experimental investigation into the impact of density wave oscillations on flow boiling system dynamic behavior and stability, *Int. J. Heat Mass Transfer* 120 (2018) 144-166.
- [55] L.E. O'Neill, I. Mudawar, Mechanistic model to predict frequency and amplitude of Density Wave Oscillations in vertical upflow boiling, *Int. J. Heat Mass Transfer* 123 (2018) 143-171.
- [56] L.E. O'Neill, I. Mudawar, M.M. Hasan, H.K. Nahra, B. Ramaswamy, J.R. Mackey, Experimental investigation of frequency and amplitude of density wave oscillations in vertical upflow boiling, *Int. J. Heat Mass Transfer*, in review.
- [57] W. Qu, I. Mudawar, Measurement and prediction of pressure drop in two-phase micro-channel heat sinks, *Int. J. Heat Mass Transfer* 46 (2003) 2737-2753.
- [58] K.H. Chang, C. Pan, Two-phase flow instability for boiling in a microchannel heat sink, *Int. J. Heat Mass Transfer* 50 (2007) 2078-2088.
- [59] H. Lee, I. Park, I. Mudawar, M.M. Hasan, Micro-channel evaporator for space applications – 1. Experimental pressure drop and heat transfer results for different orientations in Earth gravity, *Int. J. Heat Mass Transfer* 77 (2014) 1213-1230.
- [60] V. Jovic, N. Afgan, L. Jovic, D. Spasojevic, An experimental study of the pressure drop oscillations in three parallel channel two phase flow, in: G.F. Hewitt (Ed.), *Proc. Int. Heat Transfer Conf.*, Brighton, UK, 1994 (193-198).
- [61] S. Lee, V.S. Devahdhanush, I. Mudawar, Frequency analysis of pressure oscillations in large length-to-diameter two-phase micro-channel heat sinks, *Int. J. Heat Mass Transfer*, in press.
- [62] H. Yuncu, An experimental and theoretical study of density wave and pressure drop oscillations, *Heat Transfer Eng.* 11 (1990) 45-56.

- [63] W.R. Schlichting, R.T. Lahey Jr., M.Z. Podowski, An analysis of interacting instability modes, in a phase change system, *Nucl. Eng. Des.* 240 (2010) 3178-3201.
- [64] L. Tadrist, Review on two-phase flow instabilities in narrow spaces, *Int. J. Heat Fluid Flow* 28 (2007) 54-62.
- [65] S. Kakac, B. Bon, A review of two-phase flow dynamic instabilities in tube boiling systems, *Int. J. Heat Mass Transfer* 51 (2008) 399-433.
- [66] L.C. Ruspini, C.P. Marcel, A. Clause, Two-phase flow instabilities: a review, *Int. J. heat Mass Transfer* 71 (2014) 521-548.
- [67] J. Barber, K. Sefiane, D. Brutin, L. Tadrist, Hydrodynamics and heat transfer during flow boiling instabilities in a single microchannel, *Appl. Therm. Eng.* 29 (2009) 1299-1308.
- [68] S. Lee, I. Mudawar, Transient characteristics of flow boiling in large micro-channel heat exchangers, *Int. J. Heat Mass Transfer* 103 (2016) 186-202.
- [69] S. Lee, I. Mudawar, Thermal and thermodynamic performance, and pressure oscillations of refrigeration loop employing large micro-channel evaporators, *Int. J. Heat Mass Transfer* 103 (2016) 1313-1326.
- [70] Q. Lu, D. Chen, C. Li, X. He, Experimental investigation on flow boiling heat transfer in conventional and mini vertical channels, *Int. J. Heat Mass Transfer* 107 (2017) 225-243.
- [71] G. Xia, W. Wang, L. Cheng, D. Ma, Visualization study on the instabilities of phase-change heat transfer in a flat two-phase closed thermosyphon, *App. Therm. Eng.* 116 (2017) 392-405.
- [72] K. Miyoshi, N. Takenaka, T. Ishida, K. Sugimoto, Investigation of temperature fluctuation phenomena in a stratified steam-water two-phase flow in a simulating pressurizer spray pipe of a pressurized water reactor, *Nucl. Eng. Des.* 316 (2017) 38-45.
- [73] C. Huh, J. Kim, M.H. Kim, Flow pattern transition instability during flow boiling in a single microchannel, *Int. J. Heat Mass Transfer* 50 (2007) 1049-1060.
- [74] C.A. Chen, T.F. Lin, W-M Yan, Time periodic saturated flow boiling heat transfer of R-134a in a narrow annular duct due to heat flux oscillation, *Int. J. Heat Mass Transfer* 106 (2017) 35-46.
- [75] M. Ishii, Thermally induced flow instabilities in two-phase mixtures in thermal equilibrium, Ph.D. Thesis, Georgia Institute of Technology (1971).
- [76] H. Nyquist, Regeneration theory, *Bell System Technical J.* 11 (1932) p. 126.

- [77] S. Levy, E.S. Beckjord, Hydraulic instability in a natural circulation loop with net steam generation at 1000 psia, G.E.A.P., 3215, General Electric, San Jose, California, July 15, 1959.
- [78] K. Solberg, Resultats des essais d'instabilités sur la boucle 'culine' et comparaisons avec un code de calcul, C.E.N.G., Note 225, Centre d'Etudes Nucleaires de Grenoble, France, 1966.
- [79] M.B. Carver, An analytical model for the prediction of hydro-dynamic instability in parallel heated channels, A.E.C.L., 2681, Atomic Energy Canada Limited, 1968.
- [80] K. Fukuda, T. Kobori, Classification of two-phase flow instability by density wave oscillation model, *J. Nucl. Sci. Technol.* 16 (1979) 95-108.
- [81] L.A. Belblidia, C. Bratianu, Density-wave oscillations, *Ann. Nucl. Energy* 6 (1979) 425-444.
- [82] J-L. Achard, D.A. Drew, R.T. Lahey, The analysis of nonlinear density-wave oscillations in boiling channels, *J. Fluid Mech.* 155 (1985) 213-232.
- [83] Q. Wang, X.J. Chen, S. Kakac, Y. Ding, An experimental investigation of density-wave-type oscillations in a convective boiling upflow system, *Int. J. Heat Fluid Flow* 3 (1994) 241-246.
- [84] V. Pandey, S. Singh, Characterization of stability limits of Ledinegg instability and density wave oscillations for two-phase flow in natural circulation loops, *Chem. Eng. Sci.* 168 (2017) 204 - 224.
- [85] M.M. Chen, An analytical study of laminar film condensation: Part 2 - Single and multiple horizontal tubes, *J. Heat Transfer* 83 (1961) 55-60.
- [86] J.F. Roques, V. Dupont, J.R. Thome, Falling film transitions on plain and enhanced tubes, *J. Heat Transfer* 124 (2002) 491-499.
- [87] Y.T. Kang, H. Hong, Y.S. Lee, Experimental correlation of falling film condensation on enhanced tubes with HFC134a; low-fin and Turbo-C tubes, *Int. J. Refrigeration* 30 (2007) 805-811.
- [88] M. Soliman, J.R. Schuster, P.J. Berenson, A general heat transfer correlation for annular flow condensation, *J. Heat Transfer* 90 (1968) 267-274.
- [89] M.K. Dobson, J.C. Chato, Condensation in smooth horizontal tubes, *J. Heat Transfer* 120 (1998) 193-213.

- [90] D. Jung, K. Song, Y. Cho, S. Kim, Flow condensation heat transfer coefficients of pure refrigerants, *Int. J. Refrigeration* 26 (2003) 4-11.
- [91] S. Lips, J.P. Meyer, Experimental study of convective condensation in an inclined smooth tube. Part I: Inclination effect on flow pattern and heat transfer coefficient, *Int. J. Heat Mass Transfer* 55 (2012) 395-404.
- [92] I. Park, S.M. Kim, I. Mudawar, Experimental measurement and modeling of downflow condensation in a circular tube, *Int. J. Heat Mass Transfer* 57 (2013) 567-581.
- [93] I. Park, I. Mudawar, Climbing film, flooding and falling film behavior in upflow condensation in tubes, *Int. J. Heat Mass Transfer* 65 (2013) 44-61.
- [94] I. Park, H. Lee, I. Mudawar, Determination of flow regimes and heat transfer coefficient for condensation in horizontal tubes, *Int. J. Heat Mass Transfer* 80 (2015) 688-716.
- [95] X. Quan, P. Cheng, H. Wu, Transition from annular flow to plug/slug flow in condensation of steam in microchannels, *Int. J. Heat Mass Transfer* 51 (2008) 707-716.
- [96] S.M. Kim, J. Kim, I. Mudawar, Flow condensation in parallel micro-channels - Part 1: Experimental results and assessment of pressure drop correlations, *Int. J. Heat Mass Transfer* 55 (2012) 971-983.
- [97] J. Wang, J.M. Li, Theoretical and experimental study of wavy flow during R134a condensation flow in symmetrically and asymmetrically cooled microchannels, *Int. J. Multiphase Flow* 101 (2018) 125-136.
- [98] H. Lee, I. Park, C. Konishi, I. Mudawar, R.I. May, J.R. Juergens, J.D. Wagner, N.R. Hall, H.K. Nahra, M.M. Hasan, J.R. Mackey, Experimental investigation of flow condensation in microgravity, *J. Heat Transfer* 136 (2014) 021502-1-11.
- [99] W.H. Westendorf, W.F. Brown, Stability of intermixing of high-velocity vapor with its subcooled liquid in cocurrent streams, NASA TN D-3553 (1966).
- [100] J.H. Goodykoontz, R.G. Dorsch, Local heat-transfer coefficients and static pressures for condensation of high-velocity steam within a tube, NASA TN D-3953 (1967).
- [101] M. Soliman, P. Berenson, Flow instability and gravitational effects in condenser tubes, Paper no. Cs. 1.8, in: *Proc. Fourth Int. Conf. on Heat Transfer*, 1970.
- [102] T.J. Rabas, P.G. Minard, Two types of flow instabilities occurring inside horizontal tubes with complete condensation, *Heat Transfer Eng.* 8 (1987) 40-49.

- [103] B.D. Boyer, G.E. Robinson, T.G. Hughes, Experimental investigation of flow regimes and oscillatory phenomena of condensing steam in a single vertical annular passage, *Int. J. Multiphase Flow* 21 (1995) 61-74.
- [104] C.J. Kobus, G.L. Wedekind, B.L. Bhatt, Predicting the onset of a low-frequency, limit-cycle type of oscillatory flow instability in multitube condensing flow systems, *J. Heat Transfer* 123 (2001) 319-330.
- [105] B.L. Bhatt, G.L. Wedekind, A self-sustained oscillatory flow phenomenon in two-phase condensing flow systems, *J. Heat Transfer* 102 (1980) 694-700.
- [106] B.L. Bhatt, G.L. Wedekind, K. Jung, Effects of two-phase pressure drop on the self-sustained oscillatory instability in condensing flows, *J. Heat Transfer* 111 (1989) 538-545.
- [107] G. Liang, N. Mascarenhas, I. Mudawar, Analytical and experimental determination of slug flow parameters, pressure drop and heat transfer coefficient in micro-channel condensation, *Int. J. Heat Mass Transfer* 111 (2017) 1218-1233.
- [108] H. Teng, P. Cheng, T.S. Zhao, Instability of condensate film and capillary blocking in small-diameter-thermosyphon condensers, *Int. J. Heat Mass Transfer* 42 (1999) 3071-3083.
- [109] R. Naik, A. Narain, Steady and unsteady simulations for annular internal condensing flows, part II: Instability and flow regime transitions, *Numer. Heat Transfer Part B* 69 (2016) 473-494.
- [110] G.B. Wallis, Flooding velocities for air and water in vertical tubes, No. AEEW-R-123, United Kingdom Atomic Energy Authority, Reactor Group, Atomic Energy Establishment, Winfrith, Dorset, England, 1961.
- [111] Y. Taitel, A.E. Dukler, A model for predicting flow regime transitions in horizontal and near horizontal gas-liquid flow, *AIChE J.* 22 (1976) 47-55.
- [112] J.M. Mandhane, G.A. Gregory, K. Aziz, A flow pattern map for gas-liquid flow in horizontal pipes, *Int. J. Multiphase Flow* 1 (1974) 537-553.
- [113] G. Breber, J.W. Palen, J. Taborek, Prediction of horizontal tubeside condensation of pure components using flow regime criteria, *J. Heat Transfer* 102 (1980) 471-476.
- [114] T.N. Tandon, H.K. Varma, C.P. Gupta, A new flow regimes map for condensation inside horizontal tubes, *J. Heat Transfer* 104 (1982) 763-768.
- [115] H.M. Soliman, On the annular-to-wavy flow pattern transition during condensation inside horizontal tubes, *Can. J. Chem. Eng.* 60 (1982) 475-481.

- [116] H.M. Soliman, The mist-annular transition during condensation and its influence on the heat transfer mechanism, *Int. J. Multiphase Flow* 12 (1986) 277-288.
- [117] Q. Chen, R.S. Amano, M. Xin, Experimental study of flow patterns and regimes of condensation in horizontal three-dimensional micro-fin tubes, *Heat Mass Transfer* 43 (2006) 201-206.
- [118] A. Cavallini, G. Censi, D. Del Col, L. Doretti, G.A. Longo, L. Rossetto, In-tube condensation of halogenated refrigerants, *ASHRAE Trans.* 108 (2002) 146-161.
- [119] W.W.W. Wang, T.D. Radcliff, R.N. Christensen, A condensation heat transfer correlation for millimeter-scale tubing with flow regime transition, *Exp. Therm. Fluid Sci.* 26 (2002) 473-485.
- [120] J. El Hajal, J.R. Thome, A. Cavallini, Condensation in horizontal tubes, part 1: two-phase flow pattern map, *Int. J. Heat Mass Transfer* 46 (2003) 3349-3363.
- [121] J.W. Coleman, S. Garimella, Two-phase flow regimes in round, square, and rectangular tubes during condensation of refrigerant R134a, *Int. J. Refrigeration* 26 (2003) 117-128.
- [122] Q. Song, G. Chen, Z. Yang, H. Wang, M. Gong, New adiabatic and condensation two-phase flow pattern maps of R14 in a horizontal tube, *Int. J. Heat Mass Transfer* 127 (2018) 910-924.
- [123] L. Liebenberg, J.R. Thome, J.P. Meyer, Flow visualization and flow pattern identification with power spectral density distributions of pressure traces during refrigerant condensation in smooth and microfin tubes, *J. Heat Transfer* 127 (2005) 209-220.
- [124] L. Liebenberg, J.P. Meyer, The characterization of flow regimes with power spectral density distributions of pressure fluctuations during condensation in smooth and micro-fin tubes, *Exp. Therm. Fluid Sci.* 31 (2006) 127-140.
- [125] Y. Chen, C.B. Sobhan, G.P. Peterson, Review of condensation heat transfer in microgravity environments, *J. Therm. Heat Transfer* 3 (2006) 353-360.
- [126] S. Lips, J.P. Meyer, Two-phase flow in inclined tubes with specific reference to condensation: A review, *Int. J. Multiphase Flow* (2011) 845-859.
- [127] J.A. Albers, R.P. Macosko, Experimental pressure-drop investigation of nonwetting, condensing flow of mercury vapor in a constant-diameter tube in 1-g and zero-gravity environments, *NASA TN D-2838* (1965) 1-32.

- [128] J.A. Albers, R.P. Macosko, condensation pressure drop of nonwetting mercury in a uniformly tapered tube in 1-g and zero-gravity environments, NASA TN D-3185 (1966) 1-38.
- [129] D. Namkoong, H.B. Block, R.P. Macosko, C.C. Crabs, Photographic study of condensing mercury flow in 0- and 1-g environments, NASA TN D-4023 (1967) 1-31.
- [130] E.G. Keshock, Experimental and analytical investigation of 0-g condensation in a mechanical refrigeration system application, TR 75-T6, Old Dominion University, Contract NAS9-13410 (1975) 1-92.
- [131] H. Lee, I. Mudawar, M.M. Hasan, Experimental and theoretical investigation of annular flow condensation in microgravity, *Int. J. Heat Mass Transfer* 61 (2013) 293-309.
- [132] B.-X. Wang, X.-Z. Du, Study on laminar film-wise condensation for vapor flow in an inclined small/mini-diameter tube, *Int. J. Heat Mass transfer* 43 (2003) 1859-1868.
- [133] S. Lips, J.P. Meyer, Experimental study of convective condensation in an inclined smooth tube. Part II: Inclination effect on pressure drops and void fractions, *Int. J. Heat Mass Transfer* 55 (2012) 405-412.
- [134] J. Kurita, M. Kivisalu, S. Mitra, R. Naik, A. Narain, Experimental results on gravity driven fully condensing flows in vertical tubes, their agreement with theory, and their differences with shear driven flows' boundary-condition sensitivities, *Int. J. Heat Mass Transfer* 54 (2011) 2932-2951.
- [135] S. Mitra, A. Narain, R. Naik, S.D. Kulkarni, A quasi one-dimensional method and results for steady annular/stratified shear and gravity driven condensing flows, *Int. J. Heat Mass Transfer* 54 (2011) 3761-3776.
- [136] I. Park, L.E. O'Neill, C.R. Kharangate, I. Mudawar, Assessment of body force effects in flow condensation, Part I: Experimental investigation of liquid film behavior for different orientations, *Int. J. Heat Mass Transfer* 106 (2017) 295-312.
- [137] L.E. O'Neill, I. Park, C.R. Kharangate, V.S. Devahdhanush, V. Ganesan, I. Mudawar, Assessment of body force effects in flow condensation, part II: Criteria for negating influence of gravity, *Int. J. Heat Mass Transfer* 106 (2017) 313-328.
- [138] S.M.A. Noori Rahim Abadi, J.P. Meyer, J. Dirker, Effect of inclination angle on the condensation of R134a inside an inclined smooth tube, *Chem. Eng. Res. Des.* 132 (2018) 346-357.

- [139] I. Mudawar, Flow boiling and flow condensation in reduced gravity, *Advances in Heat Transfer* 49 (2017) 225-306.
- [140] S.M. Kim, I. Mudawar, Universal approach to predicting saturated flow boiling heat transfer in mini/micro-channels – Part II. Two-phase heat transfer coefficient, *Int. J. Heat Mass Transfer* 64 (2013) 1239-1256.
- [141] S.M. Kim, I. Mudawar, Theoretical model for local heat transfer coefficient for annular flow boiling in circular mini/micro-channels, *Int. J. Heat Mass Transfer* 73 (2014) 731-742.
- [142] C.R. Kharangate, L.E. O'Neill, I. Mudawar, Effects of two-phase inlet quality, mass velocity, flow orientation, and heating perimeter on flow boiling in a rectangular channel: Part 1 – Two-phase flow and heat transfer results, *Int. J. Heat Mass Transfer* 103 (2016) 1261-1279.
- [143] J. Lee, L.E. O'Neill, S. Lee, I. Mudawar, Experimental and computational investigation on two-phase flow and heat transfer of highly subcooled flow boiling in vertical upflow, *Int. J. Heat Mass Transfer* 136 (2019) 1199-1216.
- [144] S.-M. Kim, I. Mudawar, Universal approach to predicting two-phase frictional pressure drop for mini/micro-channel saturated flow boiling, *Int. J. Heat Mass Transfer* 55 (2013) 718-734.
- [145] H. Zhang, I. Mudawar, M.M. Hasan, Experimental assessment of the effects of body force, surface tension force, and inertia on flow boiling CHF, *Int. J. Heat Mass Transfer* 45 (2002) 4079-4095.
- [146] H. Zhang, I. Mudawar, M.M. Hasan, Experimental and theoretical study of orientation effects on flow boiling CHF, *Int. J. Heat Mass Transfer* 45 (2002) 4463-4478.
- [147] C. Konishi, I. Mudawar, Review of flow boiling and critical heat flux in microgravity, *Int. J. Heat Mass Transfer* 80 (2015) 469-493.
- [148] C.R. Kharangate, L.E. O'Neill, I. Mudawar, M.M. Hasan, H.K. Nahra, R. Balasubramaniam, N.R. Hall, A. M. Macner, J.R. Mackey, Effects of subcooling and two-phase inlet on flow boiling heat transfer and critical heat flux in a horizontal channel with one-sided and double-sided heating, *Int. J. Heat Mass Transfer* 91 (2015) 1187-1205.

- [149] C.R. Kharangate, L.E. O'Neill, I. Mudawar, M.M. Hasan, H.K. Nahra, R. Balasubramaniam, N.R. Hall, A. M. Macner, J.R. Mackey, Flow boiling and critical heat flux in horizontal channel with one-sided and double-sided heating, *Int. J. Heat Mass Transfer* 90 (2015) 323-338.
- [150] C.R. Kharangate, C. Konishi, I. Mudawar, Consolidated methodology to predicting flow boiling critical heat flux for inclined channels in Earth gravity and for microgravity, *Int. J. Heat Mass Transfer* 92 (2016) 467-482.
- [151] C.R. Kharangate, L.E. O'Neill, I. Mudawar, Effects of two-phase inlet quality, mass velocity, flow orientation, and heating perimeter on flow boiling in a rectangular channel: Part 2 – CHF experimental results and model, *Int. J. Heat Mass Transfer* 103 (2016) 1280-1296.
- [152] H. Lee, C.R. Kharangate, N. Mascarenhas, I. Park, I. Mudawar, Experimental and computational investigation of vertical downflow condensation, *Int. J. Heat Mass Transfer* 85 (2015) 865-879.
- [153] C.R. Kharangate, H. Lee, I. Park, I. Mudawar, Experimental and computational investigation of vertical upflow condensation in a circular tube, *Int. J. Heat Mass Transfer* 95 (2016) 249-263.
- [154] C.R. Kharangate, I. Mudawar, Review of computational studies on boiling and condensation, *Int. J. Heat Mass Transfer* 108 (2017) 1164-1196.
- [155] S.M. Kim, I. Mudawar, Universal approach to predicting two-phase frictional pressure drop for adiabatic and condensing mini/micro-channel flows, *Int. J. Heat Mass Transfer* 55 (2012) 3246-3261.
- [156] S.M. Kim, I. Mudawar, Universal approach to predicting heat transfer coefficient for condensing mini/micro-channel flow, *Int. J. Heat Mass Transfer* 56 (2013) 238-250.
- [157] J.D. Lee, C. Pan, Dynamics of multiple parallel boiling channel systems with forced flows, *Nucl. Eng. Des.* 192 (1999) 31-44.
- [158] D. Bogojevic, K. Sefiane, A.J. Walton, H. Lin, G. Cummins, Two-phase flow instabilities in a silicon microchannels heat sink, *Int. J. Heat Fluid Flow* 30 (2009) 854-867.
- [159] “SciPy v0.14.0 Reference Guide, Signal processing, [scipy.signal.butter](https://docs.scipy.org/doc/scipy-0.14.0/reference/generated/scipy.signal.butter.html)”, The scipy community (2014), accessed September 2017, <https://docs.scipy.org/doc/scipy-0.14.0/reference/generated/scipy.signal.butter.html>.

- [160] “Simple real Fourier series approximation”, Matt Tearle (2016), accessed September 2017, <https://www.mathworks.com/matlabcentral/fileexchange/31013-simple-real-fourier-series-approximation?focused=6790998&tab=function>.
- [161] M.V.C. Alves, P.J. Waltrich, T.R. Gessner, G. Falcone, J.R. Barbosa Jr., Modeling transient churn-annular flows in a long vertical tube, *Int. J. Multiphase Flow* 89 (2017) 399-412.
- [162] C.F. Colebrook, Turbulent flow in pipes, with particular reference to the transition region between the smooth and rough pipe laws, *J. Inst. Civil Engineers* 11 (1939) 133-156.
- [163] G.B. Wallis, *One-dimensional two-phase flow*, McGraw-Hill, New York, 1969.
- [164] W.W. Akers, H.A. Deans, O.K. Crosser, Condensing heat transfer within horizontal tubes, *Chem. Eng. Prog.* 54 (1958) 89-90.
- [165] S.M. Zivi, Estimation of steady-state steam void-fraction by means of the principle of minimum entropy production, *J. Heat Transfer* 86 (1964) 247-252.
- [166] S.W. Chen, T. Hibiki, M. Ishii, M. Mori, F. Watanabe, Experimental investigation of void fraction variation in subcooled boiling flow under horizontal forced vibrations, *Int. J. Heat Mass Transfer* 115 (2017) 954-968.
- [167] J.R. Thome, J. El Hajal, A. Cavallini, Condensation in horizontal tubes, part 2: new heat transfer model based on flow regimes, *Int. J. Heat Mass Transfer* 46 (2003) 3365-3387.
- [168] M.M. Shah, An improved and extended general correlation for heat transfer during condensation in plain tubes, *HVAC&R Research* 15 (2009) 889-913.
- [169] J.P. Meyer, D.R.E. Ewim, Heat transfer coefficients during the condensation of low mass fluxes in smooth horizontal tubes, *Int. J. Multiphase Flow* 99 (2018) 485-499.
- [170] Y. Camaraza-Medina, A. Hernandez-Guerrero, J.L. Luviano-Ortiz, K. Mortensen-Carlson, O.M. Cruz-Fonticiella, O.F. Garcia-Morales, New model for heat transfer calculation during film condensation inside pipes, *Int. J. Heat Mass Transfer* 128 (2019) 344-353.
- [171] P.L. Kapitza, S.P. Kapitza, Wave flow in thin layers of a viscous fluid, *Zh. Exper. Teor. Fiz.* 19 (1949) 105.
- [172] V. Balakotaiah, S. S. Jayawardena, Stability of wavy films in gas-liquid two-phase flows at normal and microgravity conditions, *Third Microgravity Fluid Physics Conf.* (1996) 103-108.

- [173] N. Nusselt, Die oberflächenkondensation des wasserdampfes, Z. Ver. Dt. Ing. 60 (1916) 541-569.
- [174] T. Ueda, T. Tanaka, Studies of liquid film flow in two-phase annular and annular-mist flow regions (Part 1, downflow in a vertical tube), Bull. of JSME 17 (1974) 603-613.
- [175] I.A. Mudawwar, M.A. El-Masri, Momentum and heat transfer across freely-falling turbulent liquid films, Int. J. Multiphase Flow 12 (1986) 771-790.
- [176] T.H. Lyu, I. Mudawwar, Statistical investigation of the relationship between interfacial waviness and sensible heat transfer to a falling liquid film, Int. J. Heat Mass Transfer 34 (6) (1991) 1451-1464.
- [177] A. Miyara, Numerical analysis on flow dynamics and heat transfer of falling liquid films with interfacial waves, Heat and Mass Transfer 35 (1999) 298-306.
- [178] R.K. Shah, A.L. London, Laminar flow forced convection in ducts: A source book for compact heat exchanger analytical data, Academic Press, New York, 1978.
- [179] S.-M. Kim, I. Mudawwar, Review of databases and predictive methods for heat transfer in condensing and boiling mini/micro-channel flows, Int. J. Heat Mass Transfer 77 (2014) 627-652.
- [180] W.W. Akers, H.F. Rosson, Condensation inside a horizontal tube, Chem. Eng. Prog. Symp. 56 (1960) 145-149.
- [181] A. Cavallini, R. Zecchin, A dimensionless correlation for heat transfer in forced convection condensation, Proc. Fifth Int. Heat Transfer Conf., Tokyo, Japan, Vol. 3 (1974) 309-313.
- [182] M.M. Shah, A general correlation for heat transfer during film condensation inside pipes, Int. J. Heat Mass Transfer 22 (1979) 547-556.
- [183] H. Haraguchi, S. Koyama, T. Fujii, Condensation of refrigerants HCFC 22, HFC 134a and HCFC 123 in a horizontal smooth tube (2nd report), Trans. JSME (B) 60 (1994) 245-252.
- [184] K.W. Moser, R.L. Webb, B. Na, A new equivalent Reynolds number model for condensation in smooth tubes, J. Heat Transfer 120 (1998) 410-417.
- [185] L. Friedel, Improved friction pressure drop correlations for horizontal and vertical two phase pipe flow, Paper E2, European Two Phase Flow Group Meeting, Ispra, Italy (1979).
- [186] S. Koyama, K. Kuwahara, K. Nakashita, K. Yamamoto, An experimental study on condensation of refrigerant R134a in a multi-port extruded tube, Int. J. Refrig. 24 (2003) 425-432.

- [187] X. Huang, G. Ding, H. Hu, Y. Zhu, H. Peng, Y. Gao, B. Deng, Influence of oil on flow condensation heat transfer of R410A inside 4.18 mm and 1.6 mm inner diameter horizontal smooth tubes, *Int. J. Refrig.* 33 (2010) 158-169.
- [188] T. Bohdal, H. Charun, M. Sikora, Comparative investigations of the condensation of R134a and R404A refrigerants in pipe minichannels, *Int. J. Heat Mass Transfer* 54 (2011) 1963-1974.
- [189] J.E. Park, F. Vakili-Farahani, L. Consolini, J.R. Thome, Experimental study on condensation heat transfer in vertical minichannels for new refrigerant R1234ze€ versus R134a and R236fa, *Exp. Therm. Fluid Sci.* 35 (2011) 442-454.
- [190] I. Mudawar, Recent advances in high-flux, two-phase thermal management, *J. Therm. Sci. Eng. Appl.* 5 (2) (2013) 021012.
- [191] D.E. Maddox, I. Mudawar, Single- and two-phase convective heat transfer from smooth and enhanced microelectronic heat sources in a rectangular channel, *J. Heat Transfer* 111 (1989) 533-542.
- [192] I. Mudawar, D.E. Maddox, Enhancement of critical heat flux from high power microelectronic heat sources in a flow channel, *J. Electronic Packaging* 112 (1990) 241-248.
- [193] C.O. Gersey, I. Mudawar, Effects of heater length and orientation on the trigger mechanism for near-saturated flow boiling critical heat flux – I. Photographic study and statistical characterization of the near-wall interfacial features, *Int. J. Heat Mass Transfer* 38 (1995) 629-641.
- [194] J.C. Sturgis, I. Mudawar, Critical heat flux in a long, rectangular channel subjected to one-sided heating – I. Flow visualization, *Int. J. Heat Mass Transfer* 42 (1999) 1835-1847.
- [195] J.C. Sturgis, I. Mudawar, Critical heat flux in a long, rectangular channel subjected to one-sided heating – II. Analysis of critical heat flux data, *Int. J. Heat Mass Transfer* 42 (1999) 1849-1862.
- [196] D.D. Hall, I. Mudawar, Ultra-high critical heat flux (CHF) for subcooled water flow boiling – II: high-CHF database and design equations, *Int. J. Heat Mass Transfer* 42 (1999) 1429-1456.

- [197] S. Mukherjee, I. Mudawar, Smart, low-cost, pumpless loop for micro-channel electronic cooling using flat and enhanced surfaces, Proc. I-THERM 2002, San Diego, California, pp. 360-370.
- [198] W. Qu, I. Mudawar, S.Y. Lee, S.T. Wereley, Experimental and computational investigation of flow development and pressure drop in a rectangular micro-channel, J. Electronic Packaging 128 (2005) 1-9.
- [199] D.D. Hall, I. Mudawar, Experimental and numerical study of quenching complex-shaped metallic alloys with multiple, overlapping sprays, Int. J. Heat Mass Transfer 38 (1995) 1201-1216.
- [200] M.K. Sung, I. Mudawar, Single-phase hybrid micro-channel/micro-jet impingement cooling, Int. J. Heat Mass Transfer 51 (2008) 4342-4352.
- [201] X.R. Zhuang, G.F. Chen, H. Guo, Q.L. Song, Q.X. Tang, Z.Q. Yang, X. Zou, M.Q. Gong, Experimental investigation on flow condensation of zeotropic mixtures of methane/ethane in a horizontal smooth tube, Int. J. Refrig. 85 (2018) 120-134.
- [202] W.-X. Chu, C.-Y. Chen, Y.-H. Liao, C.-C. Wang, A novel micro-channel heat sink with trapezoid drainage for enhancing condensation heat transfer of dielectric fluid, Exp. Therm. Fluid Sci. 106 (2019) 11-24.
- [203] S.M. Kim, I. Mudawar, Flow condensation in parallel micro-channels - Part 2: Heat transfer results and correlation technique, Int. J. Heat Mass Transfer 55 (2012) 984-994.
- [204] M.A. Vanderputten, T.A. Jacob, M. Sattar, N. Ali, B.M. Fronk, Two-phase flow regimes of condensing R-134a at low mass flux in rectangular microchannels, Int. J. Refrig. 84 (2017) 92-102.
- [205] A. Umur, P. Griffith, Mechanism of Dropwise Condensation, J. Heat Transfer 87 (1965) 275-282.
- [206] J.W. Rose, L.R. Glicksman, Dropwise condensation - The distribution of drop sizes, Int. J. Heat Mass Transfer 16 (1973) 411-425.
- [207] X. Chen, M.M. Derby, Droplet departure modeling and a heat transfer correlation for dropwise flow condensation in hydrophobic min-channels, Int. J. Heat Mass Transfer 125 (2018) 1096-1104.
- [208] S. Kakac, T.N. Veziroglu, A review of two-phase flow instabilities, Adv. Two-Phase Flow and Heat Trans. vol. II (1983) 577-667.

- [209] H. Yuncu, S. Kakac, Fundamentals of two-phase flow instabilities, Two-Phase Flow Heat Exchangers (1988) 375-406.
- [210] E.M. Chiapero, M. Fernandino, C.A. Dorao, Review on pressure drop oscillations in boiling systems, Nuc. Eng. Des. 250 (2012) 436-447.
- [211] J. March-Leuba, J.M. Rey, Coupled thermohydraulic-neutronic instabilities in boiling water nuclear reactors: a review of the state of the art, Nucl. Eng. Des. 145 (1993) 97-111.
- [212] G.V. Durga Prasad, M. Pandey, M.S. Kalra, Review of research on flow instabilities in natural circulation boiling systems, Prog. Nucl. Eng. 49 (2007) 429-451.
- [213] A.K. Nayak, P.K. Vijayan, Flow instabilities in boiling two-phase natural circulation systems: A review, Sci. Tech. Nucl. Installations vol. 2008 (2008) 1-15.
- [214] N. Liang, S. Shao, H. Xu, C. Tian, Instability of refrigeration system - A review, Energy Conv. Management 51 (2010) 2169-2178.
- [215] Y.K. Prajapati, P. Bhandari, Flow boiling instabilities in microchannels and their promising solutions - A review, Exp. Therm. Fluid Sci. 88 (2017) 576-593.
- [216] M.R. Özdemire, Ö.R. Sözbir, A review of single-phase and two-phase pressure drop characteristics and flow boiling instabilities in microchannels, J. Therm. Eng. 4 (no. 6) (2018) 2451-2463.
- [217] C.L. Ong, J.R. Thome, Macro-to-microchannel transition in two-phase flow: Part 1 - Two-phase flow patterns and film thickness measurements, Exp. Therm. Fluid Sci. 35 (2011) 37-47.
- [218] P. Kew, K. Cornwell, Correlations for prediction of flow boiling heat transfer in small-diameter channels, Appl. Therm. Eng. 17 (1997) 705-715.
- [219] N. Brauner, A. Ullmann, The prediction of flow boiling maps in minichannels, 4th Japanese-European Two-Phase Flow Group Meeting, Kyoto, 2006.
- [220] J. Li, B. Wang, Size effect on two-phase flow regime for condensation in micro/mini tubes, Heat Transfer - Asian Research 32 (2003) 65-71.
- [221] K.A. Triplett, S.M. Ghiaasiaan, S.I. Abdel-khalik, D.L. Sadowski, Gas-liquid two-phase flow in microchannels. Part I: Two-phase flow patterns, Int. J. Multiph. Flow 25 (1999) 377-394.
- [222] S.G. Kandlikar, W.J. Grande, Evolution of microchannel flow passages -- thermohydraulic performance and fabrication technology, J. Heat Trans. Eng. 24 (2003) 3-17.

- [223] P. Cheng, H.Y. Wu, Mesoscale and microscale phase-change heat transfer, *Adv. Heat Transfer* 39 (2006) 461-563.
- [224] T. Harirchian, S.V. Garimella, A comprehensive flow regime map for microchannel flow boiling with quantitative transition criteria, *Int. J. Heat Mass Transfer* 53 (2010) 2694-2703.
- [225] C.B. Tribica, G. Ribatski, Flow boiling phenomenological differences between micro- and macroscale channels, *J. Heat Trans. Eng.* 36 (2015) 937-942.
- [226] J. Barber, D. Brutin, K. Sefiane, L. Tadrist, Bubble confinement in flow boiling of FC-72 in a "rectangular" microchannel of high aspect ratio, *Exp. Therm. Fluid Sci.* 34 (2010) 1375-1388.
- [227] G.P. Celata, S.K. Saha, G. Zummo, D. Dossevi, Heat transfer characteristics of flow boiling in a single horizontal microchannel, *Int. J. Therm. Sci.* 49 (2010) 1086-1094.
- [228] X. Hu, G. Lin, Y. Cai, D. Wen, Experimental study of flow boiling of FC-72 in a parallel minichannels under sub-atmospheric pressure, *Appl. Therm. Eng.* 31 (2011) 3839-3853.
- [229] C.Y. Park, Y. Jang, B. Kim, Y. Kim, Flow boiling heat transfer coefficients and pressure drop of FC-72 in microchannels, *Int. J. Multiph. Flow* 39 (2012) 45-54.
- [230] D.B.R. Kenning, M.G. Cooper, Saturated flow boiling of water in vertical tubes, *Int. J. Heat Mass Transfer* 32 (1989) 445-458.
- [231] I. Mudawar, M.B. Bowers, Ultra-high critical heat flux (CHF) for subcooled water flow boiling - I: CHF data and parametric effects for small diameter tubes, *Int. J. Heat Mass Transfer* 42 (1999) 1405-1428.
- [232] W. Qu, I. Mudawar, Flow boiling heat transfer in two-phase micro-channel heat sinks - I. Experimental investigation and assessment of correlation methods, *Int. J. Heat Mass Transfer* 46 (2003) 2755-2771.
- [233] B. Sumith, F. Kaminaga, K. Matsumura, Saturated flow boiling of water in a vertical small diameter tube, *Exp. Therm. Fluid Sci.* 27 (2003) 789-801.
- [234] M.E. Steinke, S.G. Kandlikar, An experimental investigation of flow boiling characteristics of water in parallel microchannels, *J. Heat Transfer* 126 (2004) 518-526.
- [235] J. Lee, I. Mudawar, Two-phase flow in high-heat-flux micro-channel heat sink for refrigeration cooling applications: Part I - pressure drop characteristics, *Int. J. Heat Mass Transfer* 48 (2005) 928-940.

- [236] B. Agostini, A. Bontemps, Vertical flow boiling of refrigerant R134a in small channels, *Int. J. Heat Fluid Flow* 26 (2005) 296-306.
- [237] A. Greco, G.P. Vanoli, Flow boiling of R22, R134a, R507, R404A and R410A inside a smooth horizontal tube, *Int. J. Refrig.* 28 (2005) 872-880.
- [238] C.L. Ong, J.R. Thome, Flow boiling heat transfer of R134a, R236fa and R245fa in a horizontal 1.030 mm circular channel, *Exp. Therm. Fluid Sci.* 33 (2009) 651-663.
- [239] S. In, S. Jeong, Flow boiling heat transfer characteristics of R123 and R134a in a micro-channel, *Int. J. Multiph. Flow* 35 (2009) 987-1000.
- [240] C.B. Tibirica, G. Ribatski, Flow boiling heat transfer of R134a and R245fa in a 2.3 mm tube, *Int. J. Heat Mass Transfer* 53 (2010) 2459-2468.
- [241] C.N. Chen, J.T. Han, T.C. Jen, L. Shao, Thermo-chemical characteristics of R134a flow boiling in helically coiled tubes at low mass flux and low pressure, *Thermochimica Acta* 512 (2011) 163-169.
- [242] S. Lee, I. Mudawar, Enhanced model for annular flow in micro-channel heat sinks, including effects of drop entrainment/deposition and core turbulence, *Int. J. Heat Mass Transfer* 133 (2019) 510-530.
- [243] M.T. Kivisalu, P. Gorgitrattanagul, S. Mitra, R.R. Naik, A. Narain, Prediction and control of internal condensing flows in the experimental context of their inlet condition sensitivities, *Micrograv. Sci. Tech.* 24 (2012) 147-155.
- [244] L.E. O'Neill, R. Balasubramaniam, H.K. Nahra, M.M. Hasan, I. Mudawar, Flow condensation heat transfer in a smooth tube at different orientations: Experimental results and predictive models, *Int. J. Heat Mass Transfer*, under review.
- [245] H. Jaster, P.G. Kosky, Condensation heat transfer in a mixed flow regime, *Int. J. Heat Mass Transfer* 19 (1976) 95-99.
- [246] H.Y. Wu, P. Cheng, Condensation flow patterns in silicon microchannels, *Int. J. Heat Mass Transfer* 48 (2005) 2186-2197.
- [247] J.W. Coleman, S. Garimella, Two-phase flow regimes in round, square and rectangular tubes during condensation of refrigerant R134a, *Int. J. Refrig.* 26 (2003) 117-128.
- [248] D. Jung, Y. Cho, K. Park, Flow condensation heat transfer coefficients of R22, R134a, R407C, and R410A inside plain and microfin tubes, *Int. J. Refrig.* 27 (2004) 25-32.

- [249] A.S. Dalkilic, O. Agra, I. Teke, S. Wongwises, Comparison of frictional pressure drop models during annular flow condensation of R600a in a horizontal tube at low mass flux and of R134a in a vertical tube at high mass flux, *Int. J. Heat Mass Transfer* 53 (2010) 2052-2064.
- [250] A. Agarwal, T.M. Bandhauer, S. Garimella, Measurement and modeling of condensation heat transfer in non-circular microchannels, *Int. J. Refrig.* 33 (2010) 1169-1179.
- [251] J.P. Meyer, J. Dirker, A.O. Adelaja, Condensation heat transfer in smooth inclined tubes for R134a at different saturation temperatures, *Int. J. Heat Mass Transfer* 70 (2014) 515-525.
- [252] S.M. Kim, I. Mudawar, Review of databases and predictive methods for pressure drop in adiabatic, condensing and boiling min/micro-channel flows, *Int. J. Heat Mass Transfer* 77 (2014) 74-97.
- [253] S.M. Kim, I. Mudawar, Review of databases and predictive methods for heat transfer in condensing and boiling mini/micro-channel flows, *Int. J. Heat Mass Transfer* 77 (2014) 627-652.
- [254] S.M. Kim, I. Mudawar, Review of two-phase critical flow models and investigation of the relationship between choking, premature CHF, and CHF in micro-channel heat sinks, *Int. J. Heat Mass Transfer* 87 (2015) 497-511.
- [255] G. Liang, I. Mudawar, Review of mass and momentum interactions during drop impact on a liquid film, *Int. J. Heat Mass Transfer* 101 (2016) 577-599.
- [256] G. Liang, I. Mudawar, Review of drop impact on heated walls, *Int. J. Heat Mass Transfer* 106 (2017) 103-126.
- [257] G. Liang, I. Mudawar, Review of spray cooling - Part 1: Single-phase and nucleate boiling regimes, and critical heat flux, *Int. J. Heat Mass Transfer* 115 (2017) 1174-1205.
- [258] G. Liang, I. Mudawar, Review of spray cooling - Part 2: high temperature boiling regimes and quenching applications, *Int. J. Heat Mass Transfer* 115 (2017) 1206-1222.
- [259] G. Liang, I. Mudawar, Pool boiling critical heat flux (CHF) - Part 1: Review of mechanisms, models, and correlations, *Int. J. Heat Mass Transfer* 117 (2018) 1352-1367.
- [260] G. Liang, I. Mudawar, Pool boiling critical heat flux (CHF) - Part 2: Assessment of models and correlations, *Int. J. Heat Mass Transfer* 117 (2018) 1368-1383.

- [261] G. Liang, I. Mudawar, Review of pool boiling enhancement with additives and nanofluids, *Int. J. Heat Mass Transfer* 124 (2018) 423-453.
- [262] G. Liang, I. Mudawar, Review of pool boiling enhancement by surface modification, *Int. J. Heat Mass Transfer* 128 (2019) 892-933.
- [263] G. Liang, I. Mudawar, Review of single-phase and two-phase nanofluid heat transfer in macro-channels and micro-channels, *Int. J. Heat Mass Transfer* 136 (2019) 324-354.
- [264] G. Liang, I. Mudawar, Review of channel flow boiling enhancement by surface modification, and instability suppression schemes, *Int. J. Heat Mass Transfer*, under review.
- [265] H. Zhang, I. Mudawar, M.M. Hasan, Experimental and theoretical study of orientation effects on flow boiling CHF, *Int. J. Heat Mass Transfer* 45 (2002) 4463-4477.
- [266] R.D. Boyd, Subcooled flow boiling critical heat flux (CHF) and its application to fusion energy components. Part I. A review of fundamentals of CHF and related data base, *Fusion Tech.* 7 (1985) 7-30.
- [267] D.H. Wolf, F.P. Incropera, R. Viskanta, Jet impingement boiling, *Adv. Heat Transfer* 23 (1993) 1-132.
- [268] H. Schnackenberg, Die Wasserverteilung in Zwanglaufheizflächen, insbesondere in Speisewasservorwärmern, *Die Wärme* 60 (1937) 481-484.
- [269] K. Mishima, H. Nishihara, I. Michiyoshi, Boiling burnout and flow instabilities for water flowing in a round tube under atmospheric pressure, *Int. J. Heat Mass Transfer* 28 (1985) 1115-1129.
- [270] M. Ishii, H.K. Fauske, Boiling and dryout behavior in a liquid-metal fast breeder reactor subassembly bundle under low heat flux and low flow conditions, *Nucl. Sci. Eng.* 84 (1983) 131-146.
- [271] P.W. Garrison, R.H. Morris, B.H. Montgomery, Natural convection boiling of sodium in a simulated FBR fuel assembly subchannel, *Proc. Int. Mtg. Fast Reactor Safety Technology*, CONF-790819 Vol. 4 (1979) p. 1686 American Nuclear Society.
- [272] K. Haga, M. Uotani, K. Yamaguchi, M. Hori, Decay heat removal under boiling conditions in a pin-bundle geometry, *Proc. Ninth Mtg. Liquid Metal Boiling Working Group*, Casaccia, Italy (1980).
- [273] X. Genglei, P. Minjun, G. Yun, Research of two-phase flow instability in parallel narrow multi-channel system, *Ann. Nucl. Energy* 48 (2012) 1-16.

- [274] P. Saha, N. Zuber, Point of net vapor generation and vapor void fraction in subcooled boiling, *Heat Transfer* 4 (1974) 175-179.
- [275] B.W. Yang, T. Dougherty, C. Fighetti, S. Kokolis, G.D. Reddy, E.V. McAssey Jr., A. Coutts, Flow instability and critical heat flux in a ribbed annulus, No. WSRC-RT-93-506; CONF-940809-3, Westinghouse Savannah River Co., Aiken, SC, 1993.
- [276] M. Siman-Tov, D. Felde, J.L. McDuffee, G.L. Yonder, Experimental study of static flow instability in subcooled flow boiling in parallel channels, No. CONF-9501130-1, Oak Ridge National Lab, TN, 1995.
- [277] J. Costa, M. Courtaud, S. Elberg, J. Lafay, ORNL/TR-90/13, Martin Marietta Energy Systems, Inc., Oak Ridge National Laboratory, Oak Ridge, TN, 1967.
- [278] R. Stelling, E.V. McAssey, T. Dougherty, B.W. Yang, The onset of flow instability for downward flow in vertical channels, *J. Heat Transfer* 118 (1996) 709-714.
- [279] J.E. Kennedy, G.M. Roach Jr., M.F. Dowling, S.I. Abdel-Khalik, S.M. Ghiaasiaan, S.M. Jeter, Z.H. Quershi, The onset of flow instability in uniformly heated horizontal microchannels, *ASME J. Heat Transfer* 122 (2000) 118-125.
- [280] G.H. Yeoh, J.Y. Tu, Y. Li, On void fraction distribution during two-phase boiling flow instability, *Int. J. Heat Mass Transfer* 47 (2004) 413-417.
- [281] O.S. Al-Yahia, D. Jo, ONB, OSV, and OFI for subcooled flow boiling through a narrow rectangular channel heated on one side, *Int. J. Heat Mass Transfer* 116 (2018) 73 - 83.
- [282] H.C. Unal, Determination of the initial point of net vapor generation in flow boiling systems, *Int. J. Heat Mass Transfer* 18 (1974) 1095-1099.
- [283] R.W. Bowring, Physical model based on bubble detachment and calculation of steam voidage in subcooled region of a heated channel, Institute for Atomenergi, Halden, Norway, Report No. HPR-10, 1962.
- [284] Q. Lu, Y. Zhang, Y. Liu, L. Zhou, C. Shen, D. Chen, An experimental investigation on the characteristics of flow instability with the evolution of two-phase interface morphology, *Int. J. Heat Mass Transfer* 138 (2019) 468-482.
- [285] J. Leng, Research on the density-wave flow instability in the rectangular parallel channels, Nuclear Power Institute of China, 2008.
- [286] Y. Zhou, Research on the flow instability in the rectangular parallel multi-channels, Nuclear Power Institute of China, 2010.

- [287] J.L. Achard, D.A. Drew, R.T. Lahey Jr., The effect of gravity and friction on the stability of boiling flow in a channel, *Chem. Eng. Comm.* 11 (1981) 59-79.
- [288] R.T. Lahey Jr., G. Yadigaroglu, On the relationship between Ledinegg and density wave instability analysis, *Trans. Am. Nucl. Soc.* 41 (1982).
- [289] A.C. Fowler, Linear and non-linear stability of heat exchangers, *J. Appl. Mathematics* 22 (1978) 361-382.
- [290] P. DiMarco, A. Clausse, R.T. Lahey Jr., D.A. Drew, A nodal analysis of instabilities in boiling channels, *Int. J. Heat Technology* 8 (1990) 125-141.
- [291] P. DiMarco, A. Clausse, R.T. Lahey Jr., An analysis of nonlinear instabilities in boiling systems, *Dynam. Stab. Systems* 6 (1991) 191-216.
- [292] M.M. Padki, K. Palmer, S. Kakac, T.N. Veziroglu, Bifurcation analysis of pressure-drop oscillations and the Ledinegg instability, *Int. J. Heat Mass Transfer* 35 (1992) 525-532.
- [293] S.H. Chang, Y.I. Kim, W.P. Baek, Derivation of mechanistic critical heat flux model for water based on flow instabilities, *Int. Comm. Heat Mass Transfer* 23 (1996) 1109-1119.
- [294] W. Ambrosini, P. Di Marco, J.C. Ferreri, Linear and nonlinear analysis of density-wave instability phenomena, *Heat and Tech.* 18 (2000) 27-36.
- [295] T. Hamidouche, N. Rassoul, E.K. Si-Ahmed, H. El Hadjen, A. Bousbia-salah, Simplified numerical model for defining Ledinegg flow instability margins in MTR research reactor, *Prog. Nucl. Energy* 51 (2009) 485-495.
- [296] L.C. Ruspini, C.A. Dorao, M. Fernandino, Dynamic simulation of Ledinegg instability, *J. Nat. Gas Sci. Eng.* 2 (2010) 211-216.
- [297] L.C. Ruspini, C. Dorao, M. Fernandino, Two-phase flow instabilities in boiling and condensing systems, *J. Power Energy Syst., JSME* 6 (2) (2012) 302-313.
- [298] A.K. Nayak, P.K. Vijayan, D. Saha, V. Venkat Raj, M. Aritomi, Linear analysis of thermo-hydraulic instabilities of the Advanced Heavy Water Reactor (AHWR), *J. Nucl. Sci. Tech.* 35 (1998) 768-778.
- [299] P.T. Garrity, J.F. Klausner, R. Mei, Instability phenomena in a two-phase microchannel thermosyphon, *Int. J. Heat Mass Transfer* 52 (2009) 1701-1708.
- [300] V. Pandey, S. Singh, Characterization of stability limits of Ledinegg instability and density wave oscillations for two-phase flow in natural circulation loops, *Chem Eng. Sci.* 168 (2017) 204 - 224.

- [301] J. Zhao, Stability analysis of supercritical water cooled reactors, PhD Diss. Mass. Inst. Tech. (2005).
- [302] W. Ambrosini, J.C. Ferreri, Analysis of basic phenomena in boiling channel instabilities with different flow models and numerical schemes, Proc. 14th Int. Conf. Nucl. Eng. (2006) 889-900.
- [303] T. Ortega Gomez, A. Class, R.T. Lahey Jr., T. Schulenberg, Stability analysis of a uniformly heated channel with supercritical water, Nucl. Eng. Design 238 (2008) 1930-1939.
- [304] W. Ambrosini, On the analogies in the dynamic behaviour of heated channels with boiling and supercritical fluids, Nucl. Eng. Design 237 (2007) 1164-1174.
- [305] W. Ambrosini, Discussion on the stability of heated channels with different fluids at supercritical pressures, Nucl. Eng. Design 239 (2009) 2952-2963.
- [306] W. Ambrosini, Assessment of flow stability boundaries in a heated channel with different fluids at supercritical pressure, Ann. Nucl. Energy 38 (2011) 615-627.
- [307] E. Ampomah-Amoako, W. Ambrosini, Developing a CFD methodology for the analysis of flow stability in heated channels with fluids at supercritical pressures, Ann. Nucl. Energy 54 (2013) 251-262.
- [308] E. Ampomah-Amoako, E. H.K. Akaho, B. J.B. Nyarko, W. Ambrosini, Analysis of flow stability in nuclear reactor subchannels with water at supercritical pressures, Ann. Nucl. Energy 60 (2013) 396-405.
- [309] B.T. Swapnalee, P.K. Vijayan, M. Sharma, D.S. Pilkhwal, Steady state flow and static instability of supercritical natural circulation loops, Nucl. Eng. Design 245 (2012) 99-112.
- [310] T. Zhang, T. Tong, J.Y. Chang, Y. Peles, R. Prasher, M.K. Jensen, J.T. Wen, P. Phelan, Ledinegg instability in microchannels, Int. J. Heat Mass Transfer 52 (2009) 5661-5674.
- [311] K. Yang, A. Zhang, J. Wang, On the Ledinegg instability in parallel channels: A new and exact criterion, Int. J. Therm. Sci. 129 (2018) 193-200.
- [312] T.J. Heindel, S. Ramadhyani, F.P. Incropera, Liquid immersion cooling of a longitudinal array of discrete heat sources in protruding substrates: II - Forced convection boiling, J. Elec. Packaging 114 (1992) 63-70.

- [313] Y.K. Prajapati, M. Pathak, M.K. Khan, A comparative study of flow boiling heat transfer in three different configurations of microchannels, *Int. J. Heat Mass Transfer* 85 (2015) 711-722.
- [314] R.W. Murphy, A.E. Bergles, Subcooled flow boiling of fluorocarbons, MIT Engineering Projects Lab Report 71903-72 (1971).
- [315] A.E. Bergles, High flux boiling applied to microelectronics thermal control, *Int. Comm. Heat Mass Transfer* 15 (1988) 509-531.
- [316] D.W. Zhou, C.F. Ma, J. Yu, Boiling hysteresis of impinging circular submerged jets with highly wetting liquids, *Int. J. Heat Fluid Flow* 25 (2004) 81-90.
- [317] P.G. Kosky, D.N. Lyon, Pool boiling heat transfer to cryogenic liquids; I. Nucleate regime data and a test of some nucleate boiling correlations, *AIChE J.* 14 (1968) 372-379.
- [318] G. Hetsroni, M. Gurevich, A. Mosyak, R. Rozenblit, L.P. Yarin, Subcooled boiling of surfactant solutions, *Int. J. Multiphase Flow* 28 (2002) 347-361.
- [319] Z.H. Ayub, A.E. Bergles, Nucleate pool boiling curve hysteresis for GEWA-T surfaces in saturated R-113, *Exp. Therm. Fluid Science* 3 (1990) 249-255.
- [320] J. Tehver, H. Sui, V. Temkina, Heat transfer and hysteresis phenomena in boiling on porous plasma-sprayed surface, *Exp. Therm. Fluid Science* 5 (1992) 714-727.
- [321] S. Ndao, Y. Peles, M.K. Jensen, Experimental investigation of flow boiling heat transfer of jet impingement on smooth and micro structured surfaces, *Int. J. Heat Mass Transfer* 55 (2012) 5093-5101.
- [322] M. Lee, L.S.L. Cheung, Y.K. Lee, Y. Zohar, Height effect on nucleation-site activity and size-dependent bubble dynamics in microchannel convective boiling, *J. Micromech. Microeng.* 15 (2005) 2121.
- [323] A. Kosar, Y. Peles, Convective flow of refrigerant (R-123) across a bank of micro pin fins, *Int. J. Heat Mass Transfer* 49 (2006) 3142-3155.
- [324] Y. Wang, Y. Peles, Subcooled flow boiling in a microchannel with a pin fin and a liquid jet in crossflow, *Int. J. Heat Mass Transfer* 86 (2015) 165-173.
- [325] M.M. Hasan, C.S. Lin, R.H. Knoll, M.D. Bentz, J.S. Meserole, Nucleate pool boiling in the long duration low gravity environment of the space shuttle, *AIAA Paper* 93-0465 (NASA TM-105973), Jan. 1993.

- [326] M.M. Hasan, C.S. Lin, R.H. Knoll, M.D. Bentz, Tank pressure control experiment: thermal phenomena in microgravity, NASA TM 3564 (1996).
- [327] J.L. Plawsky, P.C. Wayner Jr., Explosive nucleation in microgravity: The Constrained Vapor Bubble experiment, *Int. J. Heat Mass Transfer* 55 (2012) 6473-6484.
- [328] L.E. O'Neill, I. Mudawar, M.M. Hasan, H.K. Nahra, R. Balasubramaniam, J.R. Mackey, Flow condensation pressure oscillations at different orientations, *Int. J. Heat Mass Transfer* 127 (2018) 784-809.
- [329] L.E. O'Neill, R. Balasubramaniam, H.K. Nahra, M.M. Hasan, J.R. Mackey, I. Mudawar, Identification of condensation flow regime at different orientations using temperature and pressure measurements, *Int. J. Heat Mass Transfer* 135 (2019) 569-590.
- [330] Y. Abe, S. Saitho, Vapor explosion between high-temperature molten liquid droplet and water pool, *Research Advances Chap. 6.15* (2017) 682-705.
- [331] M. Furuya, Vapor explosion, *Research Advances Chap. 6.16* (2017) 706-731.
- [332] A.K. Nayak, P.K. Vijayan, V. Jain, D. Saha, R.K. Sinha, Study on the flow-pattern-transition instability in a natural circulation heavy water moderated boiling light water cooled reactor, *Nucl. Eng. Des.* 225 (2003) 159-172.
- [333] C. Tompkins, M. Corradini, Flow pattern transition instabilities in a natural circulation cooling facility, *Nucl. Eng. Des.* 332 (2018) 267 - 278.
- [334] S. Fabrega, Etude experimentale des instabilites hydrodynamiques survenant dans les reacteurs nucleaires a ebullition, CEA-R-2884 (1964).
- [335] F.A. Jeglic, T.M. Grace, Onset of flow oscillations in forced flow subcooled boiling, NASA-TN-D 2821 (1965).
- [336] S. Lee, V.S. Devahdhanush, I. Mudawar, Investigation of subcooled and saturated boiling heat transfer mechanisms, instabilities, and transient flow regime maps for large length-to-diameter ratio micro-channel heat sinks, *Int. J. Heat Mass Transfer* 123 (2018) 172-191.
- [337] B.R. Fu, C. Pan, Flow pattern transition instability in a microchannel with CO<sub>2</sub> bubbles produced by chemical reactions, *Int. J. Heat Mass Transfer* 48 (2005) 4397-4409.
- [338] L.G. Neal, S.M. Zivi, R.W. Wright, The Mechanisms of Hydrodynamic Instabilities In Boiling Systems, *Proceedings of the Symposium on Two-Phase Flow Dynamics, EURATOM - The Technological University of Eindhoven, The Netherlands, 1967.*

- [339] T. Dogan, S. Kakac, T.N. Veziroglu, Analysis of forced-convection boiling flow instabilities in a single-channel upflow system, *Int. J. Heat Fluid Flow* 4 (1983) 145-156.
- [340] M. Colombo, A. Cammi, D. Papini, M.E. Ricotti, RELAP5/MOD3.3 study on density wave instabilities in single channel and two parallel channels, *Prog. Nucl. Energy* 56 (2012) 15-23.
- [341] K.C. Jain, M. Petrick, D. Miller, S.G. Bankoff, Self-sustained hydrodynamic oscillations in a natural-circulation boiling water loop, *Nucl. Eng. Des.* 4 (1966) 233-252.
- [342] A.B. Jones, Hydrodynamic stability of a boiling channel, KAPL-2170, October 1961.
- [343] A.B. Jones, D.G. Dight, Hydrodynamic stability of a boiling channel, Part 2, KAPL-2208, April 1962
- [344] S. Jahnberg, A one-dimensional model for calculation of non-steady two-phase flow, EAES Symposium, Studsvik, Sweden, October 1963.
- [345] P. Saha, M. Ishii, N. Zuber, An experimental investigation of the thermally induced flow oscillations in two-phase systems, *J. Heat Transfer - Trans. ASME* 98 (1976) 616-622.
- [346] S. Guanghui, J. Dounan, K. Fukuda, G. Yujun, Theoretical and experimental study on density wave oscillation of two-phase natural circulation of low equilibrium quality, *Nucl. Eng. Des.* 215 (2002) 187-198.
- [347] A.K. Nayak, D. Lathouwers, T.H.J.J. van der Hagen, F. Schrauwen, P. Molenaar, A. Rogers, A numerical study of boiling flow instability of a reactor thermosyphon systems, *Appl. Therm. Eng.* 26 (2006) 644-653.
- [348] S. Chen, X. Chen, G. Luo, K. Zhu, L. Chen, Y. Hou, Flow boiling instability of liquid nitrogen in horizontal mini channels, *J. Appl. Therm. Eng.* 144 (2018) 812-824.
- [349] Q. Wang, X.J. Chen, S. Kakac, Y. Ding, An experimental investigation of density-wave-type oscillations in a convective boiling upflow system, *Int. J. Heat Fluid Flow* 3 (1994) 241-246.
- [350] O. Comakli, S. Karsli, M. Yilmaz, Experimental investigation of two phase flow instabilities in a horizontal in-tube boiling system, *Energy Conv. Manag.* 43 (2002) 249-268.
- [351] S. Karsli, M. Yilmaz, O. Comakli, The effect of internal surface modification on flow instabilities in forced convection boiling in a horizontal tube, *Int. J. Heat Fluid Flow* 23 (2002) 776-791.

- [352] S. Karagoz, S. Karsli, M. Yilmaz, O. Comakli, Density-wave flow oscillations in a water boiling horizontal tube with inserts, *J. Enhanc. Heat Transfer* 16 (2009) 331-350.
- [353] N. Liang, S. Shuangquan, C. Tian, Y.Y. Yan, Two-phase flow instabilities in horizontal straight tube evaporator, *Appl. Therm. Eng.* 31 (2011) 181-187.
- [354] C.A. Dorao, Effect of inlet pressure and temperature on density wave oscillations in a horizontal channel, *Chem. Eng. Sci.* 134 (2015) 767-773.
- [355] M. Sorum, C.A. Dorao, Experimental study of the heat transfer coefficient deterioration during Density Wave Oscillations, *Chem. Eng. Sci.* 132 (2015) 178-185.
- [356] L. Zhang, Y. Wang, Z. Yu, Regulation of gas-liquid stratified flow boiling dynamic instabilities in horizontal tube: Effects of heat load distribution and wall thermal capacity, *Int. J. Heat Mass Transfer* 127 (2018) 426-436.
- [357] I.W. Park, M. Fernandino, C.A. Dorao, Experimental study on the characteristics of pressure drop oscillations and their interaction with short-period oscillation in a horizontal tube, *Int. J. Refrig.* 91 (2018) 246-253.
- [358] I.W. Park, M. Fernandino, C.A. Dorao, On the occurrence of superimposed density wave oscillations on pressure drop oscillations and the influence of a compressible volume, *AIP Advances* 8 (2018) 075022.
- [359] L. Zhang, Y. Wang, Z. Yu, Experimental study of flow boiling instabilities in horizontal tubes under gas-liquid stratification condition: Effects of heat flux and inlet subcooling degree, *Int. J. Heat Mass Transfer* 118 (2018) 1040-1045.
- [360] Q. Lu, Y. Liu, H. Huang, C. Shen, H. He, L. Zhou, D. Chen, Visual investigation on the boiling crisis post the flow instability in the channel with bypass, *Ann. Nucl. Energy* 131 (2019) 171-184.
- [361] M. Furuya, F. Inada, T.H.J.J. Van Der Hangen, Characteristics of type-I density wave oscillations in a natural circulation BWR at relatively high pressure, *J. Nucl. Sci. Tech.* 42 (2005) 191-200.
- [362] M. Furuya, F. Inada, T.H.J.J. van der Hagen, Flashing-induced density wave oscillations in a natural circulation BWR - mechanism of instability and stability map, *Nucl. Eng. Des.* 235 (2005) 1557-1569.

- [363] S.Z. Wen, L.P. Huang, Z.R. Wang, X.B. Zhang, W.C. Xiong, Z.H. He, Experimental investigation of the oscillation characteristics of natural circulation of R134A in a two-phase loop, *Exp. Therm. Fluid Sci.* 99 (2018) 129-139.
- [364] L.A. Belblidia, C. Bratianu, Density-wave oscillations, *Ann. Nucl. Energy* 6. (1979) 425-444.
- [365] Rizwan-Uddin, J.J. Dorning, Some nonlinear dynamics of a heated channel, *Nucl. Eng. Design* 93 (1986) 1-14.
- [366] S. Nakanishi, M. Kaji, S. Yamauchi, An approximation method for construction of a stability map of density-wave oscillations, *Nucl. Eng. Des.* 95 (1986) 55-64.
- [367] Rizwan-Uddin, J.J. Dorning, A chaotic attractor in a periodically forced two-phase flow system, *Nucl. Sci. Eng.* 100 (1988) 393-404.
- [368] W.R. Schlichting, An analysis of the effect of gravity on interacting DWO/PDO instability modes, Ph.D. Thesis, Rensselaer Polytechnic Institute (2009).
- [369] S. Paruya, S. Maiti, A. Karmakar, P. Gupta, J.P. Sarkar, Lumped parameterization of boiling channel - Bifurcations during density wave oscillations, *Chem. Eng. Sci.* 74 (2012) 310-326.
- [370] D. Papini, A. Cammi, M. Colombo, M.E. Ricotti, Time-domain linear and non-linear studies on density wave oscillations, *Chem. Eng. Sci.* 81 (2012) 118-139.
- [371] S. Paul, S. Singh, Linear stability analysis of flow instabilities with a nodalized reduced order model in heated channel, *Int. J. Therm. Sci.* 98 (2015) 312-331.
- [372] S. Paruya, N. Goswami, S. Pushpavanam, D.S. Pillai, O. Bidyarani, Periodically-forced density wave oscillations in boiling flow at low forcing frequencies: Nonlinear dynamics and control issues, *Chem. Eng. Sci.* 140 (2016) 123-133.
- [373] D. Paul, S. Singh, S. Mishra, Impact of system pressure on the characteristics of stability boundary for a single-channel flow boiling system, *Nonlinear Dynamics* (2019) 1-10.
- [374] G. Dutta, C. Zhang, J. Jiang, Analysis of flow induced density wave oscillations in the CANDU supercritical water reactor, *Nucl. Eng. Design* 286 (2015) 150-162.
- [375] J. Liu, H. Li, X. Lei, K. Guo, L. Li, Numerical study on the effect of pipe wall heat storage on density wave instability of supercritical water, *Nucl. Eng. Des.* 335 (2018) 106-115.

- [376] R. Khodabandeh, R. Furberg, Instability, heat transfer and flow regime in a two-phase flow thermosyphon loop at different diameter evaporator channel, *Appl. Therm. Eng.* 30 (2010) 1107-1114.
- [377] H. He, P.F. Li, R.G. Yan, L.M. Pan, Modeling of reversal flow and pressure fluctuation in rectangular microchannel, *Int. J. Heat Mass Transfer* 102 (2016) 1024-1033.
- [378] D. Brutin, F. Topin, L. Tadriss, Experimental study of unsteady convective boiling in heated minichannels, *Int. J. Heat Mass Transfer* 46 (2003) 2957-2965.
- [379] G. Wang, P. Cheng, H. Wu, Unstable and stable flow boiling in parallel microchannels and in a single microchannel, *Int. J. Heat Mass Transfer* 50 (2007) 4297-4310.
- [380] G. Wang, P. Cheng, An experimental study of flow boiling instability in a single microchannel, *Int. Comm. Heat Mass Transfer* 35 (2008) 1229-1234.
- [381] Y.F. Fan, I. Hassan, Experimental investigation of flow boiling instability in a single horizontal microtube with and without inlet restriction, *J. Heat Transfer* 134 (2012) 081501.
- [382] H. Li, P. Hrnjak, Modeling of bubble dynamics in single diabatic microchannel, *Int. J. Heat Mass Transfer* 107 (2017) 96-104.
- [383] T. Van Oevelen, J.A. Weibel, S.V. Garimella, Predicting two-phase flow distribution and stability in systems with many parallel heated channels, *Int. J. Heat Mass Transfer* 107 (2017) 557-571.
- [384] T. Van Oevelen, J.A. Weibel, S.V. Garimella, The effect of lateral thermal coupling between parallel microchannels on two-phase flow distribution, *Int. J. Heat Mass Transfer* 124 (2018) 769-781.
- [385] S. Hayama, A study on the hydrodynamic instability in boiling channels: 3rd report, the modes of vibration in multi-channel system and the reverse flow, *Bulletin of JSME* 10 (1967) 308-319.
- [386] M. Aritomi, S. Aoki, A. Inoue, Instabilities in parallel channel of forced-convection boiling upflow system, (I) Mathematical model, *J. Nucl. Sci. Tech.* 14 (1977) 22-30.
- [387] M. Aritomi, S. Aoki, A. Inoue, Instabilities in parallel channel of forced-convection boiling upflow system, (II) Experimental results, *J. Nucl. Sci. Tech.* 14 (1977) 88-96.
- [388] M. Aritomi, S. Aoki, A. Inoue, Instabilities in parallel channel of forced-convection boiling upflow system, (III) System with different flow conditions between two channels, *J. Nucl. Sci. Tech.* 16 (1979) 343-355.

- [389] M. Aritomi, S. Aoki, T. Narabayashi, Instabilities in parallel channel of forced-convection boiling upflow system, (IV) Instabilities in multi-channel system and with boiling in downcomer, *J. Nucl. Sci. Tech.* 18 (1981) 329-340.
- [390] M. Aritomi, S. Aoki, A. Inoue, Instabilities in parallel channel of forced-convection boiling upflow system, (V) Consideration of density wave instability, *J. Nucl. Sci. Tech.* 20 (1983) 286-301.
- [391] K. Fukuda, S. Hasegawa, Analysis on two-phase flow instability in parallel multichannels, *J. Nucl. Sci. Technol.* 16 (1979) 190-199.
- [392] K. Fukuda, A. Kato, S. Hasegawa, Two-phase flow instability at low flow rate conditions, *J. Nucl. Sci. Tech.* 21 (1984) 491-500.
- [393] G. Guido, J. Converti, A. Clausse, Density-wave oscillations in parallel channels - an analytical approach, *Nucl. Eng. Des.* 125 (1991) 121-136.
- [394] Y.J. Zhang, G.H. Su, X.B. Yang, S.Z. Qiu, Theoretical research on two-phase flow instability in parallel channels, *Nucl. Eng. Design* 239 (2009) 1294-1303.
- [395] T.J. Zhang, J.T. Wen, A. Julius, Y. Peles, M.K. Jensen, Stability analysis and maldistribution control of two-phase flow in parallel evaporating channels, *Int. J. Heat Mass Transfer* 54 (2011) 5298-5305.
- [396] V. Jain, A.K. Nayak, P.K. Vijayan, D. Saha, R.K. Sinha, Experimental investigation on the flow instability behavior of a multi-channel boiling natural circulation loop at low-pressures, *Exp. Therm. Fluid Sci.* 34 (2010) 776-787.
- [397] M. Ozawa, K. Akagawa, T. Sakaguchi, Flow instabilities in parallel-channel flow systems of gas-liquid two-phase mixtures, *Int. J. Multiph. Flow* 15 (1989) 639-657.
- [398] T. Xiong, X. Yan, Z. Xiao, Y. Li, Y. Huang, J. Yu, Experimental study on flow instability in parallel channels with supercritical water, *Ann. Nucl. Energy* 48 (2012) 60-67.
- [399] B. Xie, D. Yang, W. Wang, X. Nie, W. Liu, Numerical analysis on the flow instability of parallel channels in water wall of an ultra-supercritical CFB boiler, *Int. J. Heat Mass Transfer* 110 (2017) 545 - 554.
- [400] D. Papini, M. Colombo, A. Cammi, M.E. Ricotti, Experimental and theoretical studies on density wave instabilities in helically coiled tubes, *Int. J. Heat Mass Transfer* 68 (2014) 343-356.

- [401] Z. Ma, L. Zhang, S. Bu, W. Sun, D. Chen, L. Pan, A study of the heat flux profile effect on parallel channel density wave oscillation in sodium heated heat exchanger, *Prog. Nucl. Energy* 112 (2019) 135-145.
- [402] A. Hotta, Y. Suzawa, H. Takeuchi, Development of BWR regional instability model and verification based on ringhals 1 test, *Ann. Nucl. Energy* 24 (1997) 1403-1427.
- [403] A.K. Nayak, P.K. Vijayan, D. Saha, V. Venkat Raj, M. Aritomi, Analytical study of nuclear-coupled density-wave instability in a natural circulation pressure tube type boiling water reactor, *Nucl. Eng. Des.* 195 (2000) 27-44.
- [404] J.L. Munoz-Cobo, O. Rosello, R. Miro, A. Escriva, D. Ginestar, G. Verdu, Coupling of density wave oscillations in parallel channels with high order modal kinetics: application to BWR out of phase oscillations, *Ann. Nucl. Energy* 27 (2000) 1345-1371.
- [405] J.L. Munoz-Cobo, M.Z. Podowski, S. Chiva, Parallel channel instabilities in boiling water reactor systems: boundary conditions for out of phase oscillations, *Ann. Nucl. Energy* 29 (2002) 1891-1917.
- [406] J.L. Munoz-Cobo, S. Chiva, A. Sekhri, A reduced order model of BWR dynamics with subcooled boiling and modal kinetics: application to out of phase oscillations, *Ann. Nucl. Energy* 31 (2004) 1135-1162.
- [407] G. Dutta, J.B. Doshi, Nonlinear analysis of nuclear coupled density wave instability in time domain for a boiling water reactor core undergoing core-wide and regional modes of oscillations, *Prog. Nucl. Energy* 51 (2009) 769-787.
- [408] H.Y. Wu, P. Cheng, Visualization and measurements of periodic boiling in silicon microchannels, *Int. J. Heat Mass Transfer* 46 (2003) 2603-2614.
- [409] Y. Peles, Two-phase boiling flow in microchannels: instabilities issues and flow regime mapping, *ICMM2003-1069* (2003) 559-566.
- [410] H.Y. Wu, P. Cheng, Boiling instability in parallel silicon microchannels at different heat flux, *Int. J. Heat Mass Transfer* 47 (2004) 3631-3641.
- [411] H.Y. Wu, P. Cheng, H. Wang, Pressure drop and flow boiling instabilities in silicon microchannel heat sinks, *J. Micromech. Microeng.* 16 (2006) 2138-2146.
- [412] W. Qu, I. Mudawar, Measurement and correlation of critical heat flux in two-phase micro-channel heat sinks, *Int. J. Heat Mass Transfer* 47 (2004) 2045-2059.

- [413] G. Hetsroni, A. Mosyak, E. Pgrebnyak, Z. Segal, Periodic boiling in parallel micro-channels at low vapor quality, *Int. J. Mult. Flow* 32 (2006) 1141-1159.
- [414] H.J. Lee, D.Y. Liu, S. Yao, Flow instability of evaporative micro-channels, *Int. J. Heat Mass Transfer* 53 (2010) 1740-1749.
- [415] A. Kosar, C.-J. Kuo, Y. Peles, Suppression of boiling flow oscillations in parallel microchannels by inlet restrictors, *J. Heat Transfer* 128 (2005) 251-260.
- [416] S. Szczukiewicz, N. Borhani, J.R. Thome, Two-phase heat transfer and high-speed visualization of refrigerant flows in 100 x 100  $\mu\text{m}^2$  silicon multi-microchannels, *Int. J. Refrig.* 36 (2013) 402-413.
- [417] S. Szczukiewicz, N. Borhani, J.R. Thome, Two-phase flow operational maps for multi-microchannel evaporators, *Int. J. Heat Fluid Flow* 42 (2013) 176-189.
- [418] A. Kaya, M.R. Ozdemir, M. Keskinoz, A. Kosar, The effects of inlet restriction and tube size on boiling instabilities and detection of resulting premature critical heat flux in micro-tubes using data analysis, *Appl. Therm. Eng.* 65 (2014) 575-587.
- [419] K. Balasubramaniam, P.S. Lee, L.W. Jin, S.K. Chou, C.J. Teo, S. Gao, Experimental investigations of flow boiling heat transfer and pressure drop in straight and expanding microchannels - A comparative study, *Int. J. Therm. Sci.* 50 (2011) 2413-2421.
- [420] P.C. Lee, C. Pan, Boiling heat transfer and two-phase flow of water in a single shallow microchannel with a uniform or diverging cross section, *J. Micromech. Microeng.* 18 (2007) 025005.
- [421] C.T. Lu, C. Pan, Convective boiling in a parallel microchannel heat sink with a diverging cross section and artificial nucleation sites, *Exp. Therm. Fluid Sci.* 35 (2011) 810-815
- [422] C.-J. Kuo, Y. Peles, Flow boiling instabilities in microchannels and means for mitigation by reentrant cavities, *J. Heat Transfer* 130 (2008) 072402.
- [423] R.J. Jones, D.T. Pate, N. Thiagarajan, S.H. Bhavnani, Heat transfer and pressure drop characteristics in dielectric flow in surface-augmented microchannels, *J. Enhanced Heat Transfer* 16 (2009) 225-236.
- [424] D. Deng, W. Wan, Y. Tang, Z. Wan, D. Liang, Experimental investigations on flow boiling performance of reentrant and rectangular microchannels - a comparative study, *Int. J. Heat Mass Transfer* 82 (2015) 435-446.

- [425] D. Deng, R. Chen, Y. Tang, L. Lu, T. Zeng, W. Wan, A comparative study of flow boiling performance in reentrant copper microchannels and reentrant porous microchannels with multi-scale rough surface, *Int. J. Multi Flow* 72 (2015) 275-287.
- [426] D. Deng, Y. Xie, Q. Huang, W. Wan, On the flow boiling enhancement in interconnected reentrant microchannels, *Int. J. Heat Mass Transfer* 108 (2017) 453-467.
- [427] S. Zhang, W. Yuan, Y. Tang, J. Chen, Z. Li, Enhanced flow boiling in an interconnected microchannel net at different inlet subcooling, *Appl. Therm. Eng.* 104 (2016) 659-667.
- [428] S. Zhang, Y. Tang, W. Yuan, J. Zeng, Y. Xie, A comparative study of flow boiling performance in the interconnected microchannel net and rectangular microchannels, *Int. J. Heat Mass Transfer* 98 (2016) 814-823.
- [429] Y. Tang, C. Can, S. Zhang, Y. Sun, J. Zeng, W. Yuan, Z. Li, Effects of structural parameter on flow boiling performance of interconnected microchannel net, *Appl. Therm. Eng.* 112 (2017) 164-173.
- [430] A.H. Stenning, T.N. Veziroglu, Flow oscillation modes in forced-convection boiling, *Proc. 1965 Heat Transfer and Fluid Mechanic Institute* (1965), 301, Stanford Press.
- [431] J.S. Maulbetsch, P. Griffith, System-induced instabilities in forced-convection flows with subcooled boiling, *Proc. Third Int. Heat Trans. Conf.* (1966) 247-257.
- [432] G.M. Callahan, A.H. Stenning, T.N. Veziroglu, "Pressure-drop" oscillations in forced convection flow with boiling, EURATOM Report, *Proc. Symp. On Two-Phase Flow Dynamics*, Eindhoven (1967) 405.
- [433] M.E. Rahman, S. Singh, Flow excursions and pressure drop oscillations in boiling two-phase channel, *Int. J. Heat Mass Transfer* 138 (2019) 647-658.
- [434] B. Srinivas, S. Pushpavanam, Determining parameters where pressure drop oscillations occur in a boiling channel using singularity theory and the D-partition method, *Chem. Eng. Sci.* 55 (2000) 3771-3783.
- [435] C.-J. Kuo, Y. Peles, Pressure effects on flow boiling instabilities in parallel microchannels, *Int. J. Heat Mass Transfer* 52 (2009) 271-280.
- [436] H. Grzybowski, R. Mosdorf, Dynamics of pressure drop oscillations during flow boiling inside minchannel, *Int. Comm. Heat Mass Trans.* 95 (2018) 25-32.
- [437] X. Chen, P. Gao, S. Tan, Z. Yu, C. Chen, An experimental investigation of flow boiling instability in a natural circulation loop, *Int. J. Heat Mass Transfer* 117 (2018) 1125-1134.

- [438] H. Yuncu, O.T. Yildirim, S. Kakac, Two-phase flow instabilities in a horizontal single boiling channel, *Appl. Sci. Research* 48 (1991) 83-104.
- [439] Y. Ding, S. Kakac, X.J. Chen, Dynamic instabilities of boiling two-phase flow in a single horizontal channel, *Exp. Therm. Fluid. Sci.* 11 (1995) 327-342.
- [440] S. Kakac, T.N. Veziroglu, M.M. Padki, L.Q. Fu, X.J. Chen, Investigation of thermal instabilities in a forced convection upward boiling system, *Exp. Therm. Fluid Sci.* 3 (1990) 191-201.
- [441] H.T. Liu, S. Kakac, An experimental investigation of thermally induced flow instabilities in a convective boiling upflow system, *Warme - und Stoffubertragung* 26 (1991) 365-376.
- [442] M.M. Padki, H.T. Liu, S. Kakac, Two-phase flow pressure-drop type and thermal oscillations, *Int. J. Heat Fluid Flow* 12 (1991) 240-248.
- [443] K. Cheng, T. Meng, C. Tian, H. Yuan, S. Tan, Experimental investigation on flow characteristics of pressure drop oscillations in a closed natural circulation loop, *Int. J. Heat Mass Transfer* 122 (2018) 1162-1171.
- [444] R.S. Daleas, A.E. Bergles, Effect of upstream compressibility on subcooled critical heat flux, *ASME Paper No. 65-HT-67* (1965).
- [445] J.S. Maulbetsch, P. Griffith, A study of system-induced instabilities in forced-convection flows with subcooled boiling, *MIT Engineering Projects Lab Report 5382-35* (1965).
- [446] J.S. Maulbetsch, P. Griffith, Prediction of the onset of system-induced instabilities in subcooled boiling, *EURATOM Report, Proc. Symp. On Two-phase flow dynamics* (1967) 405-427.
- [447] L. Yu, A. Sur, D. Liu, Flow boiling heat transfer and two-phase flow instability of nanofluids in a minichannel, *J. Heat Transfer* 137 (2015) 051502.
- [448] S. Kakac, L. Cao, Analysis of convective two-phase flow instabilities in vertical and horizontal in-tube boiling systems, *Int. J. Heat Mass Transfer* 52 (2009) 3984-3993.
- [449] L. Cao, S. Kakac, H.T. Liu, P.K. Sarma, The effects of thermal non-equilibrium and inlet temperature on two-phase flow pressure drop type instabilities in an upflow boiling system, *Int. J. Therm. Sci.* 39 (2000) 886-895.
- [450] H.T. Liu, Parametric study of two-phase flow instabilities in a force-convective boiling upflow system, *M.S. Thesis, University of Miami, Coral Gables, FL, 1989.*

- [451] T. Zhang, Y. Peles, J.T. Wen, T. Tong, J.-Y. Chang, R. Prasher, M.K. Jensen, Analysis and active control of pressure-drop flow instabilities in boiling microchannel systems, *Int. J. Heat Mass Transfer* 53 (2010) 2347-2360.
- [452] S. Lee, V.S. Devahdhanush, I. Mudawar, Experimental and analytical investigation of flow loop induced instabilities in micro-channel heat sinks, *Int. J. Heat Mass Transfer* 140 (2019) 303-330.
- [453] H. Firstenberg, Boiling songs and associated mechanical vibrations, NDA 2131-12 (1960).
- [454] B. Ward, D.C. Emmony, Direct observation of the pressure developed in a liquid during cavitation-bubble collapse, *Appl. Phys. Lett.* 59 (1991) 2228-2230.
- [455] A. Prosperetti, Vapor bubbles, *Annual Review Fluid Mech.* 49 (2017) 221-248.
- [456] A.E. Bergles, P. Goldberg, J.S. Maulbetsch, Acoustic oscillations in a high pressure single channel boiling system, EURATOM Report, Proc. Symp. On Two-phase flow dynamics at Eindhoven (1967) 535-550.
- [457] T. Aoki, J.R. Welty, Frequency distribution of boiling-generated sound, *J. Heat Transfer* 92 (1970) 542-544.
- [458] H.F. Smirnow, V.V. Zrodnikov, I.L. Boshkova, Thermoacoustic phenomena at boiling subcooled liquid in channels, *Int. J. Heat Mass Transfer* 40 (1997) 1977-1983.
- [459] D.W. Fogg, K.E. Goodson, Bubble-induced water hammer and cavitation in microchannel flow boiling, *J. Heat Transfer* 131 (2009) 121006-1 - 11.
- [460] E. Ory, H. Yuan, A. Prosperetti, S. Popinet, S. Zaleski, Growth and collapse of a vapor bubble in a narrow tube, *Phys. Fluids* 12 (2000) 1268-1277.
- [461] H. Lamb, *Hydrodynamics*, sixth ed., Dover Publications, New York, 1945, p. 371.
- [462] C.W. Deane IV, W.M. Rohsenow, Mechanism and behavior of nucleate boiling heat transfer to the alkalai liquid metals, MIT Engineering Projects Lab Report 76303-65 (1969).
- [463] T. Aoki, J.R. Welty, Energy transfer mechanisms in transition pool boiling, *Int. J. Heat Mass Transfer* 13 (1970) 1237-1240.
- [464] Y.A. Buyevich, I.A. Natalukha, Self-oscillating regimes of nucleate, transition and film boiling, *Int. J. Heat Mass Transfer* 39 (1996) 2363-2373.
- [465] P. Griffith, Geysering in liquid-filled lines, ASME Paper 62-HT-39 (1962).
- [466] M. Aritomi, J.H. Chiang, M. Mori, Geysering in parallel boiling channels, *Nucl. Eng. Des.* 141 (1993) 111-121.

- [467] C. Casarosa, E. Latrofa, A. Shelginski, The geyser effect in a two-phase thermosyphon, *Int. J. Heat Mass Transfer* 26 (1983) 933-941.
- [468] T.F. Lin, W.T. Lin, T.L. Tsay, J.C. Wu, R.J. Shyu, Experimental investigation of geyser boiling in an annular two-phase closed thermosyphon, *Int. J. Heat Mass Transfer* 38 (1995) 295-307.
- [469] M.R. Sarmasti Emami, S.H. Noie, M. Khoshnoodi, M.T. Hamed Mosavian, A. Kianifar, Investigation of geyser boiling phenomenon in a two-phase closed thermosyphon, *Heat Trans. Eng.* 30 (2009) 408-415.
- [470] I. Khazaei, R. Hosseini, S.H. Noie, Experimental investigation of effective parameters and correlation of geyser boiling in a two-phase closed thermosyphon, *Appl. Therm. Eng.* 30 (2010) 406-412.
- [471] H. Jouhara, B. Fadhl, L.C. Wrobel, Three-dimensional CFD simulation of geyser boiling in a two-phase closed thermosyphon, *Int. J. Hydrogen Energy* 41 (2016) 16463-16476.
- [472] C. Tecchio, J.L.G. Oliveira, K.V. Paiva, M.B.H. Mantelli, R. Galdolfi, L.G.S. Ribeiro, Geyser boiling phenomenon in two-phased closed loop-thermosyphons, *Int. J. Heat Mass Transfer* 111 (2017) 29-40.
- [473] G.B. Wallis, J.H. Heasley, Oscillations in two-phase flow systems, *J. Heat Transfer* 83 (1961) 363-369.
- [474] J.A. Boure, Oscillatory two-phase flows, No. CEA-CONF-3539, CEA Centre d'Etudes Nucleaires de Grenoble (1974).
- [475] G.C. Gardner, Flooded countercurrent two-phase flow in horizontal tubes and channels, *Int. J. Multiph. Flow* 9 (1983) 367-382.
- [476] R.N. de Mesquita, P.H.F. Masotti, R.M.L. Penha, D.A. Andrade, G. Sabundjian, W.M. Torres, L.A. Macedo, Classification of natural circulation two-phase flow patterns using fuzzy inference on image analysis, *Nucl. Eng. Des.* 250 (2012) 592-599.
- [477] V. Tanskanen, A. Jordan, M. Puustinen, R. Kyrki-Rajamaki, CFD simulation and pattern recognition analysis of the chugging condensation regime, *Ann. Nucl. Energy* 66 (2014) 133-143.
- [478] L.E. O'Neill, I. Mudawar, Review of two-phase flow instabilities in macro- and micro-channel systems, *Int. J. Heat Mass Transfer*, under review.

## **APPENDIX A: REVIEW OF TWO-PHASE FLOW INSTABILITIES IN MACRO- AND MICRO-CHANNEL SYSTEMS**

### **A.1 Introduction**

#### *A.1.1 Phase Change Heat Transfer and Multiphase Flow*

Engineers and scientists worldwide are transitioning away from traditional single-phase heat transfer systems towards those utilizing phase change due to orders-of-magnitude improvement in both heat transfer coefficient and thermal transport capacity. These improvements have allowed innovative advancements in thermal management and transport solutions across industries including electronics thermal management, nuclear power, and heating, ventilation, air-conditioning, and refrigeration (HVAC&R) [1,190].

Along with these advantages in performance have come challenges associated with accurate prediction of important design parameters including critical heat flux (CHF), heat transfer coefficient, and pressure drop, each necessitating detailed investigation. Numerous studies have been conducted on boiling in a variety of configurations including pool boiling [5,6], flow boiling in macro- [11,191-195] and micro-channels [3,12-15,196-198], jet impingement [18,19], spray cooling [21,23,25,27,199], and hybrid schemes involving multiple approaches [29,200]. Similarly, condensation configurations include falling film [85-87], flow through single mini-channels [88-90,92-94,113,201], flow through parallel micro-channel arrays [96-97,107,202-204], and dropwise condensation [205-207].

Despite the proliferation of studies investigating boiling and condensation heat transfer (as well as numerous on multiphase flow without phase change), one area of deficiency in existing literature is multiphase instabilities and dynamic behavior. Whether brought on by boiling (or any mode of phase change) within the system or inherent to multiphase flow, there are numerous different instability modes that may manifest depending on operating conditions.

#### *A.1.2 Study of Two-Phase Flow Instabilities*

The study of two-phase flow instabilities is relevant to engineers and scientists in all fields encountering phase change heat transfer and multiphase flow. Often adopted for their superior transport (heat and/or mass) capabilities, systems relying on multiphase flow are prone to several

unique modes of instability. These may render some combinations of operating conditions unachievable or lead to significant oscillatory behavior in others, which may adversely affect system performance and safety. As such, knowledge and understanding of different instability modes and the conditions under which they are encountered is critical to design and operation of multiphase flow systems.

Prior reviews on the field of two-phase flow instabilities provide overviews on state-of-the-art (at the time the review was written) understanding of instabilities. One of the earliest and most influential of these was prepared by Boure *et al.* [50]. They structured their review around an important distinction between *Static Instabilities*, which involve departure from one unstable operating condition to a new, stable operating condition, and *Dynamic Instabilities*, which involve feedback between competing influences on flow (*i.e.*, body force, void fraction, flowrate) and lead to periodic fluctuations around a near-constant operating point. They also provided guidelines on expected frequencies for different dynamic instabilities that contributed to a proliferation of frequency-based analysis by current researchers leveraging more advanced data acquisition and signal processing capabilities.

Many other reviews in the interim have served to provide updated summaries on literature regarding two-phase flow instabilities, both for general instability analysis [64-66,208-209] as well as those focused on specific instability modes [210], and instabilities in nuclear power systems [211-213], refrigeration systems [214], and parallel micro-channel heat sinks [215,216]. Despite these works seeking to provide updated, unified analysis of existing instability literature, significant disagreement remains in modern literature regarding how to properly classify unstable behavior observed during experimentation or practical implementation.

In particular, much work remains to rectify the classical approach developed in macro-scale systems (often associated with nuclear reactor design) with phenomena observed in micro-scale systems (particularly parallel micro-channel heat sinks). As this is a major focus of the current work, a brief explanation of key differences between mini/macro-scale and micro-scale systems will be provided in the following subsection.

### *A.1.3 Classification of Macro- and Micro-Scale Systems*

With advances in manufacturing capabilities and increasing adoption of two-phase flow thermal management for electronics has come the increasing popularity of micro-channels and

parallel micro-channel heat sinks. Significant reductions to hydraulic diameter and inclusion of multiple flow passages allow micro-channel heat sinks to offer superior heat transfer performance compared to traditional, macro-channel systems with the same footprint. This reduction in channel diameter, however, can lead to differences in key two-phase flow mechanisms as compared to macro-channel systems. These differences are important for thermal, hydraulic, and stability reasons, so it is critical to be able to distinguish whether a given set of operating conditions will behave as a ‘macro-channel system’ or a ‘micro-channel system’.

Parameters most commonly used to distinguish between mini/macro- and micro-channel systems are confinement number,

$$Co = \frac{1}{D_h} \sqrt{\frac{\sigma}{g(\rho_f - \rho_g)}}, \quad (3.2)$$

Bond number,

$$Bo = \frac{g(\rho_f - \rho_g)D_h^2}{\sigma}, \quad (4.32)$$

Eötvös number,

$$Eö = \frac{g(\rho_f - \rho_g)D_h^2}{8\sigma}, \quad (A.1)$$

and capillary length,

$$L_{cap} = \sqrt{\frac{\sigma}{g(\rho_f - \rho_g)}}. \quad (A.2)$$

As pointed out by Ong and Thome [217], Eq.’s (3.2), (4.32), and (A.1) are all related to one another by the relationship

$$Eö = \frac{Bo}{8} = \frac{1}{8Co^2}, \quad (A.3)$$

and it is also clear capillary length  $L_{cap}$  is present in each dimensionless group. They decided to express their own transition criteria and that of Kew and Cornwell [218], Brauner and Ullmann [219], and Li and Wang [220] in terms of confinement number to offer a unified summary of transition criteria present in the literature. Transition criteria listed above, as well as others found in available literature, are provided in Table A.1.

Table A.1: Mini/macro- to micro-channel transition criteria.

Study	Transition Criteria	Notes
Kew & Cornwell, 1997 [218]	$Co > 0.5$ for microscale $Co < 0.5$ for macroscale	Early transition criteria, state if hydraulic diameter is less than half the capillary length, flow is confined (micro-channel), more than half, flow is not confined (mini/macro-channel).
Triplett <i>et al.</i> , 1999 [221]	$Co > 1$ for microscale $Co < 1$ for macroscale	Similar to Kew and Cornwell [218], but transition point is taken to be $Co = 1$ . This criterion is omitted here as it is the same as the upper limit of Ong and Thome [217].
Li & Wang, 2003 [220]	$Co > 4.46$ for microscale $4.46 > Co > 0.57$ for transition $Co < 0.57$ for macroscale	The first authors to include a 'transition region' (later referred to as meso-scale by Ong and Thome [217]) between micro-channel (confined) behavior and mini/macro-channel (non-confined). Based their criteria on condensation data.
Kandlikar & Grande, 2003 [222]	$D_h > 3$ mm for macroscale $3$ mm $\geq D_h > 0.2$ mm for miniscale $0.2$ mm $\geq D_h > 10$ $\mu$ m for microscale $10$ $\mu$ m $\geq D_h > 1$ $\mu$ m for transitional microscale $1$ $\mu$ m $\geq D_h > 0.1$ $\mu$ m for transitional nanoscale $0.1$ $\mu$ m $\geq D_h$ for nanoscale	Does not take fluid properties into account making it less applicable than alternatives. Based loosely on Knudsen number (molecular mean-free path divided by hydraulic diameter).
Brauner & Ullmann, 2006 [219]	$Co > 0.79$ for microscale $Co < 0.79$ for macroscale	Similar to Kew and Cornwell [218], but transition point $Co = 0.79$ is used.
Cheng & Wu, 2006 [223]	$Co > 4.472$ for microscale $4.472 > Co > 0.577$ for transition $Co < 0.577$ for macroscale	Included a meso-scale transition region between $Co < 4.472$ and $Co > 0.577$ . Compared to later relationships, offers a much more stringent confinement number relationship for microscale phenomenon.
Harirchian & Garimella, 2010 [224]	'Convective Confinement Number' $Bo^{0.5} Re_f = \frac{Re_f}{Co} = \left( \frac{g(\rho_f - \rho_g)}{\sigma} \right)^{0.5} \frac{GD_h^2}{\mu_f}$ $Re_f / Co < 160$ for microscale $Re_f / Co > 160$ for macroscale	Attempted to incorporate flow inertia into a confinement criterion, but has the implication all low velocity flows are well described by assuming confined flow (this is not true). Omitted from current analysis.
Ong & Thome, 2011 [217]	$Co > 1$ for microscale $1 > Co > \sim 0.3-0.4$ for transition $Co < \sim 0.3-0.4$ for macroscale	Found a meso-scale transition region between $Co < 1$ and $Co > \sim 0.3-0.4$ where flow is not well described by macroscale phenomena but is not fully confined either.
Mudawar 2011 [28]	Used Weber number instead of Confinement: $We_{min} = \frac{160}{9} \frac{1}{\left(1 + \frac{160}{3Re_{min}}\right)}$ or $D_{min} = \frac{160(\sigma\rho_f - 3\mu_f G)}{9G^2}$	Defined transition from mini/macro-channel to micro-channel in terms of surface tension and flow inertia (neglecting body force). Derivation based on equating liquid drag force on bubble to surface tension force on the same.
Tribica & Ribatski, 2015 [225]	Modified Confinement Number $Co^* = Co \sqrt{8 \cos(\theta_f)}$ $Co^* > 1$ for microscale, $Co^* < 1$ for macroscale	Modified characteristic length scale by multiplication with contact angle $\theta_f$ . Difficult to evaluate dynamic contact angle as a function of operating conditions, omitted here.

A general conclusion which may be drawn from analysis of the transition criteria in Table A.1 is that a micro-channel is defined as a system where capillary length  $L_{cap}$  is approximately equal to the hydraulic diameter (resulting in  $Co \sim 1$ ). This makes intuitive physical sense, as the capillary length is often used as a characteristic length associated with bubble formation (Taylor wavelength in Rayleigh-Taylor instability), meaning experimental setups with  $Co \sim 1$  produce bubbles of a size similar to that of the channel cross-section. This leads to fundamental differences compared with traditional mini/macro systems, where bubbles are appreciably smaller than the channel, and liquid displacement due to nucleation is a much less appreciable phenomenon as compared to micro-channels.

This definition is not necessarily apt for flow condensation, however, where bubble dynamics are significantly different than for flow boiling. The only criterion in Table A.1 defined based on condensation data is that of Li and Wang [220], and it shows a stringent value of  $D_h < L_{cap}/4.46$  for transition to micro-channel flow. This transition for flow condensation warrants investigation in future work.

Figure A.1(a) and A.1(b) provide samples of transition criteria for flow boiling and flow condensation, respectively, plotted as diameter versus reduced pressure for FC-72, water, and R134a. Superimposed on each plot are representative operating conditions taken from many commonly cited flow boiling and flow condensation works to give a feel for how different setups may be classified as mini/macro- or micro-channel depending on working fluid and operating pressure.

Figure A.1(c) also provides a sample of differences between observed behavior near the transition between macro- and micro-channels for both water and FC-72 (adapted from Mukherjee and Mudawar [14]). Visualization images show the significantly large size of bubbles formed using water as compared to FC-72, explaining its propensity to perform as a micro-channel for larger diameters where FC-72 will exhibit macro-channel behavior.

For the sake of the current study, it is sufficient to recognize there are fundamental differences between macro-channel flows and those in micro-channels, largely attributable to the relative sizes of capillary length and hydraulic diameter. Discussion of the influence of channel classification on the mechanisms behind formation and propagation of various instability modes will be discussed at length in later sections.

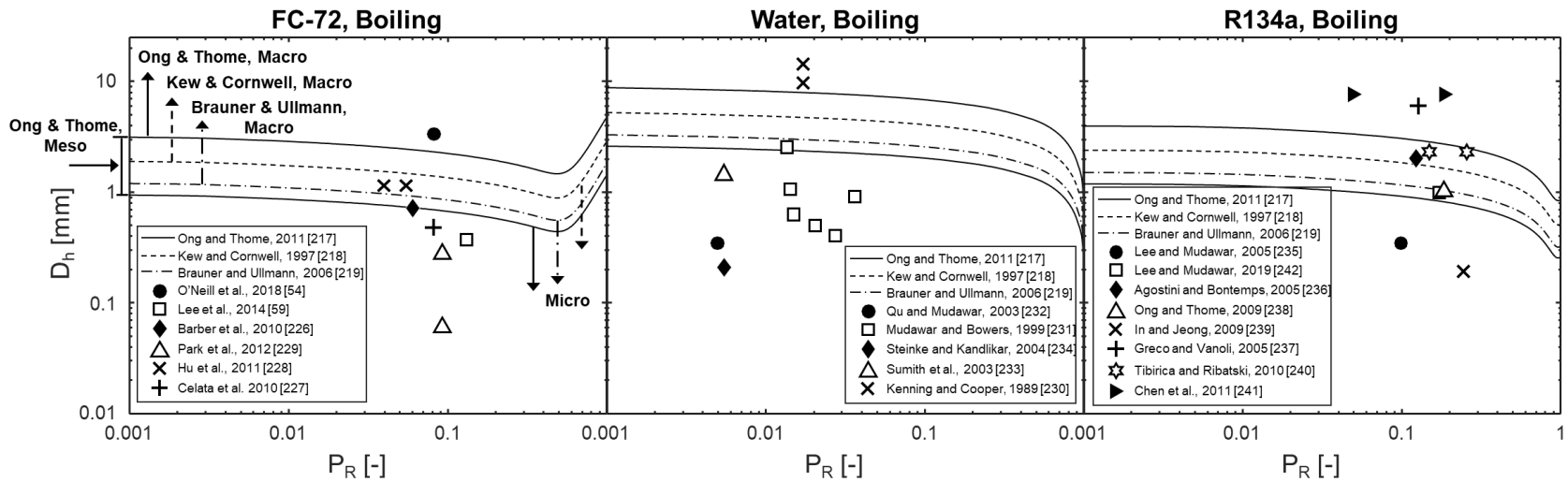


Figure A.1: Plots of channel hydraulic diameter and reduced pressure representing operating conditions for many common studies on (a) flow boiling and (b) flow condensation with FC-72, water, and R134a as working fluids. Mini/macro-to-micro channel transition criteria of Ong and Thome [217], Kew and Cornwell [218], Brauner and Ullmann [219] are superimposed with boiling studies, while that of Li and Wang [220] is superimposed for condensation studies. Provided in (c) are flow visualization images highlighting differences between macro- to micro-channel transition for FC-72 and water (adapted from Mukherjee and Mudawar [14]).

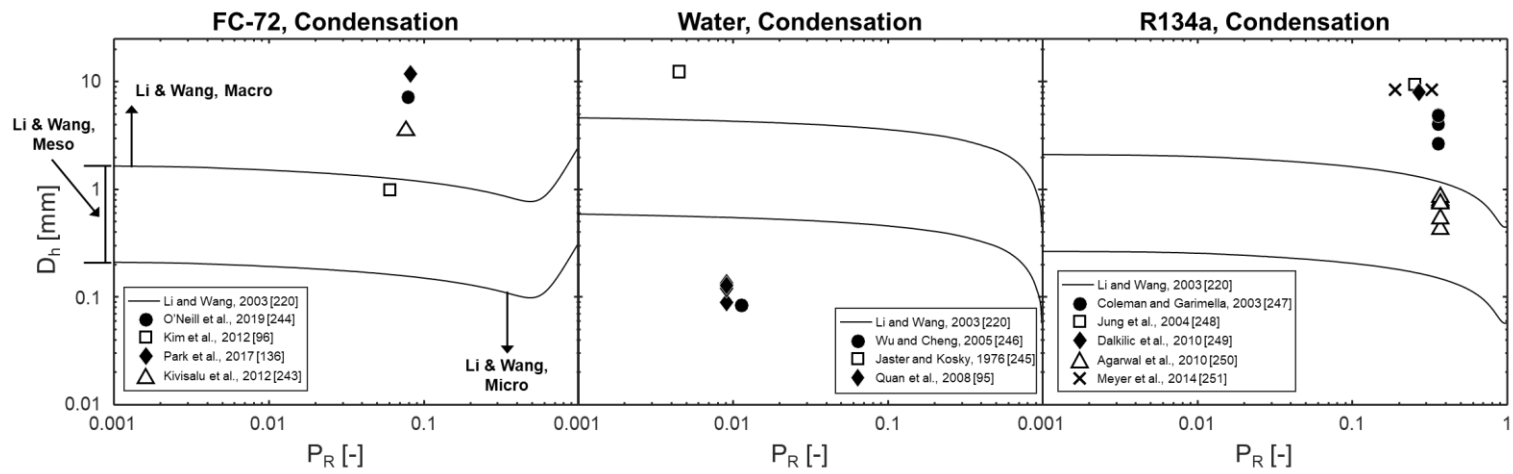


Figure A.1 (b).

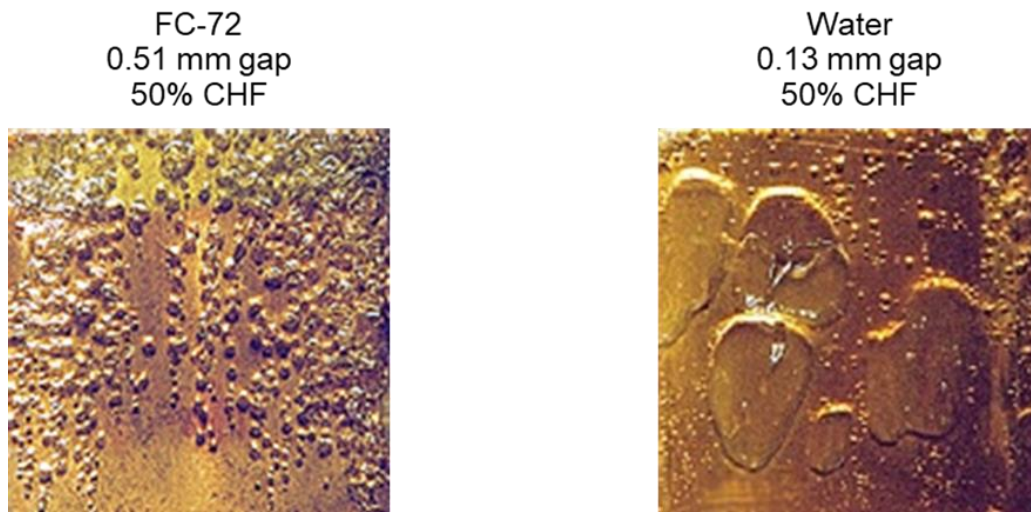


Figure A.1 (c).

#### A.1.4 Objectives of the Present Review

The present review aims to present a comprehensive summary of literature dealing with two-phase flow instabilities and dynamic behavior. Efforts will be focused on providing a fundamental, physics-based description of all key instabilities prior to detailing relevant studies concerning each instability mode. Special emphasis will be placed on presenting works which display relevant theoretical work (*i.e.*, modeling) alongside experimental results, and focus will be placed on examining similarities and differences between manifestation of instability modes in macro- and micro-channel systems.

Basic structure of the review will be based on that used by Boure *et al.* [50] in their seminal work: namely, dividing the field of study into *Static* and *Dynamic* instabilities. These two broad categories will be further subdivided by key instability types, with an additional section provided for detailed summary of the field. Table A.2 provides an overview of the structure described here, with brief notes on each instability type provided.

The present review is one in a recent series prepared by the Purdue University Boiling and Two-Phase Flow Laboratory (PU-BTPFL) covering a broad spectrum of fundamental topics in boiling and condensation. Topics include predictive tools for flow boiling and flow condensation pressure drop and heat transfer [252,253], CHF in microgravity [147] and general microgravity boiling and condensation [139], flow boiling critical flow and dryout [254], computational studies on boiling and condensation [154], droplet impact on liquid films and heated walls [255,256], spray cooling [257,258], pool boiling CHF [259,260], pool boiling enhancement via additives and surface modification [261,262], and flow boiling enhancement via nanofluids and surface modification [263,264]. These studies all provide descriptions of associated fundamental physical processes and summarize key works investigating each topic and serve as excellent starting points for delving into boiling and condensation.

It should also be noted that a primary motivation for investigation into two-phase flow instabilities by the present author is the upcoming Flow Boiling and Condensation Experiment (FBCE). A collaborative effort between the Purdue University Boiling and Two-Phase Flow Laboratory (PU-BTPFL) and NASA Glenn Research Center, FBCE will place a test bed on the International Space Station (ISS) capable of gathering long-duration microgravity flow boiling and condensation results. In addition to its key aim of exploring the impact of body force effects on flow boiling CHF (to augment prior work at multiple orientations in 1-g [145,265] and in parabolic

flight [35]), it will also offer the possibility of exploring both boiling and condensation instabilities in the absence of gravity.

Table A.2: Key topics in two-phase flow instabilities and dynamic behavior.

Type	Brief Description	Key Characteristics	Present in:
<b>Static Instabilities</b>			
Critical Heat Flux (CHF), 2.1	Also called boiling crisis, occurs when vapor production occludes liquid access to a heated wall.	Rapid, unstable temperature rise, commonly spanning an order of magnitude. May lead to heater burnout and/or other material failure.	All boiling configurations (flow, pool, spray, etc.).
Ledinegg Instability, 2.2	Also called flow excursion or excursive instability, occurs when slope of pump pressure versus flowrate curve is greater than that of system internal characteristic curve.	Significant, single-event increase or decrease in flowrate to stable system operating point. Decrease may lead to CHF.	Flow boiling only.
Boiling Curve Hysteresis, 2.3	For testing with low contact angle fluid/surface combinations and all other conditions held constant, increasing versus decreasing heat flux leads to different boiling curves, primarily near the boiling incipience point.	Initial onset of nucleation requires a higher heat flux than deactivation of nucleation sites.	All boiling configurations.
Vapor Burst, 2.3	For well de-gassed, low contact angle fluids, onset of boiling may involve significant pressure 'shock' within the system.	Amplitude of pressure spike depends on volume of system relative to that of newly produced vapor.	All boiling configurations.
Flow Pattern Transition Instability, 2.4	Operating near a boundary between dissimilar flow regimes allows the possibility of transition from one to the other for a small change in operating conditions, leading to (potentially) significant differences in pressure drop and heat transfer.	Commonly classified as a static instability, it is also possible for it to manifest in dynamic fashion (repeated, cyclical transition between regimes).	Flow boiling and flow condensation.
<b>Dynamic Instabilities</b>			
Density Wave Oscillation (DWO), 3.1	Also referred to as Density Wave Instability (DWI). Results from unstable feedback mechanisms present in multiphase flows. For macro-channels, this relates to relative magnitude of single- and two-phase pressure drop (which oscillate out of phase). For micro-channels, this is due to rapid expansion of confined bubbles towards the inlet.	These typically have periods of oscillation on the order of 1-2 times liquid transit time through the flow channel. They most commonly occur on positive-slope regions of the internal characteristic curve. Many different factors may lead to their occurrence depending on operating conditions and orientation.	Flow boiling and flow condensation.
Parallel Channel Instability (PCI), 3.2	Static mode (Flow Maldistribution) is Ledinegg instability, dynamic mode results from interacting DWOs in channels. More likely to lead to backflow compared to single-channel DWOs due to presence of parallel flow paths. Also, mechanistically different in micro- versus macro-channels.	As the fundamental mechanism is DWOs, many parametric trends for onset and characteristics are the same as those outlined in section 3.1. In parallel micro-channel heat sinks, usually manifest as oscillations in inlet pressure but not outlet.	Flow boiling and flow condensation.
Pressure Drop Oscillation (PDO), 3.3	Occurs when operating on negative-slope portion of internal characteristic curve with a compressible volume (e.g., surge tank) present in the system.	Flowrate and pressure oscillate 180° out-of-phase. Period of oscillation is typically long compared to other oscillatory phenomena, amplitudes are large.	Flow boiling only.

Table A.2: Continued.

<p>Acoustic Oscillation, 3.4</p>	<p>Usually generated by vapor bubble collapse in subcooled flow boiling, liquid droplet impingement on liquid films, and presence of rotating machinery in two-phase flow loops.</p>	<p>Generally used as a catch-all term for high-frequency (~ 20 – 10,000 Hz) oscillations observed during two-phase flow. Amplitude of oscillations is typically low.</p>	<p>Flow boiling and flow condensation.</p>
<p>Other Reported Dynamic Behavior, 3.5</p>	<p><i>Bumping, geysering, chugging, flashing, and thermal oscillations</i></p>	<p><i>Bumping and geysering</i> are unique instabilities occurring only in very specific situations. <i>Chugging</i> is largely a misnomer. <i>Flashing</i> is not an instability, but its occurrence may impact manifestation of instabilities. <i>Thermal oscillations</i> usually occur as a part of or result of other dynamic instabilities, and are important in thermal management applications.</p>	<p><i>Bumping and geysering</i> are boiling only. <i>Chugging, flashing, and thermal oscillations</i> may occur in boiling or condensation.</p>

## A.2 Static Instabilities

As mentioned in the preceding section, *Static Instabilities* are commonly characterized as a single-event departure from one unstable operating condition to a new, distinctly different operating condition. Important to note here is the key distinction between *Static* and *Dynamic* instabilities: Namely, *Static Instabilities* are best represented as a one-time departure from operating conditions *A* to a distinctly different set of conditions *B* in response to an incremental perturbation at point *A*.

To best illustrate the nature of *Static Instabilities* it is helpful to first discuss Critical Heat Flux (CHF, also referred to as Boiling Crisis). This commonly investigated facet of all boiling systems (flow boiling, pool boiling, *etc.*) is in fact a *Static Instability*.

### A.2.1 Critical Heat Flux (CHF)

Arguably the most studied aspect of boiling, CHF is commonly described as a rapid, unstable rise in heated wall temperature once vapor production becomes so vigorous as to prevent liquid contact with the heated surface. For lower heat flux values, nucleate boiling is the dominant heat transfer mechanism, but, as CHF is approached, vapor production becomes more vigorous and liquid access to the heated surface becomes restricted.

Just prior to CHF, a minimal amount of liquid accesses the heated wall and boiling is still the dominant mechanism for energy removal. A slight increase in heat flux at this point causes the onset of the CHF transient, however, where vapor production entirely occludes liquid access to the heated wall and the wall temperature rises rapidly (as the dominant heat transfer mechanism is now single-phase convection of vapor at the wall, possessing a much smaller heat transfer coefficient than boiling).

At the new, stable operating condition after CHF, wall superheat (defined as the difference between wall temperature and local saturation temperature) may be several hundred degrees. This often leads to material failure and is almost never a desired operating point for systems employing phase change heat transfer. Due to these adverse conditions, significant research efforts have focused on predicting CHF in a variety of boiling configurations, and it is considered a subfield of phase change heat transfer separate from instabilities and dynamic behavior. As such, additional space will not be devoted to it here, but, for those interested, studies by Liang and Mudawar

[259,260] are recommended for review of pool boiling CHF mechanisms and predictive tools, those by Boyd [266] and Konishi and Mudawar [147] for flow boiling CHF, Liang and Mudawar [257] for spray cooling CHF, and Wolf *et al.* [267] for jet impingement CHF.

It should be noted that CHF discussed in this section is intended to describe ‘classic’ CHF, not CHF brought on by other instability modes. CHF induced by other instabilities present in the system will be treated separately later in this review.

### A.2.2 Ledinegg (*Excursive*) Instability

Prior to discussing Ledinegg instability (also referred to as Flow Excursion Instability or Excursive Instability) it is useful to first provide discussion on internal and external characteristic pressure curves. These are relevant to understanding Ledinegg instability and will also be referred to when discussing later instability modes.

Also, it is worth noting that as Ledinegg instability is a system level instability, its behavior is near-identical in two-phase flow systems employing either traditional macro-channels or micro-channels. Some commentary will be provided at the end of this section discussing potential differences for micro-channel systems, although this warrants further investigation.

#### A.2.2.1 Characteristic Pressure Curves

Used in analysis of stability for flow boiling and flow condensation systems, characteristic pressure curves indicate how pressure responds to changes in flowrate when other operating conditions are fixed. Two-phase flow instability researchers typically refer to two key pressure characteristic curves: That of the flow loop (primarily the test section), referred to as an *Internal Pressure Characteristic Curve*, and that of the external, driving force for the flow loop as seen by the test section, referred to as an *External Pressure Characteristic Curve*. It is the intersection of these internal and external curves that determines whether a given operating point is stable or if it will experience an excursion (Ledinegg instability) to a stable operating point.

Figures A.2(a), A.2(b), and A.2(c) provide qualitative depictions of internal pressure curves for boiling and condensation, and external pressure curves for different types of systems, respectively. Figure A.2(a), corresponding to an internal characteristic curve for a boiling test section, is easiest to interpret by moving from right to left. For a fixed, nonzero heat flux, very

high mass velocities will exhibit no boiling behavior, and pressure drop will be near-identical to that for single-phase liquid flow. As mass velocity decreases, boiling begins to occur, pressure drop behavior begins to deviate from that for single-phase flow, and several key points are encountered: *Onset of Nucleate Boiling (ONB)*, *Onset of Significant Vapor/Void (OSV)*, and *Onset of Flow Instability (OFI)*. The ONB point is self-explanatory, the OFI point is defined as the local minimum in the pressure drop versus flowrate curve, and OSV has a varying definition but always falls between ONB and OFI. The implications of these locations for system stability analysis will be discussed further in later subsections.

As mass velocity is reduced further in Fig. A.2(a), pressure drop begins to increase due to added body force and acceleration effects present in two-phase flows. Past a point, however, pressure drop begins to decrease again, as void fraction is sufficiently large that flow begins to approximate that of single-phase vapor within much of the channel.

It is the negative slope region of Fig. A.2(a) that differentiates boiling flows from those for single-phase liquid and vapor, and well as condensing flows as shown in Fig. A.2(b). In all other cases, internal pressure drop exhibits a monotonic increase with flowrate, and it is the presence of this region of decreasing pressure drop with increasing flowrate that may lead to Ledinegg instability.

It is not enough to simply analyze the system internal pressure characteristics, however, as external pressure is equally important in determining whether a system will be prone to Ledinegg instability. Figure A.2(c) shows pressure curves for the three most common types of two-phase flow system ‘drivers’: *Positive Displacement Pumps (i.e., gear pumps)*, *Centrifugal Pumps*, and *Fixed Pressure Systems (i.e., those with many parallel tubes between inlet and exit manifolds)*.

*Positive Displacement Pumps* are shown as having a near-infinite negative slope on pressure drop versus flowrate curves. This is due to the fact they operate by displacing a finite volume of fluid at a given speed, meaning flowrate is fixed and pressure provided is sufficient to achieve that flowrate.

*Centrifugal Pumps*, meanwhile, operate at a fixed speed and exhibit coupled pressure drop and flowrate characteristics. Figure A.2(c) shows how, as flowrate approaches zero, centrifugal pumps provide a max (still finite) pressure head, and as flowrate increases significantly, pressure increase across the pump approaches zero.

Finally, *Fixed Pressure Systems* exhibit a flat (zero-slope) response to changes in flowrate. As mentioned previously, this is characteristic of systems with many parallel channels sharing inlet and exit plenums, a common configuration for many early boilers, nuclear power systems, and still relevant to applications with parallel micro-channel heat sinks.

Having established basics of internal and external pressure characteristics for boiling and condensing systems, it is possible to provide an explicit description of Ledinegg instability and the conditions under which it occurs.

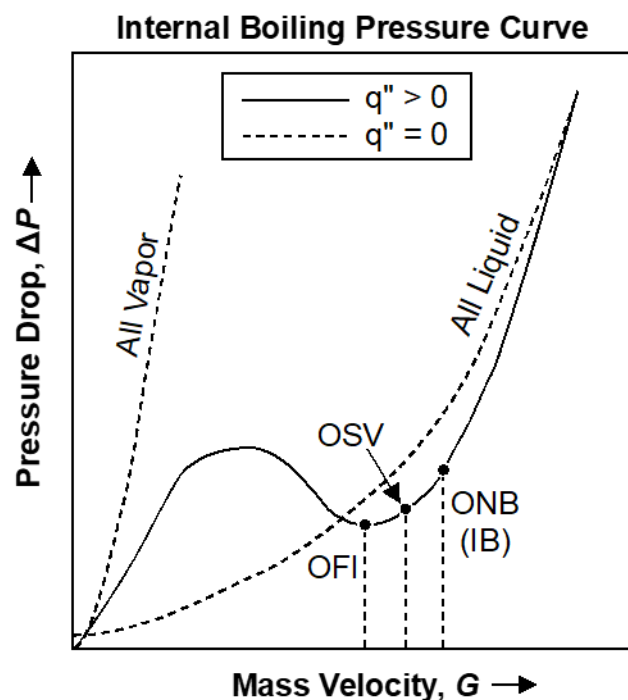


Figure A.2: Pressure versus mass velocity characteristic curves for (a) flow boiling (internal characteristic,  $q'' > 0$ ), (b) flow condensation (internal characteristic,  $q'' < 0$ ), (c) different pump types (external characteristic), and (d) sample cases for describing existence/non-existence of Ledinegg instability with (1) positive displacement pump, (2) centrifugal pump, and (3) fixed pressure drop boundary condition.

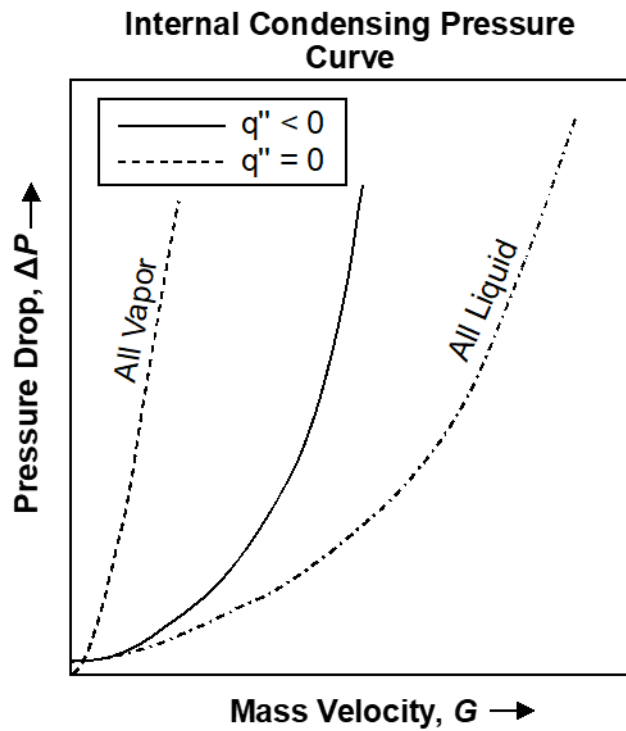


Figure A.2 (b).

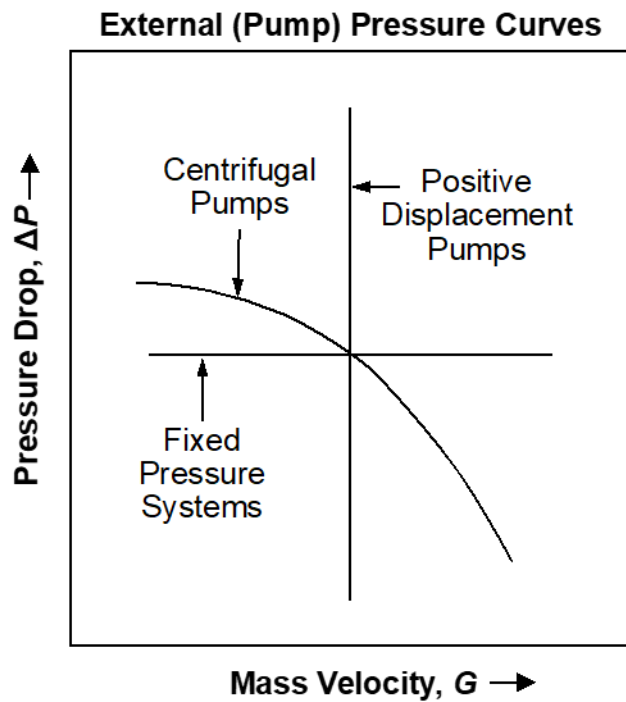


Figure A.2 (c).

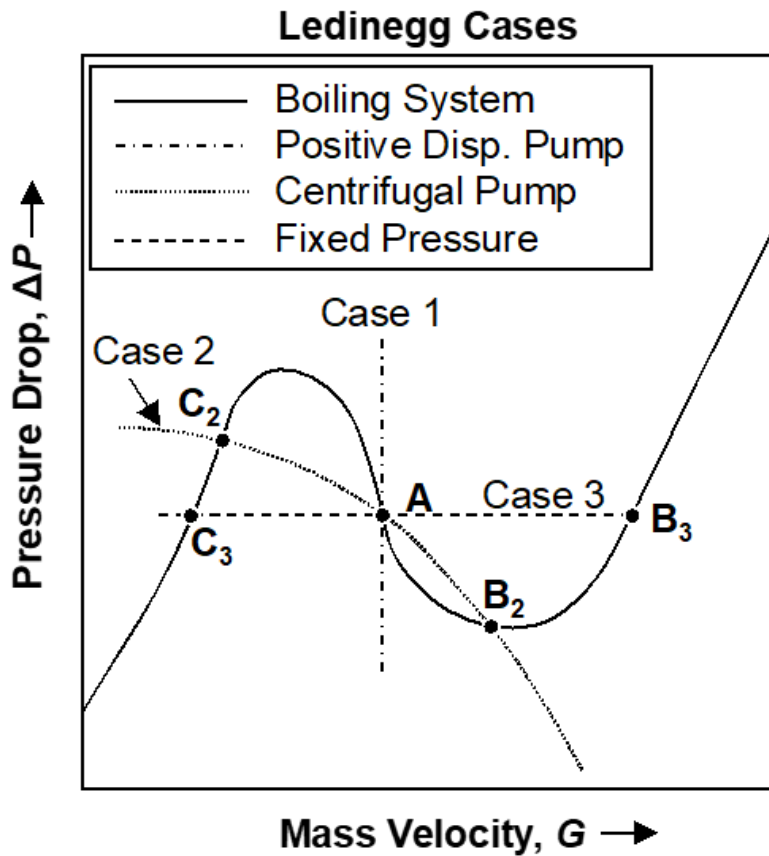


Figure A.2 (d).

#### A.2.2.2 Existence and Characteristics of Ledinegg Instability

Mathematical formulation of Ledinegg instability is straightforward and may be found in many relevant works on the topic. A brief overview will be provided here, based largely on the explanation provided by Lahey and Podowski [47].

The transient momentum equation for a flow loop may be written in the simplified form

$$I \frac{d\dot{m}}{dt} = (\Delta P_{pump} - \Delta P_{loop}), \quad (\text{A.4})$$

where  $\dot{m}$  is mass flowrate,  $\Delta P_{pump}$  pump pressure rise,  $\Delta P_{loop}$  loop pressure drop, and  $I$  inertia of the loop given by

$$I = \sum_{i=1}^n \frac{L_i}{A_i}, \quad (\text{A.5})$$

with  $L_i$  and  $A_i$  representing the length and area, respectively, of flow section  $i$ . In the case of true steady flow, the right-hand side of Eq. (A.4) is equal to zero. Perturbations from mechanical (or other sources) are common, however, so it is relevant to consider the case of a small perturbation in mass flowrate

$$\dot{m}(t) = \dot{m}_0 + \delta\dot{m}(t). \quad (\text{A.6})$$

Combing Eqs. (A.6) and (A.4) simplifies to

$$I \frac{d(\delta\dot{m})}{dt} + \left[ \frac{\partial(\Delta P_{loop})}{\partial\dot{m}} \Big|_{\dot{m}_0} - \frac{\partial(\Delta P_{pump})}{\partial\dot{m}} \Big|_{\dot{m}_0} \right] \delta\dot{m} = 0, \quad (\text{A.7})$$

which has the solution

$$\delta\dot{m}(t) = \delta\dot{m}(0) \left\{ \exp \left( - \left[ \frac{\partial(\Delta P_{loop})}{\partial\dot{m}} \Big|_{\dot{m}_0} - \frac{\partial(\Delta P_{pump})}{\partial\dot{m}} \Big|_{\dot{m}_0} \right] \frac{t}{I} \right) \right\}. \quad (\text{A.8})$$

This system is then said to be stable at a given operating point  $\dot{m}_0$  if

$$\lim_{t \rightarrow \infty} \delta\dot{m}(t) \rightarrow 0, \quad (\text{A.9})$$

a condition which is satisfied when

$$\frac{\partial(\Delta P_{loop})}{\partial\dot{m}} \Big|_{\dot{m}_0} > \frac{\partial(\Delta P_{pump})}{\partial\dot{m}} \Big|_{\dot{m}_0}. \quad (\text{A.10})$$

In plain English, Eq. (A.10) states the system will be stable operating at mass flowrate  $\dot{m}_0$  if the slope of the internal pressure curve is greater than the external (pump) pressure curve. Based on the characteristic curves presented in Figs. A.2(a) and A.2(b), this is always the case for single-phase flow and flow condensation, but there is the possibility of flow boiling systems failing to satisfy this condition (depending on specific operating conditions) due to the negative slope region of their characteristic curves.

Figure A.2(d) provides a closer look at internal and external pressure curves for boiling systems to illustrate situations when Ledinegg instability will manifest. Again drawing from the example of Lahey and Podowski [47], three cases are shown: A flow boiling system with (1) a positive displacement pump, (2) a centrifugal pump, and (3) operated with a constant pressure

difference (*i.e.*, parallel tubes). In these examples, point **A** represents the operating conditions of interest (equivalent to  $\dot{m}_0$  in the above derivation).

In case 1, the system is stable at point **A** due to the slope of the external pressure curve approaching  $-\infty$  while that of the boiling system remains a finite negative value. In physical terms, a slight increase in mass flowrate ( $+\delta\dot{m}$ ) within the system will decrease internal pressure drop. Pump pressure will decrease further, however, driving flowrate back towards the original operating point **A**.

In case 2, however, slope of the external pressure curve is now less negative than that of the internal curve at point **A**. This means that, for a slight increase in mass flowrate within the system, system pressure drop will decrease more than pump pressure head at that new flowrate. This will drive the flowrate to increase further and further until a point is reached at which system pressure drop is equal to pump pressure *and* slope of the system curve is greater than that of the external curve. For case 2, this point is labelled as **B<sub>2</sub>** on Fig. A.2(d).

Similarly, a slight decrease in mass flowrate ( $-\delta\dot{m}$ ) at point **A** for conditions associated with case 2 will lead to an increase in system pressure drop. Pump pressure will also increase, but not enough to compensate for the new system pressure drop, leading flowrate to decrease until stable point **C<sub>2</sub>** is reached.

Case 3, corresponding to a fixed pressure condition, will exhibit behavior similar to that of Case 2 for perturbations in mass flowrate about point **A**. This time, however, new stable operating conditions **B<sub>3</sub>** and **C<sub>3</sub>** will be even farther from the desired condition **A**. Point **C<sub>3</sub>** is dangerous, as the low flowrate and correspondingly high void fraction commonly lead to CHF and system failure. Thankfully, many researchers have investigated Ledinegg instability over the years, and a wide variety of strategies exist to combat its negative influence on safe system operation.

### A.2.2.3 Studies Investigating Ledinegg Instability

Although apparently first reported by Schnackenberg in 1937 [268], origination of analysis on the excursive instability commonly referred to as Ledinegg instability is frequently attributed to the 1938 work of Ledinegg [44]. As with these early studies, much of the work on Ledinegg instability focuses on prevention to avoid premature CHF and system failure associated with excursion to a lower flowrate, higher void fraction operating point. Figure A.3, adapted from the work of Mishima *et al.* [269], provides an excellent example of both CHF encountered during

nominal system operation, Fig. A.3(a), and that brought on by Ledinegg instability, Fig. A.3(b). Figure A.3(b) clearly shows the rapid, unsteady rise in heated wall temperature is brought on by a sharp decrease in flowrate just prior to CHF (identified as ‘Flow Excursion’ in the figure).

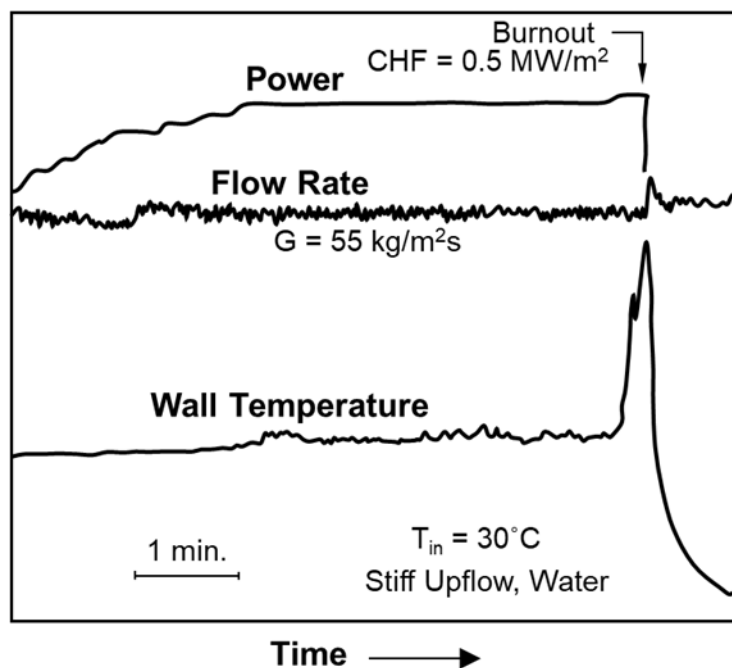


Figure A.3: Sample test cases indicating (a) nominal progression of heat flux increments leading to CHF, and (b) Ledinegg instability (Flow Excursion) leading to CHF. Adapted from Mishima *et al.* [269].

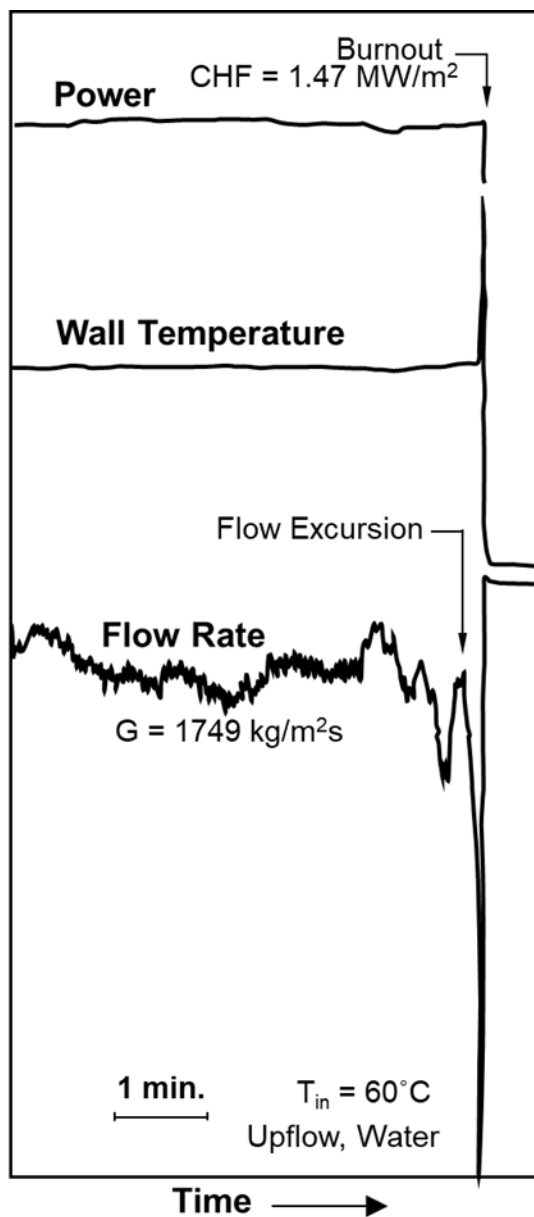


Figure A.3 (b).

Many researchers have devoted time to analysis of Ledinegg instability, but relatively few have provided experimental evidence of its occurrence. In addition to the work of Mishima *et al.* [269] referenced above, notable experimental works include those of Whittle and Forgan [40], Lee *et al.* [43], Ishii and Fauske [270], and Shin and No [52].

In their 1967 work involving water flow circulated through a single, rectangular boiling channel by use of a centrifugal pump, Whittle and Forgan [40] provided clear evidence of a stable

flow experiencing an excursive instability after being subjected to a small change in operating conditions. They showed this transition point occurred at the minima in the pressure drop – flow rate characteristic curve (the OFI point) and investigated how changes in operating conditions affect the location of this point. They used their results to generate one of the most commonly referenced OFI correlations in literature.

Lee *et al.* [43] recently offered an updated version of the approach taken by Whittle and Forgan [40]. By investigating water flow circulated using a centrifugal pump through a single rectangular channel (using channels of three different aspect ratios) they were able to experimentally observe Ledinegg instability, evaluate the correlation of Whittle and Forgan [126], and offer their own, updated correlation for OFI.

Ishii and Fauske [270] investigated natural circulation in Liquid Metal Fast Breeder Reactors (LMFBRs) to determine the dominant mechanisms leading to burnout in these systems. Natural circulation represents a particularly interesting case for Ledinegg instabilities, as both internal and external pressure characteristics change significantly with operating conditions. They found that in many cases burnout may be due to flow excursion leading to a high quality, low flowrate condition, and developed an extensive model for both internal and external system pressure characteristics to better predict flow excursion. They compared their model predictions to experimental results of Garrison *et al.* [271] and Haga *et al.* [272] and found good agreement between their Ledinegg instability model predictions and the experimental burnout values.

Shin and No [52] recently investigated flow instabilities with water in a Printed Circuit Heat Exchanger (PCHE), a parallel microchannel heat exchanger designed specifically for application with Small Modular Reactors (SMRs). They clearly demonstrated the occurrence of Ledinegg instability within their experimental system and developed a model for predicting system internal pressure curves.

The majority of studies on Ledinegg instability avoid directly encountering the instability mode and instead focus on how it may be avoided. Avoidance strategies may be classified into two broad categories: *Modifications to the System* and *Knowledge of Operating Boundaries*.

*Modifications to the System* are focused on eliminating the negative slope portion of the internal pressure curve altogether, commonly accomplished by including a throttling valve upstream of the test section (increasing frictional pressure drop to where it dwarfs two-phase effects and eliminates the negative slope portion) or raising system pressure. Figure A.4(a)

presents an example of the effect of raising system pressure on the shape of the internal pressure curve, adapted from the work of Genglei *et al.* [273]. They investigated boiling instabilities in systems with parallel, narrow channels using the RELAP5 analysis code (commonly used for analysis of nuclear thermohydraulic systems). They undertook extensive parametric analysis, one of the conclusions of which was increases in system pressure, as shown in Fig. A.4(a), lead to reductions in density ratio between phases and Ledinegg instability (indicated with star symbols in Fig. A.4(a)) no longer manifesting

The other approach to *Modifications to the System* mentioned above, inclusion of a throttling valve at the channel inlet, leads to a family of curves similar to those shown in Fig. A.4(a) (this time with increasing inlet restriction coefficient replacing increasing pressure). Practically, inclusion of throttling valves with large pressure drops has led to the elimination of Ledinegg instability and significant improvements in system performance. Figure A.4(b) provides an example of this, taken from the work of Mishima *et al.* [269]. They provide flow boiling CHF results for both vertical upflow and downflow orientations using no inlet restriction (Soft System) and a throttling valve at the channel inlet (Stiff System). At low flow velocities, Fig. A.4(b) shows CHF values are similar for both systems, but, as velocity is increased, significant differences are seen between ‘Soft’ and ‘Stiff’ system results. Mishima *et al.* state this difference is due to the occurrence of Ledinegg instability in the ‘Soft’ system, yielding burnout at lower heat fluxes than those encountered for the ‘Stiff’ system at a similar mass velocity.

*Modifications to the System* offer methods for eliminating the possibility of Ledinegg instability occurring within a system, but usually come with their own incurred costs: Raising system pressure may require changes to flow loop hardware to accommodate heightened pressures and temperatures (as boiling point increases with increasing pressure). Similarly, inclusion of a throttling valve at the channel inlet may require a larger pump (larger driving pressure head) to accommodate the increased pressure drop. Because of these adverse side effects, significant effort has been devoted to *Knowledge of Operating Boundaries*, or understanding what operating conditions may lead to Ledinegg instabilities in a given system.

The most straightforward method employed to gain *Knowledge of Operating Boundaries* is use of ‘Onset of Flow Instability’ (OFI) correlations. As described in preceding subsections, the OFI point is the local minimum in the internal pressure drop versus flowrate characteristic curve. Correlations for this point allow system designers and/or operators to know, for all other

operating conditions held constant, the minimum mass velocity allowable for the system to remain on the positive-slope region of the internal characteristic curve (thus avoiding the potential for Ledinegg instability).

One of the earliest works to provide an OFI correlation was that of Whittle and Forgan [40] and, as such, their work has influenced many subsequent investigators. One of the best, most recent examples is the work of Lee *et al.* [43]. They provided experimental evidence their system was susceptible to Ledinegg instability, generated a database of conditions where the onset of Ledinegg instability was observed, evaluated prior correlations for OFI, and presented a new correlation of their own. Figure A.4(c) provides a plot of data reduction used to generate their new correlation, including data for three different gap spacings ( $b$ ) in their rectangular boiling channel and statistics for the curve fit performed.

Many authors generated databases of OFI points, evaluated common correlations, and even proposed new correlations to best fit existing results. Table A.3 presents much of the relevant work regarding experimental determination and correlation of OFI points. All works included have utility, but those of Whittle and Forgan [40], Siman-Tov *et al.* [276], Stelling [278], Kennedy [279], and Lee *et al.* [43] are strongly recommended.

The other common method for gaining *Knowledge of Operating Boundaries* involves formulating a detailed model for internal system pressure drop, such as the previously mentioned work by Ishii and Fauske's [270] on natural circulation. One early example of this approach may be found in the work of Achard *et al.* [287]. Their approach (which follows that established by earlier works in the field, including Ishii [75] and Yadigaroglu [49]) involves formulating equations of motion within the heater, including both single-phase and boiling regions. By non-dimensionalizing these equations, several key dimensionless numbers appear, including:

$$Eu = \frac{\Delta P}{\rho_f U_f^2}, \quad (\text{A.11})$$

$$Fr = \frac{U_f^2}{gL_H}, \quad (\text{A.12})$$

$$\mathcal{L} = \frac{fL_H}{2D_h}, \quad (\text{A.13})$$

and

$$N_{sub} = \frac{v_{fg}(h_f - h_i)}{v_f h_{fg}}, \quad (1.1)$$

where  $Eu$  is Euler number,  $Fr$  Froude number,  $\Lambda$  friction number, and  $N_{sub}$  subcooling number.

By linearizing their equation of motion and applying the D-partition method (determining roots of governing equations as a function of operating parameters, allowing presentation of stability bounds for varying conditions), they generate information on stability of the boiling system for different ranges of operating conditions. This approach is similar to that applied in control theory for determining stability/instability of dynamic system controls.

One of the most common ways this information is utilized is through formulation of ‘stability maps’. One of the maps generated by Achard *et al.* [287] is shown in Fig. 4(d), consisting of a plot of friction number versus subcooling number, and including boundaries showing what combinations of conditions will lead to stable or unstable operating conditions. They explicitly identify the region pertaining to Ledinegg instability, which, for the system they modeled, corresponds to very high friction numbers. Other unstable regions identified ( $D_2$ ,  $D_3$ ,  $D_4$ ) likely correspond to the onset of Density Wave Oscillations (DWOs); these will be discussed in more detail later, but for now it should be mentioned other researchers analytically show Ledinegg instability as the 0-frequency limit of DWOs [288].

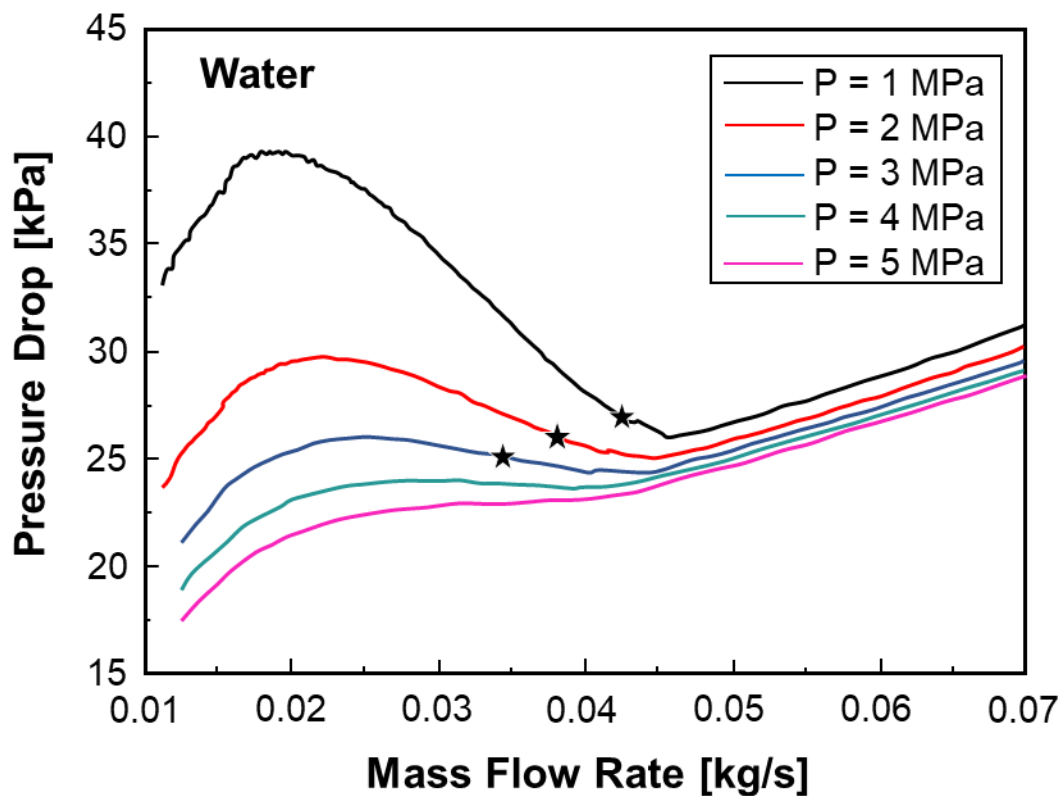


Figure A.4: Avoidance of Ledinegg instability may be achieved through elimination of the negative slope of the boiling curve as shown in (a) (adapted from Genglei *et al.* [273]) which may result in appreciable improvements in CHF values (b) as seen by Mishima *et al.* [269]. Also shown are methods for avoiding operating conditions where Ledinegg instability is likely to occur (negative-slope region), including (c) correlation for Onset of Flow Instability (OFI), adapted here from Lee *et al.* [43], and (d) stability maps, adapted here from Achard *et al.* [287].

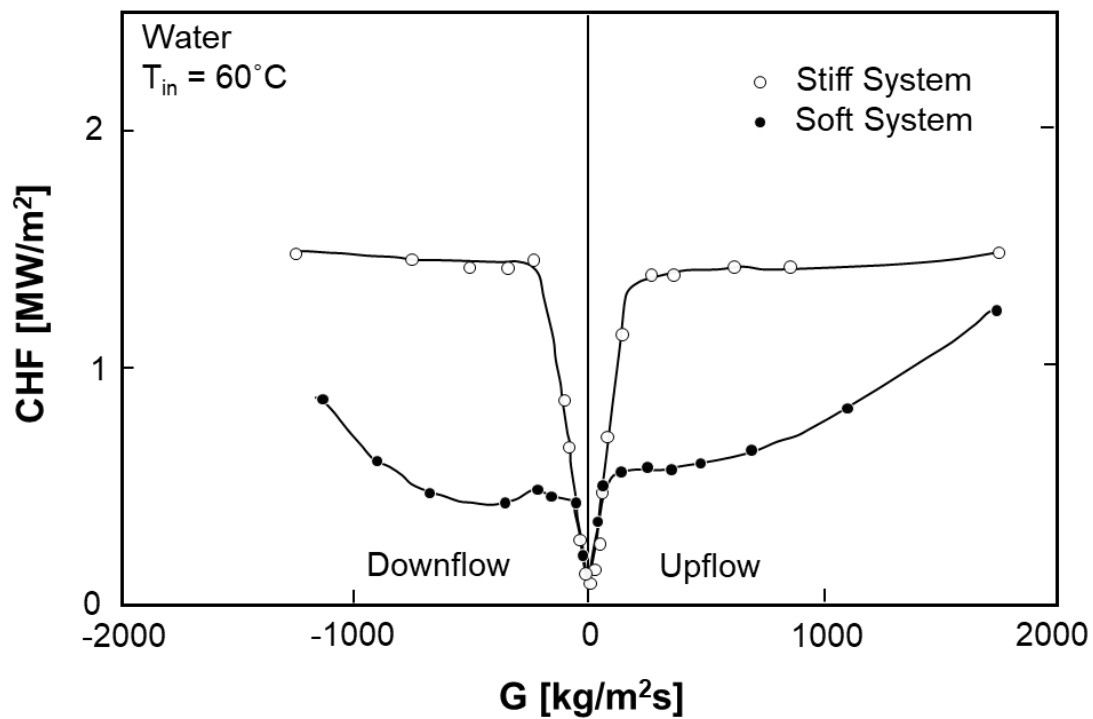


Figure A.4 (b).

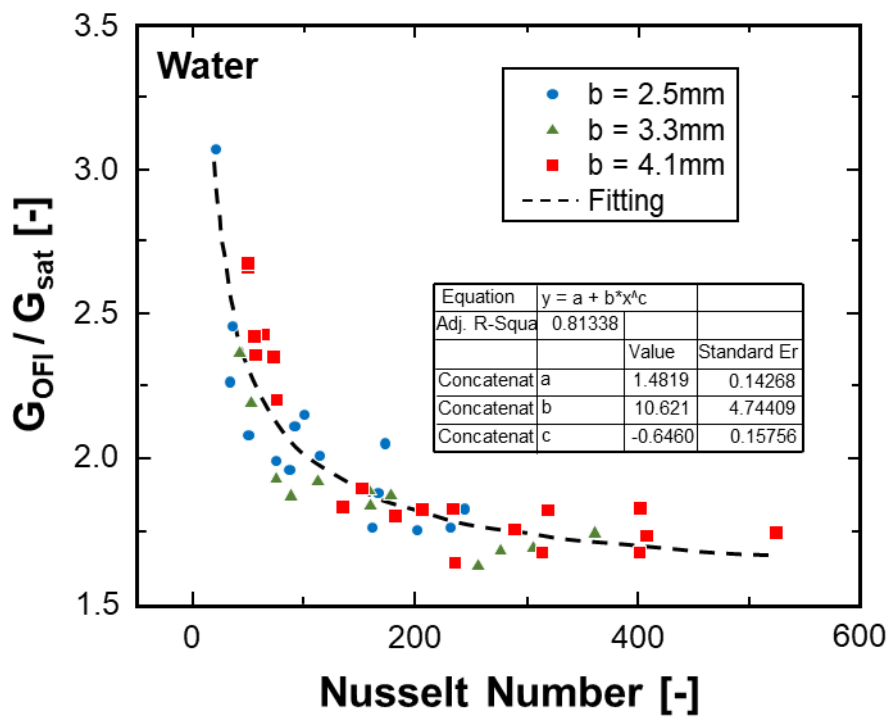


Figure A.4 (c).

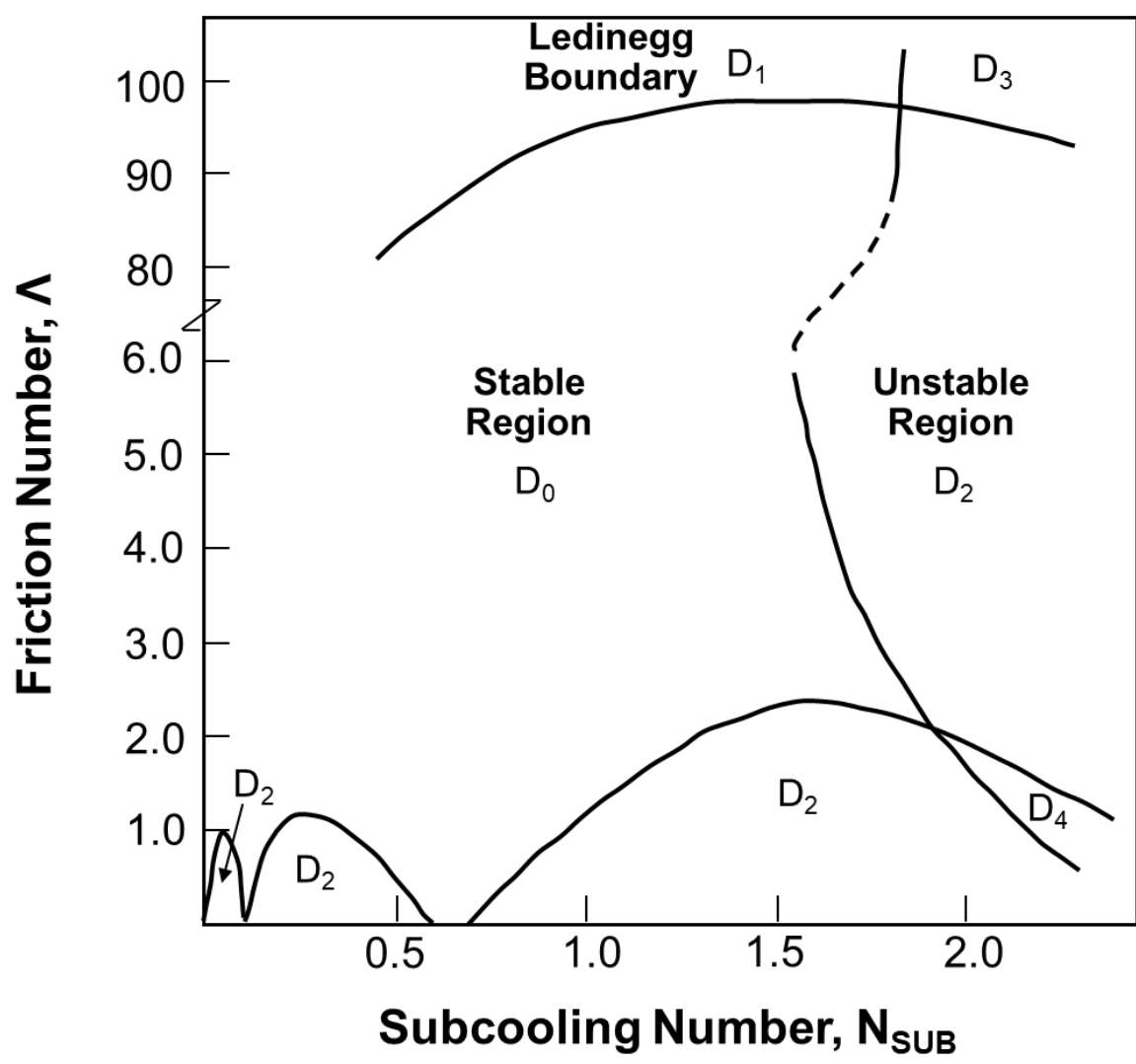


Figure 5.4 (d).

Table A.3: Works dealing with OFI correlations.

Authors	Correlation	Correlation(s) Evaluated	Comments
Whittle & Forgan [40], 1967	$R = \frac{\Delta T_c}{\Delta T_{sat}} = \frac{1}{1 + \eta / (L_H / D_H)}$ $\eta = 25, \Delta T_{sat} = T_{sat} - T_{in},$ $\Delta T_c = T_{out} - T_{in}$	Whittle & Forgan [126]	Investigated subcooled water flowing in narrow ( $L_H/D_H = 94.5, 83, 100, 191, 95$ ) channels. Vertical upflow orientation. Show direct evidence of Ledinegg instability, tabulate results for OFI point.
Saha & Zuber [274], 1974	$St = \frac{q''}{\rho_f c_{p,f} U_f (T_{sat} - T_{f,fd})}$ $DT_{sub,OSV} = T_{sat} - T_{in} = 0.0022 \frac{q'' D}{k_f}, \text{ for } Pe \leq 70,000$ $DT_{sub,OSV} = T_{sat} - T_{in} = 154 \frac{q''}{Gc_{p,f}}, \text{ for } Pe > 70,000$ <p><math>U_f =</math> Liquid Velocity,  <math>T_{f,fd} =</math> Temp. @ fully developed subcooled boiling</p>	NA	Correlation originally for OSV, commonly used in/with correlations for OFI. Included here for reference.
Yang <i>et al.</i> [275], 1993	Modified Saha-Zuber: $Q_{OFI} = \dot{m} c_{p,f} (T_{sat} - T_{in}) \left[ 1 + \frac{0.25 D_h}{St L} \right]^{-1}$	Saha & Zuber [274]	Vertical downflow of water in annulus, one without ribs (73.64-mm OD, 59.61-mm ID, 3.66-m length), and one with ribs (73.46-mm OD, 59.61-mm ID, 3.66-m length).
Siman-Tov <i>et al.</i> [276], 1995	Proposed a modification to the Saha and Zuber correlation to account for inlet subcooling: for $Pe > 70,000$ : $St_{OFI} = \frac{q''_{OFI}}{G_{OFI} c_{p,f} (T_{sat} - T_{in})} = 0.0065 h_{sub} = 0.0065 \left[ 0.55 + \frac{11.21}{T_{sat} - T_{in}} \right],$ for $Pe \leq 70,000$ : $Nu_{OFI} = \frac{q''_{OFI} D_h}{k (T_{sat} - T_{in})} = 455 h_{sub} = 455 \left[ 0.55 + \frac{11.21}{T_{sat} - T_{in}} \right],$	Costa [277], Whittle & Forgan [40], Saha & Zuber [274], Siman-Tov <i>et al.</i> [276]	Vertical upflow of water in a single channel, 507-mm long, 12.7-mm wide, and 1.27-mm gap. Include 'soft' and 'stiff' configurations to show cases with and without Ledinegg instability. Used a database from authors in the 1950's and 1960's to develop and evaluate their correlation. Found it was necessary to account for high inlet subcooling in their correlation.
Stelling <i>et al.</i> [278], 1996	$Q_{ratio} = \frac{q'' \pi DL}{\dot{m} c_{p,f} (T_{sat} - T_{in})} = \frac{1}{\left( 1 + 0.25 \left[ St_{OSV} (L_H / D_H) \right] \right)^{-1}}$ $St_{OSV} = 0.0065 \text{ for } Pe \geq 70,000 \text{ (Saha \& Zuber [88])}$ $Pe = Re Pr = \frac{r_f U_f D_H}{m_f} Pr$	Stelling <i>et al.</i> [278]	Vertical downflow of water in stainless-steel and Inconel tubes. Tube diameters of 25.4, 19, 15.5, 9.1, 28, 15.2, and 15.8 mm used.

Table A.3 Continued.

<p>Kennedy <i>et al.</i> [279], 2000</p>	$q''_{OFI} = 0.9q''_{sat} = 0.9 \frac{GA(h_f - h_{in})}{p_H L_H}$ $G_{OFI} = 1.11G_{sat} = 1.11 \frac{q'' p_H L_H}{A(h_f - h_{in})}$	<p>Saha &amp; Zuber [274], Kennedy <i>et al.</i> [279]</p>	<p>Water flow through 1.17-mm and 1.45-mm diameter tubes, 16-cm heated length. Horizontal flow.</p>
<p>Yeoh <i>et al.</i> [280], 2004</p>	$\alpha_{out,OFI} \sim 0.1$	<p>None</p>	<p>Compare model predictions with experimental results from CEA-Grenoble. Vertical upflow, 600-mm heated length, 38-mm wide, 3.6-mm deep, water flow.</p>
<p>Wang <i>et al.</i> [42], 2011</p>	<p>Proposed modification technique for existing correlations (only applied for OSV correlations) to account for single-sided heating configuration. This involved multiplication by ratio of wetted to heated perimeters.</p>	<p>Kennedy <i>et al.</i> [279]</p>	<p>Vertical upflow of water in 470-mm long, 40-mm wide, 3-mm deep channel. Note OFI may be predicted well by transition from Bubbly to Bubbly-Churn flow regime at channel exit. Should be noted they define OFI as location where mass flowrate fluctuations become larger with increasing flowrate.</p>
<p>Lee <i>et al.</i> [43], 2013</p>	$G_{OFI} = G_{sat} \left[ 1.48 + \frac{10.6}{Nu^{0.65}} \right]$ $Nu = \frac{q'' D_h}{k_f \Delta T_{OSV}}$ $\Delta T_{OSV} = T_{sat} - \left( T_{in} + \frac{p_H L_H q''}{Ac_{p,f} G_{OSV}} \right)$	<p>Whittle &amp; Forgan [40], Saha &amp; Zuber [274], Kennedy <i>et al.</i> [279], Lee <i>et al.</i> [43]</p>	<p>Vertical downflow of water through a narrow rectangular channel 40-mm wide, 350-mm long, with gap sizes of 2.5-mm, 3.3-mm, and 4.1-mm.</p>
<p>Al-Yahia <i>et al.</i> [281], 2018</p>	<p>For constant flowrate and varying heat flux:</p> $q''_{OFI} = q''_{sat} \left[ 0.8 \left( \frac{p_H}{p_w} \right) \left( \frac{P}{1.12} \right)^{0.4} \right]$ <p>where <math>P</math> is pressure in bar, <math>p_H</math> is heated perimeter, and <math>p_w</math> wetted perimeter.</p> <p>For constant heat flux and varying flowrate:</p> $G_{OFI} = G_{sat} \left[ 1.25 \left( \frac{p_w}{p_H} \right) \left( \frac{1.12}{P} \right)^{0.4} \right]$	<p>Whittle &amp; Forgan [40], Kennedy <i>et al.</i> [279], Unal <i>et al.</i> [282], Lee <i>et al.</i> [43], Bowring [283], Saha &amp; Zuber [274]. Included modified predictions similar to Wang <i>et al.</i> [42].</p>	<p>Vertical upflow of water in a 566-mm long, 54-mm wide, 2.35-mm tall rectangular channel. Should be noted they define OFI as location where pressure fluctuations become larger with increasing heat flux/flow rate. Declared OSV is a good indicator of OFI, used several OSV correlations (Unal [282], Saha &amp; Zuber [274], Bowring [283]).</p>

Table. A.3 Continued.

<p>Lu <i>et al.</i> [284], 2019</p>	$N_{pch,OFI} = N_{conf}^{-0.24} \left[ 4.84 N_{sub}^{0.60} + 1.98 We^{-0.84} \left( \frac{\rho_f}{\rho_g} \right)^{0.64} \right],$ $N_{pch} = \frac{Q}{GA_c h_{fg}} \frac{\rho_f - \rho_g}{\rho_g}, \text{ is phase change number,}$ $N_{sub} = \frac{c_{p,f} \Delta T_{sub}}{h_{fg}} \frac{\rho_f - \rho_g}{\rho_g}, \text{ is subcooling number}$ <p>and <math>We = \frac{\rho_f u_f^2 D_h}{\sigma}</math> is Weber number.</p>	<p>Lu <i>et al.</i> [284], Leng [285], Zhou [286]. Original references for Leng [285] and Zhou [286] not accessible.</p>	<p>Define OFI as the point past which significant flow oscillations are observed. Appears (from experimental results) to sometimes correspond to Ledinegg followed by DWO.</p>
-------------------------------------	---	--	--

Key to note when attempting to formulate and/or use existing stability maps is the 2-D nature of the maps, while the problem depends on four dimensionless groups (commonly Eqs. (A.11)-(A.13), (1.1), although sometimes more depending on model formulation). This means stability maps formulated for a specific test fluid, test section, and operating conditions rarely offer utility when any of these parameters is changed. Because of this, stability maps are not generally applicable design tools. Rather, it is the modeling and stability analysis approach that may be broadly applied, resulting in specific stability boundaries for individual systems.

This analytic approach to determine stability limits is very prolific in existing literature. Many works have taken a similar approach for conventional macro-channel tubes (modelled using a constant pressure drop assumption to mimic that in banks of tubes) [41,63,287-297], natural circulation driven systems [270,298-300], systems with supercritical flows where temperature-dependent density variations allow flow to be modelled as pseudo-multiphase [301-306] (recently augmented with CFD predictions [307,308]), natural circulation driven supercritical systems [309], and parallel micro-channel heat sinks [52,273,310-311]. Although comparatively little work has been performed investigating Ledinegg instability in parallel micro-channel heat sinks, their proliferation in recent years warrants a short discussion on their potential differences compared to traditional macro-channel systems (where boiling occurs in tubes designated as macro-channels based on criteria in section A.1.3).

#### A.2.2.4 Differences in Micro-Channel Systems

As discussed in sections A.2.2.1 and A.2.2.2, Ledinegg instability is a system level instability, meaning it depends on interaction between external and internal system characteristics to manifest. Explanations of internal and external pressure curves and how they may interact to yield Ledinegg instability are applicable to single micro-channels as well as parallel micro-channel heat sinks, and the same approaches for mitigation and avoidance outlined in section A.2.2.3 may be successfully utilized to avoid encountering this instability.

Some recent evidence suggests, however, that determination of external pressure curves for systems using parallel micro-channel heat sinks may not be straightforward. In the case of parallel macro-channel tubes, it is common to use a constant pressure drop assumption across the tube bank, but in the case of parallel micro-channel heat sinks, Zhang *et al.* [310] found increasing the number of parallel micro-channels increases system susceptibility to Ledinegg instability.

They stated that, for a system with a constant displacement pump and a parallel micro-channel heat sink, the external pressure curve will be neither zero (constant pressure drop, case 3 in Fig. A.2(d)) nor infinite (positive displacement pump, case 1 in Fig. A.2(d)), but somewhere in between depending on heat sink design.

Although only a single source, their experimental evidence is very compelling, and it is recommended future research be performed to address the exact impact of micro-channel heat sink design on external pressure curve definition.

#### A.2.2.5 Concluding Remarks on Ledinegg Instability

The preceding subsections highlight the impressive amount of research work focused on Ledinegg instability available in literature. Both practical guidelines for avoiding the instability (inlet throttling, operating at higher pressure) and advanced predictive tools (OFI correlations, full system models) are available to assist system designers in understanding and mitigating potential adverse effects of Ledinegg instability.

In particular, development of full system models is thought to be the safest way to fully understand and avoid Ledinegg instability in any given system. After review of prior works, three key areas (other than intended application) may be used to distinguish between full system models:

- 1) *Model Formulation* – When establishing the governing equations, do the models use Homogeneous Equilibrium Model (HEM) assumptions (most common), Drift-Flux model assumptions, take a purely correlation based approach, or use some other method for expressing relevant pressure drop terms?
- 2) *Method for Evaluation/Determination of Stability* – Do the models linearize the system and undertake stability analysis (frequency domain analysis)? Or, do they directly evaluate steady-state conditions to generate an internal pressure characteristic curve and look for the OFI point (time domain analysis)?
- 3) *Comparison with Experimental Results* – Were any experimental results used for evaluation? This is arguably the most important aspect to look for, as unverified model predictions do little to reinforce confidence in the model.

Overall, all studies referenced above offer valuable information on modeling approaches for determining system susceptibility to Ledinegg instability, but those that do the best job of including experimental verification are works by Ishii [270], Zhang [310], and Shin [52].

Finally, to conclude this section dealing with Ledinegg instability, many of the studies referenced here include findings either not reported in most literature or in direct contradiction with statements made in other places. These are outlined in Table A.4.

Table A.4: Uncommon findings related to Ledinegg Instability.

Finding	Implications/Relevance	Relevant References
Ledinegg instability may occur on the positive slope portion of the internal pressure characteristic curve for sufficiently high subcooling.	This is in contradiction to the common understanding of how Ledinegg instability occurs (outlined in Section 2.2.2). No experimental verification of this has been found in literature by the present author.	Fowler [289], 1978
Care must be taken when determining an external pressure curve to apply. In the case of a bank of parallel tubes, a constant pressure drop assumption may be applied and behavior in the tube analyzed. In the case of natural circulation, flowrate and pressure drop will depend on pressure drop throughout the loop, and the entire system (including boiling and condensation lengths) must be included in analysis. Systems driven by centrifugal pumps also must be analyzed in their entirety. Systems driven by constant-displacement pumps may be assumed not to experience Ledinegg instability, except in the case of parallel micro-channel heat sinks, where behavior becomes more complicated (see next row).	It is important to understand how any specific system is similar to / different from those present in other studies. Valid modeling applied on an incorrectly defined system may lead to incorrect predictions of stable or unstable behavior.	Ishii & Fauske [270], 1983 Lahey & Podowski [47], 1989 Zhang <i>et al.</i> [310], 2009
Ledinegg instability in parallel micro-channel heat sinks may require analysis different from that for traditional boiling systems. Stability boundaries clearly depend on the number of parallel channels, and the external pressure curve (as seen by the micro-channel heat sink) is thought to depend on specific heat-sink operating conditions.	As micro-channel heat sinks are increasingly becoming the go-to solution for evaporation in a variety of applications, additional experimental investigation of Ledinegg instability in these systems is necessary. Internal pressure curve modeling is understood, but the dependence of the external curve (as seen by the heat sink) on heat sink geometry must be studied.	Zhang <i>et al.</i> [310], 2009 Genglei <i>et al.</i> [273], 2012 Shin <i>et al.</i> [52], 2017
Commonly accepted theory indicates it is possible for Ledinegg instability to lead to a higher flowrate (trending back towards single-phase liquid flow) or a lower flowrate (often leading to premature CHF). Experimental sources seem to indicate a decrease in flowrate is much more common than an increase.	This is likely related to the location on the internal pressure curve where the instability manifests. If the external pressure curve is flat, Ledinegg instability may occur at the OFI point, and only one stable solution exists (lower flowrate). Additional exploration is needed for cases with external pressure curves of intermediate slope (which may yield two stable solutions after flow excursion) to see if a bias still exists.	Theory: Ruspini <i>et al.</i> [296], 2010 Experiments: Whittle & Forgan [40], 1967 Mishima <i>et al.</i> [269], 1985 others

### A.2.3 Boiling Curve Hysteresis and Vapor Burst

Unlike the prior section, which was concerned primarily with OFI, Boiling Curve Hysteresis and Vapor Burst are both boiling instability modes which occur at the ONB point of the curve shown in Fig. A.2(a). As vapor burst is (when it manifests) a byproduct of boiling curve hysteresis, boiling curve hysteresis will be discussed first.

Boiling curve hysteresis commonly occurs with low contact angle combinations of fluid and heated surface in a variety of boiling configurations [312-324], and may be simply described as resulting from difference in wall superheat required for nucleation to begin versus that at which it ends (it takes a higher wall superheat to start nucleation than the heat flux wall superheat at which nucleation ends). The main corporate for hysteresis is flooding of surface cavities by low contact angle fluids, which deprives the cavities from viable vapor embryos capable of initiating the bubble nucleation. This would require increasing the wall superheat further to ultimately initiate properly sized embryos and commence nucleation. But, once the nucleation occurs, it propagates violently across the wall, greatly improving heat transfer and resulting in a sharp decrease in the wall superheat. This process leads to a ‘hysteresis’ in boiling curves traced with ascending versus descending heat fluxes, manifest near the incipience point. An example of this from Heindel *et al.* [312] (who investigated flow boiling of FC-72) is shown in Fig. A.5(a).

In the case of a well de-gassed low contact angle fluid with a relatively low heat flux applied over a large area, it is possible to encounter Vapor Burst. In this case, suppression of nucleation associated with boiling curve hysteresis leads to ‘liquid superheat’, where bulk fluid significantly exceeds saturation temperature at local pressure. Incipient boiling is now accompanied by violent flashing of a large fraction of liquid to vapor, which can significantly affect system pressure. Although not as common as boiling curve hysteresis, documented accounts of this phenomenon do exist [325-327], and an example is shown in Fig. A.5(b) corresponding to flow boiling of FC-72 through a circulation heater [244,328-329]. Vapor burst manifestation in quenching and nuclear fuel cooling represent a field of study on their own [330,331].

Both boiling curve hysteresis and vapor burst are commonly treated with practical solutions for two-phase system design and operation, both through awareness of their potential to occur and operation away from conditions that may cause them to impact operation. Unlike Ledinegg instability, detailed design tools are not available for these two phenomena, and more information

on fundamentals of boiling incipience is warranted for development of reliable predictive models for both.

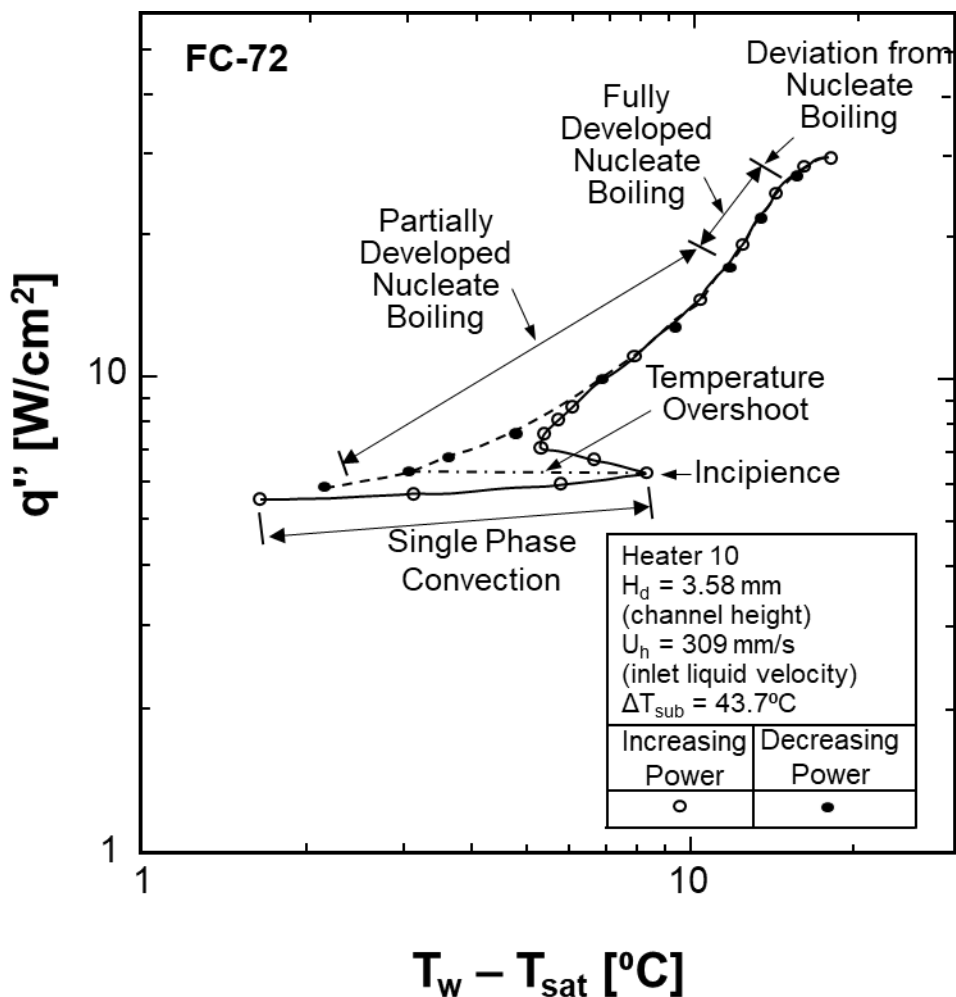


Figure A.5: Examples highlighting key features of boiling curve hysteresis. (a) Differences in ascending and descending boiling curves for flow boiling of FC-72 (adapted from Heindel *et al.* [312]). (b) ‘Vapor Burst’ phenomenon associated with flow boiling of FC-72 [244,328-329]).

The sharp pressure increase in (b) due to rapid vaporization of a significant mass of liquid is observable in most boiling configurations with well de-gassed, low contact angle working fluids.

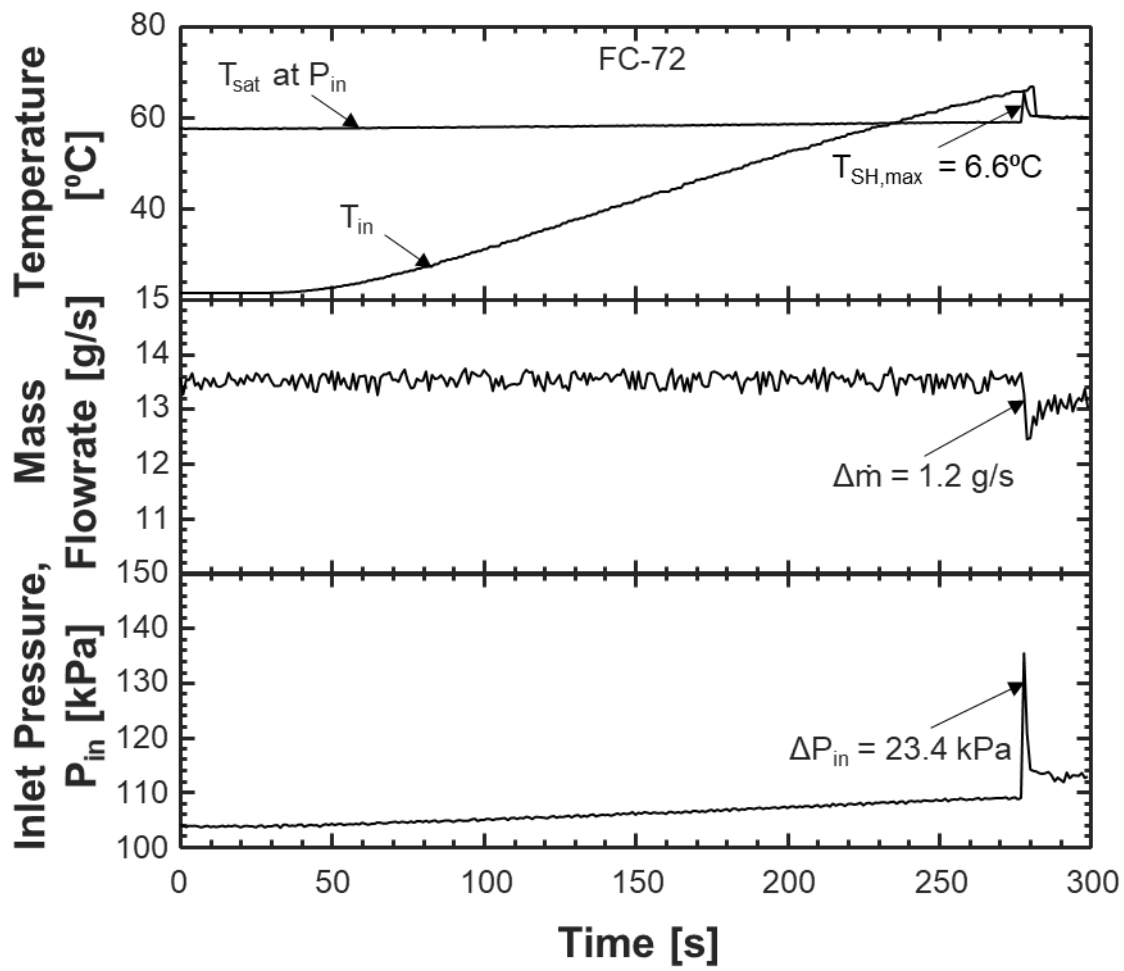


Figure A.5 (b).

#### A.2.4 Flow Regime Transition Instability

Mention of flow regime transition instability is often a source of confusion in two-phase instability literature due to three key reasons: 1) the ability for it to manifest as either a static or dynamic instability mode, 2) the differences present between flow regimes in macro- versus micro-channels, and 3) whether it is a unique, self-sustaining oscillatory mode, or a byproduct of other instability(s). Following are key observations concerning each:

*Static versus Dynamic:* Flow regimes are an inherent part of two-phase flow that distinguish it from traditional single-phase flows. Depending on geometry, working fluid, phase velocities, mass fractions of vapor and liquid, and other factors, distribution of liquid and vapor phases can differ greatly. For example, a small increase in heat flux may lead to slightly larger quality, transitioning flow from *slug* to *annular* (thus a small perturbation in operating conditions leads to a large change in flow behavior), the latter having distinctly different pressure drop and heat transfer coefficient than the former. This static-type instability is fairly well predicted by existing flow regime maps available in literature.

In the dynamic type manifestation, changes in operating state may lead to a self-sustaining oscillation between operating points. Nayak *et al.* [332] provided a compelling description for this, but the majority of literature indicates dynamic changes in flow regime are in fact a response to other instability modes [50,333-335].

*Macro- versus Micro-Channels:* Due to confinement effects described in section A.1.3, it is possible for single bubbles to occupy the entire cross-section in micro-channels, leading to abrupt transitions between flow regimes due not to bulk-flow changes, but to single-bubble formation and expansion. Lee *et al.* [336] discussed transient changes in flow regime within a micro-channel extensively in their recent study. Other authors have also addressed these transient changes for micro-channels [73,337], but it appears these changes in flow regime are largely attributable to Density Wave Oscillations in micro-channels (to be discussed in a later section).

*Unique Instability versus Byproduct of Other Dynamic Instability(s):* This item has been touched on in the preceding two points, and while conclusive proof is not available in literature, most studies indicate transient changes in flow regime are attributable to other dynamic instabilities. This means flow regime transition should not be considered a unique dynamic instability type, although changes in flow regime will be discussed along with other dynamic instabilities in the next section.

### A.3 Dynamic Instabilities

Unlike *Static Instabilities*, which involve a one-time excursion from an unstable operating point to a new, stable condition, *Dynamic Instabilities* are best characterized by continuous cycling between marginally unstable operating points. In their seminal review, Boure *et al.* [50] used frequency ranges to help classify *Dynamic Instabilities* into different classes. Frequency information is one of the most important pieces of information (along with amplitude) for evaluating potential impact of different dynamic instability modes, but is not a reliable method for classifying different instability modes. In fact, 46 years of continued scientific investigation since the publication of Boure *et al.*'s review has shown frequency of *Density Wave Oscillations* in one system may be similar to *Pressure Drop Oscillations* in another, which in turn may be similar to *Parallel Channel Instability* in a third system. Complicating matters is the potential for mechanically-induced vibrations (by fluid machinery, external factors, or otherwise) appearing alongside physical oscillatory phenomena.

The present section aims to provide physical descriptions of the underlying mechanisms behind common *Dynamic Instabilities*, allowing for classification based on cause (physical mechanisms) rather than effect (*i.e.*, frequency of oscillations). A summary of relevant experimental and analytic works on each instability mode will also be provided, and subsections will conclude with summaries of key findings and recommendations for new/continuing work.

#### A.3.1 *Density Wave Oscillations*

Commonly reported as the first dynamic instability mode investigated in two-phase flow literature [48], *Density Wave Oscillations* (DWOs), or *Density Wave Instability*, are sometimes referred to as *Flow-void Feedback Instabilities* [338] for reasons that will be explained shortly. Good discussions on the physical mechanisms for *Density Wave Oscillations* may be found in the works of Boure *et al.* [50] and Lahey and Podowski [47], but the present work will provide a slightly more descriptive approach to better illustrate how this oscillatory mode manifests.

Also, tying in with the discussion of flow regime transition instability in section 2.4, clear mechanistic differences have been observed for DWOs in macro-channels versus micro-channels, as well as for parallel- versus single-channel systems. Parallel-channel systems will be addressed

in a separate section on Parallel Channel Instability, while the present section will split study of DWOs in macro- and micro-channels into separate subsections.

#### A.3.1.1 Existence and Characteristics of Density Wave Oscillations in Macro-Channels

Figures A.6(a) and A.6(b) provide schematics and plots, respectively, outlining how DWOs occur in a simplified boiling system. A single channel subjected to constant pressure drop and constant heat flux boundary conditions is considered. Flow at the inlet has some constant subcooling level, meaning flow along the channel may be divided into single-phase and two-phase lengths ( $L_{1\phi}$  and  $L_{2\phi}$ ). At time  $t = t_0$ , the inlet velocity ( $U_{1\phi,in}$ ) is slightly perturbed (by  $\delta U$ ), as shown in Fig. A.6(a). The perturbation in velocity causes formation of a low-enthalpy (heat flux remains the same as velocity is increased, meaning local enthalpy has to decrease) wave that propagates downstream. At time  $t = t_1$ , this wave reaches the ‘boiling boundary’ separating the single-phase and two-phase regions. Due to its reduced enthalpy, the passage of this wave serves to move the boiling boundary downstream within the channel. As this wave continues through the channel, a new boiling boundary is established (time  $t = t_2$ ) and local void fraction is altered in its wake. This continues until the low-enthalpy wave exits the channel at time  $t = t_3$ .

At the same time, due to the significant delay in decrease of pressure drop in  $L_{2\phi}$  due to the delay in propagation of the low-enthalpy front, a high-enthalpy front is formed and moves along the channel (between  $t_1$  and  $t_2$ ) due to the now reduced velocity. As the initial low-enthalpy front moves out of the channel between  $t_2$  and  $t_3$ , the high-enthalpy front now causes the boiling boundary to shift upstream towards the channel inlet, and, at time  $t = t_3$ , the two-phase length is larger than it was initially (while another low-enthalpy front forms and begins moving along the channel).

Figure A.6(a) clearly captures the motion of these high/low-enthalpy fronts and their impact on boiling within the flow channel. In a single-phase, adiabatic case with constant pressure drop, any perturbation in velocity would be met by an increase in pressure drop, driving velocity back to its nominal value. In the present case, however, this reduction in inlet flow velocity occurs along with the low enthalpy wave reducing the boiling length  $L_{2\phi}$  and associated pressure drop  $\Delta P_{2\phi}$ . This, in turn, causes flow rate to attempt to increase, however, reduction in flowrate around time  $t = t_1$  causes the formation of a high enthalpy wave, which propagates through the channel and causes the two-phase length to increase once again, leading to the cycle repeating itself.

Schematics in Fig. A.6(b) show these changes in important flow-field parameters corresponding to the schematics shown in Fig. A.6(a), including ‘Desired’ and ‘Imposed’ pressure drop, which indicate how the fixed pressure drop channel will respond to changes in flowrate (*i.e.*, the increase in flow velocity at  $t_0$  causes desired pressure drop to increase as this will lead to a new stable condition, but the difference between desired and imposed means inlet velocity will decrease towards its nominal stable value). Only the first half of the entire oscillatory phenomenon is shown, spanning  $t_0 - t_3$ . These steps are followed by the inverse process mentioned above (the formation and motion of another low enthalpy wave through the system, leading to a shift in the boiling boundary upstream and associated changes in pressure drop components and flowrate).

The motion of these high and low enthalpy fronts through the channel occur at a wave-speed  $c_k$ . For single-phase flow, this is equal to the speed of sound within the fluid, but, for two-phase flow, it is difficult to define. This difference in propagation speed (exemplified in the differences between  $t_1 - t_2$  and  $t_2 - t_3$ ) is what allows DWOs to occur, and, for the two-phase portion of flow,  $c_k$  is commonly approximated as 1 – 1.5 times bulk liquid velocity. Because of this, the period (inverse of frequency) of DWOs is commonly 1.5 – 2 times liquid transport time (based on liquid inlet velocity) through the channel [47].

To expand on this, it is often said DWOs occur due to perturbations being amplified and resulting in oscillatory phenomena due to the two-phase portion responding out of phase with the single-phase portion of the channel (due to the differences in propagation speed). This requires  $\Delta P_{2\phi}$  to be of the same order as  $\Delta P_{1\phi}$ , as otherwise their changes will become closer to in-phase with one another and any perturbation will decay back to the initial value. Thermal inertia of heated surfaces, inlet/exit restrictions, local phase non-equilibrium (manifest differently for subcooled boiling versus saturated boiling), and a variety of other factors also influence whether a given operating point is stable to perturbations. These effects will be discussed further in the following subsections.

Finally, it should be noted here that the ‘flow-void’ feedback depicted in Fig. A.6(b) is only one feedback mechanism capable of leading to *Density Wave Oscillations*. In their classic experimental and analytic work, Fukuda and Kobori [80] reported five separate types of DWOs in their system, distinguished by the terms leading to instability. Their system included vertical and horizontal, adiabatic and diabatic sections, and they found acceleration in the heated section, friction in the heated section, friction in the riser section, gravity in the heated section and inertia

of single-phase fluid, and gravity in the riser section all could lead to unstable feedback mechanisms (DWOs).

Many authors choose to classify DWOs into 'Type-I' and 'Type-II', stating Type-I DWOs occur at low exit qualities (high flowrates for a fixed heat flux) and Type-II at high exit qualities (low flowrates for a fixed heat flux). The frequency with which this classification is used (particularly in nuclear-oriented investigations) warrants their acknowledgement, but in reality there are far more than two types of Density Wave Oscillations.

This concept will be revisited in subsections below, as the potential for complicated, atypical DWOs will be shown to relate to unique opportunities for unstable feedback mechanisms. For now, however, it is relevant to present standard experimental examples of DWOs taken from literature to help provide an understanding of key instability characteristics.

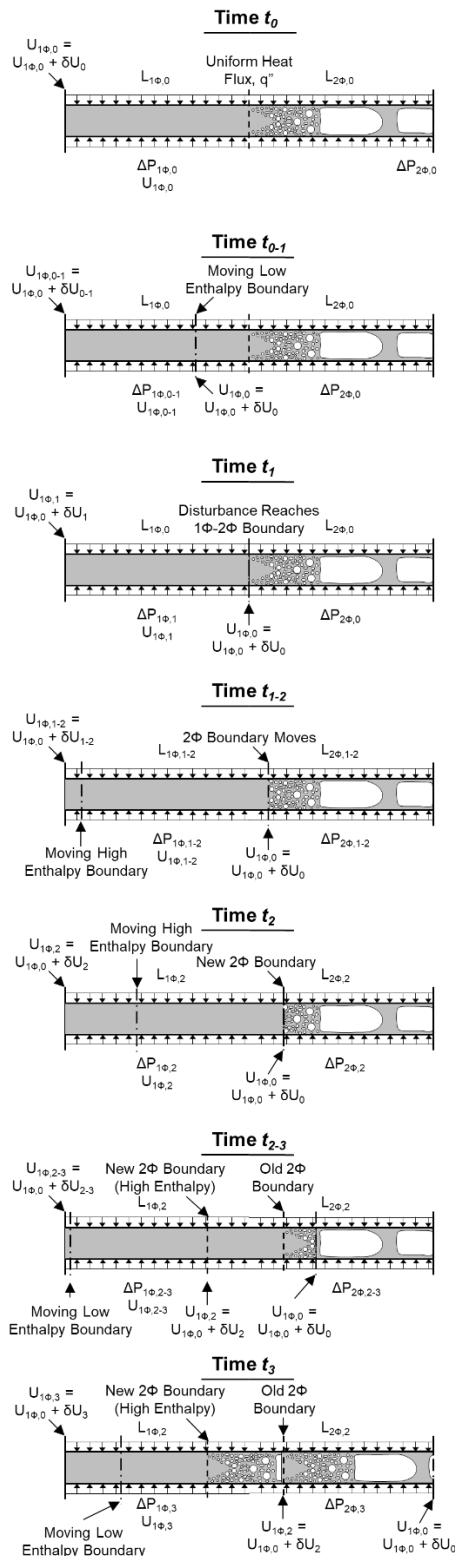


Figure A.6:: Illustration of simplified Density Wave Oscillation (DWO) process. Information corresponds to a half-cycle of the instability, and includes (a) schematics and (b) plots of representative parameters.

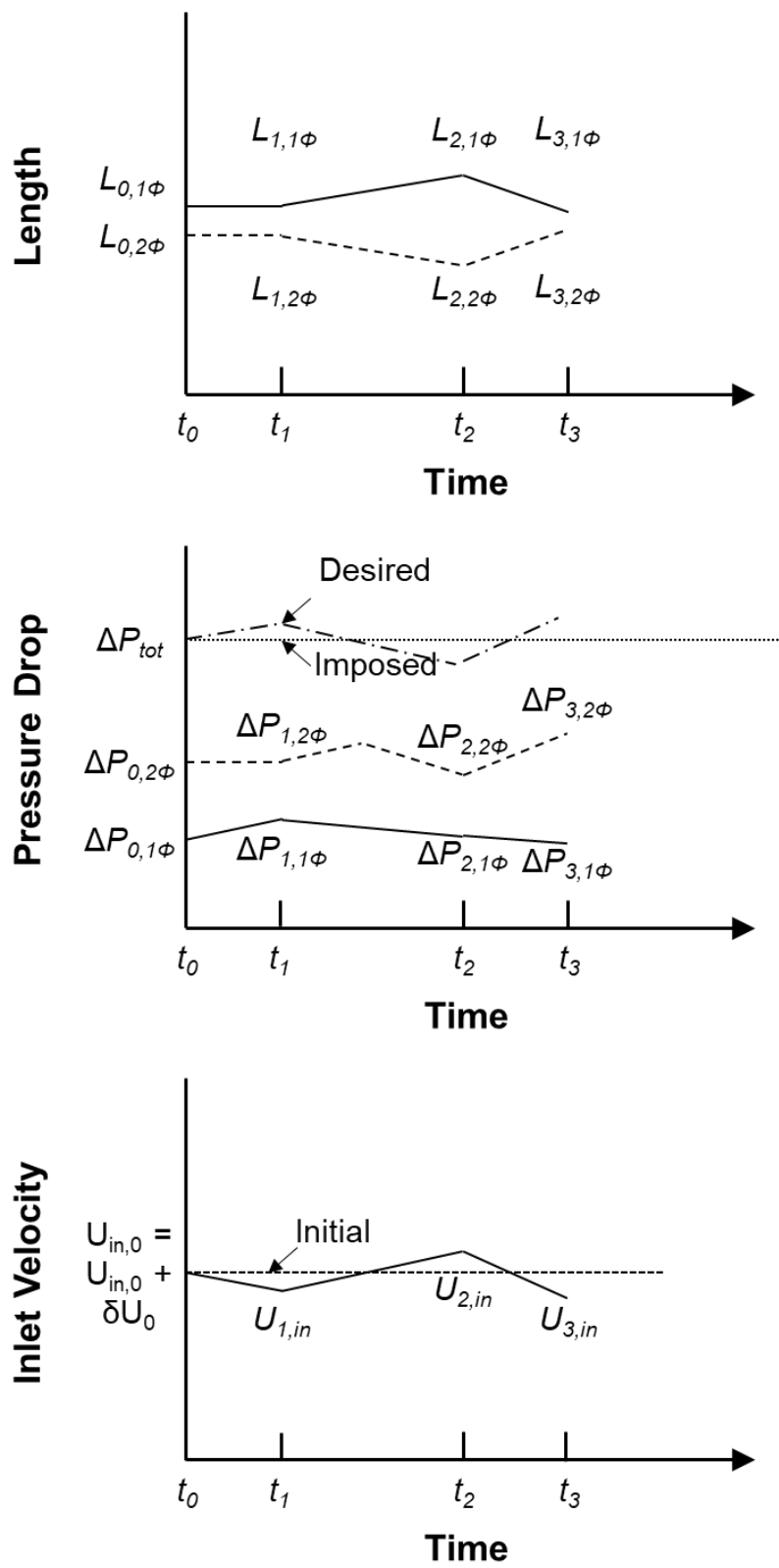


Figure A.6 (b).

### A.3.1.2 Existence and Characteristics of Density Wave Oscillations in Macro-Channels

Having provided a mechanistic basis for the existence of DWOs in classic macro-channels, examples of experimentally captured occurrences of DWO are provided in Fig. A.7. Figure A.7(a) shows DWO induced fluctuations in heater inlet pressure and flowrate captured by Dogan *et al.* [339] for vertical upflow of Freon-11. DWOs in their system had a period of 1-2 s (frequency of 0.5 – 1 Hz) depending on operating conditions.

It is also possible for DWOs to occur in response to other oscillatory modes. Figure A.7(b), adapted from Yuncu [62], shows DWOs (high frequency mode) superimposed on *Pressure Drop Oscillations* (PDOs, low frequency mode). These will be discussed in more detail in following subsections, but, for now, it is sufficient to note they serve to shift operation from the negative-slope portion of the system pressure drop curve (stable for DWOs, unstable for PDOs) to the low-flowrate, positive slope portion (potentially unstable for DWOs). This behavior is characterized in Fig. A.7(c), also taken from Yuncu [62].

Figure A.7(d), adapted from Mishima *et al.* [269], shows DWOs occurring after a Ledinegg excursion (again shifting system operation to the low flowrate, positive slope portion of the system characteristic curve). Amplitude of DWO-induced flowrate oscillations is seen to increase with increasing heat flux until CHF (burnout) is encountered.

Across the examples shown in Fig. A.7(a) – 7(d), it is important to note (1) the relative consistency of frequency and amplitude of DWOs for a given set of operating conditions, (2) the changes of frequency and amplitude of DWOs in response to changes in system operating conditions, and (3) the ability of DWOs to interact with other instability modes. These are all key facets of DWOs that will be explored further.

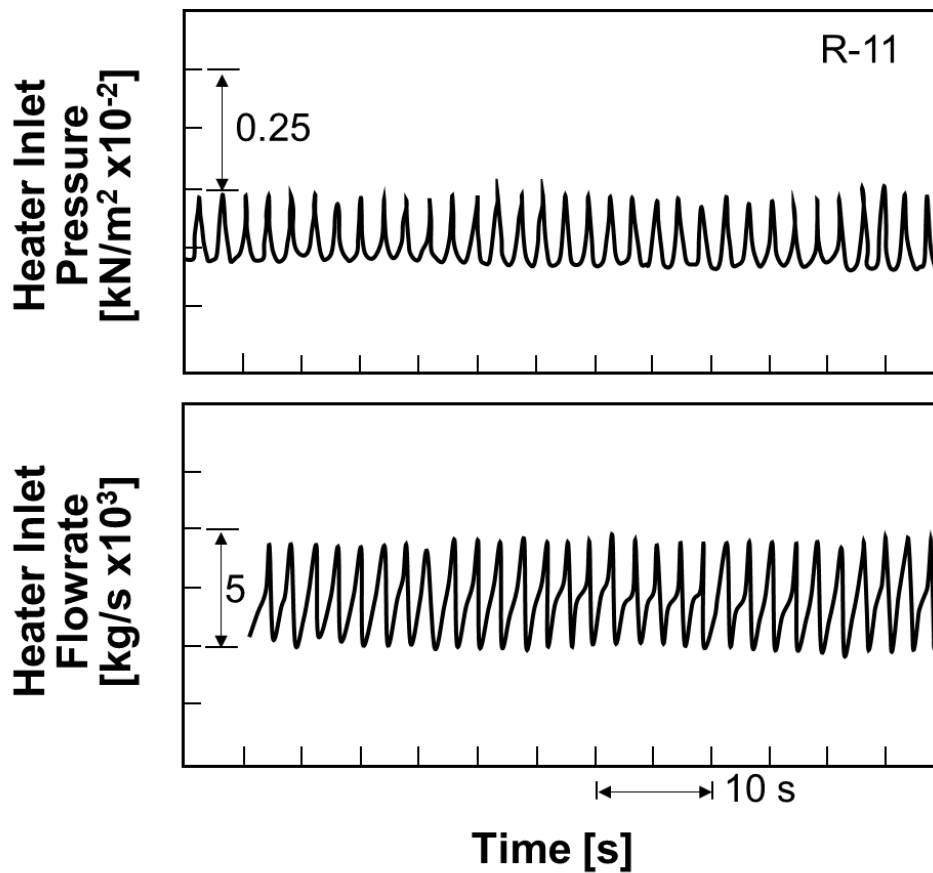


Figure A.7: Experimental examples of Density Wave Oscillations (DWOs), including (a) isolated DWOs, adapted from Dogan *et al.* [339], (b) DWOs induced by PDOs, adapted from Yuncu [62] with (c) superposition of PDO and DWO conditions on system pressure curves, also from Yuncu [62], and (d) DWO following Ledinegg instability, adapted from Mishima *et al.* [269].

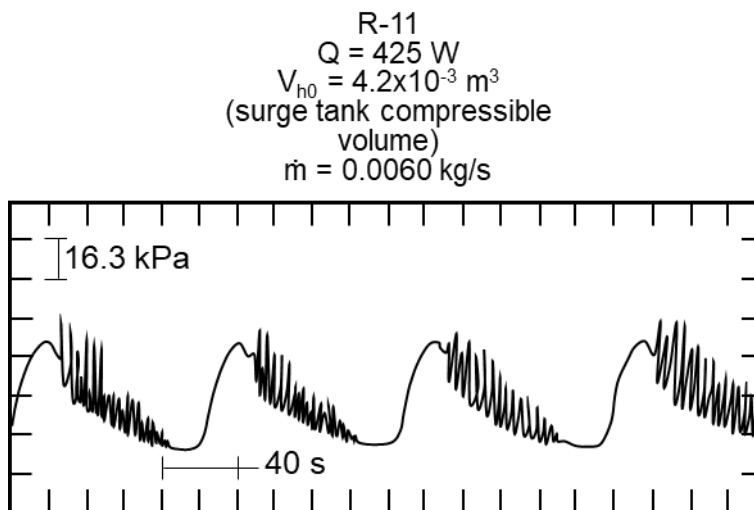


Figure A.7 (b).

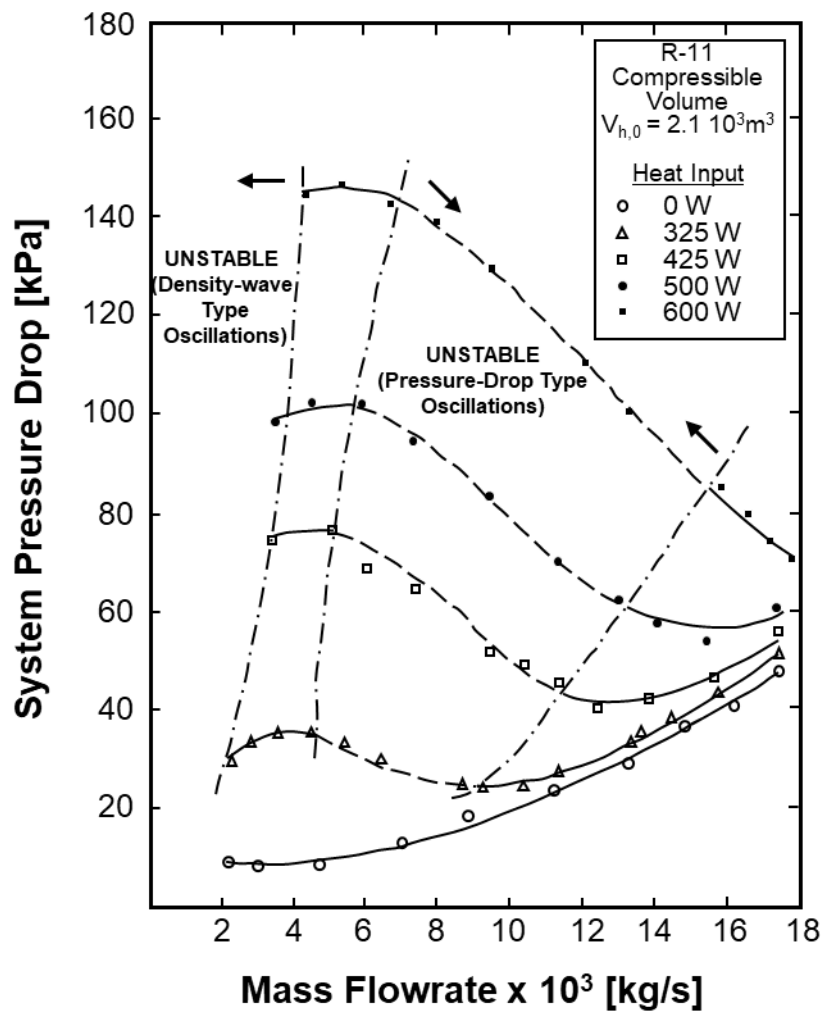


Figure A.7 (c).

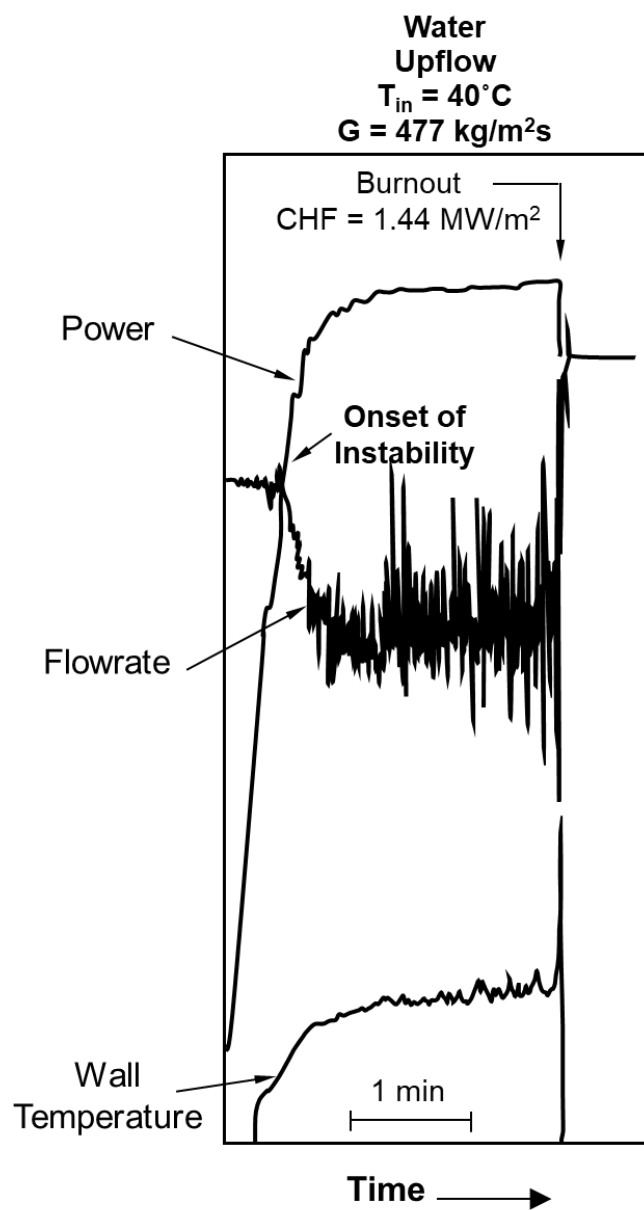


Figure A.7 (d).

Unlike Ledinegg instability, where the problem may be avoided by modifying the system to eliminate the negative slope portion of the internal characteristic curve, *Knowledge of Operating Boundaries* is the only option available for DWOs. Further, there are no simple correlations available for DWO stability boundaries (as were presented for OFI point associated with Ledinegg instability), as DWOs appear only for specific combinations of operating conditions dependent on a wider variety of factors. The only viable option for design tools capable of determining whether a system will experience DWOs are full system models (as discussed alongside the stability map of Achard *et al.* [287] in Fig. A.4 (d)). These are developed in exactly the same way as described for prediction of Ledinegg instability in section A.2.2, only now they are concerned not with what operating conditions fall on the negative slope portion of the boiling curve, but with what combinations of conditions will lead to unstable feedback mechanisms on the positive slope regions. This is typically determined in two ways: 1) transforming the governing equations into frequency domain and performing stability analysis (D-partition, Nyquist plots, *etc.*), or 2) directly solving the governing equations in time domain and determining for which operating conditions unstable oscillatory phenomena is observed.

One of the earliest works outlining an analytic approach to determining DWO stability boundaries for a given boiling system was provided by Ishii [75]. He presented his results in the form of a stability map [37], shown here in Fig. A.8(a), along with validation using experimental results of Solberg [78]. Ishii's use of phase change number,

$$N_{pch} = \frac{Q}{GA_c h_{fg}} \frac{r_f - r_g}{r_g}, \quad (1.2)$$

versus subcooling number  $N_{sub}$  (provided in Eq. (1.1)) became very popular as these two groups map possible operating conditions a fixed (meaning constant diameter, length, and working fluid) system may encounter.

Figure A.8(b) provides transient model results adapted from the work of Colombo *et al.* [340]. For a single boiling channel with a constant pressure drop boundary condition, Fig. A.8(b) shows how increases in heating power (leading to reductions in mass flowrate on the y-axis) eventually destabilize the system. By keeping track of which conditions lead to destabilizing the system, Colombo *et al.* [340] were able to use their transient model predictions to create stability maps similar to those of Ishii and Zuber [37].

It is important to recognize stability maps (and predictions of system stability in general) are only valid for given combinations of working fluid, test section length, diameter, boundary conditions, orientation, and others (typically governed by Froude number, confinement number, Euler number, friction number, *etc.*). Due to 2-D limitations associated with presentation of stability maps and the higher-dimensional nature of DWO stability problems, it is critical to understand individual stability maps are not generalizable design tools; it is the methodology used to develop them that may be applied to other systems to determine their stability.

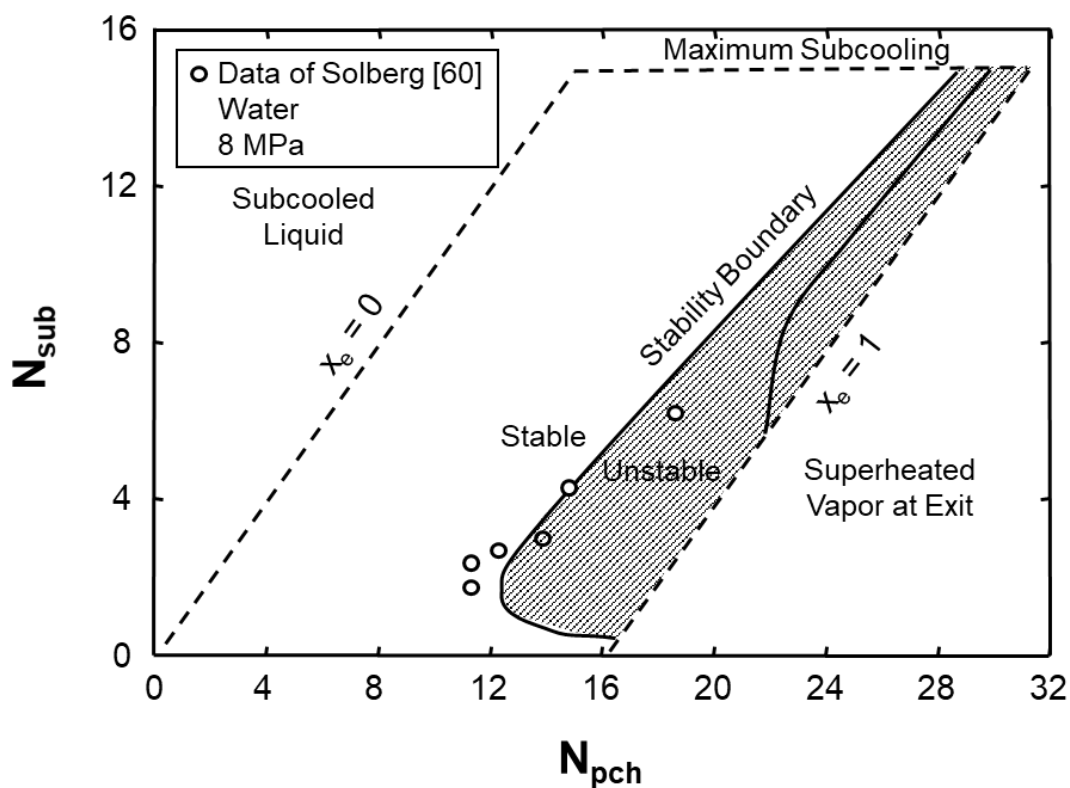


Figure A.8: Examples of results from analytic models used to determine under what conditions Density Wave Oscillations will occur in a given system: (a) stability map of Ishii and Zuber [37] and (b) transient model results of Colombo *et al.* [340].

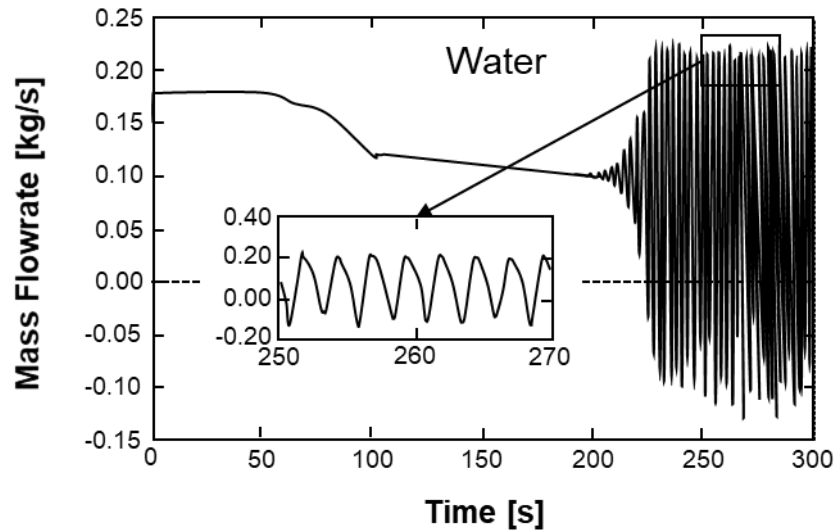


Figure A.8 (b).

Having provided some examples of experimental characteristics of DWOs and the main methodology used to model them, it is now useful to provide a full summary of existing literature on DWOs in macro-channels. A multitude of studies on DWOs exist in literature, so these will be grouped by experiment-focused, modeling-focused, and combination experimental-modeling studies, with care taken to point out particularly useful studies in each group. This subsection will conclude with a table outlining influences of different key operating parameters on DWO behavior.

Some of the best literature to begin understanding DWOs provides both high-quality experimental results and detailed analytic modeling of the instability mode. One of the earliest works providing both experimental and analytic results for DWOs comes from *Jain et al.* [341], who investigated boiling of water in a natural circulation loop. They compared their experimental results with models developed by Jones (frequency domain solution approach) [342,343] and Jahnberg (time domain solution approach) [344], and found that of Jones yielded better agreement with their experimentally determined stability boundaries.

Another early work came from Yadigaroglu and Bergles [49], who investigated flow boiling of Freon-113. Their work is notable for experimental and theoretical evidence of higher-order DWOs, or oscillations whose frequencies are multiples of the fundamental DWO mode.

Yuncu [62] provided another comparison of experimental and analytic instability results for flow boiling of R-11 in a horizontal channel. His work is notable for its inclusion of Pressure Drop Oscillations along with DWOs.

Other relevant works including both experimental and analytic investigation of DWOs include those of Saha *et al.* [345], Fukuda and Kobori [80], and Dogan *et al.* [339] for forced flow, Guanhai *et al.* [346] and Nayak *et al.* [347] for natural circulation, and Chen *et al.* [348] for cryogenic flow boiling.

Many other authors choose to focus primarily on experimental evidence of DWOs. These include studies on both forced convection [284,349-360] and natural circulation [361-363]. Of note among these are the studies of Sorum and Dorao [355] and Lu *et al.* [360] for their experimental evidence of the impact of DWOs on deteriorating heat transfer coefficient and CHF, respectively. Another high-quality experimental work from this group is that of Wang *et al.* [349], who studied DWOs in vertical upflow boiling of water.

Of practical interest from this group are the works of Karsli [351] and Karagoz [352], who investigate DWOs in flow boiling channels with surface enhancement and inserts, respectively. Both show clear changes in stability boundaries for different surface modifications and inserts, indicating 1) theory must be adapted to accommodate systems with atypical surfaces and/or inserts, and 2) the potential to improve system stability through selective use of modifications and inserts. Additional work in this area is recommended.

Finally, a wealth of analytic work has been performed with the aim of better predicting and modeling DWOs [51,63,290-291,294,340,364-373]. These are primarily studies modeling forced convection (often with a constant pressure drop assumption), although a significant amount of analytic work has also been done modeling DWOs in supercritical flows [302-309,374-375] (there is significant overlap with the supercritical Ledinegg instability references provided in section A.2.2).

When investigating analytic studies on DWOs, all approaches have strengths and weaknesses, and distinctions may be drawn between them based on a variety of factors including:

- 1) Modeling approach taken (*e.g.*, Homogeneous Equilibrium Model, Drift-Flux Model, friction factor correlation(s) used, 1-D, 2-D, *etc.*).
- 2) Linear or non-linear treatment of governing equations.
- 3) Solution in time-domain or frequency-domain (as mentioned previously).

Across all the studies on classic DWOs in single macro-channels cited here, it can be seen most DWO literature only reports the fundamental modes for DWO, and contains similar types of information:

- 1) Experimental results depicting conditions for which DWOs will occur.
- 2) Analytic modeling for the system, allowing prediction (and comparison with experimental results) of conditions that will lead to DWOs.
- 3) Parametric analysis of experimental results and/or model(s) to assess the impact of variations in key operating parameters on DWO occurrence and behavior within the system.

Item number three is relevant for system designers, and a summary of key parametric trends taken from studies cited here is provided in Table A.5. A discussion of parametric trends is also provided in the work of Boure *et al.* [50]. Their conclusions match well with those in the present work, indicating much of the relevant understanding for classic DWOs has been in place for decades. Key areas for additional study on classic macro-channel DWOs as identified in the current work include (1) orientation effects (2) heated wall thermal mass effects, and (3) impact of surface enhancements.

Despite the wealth of literature focused on DWOs in boiling channels, recent work has found DWOs resulting from atypical feedback mechanisms not well described by classic theory. Atypical mechanisms in macro-channels are described in the following section.

Table A.5: Parametric trends for traditional (macro-channel) Density Wave Oscillations.

Parameter	Effect	Mechanism	References
Heating Power	Increase in heating power acts to destabilize flow (up to the point where CHF/dryout occurs).	Increasing heating power leads to more vigorous boiling and larger two-phase pressure drop, commonly leading to a negative shift in marginal stability boundary and/or increase in amplitude of oscillations.	Colombo, 2012 [340] Boure <i>et al.</i> , 1973 [50]
Inlet Subcooling	Increasing subcooling is often stabilizing for high initial subcooling, destabilizing for low initial subcooling.	The nonlinear effect associated with changes to inlet subcooling may be attributed to changes in the relative lengths of single-phase and two-phase regions.	Wen, 2018 [363] Guanghui, 2002 [346] Comakli, 2002 [350] Colombo, 2012 [340] Boure <i>et al.</i> , 1973 [50]
Mass Flowrate	Increasing mass flowrate improves stability. If flow is already unstable, increasing mass flowrate increases amplitude and period of oscillations (may decrease period, depending on DWO mechanism).	For a given heat flux, increasing mass flowrate reduces the two-phase length and may improve stability. However, for conditions already exhibiting DWO, higher mass flowrate means the instability manifests with additional energy (increasing amplitude). Effect on frequency depends on DWO type.	Guanghui, 2002 [346] Comakli, 2002 [350] Boure <i>et al.</i> , 1973 [50]
Operating Pressure	Increasing operating pressure has a stabilizing effect. Once the instability manifests, increasing pressure leads to increased period.	Increasing operating pressure leads to a slight positive shift in marginal stability boundary due to the reduction in density difference between phases and reduction in void fraction (for a constant heating power).	Guanghui, 2002 [346] Furuya, 2005 [361] Colombo, 2012 [340] Dorao, 2015 [355] Boure <i>et al.</i> , 1973 [50]
Inlet Throttling	Increasing inlet throttling has a stabilizing effect.	Increasing the single-phase pressure drop (relative to the two-phase) improves stability of the channel.	Colombo, 2012 [340] Boure <i>et al.</i> , 1973 [50]
Outlet Throttling	Increasing exit throttling has a destabilizing effect.	Increasing the two-phase pressure drop (relative to the single-phase) reduces stability of the channel.	Colombo, 2012 [340] Boure <i>et al.</i> , 1973 [50]
Orientation	Changes in orientation may be stabilizing or destabilizing, depending on other factors.	Changes in orientation often lead to changes in dominant feedback mechanism(s) causing DWO. This may be a positive or negative depending on specifics. Additional study necessary.	Fukuda & Kobori, 1979 [80]
Channel Length	There exists a critical channel length, prior to which increases in length destabilize flow, after which increases to length stabilize flow.	Deals with relative contribution of single-phase and two-phase lengths. This needs experimental verification.	Liu <i>et al.</i> , 2018 [375] Comakli <i>et al.</i> , 2002 [350] Paruya <i>et al.</i> , 2012 [369] Boure <i>et al.</i> , 1973 [50]
Heated Wall Thermal Mass	Changes in thermal mass of heated wall(s) will alter stability characteristics of a given channel.	Numerical results show stability increasing with wall thermal mass, but experimental results show non-linear trend (first decreases, then increases). Needs additional verification.	Liu <i>et al.</i> , 2018 [375] Zhang <i>et al.</i> , 2018 [359]

Table A.5 Continued.

Channel Hydraulic Diameter	Hydraulic diameter affects stability in the sense increases or decreases will require more or less heater power to establish similar single-phase and two-phase lengths. Once it becomes a micro-channel, however, DWOs exhibit very different characteristics.	Diameter does not directly impact channel stability, only in conjunction with other operating conditions.	Nayak <i>et al.</i> , 2006 [347]
Compressible Volume	Typically important for occurrence of Pressure Drop Oscillations, some results indicate it may increase DWO amplitude.	Resonance of compressible volume with DWO acts to increase amplitude (in the absence of PDO). Needs additional verification.	Park <i>et al.</i> , 2018 [358]
Surface Enhancement/Modification	Stability boundaries may be positively or negatively affected. Oscillatory characteristics also impacted.	Result depends on relative impact to single-phase and two-phase portions of boiling channel. Additional study necessary.	Karsli <i>et al.</i> , 2002 [351] Karagoz <i>et al.</i> , 2009 [352]

### A.3.1.3 Atypical Density Wave Oscillations in Macro-Channels

Extensive use of high-speed imaging during flow boiling testing over the past decades have revealed the existence of atypical feedback mechanisms leading to DWOs during flow boiling.

One example of this is found in the work of Khodabandeh and Furberg [376], who investigated flow boiling of R-134a in a thermosyphon. They used test sections with hydraulic diameters spanning 1.2 – 2.7 mm and observed a transition from macro- to micro-channel behavior. Within their macro-channels, they observed flow oscillations due to backflow of liquid into their vertically oriented evaporator at low heating powers (corresponding to low flowrates as thermosyphons are natural circulation systems). This instability mode is characterized by low intensity nucleate boiling followed by liquid rushing into the channel from the exit (backflow) and collapsing vapor back to single-phase liquid flow. After a short period of time, boiling begins again, and the process repeats.

Similar atypical periodic behavior was reported by Aritomi *et al.* [387] during their work with flow boiling of water in a parallel channel system. They found that, during downflow boiling, the oscillatory mode was fundamentally different from that for upflow. They termed it ‘slug excursion’ and characterized it by vapor generation forming a vapor slug that excluded the channel. Buoyancy force caused the slug to stagnate and expand towards the channel inlet, where exposure to subcooled liquid led to its rapid collapse and flow of liquid back into the channel. This periodic process occurred only at low flow velocities (less than 30 cm/s) and is representative of an atypical DWO mode.

Fukuda and Kobori [80] reported in their classic study that DWOs may be brought on by feedback between inertia and gravitational effects but provided no examples or modeling of the case experienced by Khodabandeh and Furberg [376] involving liquid backflow into the channel and vapor collapse (nor that of Aritomi *et al.* [387]). It is these types of mechanisms that may be classified as DWOs (as they are device-level instability mechanisms with period similar to fluid transport time through the test section) but may be considered atypical compared to classic work in the field.

Another recent example may be found in the work of O’Neill *et al.* [53-56], who investigated vertical upflow boiling of FC-72 in a rectangular channel. They observed a characteristic oscillatory mode with period ~ 1.5–2 times fluid transport time through the channel

[54] (characteristic of DWOs [47,50]), but largely independent of heat flux within the channel. Extensive analysis of flow visualization images and oscillatory characteristics [255] allowed a mechanistic description of the phenomenon to be formed, presented here in Fig. A.9.

Figure A.9(a) provides flow visualization images captured at 2000 frames per second covering the ~11-cm heated length of their test section. Clearly visible is the alternating passage of liquid-dominant (high-density, optically opaque) and vapor dominant (low-density, optically clear) fronts. These high-density, optically opaque regions were termed High-Density Fronts (HDFs), and by identifying consecutive fronts, single-event frequencies were found and seen to match with peak oscillatory frequency of pressure measurements upstream and downstream of the heated length.

Through extensive analysis [54,56], an understanding of the mechanisms responsible for this oscillatory mode was developed, presented schematically in Fig. A.9(b). In essence, separated flow within the entire channel (~33-cm adiabatic developing length and ~11-cm heated length) lead body force to drive liquid accumulation at the channel inlet and vapor to exit the channel. This created an instantaneous imbalance for conservation of mass (with the channel effectively beginning to fill with liquid), driving pressure buildup at the inlet and excursion of a liquid slug through the channel, rewetting the walls and satisfying conservation of mass in a time-averaged fashion.

O'Neill and Mudawar developed a model [55] based on this understanding and found excellent agreement for predictions of frequency and amplitude using their experimental datasets.

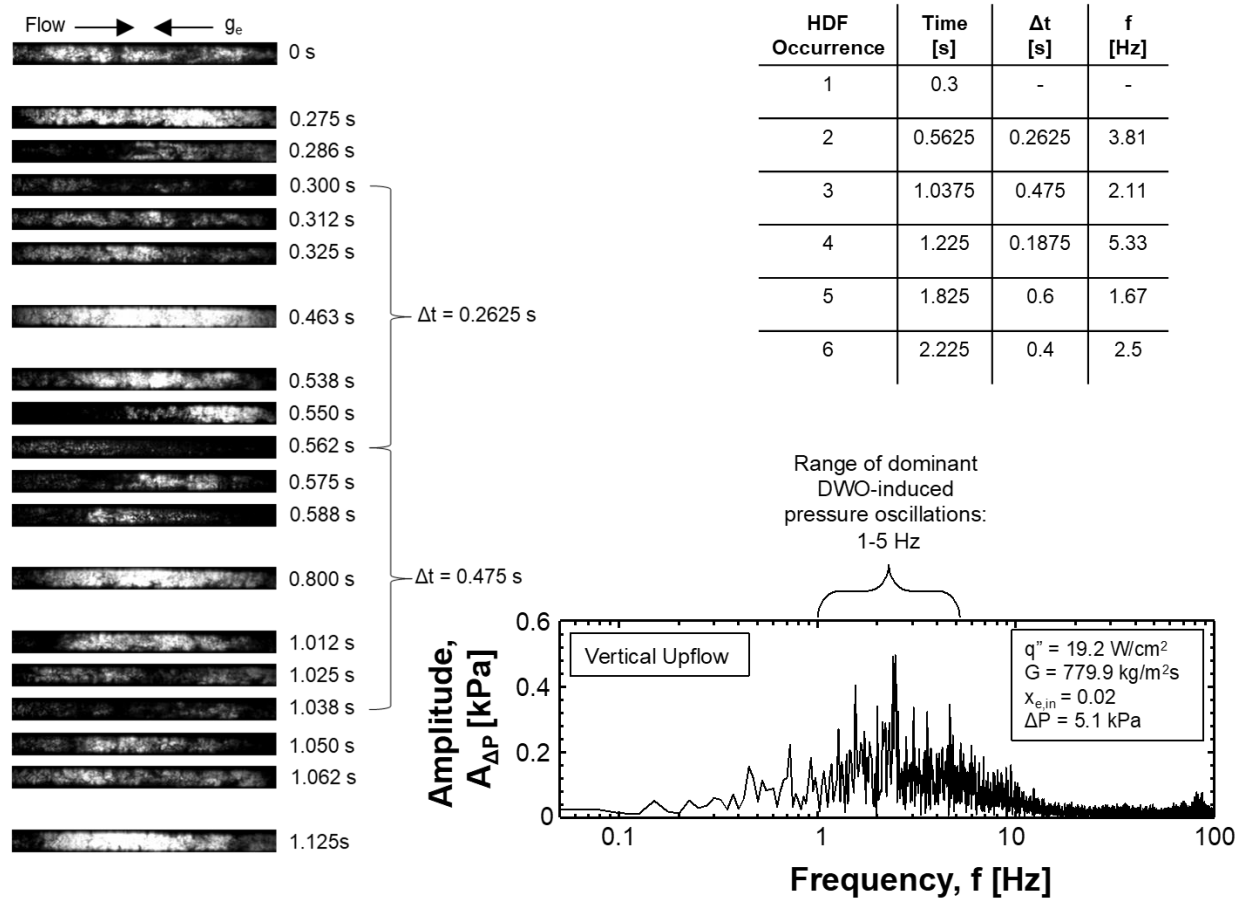


Figure A.9: (a) Experimental evidence for and (b) explanation of an atypical DWO mechanism investigated in a series of studies by O'Neill *et al.* [53-56].

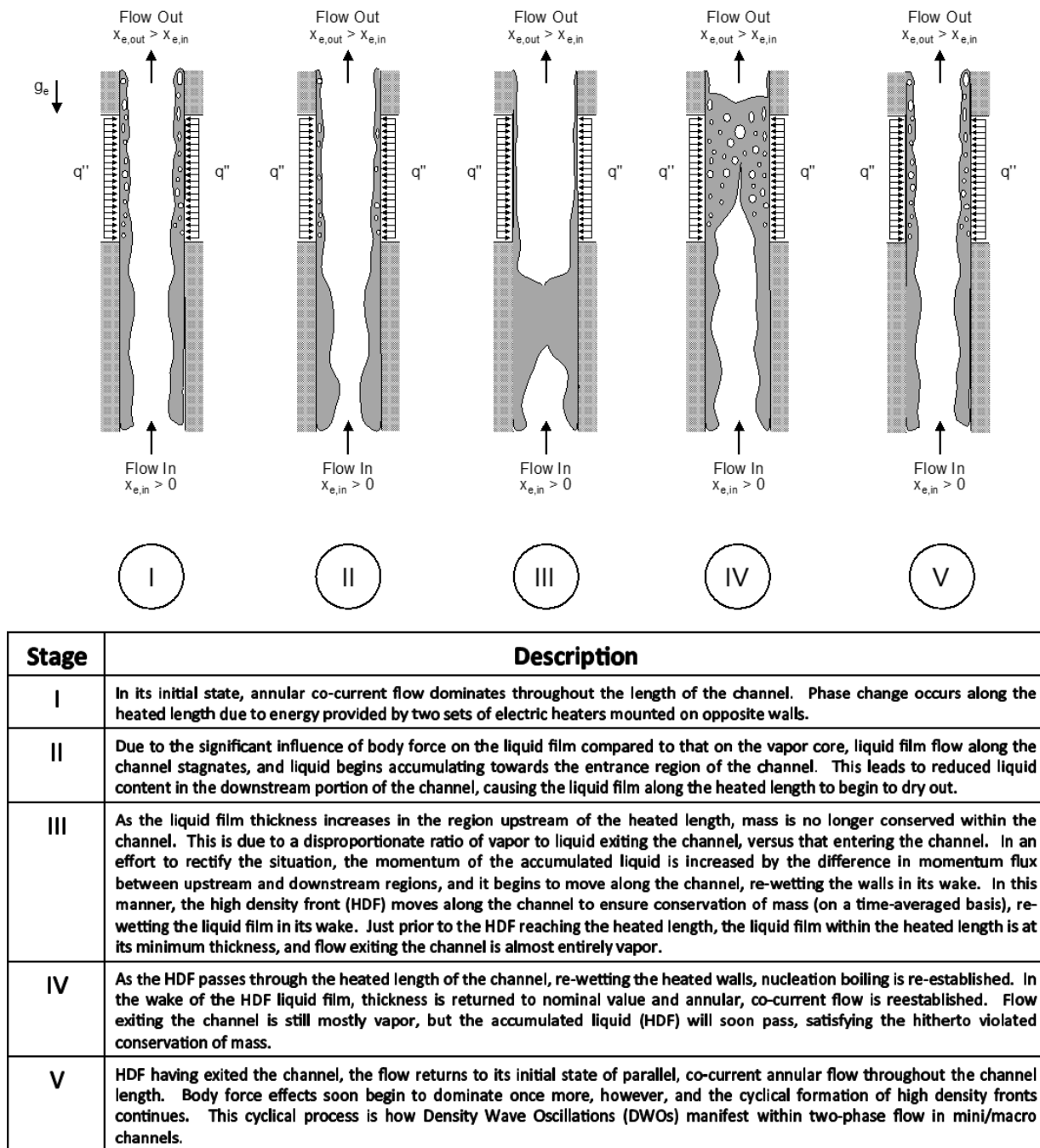


Figure A.9 (b).

The key takeaway for these atypical DWO mechanisms is the inability of classic modeling approaches to properly account for them (primarily due to non-continuum effects, such as liquid accumulation in the inlet region for O'Neill *et al.* and backflow of subcooled liquid collapsing vapor for Khodabandeh and Furberg [376]. Fukuda and Kobori [80] famously identified numerous different forcing mechanisms for DWOs (depending on orientation and operating conditions), but all of these could be captured using classic modeling approaches.

There clearly exist feedback mechanisms in two-phase flow leading to DWOs that are not well understood using classic analysis discussed in sections A.3.1.1 and A.3.1.2. Perhaps no better example of this exists than flow boiling in micro-channels.

#### A.3.1.4 Existence and Characteristics of Density Wave Oscillations in Micro-Channels

As discussed in section A.1.3, flow boiling in micro-channels is fundamentally different from that in macro-channels due to the comparable size of bubble and hydraulic diameter in the former. This leads to a distinctly different mechanism for DWOs in micro-channels.

Figure A.10(a) provides a set of schematics illustrating key concepts behind the dominant mechanism for DWOs in micro-channels. This description draws largely from the work of He *et al.* [377], who developed a model for bubble growth leading to flow reversal and pressure fluctuations in a micro-channel (DWOs).

He *et al.* describe bubble growth in a micro-channel occurring in three stages or states:

- 1) *Free growth*, where the bubble is unconstrained and expands in a spherical fashion (as it would in a macro-channel).
- 2) *Partially confined growth*, where the bubble growth becomes inhibited by the channel cross-section along one dimension (the width in Fig. A.10(a)).
- 3) *Fully confined growth*, where the bubble occupies the entire cross-section of the channel and must expand axially in response to any additional phase change.

It is important to recognize these three states correspond to both (i) the nucleation process of a single bubble at high heat flux and low flowrate (continuing to expand from state 1 through 3) and (ii) changes in nucleation behavior at a single location in response to increasing heat flux (at low heat flux, the bubble may depart during free growth and be advected through the channel, while increasing heat flux will lead to partial or full confinement before exiting the channel).

The final schematic in Fig. A.10(a) shows an axial view of the fully confined growth case, illustrating how, for high heat fluxes, phase change will cause the bubble to expand towards the channel exit as well as inlet. It is this case (and specifically the bubble expansion towards the channel inlet) which leads to DWOs in micro-channels. Fully confined bubble growth towards the channel inlet reduces flowrate (potentially leading to backflow). This leads to further bubble expansion towards the inlet, causing inlet pressure to build. Eventually inlet pressure reaches a level sufficient to overcome the fully-confined bubble, and liquid rushes back into the channel, advecting the bubble out of the micro-channel. High frictional pressure drop associated with this liquid surge causes flowrate in the channel to decrease back to a nominal level, bubble growth begins again, and the process repeats.

This phenomenon is undoubtedly a DWO, although fundamentally different than that observed in single macro-channels. The following subsection will provide a summary of literature investigating DWOs in single micro-channels. It should be mentioned, however, that most work on DWOs in micro-channels corresponds to parallel micro-channel heat sinks and will be addressed separately in a section on Parallel Channel Instability (PCI).

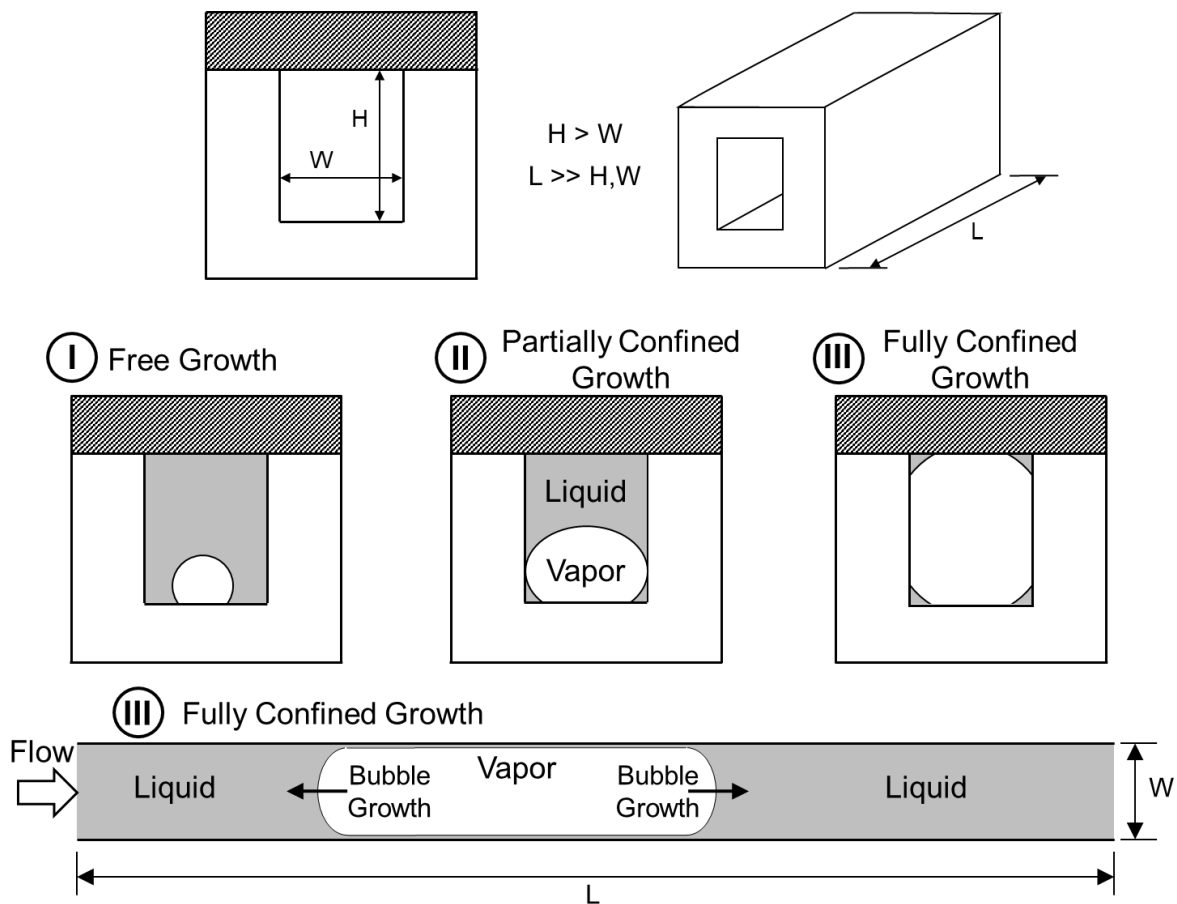
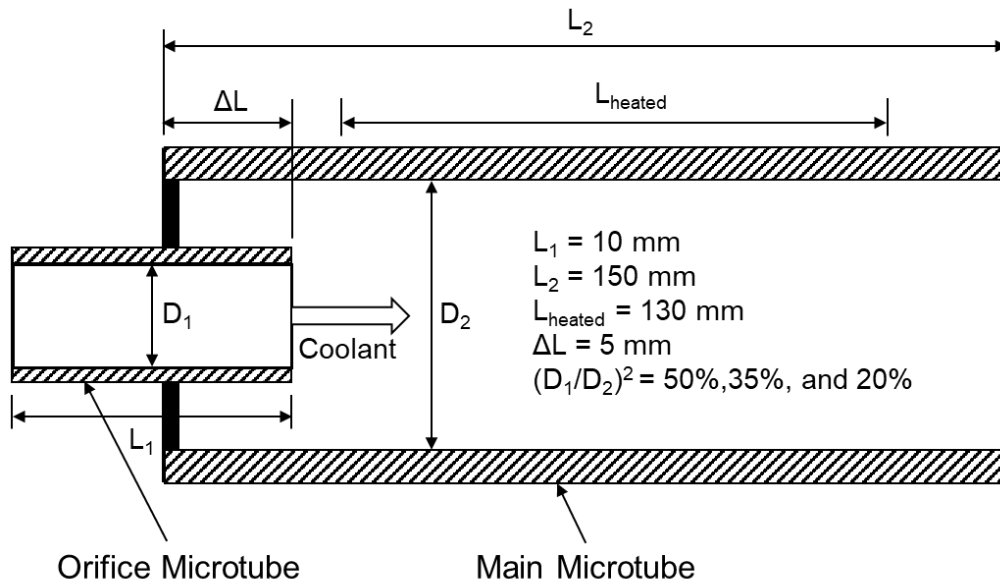


Figure A.10: (a) Schematic illustrating the key condition for Density Wave Oscillation in a micro-channel (presence of fully confined vapor growth) based on the work of He *et al.* [377]. (b) Illustration of orifice use at inlet to micro-channel, and (c) experimental results depicting impact of inlet orifice on damping/elimination of DWOs in the micro-channel, adapted from Fan and Hassan [381].



Nominal name	D <sub>1</sub> (mm)	D <sub>2</sub> (mm)	Area ratio (%)
Without orifice	0.889	0.889	100
50% orifice	0.635	0.889	51.02
35% orifice	0.5334	0.889	36
20% orifice	0.4064	0.889	20.9

Figure A.10 (b).

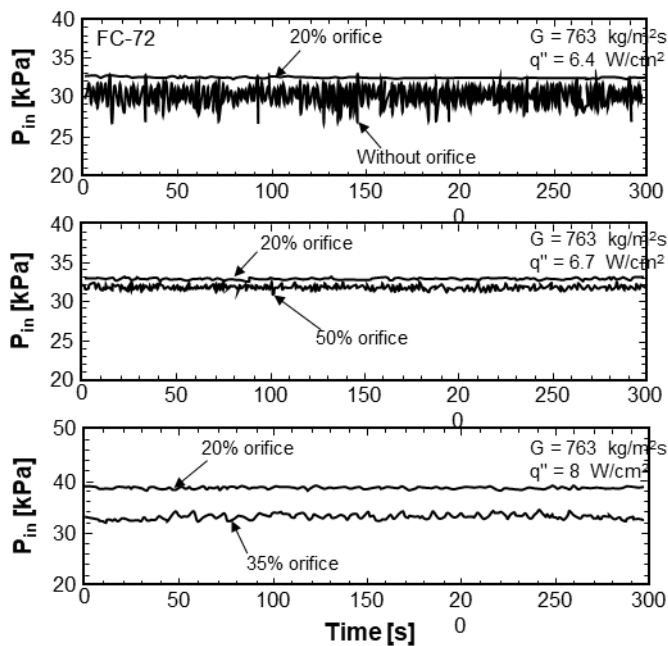


Figure A.10 (c).

### A.3.1.5 Studies Investigating Density Wave Oscillations in Micro-Channels

One of the earliest investigations of flow instability in a single micro-channel was done by Brutin *et al.* [38,378]. They studied flow boiling of n-pentane in a channel with hydraulic diameter  $D_h = 0.889$  mm and observed significant inlet pressure fluctuations corresponding to confined-growth phenomena similar to those described in Fig. A.10(a). They also showed clearly how confined growth could lead to a rapid transition from bubbly flow to annular flow and near-dryout prior to liquid rushing back into the channel, something Mudawar [28] also identified as a key concern when utilizing micro-channel heat sinks as it may lead to premature CHF.

Another important early work is that of Wang *et al.* [379], who studied flow boiling of water in both single and 8 parallel trapezoidal micro-channels with  $D_h = 0.186$  mm. They also reported a similar mechanism of confined vapor growth leading to instability and backflow towards the inlet in unstable cases, while stable cases showed isolated bubbles being generated and advected out of the channel.

Wang and Cheng [380] investigated flow boiling of water in a channel with  $D_h = 0.155$  mm. They attributed oscillations in their system to Pressure Drop Oscillations (PDOs) with superimposed DWO.

Barber *et al.* [67] studied flow boiling of n-pentane in a channel with  $D_h = 0.727$  mm. Their work included the interesting observation that deformation of the liquid-vapor interface in the case of confined bubble growth could play a significant role in high-frequency pressure oscillations observed in micro-channel flow boiling.

Relevant in the context of section A.2.4 (dealing with flow regime transition instability) is the work of Celata *et al.* [227], who found that, while a variety of flow regimes occurred in their channel (FC-72,  $D_h = 0.48$  mm), changes in flow regime did not necessarily correspond to instability. This further reinforces the idea presented in section A.2.4 that most fluctuations in flow regime are a result of other instability modes, and though they may act to amplify pressure/flowrate/temperature fluctuations, they are not a fundamental instability.

One of the most interesting works on flow boiling in a single micro-channel comes from Fan and Hassan [381]. They studied flow boiling of FC-72 in a single micro-channel with  $D_h = 0.889$  mm and included inserts to provide inlet orifices for their test section. This is shown schematically in Fig. A.10(b), with Fig. A.10(c) illustrating how these orifices act to damp out or even eliminate DWOs depending on percent inlet restriction. This is a very important practical

conclusion as it provides a way to avoid the adverse impact of DWOs in micro-channels (although coming at the expense of heightened pressure drop). This method shows clear parallels with the tactic of adding a throttling valve at the channel inlet for macro-channels, which extensive literature in section A.3.1.3 showed to have a stabilizing effect on DWOs (and also to help prevent Ledinegg and PDO).

Theoretical approaches to predicting onset of DWOs in micro-channels are limited compared to those for DWOs in macro-channels. He *et al.* [377] developed their model for expansion of a single bubble, but did not adapt it to account for the realistic effects often encountered in micro-channels (*e.g.*, bubble merger prior to confined expansion [38,378-379]).

Li and Hrnjak [382] also undertook modeling based on a mechanistic definition similar to that of He *et al.* [377] and provided some comparison with flow visualization images. Additional work is recommended, however, with efforts focused on matching qualitatively (vapor fraction and distribution) and quantitatively (inlet and exit pressure, interface speed) with experimental results.

This and the preceding section provided the fundamental basis for DWOs in a single micro-channel. Results discussed here will become relevant again when discussing parallel channel instability in micro-channel heat sinks (for which work has been far more prolific), where feedback effects between DWOs in individual micro-channels act to further destabilize the system.

#### A.3.1.6 Density Wave Oscillations in Flow Condensation

Thus far in the present review, flow condensation has been mentioned only in the section discussing flow regime transition instability. As shown in Fig. A.2(b), condensing flows cannot manifest a negative slope portion of their internal characteristic curve, meaning they are not subject to Ledinegg instability (or Pressure Drop Oscillations, as will be discussed in a future section). They also do not possess many of the local instabilities associated with boiling, such as CHF, vapor burst, or rapid bubble growth, meaning condensation is generally much more stable than boiling.

Despite this, one instability mode condensing flows manifest is DWOs. Although receiving far less attention than boiling DWOs, their existence has been confirmed through several experimental and theoretical studies.

In the 1960's, Westendorf and Brown [99] observed high and low frequency oscillatory modes present in direct condensation of saturated water vapor and subcooled liquid and found the modes could be related to liquid subcooling.

Goodykoontz and Dorsch [100] studied flow condensation in a traditional tube-in-tube configuration and observed pressure oscillations with frequencies in the 1-10 Hz range, although only for what they termed moderate condensation lengths (1.7 – 3.7 feet). This restriction to a specific length range corresponds well to the theoretical understand of DWOs in macro-channels presented in section A.3.1.1, with DWOs only manifesting for cases where single-phase and two-phase lengths were comparable and provided pressure drop contributes which oscillate out-of-phase.

Around this time, Soliman and Berenson [101] investigated flow condensation of R-113 in a multi-tube condenser in vertical upflow, vertical downflow, and horizontal flow orientations. They observed two distinct oscillatory modes, one for vertical upflow and another for horizontal and vertical downflow orientations, and noted amplitude of pressure oscillations always remained below 5% of nominal inlet pressure for horizontal and vertical downflow orientations, and below 10% for vertical upflow.

These conclusions are similar to those from a recent study by O'Neill *et al.* [328], who performed flow condensation testing using FC-72 in a circular tube in vertical upflow, downflow, and horizontal orientations. Clearly differences were seen between oscillatory mode in vertical upflow with those in horizontal and vertical downflow. In a follow up study, O'Neill *et al.* [329] were able to leverage the differences in oscillatory mode in vertical upflow to develop a criterion for determining whether flow is *co-current* or *counter-current*, which is of great practical relevance in situations when flow regime may not be determined optically.

A variety of other studies have investigated transient flow condensation behavior, including in U-tube condensers [102], flow through an annulus [103], multi-tube condensers [104], and micro-channels [95]. Some analytic work has also been performed, including standard stability models [105,106], and those seeking to assess the impact of classic hydrodynamic instability present in condensing flows [107] on system pressure fluctuations and flow regime transition [104,108-109].

Across these works, key takeaways are the existence of DWOs in condensing flows and the impact of flow orientation on instability characteristics. It is also important to note DWOs in

condensing flows are typically considered far less dangerous than those in boiling flows as there is no potential for them to trigger burnout or any other catastrophic system failure.

#### A.3.1.7 Summary of Findings Relating to Density Wave Oscillations

The current section is by far the longest in the present work, reflecting both the pervasive nature of DWOs in boiling systems and the complexity in determining exactly which factors may lead to their occurrence. Key conclusions from this section are:

- 1) DWOs occur in macro-channels due to out-of-phase oscillations of pressure drop in single-phase and two-phase portions of the channel. These may occur in both boiling and condensing flows.
- 2) Theoretical modeling of DWOs is a well-developed field, and a variety of approaches exist to determining stability boundaries for classic DWOs in macro-channels. Parametric influences are also well understood, with information summarized in Table 5.
- 3) Atypical DWOs exist and are commonly related to backflow and pseudo-compressibility effects in macro-channels. In micro-channels, these are related to rapid expansion of confined bubbles towards the channel inlet.

Further highlighting their importance as a fundamental two-phase flow instability, DWOs will feature prominently in the following section dealing with Parallel Channel Instability. Here, feedback effects between out-of-phase DWOs occurring in parallel boiling channels will be seen to lead to significant adverse effects in two-phase flow systems.

### A.3.2 *Parallel Channel Instability*

Similar to Flow Pattern Transition Instability discussed in section A.2.4, Parallel Channel Instability (PCI) may refer to either static or dynamic phenomenon. The following subsection provides a brief description of the fundamental mechanisms behind these instability modes.

#### A.3.2.1 Existence and Characteristics of Parallel Channel Instability

Instability modes in parallel channels are identical in mechanism to those in single channels, but with interactions across multiple channels adding complexity. Figure A.11(a) provides a schematic of a sample case with boiling in two parallel channels connected by inlet and exit

plenums. For nominal, stable operating conditions, Fig. A.11(a) shows how flow is split evenly between the two boiling channels, with equal vapor generation and flowrate in each.

For operation on the negative slope portion of the internal characteristic curve with a constant pressure drop boundary condition (characteristic of many parallel channel systems, as discussed in section A.2.2), a perturbation in one or more boiling channels will lead to Ledinegg instability. In a single-tube system this would mean the entire system departs to either a lower- or higher-flowrate condition, after which burnout may be encountered. Figure A.11(b), however, shows how, in parallel channel systems, this is not the only possible outcome: The presence of multiple flow paths means total flowrate may be maintained, while flow distribution across the two channels becomes drastically different (as indicated by  $G_1 \ll G_2$  in Fig. A.11(b)). This is often termed ‘Flow Maldistribution’ in literature, and its mechanism is identical to Ledinegg instability (covered in section A.2.2 of the present review).

The final (and most relevant) case is that of boiling in a parallel channel system where Density Wave Oscillations (DWOs) may occur. Interaction between parallel channels may lead to either 1) total flowrate held constant while flowrates in individual channels oscillate out-of-phase, or 2) total flowrate oscillating as individual channel flowrates remain equal but oscillate in-phase. Figure A.11(c) presents schematics corresponding to the first case, showing how boiling boundary position oscillates out-of-phase between the two channels.

It is this dynamic, oscillatory mode depicted in Fig. A.11(c) which is commonly termed *Parallel Channel Instability* (PCI), and which will be addressed at length in the current section. Its dependence on DWOs as the fundamental mechanism means much of the modeling approach and theoretical analysis have already been presented in section A.3.1, but the interactions between parallel channels, in-phase versus out-of-phase behavior, and, in particular, its manifestation in micro-channel heat sinks (where it may lead to premature CHF) mean PCI warrants separate analysis from that provided for DWOs in the prior section.

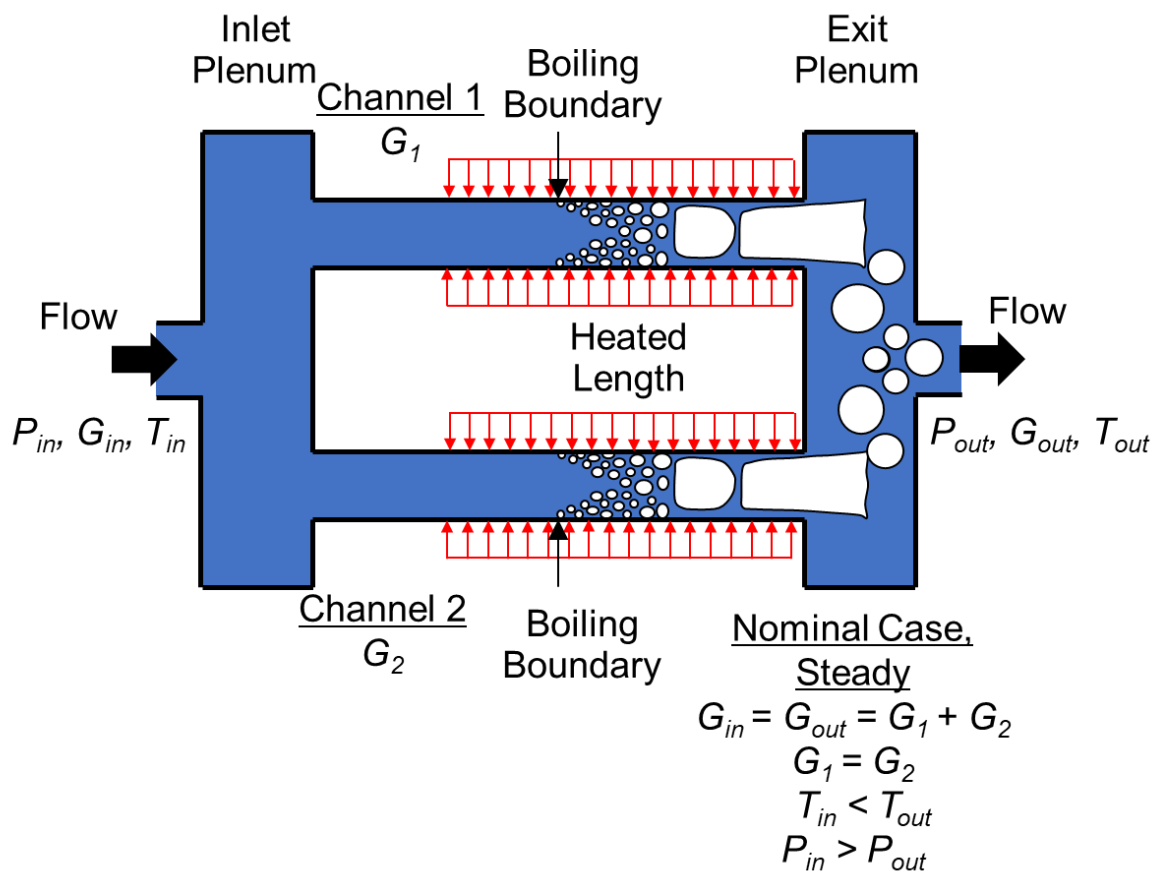


Figure A.11: Schematics depicting (a) nominal operation of two parallel boiling channels, (b) parallel boiling channels experiencing Flow Maldistribution (Ledinegg instability), and (c) parallel channels exhibiting out-of-phase Density Wave Oscillations (DWOs), referred to as Parallel Channel Instability (PCI).

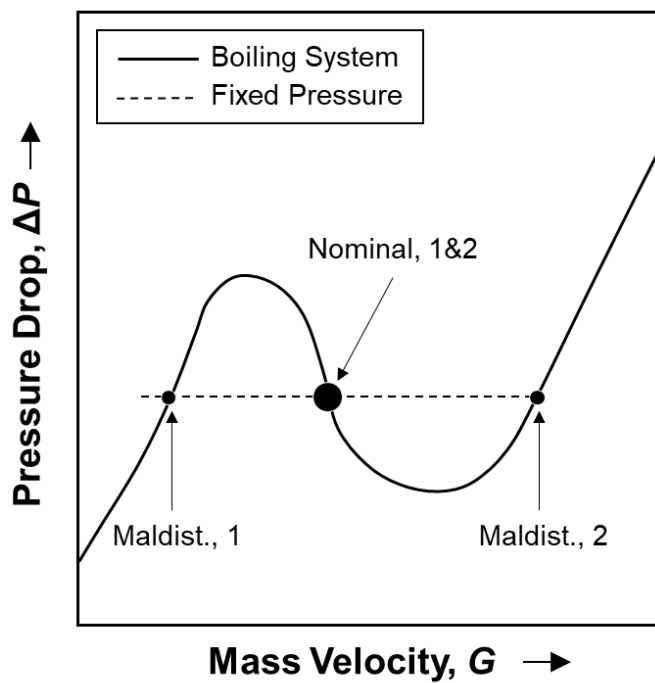
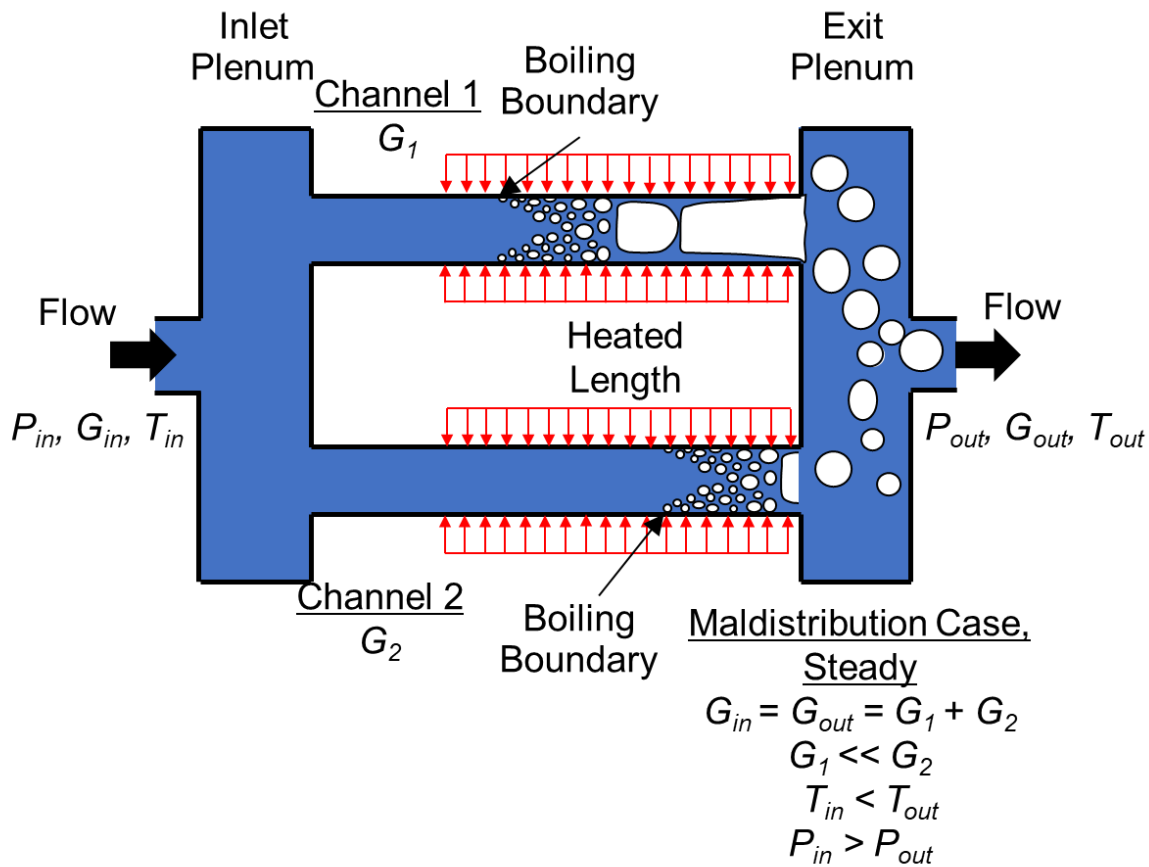


Figure A.11 (b).

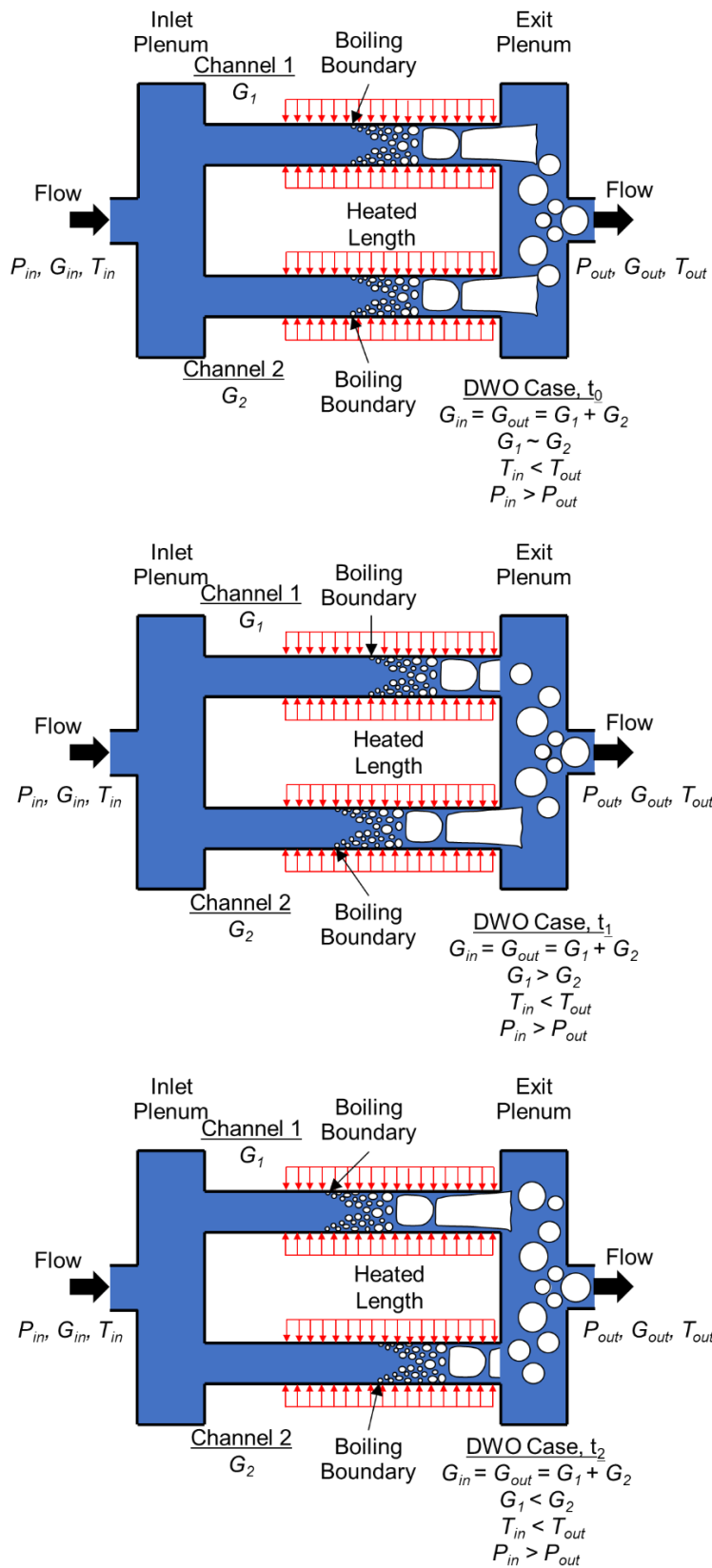


Figure A.11 (c).

### A.3.2.2 Studies on Parallel Channel Instability in Macro-Channel Systems

Similar to Density Wave Oscillations (in fact, *because* of DWOs), Parallel Channel Instability (PCI) manifests differently in macro- and micro-channel systems. The present section aims to provide an overview of relevant literature dealing with PCI in macro-channel systems. As mentioned in the preceding subsection, the ‘Flow Maldistribution’ instance of PCI is a static instability, and literature regarding it is covered in section A.2.2 [52,276,287,289,298,311]. Recent analytic work on this topic specific to micro-channels is also available from Oevelen *et al.* [383,384].

One of the earliest works dealing with PCI is that of Hayama in 1967 [385]. Analytic modeling in his study established that, for a system of  $N$  parallel channels, there will be  $N$  possible modes of oscillatory flow, one with oscillations in-phase between all channels, and  $N-1$  with different phases and amplitudes across channels.

This concept was reinforced in a series of studies by Aritomi *et al.* [386-390]. They studied flow boiling of water in parallel channels both experimentally and analytically. Figure A.12(a) provides a sample of their experimental results, highlighting how flowrates in parallel channels oscillate  $180^\circ$  out-of-phase, maintaining a constant combined flowrate.

Similar work was carried out by Fukuda and Hasegawa [391,392]. Their 1984 work in particular [392] does an excellent job of comparing analytic and experimental results, focusing discussion on initial difficulties in capturing DWO characteristics in parallel channel systems.

Additional refinement to analytic modeling of PCI occurred over recent decades, including the works of Guido *et al.* [393], Nayak *et al.* [298], Lee and Pan [157], Zhang *et al.* [394], and Zhang *et al.* [395]. Figure 12(b) provides a sample of results from Lee and Pan [157] showing oscillatory modes for a simulated 5-channel system. Interesting to note is four of the five channels (2–5) oscillate in-phase, while the fifth (channel 1) oscillates  $180^\circ$  out-of-phase while maintaining amplitude equal to that of the first four combined.

Experimental verification of this predicted behavior is found in the work of Jain *et al.* [396] who studied natural circulation flow boiling of water through four parallel channels. They saw similar behavior in their system, with different cases showing different combinations of channels oscillating in-phase versus out-of-phase. They also noted phase difference(s) between channels could change slightly over the duration of experiments.

Other works on macro-channel PCI include those of Ozawa *et al.* on adiabatic gas-liquid two phase flow [397], Xiong *et al.* [398] and Xie *et al.* [399] on PCI in supercritical flows (Xiong *et al.* in particular do an excellent job of presenting experimental evidence of PCI), Papini *et al.* [400] in parallel vertical helically-coiled tubes, and Ma *et al.* [401] on the effects of heat flux profile (generated by counterflow of liquid sodium) on PCI. It is also worth recognizing the significant work on PCI including the effect of neutron-kinetics, relevant for nuclear reactor design [402-407]. These will not be analyzed here as they represent a specific subcase of PCI, but recognition of their existence is important for engineers working in the nuclear field.

Across all works on PCI in macro-channels, parametric trends for onset of PCI and oscillatory characteristics (amplitude, frequency) resemble those for DWOs in solitary channels. This makes intuitive sense, as DWOs are the fundamental mechanism leading to the onset of PCI. Because of this, Table A.5 contains relevant information for trends relating to PCI.

One interesting addition is repeated mention of intentional differences to channel characteristics leading to improved system stability [388] (or in the case of Zhang *et al.* [395] the ability to use flow-control to suppress PCI). In their early work, Aritomi *et al.* [388] showed that different heat flux and/or inlet throttling values applied to parallel channels led to a new stability boundary roughly equivalent to that of the average values applied to both channels.

One area that remains somewhat unclear is the impact of increasing channel number on marginal stability boundary (MSB) of the system. The analytic work of Lee and Pan [157] showed complex, non-monotonic changes to stability boundary as the number of parallel channels increased, but this has not been rigorously verified by experimental results. This trend will be discussed further in the following subsection dealing with PCI in micro-channels.

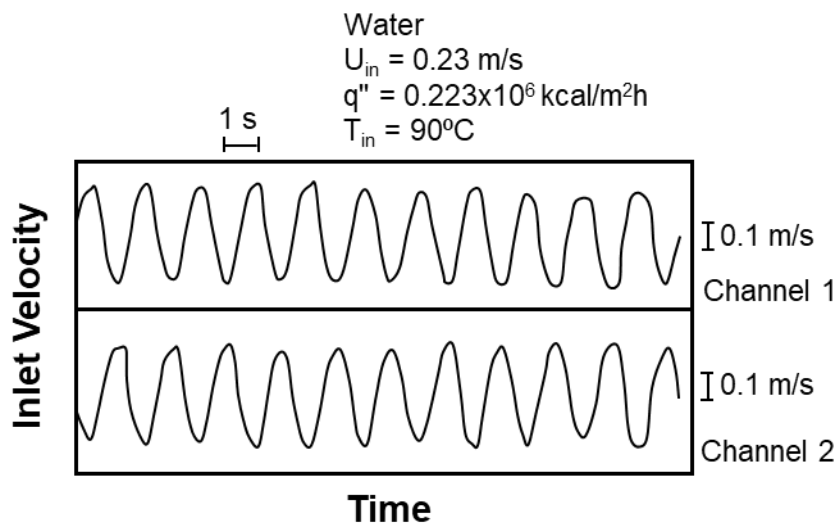


Figure A.12: Plots of (a) inlet velocity versus time showing Parallel Channel Instability  $180^\circ$  out-of-phase between two channels, adapted from Aritomi *et al.* [386-390], (b) fluctuations in non-dimensional inlet velocity versus non-dimensional time showing PCI in a five-channel system, adapted from analytic work of Lee and Pan [157], and (c) experimental results highlighting the difference between Pressure Drop Oscillations (left) and PCI (right) in parallel micro-channel heat sinks, adapted from Qu and Mudawar [57].

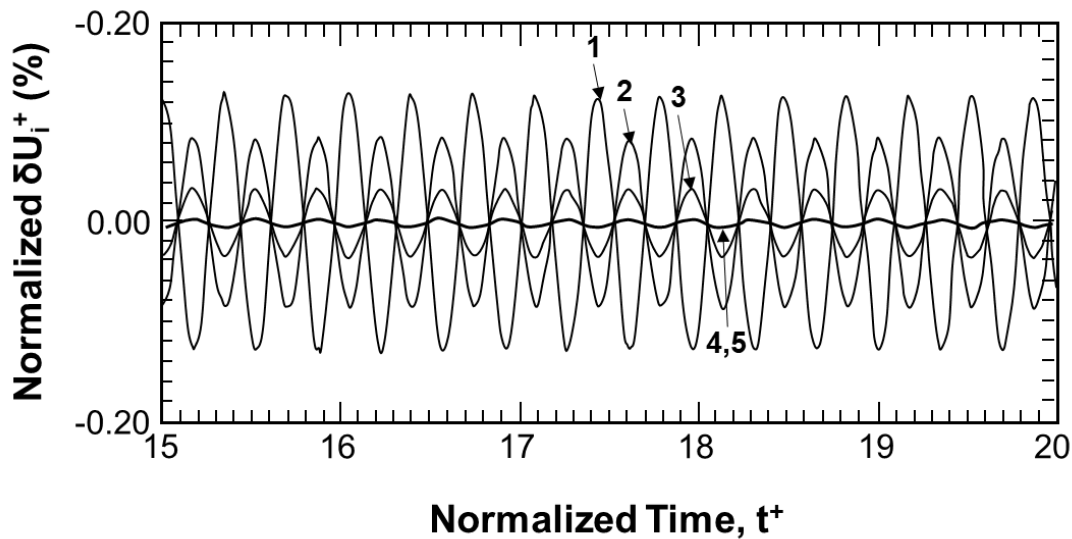


Figure A.12 (b).

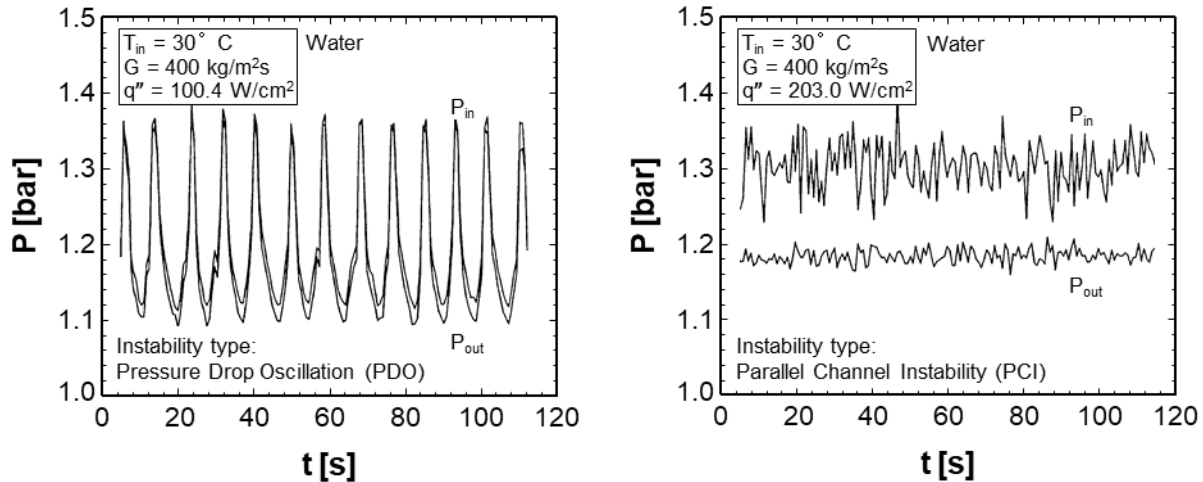


Figure A.12 (c).

### A.3.2.3 Studies on Parallel Channel Instability in Micro-Channel Systems

Prior to discussing literature investigating PCI in micro-channels, it is necessary to mention proper identification of PCI in micro-channels. Unlike macro-channel systems, it is currently impossible to include independent flow meters and/or pressure measurements in parallel channels for micro-channel heat sinks. Because of this, common measurements used for identifying instabilities in micro-channel heat sinks are inlet and exit plenum pressure measurements (as well as direct optical access, although these are rarely used in a quantitative fashion).

Figure A.12(c) provides plots of inlet and exit plenum pressure versus time adapted from the work of Qu and Mudawar [57], who investigated flow boiling of water in a micro-channel heat sink with  $N = 21$  channels of  $D_h = 0.349$  mm. The first plot clearly shows both inlet and exit pressure oscillating with high amplitude and low pressure, and corresponds to Pressure Drop Oscillations (PDOs, to be discussed in detail in the following section). The second plot represents similar flowrate and inlet temperature, now with a throttling valve upstream of the test section to eliminate PDOs (by eliminating the negative slope region on the internal pressure curve). In this case, inlet pressure oscillates with moderate amplitude while exit pressure hardly oscillates at all. This is similar to behavior observed for DWOs in single micro-channels discussed in section A.3.1.5 and is representative of PCI occurring in a micro-channel heat sink. It is this type of inlet pressure oscillation that is commonly used to identify the presence of PCI in micro-channels.

The early work of Qu and Mudawar [57] is joined by studies from Wu and Cheng [408] and Peles [409], who presented evidence of PCI in micro-channel heat sinks around the same time. The ability of parallel micro-channel heat sinks to offer greatly improved heat transfer performance for small surface areas meant the amount of literature on the topic proliferated in the following years with many authors showing 1) the advantages of micro-channel heat sinks from a heat transfer standpoint, and 2) the limiting effects of PCI in these heat sinks.

Notable experimental works characterizing PCI in micro-channels include those by Cheng and co-authors [39,379,410-411], Mudawar and co-authors [59,61,68,235,412], Hetsroni *et al.* [413], Chang and Pan [58], Bogojevic *et al.* [158], and Lee *et al.* [414]. From these works, many of the dominant trends relating to onset of PCI as well as PCI characteristics are summarized as:

- 1) Decreasing mass velocity and/or increasing heat flux (*i.e.*, increasing exit quality) leads to onset of PCI in micro-channel heat sinks.
- 2) Frequency and amplitude of oscillations are dominated by heat flux (increasing as heat flux increases), although mass velocity also plays a non-linear role on amplitude [61].
- 3) Generally, frequency and amplitude are governed by the length of liquid upstream of confined bubble growth, with longer liquid lengths yielding lower frequencies and amplitudes [61].
- 4) Vapor backflow into the inlet occurs primarily for very high heat fluxes [412], and significantly affects dynamics of inlet plenum [61].

Many of the authors listed above present criteria and/or stability maps for detailing the onset of PCI. Several of these are expressed as transition criteria using a ratio of heat flux to mass velocity ( $q''/G$ ) [158] or exit quality [39], both of which involve the dominant parameters of flowrate and heat flux. These are not expected to generalize well, however, due to their omission of differences in surface tension and diameter effects critical to the onset and characteristics of DWOs in micro-channels (see section A.3.1.5) which in turn cause PCI in parallel micro-channel heat sinks.

A more sophisticated approach is that recommended by Lee *et al.* [414], who introduced a parameter  $R$  defined as the ratio of force terms acting backwards (towards the inlet) to the force terms acting forwards (including expansion and inlet orificing components). Formally, this was expressed as

$$R = \sqrt{\frac{F_{back}}{F_{forward} + F_{exp} + F_{orf}}}, \quad (\text{A.14})$$

with individual terms defined as

$$F_{back} = \frac{1}{4\rho_g A_c} \left( \frac{Q}{h_{fg}} \right)^2, \quad (\text{A.15})$$

where  $A_c$  is the channel cross-sectional area and  $Q$  total heat input in a channel,

$$F_{forward} = \frac{G^2 A_c}{\rho_f}, \quad (\text{A.16})$$

$$F_{exp} = \sigma \left( \frac{1}{W_1} - \frac{1}{W_2} \right) A_{c,1}, \quad (\text{A.17})$$

where  $W_1$  and  $W_2$  represent changing widths of the micro-channel and  $A_{c,1}$  is cross-sectional area in the upstream portion (Eq. (A.17) deals with expanding microchannels, discussed further in section A.3.2.4), and

$$F_{orf} = \frac{1}{2\rho_f} \left( \frac{GA_{c,1}}{A_{c,orf}} \right)^2 K_{orf} A_{c,1}, \quad (\text{A.18})$$

where  $A_{c,orf}$  is the cross-sectional area of an inlet orifice (such as that shown in Fig. A.10(b)) and  $K_{orf}$  the inlet orifice loss coefficient. More information on defining and evaluating these terms may be found in the original work [414].

Lee *et al.* [414] used this parameter to predict whether PCI would occur (if  $R > 1$ , forces acting to drive backflow are greater than those for forward motion and DWOs should occur) in straight micro-channels, expanding micro-channels, and micro-channels with inlet orifices, and showed excellent agreement with their experimental results. More than this agreement, however, is the relatively simple yet comprehensive modelling approach adopted: By capturing important effects relating to channel flow area, inlet restriction, surface tension, and vapor generation rate, they provided fundamental groundwork for researchers seeking to begin optimizing parallel micro-channel heat sink design to provide stable flow while minimizing pressure drop through inclusion of geometry modifications.

Unlike PCI in macro-channels (and almost all other instability modes discussed in this study), PCI in micro-channel heat sinks has received relatively little analytic focus in literature.

Instead, researchers have focused on exploring practical modifications to heat sink geometry to reduce and/or eliminate PCI.

#### A.3.2.4 Geometry Modifications to Suppress/Eliminate PCI in Parallel Micro-Channel Heat Sinks

Despite the (comparative) lack of theoretical work related to PCI in micro-channel heat sinks, extensive mitigation methods are available in the form of geometry modifications. These are summarized in a recent review by Liang and Mudawar [264] and presented at length in the work of Prajapati and Bhandari [215]. Specifically, Table 3 in the work of Prajapati and Bhandari [215] does an excellent job of providing a summary of proposed mitigation techniques and the studies investigating them. For the sake of the current work, two of the more common configurations will be discussed, and their respective impact on PCI assessed.

Continuing with the fundamental understanding of forces developed by Lee *et al.* [414], it is clear the purpose of geometric modifications to micro-channel heat sinks is to increase the resistance to vapor expansion towards the channel inlet (which leads to flow reduction or backflow depending on intensity of vapor generation as discussed in section A.3.1.5). The most commonly used schemes for this purpose are inlet restriction/orificing and diverging channels. An early study by Wang *et al.* [39] showed the ability of added orifices at individual channel inlets to suppress PCI (and thus backflow). They also came to the interesting conclusion that flow into the inlet plenum and leaving the exit plenum affect stability characteristics significantly, with flow entering parallel to channels (*e.g.*, that in Fig. A.11) exhibiting greater stability than that entering/leaving plenums at a 90° angle to channel direction (from the bottom of the inlet plenum).

Other studies involving inlet orificing include those of Kosar *et al.* [415], Szczukiewicz *et al.* [416,417] and Kaya *et al.* [418]. Figure A.13(a) provides an image of micro-channel inlet restrictions implemented by Szczukiewicz *et al.* [416,417] for their work and representative of those included in other works. The impact of these restrictions on flow stability is similar to that shown for the work of Fan and Hassan [381] in Figs. A.10(b) and A.10(c), which showed fluctuations eliminated by aggressive inlet orificing. Kaya *et al.* [418] went further and illustrated how, for high heat flux values in micro-channel heat sinks, CHF values increased exponentially with increased inlet restriction ratio due to inlet orificing preventing backflow (which commonly causes premature CHF in micro-channel heat sinks).

Many additional studies exist detailing advantages of inlet orificing for suppressing PCI, but, for the scope of the current work, it is sufficient to understand the following: Increasing inlet orificing for individual micro-channels in parallel micro-channel heat sinks suppresses PCI at the cost of increased pressure drop. More detailed modeling on DWO formation and characteristics in micro-channels (which manifest as PCI in parallel micro-channel systems) is needed to optimize this trade-off.

The second commonly used modification is that of expanding channels. These serve to bias vapor expansion towards the downstream portion of the test section, and often have less adverse impact on pressure drop than inlet orificing. However, due to the increase in flow area downstream, flow velocity is reduced, which may impact heat transfer coefficients (this is largely speculative, and some work has shown heat transfer to improve due to increased flow stability [419]).

One early study to incorporate expanding flow in the downstream region is that of Lee and Pan [420]. They compared straight to expanding channels in a single micro-channel flow boiling configuration and saw significantly reduced inlet temperature oscillations in the expanding channel case (attributed to the absence of backflow into the inlet plenum).

Other studies investigating the impact of diverging micro-channels on heat sink stability include those of Prajapati *et al.* [313] and Lu and Pan [421], both of whom found advantages to using expanding microchannels. Figure A.13(b) shows a schematic of a micro-channel heat sink with diverging channels, adapted from Lu and Pan [421].

Overall, the standard for studies dealing with impact of inlet restriction and expanding channels on PCI is that of Lee *et al.* [414]. In addition to their mechanistic modeling mentioned previously, they provide excellent comparison of results for plain channels, diverging channels, and those with inlet restrictions, clearly showing the tradeoffs between each configuration in Fig. A.13(c). Their work is strongly recommended as an entry-point for researchers looking to apply inlet restrictions and/or channel expansion to help stabilize flow.

Many other modification techniques exist to help suppress and/or eliminate PCI in micro-channel heat sinks. These include the use of reentrant cavities [422-426], interconnected micro-channels [427-429], and a plethora of direct surface-enhancement (*e.g.*, nanotubes) studies. Those interested in further reading on these topics should consult the reviews of Liang and Mudawar [264] and Prajapati and Bhandari [215].

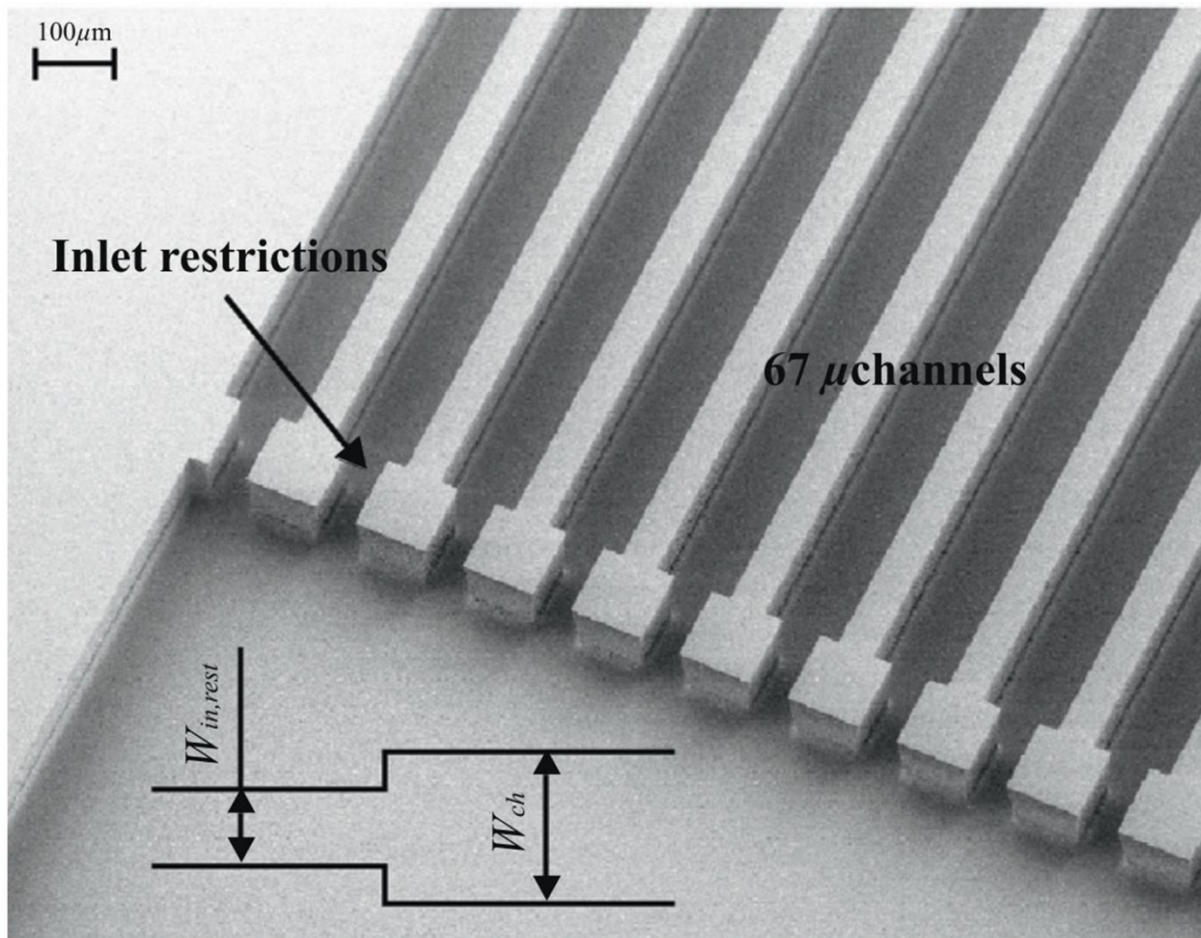


Figure A.13: Image of (a) parallel micro-channels with inlet restrictions adapted from Szczukiewicz *et al.* [416], (b) schematic of expanding parallel micro-channels adapted from Lu and Pan [421], and (c) comparison of results for straight micro-channels with expanding micro-channels (top) and those with inlet orificing (bottom), adapted from Lee *et al.* [414].

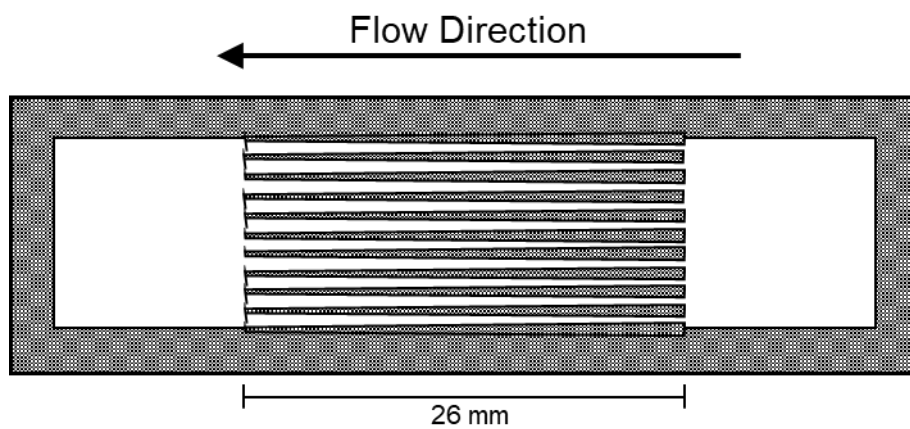
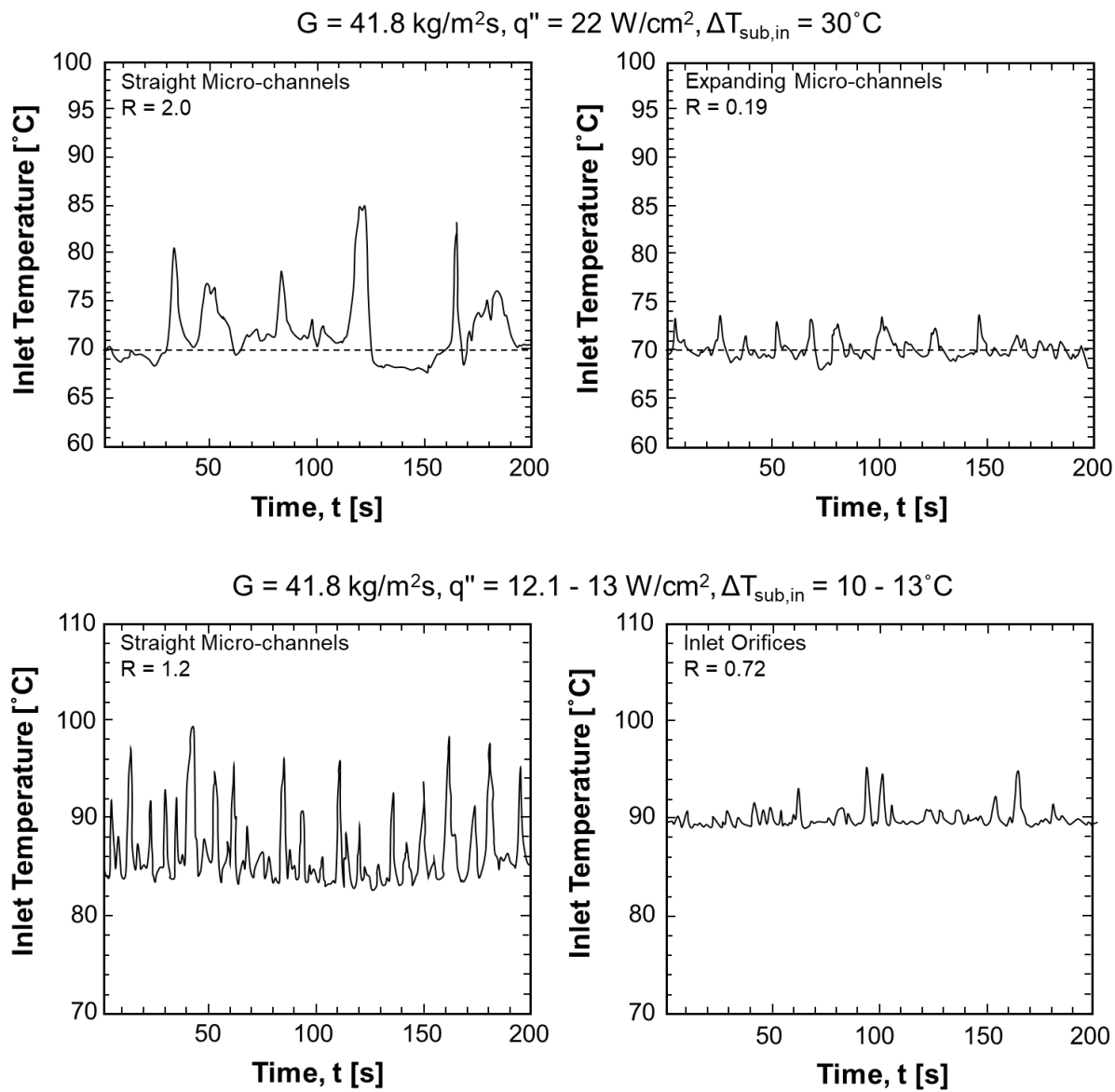


Figure A.13 (b).



#### A.3.2.5 Summary of Key Information Related to Parallel Channel Instability

Parallel Channel Instability has been shown to refer to both static (flow maldistribution) and dynamic type instabilities in the preceding subsections. Analysis here focused on the dynamic type instability, as section A.2.2 (Ledinegg instability) covered studies dealing with static type. Key conclusions are listed below:

- 1) DWOs interacting across parallel channels were discussed as the mechanism leading to PCI. Many classic experimental and analytic studies were referenced, with key trends relating to onset of PCI and oscillatory characteristics found to be near-identical to those for DWOs in single macro-channels.
- 2) Like DWOs, PCI is mechanistically different in micro-channel systems, but is again attributable to DWOs acting in parallel channels (this time with the dominant DWO mechanism related to rapid confined bubble growth).
- 3) Dominant parameters influencing PCI onset and characteristics in parallel micro-channel heat sinks are heat flux and mass velocity. Some mechanistic modeling is provided (from the work of Lee *et al.* [415]) showing the different parameters influencing whether bubble growth will expand towards the channel inlet (destabilizing flow), and the effects of geometric modifications on these.
- 4) A brief overview of common geometry modifications for suppressing PCI was provided, with inclusion of inlet orificing and expanding channels identified as promising solutions.
- 5) Additional modeling work is needed to optimize the tradeoffs between increased pressure drop and improved stability associated with common geometry modifications.

#### A.3.3 Pressure Drop Oscillations

Pressure drop oscillations (PDOs) are another pervasive two-phase flow instability. First reported in the 1960's [430-432], PDOs are a system-level instability (as opposed to device level instabilities such as DWOs and PCI). Similar to Ledinegg instability, it requires the system to be operating on the negative slope portion of the internal characteristic curve and have an external pressure curve with higher (less-negative) slope than the internal curve. Additional details on these conditions can be found in sections A.2.2.1 and A.2.2.2.

Unlike Ledinegg instability, which is a static instability characterized by a one-time excursion in operating conditions to a new stable state, the presence of compressible volume within the system causes PDOs to manifest as a dynamic instability mode. As compressible volumes are necessary for closed systems that undergo phase change (in order to accommodate the increased volume of fluid present without prohibitive increases to operating pressure), this instability mode is very common in two-phase literature. A detailed description (again drawing heavily on the explanation of Lahey and Podowski [47]) of the mechanisms behind it is provided in the following subsection.

### A.3.3.1 Existence and Characteristics of Pressure Drop Oscillations

A brief sample case outlining the mechanisms behind PDOs is captured in Fig. A.14. Figure A.14(a) shows the nominal operating conditions under consideration: The system is driven by a centrifugal pump (case 2 in Fig. A.2(d)), currently operating in the middle of the negative slope region of the boiling curve (point **A**), liquid level in the surge tank (closed reservoir or accumulator) is constant, and pressure in the tank is in equilibrium with that along the flow path. Figure A.14(b) shows the system experiencing a perturbation (slight increase) in mass velocity, which destabilizes the operating condition (as was discussed with case 2 in Fig. A.2(d), section A.2.2.2). The increase in flowrate reduces pump pressure head, meaning pressure inside the tank is now higher than that along the flowpath, and liquid flows out of the tank.

Due to the inertia of liquid within the tank, however, tank pressure undershoots what would be a new stable value. Figure A.14(c) shows how, at its maximum flowrate condition (**B'**, where **B** is the stable post-Ledinegg-excursion point from case 2 in Fig. A.2 (d)), tank pressure is now less than bulk flow pressure, meaning flow will be diverted back into the tank. Figure A.14(d) illustrates this process, with flow diverted back into the tank and operating condition moving back towards lower flowrate and higher pressure.

Once again due to inertial effects associated with liquid motion, tank fill level overshoots its stable value, and Fig. A.14(e) shows tank pressure once again exceeding bulk flow pressure (point **C'**, where **C** is the stable post-Ledinegg-excursion point from case 2 in Fig. A.2 (d)). This leads to outflow from the tank (Fig. A.14(f)), driving system flowrate up and pressure down, causing the system to continue its cycle between points **C'** and **B'**.

It is worth noting here that the present explanation for PDOs depends on the system's predilection for Ledinegg instability in the absence of a compressible volume. This is not totally confirmed within literature: In fact, one early analytic work asserted the external pressure curve *must* be steeper than internal (Case 1 in Fig. A.2(d)) for PDOs to occur [292]. This has been disproved by experimental work showing PDO occurring for conditions that yielded Ledinegg prior to the inclusion of a compressible volume [269], but conclusive proof that PDOs will *only* occur under conditions that would have led to Ledinegg instability is absent in existing literature.

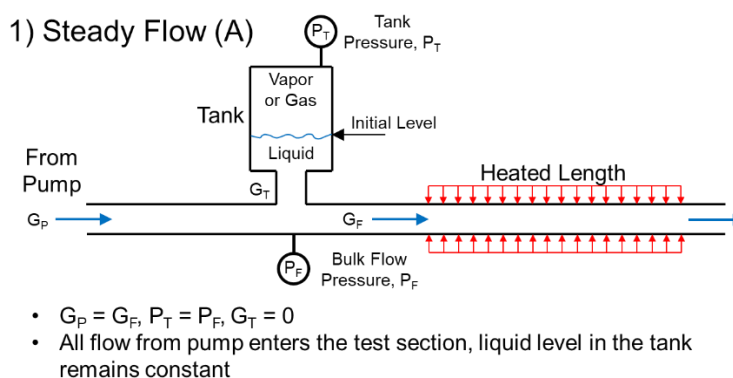
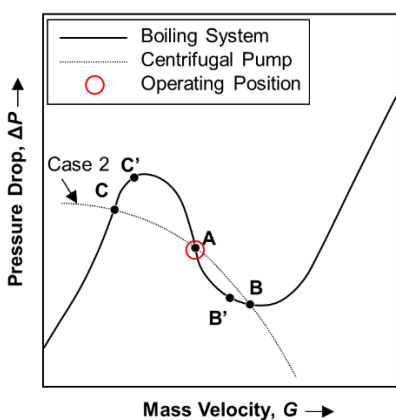


Figure A.14: Series of schematics presenting the process of Pressure Drop Oscillations, from (a) nominal operation, (b) attempting flow excursion, (c) max flowrate condition, (d) reduction in flowrate, (e) minimum flowrate condition, and (f) continuation of the cycle

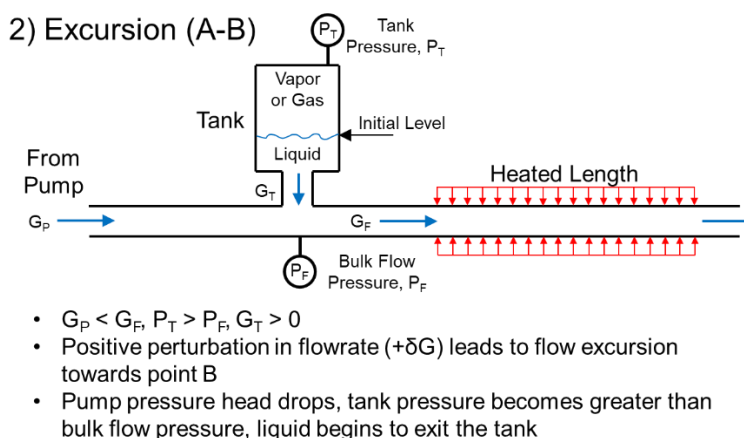
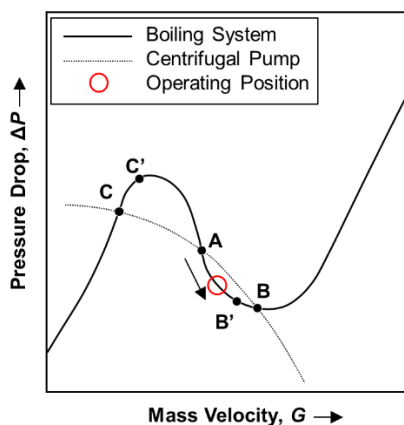
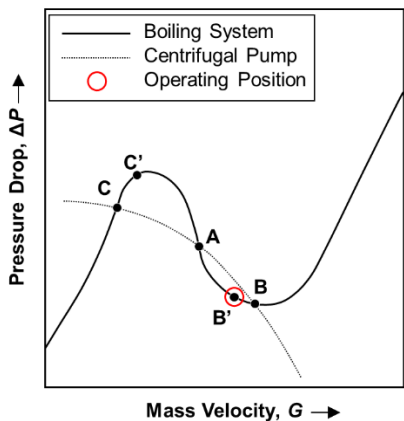
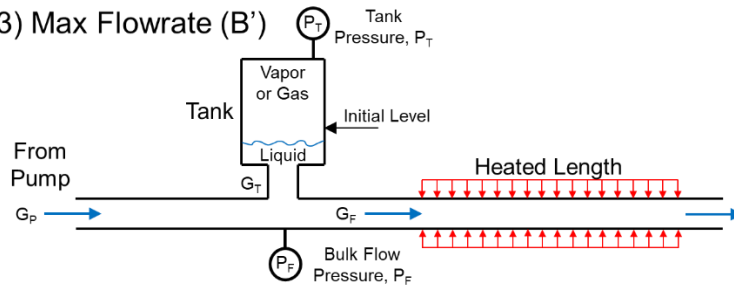


Figure A.14 (b).

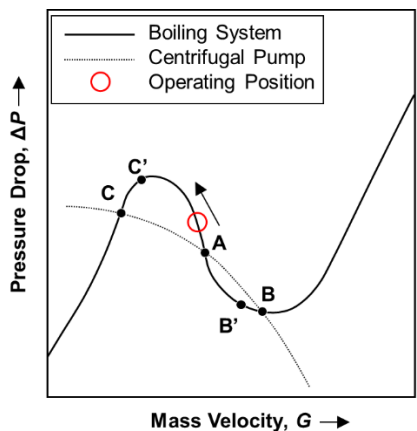


3) Max Flowrate (B')

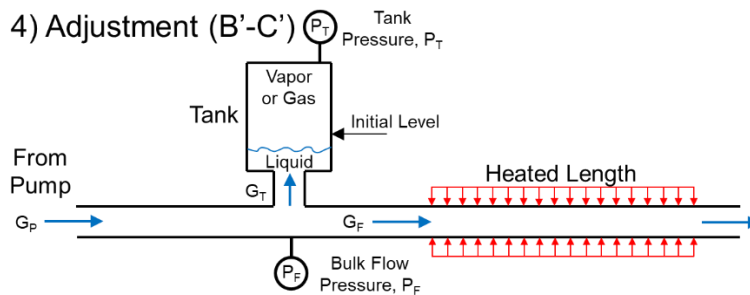


- $G_p = G_f, P_T < P_F, G_T = 0$
- Inertia of liquid tank causes tank pressure to undershoot new steady-state value
- Instead of reaching new stable operating point B, some flow will be diverted into the tank to re-establish equilibrium

Figure A.14 (c).

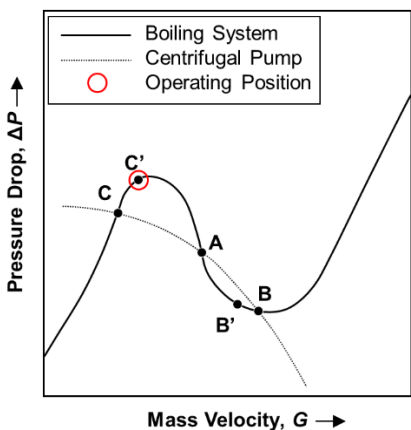


4) Adjustment (B'-C')

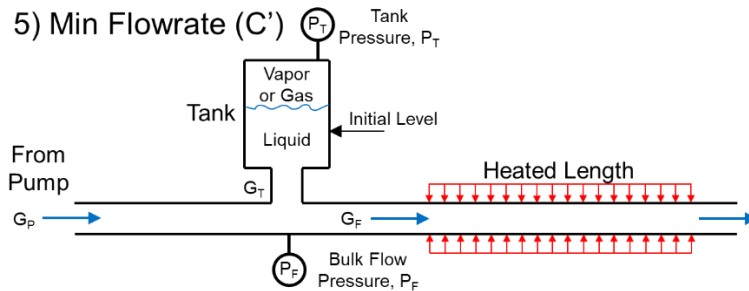


- $G_p > G_f, P_T < P_F, G_T < 0$
- Low pressure in tank causes liquid to flow into it, refilling

Figure A.14 (d).



5) Min Flowrate (C')



- $G_p = G_f, P_T > P_F, G_T = 0$
- Liquid inertia again causes the tank to overshoot its initial position

Figure A.14 (e).

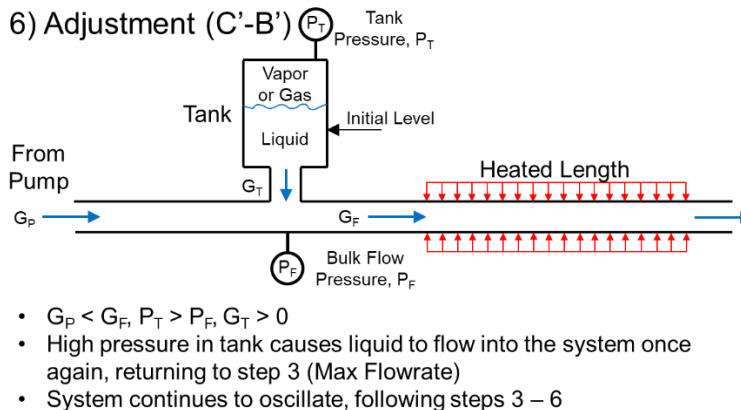
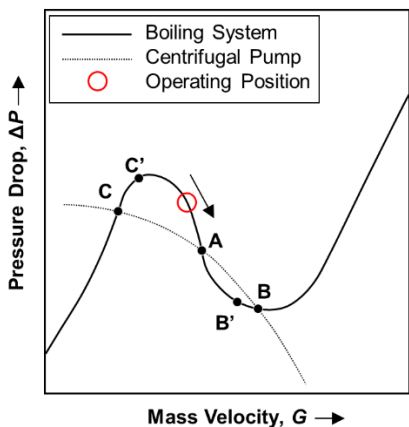


Figure A.14 (f).

### A.3.3.2 Comments on Ledinegg Instability versus Pressure Drop Oscillations

The mechanistic description of PDOs in the preceding subsection can be summarized as ‘the system attempts to undergo Ledinegg instability, but the presence of an underdamped compressible volume causes it to experience limit cycle oscillations instead’. This implies the presence of a compressible volume in the system precludes the existence of Ledinegg instability and means operating conditions that would have led to Ledinegg now yield PDOs (in the system pressure curves shown in Fig. A.14, Ledinegg instability would cause the system to shift from **A** to **B** or **C**, but the inclusion of a compressible volume leads to oscillations between intermediate points **B'** and **C'** instead). This is true in most cases, but it is necessary to point out cases for which it does not hold and explain the conditions that may lead to a middle ground between Ledinegg and PDOs.

Recent analytic work by Rahman and Singh [433] discussed the existence of Flow Excursion with Compressible Volume (FECV). These are cases where a Ledinegg-like flow excursion takes place despite the presence of a compressible volume in the system. Fig. A.15(a) shows a stability map generated from their work, illustrating how changes to an inlet restriction value  $K_I$  (resistance located between their supply tank and surge tank just upstream of a vertical test section) lead to manifestation of different instability types resulting from interplay between flow excursion and compressible volume.

Little experimental evidence of this phenomenon is available, but one study where it seems to appear (although not identified as such) is the work of Mishima *et al.* [269]. Figures A.15(b)

and A.15(c) present results from their work, with Fig. A.15(b) showing PDOs encountered during vertical downflow boiling. In this case, their large inlet plenum (despite only using a single boiling channel) acts as the compressible volume resulting in PDOs.

Figure A.15(c), however, shows more complex behavior. It corresponds to a case with vertical upflow boiling and a significant compressible volume located just upstream of the test section. For this case, the point they identify as ‘Onset of Instability’ exhibits a flow excursion followed by DWOs. As they continue to increase heat flux, 4-5 additional flow excursions are identifiable (each followed by unsteady boiling exhibiting DWOs), until CHF (burnout) finally occurs. In their work, Mishima *et al.* postulate these multiple small flow excursions are a result of the compressible volume: increasing heat flux triggers Ledinegg instability (shown here in Fig. A.3(b)), but the presence of the large compressible volume stabilizes the system prior to full excursion. Referring to the mechanistic description provided in the prior subsection, this corresponds to a case where the compressible volume is overdamped (as opposed to the underdamped case that leads to PDOs).

The potential for compressible volume to interact with the system in an overdamped fashion receives virtually no attention in two-phase literature. Some experimental works on PDOs vary compressible volume (as will be discussed in the following section), but none identify a boundary between PDO and FECV as depicted in Fig. A.15.

Analytically, Padki *et al.* [292] first mention the potential for Ledinegg-type excursive behavior to occur even in the presence of a compressible volume, but only for very high heat fluxes (based on their model and system). Srinivas and Pushpavanam [434] discuss infinitely large compressible volumes resulting in order-of-magnitude larger periods for PDO compared to finite tanks; it is possible this relates to the occurrence of FECV, but additional work is necessary on the topic. For the sake of the current review section, the remainder of discussion will focus on works where the inclusion of a compressible volume results in PDOs.

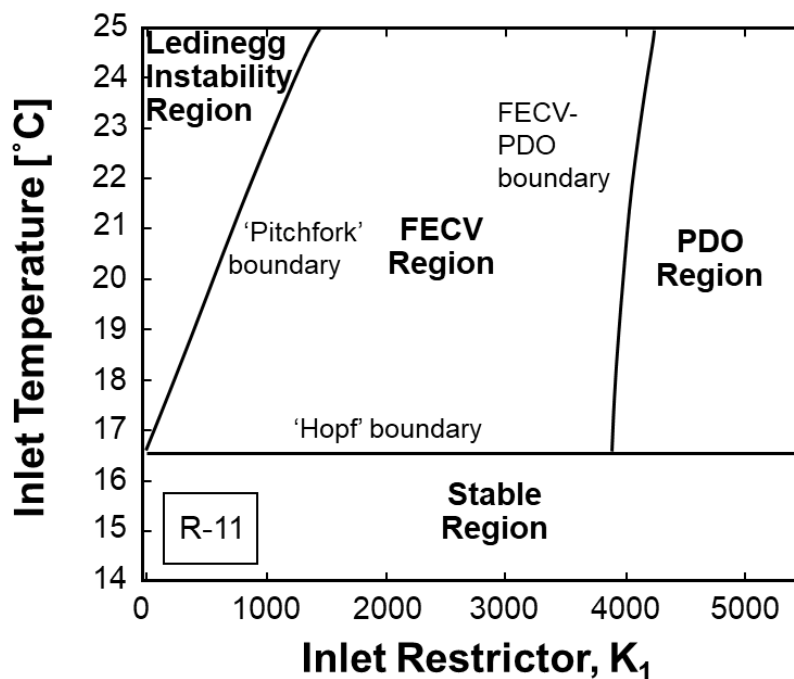


Figure A.15: (a) Stability map (for fixed mass flowrate, pressure, and heat flux) showing conditions for which Ledinegg instability, Flow Excursion with Compressible Volume (FECV), and Pressure Drop Oscillations will occur (adapted from Rahman and Singh [433]). (b) Operating conditions exhibiting PDOs, and (c) operating conditions showing FECV, adapted from Mishima *et al.* [269].

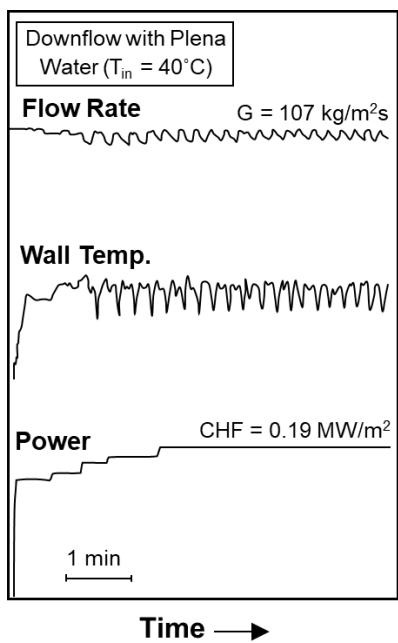


Figure A.15 (b).

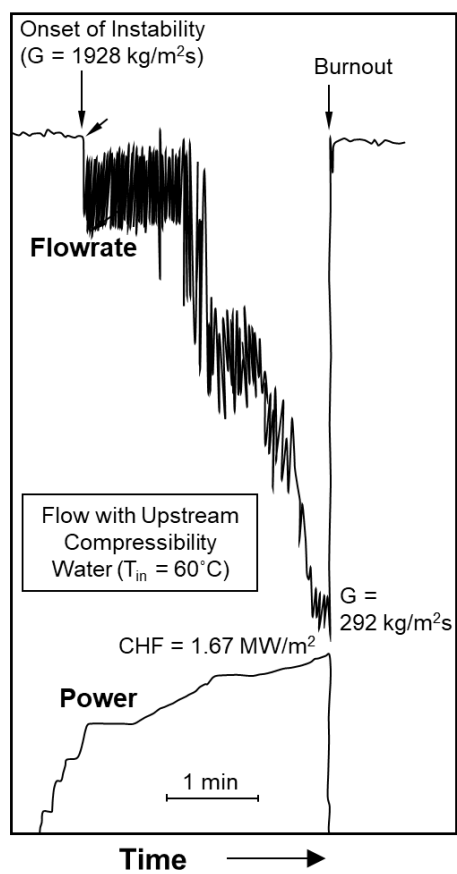


Figure A.15 (c).

### A.3.3.3 Studies Investigating Pressure Drop Oscillations

PDOs have been investigated extensively. Since their initial presentation in 1960's [430-432], numerous studies on two-phase flow instabilities and dynamic behavior have analyzed them, often alongside Ledinegg instability (refs. [63,269,292,303] from section A.2.2), DWOs (refs. [38,62,339,348-350,353,357-359,368,380-381] from section A.3.1), and PCI (ref. [57] from section A.3.2).

Experimental examples of PDOs are provided in Figs. A.7(b) and A.7(c) (adapted from the work of Yuncu [62]), Fig. A.12(c) (adapted from the work of Qu and Mudawar [57]), and Fig. A.15(b) (adapted from the work of Mishima *et al.* [269]). Relative to DWOs and PCI, they are best characterized by their low frequency and high amplitude of oscillation.

Unlike DWOs and PCI in the prior sections, PDOs do not require mechanistic distinction between occurrence in macro- and micro-channel systems. As discussed for Ledinegg, they are 'system-level' instabilities, meaning they are dependent on interplay between system components (in this case test section and compressible volume). Works such as those by Qu and Mudawar [57], Fan and Hassan [381], Kuo and Peles [435], and Grzybowski and Mosdorf [436] illustrate how PDOs in microchannel systems are mechanistically identical to those in macro-channels. The one potential difference, however, is the impact of parallel micro-channel heat sinks on external pressure curves discussed in section A.2.2 [395]. More investigation on this is needed.

When discussing parametric trends leading to the onset of PDOs, key conclusions resemble those drawn for Ledinegg instability (as presence of a negative slope region on the internal pressure curve is necessary for the existence of PDOs). Increased inlet throttling and increased system pressure [381,435,437] act to stabilize the system against PDOs, increased heat flux is destabilizing [359,437].

Assuming PDOs have manifested within a system, guidance exists on how changes to operating conditions will affect PDO characteristics. In their recent review on PDOs, Chiapero *et al.* [210] summarized important experimental trends from the works of Yuncu *et al.* [438], Comakli *et al.* [350], and Ding *et al.* [439] for horizontal channels, and Kakac *et al.* [440], Liu and Kakac [441], and Padki *et al.* [442] for vertical channels. These changes are minor compared to existence versus non-existence of PDOs, however, and most studies focus on avoiding them entirely.

One factor affecting PDOs that is under-explored in literature is the size and position of compressible volume on the impact of PDOs. Cheng *et al.* [443] recently showed that moving the

compressible volume downstream of the test section (as opposed to placing it just upstream as in Fig. A.14) can significantly increase system stability to PDOs. More rigorous investigation on this is necessary, however, to fully understand the impact of compressible volume position on PDOs.

Similarly, it has long been known inclusion of even a very small compressible volume may trigger PDOs in boiling systems [444], but extended experimental analysis of compressible volume magnitude on PDO characteristics (frequency and amplitude) is lacking. A related area needing clarification is the statement of Maulbetsch and Griffith in their early works [445,446] that test sections with large length-to-diameter ratios ( $L/D > 150$ ) may act as their own compressible volumes. This statement is often repeated in literature, but has not been verified by other researchers.

Other underexplored areas include the effects of nano-fluids and surface enhancements on PDOs. Yu *et al.* [447] studied  $Al_2O_3$  nanoparticles in water and showed their ability to delay the occurrence of PDOs. This was accomplished by filling of nucleation sites with nano-particles (delaying ONB and OFI), meaning it is debatable whether it is advantageous or not. Kakac and Cao [448] used both coated and uncoated test sections in their work, but did not provide any extended analysis on the impact on PDO characteristics.

Analytic tools for prediction of PDOs are very robust. For occurrence of PDOs, it is possible to use OFI correlations outlined in Table A.3 (as they occur on the negative slope portion of the internal boiling curve). More common, however, is the development of full transient system models for PDOs (similar to that done for DWOs and sometimes Ledinegg). These models necessarily include transient equations governing mass storage (and associated pressure) within the loop compressible volume, and key points of differentiation between modeling approaches again include HEM versus Drift-flux formulation, linear versus non-linear approach, inclusion of thermal non-equilibrium effects, *etc.*

Model results for one of the earliest works is shown in Fig. A.16(a), adapted from Ozawa *et al.* [46]. Their work was clearly able to capture general behavior of PDOs but misses somewhat on oscillation period.

Over the ensuing decades, many other researchers presented analytic models for PDOs. Notable works include those of Yuncu [62], Padki *et al.* [292], Cao [449] (who used experimental results from Liu [450]), Schlichting *et al.* [63] and Kakac and Cao [448]. One of the best recent examples of PDO modeling comes from the work of Zhang *et al.* [451]. Figure A.16(b) shows a

sample of their model predictions alongside experimental results, indicating a near-perfect match between the two.

Despite the wealth of works that exist dealing with PDOs, researchers continue to discover new, atypical interactions between compressible volumes and two-phase flow systems that lead to unstable operation.

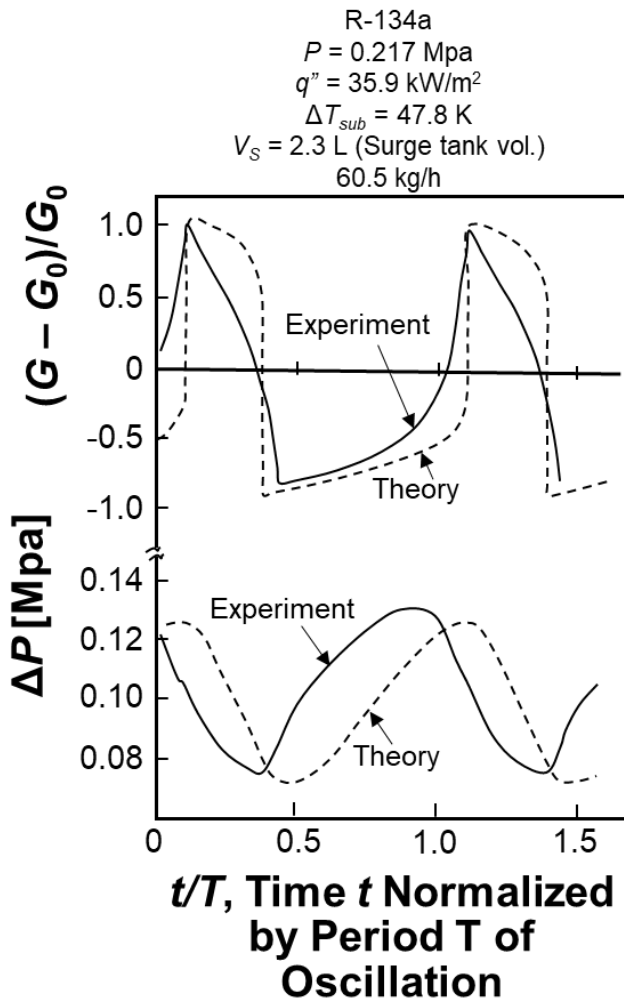


Figure A.16:: Examples of analytic model results for Pressure Drop Oscillations adapted from (a) Ozawa *et al.* [46] and (b) Zhang *et al.* [451]. Also, (c) example of atypical interaction between compressible volume and system dynamic behavior resulting in a new instability mode termed *Charge Transition Instability (CTI)*, adapted from Lee *et al.* [452].

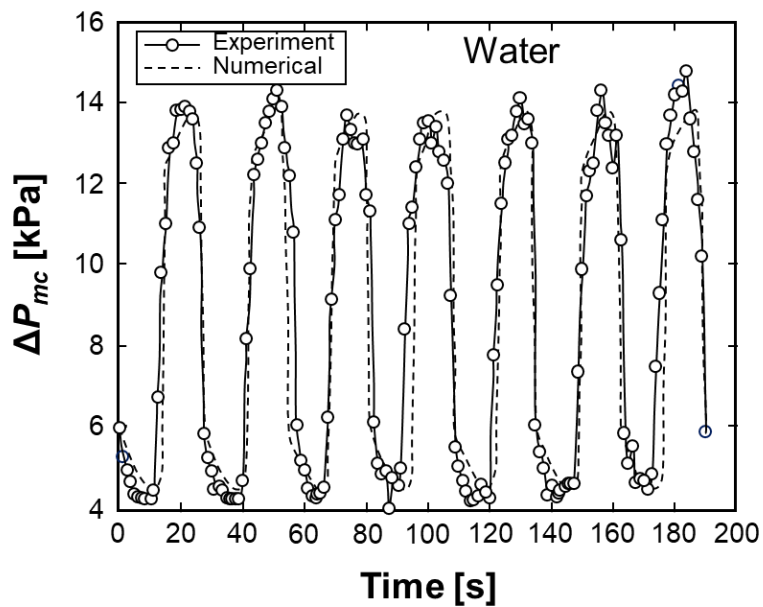


Figure A.16 (b).

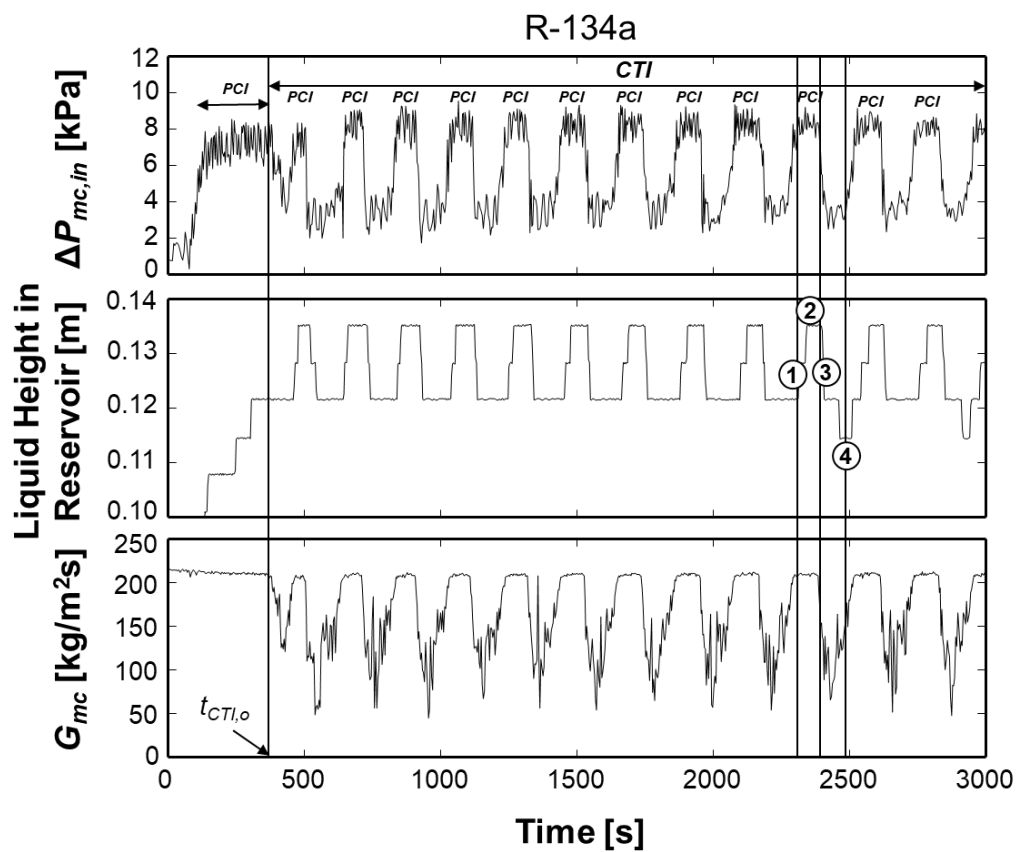


Figure A.16 (c).

#### A.3.3.4 Atypical Interactions between Boiling Systems and Compressible Volume(s)

In a recent study, Lee *et al.* [452] clearly showed how the presence of a closed liquid reservoir just downstream of the condenser in their two-phase pumped loop flow boiling (micro-channel heat sink) test facility could trigger what they term *Charge Transition Instability* (CTI). They systematically prove this is a fundamentally different instability from PDOs (their system has no negative slope region on the internal pressure curve, and pressure drop and mass velocity oscillate in phase during CTI) and show it is related to transient fluctuations in the liquid level in their closed liquid reservoir. Figure A.16(c) shows sample experimental results from their study, highlighting how pressure drop across the micro-channel test section ( $\Delta P_{mc}$ ), reservoir height ( $H_{res}$ ) and system mass flowrate ( $G_{mc}$ ) behave during CTI.

Figure A.16(c) also clearly highlights the existence of Parallel Channel Instability (PCI) during peaks and troughs of CTI. CTI clearly occurs on a much longer timescale than PCI (similar to PDO), but, due to the aforementioned characteristics, it is inherently different from PDOs. Lee *et al.* included analysis of experimental results and analytic modeling for charge distribution within their system and showed occurrence of CTI is associated with vapor pockets at the exit of their condenser interacting with the compressible volume.

The work of Lee *et al.* [452] is particularly important as it highlights the need for more thorough investigation of the influence of compressible volume position on two-phase loop dynamics. Based on current (limited) investigation, changes in compressible volume position have been shown to delay the onset of PDOs [443] or lead to a fundamentally different system-level instability mode [452].

#### A.3.3.5 Summary of Important Findings Related to PDOs

Having analyzed literature relating to PDOs in flow boiling systems, several key conclusions may be drawn:

- 1) The existence of PDOs requires a compressible volume within the system and a negative-slope portion of the internal pressure curve. Some disagreement exists as to the exact relationship between Ledinegg instability and PDOs, but, if a system possesses a compressible volume and operates on the negative slope region, it is safe to assume PDOs will manifest.

- 2) Numerous experimental and analytic investigations into PDOs have established a detailed understanding of the effect of changes to mass velocity, inlet temperature, heat flux, and operating pressure on the existence and characteristics of PDOs.
- 3) The primary recommendation for future work on PDOs involves parametric analysis of changes to position and size of compressible volume(s) used within flow boiling systems.

#### A.3.4 *Acoustic Oscillations*

Used as a general term for most oscillatory phenomena observed at frequencies above ~20 Hz (depending on specific source), *Acoustic Oscillations* are one of the most pervasive and least impactful dynamic instability modes in two-phase flow. One of the earliest works on the topic by Firstenberg [453] investigated oscillations in the range from 1000 – 10,000 Hz (leading him to term them ‘boiling songs’). He saw these oscillations were occasionally accompanied by vibrations of the flow channel.

Generally speaking, most oscillatory modes present in two phase flow fall in the range of 0 Hz (static type) to ~20 Hz (for DWO, PCI, or PDO, depending on system geometry and operating conditions), and any observed oscillatory modes above this frequency are described as ‘acoustic oscillations’. One of the most common causes for these high-frequency modes is bubble collapse during subcooled boiling. Bubble collapse has long been known to release energy in the form of acoustic pressure waves in the surrounding fluid [454,455] (this is a field of study on its own), and, depending on the level of subcooling and intensity of nucleate boiling, this may manifest in traditional macro-channel systems as a high-frequency oscillatory mode. Evidence for this mechanism has been provided in several macro-channel works [54,456-458]. Its impact on micro-channels (and small-scale systems in general) is potentially larger due to the relative size of bubbles to the flow channel and remains under investigation [459,460].

Other sources for acoustic oscillations include those originating from rotating machinery within the flow loop [53] as well as droplet impact on liquid films due to liquid film breakup, entrainment, and deposition mechanisms during annular flow [328,461].

Overall, acoustic oscillations can be described as a catch-all category for high-frequency oscillatory modes having little impact on bulk fluid behavior (with the possible exception of Bergles *et al.* [456] who observed a high-frequency, high-amplitude mode on the negative slope portion of the internal curve; additional verification of the causes contributing to this is required).

These high-frequency oscillations are commonly related to (1) manifestation of micro-scale phenomenon (bubble growth, collapse, film breakup, droplet impingement) in macro-channels and/or (2) mechanically-induced vibrations within the system.

#### A.3.5 Other Reported Two-Phase Dynamic Instabilities

Other dynamic type instabilities are occasionally reported in literature, falling under topics such as *Bumping*, *Geysering*, *Chugging*, *Flashing*, and *Thermal Oscillations*. Boure *et al.* [50] provided a brief discussion on the first four (under the common header *Compound Relaxation Instability*), the general takeaway being they are resultant from combinations of other commonly reported static and/or dynamic instabilities, primarily vapor burst and flow regime transition. *Thermal Oscillations* are slightly more complex and are only self-sustaining under certain conditions (primarily in pool boiling and natural circulation). A brief description of each and a short summary of relevant works is provided below.

*Bumping* is an oscillatory (although not necessarily periodic) fluctuation between natural convection and boiling. Boure *et al.* [50] highlighted the work of Deane and Rohsenow [462] with boiling of liquid metals. For low operating pressures and a narrow heat flux range, they observed a self-sustaining oscillation between natural convection and nucleate boiling, possessing associated variations in temperature and pressure depending on heat transfer mode. Although not referred to as *bumping*, this is very similar in nature to self-sustaining oscillations observed for transition (between nucleate and film) pool boiling [463,464]. These oscillatory modes will be discussed again alongside *thermal oscillations*.

*Geysering* is one of the more well-understood two-phase instabilities, occurring only in closed-end, vertical tubes heated at the bottom [50]. Once boiling initiates in the bottom of the tube, liquid is displaced from the top of the tube. This reduces the hydrostatic head, lowering pressure in the bottom of the tube and causing phase change to occur faster, leading to rapid liquid expulsion from the top of the channel. Subcooled liquid then returns to the tube, allowing for the process to begin again.

The work of Griffith [465] is commonly cited as an early investigation on *geysering*. The subject has received some analysis for forced flows and natural circulation [466] (key takeaways being it occurs for low flowrates and during startup, respectively), but in recent years it has been most relevant to analysis of thermosyphon design and operation [467-472].

Many of the two-phase thermosyphon references listed above [467-472] performed parametric analysis on factors leading to geysering in thermosyphons. Key takeaways are that, for a given geometry, geysering only occurs for relatively low heat fluxes and is strongly dependent on fill ratio and operating pressure.

*Chugging* is largely a misnomer in two-phase flow literature. One of the earliest uses of the term comes from the work of Wallis and Heasley [473]. They use the term extensively to refer to two-phase flow instability, which, based on their modeling approach, seems to be DWOs. By the time of Boure *et al.*'s seminal review [50], the term was commonly used to denote periodic expulsion of coolant from a flow channel. In a later work, Boure [474] attributed this primarily to vapor burst, describing a mechanism of rapid bubble growth pushing liquid from a channel similar to that of geysering.

Herein lies the issue with use of the term *chugging*: It refers to two-phase flow conditions where coolant is expelled from the channel in a periodic fashion, but this expulsion could be due to a wide variety of different causes (DWOs [473], geysering [474], counterflow configurations [475], *etc.*). Any of the instability modes described in this study that could lead to variations in mass flowrate may be technically described as causing chugging. The term is still used in some contemporary studies dealing with two-phase flow oscillations and instabilities [476,477], but it is the recommendation of the current author that its use be avoided when possible and observed oscillatory phenomenon be classified as more fundamental instability modes.

*Flashing* in the fundamental sense is not an instability at all, but a known phenomenon in liquid-vapor flow whereby sharp pressure drop causes a significant fraction of saturated liquid to convert to vapor (a near-vertical movement on a  $P$ - $h$  diagram). *Flashing* has been shown to impact oscillatory characteristics of DWOs [361,362], however, so despite it not being a unique instability mode, its potential impact should be considered when modeling other dynamic instabilities.

Finally, *thermal oscillations* are reported in a wide variety of two-phase flow literature included in the current section on dynamic instabilities. A common misconception is that they are a unique instability mode, when they are actually either 1) a result of hydrodynamic instability or 2) intrinsic parts of other instabilities.

*Thermal oscillations* are important to consider when designing devices for thermal control and are an interesting coupling of heat transfer and hydrodynamics. Similar to the impact of heated wall thermal mass on DWO characteristics discussed in section A.3.1 [356,375], thermal mass has

the potential to significantly affect manifestation of *thermal oscillations*. O'Neill *et al.* [54] provided evidence of thermal oscillations only manifesting alongside DWOs for cases with high heat flux, and they attribute this to the thermal mass of their heated walls.

Although not an independent mode of two-phase flow instability, *thermal oscillations* warrant further investigation, particularly on the affects of heated wall thermal mass on their manifestation.

#### A.4 Current State of Instability Literature

This study has presented key mechanisms behind two-phase instabilities and provided summaries of existing literature on each, including mention of topics for future study where they become apparent. Due to the length of this work, however, it is beneficial to consolidate these in the present section to better help inform researchers working in the field.

Table A.6 provides an overview of the current state of instability literature. This includes assessment of fundamental understanding for the mechanisms leading to each instability mode, predictive tools available for system designers, differences between macro- and micro-channels, and key areas for future study. To expand on items for future study, several topics are discussed in depth below:

*Ability of parallel micro-channels to influence external pressure curve* – As discussed in section A.2.2, results in literature indicate the ability of parallel micro-channel heat sinks to impact the external pressure curve, with increasing number of channels decreasing stability. This requires additional experimental investigation as it impacts both Ledinegg and PDO instabilities.

*Mechanisms behind/leading-to Flow Regime Transition Instability* – Much existing literature indicates dynamic flow regime transition instability to be a result of DWOs (and not a fundamental instability on its own), but some disagreement exists on this.

*Identification of atypical DWOs* – As discussed in section A.3.1, understanding of classic DWOs in macro-channels is fairly complete, but work remains necessary on proper identification of feedback mechanisms leading to DWOs in atypical configurations.

*Impact of parallel channels on stability boundaries* – While mechanisms for PCI are relatively well understood (as they result from DWOs interacting across multiple channels), exact influence of number of parallel channels on stability boundaries needs additional investigation,

particularly in parallel micro-channels where some evidence exists increasing number of parallel channels destabilizes the system.

*Position and size of compressible volume in system* – Presence of a compressible volume is recognized as requisite for occurrence of PDOs, but exact influence of its size and position is poorly understood. Further parametric study is recommended on size and position of compressible volume to determine 1) relationship between Ledinegg instability and PDOs and the influence compressible volume has on this, 2) optimal size and positioning of compressible volume to increase system stability, and 3) potential for placement of compressible volume to initiate atypical instability modes such as *Charge Transition Instability* (CTI).

Table A.6: Overview of strengths and weaknesses of current instability literature.

<b>Instability</b>	<b>Understanding of Fundamental Mechanism</b>	<b>Experimental Evidence</b>	<b>Predictive Tools for Onset of Instability</b>	<b>Predictive Tools for Instability Characteristics</b>	<b>Differences Between Macro- and Micro-channels</b>	<b>Key Area(s) for Future Study</b>
Critical Heat Flux (Device Level)	Mechanisms behind CHF are well understood.	Extensive experimental evidence exists.	Many different empirical, semi-empirical, and analytic tools exist for prediction of CHF.	Instability characteristics are usually not a focus of analysis for CHF, as burnout usually occurs before the system reaches a new stable operating state.	Phenomenon is similar in macro- and micro-channels.	CHF is largely considered a separate field of study. Consult section 2.1 for dedicated reviews which may better inform areas for future study.
Ledinegg Instability (System Level)	Mechanisms behind Ledinegg instability are well understood.	Experimental evidence exists.	Extensive predictive tools exist for determining onset of Ledinegg instability.	Few predictive tools exist for predicting/quantifying the magnitude and rate of flow excursion due to Ledinegg instability.	Phenomenon is similar in macro- and micro-channels.	The impact of parallel channels on external pressure curve (discussed in section 2.2) needs further investigation.
Boiling Curve Hysteresis (Device Level)	Mechanisms behind Boiling Curve Hysteresis are well understood.	Experimental evidence exists.	Few predictive tools exist --- Boiling curve hysteresis is treated practically rather than theoretically.		Phenomenon is similar in macro- and micro-channels.	Better understanding of nucleate boiling incipience is necessary for modeling of Boiling Curve Hysteresis.
Vapor Burst (Device Level)	Mechanisms are well understood.	Limited experimental evidence exists.	Few predictive tools exist. Like boiling curve hysteresis, vapor burst is treated practically rather than theoretically.		Phenomenon is similar in macro- and micro-channels.	Extended experimental investigation is necessary to determine parametric trends and begin modeling.
Flow Regime Transition Instability (Device Level)	Mechanisms are disputed, with many believing dynamic flow regime transition instability to be the result of other instability modes (DWOs, PDOs).	Experimental evidence exists.	Many predictive tools (flow regime maps) exists for prediction of relevant operating boundaries.	As these are often the result of other dynamic instabilities, few predictive tools exist expressly for flow regime transition instability.	Phenomenon is clearly different in macro- versus micro-channels. This is due to confinement effects in micro-channels.	Sophisticated experiment design is needed to determine whether flow regime transition is a self-sustaining instability or is a result of other dynamic instabilities as commonly hypothesized.

Table 5.6 Continued.

<p>Density Wave Oscillations (Device Level)</p>	<p>Mechanisms behind DWOs are well understood, although some atypical configurations require additional investigation.</p>	<p>Extensive experimental evidence exists.</p>	<p>Many predictive tools exist for onset of classic (<i>i.e.</i>, 'Flow-void feedback') DWOs. Additional work needed for atypical and micro-channel DWOs.</p>	<p>Instability characteristics are well predicted in the classic case. Atypical and micro-channel DWOs need additional study.</p>	<p>Phenomenon is fundamentally different in macro-channels versus micro-channels. In macro-channels, instability is commonly associated with oscillation of the boiling boundary, while in micro-channels, rapid confined bubble expansion towards the inlet is the key mechanism.</p>	<p>Additional modeling of DWOs in micro-channels is needed to provide useful design tools.</p>
<p>Parallel Channel Instability (Device Level)</p>	<p>Mechanisms behind PCI are well understood, both in the static (Flow Maldistribution, due to Ledinegg) and dynamic (due to interacting DWOs across channels) modes.</p>	<p>Extensive experimental evidence exists.</p>	<p>Many tools exist for macro-channels, and some limited tools exist for micro-channels.</p>	<p>Similar to DWOs, instability characteristics are well predicted in the classic case, but micro-channel PCI needs additional modeling.</p>	<p>Phenomenon is fundamentally different due to the difference between DWOs in macro- versus micro-channels discussed above.</p>	<p>Additional modeling of PCI in micro-channels is necessary. Also, further experimental study on effect of channel number on stability boundaries is recommended.</p>
<p>Pressure Drop Oscillations (System Level)</p>	<p>Broad concepts behind PDOs are well understood (presence of compressible volume, operation on the negative-slope portion of the boiling curve), but specifics regarding the influence of external pressure curve are lacking.</p>	<p>Extensive experimental evidence exists.</p>	<p>Many tools exist for predicting onset of PDOs.</p>	<p>Modeling approaches exist for determining PDO characteristics.</p>	<p>Mechanisms are similar in macro- and micro-channel systems.</p>	<p>Experimental work is needed to determine the exact influence of external pressure curve on the occurrence of PDOs. Also, like Ledinegg instability, potential for parallel micro-channels to alter this external characteristic must be studied. Exact influence of size and position of compressible volume is also uncertain, including potential to incite atypical instability modes such as CTI.</p>

Table. 5.6 Continued.

Acoustic Oscillations (Device or System Level)	Various mechanisms are known to result in observed Acoustic Oscillations.	Experimental evidence exists.	Predictive tools are not commonly used for acoustic oscillations. These occur for a variety of reasons (section 3.4) and are largely unavoidable in two-phase flows.	No differences between macro- and micro-channel systems.	These have little impact on system performance, and as such additional investigation is not a priority.
Other Dynamic Behavior	This refers to a range of other reported instability modes. These are discussed at length in section 3.5, and it is believed further study may be necessary for specific subfields of research ( <i>e.g.</i> , investigation on <i>geysering</i> by researchers studying thermosyphons) but generally additional work is not a priority.				

## A.5 Conclusions

This study provided a systematic overview of dominant instability modes occurring during boiling (and to a lesser extent condensation) in a variety of configurations. Key emphasis was placed on distinguishing between macro- and micro-channel flows, as this difference was shown to impact mechanisms behind commonly observed instabilities.

Instabilities were grouped into static and dynamic types, and key experimental and analytic works were discussed for each instability mode. Overall, extensive work was shown to exist for all key two-phase instability modes, although some gaps in understanding remain. Conclusions for each subsection typically included recommendations for future work, which were further highlighted in section A.4. Key conclusions from the present study are:

- 1) Strategies for classification of flow boiling and condensation into macro- or micro-channel flow were provided. This distinction is important as it impacts the mechanism behind observed instability modes.
- 2) Internal and external pressure curves remain the best method for assessing potential for system-level instabilities (*i.e.*, those involving interaction between test section and driving head), primarily Ledinegg instability and Pressure Drop Oscillations. Parallel micro-channels with inlet plenums have shown some potential to affect shape of external pressure curve; additional study on this is strongly recommended.
- 3) Device-level instabilities (*i.e.*, those occurring within a boiling/condensing channel due to inherent two-phase mechanisms) are shown to occur for a variety of reasons in many different two-phase configurations. Some show strong differences for macro- versus micro-channels (Density Wave Oscillations, Parallel Channel Instability), while others do not (Boiling Curve Hysteresis, Vapor Burst).
- 4) Density Wave Oscillations in micro-channels (and associated Parallel Channel Instability in micro-channel heat sinks) are a key topic of study. Further analytic/mechanistic modeling is recommended to better optimize trade-offs between their mitigation (commonly achieved through inlet throttling and/or expanding channels) and system performance.
- 5) Pressure Drop Oscillations require additional investigation on the influence of size and position of compressible volume on their occurrence. Section 3.3 discusses these issues at

length, as well as the potential for placement of compressible volume to initiate other atypical oscillatory modes such as *Charge Transition Instability* (CTI) [452].

- 6) While impressive volume and quality of work already exists on two-phase flow instabilities, key areas for future study have been identified. Completion of these will provide appreciable value for system designers looking to leverage phase change heat transfer technologies.

Finally, it should be noted the material presented in the present appendix is available in polished form in a forthcoming publication [478].

## VITA

### EDUCATION

- Doctor of Philosophy in Mechanical Engineering (3.89/4.00)** August 2019  
 College of Engineering, Purdue University West Lafayette, IN  
 Thesis Titled: *Experimental Investigation and Modeling of Key Design Parameters in Flow Boiling and Condensation*
- Master of Science in Mechanical Engineering (3.91/4.00)** May 2016  
 College of Engineering, Purdue University West Lafayette, IN  
 Thesis Titled: *Analysis of Body Force Effects on Flow Boiling and Condensation with Finite Inlet Quality*
- Bachelor of Science in Mechanical Engineering (3.85/4.00)** August 2014  
 College of Engineering, Auburn University Auburn, AL  
 Minor in Asian Studies (Chinese Language Emphasis)

### RESEARCH EXPERIENCE

- Graduate Research Assistant, Boiling and Two Phase Flow Lab** August 2014 - Present  
 Purdue University West Lafayette, IN
- Experimental study of flow boiling and condensation heat transfer for space cooling systems
  - Theoretical modeling to predict important design parameters such as heat transfer coefficient, pressure drop, critical heat flux, and system stability
  - Use of numerical tools, such as ANSYS-FLUENT, capable of predicting fluid behavior and heat transfer for flow boiling and condensation
  - Maintenance of the Science Requirements Document for NASA's Flow Boiling and Condensation Experiment and communication with the engineering team at NASA Glenn Research Center developing the experiment payload for the International Space Station

### WORK EXPERIENCE

- NASA Glenn Research Center** Cleveland, OH  
*Visiting Technologist* July 2018 – October 2018
- Participation in testing of Flow Boiling and Condensation Experiment (FBCE) flight-functional hardware to assist software team in troubleshooting of International Space Station (ISS) experiment control software
  - Provide input to contractors working to develop ground-station user interface for ISS experiment monitoring and control due to prior experience conducting ground-based tests
  - Establishment of data reduction technique for calculation of flow condensation heat transfer coefficient to be used when processing ISS data
- Visiting Technologist* June 2017 – August 2017
- Conduction of flow condensation experiments at multiple orientations to characterize performance of the Flow Boiling and Condensation Experiment (FBCE) brassboard facility and provide scientific data
  - Utilization of outcomes from experimental testing to create Engineering Parameter Master Table for flow condensation experiments to be conducted on the International Space Station

- Participation in Concept of Operations and Software Architecture Design meetings, providing input on ISS experiment operations based on experience performing ground-based testing

*Visiting Technologist*

May 2016 – August 2016

- Design and construction of flow boiling test loop for the characterization of two-phase flow cooling system stability and transient behavior
- Design and implementation of full data acquisition system for detailed measurement of important flow characteristics, such as temperature, pressure, and flow rate
- Work with FBCE team to assist in the development of ISS experimental payload

## SCHOLARSHIP

### Publications

1. C. Kharangate, **L.E. O'Neill**, I. Mudawar, M.M. Hasan, H. Nahra, R. Balasubramaniam, N. Hall, A. Macner, J. Mackey, "*Flow boiling and critical heat flux in horizontal channel with one-sided and double-sided heating*," International Journal of heat and Mass Transfer, Vol. 90, pp. 323-338, 2015.
2. C. Kharangate, **L.E. O'Neill**, I. Mudawar, M.M. Hasan, H. Nahra, R. Balasubramaniam, N. Hall, A. Macner, J. Mackey, "*Effect of subcooling and two-phase inlet on flow boiling heat transfer and critical heat flux in a horizontal channel with one-sided and double-sided heating*," International Journal of Heat and Mass Transfer, Vol. 91, pp. 1187-1205, 2015.
3. **L.E. O'Neill**, C. Kharangate, I. Mudawar, "*Time-averaged and transient pressure drop for flow boiling with saturated inlet conditions*," International Journal of Heat and Mass Transfer, Vol. 103, pp. 133-153, 2016.
4. C. Kharangate, **L.E. O'Neill**, I. Mudawar, "*Effects of two-phase inlet quality, mass velocity, flow orientation, and heating perimeter on flow boiling in a rectangular channel: Part 1 – Two-phase flow and heat transfer results*," International Journal of Heat and Mass Transfer, Vol. 103, pp. 1261-1279, 2016.
5. C. Kharangate, **L.E. O'Neill**, I. Mudawar, "*Effects of two-phase inlet quality, mass velocity, flow orientation, and heating perimeter on flow boiling in a rectangular channel: Part 2 – CHF experimental results and model*," International Journal of heat and Mass Transfer, Vol. 103, 1280-1296, 2016.
6. I. Park, **L.E. O'Neill**, C. Kharangate, I. Mudawar, "*Assessment of body force effects in flow condensation, part I: Experimental investigation of liquid film behavior for different orientations*," International Journal of Heat and Mass Transfer, Vol. 106, pp. 295-312, 2017.
7. **L.E. O'Neill**, I. Park, C. Kharangate, V.S. Devahdhanush, V. Ganesan, I. Mudawar, "*Assessment of body force effects in flow condensation, part II: Criteria for negating influence of gravity*," International Journal of Heat and Mass Transfer, Vol. 106, pp. 313-328, 2017.
8. **L.E. O'Neill**, I. Mudawar, M.M. Hasan, H.K. Nahra, R. Balasubramaniam, N.R. Hall, A. Lokey, J.R. Mackey, "*Experimental investigation into the impact of density wave oscillations on flow boiling system dynamic behavior and stability*", International Journal of Heat and Mass Transfer, Vol. 120, pp. 144-166, 2018.
9. **L.E. O'Neill**, I. Mudawar, "*Mechanistic model to predict frequency and amplitude of density wave oscillations in vertical upflow boiling*", International Journal of Heat and Mass Transfer, Vol. 123, pp. 143-171, 2018.

10. **L.E. O'Neill**, I. Mudawar, M.M. Hasan, H.K. Nahra, R. Balasubramaniam, J.R. Mackey, "*Experimental investigation of frequency and amplitude of density wave oscillations in vertical upflow boiling*", International Journal of Heat and Mass Transfer, Vol. 125, pp. 1240-1263, 2018.
11. **L.E. O'Neill**, I. Mudawar, M.M. Hasan, H.K. Nahra, R. Balasubramaniam, J.R. Mackey, "*Flow condensation pressure oscillations at multiple orientations*", International Journal of Heat and Mass Transfer, Vol. 127, pp. 784-809, 2018.
12. **L.E. O'Neill**, R. Balasubramaniam, H.K. Nahra, M.M. Hasan, J.R. Mackey, I. Mudawar, "*Identification of condensation flow regime at different orientations using temperature and pressure measurements*", International Journal of Heat and Mass Transfer, Vol. 135, pp. 569-590, 2019.
13. J. Lee, **L.E. O'Neill**, S. Lee, I. Mudawar, "*Experimental and computational investigation on two-phase flow and heat transfer of highly subcooled flow boiling in vertical upflow*", International Journal of Heat and Mass Transfer, Vol. 136, pp. 1199-1216, 2019.
14. **L.E. O'Neill**, R. Balasubramaniam, H.K. Nahra, M.M. Hasan, I. Mudawar, "*Flow condensation heat transfer in a smooth tube at different orientations: Experimental results and predictive models*", International Journal of Heat and Mass Transfer, in press.
15. **L.E. O'Neill**, I. Mudawar, "*Review of two-phase flow instabilities in macro- and micro-channel systems*", International Journal of Heat and Mass Transfer, under review.

#### **Posters & Presentations**

1. **L.E. O'Neill**, C. Kharangate, C. Konishi, I. Mudawar, M.M. Hasan, H. Nahra, N. Hall, R. Balasubramaniam, J. Mackey, "*Flow Boiling and Condensation Experiment for the International Space Station*," 31<sup>st</sup> Annual Meeting of American Society for Gravitational and Space Research, Alexandria, VA, November 2015.
2. H. Nahra, M.M. Hasan, R. Balasubramaniam, M. Patania, N. Hall, J. Wagner, J. Mackey, B. Frankenfield, D. Hauser, G. Harpster, D. Nawrocki, R. Clapper, J. Kolacz, R. Butcher, R. May, D. Chao, I. Mudawar, **L.E. O'Neill**, C. Kharangate, "*Development and Capabilities of ISS Flow Boiling and Condensation Experiment*," 31<sup>st</sup> Annual Meeting of American Society for Gravitational and Space Research, Alexandria, VA, November 2015.
3. **L.E. O'Neill**, I. Mudawar, N.R. Hall, M.M. Hasan, H.K. Nahra, A. Lokey, J.R. Mackey, "*Development of Flow Boiling Test Loop to Investigate System Transient Behavior and Stability*", 32<sup>nd</sup> Annual Meeting of American Society for Gravitational and Space Research, Cleveland, OH, October 2016.
4. I. Mudawar, **L.E. O'Neill**, M.M. Hasan, H.K. Nahra, N.R. Hall, R. Balasubramaniam, J.R. Mackey, "*Flow Boiling and Condensation Experiment (FBCE) for the International Space Station*", 32<sup>nd</sup> Annual Meeting of American Society for Gravitational and Space Research, Cleveland, OH, October 2016.
5. M.M. Hasan, H.K. Nahra, J.R. Mackey, N.R. Hall, M. Talmor, R. Balasubramaniam, B. Frankenfield, G. Harpster, R. May, I. Mudawar, C. Kharangate, **L.E. O'Neill**, "*Performance Evaluation of the International Space Station Flow Boiling and Condensation Experiment (FBCE) Test Facility*", 32<sup>nd</sup> Annual Meeting of American Society for Gravitational and Space Research, Cleveland, OH, October 2016.
6. I. Mudawar, **L.E. O'Neill**, S. Lee, V.S. Devahdhanush, V. Ganesan, J. Lee, M.M. Hasan, H.K. Nahra, R. Balasubramaniam, J.R. Mackey, "*Flow Boiling and Condensation Experiment for the International Space Station*", 33<sup>rd</sup> Annual Meeting of American Society for Gravitational and Space Research, Seattle, WA, October 2017.

7. **L.E. O'Neill**, I. Mudawar, M.M. Hasan, H.K. Nahra, R. Balasubramaniam, J.R. Mackey, “*Experimental Investigation and Modeling of Density Wave Oscillations in Vertical Upflow Boiling*”, 34<sup>th</sup> Annual Meeting of American Society for Gravitational and Space Research, Bethesda, MD, November 2018.
8. H.K. Nahra, R. Balasubramaniam, M.M. Hasan, J.R. Mackey, I. Mudawar, **L.E. O'Neill**, “*Flow Boiling Experiments Using the Flow Boiling and Condensation Experiment (FBCE) Breadboard Test Bed*”, 34<sup>th</sup> Annual Meeting of American Society for Gravitational and Space Research, Bethesda, MD, November 2018.
9. **L.E. O'Neill**, I. Mudawar, “*Analysis of Temperature Rise and Peak Temperature Position during the CHF Transient for Subcooled Flow Boiling in 1-g and Microgravity*”, Gordon Research Conference on Micro- and Nano-Scale Phase Change Heat Transfer, Barga, Italy, February 2019.

### HONORS AND AWARDS

- Honorable Mention, ASGSR Graduate Student Poster Competition October 2016
- NASA Space Technology Research Fellow August 2015 - Present
- Member of Phi Beta Kappa Academic Honor Society May 2014
- Purdue Arasmith Fellowship Recipient August 2014
- Graduated Summa Cum Laude from Auburn University August 2014
- Named Graduation Marshall for the College of Engineering August 2014
- O’Neal-Austin Best Student Award Recipient December 2013
- Alabama Space Grant Consortium Scholarship recipient August 2013 – May 2014
- Birdsong Study Abroad Fellowship Recipient April 2013
- Member of Pi Tau Sigma Mechanical Engineering Honor Society October 2012 - Present
- Auburn University Dean’s List 7x August 2011 – August 2014
- Dean of Engineering Scholarship recipient August 2011 – August 2014
- Presidential Scholar Scholarship recipient August 2011 – August 2014
- National Merit Scholar April 2011
- STAR Student in the State of Mississippi April 2011

### SKILLS AND PROFICIENCIES

- Design of experiments (including test section, facility, and data acquisition), experiment conduction, and data post-processing for fluid physics and heat transfer applications
- Development and use of empiric, semi-empiric, data-driven, mechanistic, analytic, and computational predictive tools for fluid physics and heat transfer applications
- Matlab, Python, LabView, ANSYS-Fluent, Microsoft Office
- Teamwork, communication, public speaking, technical writing

## PUBLICATIONS

### Publications

1. C. Kharangate, **L.E. O'Neill**, I. Mudawar, M.M. Hasan, H. Nahra, R. Balasubramaniam, N. Hall, A. Macner, J. Mackey, “*Flow boiling and critical heat flux in horizontal channel with one-sided and double-sided heating*,” International Journal of heat and Mass Transfer, Vol. 90, pp. 323-338, 2015.
2. C. Kharangate, **L.E. O'Neill**, I. Mudawar, M.M. Hasan, H. Nahra, R. Balasubramaniam, N. Hall, A. Macner, J. Mackey, “*Effect of subcooling and two-phase inlet on flow boiling heat transfer and critical heat flux in a horizontal channel with one-sided and double-sided heating*,” International Journal of Heat and Mass Transfer, Vol. 91, pp. 1187-1205, 2015.
3. **L.E. O'Neill**, C. Kharangate, I. Mudawar, “*Time-averaged and transient pressure drop for flow boiling with saturated inlet conditions*,” International Journal of Heat and Mass Transfer, Vol. 103, pp. 133-153, 2016.
4. C. Kharangate, **L.E. O'Neill**, I. Mudawar, “*Effects of two-phase inlet quality, mass velocity, flow orientation, and heating perimeter on flow boiling in a rectangular channel: Part 1 – Two-phase flow and heat transfer results*,” International Journal of Heat and Mass Transfer, Vol. 103, pp. 1261-1279, 2016.
5. C. Kharangate, **L.E. O'Neill**, I. Mudawar, “*Effects of two-phase inlet quality, mass velocity, flow orientation, and heating perimeter on flow boiling in a rectangular channel: Part 2 – CHF experimental results and model*,” International Journal of heat and Mass Transfer, Vol. 103, 1280-1296, 2016.
6. I. Park, **L.E. O'Neill**, C. Kharangate, I. Mudawar, “*Assessment of body force effects in flow condensation, part I: Experimental investigation of liquid film behavior for different orientations*,” International Journal of Heat and Mass Transfer, Vol. 106, pp. 295-312, 2017.
7. **L.E. O'Neill**, I. Park, C. Kharangate, V.S. Devahdhanush, V. Ganesan, I. Mudawar, “*Assessment of body force effects in flow condensation, part II: Criteria for negating influence of gravity*,” International Journal of Heat and Mass Transfer, Vol. 106, pp. 313-328, 2017.

8. **L.E. O'Neill**, I. Mudawar, M.M. Hasan, H.K. Nahra, R. Balasubramaniam, N.R. Hall, A. Lokey, J.R. Mackey, "*Experimental investigation into the impact of density wave oscillations on flow boiling system dynamic behavior and stability*", International Journal of Heat and Mass Transfer, Vol. 120, pp. 144-166, 2018.
9. **L.E. O'Neill**, I. Mudawar, "*Mechanistic model to predict frequency and amplitude of density wave oscillations in vertical upflow boiling*", International Journal of Heat and Mass Transfer, Vol. 123, pp. 143-171, 2018.
10. **L.E. O'Neill**, I. Mudawar, M.M. Hasan, H.K. Nahra, R. Balasubramaniam, J.R. Mackey, "*Experimental investigation of frequency and amplitude of density wave oscillations in vertical upflow boiling*", International Journal of Heat and Mass Transfer, Vol. 125, pp. 1240-1263, 2018.
11. **L.E. O'Neill**, I. Mudawar, M.M. Hasan, H.K. Nahra, R. Balasubramaniam, J.R. Mackey, "*Flow condensation pressure oscillations at multiple orientations*", International Journal of Heat and Mass Transfer, Vol. 127, pp. 784-809, 2018.
12. **L.E. O'Neill**, R. Balasubramaniam, H.K. Nahra, M.M. Hasan, J.R. Mackey, I. Mudawar, "*Identification of condensation flow regime at different orientations using temperature and pressure measurements*", International Journal of Heat and Mass Transfer, Vol. 135, pp. 569-590, 2019.
13. J. Lee, **L.E. O'Neill**, S. Lee, I. Mudawar, "*Experimental and computational investigation on two-phase flow and heat transfer of highly subcooled flow boiling in vertical upflow*", International Journal of Heat and Mass Transfer, Vol. 136, pp. 1199-1216, 2019.
14. **L.E. O'Neill**, R. Balasubramaniam, H.K. Nahra, M.M. Hasan, I. Mudawar, "*Flow condensation heat transfer in a smooth tube at different orientations: Experimental results and predictive models*", International Journal of Heat and Mass Transfer, in press.
15. **L.E. O'Neill**, I. Mudawar, "Review of two-phase flow instabilities in macro- and micro-channel systems", International Journal of Heat and Mass Transfer, under review.

#### **Posters & Presentations**

1. **L.E. O'Neill**, C. Kharangate, C. Konishi, I. Mudawar, M.M. Hasan, H. Nahra, N. Hall, R. Balasubramaniam, J. Mackey, "*Flow Boiling and Condensation Experiment for the International Space Station*," 31<sup>st</sup> Annual Meeting of American Society for Gravitational and Space Research, Alexandria, VA, November 2015.

2. H. Nahra, M.M. Hasan, R. Balasubramaniam, M. Patania, N. Hall, J. Wagner, J. Mackey, B. Frankenfield, D. Hauser, G. Harpster, D. Nawrocki, R. Clapper, J. Kolacz, R. Butcher, R. May, D. Chao, I. Mudawar, **L.E. O'Neill**, C. Kharangate, “*Development and Capabilities of ISS Flow Boiling and Condensation Experiment*,” 31<sup>st</sup> Annual Meeting of American Society for Gravitational and Space Research, Alexandria, VA, November 2015.
3. **L.E. O'Neill**, I. Mudawar, N.R. Hall, M.M. Hasan, H.K. Nahra, A. Lokey, J.R. Mackey, “*Development of Flow Boiling Test Loop to Investigate System Transient Behavior and Stability*”, 32<sup>nd</sup> Annual Meeting of American Society for Gravitational and Space Research, Cleveland, OH, October 2016.
4. I. Mudawar, **L.E. O'Neill**, M.M. Hasan, H.K. Nahra, N.R. Hall, R. Balasubramaniam, J.R. Mackey, “*Flow Boiling and Condensation Experiment (FBCE) for the International Space Station*”, 32<sup>nd</sup> Annual Meeting of American Society for Gravitational and Space Research, Cleveland, OH, October 2016.
5. M.M. Hasan, H.K. Nahra, J.R. Mackey, N.R. Hall, M. Talmor, R. Balasubramaniam, B. Frankenfield, G. Harpster, R. May, I. Mudawar, C. Kharangate, **L.E. O'Neill**, “*Performance Evaluation of the International Space Station Flow Boiling and Condensation Experiment (FBCE) Test Facility*”, 32<sup>nd</sup> Annual Meeting of American Society for Gravitational and Space Research, Cleveland, OH, October 2016.
6. I. Mudawar, **L.E. O'Neill**, S. Lee, V.S. Devahdhanush, V. Ganesan, J. Lee, M.M. Hasan, H.K. Nahra, R. Balasubramaniam, J.R. Mackey, “*Flow Boiling and Condensation Experiment for the International Space Station*”, 33<sup>rd</sup> Annual Meeting of American Society for Gravitational and Space Research, Seattle, WA, October 2017.
7. **L.E. O'Neill**, I. Mudawar, M.M. Hasan, H.K. Nahra, R. Balasubramaniam, J.R. Mackey, “*Experimental Investigation and Modeling of Density Wave Oscillations in Vertical Upflow Boiling*”, 34<sup>th</sup> Annual Meeting of American Society for Gravitational and Space Research, Bethesda, MD, November 2018.
8. H.K. Nahra, R. Balasubramaniam, M.M. Hasan, J.R. Mackey, I. Mudawar, **L.E. O'Neill**, “*Flow Boiling Experiments Using the Flow Boiling and Condensation Experiment (FBCE) Breadboard Test Bed*”, 34<sup>th</sup> Annual Meeting of American Society for Gravitational and Space Research, Bethesda, MD, November 2018.

9. **L.E. O'Neill, I. Mudawar**, “*Analysis of Temperature Rise and Peak Temperature Position during the CHF Transient for Subcooled Flow Boiling in 1-g and Microgravity*”, Gordon Research Conference on Micro- and Nano-Scale Phase Change Heat Transfer, Barga, Italy, February 2019.